Reaction Kinetics for High-Pressure Hydrogen and Methane Oxy-combustion in the Presence of High Levels of H_2O and CO_2

by

Ashkan Beigzadeh

A thesis
presented to the University of Waterloo
in fulfillment of the
thesis requirement for the degree of
Doctor of Philosophy
in
Chemical Engineering

Waterloo, Ontario, Canada, 2021

EXAMINING COMMITTEE MEMBERSHIP

The following served on the Examining Committee for this thesis. The decision of the Examining Committee is by majority vote.

External Examiner	Professor Laurent Catoire Unité de Chimie et Procédés, ENSTA ParisTech
Supervisor(s)	Professor Eric Croiset Department of Chemical Engineering, University of Waterloo
Internal Member	Professor Peter Douglas Department of Chemical Engineering, University of Waterloo
Internal Member	Professor Luis Ricardez-Sandoval Department of Chemical Engineering, University of Waterloo
Internal-external Member	Professor Cecile Devaud Department of Mechanical and Mechatronics Engineering, University of Waterloo

AUTHOR'S DECLARATION

I hereby declare that I am the sole author of this thesis. This is a true copy of the thesis, including any required final revisions, as accepted by my examiners.

I understand that my thesis may be made electronically available to the public.

Abstract

Continued use of fossil fueled heat and power generation calls for a multi-faceted approach to ensure their associated emissions, in particular CO_2 emissions, are mitigated in an economically viable manner. A path to sustainable development, not only demands switching from carbon intensive fuels such as coal to the likes of natural gas or biofuels, it also requires equipping fossil-fueled systems with carbon capture, utilization and storage (CCUS) technologies. One promising carbon capture technology, is oxy-fuel combustion with cooling and compression CO_2 capture. Oxy-fuel combustion entails reacting the fuel with nearly pure oxygen (95-99 mole %), producing a flue gas composed mostly of CO_2 and H_2O, with smaller quantities of N_2 and Ar. As the flue gas is CO_2-rich and is not diluted by large quantities of N_2, it can be separated physicaly through compression, cooling, and auto-refrigeration steps. Pressurized variants of oxy-combustion technologies enable integration of CO_2 capture and compression with the combustion process, and hold prospects for improved economics and reduced footprint. On the path for these promising technologies to reach their full potential, one of the knowledge gaps lies within the understanding of their combustion chemistry. This is due to the presence of high concentrations of H_2O (up to 65%) and/or CO_2 (up to 90%) in these systems. The impact of high H_2O concentrations on pressurized oxy-combustion kinetics has not been explored. This research aims to fill this knowledge gap by generating new experimental data and developing experimentally-validated reaction mechanisms able to better characterize and model pressurized oxy-combustion kinetics behavior in presence of large quantities of H_2O and CO_2.

To this end, novel shock tube experimental ignition delay time (IDT) test data were generated in collaboration with King Abdullah University of Science and Technology (KAUST) for reactive mixtures involving 4% H_2, 0.48-3.44% CH_4, at equivalence ratios (φ) of 0.93-1, to delineate the effect of high concentrations of H_2O, CO_2, and pressure on combustion kinetics. A hierarchical model development and validation approach is presented for high-pressure combustion kinetics in the presence of high levels of H_2O and CO_2. Two models, one for H_2/CO and the other for CH_4 high-pressure combustion kinetics were developed with particular attention to pressure- and bath gas-dependent reaction rates.

High-pressure H_2 IDT experiments were performed at temperatures of 1084-1242 K and pressures of 37-43.8 bar at φ of 1. IDT data for four different bath gases, namely: Ar, 45%H_2O/Ar, 30%H_2O/15%CO_2/Ar, and 45%CO_2/Ar are provided. Low-pressure H_2 IDT experiments were also conducted across a temperature range of 917-1237 K, pressure range of 1.6-2.4 bar, at φ of 1 in Ar and 45%CO_2/Ar bath gases. A minimally-tuned H_2/CO reaction mechanism, CanMECH 1.0, targeting high-pressure combustion in the presence of large concentrations of H_2O and CO_2 is developed. CanMECH 1.0 is validated against both the shock tube IDT data of this work, and other H_2 and H_2/CO shock tube IDT datasets from literature. CanMECH 1.0 performance is compared to a well-cited incumbent syngas oxidation kinetics mechanism (Keromnes et al., Combust. Flame 160 (2013) 995-1011). It outperformed the incumbent for 16 out of 25 data subsets, and exhibited a similar performance for another two. CanMECH 1.0 improved model predictions of this work's shock tube IDT data for H_2O- and CO_2- laden reactive mixtures, as well as all IDT data at pressures of 17-43.8 bar, which are of particular value to pressurized oxy-fuel combustion applications relevant to this work. Overall CanMECH 1.0 brought about a 26% improvement relative to the incumbent in predicting all the IDT validation data considered in this work.

High-pressure CH_4 IDT experiments were performed at CH_4 concentrations of 0.48-0.5%, temperatures of 1536-1896 K, pressures of 37-53 bar, φ of 0.93-1, in the presence of Ar, 45%H_2O/Ar, 30%H_2O/15%CO_2/Ar, and 45%CO_2/Ar. Low-pressure IDT experiments were also conducted at temperatures of 1486-1805 K, pressures of 1.8-2.4 bar, CH_4 concentrations of 3-3.44%, at φ of 1 in bath gases composed of Ar and 45%CO_2/Ar. An improved CH_4 reaction mechanism, CanMECH 2.0, is developed, by embedding CanMECH 1.0 (H_2/CO mechanism) into a recent and well-validated C_1-C_4 detailed kinetics mechanism, AramcoMECH 2.0. CanMECH 2.0 performance is evaluated and compared with AramcoMECH 2.0, in addition to AramcoMECH 3.0, in predicting the shock tube IDT validation targets. CanMECH 2.0 is shown to improve the overall performance of the two incumbent mechanisms by 1% and 3%, respectively.

Acknowledgements

This work was supported by Natural Resources Canada's (NRCan) Office of Energy Research and Development's (OERD) Program of Energy Research and Development (PERD).

The experimental portion of this work was also partially supported by the Office of Sponsored Research (OSR) at King Abdullah University of Science and Technology (KAUST).

I would like to acknowledge Professor Eric Croiset, for his thoughtful insights, kind supervision, direction, as well as for his reviews and comments, which collectively culminated in significantly improving the quality of this manuscript.

I also would like to acknowledge Dr. Kourosh Zanganeh at NRCan, for allocating the necessary funds to support the research and experimental work.

I would like to thank the examining committee members, Professors Laurent Catoire, Cecile Devaud, Peter Douglas, and Luis Ricardez-Sandoval, for reviewing and providing their input on this manuscript.

I would like to also thank Ms. Sara Baghbanzadeh, for sharing her expertise in programming to help automate some repetitive calculation and data processing tasks.

Dedication

To my parents, Mrs. Iran Fareghi-Naeini, and Colonel Ghasem Beigzadeh.

Table of Contents

List of Figures

List of Tables

Chapter 1

Introduction

In today's carbon-constrained world, continued use of fossil fuels for heat and power generation calls for a multi-faceted approach to ensure their associated emissions are mitigated in an economically viable manner. The "International Energy Agency's (IEA) World Energy Outlook (WEO) 2020" projects that for a Sustainable Development Scenario (SDS), a surge in clean energy policies and investments are required to put the energy system back on track with the objectives of the Paris Agreement [1]. In light of the impacts of Covid-19, WEO-2020 forecasts a global energy demand growth of 4-9% for the period of 2019-2030. The bounds of this growth range are determined based on the assumption that the global economy returns to its pre-crisis levels either by 2023 or earlier by the end of 2021.

According to WEO-2020, by the end of this decade the share of coal in energy mix is expected to fall from 37% in 2019 to 15-28%, but the use of oil as a feedstock will likely rise despite the current uncertainity about the fate of this energy source. In contrast, a 30% increase in global natural gas (NG) demand is expected by 2040 [1]. However, for a rising number of countries on a net-zero pathway by mid-century, continued use of NG demands retooling of the gas industry by demonstrable progress in technologies like carbon capture, utilization and storage (CCUS), use of alternative gases such as biomethane and low carbon hydrogen, among others [1].

In order to enable continued deployment of NG-fired heat and power generation technologies into the middle of the 21st century, their carbon emission intensities would need to be decreased through CO_2 capture in an economically competitive manner. Conventionally, to capture CO_2 from these processes, post-combustion solvent absorption, as well as oxy-fuel combustion with cooling and compression CO_2 capture have been proposed as economically viable options [2, 3]. The high-purity captured CO_2 can then be either stored or follow one of many utilization pathways. The IEA Energy Technology Perspectives Flagship report 2020 highlights that under an SDS scenario CCUS accounts for up to 15% of the emissions reductions compared with the current Stated Policies Scenario (STEPS), and the power sector accounts for around 40% of the captured CO_2 [4].

As one promising carbon capture pathway for the power sector, oxy-fuel combustion entails reacting the fuel with pure oxygen (95-99 mole %), producing a flue gas composed mostly of CO_2 and H_2O, with smaller quantities of other species such as N_2 and Ar. N_2 and Ar are commonly introduced via air in-leakage in plants operating at near atmospheric pressures, and/or by the impurities of the O_2 feed stream. As the flue gas is CO_2-rich, and N_2-lean it can be efficiently separated, through a series of compression, and cooling steps [5]. In oxy-fuel combustion removal of N_2 from the oxidizer stream translates to impractically high adiabatic flame temperatures, e.g. >3000 K for NG and O_2 [6], which far exceed the maximum allowable working temperature of combustor materials. To moderate this temperature a practical workaround that does not reduce the concentration of CO_2 in the exhaust, is to dilute the combustion mixture with recycled de-energized flue gas; i.e., recycling flue gases after heat and/or work extraction by direct or indirect power cycles, or other heat utilization processes.

While near-atmoshperic oxy-fuel combustion, as a CCUS enabling technology, brings about improved emissions profiles relative to their CO_2 intensive conventional counterparts, its economics suffer due to its associated increased capital expenditure (CAPEX), operational expenditure (OPEX), and lower net plant efficiencies. To circumvent these concerns, highly-pressurized variants of oxy-fuel plants are currently under development that utilize a working fluid that comprises supercritical CO_2 as one of its main constituents. These plants, are categorized into direct and indirect cycles [7, 8, 9]. In direct cycles, semi-closed loop Brayton cycles can be used, in which the working fluid is the hot combustion product gases exiting a highly pressurized combustor that are directed to a power turbine at pressures as high as 300 bar [10]. In constract, in indirect cycles the thermal energy is transferred from hot highly pressurized combustion gases (100-300 bar) via a heat exchanger to a closed loop Brayton cycle that commonly utilizes supercritical CO_2 (sCO_2) as its working fluid [11]. Figure 1 provides a schematic of one such indirect pressurized oxy-fuel technology coupled with a sCO_2 power cycle.

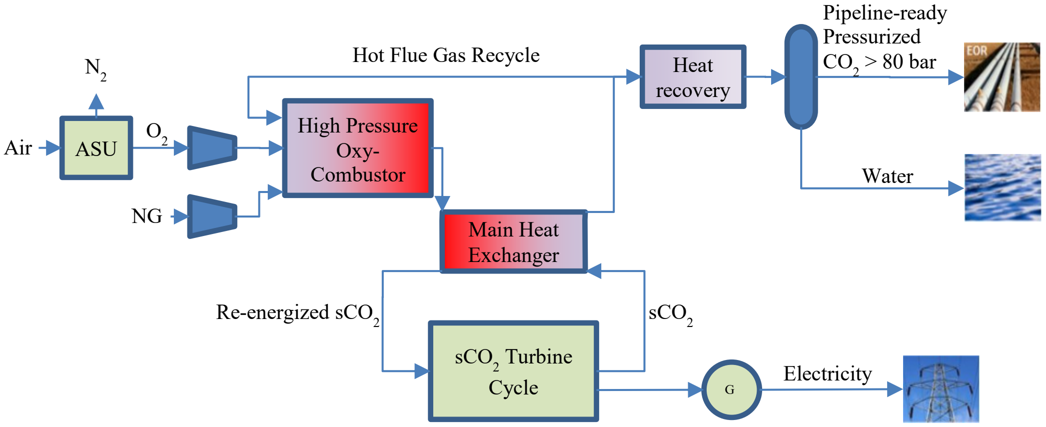

Figure 1: Sample indirect pressurized oxy-fuel with sCO_2 power cycle

Pressurized oxy-combustion enables integration of CO_2 capture and compression into the combustion process, thus eliminating the undesirable air ingress observed in their near-atmospheric pressure counterparts. However, since increasing the pressure decreases the maximum allowable operating temperature for materials of construction used in unit operations, it is necessary to moderate the combustor exhaust temperatures by recycling a portion of flue gas and thus diluting the exhaust gases [12]. With increased dilution rates, the composition of the diluents gain importance as an important design parameter, because they directly impact the combustion chemistry. Diluent compositions can have very high concentration of CO_2, as proposed in direct cycles that remove water before recycling a portion of the flue gas, or have very high concentration of water with smaller concentrations of CO_2 for indirect cycles with hot flue gas recycle [7].

Among pressurized oxy-fuel power cycles, the indirect approach enables easy recovery of large quantities of latent heat as well as water, when its flue gas is recycled hot and wet, i.e. without removing any heat or water [8]. As the combustion cycle operates at very high pressures, the dew point of the flue gas mixture increases with pressure such that the water can be condensed out and separated from the exhaust stream at high recovery rates, using a heat recovery or dry cooling system. The amount of water produced decreases with the C/H ratio of the fuel, hence for fuels such as CH_4 (hydrocarbon with lowest C/H ratio) large quantities of water is produced. This renders these net water producing power generation cycles highly advantageous, in particular for applications in arid regions. With reduced footprints due to their pressurized nature, and 30-40 times smaller turbomachineries of the sCO_2 power cycles relative to those of steam power cycles, these high-pressurized power cycle technologies hold the promise of significant reductions in CAPEX, and OPEX relative to other incumbent power generation technologies. Using currently available materials, cycle efficiencies of 50% or higher are expected for these transformative power cycles. The potential for higher efficiencies is envisioned in the near future through development of cost-effective materials for higher cycle operating temperatures [8].

In a quest to unearth the true potential of these promising technologies, one of the knowledge gaps lies with the reliability of designing such combustors, which stems from the lack of understanding their combustion chemistry. To avoid temporal and spatial miss-predictions of temperature and composition profiles of the combustion chamber, it is imperative to characterise the detailed reaction kinetics encountered under the peculiar operating conditions of these technologies, and utilize them in combustor design. While the body of research is growing rapidly for direct pressurized oxy-fuel combustion chemistry, little attention has been given to the combustion kinetics of the indirect cycles [13, 14, 15, 16, 17]. The main difference between the two lies with the high H_2O concentrations of up to 65% by mole in addition to large CO_2 concentrations (~33% for CH_4 and ~48% for diesel) for indirect cycles, versus higher CO_2 concentrations of approximately 90% by mole in their direct counterparts [7, 8]. The impact of high H_2O concentrations on oxy-combustion kinetics has not yet been explored. This research aims to generate a novel set of experimental data and develop experimentally-validated models to enable better characterization and prediction of pressurized oxy-combustion kinetics applicable to indirect power cycles.

In this context, the next chapter (Chapter 2) reviews the literature and provides a comprehensive background, to help expose some of the knowledge gaps relevant to high-pressure oxy-combustion kinetics. Appropriate modelling techniques and experimental tools available to address these gaps are also summarized. Chapter 3 details the kinetics modelling and simulation approach utilized in this research. Chapter 4 discusses the experimental setup used to generate the data required for the validation of the kinetic models for high-pressure oxy-combustion of hydrogen and methane in high H_2O- and CO_2-diluted mixtures. Chapter 5 details the results of the experimental and modelling work carried out for H_2/CO mechanism tuning and validation. Chapter 6 investigates the reaction pathways involved in hydrogen combustion, to characterize the impact of pressure as well as the presence of CO_2 and H_2O in large concentrations. Chapter 7 provides the results of the experimental and model validation work performed for the CH_4 mechanism. Lastly, Chapter 8 presents the concluding remarks and recommendations for the continuation of this research.

Chapter 2

Literature Review

Due to hydrocarbon's (HC) abundant utilization a significant body of research has been dedicated to fossil-fueled combustion to enable effective design and deployment of combustors targeting applications in transportation, fossil power, oil and gas as well as other industry sectors. Such designs must capture the interplay of fluid mechanics with the oxidative chemistry of the fuel. However, with limited computational power, gaining an in-depth understanding of either the HC combustion chemistry or the fluid mechanic complexities commonly requires them to be decoupled. As such there is commonly a compromise between the levels of detail considered for one aspect of the combustion model versus another [18]. As reaction propagation requires effective heat and mass transport, their interplay dictates the extent and efficiency of heat release as a consequence of oxidation of HC to H_2O and CO_2. Combustion systems are commonly subsonic, can vary in pressure from atmospheric to 40 bar, and are designed to operate at temperatures higher than 1000 K. [19]. The high-pressure variants are common to the gas turbine industry. In gas turbine design, having a good understanding of the chemistry is critical, from efficiency, emissions, and safe design stances. While this understanding is important for the design of low-emission stable high-pressure non-premixed aero-derivative gas turbines, it is even more critical for the safe design of premixed gas turbines, considering their thermal hydrodynamic instabilities and elevated pressures [20].

Similarly pressurized oxy-combustors with hot and wet flue gas recycle targeted in this research face the same concerns as their air-fired gas turbine combustor predecessors. As N_2 constitutes nearly three quarters of the combustion gas, and is being replaced completely by combustion flue gases at potentially very high pressures, i.e. 40 to 300 bar, a critical review of all aspects of kinetics model generation and validation is necessary. These combustors have the prospects to either be premixed or non-premixed, so it is of paramount importance to understand the chemistry of these highly energy dense energy conversion systems. As consumption of NG is expected to grow more than other fossil fuels, the research targeted combustion kinetics of its largest constituent CH_4. In the case of oxy-combustion of methane the flue gases include up to 65% by volume water, which puts the kinetics mechanism into completely unchartered territories. Building kinetics models for such unexplored conditions requires a critical review of all relevant kinetics model development steps, and embedded assumptions. Consequently, kinetics model architectures appropriate for generating new kinetics models are discussed first. This is followed by a brief introduction of the experimental tools commonly employed for analyzing and validating combustion kinetic models, along with their limitations. Finally, the results of a review of literature on the impacts of variations of temperature, pressure, and combustion bath gas composition on the combustion kinetics are discussed.

2.1 Kinetics mechanisms and their architecture

Leclerc et al. [18] noted that detailed mechanisms follow a definite structure classifying sets of reactions called sub-mechanisms which interact with each other and collectively produce the mechanism. The interactions of sub-mechanisms are such that the reacting species of one, are the products of the other, with these species either consumed through one or multiple sub-mechanisms. Furthermore, under varying conditions different sub-mechanisms may be constructed to capture different aspects of the reactivity of the process. For example an architecture may be such that it includes separate sub-mechanisms for high- and low-temperature chemistry targeted for different applications. Consequently the authors grouped the classification of mechanisms based on the following criteria [18]:

1) Hierarchical in terms of size of reactants
2) Primary, secondary and base mechanisms, an extension of hierarchical mechanism, based on sequence of reactions starting from reactants to products, with intermediates following the secondary reaction consumed in the base mechanism.
3) Pathways, which is based on chain reaction pathways ensuring a realistic pathway to products is present in the model.
4) Reaction and molecule classes, such as hydrogen abstraction vs. aldehyde sub-mechanism class of reactions.

In recent years, in order to effectively capture the chemistry involved in combustion, models are constructed hierarchically. Their development starts from a reaction mechanism model for a simple fuel, e.g. H_2. Upon validation, additional reaction and species sets are added to the mechanism for the next more complex fuels, e.g. CO. This process is repeated until the model contains the necessary species and reactions and is able to predict the phenomena observed in experiments [18, 21]. Metcalfe et al. [22] note it is important to develop comprehensive mechanisms with subsequent validation by a wide range of experimental means, with emphasis on the hierarchical structure of mechanisms for expansion to enable modeling complex fuels' kinetics [18]. It should be noted that for extending the range of application of chemical kinetics mechanisms, it is important to ensure the mechanism is validated by experimental means for the intended range of application as temperature, pressure, and equivalence ratio as the dependence of kinetics of HC oxidation is not monotonic. Equivalence ratio is the ratio of fuel to oxygen relative to their stoichiometric values.

Since detailed kinetic models are composed of elementary reactions, determining their rates accurately directly impacts the prediction ability of the overall model. Numerous research papers have looked into determining individual elementary reaction rates using experimental, and/or theoretical means. In addition, major reviews have been performed of large sets of elementary reaction rate determinations relevant to combustion collaboratively with expert reviewing panels at times exceeding a dozen members. A few notable ones are the high-temperature kinetics databases for high temperature combustion prepared by Cohen and Westberg [23], Tsang and Hampson [24], and a few by Baulch et al. [25, 26]. However as noted by Metcalfe et al. [22] the reviews never address the combined effects of these elementary reaction rates within a single model, and such could constitute the worst case scenario. Instead Metcalfe et al. [22] adopted a hierarchical model structure for the highly cited AramcoMech 1.3 and conducted sensitivity analyses to identify the most sensitive reactions. The authors reviewed the literature and extracted the most recent accurate measurements or calculations of the rates to improve reproducibility of validation targets, followed by tuning of strategic parameters within their range of uncertainty [22]. In contrast Pilling [27] noted that in a model construction exercise it is critical to utilize un-optimized and untuned reaction rates prior to validation. Another important aspect of using a hierarchical model stems from the fact that the majority of highly sensitive reaction rates are contained within the chemistry of the simplest fuels, i.e. H_2, and to a lesser extent C_1 chemistry, irrespective of the size of the HC fuel under study [22]. Keromnes et al. [28] demonstrated this is also the case for high CO syngas combustion chemistry and illustrated that at 1000 K and high pressures, of the 15 most sensitive reactions, only four involved CO, and the rest are those pertaining to the H_2 oxidation chemistry. Hong et al. [29] also noted that several sensitivity studies have shown that the H_2 oxidation reactions are critical to correct prediction of oxidation kinetics of all HC fuels. The fate of H radical is fundamental to the kinetics of oxidation process. How the first radical is formed is not critical, rather the radical’s involvement in propelling chain branching reactions towards explosive combustion must be studied rigorously [6]. These chain branching reactions however, are also accompanied by chain terminating ones, and their competition is highly impacted by the combination of temperature, pressure, and composition of bath gases surrounding the reactive participants. Consequently it is critical in such hierarchical models to have a reliable and accurate H_2 combustion mechanism able to capture the temperature, pressure, and bath gas dependence of the elementary reaction rates appropriately. These pressure, temperature and bath gas dependent rates are also present in CO, CH_4 and larger HC mechanisms.

There is currently a multitude of hydrogen and syngas oxidation mechanisms available in the literature [28, 30, 29, 31, 32, 33, 34, 35], as well as studies evaluating their relative performance [36, 37] and optimization [38]. A select number of these mechanisms have gained popularity in the recent years. These mechanisms were all built on previously developed mechanisms, commonly augmenting their predecessors with new model validation data and improvements to reaction rates. Due to the availability of numerous mechanisms, only select models are mentioned in this work. In 2004 Li et al. [39] developed a 19-step H_2 mechanism, well-validated against shock tube, flow reactor and laminar premixed flame experiments, which served as the basis for several other mechanisms [35, 30]. Their work was followed by Burke et al. [30] culminating in another updated 19-step mechanism in 2012, with comprehensive model validation, theoretical analysis of rates and thermodynamic properties, as well as identification of shortcomings of simulation software such as ChemkinPro at the time. Hong et al. conducted a multitude of shock tube experiments [40, 41] improving several critical elementary reactions' rates, which culminated in another highly cited 19-step high temperature H_2/O_2 mechanism [29]. Keromnes et al. [28] conducted ignition delay time experiments in shock tubes, rapid compression machines, as well as flame speed measurements and developed a 19-step H_2 mechanism along with a 12-step CO mechanism validated for pressures of 1-70 bar, and temperatures of 914-2220 K, and at equivalence ratios of 0.1-4. The mechanism also served as the sub-mechanism used in the AramcoMech 1.3's C_1-C_2 chemistry [22], as well as others. In 2014 Olm et al. [38] compared 19 recent hydrogen mechanisms against a large set of experimental data, and concluded that the Keromnes et al.'s models had the best overall performance. With a similar approach in 2015 Olm et al. [42] also compared the performance of 16 syngas mechanisms and concluded that Keromnes et al. had the 2nd best performance overall following NUIG-NGM-2010 in predicting large validation data set for syngas combustion. Moreover, Varga et al. [38] optimized Keromnes et al.'s model using a large set of experimental data according to sensitivity analysis carried out at each experimental data point, and optimized 30 Arrhenius parameters and 3rd body collision efficiencies of 11 reactions. Alekseev et al. [32] investigated the effect of temperature on burning velocities of diluted hydrogen flames, and generated a 20-step mechanism. Konnov extended Alekseev et al.'s model and developed a 48 step mechanism which included excited species and captured their role in predicting combustion targets [33], and its performance was shown to be near identical to that of Alekseev et al.'s. Recently Konnov [31] further updated Alekseev et al.'s model and published an updated mechanism with untuned reaction rates while incorporating insights from Varga et al.'s [38] optimization of the Keromnes et al.'s model [28]. All in all the above noted mechanisms generally share the same species, and reactions for the most part (either 19- or 20-step for H_2/O_2), but commonly differ in the elementary reaction rates and thermodynamic properties they incorporate.

One of the differences relevant to the study at hand revolves around how pressure dependence and bath gas effects are captured and implemented in these mechanisms. Pressure-dependent reactions commonly involve unimolecular/recombination and chemically activated bimolecular reactions.

Different studies express these elementary reactions and their rates differently, depending on model target validity range and accuracy, type and variety of bath gases, the size of molecules in a reaction, and finally source of rate information and its functional fitting form chosen to represent the theoretical or experimental rate data. The following elementary rate expressions are commonly employed to capture the non-Arrhenius pressure-dependent behavior, namely: 1) Lindemann, 2) Troe, 3) SRI International, 4) pressure-dependent data tabulation and logarithmic interpolation (PLOG), and 5) Chepyshev polynomials [43]. While these expressions all capture pressure dependence of elementary reactions, their versatility and applicability in capturing the impact of multiple bath gas composition significantly differ. Physically, the rates of these reactions rely heavily on the amount of energy transferred per collision with the bath gas. In the case of radical recombination reactions, for instance, the reaction has no activation energy barrier and an excited adduct is formed which can either stabilize or dissociate back to reactants. The relative rates of these two paths heavily depend on how much and how quickly the excited adduct loses energy to bath gas molecules through collisions. Changes in bath gas composition can significantly change the rate of pressure-dependent reactions; collisions with H_2O can be an order of magnitude more potent in thermalizing an adduct than those with N_2, as noted by Hong et al. [29]. To capture this effect and in order to arrive at a single overall elementary reaction rate for such a reaction, it is critical to appropriately estimate and combine the contribution of each of the collision partners. Many studies have theoretically calculated and/or experimentally determined collider-specific reaction rates, such as that of Bates et al. [44], whereas others such as Jasper et al.'s [45] have been dedicated to evaluating collision efficiencies of molecular categories, i.e. as atomic and diatomic ones. Superiority of one form of rate expression over another for incorporation into a chemical kinetics mechanism depends on:

1. Availability of rate expressions that enable implementing the important colliders relevant to a study, i.e. H_2O and CO_2 in this work. If there are collider-agnostic pressure-dependent rates they will not be capable to discern the impact of variation of concentration of different bath gases;
2. Availability of appropriate mixing rules and estimates for their parameters [46], to arrive at a combined rate for the pressure-dependent reaction of interest; and,
3. The possibility of implementing mixing rules into kinetics codes and software package(s) selected for a study, most popular of which is Chemkin-Pro.

While all of the mentioned formulations are accommodated in Chemkin-Pro, there are limitations in terms of the mixing rules the software can accommodate. Lindeman, Troe and SRI International use similar formulations for rate expressions that differ in the functional forms of parameters that capture the pressure and temperature dependence of the collisions with different collision partners. Troe formulation is the most widely adopted, and is capable of capturing the impact of collider-specific, as well as overall combined rate expressions. PLOG expressions can be used for representing pressure-dependent rates. This type of formulation utilizes tabulations of the rate data at different conditions, and performs logarithmic interpolation between the data points available to arrive at a reaction rate. However, their accuracy increase with the number of data points for a fixed pressure range. Also, for multiple bath gases, PLOG expressions are not commonly available in the literature. As such, their applicability for bath gases with multiple strong colliders, in addition to common diluents such as Ar, is limited. Similarly, Chebyshev expressions, while they are the superior choice for multi-well reaction rates, they also suffer from limitations in their ability to capture the effect of multiple bath gases and are generated for a single bath gas [43].

In this context this research adopts a hierarchical reaction mechanism in terms of size of reactants which is versatile enough to enable exploring and validating the unexplored conditions relevant to pressurized oxy-combustion with hot wet flue gas recycle. The hierarchical model starts with an H_2/CO mechanism. The reason for the inclusion of CO along with the H_2 mechanism, is due to the large presence of CO_2 as a feed to the targeted combustors and relevant validation experiments. This is to ensure potential breakdown of CO_2 is captured followed by its evolution through the CO sub-mechanism. This hierarchical model is then augmented with the missing reactions to appropriately capture the complete oxidation of CH_4 at high-pressure oxy-fuel conditions. Moreover, for the elementary rate expressions preference is given to reaction rates which:

1- have lower reported uncertainty factors, validated against experimental data where possible;

2- capture the potential pressure dependence of the reaction rate; and,

3- capture the effect of bath-gas/collider compositions such as that of Troe formulation over PLOG or Chebyshev expressions when warranted.

In the next section a review of the experimental facilities and measurement options for kinetic model validation is provided to prepare the reader for the remainder of the literature review. This review helps illustrate the rationale behind the choice of apparatus and the suitable model validation measurement targets selected for this study.

2.2 Experimental facilities and measurements for kinetics model validation

HC oxidation is highly exothermic and involves chain reactions with an exponential dependence on temperature. As the kinetics involved in HC combustion is explosive for the most part, a limited number of devices are available to assist with accurate determination of rates of both individual elementary reactions, as well as lumped overall global ones. Mechanistically, as the temperature is increased, radicals start to form, and chain branching reactions, such as $H+O_2=OH+O$, start to become dominant, causing a buildup of highly reactive radical pool containing H, OH, and O among others, propelling fuel breakdown and oxidation. Due to the mutual positive feedback of temperature increase, chain reactions with chain branching elementary reactions, as well as exothermic oxidation reactions, reactions propagate and complete at very short timescales. The short timescales add to the complexity of effectively probing reactions using direct measurement techniques. To better manage these complexities for kinetic model validations, experimental tools that enable the decoupling of the contributions of fluid mechanical effects from kinetic ones are sought. The main experimental apparatuses are shock tubes (ST), rapid compression machines (RCM), flow reactors, jet stirred reactors (JSR), and setups for various types of flame speed measurements. The common measurements include ignition delay times, species concentration evolutions, and flame speeds [18, 6]. A complementary combination of the above measurement techniques and apparatuses may be utilized for reaction mechanisms covering a wide range of temperatures, pressures, fuels, and fuel to oxygen ratios. A recently developed C_1-C_4 combustion kinetics model, AramcoMech 1.3 with high-pressure and lower temperature ignition data in mind, utilized shock tube, JSR, flow reactor, as well as flame speed measurement, but not RCM as their facilities of choice for experimental model validation [22]. A similar set of validation data composed of the apparatuses utilized for AramcoMech 1.3, was employed as performance targets, for another benchmark NG kinetics model, i.e. GRI-Mech 3.0 [47]. It should be noted that ignition delay time (IDT) is the time it takes for a reactive mixture at a given pressure and temperature to ignite and hence, is inversely related to the global reaction rate.

2.2.1 Shock tube facilities

A shock tube (ST) is approximately a 100 diameter long tube, with common internal diameters of 4-16 cm, with a driver and driven section separated by a diaphragm. Due to the higher relative pressure of the driver section, the diaphragm ruptures and the rush of the driver gas into the low-pressure driven gas culminates in the formation of a shockwave at about 10 diameters downstream into the driven section [48]. The wave traverses down the driven section, hits the end wall, reflects, and leaves behind a static sample of instantaneously heated high temperature (600-11,000°C), and pressure (sub-atmospheric – 1000 atm) gas [49].

A schematic of a shock tube along with its position-time diagram depicting the passage of the shock wave through the driven section of the shock tube resulting in the different position-time regions, is shown in Figure 2. These position-time regions or sections, are numbered for easy referencing of the conditions of the reactive gas mixture within the shock tube as a function of time. The region that is used for probing the kinetics is region 5, with its temperature and pressure referred to as T_5, and P_5.

The boundary condition is such that upon passage of the reflected shock the gas in region 5 becomes stagnant. Hence this section of the ST is in essence a homogeneous reactor, suitable for studying chemistry taking place at timescales of less than a few milliseconds, which with modifications of the ST could be extended up to a 100 ms [48]. Due to their limitations in test times, unmodified shock tubes are more often utilized for probing higher temperature experiments, i.e. above 1200 K, as discussed by Hong et al. [29] and Beerer et al. [50].

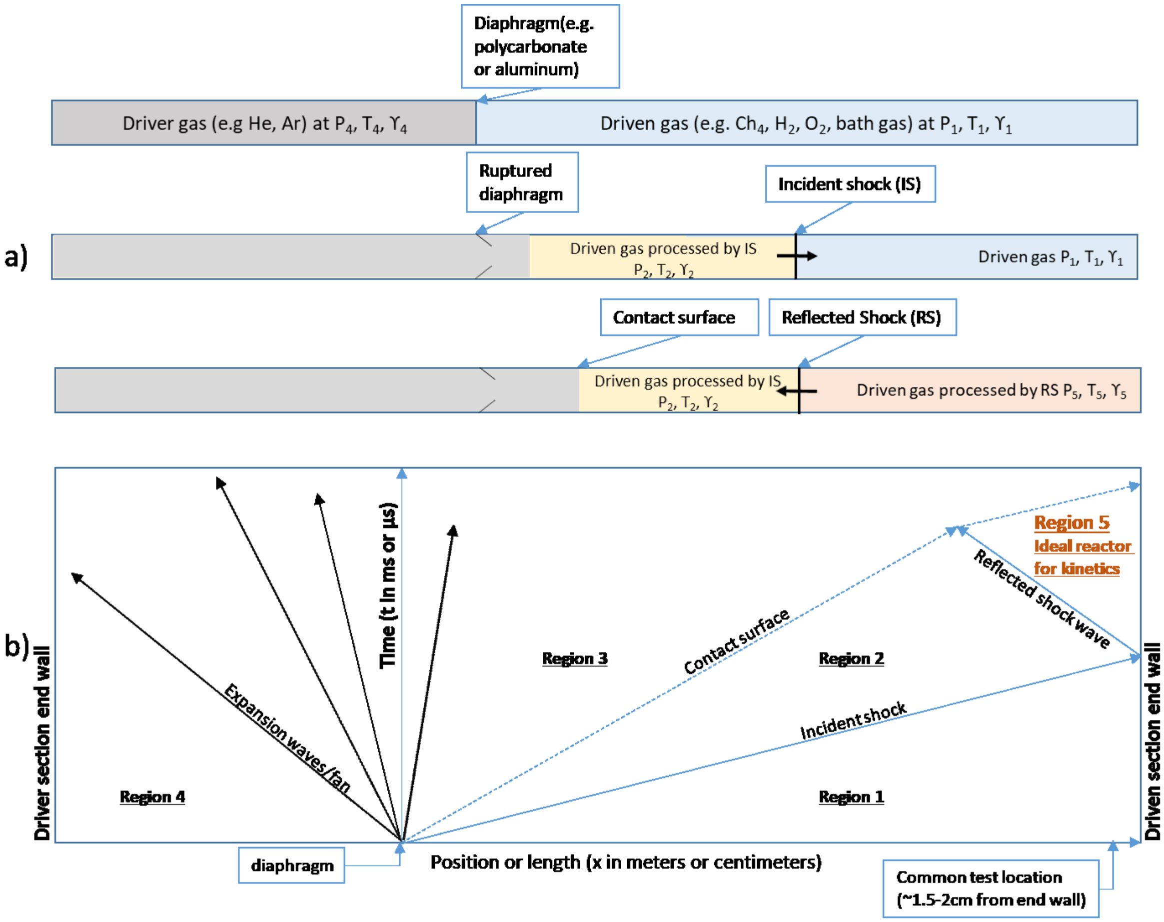

Figure 2: a) Schematic of shock tube, b) shock wave position time diagram within shock tube

STs are able to instantaneously and simultaneously heat up and pressurize the reactive mixture. The reactor in region 5 is often considered to be an adiabatic, constant volume batch reactor. Due to the short timescales probed behind reflected shock waves in STs they are immune to heat transfer effects, as well as wall-effects causing catalytic and radical termination [48]. STs are unique in that they are the only facility that have the potential to enable direct investigation of kinetics of elementary reactions and global mechanisms pertaining to hydrocarbon combustion at high pressures and temperatures, with potentially negligible fluid mechanical or heat transfer effects.

While ST facilities provide idealized reactors for kinetics research, there are five non-ideal effects, which may need to be managed and characterized for certain applications when interpreting data generated by these devices. These non-ideal effects are discussed in the following paragraphs and pertain to deviations from assumptions of:

1. constancy of pressure, known as a dP/dt effect;
2. stagnancy of the reactor contents, known as reflected shock bifurcation effect;
3. perfect cleanliness of the reactor, known as impurities effects;
4. homogenous ignition, known as pre-ignition effect; and,
5. homogenous ignition, known as mild ignition.

One is the non-constancy of pressure following the reflected shock wave passage, which exists even in non-reacting systems. That is, after the pressure jump caused by the passage of reflected shock the pressure tends to grow linearly with time, referred to as the dP/dt problem. This has been attributed to the gradual attenuation of the shock wave, due to the shock wave slowing down causing the post reflected shock pressure P_5 to gradually increase with time [49]. This deviation from pressure constancy causes discrepancies. For example, modelers typically assume that the temperature is constant, however, if the pressure varies by 3% per millisecond, the temperature will vary by ~1.2% per millisecond, which for a 10 ms ignition delay time measurement would translate to a 12% change in temperature [49]. This may be somewhat circumvented by modifying the shock tube to include what is referred to as a "driver insert" into its driver section. The insert is to modify the flow to achieve uniform temperature and pressure for reduction or possible elimination of the dP/dt problem, as demonstrated by Hong et al. [51]. Driver inserts are custom inserts added to counteract non-ideal shock tube effects to obtain near-ideal, constant-volume performance in reflected shock wave experiments at longer test times. Elimination of dP/dt effect could commonly bring about increases in experimental ignition delay times, which are inversely proportional to the overall reaction rate, of 40% [48]. This modification improves the quality of the data enabling the modeler to avoid having to correct for the gas dynamics model to correct for the dP/dt, and model the reactor as a constant internal energy and volume one [48, 49]. As noted however, since the variation in pressure with time also depends on the duration of the experiments, and the experiments in this study are expected to take in the order of 10s to 100s of microseconds, this problem tends to become less important. Pang et al. [52] investigated the dP/dt problem and concluded that for ignition delay times <0.6 ms the influence of dP/dt becomes insignificant to the point that the results from a facility with a dP/dt of 2.0%/ms are indistinguishable from those from a facility with dP/dt=6.5%/ms [28]. However, for experiments with slower kinetics such as combustion of most HCs at <1000 K kinetics conclusions become overly sensitive to correct estimation and incorporation of the dP/dt effect. Ninneman et al. [53] showed the impact of this effect for ignition delay times of H_2-O_2 systems at temperatures <980 K.

A second non-ideal effect that occurs when polyatomic bath gases constitute a significant portion of bath gases is reflected shock bifurcation. In ideal shock tubes the incident and reflected shock are assumed to occur as planes normal to the shock wave's axial motion, which process all gases in their cross section equally. Polyatomic bath gases, e.g. CO_2, have been shown to lack momentum near the boundary layer to pass through the reflected shockwave. Hence near the boundary layer these gases get pushed in front of the normal portion of the shock tube, and cause an oblique shock to form, in a direction away from the boundary layer. Subsequently, another oblique shock forms to balance the pressure bringing the flow back towards the shock tube wall. This causes a lambda shape bifurcation foot as discussed by Hargis and Petersen [54]. Hargis [55] investigated the effect of 75% dilution of a stoichiometric mixture of CH_4 and O_2 by different concentrations of CO_2 and N_2 as the bath gas, at 1 and 10 atm, and temperatures of 1450-1900 K. The author reported the following non-ideal effects:

1. the portion of the gas experiencing the bifurcated shocks do not have the same temperature and pressure conditions as the remainder of the gas;
2. the gas experiencing the bifurcation will not be quiescent and will experience vorticity and flow effects;
3. the localized impact on reactor conditions within the bifurcation foot may cause formation of hotspots and result in premature ignition (pre-ignition) perturbing the commonly targeted homogenous ignition of the bulk of the fluid for IDT determinations;
4. pressure diagnostics installed on side-wall of the shock tube are ineffective for reliable measurement of the pressure of the bulk of the fluid and in essence that of the reactor;
5. When bifurcation is really severe a portion of the gas may slip and curl up against the end-wall as observed by end-wall pressure diagnostics;
6. The authors confirmed that specific heat ratio was the main parameter impacting the severity of bifurcation;
7. End-wall pressure diagnostics indicated that a pressure dip were observed in some tests prior to the ignition event. The reason for these dips are not confirmed but is speculated to be an indicator for arrival of the contact surface. While the associated ignition delay time data for

these tests were found in-line with the overall IDT trends, they were deemed unreliable for kinetics validation; and,

8. Side-wall emission or laser diagnostics may pick up localized ignition rather than the main ignition, in the case of premature ignition occurring as a consequence of inhomogeneity caused by reflected shock bifurcation.

Hargis and Petersen [54] provided sample side- and end-wall pressure profiles for mixtures with pre-shock reactive gas mixture specific heat ratio ($\gamma = C_p/C_v$) of 1.39, 1.36, 1.33, 1.31. Decrease in γ from 1.33 to 1.31 showed the most dramatic increase in pressure fluctuations, whereas, increases in gamma beyond 1.33 suggests significantly reduced pressure fluctuations in the core bulk of the gas, as measured by end-wall pressure diagnostics [54]. It can be concluded that barring pre-ignition effects, targeting mixtures with $\gamma>1.33$ should likely provide reliable IDTs with manageable uncertainties, as far as bifurcation effects are concerned.

Peterson and Hanson [56] investigated the extent and magnitude of reflected sock bifurcation for gas mixtures with specific heat ratios 1.29-1.51, molecular weights of 14.7-44.0 g/mole, at P_5=11-265 atm and T_5=78-1740 K. They found that the size of the bifurcation zone increased with shock velocity and decreasing specific heat ratio and was not pressure-dependent. The authors also suggested laser Schlieren is more effective for time zero (t_0) determination, and bifurcation should not affect the core portion of the post-shock region [56].

More recently, Pryor et al. [14] investigated the impact of bifurcation using high-speed end-wall camera imagery in tandem with side-wall emission, pressure and laser absorption spectroscopy (LAS) of 3.5-5% CH_4 stoichiometric mixtures with 0-89.5% dilution of CO_2 with the balance Ar, at P_5=1 atm and T_5=1650-2040 K. They concluded that for mixtures with large amounts of CO_2 dilution e.g. 85-89.5%, the combustion process is no longer homogeneous. End-wall imaging shows that inhomogeneity of ignition significantly subsides for 60% CO_2 dilution [14]. For ignition delay time measurements, uncertainties increase with the severity of bifurcation, and the criterion of peak vs. onset of exponential side-wall emission rise can lead to IDT differences of over 100 us. Such difference could lead to erroneous conclusions drawn about validity of chemical kinetics models [14].

A third non-ideal effect impacting kinetics investigations is the effect of hydrocarbon impurities, even at ppm levels, entrained either along with impure feed gases, or as a result of ineffective cleaning of the apparatus. Urzay et al. [57] investigated this effect for hydrogen ignition in shock tubes and demonstrated that ppm level impurities which are unavoidable can significantly increase the reactivity of mixture. Urzay proposed different methods of quantification, however, as most validation data impacted by such impurities in the literature predate the discovery of this issue and its solution, a critical assessment and review of the data is necessary before their utilization as validation targets. Mulvihill and Petersen [58] further investigated the impact of these impurities experimentally and numerically, as well as their potential source. The authors concluded that cleaning of dirty mixing tanks are important in reducing the impact of impurities. However, even with cleaning the mixing tank, 98% diluted H_2/O_2 mixtures display 25-30% discrepancy with predicted values. The authors also showed that hydrogen ignition data in the literature from different sources are consistent for dilutions below 94%, as they were insensitive to impurities. Also CH_4/O_2 mixtures with 99% Ar dilution were also insensitive to impurities [58]. Ninnemann et al. [53] performed ignition delay time measurements using high-speed end-wall camera imaging and repeated the experimental investigation of Pang et al. [52], which had reported unexplainable results possibly impacted by inhomogeneous ignition issues. Ninnemann et al. [53] confirmed that for tests with less than 94% dilution, impurities and apparatus cleanliness effects were not of concern for H_2/O_2 systems.

A fourth non-ideal impact is referred to as pre-ignition energy release which perturbs the constancy of pressure and temperature prior to ignition and either needs to be avoided or modelled. This localized effect perturbs the intended reactor conditions and manifests itself as a non-ideal inhomogeneous ignition that is shorter than anticipated by models. To solve the chemically rooted problem while avoiding having to deal with reactive gas dynamics models, two strategies can be adopted to enable constant pressure modeling. The first strategy involves using a very small amount of fuel, highly diluted in non-reactive gas, to reduce exothermically-driven temperature and pressure changes [49]. The difficulty with this experimentation is that very sensitive diagnostics are needed with sufficient resolution to measure the diluted species' evolution. The second strategy is to use a constrained reaction volume (CRV) concept to minimize pressure perturbations, which simplifies the associated modeling [49]. In CRV instead of filling the entire driven section with the reactive mixture, which will burn upon passage of the reflected shock, only the test section volume close to the shock tube's driven section end is filled with reactive mixture, reducing the energy release and also the associated pressure change. In CRV once the incident shock comes in and reflects, the gas behind the reflected shock has no combustible components once passing the CRV section of the tube. Hence, the small pressure generated releases itself axially [48]. CRV eliminates pressure spike due to ignition of reactive gas mixture, increasing the test times and post ignition probing and monitoring the chemical evolution of combustion intermediates and products. CRV also prevents remote ignition, which may occur if the shock wave has been slowing down causing the temperature immediately behind the reflected shock to be locally higher than the temperature of the test section, which may lead to a premature ignition in the trailing region behind the shock wave, away from the test section. While driver inserts and CRV reactors provide a solution, their implementation, especially at high pressures, are expected to be difficult. For example, for effective implementation of CRV the Hanson group built a sliding valve near the end-wall, and filled both its sides to equal pressure, with the side closer to the end of the shock tube filled with a reactive gas, and the other with the non-reactive one, followed by gentle opening of the valve [49]. Considering the intrusive nature of CRV, its incorporation is cumbersome and most facilities are not equipped for it, as such the aforementioned dP/dt and heat release issues are commonly managed by modifying the combustion models instead. Pang et al. [52] developed a code which incorporates the experimental pressure trace and accounts for this pre-ignition energy release. However, the code would require availability of reliable clean pressure traces. Such pressure traces are not available for potentially bifurcating mixtures of interest in this study, namely H_2O and CO_2. Pang et al. [52] showed that pre-ignition was not an issue for stoichiometric low H_2 concentrations of ~4%, whereas this was not the case for H_2 concentrations greater than 15%. Ninnemann et al. [53] repeated experiments of Pang et al. [52] and included additional endwall imaging for further insight. They showed that while H_2 combustion was not homogeneous, i.e. it was circumferential for H_2 concentration of 4%, ignition did not occur at other locations prior to ignition at the test section. Ninnemann et al. [53] observed pre-ignition in high concentration mixtures by both the pressure traces and high speed images. The study also further confirmed the hypothesis by Walton et al. [59] that mixtures with low thermal diffusivity, are prone to pre-ignition, as local thermal energy generated cannot be dissipated fast enough, and results in flame formation. It is important to note that this issue does not exist at higher temperatures [53].

Finally, the fifth non-ideal issue is mild ignition, which takes place typically at lower temperatures (below 1000 K) for H_2/O_2 systems at high concentrations of 15% H_2 and higher, as illustrated by Ninnemann et al. [53]. Ninnemann et al. [53] observed weak deflagration flames followed by a local detonation event, and showed that for these high concentration mixtures, ignition occurred beyond the targeted ideal test location and likely before the ignition event at the test location. Moreover, Ninnemann et al. [53] observed pressure oscillations indicative of the interaction between multiple weak luminescent deflagration flames as well as detonation waves which is a characteristic of mild ignition phenomena. Both pre-ignition and mild ignition phenomena are complex to model and experimental conditions should be devised such that these phenomena can be avoided.

Despite the potential non-idealities elaborated on above, shock tubes remain the most direct means of probing the very fast kinetics of HC combustion at high temperatures and pressures.

In 1995 Petersen et al. [60] conducted two studies investigating ST ignition delay times of H_2-O_2-Ar and CH_4-O_2-Ar, while monitoring OH through tunable diode laser absorption spectroscopy (TDLAS), CH_4 through Infrared (IR) emission, as well as pressure, at Ar dilution rates of 97-99.5%, and 90-95%, at 1175-1880 K and 1250-2100 K, and 33-87atm and 8-85 atm, at equivalence ratios of 1.0, and 0.5-4.0 respectively. Additionally Petersen et al. [61] explored kinetics of CH_4-O_2-Ar at extremely high pressures of 9-480 atm, via ST ignition delay time measurements, at 90-95% dilution rates, 1410-2040 K, at the same equivalence ratios, and using the same diagnostics tools as their previous study. To put in perspective the timescales involved in such experiments, they recorded two ignition delay times of 74 μs and 150 μs at 171.5 and 177.6 atm and 1613 K and 1551 K respectively, with the full domain of their ignition delay measurements including measurements of 23-352μs. Another notable experimental test campaign exploring very high pressures is Petersen et al.'s 1999 shock tube IDT study [62] also involving measurement of CH_4 ignition delay times, at 1040-1600 K, 35-460 atm and equivalence ratios of 0.4-6.0 in the presence of bath gases Ar, N_2, and He, at dilution rates in the 50-70% range, while looking at IR emission of CH_4, visible emission from soot luminosity and C_2, laser extinction by soot and/or increased density in addition to pressure measurements.

Zhukov [21] compared different alkanes kinetics at 850 K to 1700 K, and at extreme pressures of up to 530 atm, and illustrated that the kinetics are impacted the strongest by temperature variations, pressure variations, and alkane chain size in declining order of importance. However, it is critical to understand the interplay of the aforementioned in order to be able to develop effective detailed kinetic mechanisms as a design tool [21].

It is important to also emphasize that in addition to experimentation for global mechanism validation purposes, shock tubes are more commonly employed to determine elementary reactions' rates. A noteworthy example is Hong et al.'s study [40] which determined the rate of the most important reaction in combustion chemistry, i.e. $H+O_2=OH+O$ using shock tubes at 1100-1530 K and 2 atm using TDLAS measurements of H_2O.

2.2.2 Rapid compression machine facilities

An RCM involves acceleration of piston(s) for quick compression of the reactive gas mixture in a chamber followed by rapid slow-down of the piston, with this process taking 10-70 ms [48]. It is well suited for gas phase kinetics studies and physical processes in combustion widely used at low to intermediate temperatures of 600-1100 K, and pressures of 1-70 bar. RCMs are mainly designed for ignition delay time measurements [18]. One difficulty with RCMs is the inevitable heat loss to the walls which limits test times to a range of about a few milliseconds to 500 ms [48, 18]. The other difficulty is the definition of time zero for ignition delay measurements which is commonly considered to be the time at which the peak pressure is obtained, however, this assumes non-reactivity during the 10-70 ms of compression time. As the compression is not instantaneous as is the case in a shock tube this makes it less ideal [48]. RCMs and STs have also been used in tandem to investigate ignition delay times of alkanes, with RCMs targeting lower pressures and temperatures, i.e. 10-40 atm and 700-1000 K with longer delay times of 5-300ms, and STs targeting higher temperatures and pressures leading to small delay times of 20 μs-2ms [50]. This approach was adapted by in the recent Keromnes et al. study [28] culminating in a validated H_2/CO reaction mechanism model for combustion of $H_2/CO/O_2/N_2/Ar$, at 1-70 bar, 914-2220 K, and equivalence ratios of 0.1-4.0.

2.2.3 Flow reactor facilities

Flow reactors are commonly utilized for combustion kinetics measurements [18]. Turbulent variants are used for ignition delay time measurements and laminar ones for species-time evolution measurements at the outlet of the reactor. The former commonly have maximum operating temperature and pressure of 1000 K and 30 atm [50]. Beerer et al. [50] used one such reactor to measure 997 ignition delay times of small alkanes recording times in the range of 20-600ms, in flow reactors at 785-1135 K, and 1-15 atm. In these devices ignition delay time, IDT, is measured as the difference between fuel injection time into the test section measured via IR TDLAS of HC, and time of light emission from ignition detected by photomultiplier tubes (PMT). These reactors are suitable for low to intermediate temperature combustion, with residence times larger than 20 ms [49]. Hashemi et al. [63] recently proposed a detailed kinetics mechanism for highly pressurized, low to intermediate temperature CH4 combustion using a laminar flow reactor that operates at a 100 bar and 900 K, and noted that shock tubes are typically better suited for temperatures exceeding 1100 K and high pressures [63]. Definition of time zero is commonly problematic, in both aforementioned types of flow reactors, which is taken to be coincident with the combustible mixture creation. As the device relies on in situ mixing, commencement time of chemical reaction due to the unavoidable inhomogeneities is uncertain [29, 22].

2.2.4 Jet-stirred reactor facilities

Jet-stirred reactors is a type of ideal continuously stirred tank reactors commonly targeting highly dilute flameless combustion kinetics. They are typically spherical reactors with four jets introducing fresh gas at an injection cross at the center of the sphere, ensuring perfect mixing, as detailed by Leclerc et al. [18]. Experiments are designed such that the residence time of reactants is varied from test to test, and stable intermediates and products are characterized as a function of residence time, temperature, as well as pressure at temperatures of 700-1450 K, and pressures of up to approximately 40 bar. Le Cong et al. [64] utilized JSRs to investigate kinetics of CH_4 and syngas oxidation, the results of which were utilized by Metcalfe et al. in validation of AramcoMech 1.3 [22]. Speciation is possible through GC and mass spectrometers (MS) for measurement of OH, HO_2, RO_2 and ketohydroperoxides, FTIR for H_2O, CH_2O, CO, CO_2, NO, NO_2, as well as cavity ring down spectroscopy for OH, and HO_2 measurement in the gas phase. Sampling from these reactors is critical and difficult due to change in composition of the gas between the outlet of reactor due to adsorption and reactions at the wall which brings about additional uncertainties.

2.2.5 Flame velocity facilities and measurement

Adiabatic laminar burning velocity depends on the bath gas composition, equivalence ratio, pressure, and temperature [18]. Laminar flame speeds are indirect means for refining the chemical kinetics of premixed combustion. Depending on the apparatus a flame is either anchored such as in a Bunsen burner, or the flame speed is measured through its propagation through a premixed mixture such as that of an expanding spherical one. Particle image velocimetry techniques are commonly utilized in flame speed measurements with anchored flames, in which a reacting flow is seeded with a particles, such as silicon or zirconium oxide. As utilized by Veloo et al. [65] and noted by Leclerc et al. [18] flame velocity measurements are done through two optical access points. Using a laser sheet the flow field is illuminated, and scattering of light by the particles is captured using a high speed camera and their movement is mapped. Another technique, referred to as Schlieren or shadow-graphic optical imaging, relies on interferences caused by refractive index gradients enabling detection of inhomogeneity in mixtures. In this technique this interference is captured as a shadow pattern, depicting variation of light intensity due to density variations of the burnt and unburnt fluids enabling flame speed measurements as utilized by Kochar et al. for flame speed measurements of Alkanes [20]. Kochar et al. studied speeds of Bunsen and spherically expanding flames of premixed pure and blended CH_4, C_2H_6 and C_3H_8 mixtures at 298-600 K, and 5-10 bar, which later served the validation of C4_52.0_LT, and AramcoMech1.3 models [20]. However, as these reactors and measurements are an indirect means of evaluating the kinetics, they are affected by choice of transport data and input parameters used [31], and are limited in terms of the range of pressure they are able to explore (due to stability issues of laminar flames and materials of construction in spherically expanding flames), as such they are not dwelled on in this manuscript.

2.2.6 Ignition delay time measurements

Ignition delay time is the time delay observed for a mixture of fuel and oxygen at a specific temperature and pressure before ignition or explosive reaction. This is of particular interest to engine designers which commonly rely on HC fuels' (e.g. diesel) automatic ignition as it is crucial for good control of reciprocating engines to ensure appropriate ignition timing [49]. This measurement is an indicator of the radical pool buildup time towards explosive reactivity. Such measurements are commonly obtained in shock tubes [61], rapid compression machines [66], as well as flow reactors [50]. However, the aforementioned apparatuses' limitations in operating conditions, timescales, resolution, as well as the extent and ease of quantification of uncertainties renders one superior to another for different applications. The most important challenge with ignition delay time measurements is the determination of time zero and the time of ignition. The timescales of CH_4 autoignition at pressures and temperatures relevant to this study are in the order of 10s to 100s of microsecond, i.e. in Ar, He, or N_2 baths as observed in two studies by Petersen et al. [60, 61] and another two by Zukov et al. [19, 21]. These time scales and combustion conditions render shock tubes as the only facility capable of generating these high temperature and pressure conditions almost instantaneously to enable accurate probing of the kinetics [49]. Within shock tubes the aforementioned challenges with increased uncertainties in determination of time zero, and ignition time become more pronounced in the presence of polyatomic molecules such as CO_2 and possibly H_2O at high pressures to the point that this measurement may not be quantitative enough for drawing conclusions about the kinetics. This has been recently demonstrated through several studies, conducted by research groups at Texas A&M University (TAMU) and University of Central Florida (UCF) focusing on utilizing shock tubes for ignition delay measurements at high temperature and pressures in highly diluted in CO_2 environments [54, 66, 14]. Luckily, based on the findings of the body of literature present, there are workarounds for these limitations to manage them, such that quantitative measurements can be extracted that would enable reliable conclusions to be made.

2.2.7 Species emissions and concentration time-histories measurements

Species time histories are highly desired for drawing kinetics conclusions, model validation and tuning purposes. They enable comparison of the model predicted time-histories of the same species with direct measurements. Species time-histories could involve both direct measurement of concentration time-histories, or emission time-histories of excited molecules of the species population.

For species emission time-histories the most powerful and practical measurement technique is monitoring emission in the UV and visible spectra, such as chemiluminescent emission of excited radicals such as OH*, CH*, CO_2* radicals which are direct indicators of radical pool build up, as well as reaction zone locations. These species evolution measurement is commonly utilized either directly for validation purposes or for estimation of ignition time in IDT measurements. This technique is commonly utilized in shock tubes, flow reactors, as well as flame speed measurements as demonstrated in studies by Pryor et al. [14], Beerer et al. [50], and Kochar et al. [20] respectively.

For concentration time-histories the most quantitative non-intrusive means for gaining insight into evolution of species is through laser absorption spectroscopy (LAS). LAS has limitations in terms of the species that can be probed, the composition of the mixture, i.e. including components with interfering spectra, as well as high temperature and pressure broadening effects reducing signal-to-noise ratios. At higher temperatures, higher rovibrational energy levels also become accessible to species molecules, and their fill up of the accessible energy levels follows a Boltzmann distribution. Hence target species populations spread across a larger number of rovibrational energy levels. Since lasers absorption targets a specific transition between two targeted energy level, a reduced population in those levels directly reduces signal strengths. In addition, depending on temperature, possible appearance of bandheads may densify and hinder resolving the spectrum [67, 49]. Similarly, appearance of hot bands at high temperature may further complicate the spectrum. Hot bands involve transitions between bands with more than one vibrational energy level change, which both densify the spectrum and reduce the signal to noise ratio [48]. Increasing the pressure also broadens the rovibrational spectrum of species. This pressure broadening effect is a consequence of the limited time molecules spend at an energy level at high pressures, prior to participating in an inelastic collision. This results in fuzziness in determination of the energy associated with the state of the molecule, hence widens the rovibrational transition line relative to those at low pressures [49]. As increasing the pressure significantly increases the collision frequency, this results in overlap of different transition lines which makes resolving spectral lines and their shapes for species concentration determinations difficult [67].

The most quantitative of LAS techniques applicable to combustion systems is in the IR region of the spectrum and involves tunable diode laser absorption spectroscopy (TDLAS). The advantage of working in the IR spectra is due to the fact that many combustion gases of interest, such as NO, CO, CO_2, H_2O and fuels absorb light in the IR. Since for the most parts molecules involved in simple HC oxidation studies, are small and small species have discrete spectra, TDLAS is a powerful means for their detection. TDLAS however produces a mean value of the measured quantity for a single line of sight it probes, hence it is not able to capture non-uniformities along its path length [67]. The conditions relevant to this study brings about spectroscopic challenges, which need to be overcome within the context of the experimental apparatus selected when warranted, as these techniques are well suited for shock tubes, jet stirred reactors, flow reactors, as well as RCMs [18].

A few of these challenges expected for species time histories measurements in shock tubes pertaining to the research work at hand are:

1) Pressure broadening of spectra, resulting in reduced height and broadened absorption lines, rendering integrating the line shapes out to arrive at a line strength corresponding to the concentration of species tough, due to increased overlapping of the spectra, as well as reduction of the signal to noise ratio, increasing the uncertainty associated with the measurement [48].

2) Due to the presence of H_2O or CO_2, flow non-uniformities have been shown to occur, which may cause spatial inhomogeneity, increasing the uncertainty associated with conclusions about the reactive system, from a line of sight concentration measurement stance [14].

3) Water has many vibrational modes, hence a dense and wide spectra which overlaps with absorption spectrum of other species in the IR, rendering identification of interference-free transition lines of multiple species alongside water typically more difficult [49].

Laser induced fluorescence may also be used for temperature and concentration measurements. However, it is less quantitative. Planar laser induced fluorescence (PLIF) is commonly utilized for perpendicular radial plane visualization of combustion chambers, in which a sheet of light excites the species absorbing in the incident light wavelengths, that subsequently relax and fluoresce and is commonly employed for monitoring ground state radicals like CH and OH. The advantage of these spectroscopic techniques is that they are not intrusive, hence they do not cause any perturbations in the inherent flow regime or mass balance of the environment being probed.

Other techniques common to facilities other than shock tubes, utilized in combustion kinetics studies relying on extractive sampling and measurement include Fourier transform infrared spectroscopy (FTIR) that probes the IR spectrum of molecules, and subsequently uses mathematical techniques to deconvolute the spectrum to recover individual species spectra, and determine their concentrations [48]. Although in-situ FTIR is possible, due to impractical condition specific calibration requirements, a stream of mixture is diverted to the FITR, and its temperature and pressure is adjusted to a designated condition for measurement. The reliability of measurements obtained, however, hinges on the representativeness of extracted sample, sufficiency of time and absence of catalytic surfaces for species evolution as they pass through the sampling, conditioning and measurement sections. The latter two are of concern for unstable short-lived intermediate species [18]. Successful FTIR measurements of CO, CO_2, H_2O, NO, NO_2 and CH_2O for n-heptane toluene blend oxidation in JSRs have been demonstrated by Leclerc et al. [18]. It should also be noted that FTIR has minimum flow requirements which limit its utilization at laboratory scale.

A low flow alternative, extractive technique suitable for both low and high flow apparatuses uses gas chromatograph (GC) with multiple columns, with flame ionization detectors (FID) for HC and thermal conductivity detectors (TCD) for measurement of other species. Collectively referred to as GC-TCD/FID apparatus, is able to detect CH_4, O_2, CO, CO_2, CH_3OH, and CH_3NO_2 among others. GC-TCD/FID measurements of CH_2O are difficult due to loss mechanisms, such as those pertaining to sample extraction, as noted by Rasmussen et al. [68] and Hashemi et al. [63] in their flow reactor apparatus. They estimated the uncertainties of up to 10% associated with these loss mechanisms. It has been shown that even with the usage of exclusively inert wetted materials such as Pyrex, unstable species such as HO_2 do not survive for measurement with GC-TCD/FID, the exception being jet stirred reactors (JSRs) equipped with dedicated reaction chambers coupled with mass spectrometers (MS) HO_2 measurements have been successfully made [18].

In conclusion, it can be seen that for the highly elevated target temperatures and pressures of the study at hand the only apparatus able to generate the test conditions almost instantaneously to enable effective probing of the kinetics is a shock tube. With that in mind the focus is turned to shock tubes and a few modelling challenges associated with their usage, as well as a few counter measures, which are presented in the next section. Moreover, the simplest most effective global indicator of reactivity and measurement is ignition delay times, which is targeted in this work.

Building on the knowledge of kinetics model architecture, validation targets and associated experimental facilities, the next sections summarize the results of the review of literature for insights on the kinetic effects of the temperature, pressure, and the higher concentrations of target bath gases H_2O and CO_2.

2.3 Kinetics effects of temperature

Rates of all chemical reactions as well as thermochemical properties of all species are strong functions of temperature [69]. Hence variations in temperature change the equilibrium concentrations of all reactions, as both the forward and reverse reaction rates are impacted by them. As detailed chemical kinetics involves many elementary reactions, reactants and products, with differing temperature dependencies, the response of the overall kinetics to temperature variations is not easily predictable. In order to minimize the Gibbs free energy, the dominant reactions may change and so will the reactive pathways and intermediate products generated with variations in temperature. In fact, this is the case for combustion systems which have non-monotonic temperature dependent kinetics.

Commonly HC fuel combustion reaction mechanisms are divided into three temperature ranges, of high (above 1200 K), intermediate (1000-1200 K), and low (below 1000 K), with the caveat that the aforementioned bounds move to higher temperatures with increases in pressure [18, 21]. The effect of the changing reaction pathways is demonstrated by Zhukov for the case of n-heptane [18]. For n-heptane, the overall reaction rate has been shown to decrease with increases in temperatures, at 700-1000 K for the investigated pressure range of 1-42 bar, which is referred to as the negative temperature coefficient (NTC) region. The reaction rate however increases with temperature outside the NTC region on both the low and high ends [18]. Zhukov [21] notes this observation is common to all alkanes, with the sharp increase in formation and stability of peroxides with transition from high- to low-temperature kinetics and radical recombination reaction rates to be collectively responsible for this non-monotonic kinetics' response. Zhukov [21] conducted ignition delay times of alkanes at pressures of up to ~500 atmospheres, and concluded the rate of formation, accumulation, and decomposition of H_2O_2 to be the determining factor for ignition delay times' peculiar variation at intermediate temperatures. This rate is highly sensitive to the rate of production of HO_2 and its subsequent contributions to pathways leading to production of H_2O_2, which at intermediate temperatures involve hydrogen abstraction from fuel [21]. This variation with temperature is so significant that mechanisms are commonly classified into two classes of low- and high-temperature, as noted by Leclerc et al. [18]. Even though the reaction classes within each mechanism class may differ slightly from one author to another, there is agreement between the main ones. Leclerc et al. [18] noted approximately 10 common reaction classes for high temperature mechanisms versus upwards of 30 reaction classes involved in low temperature kinetics models. This illustrates, how critical variations in temperature are to the detailed mechanism model desired, as well as the fact that the mechanism becomes more complicated for low and intermediate temperatures.

Furthermore, Wong et al. [70] investigated the dependence of the high-pressure-limit of pressure-dependent reaction rates on temperature, and illustrated that the high-pressure-limit rate is reached at higher pressures for systems at higher temperatures. The authors also showed that there is an inverse dependence between molecular size and the pressure at which high-pressure limiting rates are observed [70]. Consequently, for pressurized combustion systems involving small fuel molecules occurring at high temperatures, such as the one at hand, it is expected that many of the pressure-dependent reaction rates may be in the "fall-off" or "chemical activation" regime instead of their low- or high-pressure limits.

2.4 Kinetics effects of pressure

Pressure directly impacts the collision frequency, but the relation between reaction rates and collision frequency is not trivial, as for some elementary reactions the rate decreases with pressure whereas for others it increases.

From a thermodynamics stand point increasing the pressure will firstly force reactions in the direction of reducing molarity, following Le Chatelier's principle [69] and secondly, beyond a threshold, it may enhance intermolecular interactions, causing deviations from ideal gas behavior, depending on the temperature and composition.

Deviations from ideality also may impact the temperature-dependent evaluations of the molar enthalpy, for the various species which are assumed to be pressure-independent, as combustion typically occurs at low enough pressures. For this non-ideal behavior specific to high pressures, Moshfeghian [71] investigated the impact of pressure on pressure dependency of enthalpy for CH_4 in the range of 1 to 200 bar. It was illustrated that the impact of pressure on molar enthalpy is significant at lower temperatures, but this impact subsides at higher temperatures [71]. In order to determine the impact of pressure on CH_4's enthalpy of formation Moshfeghian used Peng-Robinson equation of state [71]. Similar investigation for CO_2, and possibly H_2O, to evaluate the impact of pressure at combustion relevant conditions is commonly ignored by the combustion modeling community, i.e. the thermochemical properties are assumed to be pressure independent [72, 73].

With increased pressure the impact of deviation from ideal-gas behavior assumption is also of interest and was evaluated by Petersen et al. [61] for determination of the conditions behind the reflected shockwave in their investigation of high temperature and pressure CH_4 ignition delay times in shock tube. Their investigation involved ignition delay times at pressures of up to 500 atm. At this pressure and a temperature of 1800 K the authors evaluated the deviation in the calculated temperature behind reflected shockwaves from ideal gas law assumption was ~-40 K. The authors showed that this deviation at 90 atm was reduced to ~-7 K, hence the authors employed Peng-Robinson as their choice of equation of state [61]. Similarly, more recently, Shao et al. [16] quantified the deviation of calculated pressures behind reflected shockwaves using ideal gas law assumption vs. Peng-Robinson. They found the deviation to peak at 2% for pure CO_2 and at pressures of 472 bar and the lowest temperature IDT measured in their work was at 1045 K.

Large enough variations in pressure also change the molecularity of reactions involving third-body with fall-off behavior. These typically involve reactions with small to no energy barrier that produce excited adducts which can isomerize and lead to a network of reactions and products, the relative fluxes of which varies with pressure, as discussed by Gao et al. [74]. Hence, a reaction could be third or second order depending on the impact of pressure on molecularity. This impact of pressure on reaction rates also may change the order of dominance of reaction paths for reactive systems. For example, reactions with higher molecularity, such as termolecular ones which are inconsequential at low pressures may become important and interfere significantly in the overall rate, as noted by Glassman and Yetter [6]. This was demonstrated by Wang and Law [75] in their investigation of the Z-shaped H_2-O_2's explosion limit curve. Wang and Law [75] showed that the 2nd limit observed in the H_2-O_2 explosion limit curve is a consequence of $H+O_2(+M)=HO_2(+M)$ becoming dominant enough to compete with the main chain branching $H+O_2=OH+O$ at higher pressures. This is due to the competition of reactions involving H radicals, which at high temperatures and pressures in the range of up to 32 bar is very sensitive to the rate of $H+O_2=O+OH$, as it is the main high-temperature chain branching reaction [28, 75, 6]. At intermediate temperatures the pressure-dependent $H+O_2(+M)=HO_2(+M)$ reaction is known to compete with $H+O_2=O+OH$ for the H radicals [75]. It should be noted that due to the pressure dependence of $H+O_2(+M)=HO_2(+M)$, the temperature range in which it starts to compete with $H+O_2=O+OH$ depends on the pressure, and HO_2 is commonly considered to be an inhibiting reaction path, but at high enough pressures it provides an important pathway for H_2O_2 production, which will further breakdown forming two highly reactive OH radicals [22, 18, 6, 75]. At temperatures below 1000 K, it is also shown that hydrogen abstraction from fuel by HO_2 radical becomes an important pathway for H_2O_2 production, followed by hydrogen peroxides decomposition as the main chain branching reaction [28].

There are two main categories of these pressure- and temperature-dependent reaction rates, namely 1) unimolecular decomposition/radical recombination reactions and 2) chemically activated bimolecular reactions. Examples of unimolecular/recombination reactions is $H+O_2(+M)=HO_2(+M)$ or $CH_3+CH_3(+M)=C_2H_6(+M)$, where there is excess energy available due to bond formation, which needs to be absorbed to stabilize or thermalize the highly excited unstable adduct [6]. Hence, thermalization through de-exciting collisions with bath gases M, is necessary for the reaction to proceed, as the transition state occurs with near-zero energy barrier, and the reaction can easily proceed in the reverse direction as well. For chemically activated bimolecular pathway for the same reactant set, such as $CH_3+CH_3(+M)=C_2H_5+H(+M)$, the path is usually endothermic, and while the reaction proceeds through the same adduct, only exciting collisions M will promote it, and thermalizing ones will stabilize the adduct, impeding its progress. There are also reactions with multi-well energy curves along the reaction coordinate, in which the excited adduct has one or more competing isomerization and dissociation pathways all of which are possible to varying extents based on the number and strengths of thermalizing/de-exciting and exciting collisions with a third body (non-reactive collision partner). Under such conditions where the collisions cause a rate limiting behavior, the phenomenological rate coefficients do not follow an Arrhenius expression, and become a function of both temperature and pressure [74], i.e. with rate constants k(T,P).

These pressure-dependent reaction rates require formulations such as those proposed by Gilbert and Troe, and Troe [76, 77], using a combination of two bounding reaction rates. One being the "low-pressure-limit", in which the reaction expression is elementary in the concentration of bath gas. The other being the "high-pressure-limit" rate representing the rate observed above a threshold pressure beyond which an increase in collision frequency with the third body does not impact the rate of reaction. Beyond this pressure the rate plateaus and becomes independent of the collider concentration. In these formulations, the low- and high-pressure-limit rates are expressed as follows:

$$k_0 = A_0 T^{n_0} exp\left(\frac{-E_0}{RT}\right) \tag{2.1}$$

$$k_\infty = A_\infty T^{n_\infty} exp\left(\frac{-E_\infty}{RT}\right) \tag{2.2}$$

Where, k_0, and k_∞ are the low- and high-pressure-limit rate constants with A_0, and A_∞, being their corresponding pre-exponential factors, respectively. T represents temperature, and R is the universal gas constant. n_0, and n_∞ are the low- and high-pressure-limit rate constants' modified Arrhenius expression temperature exponents, and E_0 and E_∞ are their activation energies, respectively. For the unimolecular/recombination reactions, the corresponding composite rate of reaction k takes the form:

$$k = k_\infty \left(\frac{P_r}{1+P_r}\right) F \tag{2.3}$$

Whereas for the chemically activated reactions the composite rate of reaction k is expressed as:

$$k = k_0 \left(\frac{1}{1+P_r}\right) F \tag{2.4}$$

The reduced pressure, P_r, is defined in terms of the concentration of the collider [M] to be:

$$P_r = \frac{k_0[M]}{k_\infty} \tag{2.5}$$

F is a parameter which takes on a different form depending on the formulation adopted. For example, in the common formulation of Troe [78], F captures the pressure and temperature dependence of the colliders through:

$$logF = logF_{cent}\left[1 + \left[\frac{logP_r + c}{n - d(logP_r + c)}\right]^2\right]^{-1} \tag{2.6}$$

Where c = -0.4 - 0.67, $logF_{cent}$, n = 0.75 - 1.271$logF_{cent}$, d = 0.14 and F_{cent} is expressed as:

$$F_{cent} = (1-\alpha)exp\left(-\frac{T}{T^{***}}\right) + \alpha exp\left(-\frac{T}{T^{*}}\right) + exp\left(-\frac{T^{**}}{T}\right) \quad (2.7)$$

The four extra parameters α, T^{***}, T^{*}, T^{**}, are fitting parameters characteristic for each molecule that must be defined in order to represent the fall-off curve.

In the above formulations two alternative means are available to capture the variation in pressure-dependent rates with changes in bath gas molecular composition. One involves having collider-specific low-pressure-limit rates which are included in the kinetics model, in which case during a simulation run an overall rate based on a linear mixing rule weighted by the relative concentrations of bath gases is used [79]. Alternatively, a single rate expression can be used, where the collision broadening factor F_{cent} is determined for a single bath gas, along with relative collision efficiencies for all other colliders relative to that bath gas'. In that latter case the value of M can be adjusted for the different colliders based on collider concentrations $[Y_i]$ through the collision efficiency parameter m_{y_i} to arrive at an effective concentration $[M]$, as follows (referred to as a Troe-embedded "mixing rule"):

$$[M] = \sum m_{y_i}[Y_i] \quad (2.8)$$

However, it should be noted that for the single bath gas formulation the broadening factor F, can vary significantly with bath gas composition, which introduces errors. Burke and Song [46] recently compared a few different mixing rules, different pressure-dependent formulations, including Troe and PLOG expressions, as well as the common software limitations and the associated error with each of the aforementioned formulations. The authors indicated that based on the various forms of expressing the rate law, inaccuracies from 50% to 2000% can be expected for the example reaction $H+O_2(+M)= HO_2(+M)$; hence it is critical to choose the appropriate formulation for expressing reaction rates [46]. The 2000% error was attributed to a single PLOG collider-agnostic rate expression. Burke and Song [46] also proposed improved modified linear and non-linear mixing rules; they illustrated multiple collider-specific reaction rates combined with their mixing rules, can bring about substantial structural enhancements resulting in increased model accuracy. Burke and song noted that most simulation software including, Chemkin-Pro, currently do not accommodate these mixing rules and in the meantime speculated that a single Troe expression with its embedded mixing rule, is a reasonably accurate approach. However, the performance of the Troe-embedded mixing rule was not evaluated vis-à-vis multiple collider-specific expressions with linear mixing rule [46].

The overall effect of increasing pressure on hydrocarbons kinetics has been investigated by multiple groups. Zhukov [21] studied simple alkanes' high-pressure combustion experimentally and developed kinetic models covering a wide temperature range of 850-1700 K and pressures of up to 530 atm, and stated that pressure plays a critical role in high-temperature oxidation. Zhukov noted that above 1200 K, going from pressures of 10 atm to pressures above 50 atm, radical recombination rates increase significantly as well as the termolecular hydroperoxyl formation reaction, $H+O_2(+M)=HO_2(+M)$. With the latter leading to HO_2 becoming the dominant radical that abstracts hydrogen from the fuel to form H_2O_2. The authors concluded, that this reaction followed by hydrogen peroxide's collision enhanced decomposition to two OH radicals, significantly contributes to radical pool build-up in the induction period [21]. Zhukov et al. also showed that at low temperatures reactions with higher activation energies slow down, resulting in the formation of peroxides (RO_2) and peroxi-hydroperoxyalkyls ($OOC_nH_{2n}OOH$), through O_2 addition to alkyl radical (R), and hydroperoxyalkyl radicals (QOOH), followed by decomposition to much smaller products. The authors also indicated that the oxidation of RO_2 and QOOH to form $OOC_nH_{2n}OOH$ increases with pressure to improve the kinetics, and for high alkanes (pentane and higher) the low temperature boundary of NTC region moves to higher temperature. Simultaneously, the authors showed that the high temperature boundary at increased pressure does not shift significantly, combination of which results in disappearance of NTC region at pressures above 200 atm [21]. Another study by Beerer et al. [50] conducted ignition delay time measurements of alkanes at intermediate to low temperatures at 7, 9 and 15 atmospheres and concluded that the ignition delay times scaled with a $P^{-1.0+/-0.1}$ dependency, where P is the absolute pressure. They also concluded that the overall activation energy very slightly decreased with increasing pressure [50]. Hashemi et al. [63] recently conducted CH_4 oxidation experiments highly diluted in N_2 in a rapid compression machine (RCM) and flow-reactor covering a temperature range of 700-1250 K, and a pressure range of 15-100 bar with equivalence ratios of 0.06-19.7. The authors proposed a high-pressure kinetic model with emphasis on peroxide chemistry [63]. The authors also used high level theory to improve thermochemical properties of CH_3OO and CH_3OOH, as well as rate constants for abstraction of $CH_3OOH+CH_3=CH_3OO+CH_4$ and $CH_3OH+CH_3=CH_3O+CH_4$. They noted that further research is desirable on reactions of CH_3O and CH_3OO due to severe model underprediction of the concentration of CH_3OH [63]. The authors found onset of methane reaction to be 725-750 K at 100 bar, and slightly dependent on stoichiometry, based on flow reactor studies in which low-pressure gas chromatographer (GC) speciation of the product gas was carried out. The study reported ignition delay time measurements of 1-100 ms, which were decreasing with increasing pressure and temperature in the range of 15-80 bar and 800-1250 K. The authors concluded based on sensitivity analyses that the methylperoxyl (CH_3OO) chemistry requires further work to improve model prediction [63].

Pryor et al. [14] recently performed shock tube ignition delay times at low pressures, in highly diluted CO_2 mixtures, and utilized GRI-Mech 3.0 and AramcoMech 1.3 to predict the pressure and temperature dependence of ignition delay times. The authors showed the two models predict different responses to variations in temperature at 300 bar, with GRI-Mech predicting a nearly monotonic increase in ignition delay times with a decrease in temperature, whereas AramcoMech 1.3 predicts significant non-monoticity at 1000-1300 K [14]. Also the study shows the onset of this behavior at 10 atm is shifted by about 300 K to 1000 K, instead of 1300 K, for simulations using AramcoMech 1.3. This illustrates both the variations of the two models' high-pressure IDT predictions, as well as their estimated onset of chemistry switch to a low-temperature chemistry, which for AramcoMECH 1.3 occurs at higher temperatures with increases in pressure [14].

2.5 Kinetics effects of H_2O dilution

H_2O is known to be a strong collider and stabilizer, and its contributions to combustion kinetics is viewed to be potentially large. A recent comprehensive paper by Klippenstein [79], looking at chemical modeling of combustion systems, analyzed the rate of the second most important chemical reaction in combustion chemistry i.e. $H+O_2(+M)=HO_2(+M)$. The author reviewed all experimental and theoretical rates in the literature associated with this reaction, and concluded that there was good agreement among the estimates, but noted that the rates were for the most part obtained with Ar as the bath gas, with a few considering N_2 and H_2 as the third body collider [79]. It was added that expanding the analysis to consider H_2O as a collider, is crucial due to H_2O's high concentrations coupled with its enhanced efficiency making it a key contributor to HO_2 stabilization [79]. The authors also noted that they are in the process of evaluating the rate of $H+O_2(+H_2O)=H+O_2(+H_2O)$, and have suggested that preliminary results show that H_2O has substantially enhanced collision efficiency, but not as enhanced as commonly conceived [79].

Glassman and Yetter [6] also noted that the presence of small quantities of water significantly enhances the kinetics of CO oxidation, as it provides new pathways for oxidation through buildup of the radical pool, culminating in two separate mechanisms developed; one for bone dry CO oxidation and another for moist CO oxidation. This suggests there may also be unknown chemical effects of H_2O at the high-pressure conditions relevant to this study.

Different studies have been conducted to evaluate the effect of moisture addition to gas turbine inlets for improved combustion performance and emissions control, also known as Humid Air Turbines (HAT) [80, 81]. These sources referenced studies indicating H_2O addition reduces NOx emissions by more than a factor of two compared to N_2 due to decreases in flame temperatures. Mazas et al. [80] investigated the effects of CO_2 and H_2O addition on premixed oxy-fuel combustion mixtures through laminar conical flame speed experiments, at atmospheric pressures with heated inlet unburnt mixtures at 373 K, at equivalence ratios of 0.5 to 1.5, and with steam molar fractions ranging from 0 to 0.45 (relative to reactive portion of mixture). However, the experiment involved further dilution of combustion mixture with H_2O, where the added H_2O did not replace any of the unreactive diluents, and observed a quasi-linear decrease in flame speed with increase in H_2O and CO_2 diluent, even at high dilution rates. The authors observed a larger reduction in burning velocity of $CH_4/O_2/N_2/H_2O$ than those of $CH_4/O_2/CO_2/H_2O$ for similar flame speeds, when the steam mole fraction was increased, and recommended further work to allow understanding of the measurements. The authors also determined that GRI-Mech 3.0 predictions were inadequate for weakly diluted, in H_2O and CO_2, CH_4/O_2 mixtures [80]. More recently, Donohoe et al. [81] investigated the effect of steam dilution on ignition of H_2, syngas and natural gas blends highly diluted Ar, through shock tube ignition delay time measurements at 730-1140 K, equivalence ratios of 0.5, 1 and 2.0. The authors investigated H_2O dilution rates of 0%, 10% and 30% of the fuel by volume, and noted that significant changes in the thermal properties of the mixtures affect reactivity, whereas no chemical effect of the steam addition was observed for the majority of mixtures.

For mixtures with pure CO, in-line with Glassman and Yetter [6] the presence of H_2O was observed to strongly influence reactivity, which was suspected by the authors to be due to formation of relatively reactive OH radicals [81].

A recent text by Turanyi et al. [82], commented on the influence of bath gases on H_2O_2 decomposition; they stated that species that have similar molecular energy levels to the rovibrationally excited H_2O_2 molecules, like H_2O_2 and H_2O, have larger collision efficiencies, whereas noble gases have typically small collision efficiencies. The general trend is that larger molecules with more excitable rovibrational frequencies have larger collision efficiency factors [82]. Baulch et al. [25] noted that there are few measurements that specifically address third-body efficiency factors, and these values can be quite uncertain. The third-body efficiency factors can also be considered as temperature-dependent [25], but even an approximate parameterization is hindered by the lack of appropriate experimental data, and the effective third-body concentration continuously changes during the course of a reaction according to the change of the mixture composition.

Very recently Shao et al. [83] conducted shock tube IDT experiments of stoichiometric 3%H_2 with 3.9-13.8%H_2O content at approximately 15 bar and1264-1376 K. This is to date the largest concentration of H_2O explored. The goal of the study was to investigate the rate of $H+O_2(+M)=HO_2(+M)$, which is one of the most important reactions in combustion chemistry and is pressure-dependent. They confirmed that the relative collision efficiency of H_2O to Ar is 23, which is in slight contrast to the Klippenstein's abovementioned speculation that H_2O's substantially enhanced collision efficiency, may not be as enhanced as commonly perceived [79]. As such, for effective modelling of systems with bath gases containing large concentrations of H_2O, there is a need for experimental validation data, that are able to distinguish the impact of such strong colliders. Moreover, from a modelling stance it is important to capture the collider-specific temperature- and pressure-dependent contribution of H_2O to reaction rates, when available. This is particularly important for reactions involving species with similar molecular energy levels such as H_2O_2 and H_2O.

2.6 Kinetics effects of CO_2 dilution

Recent modeling and experimental research campaigns conducted by the University of Central Florida (UCF) investigated the impact of CO_2 dilution rates of (0.3-0.85 mole fractions) on reaction kinetics in the range of 6-31 atm, 1300-2000 K, through ignition delay time measurements and kinetic model predictions using AramcoMech 1.3 and GRI-Mech 3.0 [13]. The authors concluded that CO_2 slows down the kinetics of ignition and this retardation is well-predicted by both mechanisms at near atmospheric pressures [13]. At 30 atm the authors demonstrated that GRI-Mech underpredicts the ignition delay times whereas AramcoMech 1.3's predictions were reasonable [13]. In another study, Koroglu et al. [15] conducted shock tube experiments at lower CO_2 dilutions 0-60%, at 1577-2144 K and 0.53-4.4 atm, and equivalence ratios of 0.5, 1, and 2, and indicated that at low pressures both of the aforementioned mechanisms generally underpredicted the activation energy at low pressures and high temperatures. Also it was shown that ignition delay time measurements using pressure measurements were unreliable in the presence of high CO_2 concentrations, as shock bifurcation took place. Therefore, Schlieren spike caused by deflection of laser was used to detect the arrival of the reflected shock, and measurement of CH* emission was used to determine the onset of ignition [15]. The authors also noted that the uncertainty with ignition delay time measurements was higher than that of the pre-ignition CH_4 decay measurements through laser absorption. As such, CH_4 decay measurements was adopted as the metric of choice for the evaluation of the impact of CO_2 dilution on kinetics, due to ignition delay times' insufficient resolution [15]. The authors also showed that the concerns with non-ideal boundary layer build up, as a consequence of bifurcation, can be circumvented, and argued that as the core section of post-shock region constitutes most of the flow area, and this portion will have the targeted temperature and pressure, T_5 and P_5 [15]. Furthermore, if the calculated P_5 (i.e. calculated through shock velocity measurements, at the driven end of the shock tube) matches the measured pressure prior to ignition, it means ignition has taken place after the bifurcation has passed over [15].

From a chemical standpoint Masunov et al. [84] recently conducted a quantum chemical study investigating the effects of supercritical CO_2 (sCO_2) on combustion kinetics, and further alluded to the unknown effect of sCO_2 on combustion kinetics. The study investigated three reactions, $H_2CO+HO_2=HCO+H_2O_2$, $HO_2+HO_2=H_2O_2+O_2$, $CO+OH=CO_2+H$, and concluded that CO_2 catalyzes all three reactions [84]. In the first two, CO_2 stabilizes transition states to direct hydrogen abstraction by HO_2, and reduces both reactions' energy barrier. As for the third above noted reaction, the authors concluded that a new reaction pathway is possible through a covalently bonded CO_2 and OH species, having a lower energy barrier, hence promoting the reaction in the reverse direction, i.e. CO_2 reacting with H. This reaction may hence negatively impact the main high temperature chain branching reaction, $H+O_2=OH+O$, by competing for hydrogen atoms, hence effecting the combustion kinetics [84].

Pryor et al. [14] also recently conducted a study in which simulations were performed using GRI-Mech 3.0 and AramcoMech 1.3 for various concentrations of CO_2 (0-89.5%) as co-diluent with Ar (0-89.5%) at 300 bar and 1000-2000 K. The authors demonstrated the two models produce significantly different results both in terms of response of ignition delay times to both variations in CO_2 concentration and for the same concentrations at different temperatures, demonstrating the need for characterizing the impact of CO_2 on both kinetics models and diagnostics tools' performance and efficacy [14]. The authors also compared the results of two diagnostics tools, namely the side-wall versus peak emissions as the metric for ignition delay times, as competing means for tuning and validation, and concluded that depending on the diagnostics employed, conflicting conclusions can be made [14]. They showed the simulated delay times at 85% CO_2, with unreactive balance of Ar, lied in between the two diagnostics' measurements, with the measurements differing by 100 microseconds. This leads to the conclusion that the choice of diagnostics may adversely impact the predicted accuracy of the models to be tested and that any subsequent parameter tuning may be completely erroneous depending on the choice of diagnostics [14].

Recently, Shao et al. [16] conducted shock tube IDT experiments of $H_2/O_2/CO_2$ at 37-311 atm and $CH_4/O_2/CO_2$ mixtures at 27-286 atm at 1045-1578 K with CO_2 concentrations of 77.5-86.17%. Shao et al. [16] concluded CH_3 and HO_2/H_2O_2 kinetics play a significant role in CH_4 and H_2 systems respectively. The authors also evaluated the performance of FFCM-2018 and Aramco mechanisms, and showed that while the models performed well in predicting the majority of the experimental data they needed improvements for lean H_2 mixture at 39 atm. Shao et al. [16] also investigated the impact of deviation from ideal gas law on calculations of ideal reactor pressure conditions, and showed that a maximum deviation of 2% at 472 atm with pure CO_2 can be expected, while utilizing ideal EOS to calculate post-reflected-shock-passage reactor conditions, P_5 and T_5.

Hargis and Petersen [54] also recently conducted shock tube experiments of oxy-CH_4 at equivalence ratio 0.5, at 1 and 10 atm, and 1450-1900 K, at CO_2 dilutions of 0-75%, with a balance of nitrogen. The authors reported higher uncertainties for ignition delay time measurements at high CO_2 dilutions. However, despite these higher uncertainties they concluded that the CO_2 slowed down the kinetics observed through longer ignition delay measurements [54]. The uncertainties were attributed to reflected-shock bifurcation, high fluid motion, suppressed pressure traces, and increase in pressure noise. The authors also emphasized the use of end-wall pressure measurements to reduce the reliance on side-wall counterparts, which may be exposed to the fluid flow underneath the bifurcation foot [54]. In addition, the authors showed that this bifurcation effect is strongly dependent on the mixture value of the specific heat, and independent of the post reflected shock temperature, T_5, with very little dependence on post reflected shock pressure P_5, consistent with Pryor et al.'s observations [13, 54]. Furthermore, a brief numerical study was conducted to identify the chemical and third-body collisional effect of CO_2, using the AramcoMech 1.3 mechanism, which concluded that high dilutions of CO_2 had negligible chemical effect and a slight collisional effect on changing the activation energy [54]. It should, however, be noted that correct evaluation of the chemical effect of a species through such simulation exercise assumes that the mechanism employed includes all the reactions, with the appropriate rates, and pressure dependencies. As noted by Wong et al. [70] the latter dependence also impacts the participation of CO_2 as a third-body collider, as some of the pressure-independent reactions in such models may in fact exhibit pressure dependencies at higher pressures which may not have been captured by the mechanism under study. Hargis and Petersen [54] also reported that CO_2's higher specific heat suppresses the ignition energy release, introducing difficulties in analysis and interpretation of the results, due to subdued pressure spikes at high CO_2 concentrations.

It should also be noted that mechanisms, such as AramcoMech 1.3, utilize PLOG expressions for some reaction rates. While these expressions are able to capture the pressure dependence of a single bath gas very well, they do not discriminate the sometimes significantly different third body colliders through incorporation of a single third body agnostic expression. In contrast, Gilbert et al.'s and Troe's [78, 76] or SRI international's, as illustrated by Stewart et al. [85], rate expression formulations with multiple collider efficiencies or collider-specific rate expressions are likely the better choice to effectively capture bath gas collider effects.

Chapter 3

Modeling Approach

Model structure is critical to the success, practicality, and expandability of a predictive chemical kinetics model. As most pressurized combustion technologies generally have dual- or multi-fuel variants, their designs demand models that can predict the kinetics of hydrocarbons of different sizes. Due to the changes in chemistry with HC size, temperature, pressure, equivalence ratio, and combustor bath gas compositions, the model generation approach needs to be focused, versatile and expandable. To ensure manageability of scope and quality, a hierarchical expandable model structure, for high temperature and pressure oxy-combustion is targeted in this study. The work involves developing two building block oxidation mechanisms, one for H_2/CO (syngas) and the other for CH_4, that capture the effect of presence of up to 45% H_2O and 45% CO_2 at high pressures and temperatures more accurately than incumbent reference models. Nevertheless, the approach is devised with the long term vision of its expansion to model larger HC fuels, as well as the more complex chemistries of NOx, SOx, and soot, in the presence of up to 65% H_2O and 45%CO_2.

Due to the unexplored conditions of this study, it is important to identify a reliable means for predicting the relevant species and reactions, a priori. Determination of species thermodynamic properties, their reaction pathways, and associated rates based on the atoms present in the fuel, oxidizer and bath gases involved, are fundamentally possible through first principles means. However, this approach quickly becomes computationally impractical as the number of species and reactions increase. Hence a compromised approach that ensures practicality with acceptable fidelity is sought. Moreover, deviations from the better characterized high-pressure high-temperature combustion kinetics are expected due to the combined effects of high pressures and high concentrations of H_2O and CO_2, which can be both chemical and non-chemical in nature. Thus, the modelling approach must also be versatile enough to capture and enable estimation of the ramifications of these deviations when possible. Figure 3 maps the reach and implications of the unique conditions under study, on the chemistry and kinetics involved as well as their potential limiting effect on the validity of common combustion modelling assumptions.

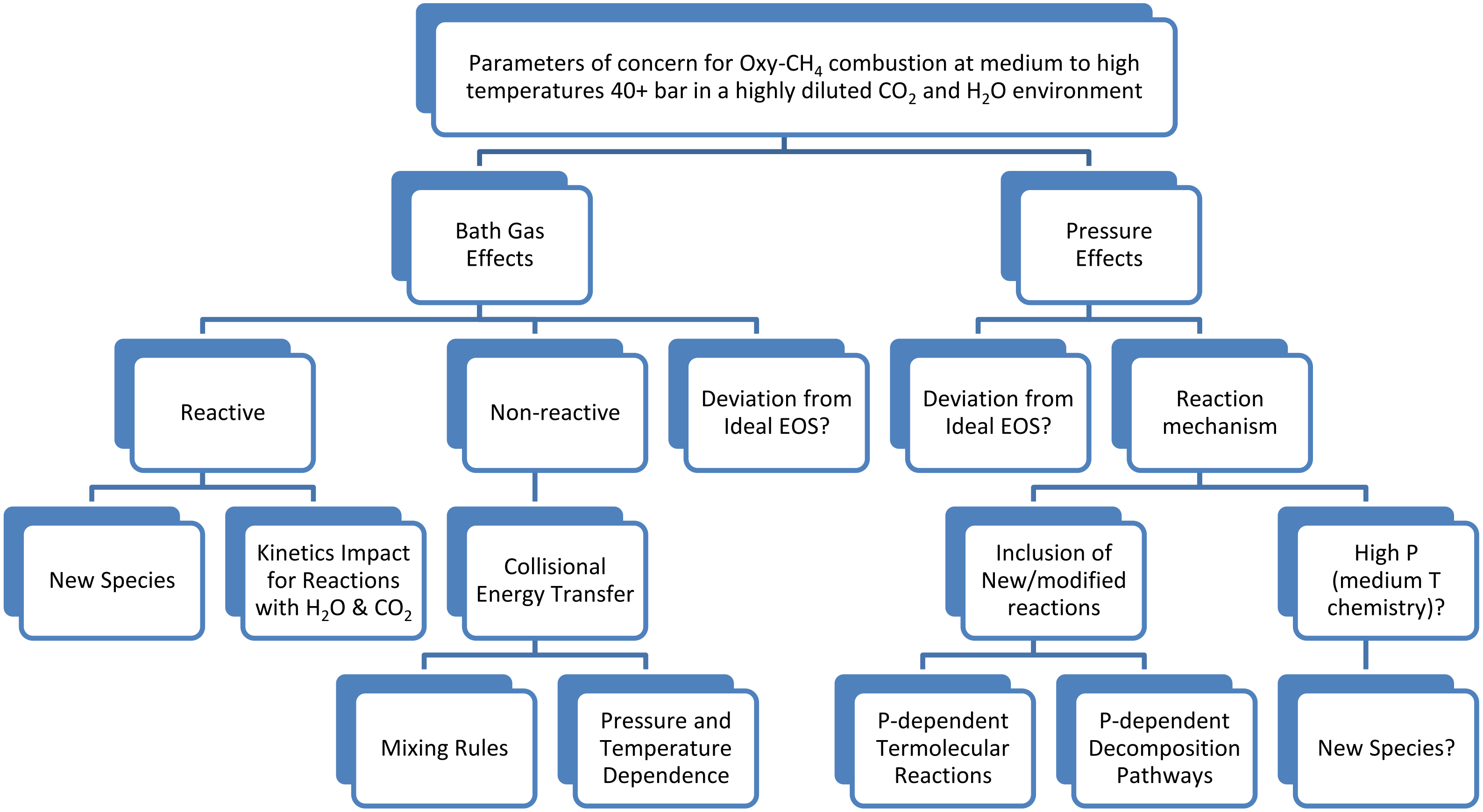

Figure 3: Combined potential effects of oxy-fuel and pressurized combustion with hot wet flue gas recycle

The effects are grouped into two main categories, namely, those pertaining to high pressures, and those related to having high CO_2 and H_2O bath gas concentrations. These effects may sometimes be a consequence of both, such as the increased likelihood of deviations from ideal gas behavior increases with pressure, as well as with higher concentrations of larger polyatomic CO_2 and polar H_2O molecules. These manifest themselves in many ways, from challenging the suitability of using an ideal gas equation of state to their impact on pressure dependency of thermochemical properties ignored in thermochemical properties databases used in both shock tube and combustion codes. Similarly, the impact of bath gases and pressure also affect the kinetics, by changes in relative rates of reactions, their molecularity, dominant reaction pathways, as well as new chemistries involving generation of new species and their reactions previously ignored. To better capture and characterize these effects, a model development and validation methodology is devised, with its workflow depicted in Figure 4. The methodology includes four clusters of activities, grouped in yellow dashed rectangles, which involve:

1- Selection of a reference base model for H_2/CO oxidation, with proven superior performance, as well as surveying the literature to collect improved elementary reaction rates and species thermochemical properties, as well as using an automatic mechanism generator, RMG [74] to detect potentially pressure-dependent reaction rates.

2- Construction and validation of the H_2/CO sub-mechanism, which involves:

    a. Untuning the reference model's adjusted kinetic parameters;

    b. Modifying the reference model to include the updated kinetics model parameters;

    c. Evaluating kinetics model's performance, identifying potential opportunities for improvements, through sensitivity analyses; and,

    d. Updating the target rate parameters either by adopting alternative untuned rates from the literature, or through conducting a parametric study to determine and incorporate an appropriate level of tuning within the uncertainty bounds of the reported rate. These last three steps are repeated until an improved H_2/CO mechanism has been developed.

3- Expansion of H_2/CO sub-mechanism to include the more complex chemistry of CH_4's oxidation. This involves selection and adoption of additional sub-mechanisms e.g. methane, formaldehyde, ethylene, etc., from a comprehensive and well accepted model from the literature (AramcoMECH 2.0 [86]). This is followed by evaluation of its performance, and identification of the critical kinetics parameters in reproducing shock tube experimental data.

Similar to the previous step, this is an iterative process involving sensitivity analyses, identifying high impact parameters, and using RMG to assess potential inclusion of missing species and/or important pressure-dependent reactions [74]. This activity is carried out to improve model fidelity, to obtain a model with improved performance relative to incumbent one(s) in the literature.

4- The last grouping of activities, carried out in parallel to the model development work, involves conducting experimental test campaigns to fill the critical knowledge gap associated with validation data for both the H_2 and CH_4 mechanisms in presence of high H_2O and CO_2 concentrations. It involves shock tube ignition delay time data generation for the targeted unique mixtures and conditions at hand. These data augment existing relevant shock tube data in the literature to enable the model development and validation targets of this work.

The proceeding sections of this chapter discuss the main elements of the model generation approach. Initially, the rationale behind the selection of the base H_2/CO model is provided. A brief comparison of the available thermochemical databases is presented, along with the chosen database for this work, and sensitivity analysis means available to evaluate impact of uncertainties or errors in these values on the overall model performance. A section is then dedicated to pressure-dependent reaction rates and automatic mechanism generation tools utilized. The section details the role of the automatic generation program (RMG), its capabilities and limitations pertinent to this work, as well as pros and cons of different formulations used for expressing pressure-dependent reaction rates in the mechanism. A critical evaluation of candidate reaction rates is performed and the collated rate parameters for both the H_2/CO as well as key ones pertaining to CH_4 oxidation chemistry are discussed. The simplified conservation equations applicable to shock tube reactors that are solved are then discussed. Finally a description of kinetics sensitivity analysis tools utilized and the in-house codes developed to streamline analysis, and post-processing of Chemkin-Pro data that enable one-to-one comparison of target experimental measurements with their model predicted values is provided.

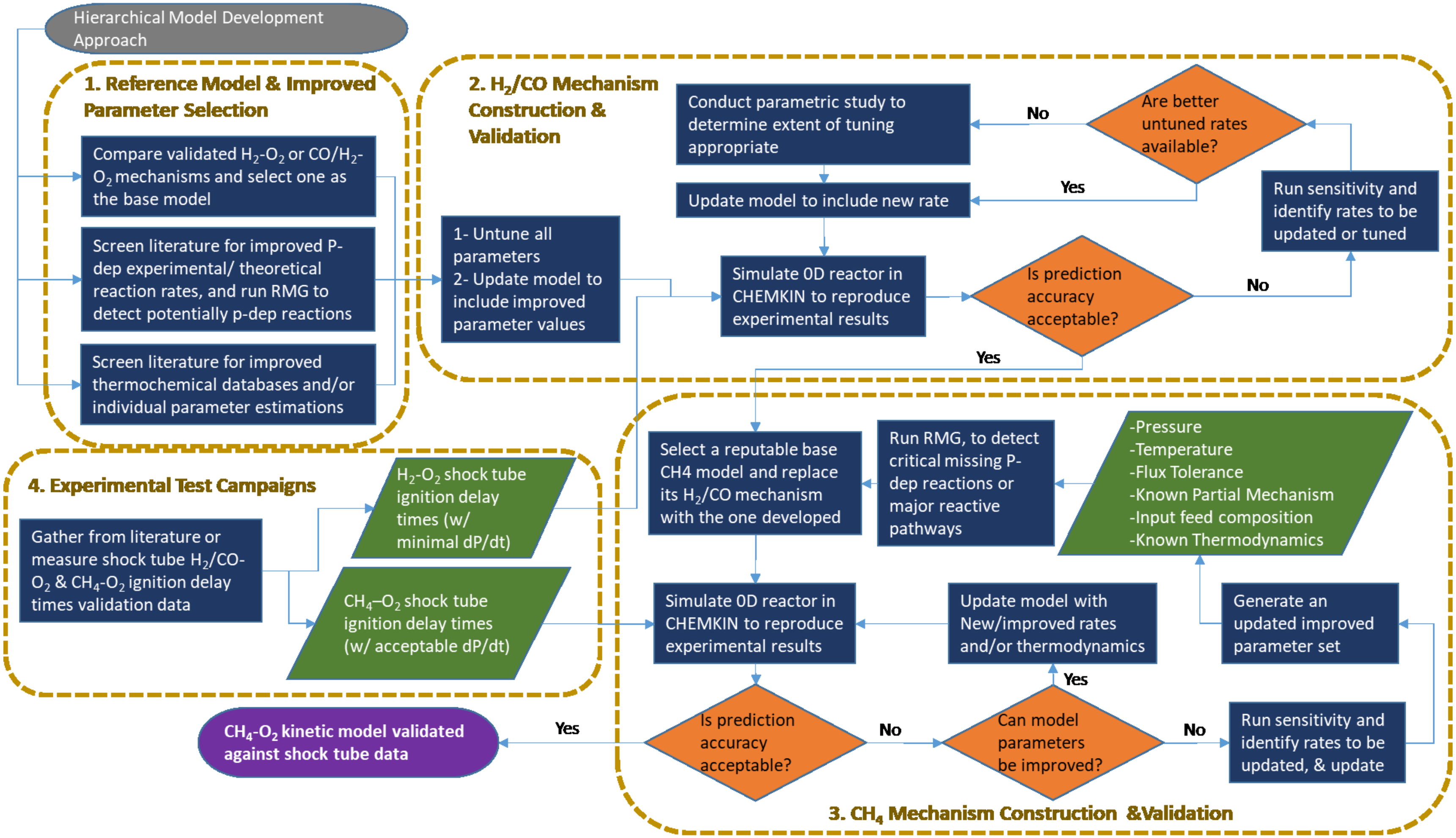

Figure 4: Model construction and validation approach

3.1 Base mechanism selection

Upon review of the literature, three high temperature chemical kinetics models were short-listed and their proposed reaction rate parameters were compared. The candidate models are detailed in the following reference publications:

1) An experimental and detailed chemical kinetic modeling study of hydrogen and syngas mixture oxidation at elevated pressure by Keromnes et al. [28];
2) Comprehensive H_2/O_2 Kinetic Model for High-Pressure Combustion by Burke et al. [30]; and,
3) An improved H_2/O_2 mechanism based on shock tube/laser absorption measurement, by Hong et al. [29];

Subsequently, each reaction noted in the above studies, were traced back to their cited references, to determine whether any uncited optimization or parameter tuning were performed. Also any errors or discrepancies identified in rate parameters were confirmed through communications with the corresponding authors of the studies. All hydrogen oxidation reactions were compared against relevant recent studies, reviewing the rate of the reaction under study in addition to major references including:

1) Li et al.'s 2004 highly cited hydrogen oxidation mechanism model [39];
2) Baulch et al.'s 2005 high temperature combustion kinetics rates database [25]; and,
3) Foundational Fuel Chemistry Model Version 1.0 (FFCM-1) [87].

It should be noted that many H_2-O_2 models, including Burke et al. [30], have been based on Li et al.'s work [39]. FFCM-1 is the result of a long-term ongoing research collaboration between Stanford University's Professor Hai Wang research group and Gregory Smith of SRI International [87]. FFCM-1 also includes estimated uncertainties for each reaction, and provides estimates for collision partner efficiencies for a wide range of common combustion species for each reaction, the latter being adopted from the GRI-Mech [87].

In this study, when uncertainties and any collision partner efficiencies were missing, recommended values of FFCM-1 were adopted.

Based on conditions of minimal reaction parameters tuning, candidate models' choice of reaction rates and approach towards proper depiction of pressure-dependent reactions, Keromnes et al.'s [28] well-validated CO/H_2 oxidation high–pressure mechanism was deemed as a suitable candidate for the "base model". The kinetics model was validated for 1-70 bar, 914-2220 K and equivalence ratios from 0.1 to

4.0, using ignition delay time data from shock tube and RCM experiments, as well as flame speed measurements using the spherically expanding flame method at 5 and 10 atm. While, Keromnes et al.'s [28] mechanism is validated for a wide range of conditions that encompass the temperatures and equivalence ratios considered for the research at hand, its validity for predicting combustion kinetics in bath gases with high H_2O and CO_2 concentrations have not been examined.

The alternative H_2/O_2 mechanism candidate mechanism by Burke et al. [30], includes the same 19-step H_2-O_2 reaction mechanism, with three of the reactions' rates provided in their reverse direction relative to Keromnes et al.'s [28]. The model also targeted high-pressure combustion, and while the validation range is not explicitly stated, ignition delay times at up to 87 atm from Petersen et al.'s study [60] were cited in the comparative model evaluation plots of the study.

The third model considered, Hong et al. [29], focused on high-temperature combustion, and ignored Chemkin-Pro's shortcoming at the time, i.e. lacking a mixing rule, resulting in over prediction of pressure-dependent reactions' overall rates when they were expressed with multiple collider-specific rates for a single reaction. The authors chose to include the $H+HO_2=H_2O+O$ reaction in their mechanism, resulting in a 20 reaction mechanism. However, the model did not target pressurized combustion.

Olm et al.'s comparisons of 19 hydrogen mechanisms in 2014 [38], and 16 syngas mechanisms in 2015 [42], included the abovementioned models and ranked Keromnes et al.'s H_2/CO [28] as the best performing hydrogen mechanism and the 2nd best performing syngas oxidation mechanism in predicting a multitude of experimental model validation targets. Konnov's [31] recent treatment of Keromnes et al.'s model [28] as the benchmark mechanism in his development of the latest H_2/O_2 mechanism is a further testament of the reliability of Keromnes et al.'s mechanism. Two recent studies by Konnov [31] and Alekseev et al. [32] have also looked at H_2/O_2 combustion kinetics more recently, and are used for comparative purposes in this work. Konnov [31] incorporated Varga et al.'s [38] optimization results of Keromnes et al.'s model to argue for inclusion of alternative rate parameters.

Finally, while the first building block of the mechanism sought in this work targets H_2 oxidation, an H_2/CO mechanism is needed as one of the dominant bath gases in oxy-fuel combustion is CO_2. CO_2's potential decomposition renders inclusion of a CO oxidation mechanism necessary hence the base model must include a CO sub-mechanism. Consequently, for this work Keromnes et al.'s model [28] is selected as the reference base mechanism. However, in-line with Alekseev et al.'s [32] , FFCM-1

[87] and Hong et al.'s [29] 20-step H_2/O_2 mechanisms, the 19-step H_2/O_2 mechanism of Keromnes et al. is augmented to include an additional step $H+HO_2=H_2O+O$. All parameter tunings implemented by Keromnes et al. [28] were untuned, and the resulting 20-step mechanism constitutes the untuned reference syngas mechanism for more detailed scrutiny and evolvement in this work.

3.2 Thermochemical properties

Detailed combustion kinetics models commonly contain a few to 100s of species, which interact in 10s-1000s of reactions. It is critical to determine the appropriate thermochemical property values, whether for a zero-dimensional simulation of the chemistry, or 3D CFD simulation of a combustor. This is due to the fact that these thermochemical properties directly impact the heat release, kinetics, and flame temperatures. These properties are species enthalpies and entropies of formation, as well as heat capacities, enthalpies and entropies, at different temperatures. These properties are directly used to calculate equilibrium constant and the reverse reaction rates of every reaction, and are necessary to determine the temperature of the mixture, the heat generated and absorbed, which impact reaction rates as well as the extent of their progression. In combustion thermodynamics literature while there are studies focusing on individual species thermochemical property determinations, there are databases that contain large collections of thermochemical properties, three of which are noteworthy as they are publically available, highly cited, and are being improved and updated often. The first is a database originally developed by Professor Alexander Burcat for species involved in HC combustion and air pollution with recommended values for ideal gas thermochemical data in NASA's polynomial format [72]. The database was published, i.e., Burcat and Ruscic [73], by the U.S. Department of Energy. An updated 2500 species version of the database is currently being maintained by Dr. Elke Goos from the German Aerospace Center's (DLR) Institute of Combustion Technology [88]. This database is also updated and checked periodically against another database called Active Thermochemical Tables (ATcT), developed by Dr. Branko Ruscic from the U.S. Argonne National Laboratory (ANL) [89]. ATcT includes internally consistent enthalpies of formation at 0 K and 298 K for 1727 species [89]. While ATcT provides the error bars for their data, DLR's Elke Goos database does not include precisely quantified uncertainty bounds, but often reports results of qualitative consistency checks with ATcT, as well as polynomial fit uncertainties when available. The third source is from the US department of commerce's National Institute of Standards and Technology (NIST) Chemistry WebBook. The website contains high accuracy “thermophysical Properties of Fluid systems” for a limited number of species [90], as well as Shomate equation parameters for polynomial expressions of many species [91].

In terms of accuracy while NIST’s high accuracy thermochemical data and ATcT are highly reliable, the former is very limited in terms of the species and the ranges of conditions it covers. ATcT includes properties for a larger set of species, but these properties are limited to enthalpies of formation at 0 and 298 K, as such cannot be directly and effectively implemented into kinetics model [89]. NIST’s Shomate equation parameters [91] while practical is not as up-to-date as the publicly available version of Burcat-DLR’s database, although it is from 2009. Alternatively for this study the thermochemical databases collected and reviewed by the National University of Ireland Galway’s (NUIG) Combustion Chemistry Centre is adopted instead [28, 92]. This is due to the fact that recently NUIG’s Burke et al. [93] conducted a comprehensive review of the literature including thermochemical properties from NIST, ATcT databases among others, to assemble a reliable database of high accuracy thermochemical properties, in addition to improving the group additivity methods they use to predict thermochemical properties for new species as well as those that do not have reliable thermochemical properties in the literature [93]. Their database includes molar entropies and enthalpies of formation, as well. As such AramcoMECH 2.0 [86], and AramcoMECH 3.0 [92] thermodynamic databases are referred to for thermodynamic property values used in this work.

In terms of representation, the common 7-coefficient NASA polynomial format is used, with values of thermochemical properties expressed as functions of temperature for two common ranges of low and high [73]. In this representation thermodynamic data are fitted for the two temperature ranges and are pinned at their connecting temperature which is commonly near 1000 K [73]. This enables smooth transition across the ranges and precludes discontinuities or jumps in properties.

These coefficients are embedded into the following polynomial forms [73]:

$$\frac{C_P^\circ}{R} = a_1 + a_2T + a_3T^2 + a_4T^3 + a_5T^4 \tag{3.1}$$

$$\frac{H_T^\circ}{RT} = a_1 + \frac{a_2T}{2} + \frac{a_3T^2}{3} + \frac{a_4T^3}{4} + \frac{a_5T^4}{5} + \frac{a_6}{T} \tag{3.2}$$

$$\frac{S_T^\circ}{R} = a_1 \ln T + a_2T + \frac{a_3T^2}{3} + \frac{a_4T^3}{4} + \frac{a_5T^4}{5} + a_7 \tag{3.3}$$

$$\frac{G_T^\circ}{RT} = \frac{H_T^\circ}{RT} - \frac{S_T^\circ}{R} = a_1(1 - lnT) - \frac{a_2T}{2} - \frac{a_3T^2}{6} - \frac{a_4T^3}{12} - \frac{a_5T^4}{20} + \frac{a_6}{T} - a_7 \tag{3.4}$$

Where, R is the universal gas constant, T is temperature, and C_P°, H_T°, S_T°, G_T° are the standard constant-pressure molar heat capacity, molar enthalpy, molar entropy and molar Gibbs free energy, respectively. a_1-a_7 are the NASA polynomial fitting parameters for representing these thermodynamic properties as a function of temperature.

Common temperature ranges involve 200-1000 K and 1000-6000 K, totaling 14 parameters per each species. However, it should be noted that the above expressions for $\frac{H_T^\circ}{RT}$ and $\frac{S_T^\circ}{R}$ can be deconstructed into two components, as the above expressions is obtained by integrating the following two equations:

$$H_k^0 = \int_{298}^{T_k} C_{pk}^0 dT + H_k^0(298) \tag{3.5}$$

$$S_k^0 = \int_{298}^{T_k} \frac{C_{pk}^0}{T} dT + S_k^0(298) \tag{3.6}$$

Where the subscript k designates species k, and $H_k^0(298)$ and $S_k^0(298)$ designate the standard enthalpy and of formation and entropy at 298 K [43]. However, the constants of integration a_6R and a_7R in equations 3.5 and 3.6, are derived from $H_k^0(298)$ and $S_k^0(298)$, respectively. Lastly, the equilibrium constant K_C or K_P are calculated using $\frac{G_T^\circ}{RT}$ in terms of concentration or pressure. For example K_C is represented as:

$$K_C = (RT)^{-\Delta v} exp\left(\Delta a_1(1 - lnT) + \frac{\Delta a_2 T}{2} + \frac{\Delta a_3 T^2}{6} + \frac{\Delta a_4 T^3}{12} + \frac{\Delta a_5 T^4}{20} + \frac{\Delta a_6}{T} - \Delta a_7\right) \quad (3.7)$$

As such the defining parameters for thermodynamic properties definition are $H_k^0(298)$, $S_k^0(298)$, and C_{pk}^0.

3.3 Deviations from ideal gas assumptions

Thermodynamic properties in combustion simulations as well as calculations embedded in shock tube reactor temperature (T_5) determinations relevant to this work, are commonly assumed to be pressure-independent. Uncertainty bounds are available for enthalpy of formation in some data bases evaluated at low pressures, such as those in ATcT. However, accurate uncertainties for entropy and heat capacities are more scarce [93]. While at high temperatures and low pressures thermodynamic properties do not exhibit pressure-dependence, such assumption of ideality may become questionable at low to intermediate temperatures and high pressures for some species. Deviations from pressure independency are commonly increased by the presence of polar molecules such as water, and more so when they are in their supercritical state. Hence, thermodynamic property deviations for H_2O serves as an appropriate worst-case-scenario example among common bath gases to bound the impact of such deviations. Moreover, as H_2O is the largest constituent among the unique bath gases in the experimental test campaigns, next to the near-ideal Ar, it is subjected to scrutiny and its thermo-physical property deviations are analyzed in detail in this section. Figure 5 illustrates the superimposed pressure-independent C_p of H_2O used in this study, with NIST REFPROP's high-accuracy C_P data for different isobars, as well as with Aspen HYSYS's Peng-Robinson equation of state for multiple isobars. It can be seen that while NIST REFPROP and the NASA polynomials' estimations converge at high temperatures of above 1700 K, depending on the parameters chosen for the cubic Peng-Robinson equation of state, it can mispredict C_P at combustion relevant temperatures. Moreover, at low to intermediate temperatures (e.g. 750-1000 K) and high pressures (e.g. 40 bar) the polynomials tend to under predict C_P of H_2O, and such deviation increases with pressure, to up to a factor of 1.5-3 at 300 bar.

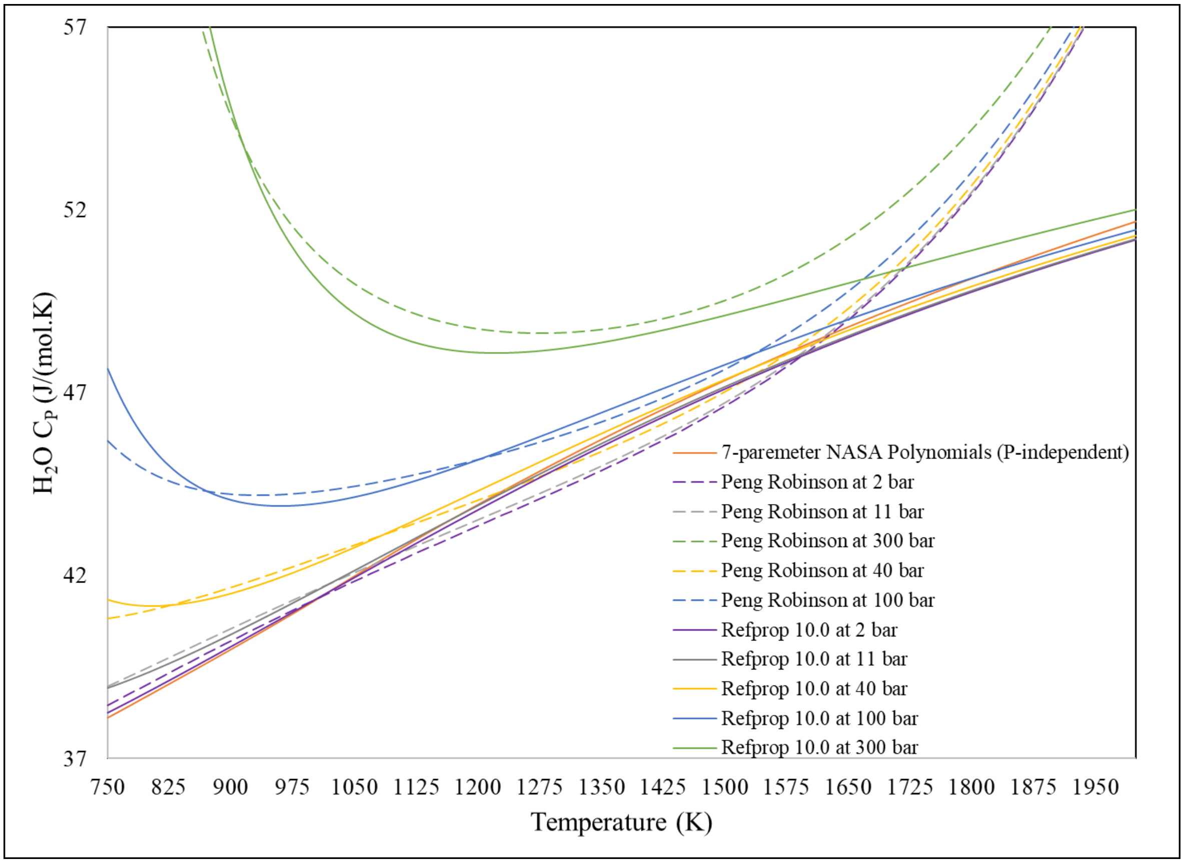

Figure 5: C_P of H_2O as a function of temperature using the 7-NASA Polynomials (pressure independent) [28], superimposed with the same property generated at pressures of 2-300 bar using NIST REFPROP 10.0 (solid lines) and using Peng-Robinson equation of state

Fortunately, potentially problematic combinations of very high pressures and intermediate temperatures are not encountered in this work, nor for any of the validation data collected from the literature. As this conclusion and the rationale behind it is important to the modelling work, it is elaborated on here. In arriving at this conclusion the following were considered:

1- Low temperatures near 750 K are only encountered at the incident shock conditions of the experimental shock tube validation data which, are commonly not at very high pressures. For instance in the 34-53 bar shock tube experimental test campaigns conducted in this study the lowest temperatures were 749 and 806 K at pressures of 11.6 and 10.7 bar for the high-pressure H_2 and CH_4 test campaigns respectively. Hence, a comparison of the C_P estimated using NASA polynomials with that of NIST REFPROP's isobar at 11 bar suggests a worst-case-scenario deviation of -2.2% for T_2=749 K from the high-pressure H_2 campaign, which quickly diminishes to -1.4% at 806 K for the lowest temperature experiment of the CH_4 high-pressure test campaign. A similar analysis conducted for CO_2 shows that at the aforementioned conditions C_p errors of -0.46 to -0.8% were observed. As such the positive uncertainty bounds of H_2O and CO_2's C_ps, were increased to +1.8% and +0.63% to capture these deviations. These adjusted uncertainty bounds were then implemented into shock tube P_5 and T_5 determinations' error bars. It should also be noted that the highest H_2O concentrations in these tests were 46%, hence, due to the presence of other bath gases, mainly Ar or N_2 as high as 50%, the effect of such uncertainties are proportionally reduced.

2- The higher pressures encountered in experiments, P_5 pressures near 40 bar, are at higher temperatures of 1106 to 1898 K, for high-pressure H_2 and CH_4 experimental test campaigns. NASA Polynomials and NIST REFPROP 10 data appear to cross over at the mid point of the aforementioned temperature range, see Figure 5. To reduce the uncertainties, use of real gas equation of state has also been proposed. While such implementation may seem reasonable, validity of such real gas equations of states and their mixing rules are uncertain. Both of which, need to be validated for binary to quaternary mixtures of Argon, N_2, CO_2, and H_2O for their successful implementation. For example while the tuned Peng-Robinson equation of state from Aspen-HYSYS, designed for methane and hydrocarbons, and includes binary interaction coefficients for species like H_2O it is not designed for such high H_2O concentrations (45%), and as such could mispredict its pure component molar heat capacity at higher temperatures, as observed from Figure 5.

3- Lastly the appropriate source for the truest value of C_P for H_2O was also critically reviewed. While NIST's REFPROP estimates, which are based on virial equations of state and validated by experimental data, are deemed reliable, so are the likes of ASPEN-HYSYS's NBS Steam fluid package which exclusively targets steam properties. While the estimates from the two disagree at some conditions, they follow a similar trends at the lower temperature end, see Figure 6. Trends of C_p data from NBS Steam however, exhibit an opposite concavity to both NASA polynomials and NIST REFPROP at the high temperatures exceeding ~1200 K. However, as C_P determinations using NASA polynomials are expected to be accurate at low pressures and Aspen-HYSYS's NBS steam's deviations increase at these conditions, in contrast to NIST REFPROP's, the latter is deemed to be a more suitable benchmark. As such to calculate error bars for experimental data, and for evaluating suitability of the NASA polynomials estimates for such combustion applications, NIST REFPROP data were referred to.

3.4 Sensitivity analysis to thermochemical properties

From equations 3.1 - 3.7 it can be concluded that, among the thermodynamic parameters, enthalpy and entropy of formation at 298 K serve as two anchoring parameters. Other thermodynamic property determinations, including those that directly impact chemical equilibria and kinetics, rely on these two parameter values. As such, in-line with Metcalfe et al.'s [22] approach any ignition delay times' sensitivities to thermodynamic parameters were evaluated by adjusting these anchoring parameters values. In this approach the temperature independent terms, namely a_6 and a_7, in equations 3.5 and 3.6 are adjusted by 2%, based on discussed maximum uncertainties for H_2O in section 3.3. This brute force sensitivity involves a two-step process:

1. evaluate $H_k^0(298)$ and $S_k^0(298)$ using equations 3.2 and 3.3,respectively; and
2. apply the intended fractional adjustments to these values which, when divided by R, provide the adjusted corresponding values of a_6 and a_7 to be used in IDT simulations. [22]

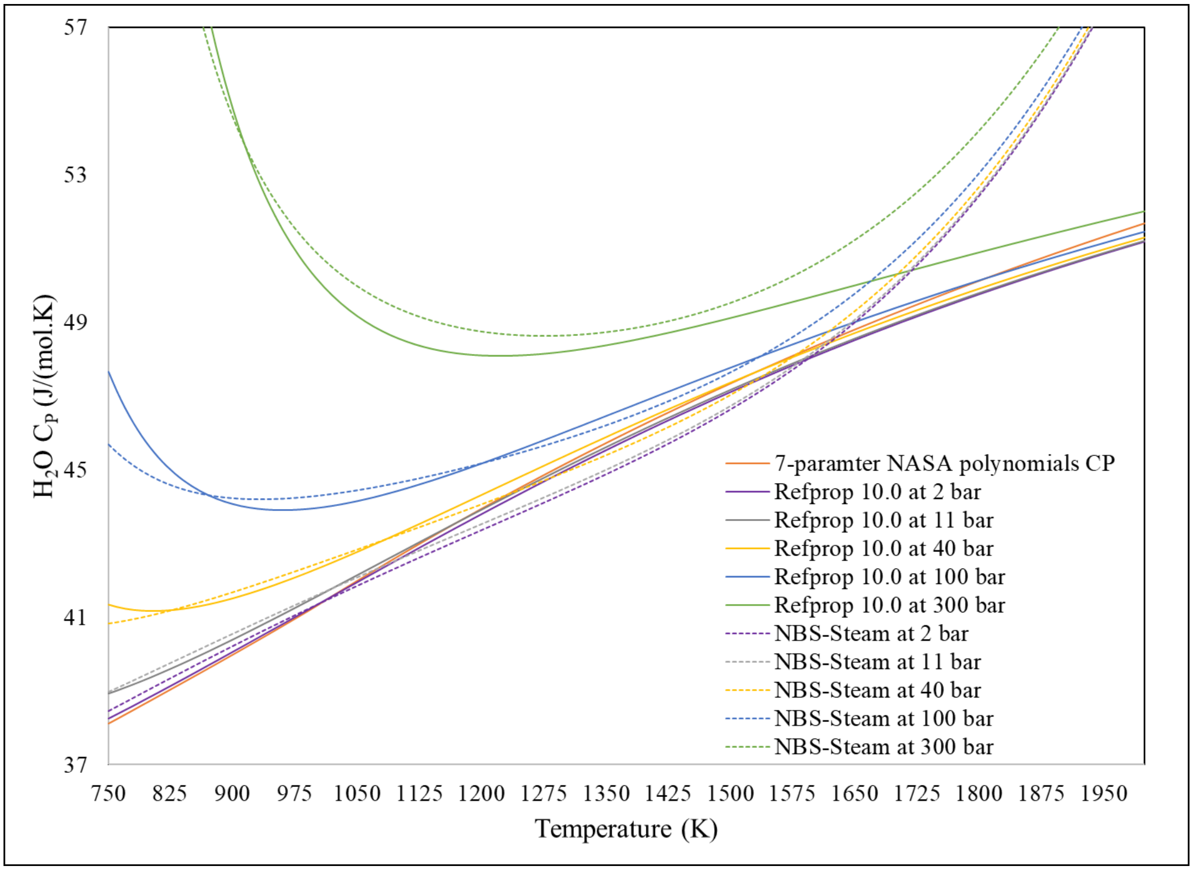

Figure 6: C_P of H_2O as a function of temperature using the 7-NASA Polynomials (pressure independent) [28], superimposed with the same property generated at pressures of 2-300 bar using NIST REFPROP 10.0 (solid lines) and using Aspen-HYSYS's NBS steam equation of state

3.5 Pressure-dependent reaction rates and automatic mechanism generation

Pressure-dependent reactions are an important feature of mechanisms involving kinetics of high-pressure oxy-combustion that include high concentrations of strong colliders like H_2O and CO_2.

Most combustion mechanisms are constructed by collecting reaction sets from the literature, which conventionally do not consider effects of pressure on rate parameters. As such it is important to have a means to detect whether a reaction's molecularity can change with pressure at the targeted conditions. To this end, an automatic reaction mechanism generator, called RMG [74], is utilized in this work to assess what reactions are relevant, and whether they may be pressure-dependent. RMG has a pressure-dependent mechanism generation mode, in which it estimates phenomenological pressure-dependent rate coefficients of reaction networks, using simplified RRKM-based calculation methods [74, 94]. Due to the large degree of simplification applied, while the estimated reaction rates may not be accurate enough for direct implementation into the model, RMG is used to identify potentially pressure-dependent reactions. These reactions may already exist in mechanisms but in the form of a low- or high-pressure-limit rate, which may not be accurately incorporating the potential impact of bath gases. It should be noted that in this work to increase the fidelity of the rate estimations, RMG's "Reservoir State Method" modelling option was selected and the maximum energy grain sizes of the micro-canonical rate determinations were reduced [94].

As discussed in sections 2.3 and 2.6, pressure-dependent effects change with temperature, pressure and bath gas composition. As RMG's automatic mechanism generation is only driven by the input reactor conditions, while using reaction families or classes, such as H-abstraction reactions, to explore all possible reactions that could take place temporally between reactants and intermediates, it is considered an "unbiased" mechanism generation means. That is the mechanism generated is not limited to reaction sets and species observed in the literature, rather it assesses all possible reaction pathways on the fly and retains significant ones using a rate-based model enlarging algorithm [74]. This is crucial as the conditions being explored in this work are novel and as such the mechanism development work must not be limited in any way in the process of constructing its mechanism. Hence, in this work, simulations are conducted in RMG to identify significant reactions and species which should be considered for inclusion in the model development work. The literature is then explored to identify more appropriate rates for these reactions, and/or quantify the extent of their pressure dependency relevant to the target conditions of this work.

Once the species and significant pressure-dependent reactions have been identified, appropriate means that enable capturing the relative effectiveness of different bath gas molecules in chemically activating or thermalizing excited adducts through collisions are needed. These relative effects could result in order of magnitude differences in the rates of reactions involving excited adducts, such as HO_2* in $H+O_2+(M)=HO_2(+M)$. As such it is imperative to be able to segregate and characterize them effectively, for example, when strong colliders such as H_2O is present in place of a weak collider like He in significant concentrations. Section 2.4, showed this requirement limits the choice of appropriate formulations to represent these reactions to those of the likes of Gilbert et al.'s [77] or Troe's [76], and SRI international's as illustrated by Stewart et al. [85]. Alternative formulations in the form of Chebyshev polynomials (utilized in RMG) and PLOG commonly fall short in delineating collider-specific rate differences either due to combustion code limitations or scarcity of collider-specific rates represented using such formulations.

Upon closer examination of Troe formulations [77, 76], single and multiple expression alternatives of the original formulations were introduced in Section 2.4. These are compared and discussed here using the example reaction H+O_2+(M)=HO_2(+M) with a hypothetical case containing two bath gases Ar and H_2O.

The "single expression" formulation, utilizes the low- and high-pressure limit rate expressions of a base bath gas, commonly Ar or N_2. It adopts the base bath gas's center broadening factor as outlined by equations 2.6 and 2.7, with its specific temperature dependency, e.g. Ar's, and applies it to all other colliders. In reality each collider has its own center broadening factor as discussed in Section 2.4 with its own distinct pressure and temperature dependency. To distinguish the enhancing or retarding effect on the rate associated with different bath gas compositions the single expression's collision efficiencies which are multipliers of the low-pressure limiting rate of the base bath gas are the adjustable feature of this treatment. The reaction-specific collision efficiencies, ε_k, that capture the relative enhanced contribution of species k to that of the base bath gas, are incorporated into the $[M]$ term of the general reduced pressure expression, see equation 2.5. For the case study reaction H+O_2(+M)=HO_2(+M) in the presence of two bath gases H_2O and Ar, equation 2.5:

$$P_r = \frac{k_0[M]}{k_\infty} \tag{2.5}$$

incorporates the $[M]$, which from equation 2.8 is:

$$[M] = [X_{H_2O}].\varepsilon_{H_2O} + [Ar].\varepsilon_{Ar}$$

and, the resulting P_r for the mixture of the sample bath gases becomes:

$$P_{r\,mix} = \frac{k_{0,Ar}\left([X_{H_2O}].\varepsilon_{H_2O} + [X_{Ar}].\varepsilon_{Ar}\right)}{k_\infty} \tag{3.8}$$

Substituting the above expression into equation 2.3, the combined pressure-dependent rate of this reaction for the mixture is expressed by:

$$k_{Mix} = k_{\infty}\left(\frac{\frac{k_{0,Ar}\left([X_{H_2O}].\varepsilon_{H_2O} + [X_{Ar}].\varepsilon_{Ar}\right)}{k_{\infty}}}{1 + \frac{k_{0,Ar}\left([X_{H_2O}].\varepsilon_{H_2O} + [X_{Ar}].\varepsilon_{Ar,i}\right)}{k_{\infty}}}\right)F_{Ar-combined} \qquad (3.9)$$

Where the broadening factor shared by all colliders has the following pressure dependency [78]:

$$logF_{Ar-combined} = logF_{cent,Ar}\left[1 + \left[\frac{logP_{r\,mix} + c}{n - d(logP_{r\,mix} + c)}\right]^2\right]^{-1} \qquad (2.6)$$

With Ar's center broadening factor $F_{cent,Ar}$, that is applied to other collider's. Moreover, $F_{cent,Ar}$ has its own temperature dependency through its three to four parameter fitting form [78]:

$$F_{cent,Ar} = (1 - \alpha_{Ar})exp\left(-\frac{T}{{T^{***}}_{Ar}}\right) + \alpha_{Ar}exp\left(-\frac{T}{{T^{*}}_{Ar}}\right) + exp\left(-\frac{{T^{**}}_{Ar}}{T}\right) \qquad (2.7)$$

The disadvantage of the above treatment, as shown by Burke and Song [46], is in the term $F_{Ar-combined}$ and the single collider-specific comprising parameters embedded in its calculations, namely: α_{Ar}, ${T^{***}}_{Ar}$, ${T^{*}}_{Ar}$, ${T^{**}}_{Ar}$ which provide a dynamic evolving broadening factor based on reaction rate parameters specific to Ar as well as reactor conditions. Burke and Song state that the differences in calculated rates due to pressure and temperature dependencies of Ar vs. H_2O for the reaction $H+O_2(+M)=HO_2(+M)$ can be ~20% and ~40%, respectively [46]. Moreover, Dove et al. [95] also discuss the inadequacy of the linear mixture rule applied when combining the low-pressure limiting rates, of the likes of $k_{0,Ar}$ and k_{0,H_2O} which could introduce up to an additional 10% of error in the overall reaction rate.

Alternatively, to address the issues of temperature and pressure dependence differences brought about by the "single expression" treatment, the "multiple expression" formulation of Troe is available in Chemkin-Pro. This formulation involves multiple low-pressure-limit expressions specific to colliders, which share a common high-pressure limiting rate. It incorporates the collider-specific center broadening factors, e.g. $F_{cent-Ar}$ and F_{cent-H_2O}, each with their distinct temperature and pressure dependencies. For the example reaction the formulation for reduced pressure becomes:

$$P_{r,H_2O} = \frac{k_{0,H_2O}[X_{H_2O}]}{k_{\infty}}$$

$$P_{r,Ar} = \frac{k_{0,Ar}[X_{Ar}]}{k_\infty}$$

Subsequently, the collider-specific pressure-dependent rate constants are:

$$k_{H_2O} = k_\infty \left(\frac{\frac{k_{0,H_2O}[X_{H_2O}]}{k_\infty}}{1 + \frac{k_{0,H_2O}[X_{H_2O}]}{k_\infty}} \right) F_{H_2O}$$

$$k_{Ar} = k_\infty \left(\frac{\frac{k_{0,Ar}[X_{Ar}]}{k_\infty}}{1 + \frac{k_{0,Ar}[X_{Ar}]}{k_\infty}} \right) F_{Ar}$$

The pressure dependency of collider-specific broadening factors take the form:

$$logF_{Ar} = logF_{cent,Ar} \left[1 + \left[\frac{logP_{r\,Ar} + c}{n - d(logP_{r\,Ar} + c)} \right]^2 \right]^{-1}$$

$$logF_{H_2O} = logF_{cent,H_2O} \left[1 + \left[\frac{logP_{r\,H_2O} + c}{n - d(logP_{r\,H_2O} + c)} \right]^2 \right]^{-1}$$

Where:

$$F_{cent,Ar} = (1 - \alpha_{Ar}) exp\left(-\frac{T}{T^{***}{}_{Ar}}\right) + \alpha_{Ar} exp\left(-\frac{T}{T^{*}{}_{Ar}}\right) + exp\left(-\frac{T^{**}{}_{Ar}}{T}\right)$$

$$F_{cent,H_2O} = (1 - \alpha_{H_2O}) exp\left(-\frac{T}{T^{***}{}_{H_2O}}\right) + \alpha_{H_2O} exp\left(-\frac{T}{T^{*}{}_{H_2O}}\right) + exp\left(-\frac{T^{**}{}_{H_2O}}{T}\right)$$

While the “multiple expression” formulation enables implementation of collider-specific rate parameters, up until recently, the associated overall rates could be overestimated up to a factor equal to the number of collider-specific rates, as discussed by Burke et al. [30], Burke and Song [46], and Konnov [31]. However, application of a linear mixture rule for combining the collider-specific expressions, embedded recently into Chemkin-Pro has solved this issue [96]:

$$\boldsymbol{R_{mix} = R_{H_2O} X_{H_2O} + R_{Ar} X_{Ar}} \tag{3.10}$$

As such, the uncertainties associated with single expression treatment, i.e., unable to capture collider-specific pressure and temperature dependencies, are anticipated to be larger than those of the “multiple expression”. This of particular relevance to oxy-fuel combustion bath gases which contain large concentrations of H_2O and CO_2. Burke and Song’s investigation [46] appears to suggest that deviations from linear mixing rule, such as that of 3.10 at a pressure of 1000 bar, may results in a limiting worst case scenario errors of up to 45-60% [46]. This worst case scenario is also limited to the case of combined presence of a strong collider H_2O in Ar, and is also limited to H_2O concentrations in the range of 10-20% [46]. This uncertainty reduces with decreasing pressure, when bath gases have similar collision strengths, and when H_2O concentrations are <10% and >20% for the reaction $H+O_2(+M)=HO_2(+M)$. As $H+O_2(+M)=HO_2(+M)$ is one of the very sensitive pressure-dependent reaction in kinetics mechanisms of HCs, the errors noted above also are expected to represent the worst case scenario on overall reactivity as well. Moreover, while the authors provide alternative mixture rules [46], they are not accommodated in current combustion codes, such as in Chemkin-Pro used in this study.

Until they do become available, to ensure the effects of such limiting case errors do not result in mechanisms with erroneous rate parameters being proposed, an approach has been devised in this work, which serves as a practical work around. This approach focuses on the selection of appropriate model validation data to limit uncertainties brought about by linear mixture rule noted by Burke and Song [46]. That is, when overall reactivity is highly sensitive to a pressure-dependent reaction rate involving multiple expression treatment, model validation data selected must avoid the abovementioned limited conditions, when they are known a priori. As an example, for reaction $H+O_2(+M)=HO_2(+M)$ which fits this category, selecting model validation data that avoids the combination of water concentrations of 10-20% and high pressures such as >60 bar, significantly reduces the peak errors discussed. For example, for validation data with 10-20% H_2O concentrations if the pressure of the validation data is limited to <16 bar (e.g. Shao et al.’s used in this study [83]) peak error in pressure-dependent rate constant for the mixture, reduces to 0-25%, from 45-60%. Alternatively, when limiting the water concentrations to less than 5% or larger than 30%, while targeting pressures lower than 100 bar (conditions of the new validation data generated in this work), the errors drop to within 0-20%.

Moreover, for applications where such conditions are encountered, in the absence of more advanced mixing rules Burke and Song recommend the single expression treatment [46]. This is due to the treatment’s slightly different linear mixing rule incorporated into the reduced pressure formula, which may reduce maximum errors [46]. As such, an alternative model is provided in this manuscript, with single expression treatment of all pressure-dependent rates when Troe formulation [78] is used.

However, in the absence of such conditions the model with multiple expression treatment of pressure-dependent rates is the more versatile choice. Also when combustion codes evolve to accommodate the new mixture rules proposed by Burke and Song [46], mechanisms with multiple expression treatment of Troe pressure-dependent rate [78] will be undisputedly the superior choice at all conditions. Hence in this work more attentions is dedicated to the model developed which incorporates the "multiple expression" treatment of pressure-dependent reaction rates.

3.6 H_2/CO oxidation mechanism

Table 1 summarizes the proposed H_2/CO sub-mechanism, CanMECH 1.0, with "multiple expression" treatment of pressure-dependent reactions using Troe formulations, when available. The table also provides a comparison of the model rate parameters proposed relative to common recent mechanisms. The model consists of 8 species, i.e. H_2, O_2, H, O, OH, HO_2, H_2O, H_2O_2, and 20 elementary chemical reactions.

It should also be noted that, relative to the reference model of Keromnes et al.'s [28] hydrogen sub-mechanism, the rate parameters of reactions R2, R4-R6, R8- R10, R12- R15, R17 were modified either by untuning them, or including multiple expression representations, or adopting rates from alternative sources, in addition to including R20. Furthermore, R8, was considered to be potentially in the fall-off regime in contrast to the other models investigated in this work, hence a pressure-dependent rate was included for this reaction. This was to ensure the potential effect of strong colliders present in this work are properly captured in the fall-off regime of this reaction. Similarly for the CO sub-mechanism, rate parameters for reactions R21, R23, R25-R30 were modified relative to the base model of Keromnes et al.'s [28]. It is noteworthy that for R25, a pressure-dependent reaction rate was implemented to further enable this mechanism to better capture the potential effects of strong colliders. The following subsections provide the rationale for the rate parameters selected in the proposed mechanism. Only the rate parameters that were either of critical importance to the mechanism, or differed from Keromnes et al.'s model [28], or could potentially be pressure-dependent are discussed.

Table 1: CanMECH 1.0 Syngas Mechanism

ID	Reaction	A	n	E_A	UF	T range	Ref.	Keromnes et al. [28]	Burke et al. [30]	Hong et al. [29]	FFCM-1 [87]	Alekseev et al. [32] + Konnov [31]	UF ref.
1	$H + O_2 = O + OH$	1.04E+14	0	1.531E+04	1.1	1100-3370	[40]	=	=	=	=	=	[40]
2	$O + H_2 = H + OH$	3.82E+12	0	7.949E+03	1.6	298-3300	[25]	[97]	=	=	=	[97]	[25]
		8.79E+14	0	1.918E+04	1.6	298-3300	[25]	NA	=	=	=	NA	[25]
3	$OH + H_2 = H + H_2O$	4.38E+13	0	6.991E+03	1.2	902-1518	[98]	=	[99]	[25]	[99]	[25]	[98]
4	$OH + OH = H_2O + O$	2.67E+06	1.82	-1.65E+03	1.4	200-2000	[100]	[97] rev	[25]	[101]	[25]	[31]	[100]
5	$H_2 + M = H + H + M$	4.58E+19	-1.4	1.0439E+05	3	600-2000	[102]	=	=	=	=	=rev*	[102]
	Relative to N_2: $\varepsilon_{He} = 0.83$, $\varepsilon_{CO2} = 3.8$, $\varepsilon_{CO} = 1.9$, $\varepsilon_{Ar} = 0$, $\varepsilon_{H2} = 0$, $\varepsilon_{H2O} = 0$						[28]						
	$H_2 + H_2 = H + H + H_2$	8.61E+17	-0.7	1.0439E+05	3	600-5000	[102]	NA	=	=	=	=rev	[102]
	$H_2 + H_2O = H + H + H_2O$	8.61E+19	-1.1	1.0439E+05	5	600-2000	[102]	NA	=	=	=	=rev	[102]
	$H_2 + Ar = H + H + Ar$	5.84E+18	-1.1	1.0439E+05	2	600-5000	[102]	NA	=	=	=	=rev	[102]
6	$O + O + M = O_2 + M$	6.2E+15	-0.5	0E+00	3	2000-10000	[24]	=	=	=	=	[103]	
	Relative to N_2: $\varepsilon_{He} = 0.83$, $\varepsilon_{H2} = 2.5$, $\varepsilon_{H2O} = 12$, $\varepsilon_{CO2} = 3.8$, $\varepsilon_{CO} = 1.9$, $\varepsilon_{Ar} = 0$, $\varepsilon_{O2} = 0$												
	$O + O + Ar = O_2 + Ar$	1.9E+13	0	-1.79E+03	3	200-4000	[24]	NA	=	=	=	NA	[25]
	$O + O + O_2 = O_2 + O_2$	8.0E+19	-1.5	0E+00	3	2000-10000	[24]	NA	NA	NA	NA	NA	[25]
7	$O + H + M = OH + M$	4.7E+18	-1	0E+00	5	300-3000	[24]	=	=	=	=	[104]	[25]
	Relative to N_2 : $\varepsilon_{He} = 0.75$, $\varepsilon_{CO2} = 3.8$, $\varepsilon_{CO} = 1.9$, $\varepsilon_{Ar} = 0.75$, $\varepsilon_{H2} = 2.5$, $\varepsilon_{H2O} = 12$												
8	$H + OH (+M) = H_2O (+M)$	2.51E+13	0.234	-1.14E+02	2	300-3000	[105]	[39]	[106] rev	[106] rev	[106] rev	[106] rev	[105]
	Ar Low Pressure Limit	3.1E+20	-1.527	3.68E+02	2	300-3000	[105]	NA	NA	NA	NA	NA	[105]
	For Ar: $F_{cent} = 0.72, T^{***} = 1.00E-30, T^{*} = 1.00E+30, T^{**} = 1.00E+30$												
	Relative to Ar : $\varepsilon_{He} = 1.1$, $\varepsilon_{H2} = 3$, $\varepsilon_{O2} = 1.5$, $\varepsilon_{N2} = 0$, $\varepsilon_{H2O} = 14$, $\varepsilon_{CO2} = 3.8$, $\varepsilon_{CO} = 1.9$,						[105]						
	N_2 low pressure limit	4.53E+21	-1.81	4.99E+02		300-3000	[105]	NA	NA	NA	NA	NA	[105]
	For N_2: $F_{cent} = 0.73, T^{***} = 1.00E-30, T^{*} = 1.00E+30, T^{**} = 1.00E+30$						[105]						
9	$H + O_2 (+M) = HO_2 (+M)$	4.7E+12	0.44	0E+00	1.2	300-2000	[107]	=	=	[44]	=	=	[107]
	N_2 low pressure limit	1.2E+19	-1.2	0E+00	1.12	1000-1400	[83]	[108]	[109]	[44]	[30]	=	[83]
	For N_2: $F_{cent} = 0.5, T^{***} = 1.00E-30, T^{*} = 1.00E+30, T^{**} = 1.00E+30$							[108]	[109]	[44]	[47]	=	
	Relative to N_2 : $\varepsilon_{He} = 0.8$, $\varepsilon_{H2} = 2$, $\varepsilon_{O2} = 0.78$, $\varepsilon_{N2} = 0$, $\varepsilon_{H2O} = 0$, $\varepsilon_{CO2} = 0$, $\varepsilon_{CO} = 1.9$, $\varepsilon_{Ar} = 0$						[107]	[108]	[30]	[109]			
	Ar Low Pressure Limit	7.8E+18	-1.2	0E+00	1.12	1000-1400	[83]x0.88	[44]	[109]	[44]	NA	NA	[83]
	For Ar: $F_{cent} = 0.5, T^{***} = 1.00E-30, T^{*} = 1.00E+30, T^{**} = 1.00E+30$						[107]	[44]	[30]	[44]			
	H_2O low Pressure limit	2.04E+20	-1.2	0E+00	1.24	1000-1400	[83]	NA	NA	[44]	NA	NA	[83]
	For H_2O: $F_{cent} = 0.8, T^{***} = 1.00E-30, T^{*} = 1.00E+30, T^{**} = 1.00E+30$						[107]			[44]			
	CO_2 low pressure limit	4.43E+19	-1.2	0E+00	1.19	1000-1400	[83]	NA	NA	NA	NA	NA	[83]
	For CO_2: $F_{cent} = 0.5, T^{***} = 1.00E-30, T^{*} = 1.00E+30, T^{**} = 1.00E+30$						[107]						
10	$H_2 + O_2 = H + HO_2$	7.395E+05	2.4328	5.3507E+04	2	400-2300	[110]	= x 0.7	=rev x 0.75	=rev	=rev	=	[87]
11	$HO_2 + H = OH + OH$	7.08E+13	0	2.95E+02	2	300-2000	[111]	=	=	=	=	=	[87]
12	$HO_2 + O = OH + O_2$	2.85E+10	1	-7.239E+02	2	300-2500	[30]	[112]	= [113] x 0.6	[25]	[25]	=	[32]
13	$HO_2 + OH = H_2O + O_2$	7.0E+12	0	-1.09E+03	1.67	250-2200	[114]	[115] x 0.85	[115]	[112]	=	=	[114]
		4.5E+14	0	1.093E+04	1.67	250-2200	[114]					=	[114]
14	$HO_2 + HO_2 = H_2O_2 + O_2$	1.03E+14	0	1.104E+04	1.67	300-1283	[116]	[117] x 0.87	[117]	[117]	=	=	[114]

		1.94E+11	0	-1.41E+03	1.67	300-1283	[116]	[117]	[117]	[117]	=	=	[114]
15	H_2O_2 (+M) = OH + OH (+M)	2.0E+12	0.9	4.8754E+04	2	500-1500	[118]	=	=	[105]	=	=	[118]
	AR low pressure limit	2.5E+24	-2.3	4.8754E+04	2	500-1500	[118]	=	=	[41, 119]	=	=	[118]
	For Ar: F_{cent} = 0.42, T*** = 1.00E-30, T* = 1.00E+30						[118]	=F_{cent} = 0.43	=		=	=	[118]
	Relative to Ar : ε_{He} = 1.1, ε_{H2} = 3.7, ε_{O2} = 1.2, ε_{N2} = 0, ε_{H2O} = 0, ε_{CO2} = 0, ε_{CO} = 1.9, ε_{H2O2} = 0						[118]	=	=	[119, 120, 121]	=	=ε_{H2O2}=7.7	[118]
	H_2O low Pressure limit	1.9E+25	-2.3	4.8754E+04	2	500-1500	[118]	=	NA	NA	NA	NA	[118]
	For H_2O: F_{cent} = 0.51, T*** = 1.00E-30, T* = 1.00E+30						[118]	=					[118]
	H_2O_2 low pressure limit	1.9E+25	-2.3	4.8754E+04	2	500-1500	[118]	NA	NA	NA	NA	NA	[118]
	For H_2O_2: F_{cent} = 0.51, T*** = 1.00E-30, T* = 1.00E+30						[118]						[118]
	CO_2 low pressure limit	3.9E+24	-2.3	4.8754E+04	2	500-1500	[118]	NA	NA	NA	NA	NA	[118]
	For CO_2: F_{cent} = 0.43, T*** = 1.00E-30, T* = 1.00E+30						[118]						[118]
	N_2 low pressure limit	3.7E+24	-2.3	4.8754E+04	2	500-1500	[118]	NA	NA	NA	NA	NA	[118]
	For N_2: F_{cent} = 0.43, T*** = 1.00E-30, T* = 1.00E+30						[118]						[118]
16	H_2O_2 + H = H_2O + OH	2E+13	0	3.974E+03	5	300-1000	[24]	=	=	[25]	=	[122]	[24]
17	H_2O_2 + H = H_2 + HO_2	5E+13	0	7.949E+03	5	300-1000	[24]	[122] mod	=	[47]	=	[122]	[24]
18	H_2O_2 + O = OH + HO_2	9.6E+06	2	3.974E+03	3	500 & above	[24]	=	=	3	=	=	[24]
19	H_2O_2 + OH = H_2O + HO_2	1.738E+12	0	3.18E+02	2	280-1640	[41]	=	=	=	=	=	[87]
		7.586E+13	0	7.273E+03	1.3	280-1640	[41]	=	=	=	=	=	[87]
20	HO_2 + H = H_2O + O	1.4E+12	0	0E+00	3	298	[25]	NA	NA	=	=	58	[87]
	CO Sub-mechanism							Keromnes et al. [28]	Li et al. [35]	Hashemi et al. [63]	FFCM-1 [87]		
21	CO+ O (+M) = CO_2(+M)	1.8E+10	0	2.43E+03	10	298-3500	[123]	= x 0.75 + E_A x 0.98	= E_A x 0.98	=	=		[87]
	N_2 low pressure limit	1.4E+21	-2.1	5.5E+03	10	298-3500	[123]	[124] x 0.87	[124]	=	=		[87]
	For N_2: F_{cent} = 1						[87]	=	=	=	=		
	Relative to N_2 : ε_{H2} = 2.5, ε_{Ar} = 0.87, ε_{CO2} = 3.8, ε_{CO} = 1.9, ε_{H2O} = 12							=ε_{He} = 0.7, ε_{Ar} = 0.7	=	ε_{Ar} = 1	=		
22	CO + O_2 = CO_2 + O	2.5E+12	0	4.7693E+04	10	1500-3000	[24]	=	=	[63]	=		[87]
23	CO + OH = CO_2 + H	7.05E+04	2.053	-2.76E+02	1.2	300-2500	[125]	= x 1.29	[35]	[126]	= x 1.29		[87]
		5.76E+12	-0.664	3.32E+02	1.5	300-2500	[125]	NA	NA	NA	=		[87]
24	CO + HO_2 = CO_2 + OH	1.57E+05	2.18	1.794E+04	2	300-2500	[127]	=	[111]	=	=		[127]
25	HCO(+M)=H+CO(+M)	4.93E+16	-0.93	1.973E+04		300-2700	[128]	NA	NA	=	NA		
	Ar low pressure limit	7.43E+21	-2.36	1.939E+04		300-2700	[128]	NA	NA	=	[129]		
	For Ar: α = 0.103, T*** = 139, T*=1.09E4, T**=4.55E3						[128]			=			
	Relative to Ar : ε_{He} = 1.3, ε_{H2} = 2, ε_{O2} = 1.5, ε_{N2} = 1.5, ε_{H2O} = 15, ε_{CO2} = 3, ε_{CO} = 1.5						[130]	ε's mod	ε's mod	=	ε's mod		
26	HCO + O_2 = CO + HO_2	6.92E+06	1.90	-1.37E+03		295-1705	[131]	[132]	[132]	=	[133]		
27	HCO + H = CO + H_2	9.0E+13	0	0E+00	2.5	298-2500	[25]	[134]	[134]	[129]	=		[25]
28	HCO + O = CO + OH	3E+13	0	0E+00	2	300-2500	[25]	[24]	[24]	[112]	=		[25]
29	HCO + O = CO_2 + H	3E+13	0	0E+00	2	300-2500	[25]	[24]	[24]	[112]	=		[25]
30	HCO + OH = CO + H_2O	1.1E+14	0	0E+00	2	296-2500	[25]	[112]	[24]	=	=		[25]
31	HCO + HO_2 = CO_2 + H + OH	3.0E+13	0	0E+00	5		[24]	=	=	=	NA		[24]
32	HCO + HCO = H_2 + CO + CO	3.0E+12	0	0E+00	1.5		[24]	=	=	NA	NA		[24]

Note: Rate constant has units of cm^3/mol/s/cal

LEGEND: “ref”: Reference, “UF”: Uncertainty Factor, “=”: Same rate parameters; “rev”: Reverse rates; “NA”: Not Available

3.6.1 R1: $H+O_2=O+OH$

This chain branching reaction is commonly referred to as the most important reaction in combustion chemistry as well as the characteristic chain branching step due to its central role in kinetics of all HC oxidation. GRI-Mech 3.0 uses this reaction rate as an optimization variable. Keromnes et al. [28] noted that the reaction dominates oxidation of all fuels at high temperatures of larger than 1000 K, and that at temperature below 1000 K it competes with R9: $H+O_2(+M)=HO_2(+M)$.

In terms of pressure dependence, automatic mechanism generation simulations were conducted in this work using RMG, and it identified R1 as being pressure-dependent. This is due to this kinetics involving chemical activation of HO_2 adduct, which can potentially tie its rate to that of R9. Burke et al. [30] investigated this using theoretical calculations and verified it was not noticeably pressure-dependent below 1000 atm. The authors also noted the portion of activated complexes decomposing to OH+O have large excess energy and decompose more rapidly than those responsible for nearly all of the formation of HO_2 through stabilization, as such R1 and R9 can be assumed to be independent, with R1 at the low-pressure limit [30]. More recently Wang et al. [135] used molecular dynamics simulations to evaluate pressure dependence and associated rates of R1 and R9 in the presence of large concentrations of supercritical CO_2 in the range of 1000-2000 K and 100-400 atm. While R1 was shown to be pressure-independent at 100-400 bar the authors noted its rate constant is two orders of magnitude lower than that at ambient pressure [135]. While their conclusions are important, their proposed rates are not considered applicable to this work. This is due to the fact that, the role of large concentrations of sCO_2 and its impacts on the kinetics of R1 is significantly less in this work, as:

1. in the present study, the concentrations of CO_2 anticipated for oxy-combustion systems with wet flue gas recycle is lower, i.e. <50%.
2. the pressures for which the mechanism is being validated at this stage are lower than those targeted by Wang et al.'s [135], and much of the validation data are at pressures below the critical point of CO_2, 31.3 °C, 73.8 bar.

It is however, important to note that as the envisioned pressures for oxy-combustion systems such as those considered in this study can reach pressures of 100-400 bar, understanding the impact of large concentration of H_2O along with smaller concentrations of CO_2, and knowing whether the targeted pressures cross H_2O's critical point, 373.9 °C and 220.1 bar, is imperative before adopting new rate parameters. As such, for the H_2-O_2 sub-mechanism Keromnes et al.'s [28] rate recommended by Hong et al. [40] is kept with a minor correction of the third and fourth significant digit of the activation energy as presented in the source study. This rate is based on Hong et al.'s shock tube measured rate for of H_2 oxidation in Ar at 1100-1530 K, combined with Masten et al.'s [136] OH absorption measurements at 1450-3370 K, producing a combined uncertainty less than 10% for temperatures 1100-3370 K. Also more recently, Wang et al. [137] conducted shock tube and laser absorption of CH_2O with simultaneous measurements of OH and CO, to determine the rate of R1 along with R24. While their rate expressions differed from Hong et al.'s [40], selected for this study, the authors noted the small deviation potentially stems from the localized fit over the limited temperature range of 1332-1685 K. Hence, they concluded it is in agreement with Hong et al.'s suggested rate, covering the wider 1100-3370 K range [40]. The wider range of temperature of the rate adopted here along with its wide adoption and validation by recent studies [28, 30, 29, 31, 87, 137] further confirms the choice made in this work. The estimated uncertainty for this rate is adopted from Hong et al.'s study [40]. This is in-line with the note of caution by [29] stating adjustments to this reactions rate constant may need to be made, as uncertainty in R10: $H+HO_2=H_2+O_2$ rate constant, is one of the sources of uncertainty in this reaction's rate constant.

In summary, in the absence of rates determined based on molecular dynamics simulations in the presence of H_2O and CO_2, similar to those of Wang et al.'s [135], the common consensus among recent studies is to adopt Hong et al.'s [40] rate, which is also the rate of choice in this work.

3.6.2 R2: $O+H_2=H+OH$

For the syngas sub-mechanism at hand the dual rate expression, valid over the temperature range of 298-3300 K with an estimated uncertainty factor of 1.6, recommended by Baulch et al. [25] is adopted. This choice is consistent with those of Burke et al., Hong et al. as well as FFCM-1 [87, 30, 29]. Baulch et al. [25] reviewed the rate of this reaction, building on their earlier review in 1992 [112]. In their earlier study they recommended rate of Sutherland et al. [97] for the temperature range 504-2495 K, adopted by Keromnes et al. [28] and Li et al. [39]. In their more recent review however, Baulch et al. [25] noted that although Sutherland et al.'s [97] previous expression extrapolates well to the more recent high temperature data, in the range of 1713-3532 K, their updated recommended rates improves the fit at the lower temperatures. Consequently, Keromnes et al.'s selection [28] is not maintained in this study. Moreover, ignition delay time sensitivity analyses performed in the range of 950-1250 K for different H_2 and syngas compositions and pressures of 1-40 bar indicate little sensitivity to R2 which diminishes at higher pressures and with increased H_2O content. As such the more inclusive rate of Baulch et al.’s 2005 [25] review is adopted in this study instead.

3.6.3 R3: $OH+H_2=H+H_2O$

Keromnes et al. [28] noted that the flame speeds are very sensitive to this reaction under fuel lean conditions. Rate of production analyses conducted in this study also indicate this reaction is a large contributor to the buildup of H radical pool. Keromnes et al. [28], used Lam et al.’s [98] recommended rate determined by shock heating of H_2 and tert-butyl hydroperoxide (TBHP) diluted in Ar, at 902-1518 K and 1.15-1.52 atm, while measuring UV laser absorption based OH time histories near 306.69 nm. Because Lam et al.’s [98] study is the most quantitative measurement, as noted by the authors, and as Keromnes et al. [28] confirmed the study is in excellent agreement with the previous studies, with improved accuracies, this recommended rate is retained in this work. Alternatively, in-line with Hong et al. [29], Alekseev et al. [32] as well as Konnov [33], Baulch et al.’s [25] recommended rate is also commonly considered. Baulch et al. recommended the rate based on Oldenborg et al.’s study [138], which involved combining their experimental data at 800-1550 K, Davidson et al.’s [139] at 1600-2500 K, and Michael et al.’s [99] along with low temperature studies to arrive at a rate. Michael et al.’s [99] rate by itself serves as another candidate which was derived from experiments at 1246-2297 K as adopted by Burke et al. [30] and Li et al. [39] and FFCM-1 [87]. While these rates, are potential alternates, Lam et al.’s [98] rate is the most recent experimental measurement of this rate, as such it is adopted in this work.

3.6.4 R4: $OH+OH=O+H_2O$

The important role of this reaction on impacting OH radical population, along with R15 $H_2O_2(+M)=OH+OH(+M)$ was noted by Hashemi et al. [63]. Baulch et al. [25] concluded this reaction path to be the more favorable relative to two alternative exothermic channels for OH recombination, i.e. $OH+OH=H_2+O_2$, -R11: $OH+OH=H+HO_2$. Keromnes et al. [28], and Li et al. [39] adopted Sutherland et al.’s [97] rate for the reverse reaction. However, Baulch et al. [25] noted considerable scatter in their adopted rate for the reverse rate of R4, as such in this study an alternative choice was sought. Baulch et al. [25] combined Wooldridge et al.’s [101] high temperature data at 1050-2380 K and Bedjanian et al.’s [140] at 230-260 K and provided a recommended rate for 298-2380 K, which served as the rate of choice in Alekseev et al. [32], Burke et al. [30], and FFCM-1 [87] mechanisms.

Wooldridge et al. [101] conducted shock tube experiments at 1050-2380 K and looked at incident shocks in HNO_3/Ar mixtures in the range 0.18–0.6 atm, and monitored [OH] by time-resolved continuous wave (CW) laser absorption. Baulch et al. [25] noted Wooldridge et al. [101] results are supported by Sutherland et al. [97], as well as other studies. More recently, Hong et al. [41] evaluated the rate of this reaction as a secondary reaction at temperatures larger than 1176 K, and noted that their results were well within the uncertainty limits of Woolridge et al.'s rate for 298-2380 K [101]. However, as Burke et al. [30] noted, Baulch et al.'s [25] predictions closely replicated those of Hong et al. [41], it remains a contender.

Hashemi et al. [63] adopted Sangwan and Krasnoperov's [141] who used a novel approach to distinguish between the two channels and minimize effects of surface reactions performing measurements in temperature range of 295-414 K and pressures of 3 and 10 bar. Sangwan and Krasnoperov [141] then combined the results with Sangwan et al.'s [142] at 298-834 K and 1-100 bar, Bedjanian et al. [140] study, and Wooldridge et al.'s study [101] to obtain a rate constant for 223-2380 K. However, Hashemi et al. [63] noted that recent analysis of Burke et al. [143], and measurements by Bahng & Mcdonald's at 293-373 K [144], and Altinay & Macdonald's at 295-701 K [100], as well as theoretical study of Nguyen and Stanton [145] indicate that rate constant for this reaction may be faster than Sangwan & Krasnoperov [141]. Altinay and Macdonald [100] noted their rate did not agree with Sangwan and Krasnoperov's [141]. They showed that their rate was in perfect agreement with Nguyen and Stanton's [145], and implemented a fit to Nguyen's theoretical data [145] with good agreement with high temperature experimental data of Woolridge [101], as well as Sutherland et al.'s [97], and provided that rate for the full temperature range of 200-2000 K. Konnov [31], recently superimposed Baulch et al.'s [25], Altinay and Macdonald's fit of theoretical data [100], as well as two rates from two optimization studies of Keromnes's H_2/O_2 and syngas mechanisms [28] by Varga et al. [146, 38] and produced a revised rate that is very close to the original studies [31]. Konnov showed that Baulch et al's rate is slightly higher than others at higher temperatures and crosses that of Altinay & Macdonald's at around 1500 K. At lower temperatures while remaining higher than, but with similar curvature to Varga's optimized syngas rate, it is lower with less of a parabolic nature as compared to Varga's optimized H_2 study [146, 38].

In terms of pressure dependence, an RMG simulation suggests a pressure-dependent rate for the reverse H-abstraction. Also IDT sensitivity analysis conducted in the range of 950-1250 K reveals that the sensitivity to this reaction increases with pressure and more so above 10 bar, and also with increased

H_2O concentration, which is important to the study at hand. However, a review of the literature, other than Nguyen and Stanton [145] who noticed in their theoretical study that fall-off may be expected, but focused on the low-pressure-limit rate determination, only revealed Sangwan et al.'s [142] as a potential option. However, while Sangwan et al.'s [142] study covered a pressure range of 1-100 bar their rate spanned low temperatures of 298-834 K. Moreover, their fall-off parameters pertained to the week collider He and enhanced collision efficiencies for H_2O and CO_2 were not provided. These features along with the disagreement reported between Altinay and Macdonald's [100] with that of Sangwan and Krasnoperov's [141] which incorporated Sangwan et al.'s [142] into their rate, this pressure-dependent rate was not implemented in this work. Instead, Altinay & Macdonald's three parameter Arrhenius fitted rate [100] is adopted. Alternatively, as the focus of this study is more towards higher temperature and pressure combustion, currently Baulch et al.'s rate [25] remains a promising second choice followed by Konnov's newly fitted rate [31]. However, an updated pressure-dependent reaction rate is really needed focusing on capturing the fall-off behavior of the colliders of interest, i.e. Ar, CO_2, H_2O.

3.6.5 R5: H_2+M=H+H+M

Glassman and Yetter [6] noted if hydrogen dissociation is the chain's initiating step, it proceed via this reaction. It is the dominant chain initiation reaction at high temperatures and only a few radicals are required to initiate the explosion. The dissociation energy of hydrogen is less than that of oxygen, so the initiation can be related to hydrogen dissociation rather than oxygen [6].

For the H_2-O_2 sub-mechanism at hand, the N_2-based rate expression from Cohen and Westberg's review [102] is adopted with collision efficiencies stated relative to that of N_2. This is consistent with Keromnes et al.'s choice [28]. The collider efficiencies of Keromnes et al.'s were adopted for He, CO, and CO_2 [28] and these values were further supplemented by those from FFCM-1 [87] for methane chemistry. For the case of H_2, Ar and H_2O, as they have different temperature dependencies than N_2 and since H_2O's role is emboldened by its large concentrations in this study, Keromnes et al.'s rates were replaced with collider-specific rates from Cohen and Westberg's rate [102]. This is in-line with Burke et al. [30], Li et al. [34] and FFCM-1 [87]. Hong et al. [29] expressed this reactions rate in terms of Ar as the reference bath gas, with the rate from Li et al. [39], rather than N_2's, and included collider-specific rates for H_2, N_2, and O_2. Alekseev et al. [32] and Konnov [31] also assumed a similar approach but implemented the reverse collider-specific reaction rates from Cohen and Westberg's rate [102]. Baulch et al. [25] noted the most reliable data would be those corresponding to Ar and H_2 bath gases, and that direct measurement of the rate are only possible using shock tube studies at 2300-8000 K. Baulch et al. [25] further noted that the third-body efficiencies of other bodies are sparse and are drawn largely from low temperature studies on H atom recombination. Tsang and Hampson [24] noted the uncertainty associated with the rate estimates were an order of magnitude larger for H_2O. With respect to the pressure dependence of this reaction, while simulations with RMG detected a pressure dependence, a review of the literature did not identify any studies that looked at pressure-dependent rate determinations for this study. While this may be a potential knowledge gap, IDT sensitivity studies did not show significant sensitivities to this reaction. As such, the low-pressure-limit rate of Cohen and Westberg's [102] is retained, with the additional collider-specific rates pertaining to Ar, H_2O, and H_2 to increase the fidelity of this reactions rate relative to that of Keromnes et al.'s [28] which adopted an N_2-based rate.

3.6.6 R6: O+O+M=O_2+M

For the H_2-O_2 sub-mechanism at hand, an N_2-based rate with collision efficiencies from the review by Tsang and Hampson [24], evaluated for temperature range of 2000-10000 K for N_2, is adopted in this study, which is in-line with Keromnes et al.'s recommendation. However, based on Tsang and Hampson [24]'s recommendation, collider-specific rates for Ar and O_2 were added as they have different temperature dependencies. This is in-line with Burke et al. [30], Hong et al. [29], Li et al. [34], and FFCM-1 [87], with the difference that the latter four studies also included an He-specific rate as well. In this study the collision efficiencies were adopted form Keromnes et al. [28]. For the missing colliders the efficiencies recommended by FFCM-1 [87] were used.

Moreover, as the N_2-based reaction rate's range of validity is for higher temperatures than encountered in the present study there is more impetus for the adoption of the separate Ar-specific rate validated for 200-4000 K by Tsang and Hampson [24], which was added in this work.

3.6.7 R8: H+OH(+M)=H_2O(+M)

Keromnes et al. [28] and Li et al. [39] both noted that flame speed calculations are very sensitive to this radical recombination reaction and that the reactivity decreases with increasing this reaction rate. Keromnes et al. [28] noted that this is due to the fact that laminar flame speeds are mainly controlled by the production and consumption of H atoms. As such, this chain terminating reaction plays a key role in competing for H with R1 and R9. Li et al. [39] also noted that, because of the large uncertainty in the rate, laminar flame speed predictions using any particular set of diffusion coefficients recommended by various authors can be forced to predict the same flame speed simply by adjusting the value of this single rate constant. Also, based on sensitivity analyses conducted in this work, and in-line with Li et al.'s [39] conclusion, shock tube ignition delay predictions are insensitive to this rate.

Simulations conducted using RMG in its pressure-dependent mechanism generation mode, recommends a pressure-dependent rate for reaction. As such in this H_2-O_2 sub-mechanism, the Ar-based pressure-dependent rate of Sellevag et al. [147], developed for the temperature range of 300-3000 K, is adopted in this work in place of Keromnes et al.'s tuned pressure-independent rate [28]. The rate adopted also includes Sellevag et al.'s [147] N_2 collider-specific low-pressure-limit rate, as well as their collision efficiencies for other bath gases. Sellevag's theoretically derived rate appears to fit the various high temperature rate data available in the literature well, including those obtained from shock tube experiments at 2196-2792 K by Srinivasan and Michael [106], as well as others in the temperature range of 1300-2300 K. Konnov [31] and Alekseev et al. [32] adopted the aforementioned pressure-independent rate by Srinivasan and Michael [106], which is reaffirming. An uncertainty factor of 2, as suggested by Sellevag et al. [147], is assigned to this reaction in this study. The collision efficiencies recommended by FFCM-1 are utilized with the exception of O_2 and H_2O. For O_2 Burke et al.'s efficiency was implemented [30], as it was not available in FFCM-1 [87]. An efficiency of 14 based on the average of commonly observed relative collision efficiencies of H_2O to Ar, was adopted in this work.

Keromnes et al. [28] reduced Li et al.'s recommended rate [39] by eight percent. Li et al.'s rate was arrived at by tuning Tsang and Hampson's rate [24] by a factor of 1.72, while implementing the collider efficiencies of GRI-Mech 3.0. Keromnes et al., Burke et al. and Hong et al. [28, 30, 29], noted that Srinivasan and Michael's [106] water decomposition shock tube study suggests +/-18% accuracy. However, an analysis by Konnov [148] estimated the uncertainty due to scatter to be in the order of a factor of 2. Keromnes et al. [28] stated that Sellevag et al.'s [147] is lower than previous recommendations. Hong et al. [29] also made note of the study but did not adopt the fall-off behavior, as the study did not have as high a pressure focus as the other reference studies. FFCM-1 [87], Burke et al. [30], Konnov [31], and Alekseev et al. [32] all adopted Srinivasan and Michael's [106] Ar-based and H_2O-based rates, along with the study's collision efficiencies but modified CO_2's efficiency from 3.8 to 4. Burke et al. [30] also investigated the effect of high-pressure falloff for the reaction by comparing model predictions through extending low-pressure-limit to include fall-off parameters of Sellevag et al. but reported that its inclusion yielded negligible differences in prediction against the present validation. It should be noted that their validation data did not involve high concentrations of the strongest collider H_2O, as is the case in this work, and very likely did not surpass Petersen et al.'s [60] 87 atm H_2-O_2 shock tube data. FFCM-1 [87] also noted that Baulch et al.'s recommended rate [25] is slower than Srinivasan and Michael's [106], bringing it closer to Sellevag et al.'s [147]. Considering the high pressures in this work, i.e. targeting 40-50 bar with large concentrations of strong colliders such as H_2O and CO_2, the choice of pressure-dependent rate is deemed justified.

Alternatively, the water decomposition rate of Srinivasan and Michael [106] can be adopted for Ar as the generic rate, with collision efficiencies from the same study, as well as an H_2O collider-specific rate in-line with Konnov [31], and Alekseev et al.'s approach [32]. These alternative rates were, however, not adopted in this work.

3.6.8 R9: $H+O_2(+M)=HO_2(+M)$

Glassman and Yetter [6] noted this reaction to be a chain propagating one, if the paths through either R11: $HO_2+H=OH+OH$ or R14: $HO_2+HO_2=H_2O_2+O_2$ followed by R15: $H_2O_2(+M)=OH+OH(+M)$ dominate. However, at other times it will be a chain terminating one competing for the H radicals with R1: $H+O_2=O+OH$. The reaction becomes more effective than R1 at higher pressures and lower temperatures and reduces reactivity constituting one of the reactions responsible for the second explosion limit (<1 atm) of H_2. Under atmospheric pressure flame speed studies, the reaction decreases flame reactivity under very lean conditions ($\varphi<=0.7$) but increases reactivity for stoichiometric and rich mixtures [6]. The reason it has a terminating effect under lean conditions is due to the reduced availability of H atoms, due to reactions R20: $HO_2+H=H_2O+O$, and R13: $HO_2+OH=H_2O+O_2$, since the reaction with OH will dominate and is chain terminating [6]. Under stoichiometric and rich conditions, H atoms are more available and HO_2 reacts with H to produce two OH radicals, hence promoting the reactivity. Glassman and Yetter [6] also noted that H_2O has a high third body efficiency due to resonance energy exchange with the HO_2 formed and tends to inhibit explosion. The reaction is sometimes referred to as the second most important reaction in combustion chemistry.

Simulations with RMG in its pressure-dependent mechanism generation mode conducted in this work, suggests a pressure-dependent network for this reaction. IDT sensitivity analyses conducted in this study indicate this reaction to be very sensitive, with maximum sensitivity being coincident with that of R1, occurring at pressures of 1-10 bar for temperatures below 1000 K. When increasing temperature the pressures at which these heightened sensitivities occur shift to higher pressures. As the pressure is further increased in particular beyond 100 bar, IDTs' sensitivities to R1 and R9's rates subside relative to other reactions, such as R17's.

In recent years Troe [107], Bates et al. [44], Sellevag et al. [147], and Fernandes et al. [108] investigated the rate of this reaction but reported significantly different high-pressure limiting rate constants, k_{∞}, as well as center broadening factors F_{cent}.

Notably, Bates et al. [44] investigated this rate at conditions where considerable scatter was present in the literature, i.e. 1050-1250 K and 7-152 bar (up to ~40 bar for H_2O as bath gas). They investigated the rate behind reflected shock waves using gas mixtures of H_2, O_2, NO with bath gases of Ar, N_2, and H_2O carefully selected to achieve NO_2 plateaus sensitive to reactions $H+O_2(+M)=HO_2(+M)$, $H+NO_2=NO+OH$, and $H+O_2=OH+O$. Bates et al. [44] augmented their experimental work with a theoretical analysis, and reported the reaction rates measured, centering factors, collider efficiencies, low- and high-pressure-limit rates calculated for Ar, N_2 and H_2O. Bates et al. [44] noted water to be 20 times more efficient than Ar as a collider and that a very good fit to H_2O and N_2 data were obtained, but not for high-pressure Ar data.

Fernandes et al. [108] conducted experiments for pressure- and temperature-dependent rate constant determinations for M=He and N_2, and further analyzed data of Hahn et al. [149] for Ar-based experiments at 300-700 K and 1-900 bar, as well as Janik et al.'s [150] experiments in water at 350°C, to determine the fall-off parameters at 1.5-950 bar and 300-900 K. Fernandes et al. also conducted theoretical calculations to extend the pressure and temperature range of validity [108].

While the differences observed in the high-pressure-limit rates are deemed inconsequential below 100 atm by Hong et al. [29] they noted more high-fidelity analysis is needed by referring to Miller et al.'s [151] work showing fall-off parameters become significant for higher pressure applications of the likes of supercritical water oxidation.

Klippenstein et al. [152] recently revisited this rate and with a focus on the impact of the choice of theoretical calculation methods on accuracy of predictions. The authors supported the rates adopted by Burke et al. [30], as well as Fernandes et al.'s [108] theoretical rate determinations i.e., identical to Troe [107]'s for the k_{∞} and center broadening factors F_{cent}. Consequently this rate is utilized for the high-pressure-limit rate in this study using their center broadening factors and their temperature and pressure dependencies. This choice is consistent with Keromnes et al. [28], Burke et al. [30], Konnov [31] and FFCM-1 [87] studies, but with a correction of their number of significant digits to match those of Fernandes et al.'s [108]. Alternatively, Hong et al. [29] adopted high-pressure-limit rates of Bates et al. [44] but a correction is warranted due to a mismatch with the source study, i.e., inconsequential for the lower pressures their mechanism targeted [153].

As for the low-pressure-limit rate, Klippenstein recently discussed the emergence of high level theory for these pressure-dependent reaction rate estimations [79], as well as the need for high level calculation of the rate of this reaction for H_2O and CO_2. Very recently, Shao et al. [83] revisited the low-pressure-limit collider-specific rates for this reaction including those pertaining to H_2O and CO_2, experimentally. Shao et al. conducted stoichiometric H_2-O_2 shock ignition delay time experiments of mixtures diluted in Ar or N_2, with up to 14% H_2O in Ar, and 20% CO_2 in Ar [83]. They combined literature data including those of Bates et al. [44] with their own higher accuracy IDT data and provided a revised low-pressure-limit rate by adopting the temperature dependency of Troe [107]. With the emergence of these new rates and the addition of a linear mixture rule in Chemkin-Pro combustion code, a multiple expression treatment, is adopted in this study using the H_2O, CO_2, Ar, and N_2-specific rate expressions. The N_2-specific low-pressure-limit rate was also augmented to capture the enhanced collision efficiencies of other colliders in bath gases. This is also in-line with Hong et al.'s [29] multiple expression approach but with Shao's updated rates [83], as well as the updated multiple bath gas formulation embedded in Chemkin-Pro using a linear mixture rule which precludes the possibility of overestimation of rates by a factor of the number of colliders near the high-pressure-limit.

For the center broadening factor for water in this study a center broadening factor of 0.8 was selected. This is based on Troe's [107] recommendation to adopt a different F_{cent} formula specifically for water which is $F_{cent}=F_{cent\text{-}strong\ collider}$. Since the $F_{cent\text{-}strong\ collider}$ is temperature dependent and varied approximately between 0.73 to 0.87, at its valley, a midpoint value of 0.8 was adopted. Incidentally, this is also in-line with Bates et al.'s [44] center broadening factor for H_2O. Moreover, for the syngas mechanism in this work, Burke et al.'s collision efficiencies [30] along with FFCM-1's [87] from a newly revised efficiency from GRI-Mech [87], were adopted for other larger HC colliders.

Alternatively, Burke et al.'s [30] low-pressure-limit rate determination involved refitting the room temperature low-pressure-limit rate data of Michael et al. [109], conducted for seven bath gases, into an Arrhenius form. Burke et al. [30] included two sets of rates, one for N_2 and another for Ar or He as the primary bath gas, each with their own collision efficiencies. The study retained the low-pressure-limit rate constant and the third body efficiencies of Li et al.'s [39]. Burke et al. [30] adopted Li et al.'s [39] fall-off parameters. However, it increased the third body efficiency of H_2O by a factor of 1.3 for their N_2- and Ar/He-based rates to improve consistency of the complete expression used with Bates et al.'s [44] high-temperature experimental data, and to improve agreement with burning rates of high-pressure laminar premixed flames sensitive to third-body efficiency of H_2O at high temperatures near the post flame zone. Burke et al. [30] noted their expression was consistent with the measurements of Bates et al. [44] in Ar, H_2, H_2O, except at the highest pressures in Ar. Burke et al. [30] also noted that none of the recently proposed expressions, i.e. Bates et al. [44], Hahn et al. [149], Sellevag et al. [147], Fernandes et al. [108], Baulch et al. [25], as well as a few other commonly referenced sources', reproduced the observed pressure dependence of the rate constant in Ar.

While Keromnes et al. [28] utilized three high-pressure-limit rates for N_2 (as the base), Ar, and He, of Fernandes et al.'s [108]. They opted for the Ar-specific low-pressure-limit rate of Bates et al. [44] instead, as the low-pressure-limit rate constant of Fernandes et al. [108] reduced reactivity in Ar, and resulted in excessively long shock tube ignition delays in the temperature range of 1000-1200 K. Secondly, Keromnes et al. [28] increased Fernandes et al.'s [108] low-pressure-limit rate of He by a factor of 1.5 to correct for over prediction of the burning rate at temperatures above 1500 K and to enable reproduction of the inverse relationship with increasing pressure. Keromnes et al. [28] noted their hybrid approach resulted in the best agreement for RCM and shock tube data, among others. Keromnes et al.'s [28] approach, however, was dismissed here as it involved multiple parameter tuning.

Hong et al. [29] included three collider-specific pressure–dependent reaction rates for N_2 (as the base), Ar, and H_2O from Bates et al.'s [44] study, including its k_0, k_∞, and F_{cent} for Ar, N_2, and H_2O. However, for the collision efficiency of H_2, and the low-pressure-limit rate of O_2, Hong et al. [29] adopted Michael et al.'s [109] rate parameters. This reaction has some controversy, as the fall-off behavior, third body collision efficiency, and Troe parameterization is not consistent with other studies.

Finally, recently, Wang et al. [135] used molecular dynamics simulations to evaluate the pressure-dependent rate R9 in the presence of supercritical CO_2, at 1000-2000 K and 100-400 atm. While Wang et al. [135]'s rigorous study produces rates likely superior for the specific bath gas of sCO_2 at 300 atm, this rate is not adopted, as the target bath gas in this study involves large concentrations of H_2O, see discussion in section 3.6.1.

3.6.9 R10: H_2+O_2=H+HO_2

Mechanisms generated in RMG identifies this H-abstraction reaction as a necessary pressure-independent reaction, see Appendix A Table A1 for a sample mechanism and the associated RMG input file. IDT sensitivity analyses indicate that at temperatures lower than 1300 K this reaction reduces the reactivity in the intermediate range of pressures in the presence of large quantities of H_2O and CO_2. Glassman and Yetter [6] recognized the reaction to be the dominant chain initiation step in the range of 1650-2100 K. Keromnes et al. [28] and Burke et al. [30] noted this reaction to play a key role with R1 and R9 in controlling H_2 flame speeds by controlling production and consumption of H and HO_2. Burke et al. [30] utilized the reverse reaction rate and concluded that at high pressures the branching between different H+HO_2 channels affects the overall branching ratio and contributes to the extended second explosion limit of H_2 in flow reactors and high-pressure flames. Hong et al. [29] noted that the uncertainty in this reactions rate is the major source of uncertainty in R1.

For the H_2-O_2 sub-mechanism at hand the rate expression from ab initio calculations of Michael et al. [110] is utilized. For the uncertainty, FFCM-1's recommended values were adopted [87]. Keromnes et al. [28], Burke et al. [30], Hong et al. [29], FFCM-1 [87], Alekseev et al. [32] and Konnov [31] all relied on Michael et al.'s [110] rate. Michael et al. [110] conducted conventional transition state theory calculations and shock tube measurements of H_2+O_2 at 1600-2000 K. They proposed an expression which agrees well with their high temperature measurements, as well as low temperature data and the reinterpretation of Baldwin & Walker's [154] results using rates constants for $k_{H+O2=OH+O}$ and $k_{HO2+HO2=H2O2+O2}$ according to the method detailed by Burke et al. [30].

Burke et al. [30], reinterpreted Baldwin and Walker's derived ratios [154] of: $(k_{R11:H+HO2=OH+OH}+k_{R20:H+HO2=H2O+O})/(k_{R1:H+O2=OH+O}+k_{R14:HO2+HO2=H2O2+O2})$ and $k_{R10:H+HO2=H2+O2}/(k_{R1:H+O2=OH+O}+k_{R14:HO2+HO2=H2O2+O2})$, as well as their static reactor experiments data at 773 K with improved values for R1 and R14 to achieve reliable expressions for R10, and R11+R20, as the above ratios involve rates for R1, R10, R11, R14, and R20. Burke et al. [30] subsequently adopted Michael et al. [110] results and reduced their A-factor by ~25% within the uncertainty, to obtain agreement with Michael et al.'s 1600-2000 K shock tube experiments, Mueller et al.'s flow reactor speciation data [155], and Baldwin and Walker's reinterpreted data using updated R1 and R14 values.

Keromnes et al. [28], reduced the rate by 30% to reduce the reactivity at low-temperatures while keeping the same reactivity at high temperatures. However, in-line with Hong et al. [29] and FFCM-

1's [87] approach and the recent study by Konnov et al. [31] that showed that with the appropriate transport properties and improved mechanisms flow reactor data can be reproduced, Keromnes et al. [28] and Burke et al.'s [30] adjustments were disregarded. This is due to the fact that this reaction's rate constant is interrelated with that of R14, R11, R20, and R1's, and in this study R20 has been added to the mechanism and a different R14 rate has been adopted relative to Keromnes et al. [28] and Burke et al.'s [30] who excluded R20.

3.6.10 R12: HO_2+O=O_2+OH

Simulations with RMG identify this reaction as a pressure-dependent one, see Appendix A Table A1. Sensitivity analysis indicates that shock tube ignition delay times of syngas and H_2 are not very sensitive to this reaction, and generally at pressures above 10 bar it slightly reduces the overall reactivity for analyses conducted in the range of 1000-1300 K. In-line with Alekseev et al. [32] and Konnov's mechanisms [31], Burke et al.'s [30] adjusted the theoretically determined value of the rate of Fernandez et al.'s [113], which is adopted for the H_2-O_2 sub-mechanism at hand. Also the two theoretical studies, Fernandez et al.'s [113] and Setokuchi et al.'s [156] are consistent qualitatively in terms of the expected high temperature behavior of this reaction. Baulch et al. [25] and Burke et al. [30] both noted that the only reliable data on this reaction have been obtained at low temperatures of ~250-400 K, where a weak negative temperature dependence of the rate constant was observed whereas the only available data at high temperatures have been obtained from flame modelling or are estimates. Baulch et al. [25] recommends their rate based on the low temperature data with small temperature coefficient for k and note that the use of this low temperature Arrhenius expression is recommended up to 1000 K but, as their estimate contains a large error limit, it likely encompasses suspected deviations at high temperatures. Also Baulch et al. noted the theoretical study by Setokuchi et al. [156] suggesting that at low temperatures the reaction proceeds by an addition mechanism giving rise to the negative temperature dependence of k, consistent with experiments, but at higher temperatures direct abstraction of H may become competitive, and be dominant above 1000 K, which would lead to a positive temperature dependence of k at high temperatures [25]. As such Baulch et al.'s rate [25] was dismissed in this study, contrary to Hong et al. [29] and FFCM-1's [87] approach.

Burke et al. [30] stated the same change in reaction pathway suggested by Baulch et al. [25] and adopted Fernandez et al.'s ab initio based rate calculations which captured the weakly negative temperature dependence at low temperatures, and the weakly positive temperature dependence expected at higher temperatures. However, Burke et al. [30] adjusted the A-factor by a factor of 0.6 to better fit the available measurements at low temperatures.

3.6.11 R13: HO_2+OH=H_2O+O_2

Simulations with RMG recognizes this H-abstraction reaction as a pressure independent contributor to the overall mechanism. Keromnes et al. [28] noted this reaction plays a key role, in addition to R1: H+O_2=OH+O, and R9: H+O_2(+M)=HO_2(+M), in controlling H_2 flame speeds at ambient conditions, as laminar flame speeds are mainly controlled by the production and consumption of H atoms. This chain terminating reaction is highly sensitive to fuel-lean flames and has been studied theoretically and experimentally, with large reported uncertainties, up to a factor of 4 at 1200 K. Significant controversy surrounded the rate of this reaction, as noted by Keromnes et al. [28], Burke et al. [30] and Hong et al. [29]. Keromnes et al. [28] reports that due to an unusual non-Arrhenius behavior as it goes through a minimum around 1250 K some have used up to five expressions in order to reproduce temperature dependence, and adopted Keyser's 1988 [115] rate and reduced it by 15%. However, two recent experimental and theoretical studies re-evaluated this rate expression, namely Hong et al. [114] and Burke et al. [143] , and significantly reduced the associated uncertainty. Hence, all previous study's findings were dismissed in this study.

In this H_2-O_2 sub-mechanism Hong et al.'s two expression rate [114] is adopted, as it is based on direct measurements and the authors mention this is in good agreement with Burke et al.'s recent theoretical study [143] claiming the rate law passes through their experimental results. Hong et al. [114] investigated the reaction experimentally by direct measurement of H_2O, OH, and HO_2 behind reflected shock waves between 1072 and 1283 K, and found no strong temperature dependency with the rate best expressed by the combination of two Arrhenius forms. Their two-expression rate was arrived at by fitting Hong et al.'s [114] experimental data over the range 1072-1283 K, Hong et al.'s earlier investigations [157] using shock tubes at 1600-2200 K, as well as a few noted low temperature experimental data. As the temperature range covered by these two experimental test campaigns covers that of target in this study, this further reaffirmed the choice valid for the temperature range 1072-2200 K. The uncertainty for this rate is extracted from the original study [114] and appears to be higher than that provided by FFCM-1 [87]. This choice is also in-line with Alekseev et al. [32]. However, Konnov [31] opted for adding the rate constant pertaining to the singlet channel of oxygen recommended by Monge-Palacios and Sarathy [158] which investigated both the triplet and singlet channels. Monge-

Palacios and Sarathy [158] investigated the impact of the singlet channel and deemed it to be significant in flames seeded with ozone. As such, this additional rate was not adopted in this study. It is unclear if Konnov adopted the triplet rate of Monge-Palacios and Sarathy [158], but it serves as a strong alternative along with Burke et al.'s rate [143] adopted by Hashemi et al.'s [159] to the current rate expression used.

3.6.12 R14: HO_2+HO_2=H_2O_2+O_2

Keromnes et al. [28] identified and attributed this reaction's varying contribution at low-temperatures and high pressures to its consumption of two HO_2 radicals form H_2O_2, which subsequently could decompose to two radicals, in contrast with HO_2+H_2=H_2O_2 followed by H_2O_2 decomposition which constitutes a chain branching path. Burke et al. [30] also considered it responsible for HO_2 consumption under higher pressures and lower temperatures, where HO_2 is present in relatively higher mole fractions but participates in a chain propagating sequence responsible for thermally driven oxidation kinetics at temperatures above the 3rd explosion limit. Hong et al. [29] warns it is subject to large uncertainties at special conditions such as oxidation of highly diluted H_2, the thermal decomposition of H_2O_2 at combustion temperatures, and instantaneously heated H_2O and O_2 mixtures. Hashemi et al. [54] identifies this recombination reaction to play a critical role in the ignition process.

For the H_2-O_2 sub-mechanism at hand, the two-expression Arrhenius rate from Hong et al. [114] which confirms Kappel et al.'s [116] consistent with Alekseev et al., Konnov, and FFCM-1 [32, 31, 87] is selected for this study. Kappel et al. conducted shock tube experiments at 950-1250 K and included low temperature data to produce their recommended rate for 300-1250 K. Hong et al. [114] recently conducted shock tube studies in the range of 1072-1283 K behind reflected shock waves; since their results were in good agreement with Troe's shock tube experiments at 950-1450 K [160] as well as Kappel et al.'s rate, the latter rate was retained for this reaction. The temperature validation range is increased to 300-1283 K as per Hong et al.'s study, and the uncertainty for this rate is adopted from FFCM-1 [87]. In terms of pressure dependence, simulations with RMG's pressure-dependent mechanism generation were conducted which identified this reaction as a pressure independent H-abstraction reaction. Moreover, while Kappel et al. [116] reported some pressure dependence at temperatures below 800 K, because most of the applications envisioned in this work are at much higher temperatures, the choice of a pressure-independent rate is deemed appropriate at this point. Finally, pressure-dependent IDT sensitivity analysis studies at pressures of 1-300 bar and 950-1300 K, conducted in the current work shows that in the presence of strong colliders such as H_2O and CO_2, R14 increases the overall reactivity at low to intermediate pressures, but at higher pressures of up to 100 bar it reduces the overall reactivity. This reaction becomes increasingly more important at pressures above 100 bar.

Hashemi et al. [159] recently adopted Zhou et al.'s rate [161], which used statistical rate theory in conjunction with high level ab initio calculations. Zhou et al.'s rate showed good agreement with studies below 500 K, as well as with studies above 1000 K, such as that of Kappel et al. [116], but showed 50% deviation from Hippler et al.'s [117] results at 700 K. Burke et al. [30] adopted Hippler et al.'s [117] rate and pointed out that the differences from Kappel et al.'s [116] of a factor of 2-3 in combustion-relevant temperatures, to result in: differences in the predicted speciation during high-pressure H_2 oxidation conditions, 10-20% differences in predicted flame speeds at high-pressure, dilute, and lean conditions. They alluded to the dependence of this reaction's rate determination on the same data used to derive the rate for R13 which is inconsistent among studies. It should be noted that as the latter was adopted by Hong et al., as well as Keromnes et al. but with a 13% reduction [28, 29]. Moreover, as Zhou et al. [161] had reported that their alternative rate did not agree well with high temperature shock tube data their rate was not considered as a candidate in this current work.

3.6.13 R15: H_2O_2 (+M) = OH + OH (+M)

Simulations with RMG's pressure-dependent automatic mechanism generation identify this reaction as an important pressure-dependent reaction. IDT sensitivity analysis carried out in this work indicates, that irrespective of the nature of the collider, at low to intermediate temperatures R15 has a promoting effect on reactivity which increases with pressure, and decreases with temperature. Hong et al. [29] identifies this reaction as the central kinetic feature in engine knock in spark ignition engines, in ignition of liquid-fueled diesel engines, and in the operation of homogeneous charge compression ignition (HCCI) engines, as it is the dominant chain-branching reaction controlling HC ignition in the intermediate temperature regimes of 850-1200 K. For high-pressure conditions, the thermal decomposition of H_2O_2 via this pressure-dependent reaction becomes the dominant chain branching reaction. Under high-pressure and low- to intermediate-temperature conditions, ignition delay times are highly sensitive to this chain branching reaction.

For the H_2-O_2 sub-mechanism at hand the pressure-dependent, Ar-based rate from a study by Troe [118], is used along with low-pressure-limit rates and centering factors for H_2O, CO_2, H_2O_2, and N_2.

Also, collision efficiencies were adopted for the remaining colliders from Troe [118] and combined with those for larger molecules from FFCM-1 [87] which recommends GRI-Mech 3.0's [47]. This approach is consistent with that of Keromnes et al. [28], Burke et al. [30], and FFCM-1 [87], with the exception of the modified center broadening factor from 0.42 to that of N_2=0.43 in Keromnes et al.'s mechanism [28].

Keromnes et al. [28] illustrated Troe's rate [118] results in accurate prediction of ignition delay times at 15, 30, and 50 bar, and alluded to the fact that Troe's derived rate included a review of Hong et al.'s [41] experimental data. This review showed Hong et al.'s results was only accurate up to 15 bar, whereas Troe's covers a wider temperature and pressure range [118]. Burke et al. [30] made note of the same experimental rate determinations of Hong et al. in addition to another theoretical study of Sellevag [105] but concluded that Troe's rate yielded better agreement than Sellevag's. The authors adopted Ar-based rate of Troe's 2011 with its third-body efficiencies for He, O_2, N_2, CO_2, H_2O, and H_2O_2 and scaled Li et al.'s [39] N_2-based third-body efficiencies for H_2 and CO to arrive at their Ar-based counterparts.

Hong et al. [29] noted that as there are no existing direct measurements of H_2O_2 decomposition rate constant at pressures much higher than 4 atm for accurate evaluation of the fall-off behavior. Although Hong et al. [29] relied on low-pressure limiting behaviour applicable to most common combustion applications, they did mention that, due to lack of reliable experimental data at high pressures, an unavoidable compromise needs to be made until better studies become available.

In this work adoption of multiple expression treatment of this pressure-dependent rate enabled the implementation of the different center broadening factors F_{cent}, for the collider-specific rates. This treatment is expected to increase the fidelity of the model at hand, in particular for its higher pressure applications, as well as those involving high concentrations of H_2O with its 20% higher broadening factor relative to its single expression treatment counterparts.

3.6.14 R17: $H_2O_2 + H = H_2 + HO_2$

This H-abstraction channel of hydrogen peroxide's reaction with H radical is interconnected with R16: H_2O_2+H=H_2O+OH. Pressure-dependent simulations for reaction mechanism generation with RMG, did not find R16 significant enough for inclusion in the mechanism, in contrast to R17. Both channels were deemed pressure-independent by RMG. Extensive sensitivity analysis identifies IDTs to be most sensitive to the rate of this reaction at low temperatures, as well as at high pressures and at intermediate to high temperatures. In fact, R17 is the most sensitive reaction at pressures above100 bar for hydrogen combustion or one of the top three for syngas combustion of the validation datasets explored. Keromnes et al. [28] identified this reaction to be important in accurate prediction of ignition delay times in the reverse direction, as it provides a pathway to H_2O_2 production. Also the reaction between fuel and HO_2 is important for most fuels at intermediate temperatures (<1100 K) in the prediction of accurate ignition delay times due to the HO_2 attack on the fuel. Hong et al. [29] noted that under high pressures (8-32 bar tested in RCMs) and low temperatures (<1100 K) hydrogen oxidation is governed by R9: $H+O_2(+M)=HO_2(+M)$, which leads to production of HO_2 which reacts with H_2 to form H_2O_2 through reverse of R17: $H_2O_2+H=H_2+HO_2$, which controls the reaction rate through decomposition through R15: $H_2O_2(+M)=OH+OH(+M)$.

For the H_2-O_2 sub-mechanism at hand, consistent with Burke et al. [30], Li et al. [39], and FFCM-1 [87], Tsang and Hampson's [24] recommended rate is adopted. The uncertainties for this reaction are large, i.e. a factor 5 at temperature above 1000 K, which drops to a factor of 2 at 773 K. This reaction's rate is controversial as the purely theoretical unadjusted rate by Ellingson et al. [122] rather than their final validated and recommended rate, was adopted by Keromnes et al. [28] to reproduce Mittal et al.'s [162] RCM auto-ignition studies of H_2 & H_2/CO oxidation at 1-50 bar and 950-1100 K and equivalence ratios of 0.36-1.6. However, this reversion of adjustment impedes reproduction of Baldwin et al.'s experimental data at 407-530°C [163]. Keromnes et al. [28] noted that Baulch et al.'s rate [25] is a factor of 3 lower than Tsang and Hampson's [24] resulting in a difference of a factor of 3 in ignition delay times at 1000 K and 50 bar. Keromnes et al. [28] also noted that Elligson et al.'s recommended rate is similar to Tsang and Hampson's [24] recommendation below 1000 K and results in ignition delay time predictions that are much more consistent with Mittal et al.'s in RCM [162].

Baulch et al. on the other hand, noted the discrepancy between their rate and that of Lee et al.'s [164], but the authors refrained from updating this rate until further data is made available. Hong et al. [29] referred to GRI-Mech 3.0's rate, which fits Li et al.'s [39] data to a T^2 temperature dependence stating such temperature dependence is expected from transition state theory. This is contradictory to Ellingson et al.'s [122] transition state theory analysis which suggests a T^1 dependence before adjustment to fit experimental data.

Finally, Lu et al. [165] revisited R17's rate and their theoretical data were fitted and superimposed by the unadjusted Ellingson et al.'s theoretical rate adopted by Keromnes et al. [28], and the fitted one adopted by both Alekseev et al. [32] and Konnov [31] as well as the rate recommended by Tsang and Hampson [24], as seen in Figure 7.

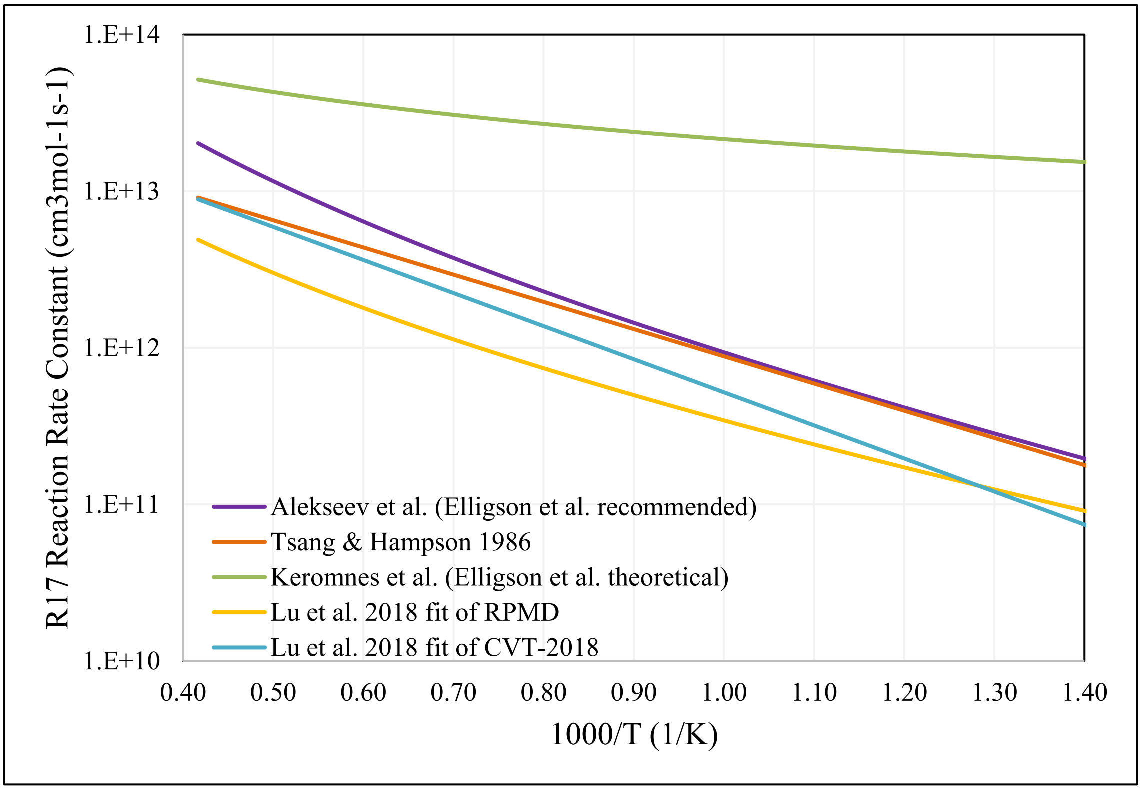

Figure 7: k of R17 as a function of temperature, generated using rate paramters of Alekseev et al. [32], Keromnes et al. [28] and Lu et al. [165]

It can be seen that the variation both in terms of the combined temperature dependency of the modified Arrhenius expressions, as well as its value is quite large, at times more than three orders of magnitude. Hence based on IDT sensitivity analyses performed it was observed that rates smaller than those of even Tsang and Hampson's [24] may be needed at temperatures of 1225 K to obtain a reasonable fit of the newly collected high-pressure H_2O-laden validation data collected in this work. As such, Tsang and Hampson's rate which is accepted by other recently developed mechanisms replaced that of the base Keromnes et al.'s [28] model used as the starting point in this work. It should also be noted that logically for R16, the same reference study was utilized as the estimates are interconnected as two potential channels for the reaction between H_2O_2 and H-radical.

3.6.15 R20: HO_2+H=H_2O+O

Burke et al. [30] estimated this reaction to be potentially responsible for less than 14% of the flux of H+HO_2, but they noted that inclusion of this reaction yields substantially faster oxidation rates at flow reactor and high-pressure flame conditions. The authors noted a few shortcomings of their theoretical calculations rendering them inconclusive and hence excluded this reaction. Burke et al. [30] deemed H+HO_2's R10 and R11 branches responsible for the majority of the flux.

Hong et al. [29] opted to adopt Baulch et al.'s rate and noted that most 19 reaction mechanisms such as that of Li et al.'s [39] did not include this reaction arguing it is kinetically similar to reaction R11: H+HO_2=OH+OH. However, Konnov et al. [148] showed that the two reactions, although not important in slow H_2 oxidation processes, have opposite signs in laminar flame sensitivities and retained this reaction. In this study, in-line with Konnov et al. [148], Hong et al. [29], and FFCM-1's [87] approach, Baulch et al.'s [25] recommended rate is adopted. Alternatively, the Conforti et al.'s [166] theoretical rate determination can be adopted in-line with Alekseev et al. [32] and Konnov's [31] mechanisms.

3.6.16 R21: CO+O(+M)=CO_2(+M)

Keromnes et al. [28] and Li et al. [35] both implemented Troe's [123] rate, yet, with a modified activation. Keromnes et al. [28] reduced the rate by a factor of 0.75, but a recent theoretical study by Jasper and Richard [167] suggests an even higher rate than Troe's [123]. As such, in this study, in-line with FFCM-1's [87] approach, the untuned rate of Troe [123] is utilized. As collider-specific rate constants are not available, a single expression Troe formulation is the only choice and FFCM-1's [87] relative efficiencies sourced from Li et al. [35] is adopted. For larger molecules' collision efficiencies GRI-Mech3.0 [47] values used by FFCM-1's are adopted [87]. As for the fall-off behavior, in line with FFCM-1[87], Lindemann fall-off with F_{cent}=1 is assumed. For the low-pressure-limit rate both Keromnes et al. [28] and Li et al. [35] refer to the theoretical rate of Westmoreland et al. [124], but, while Keromnes et al. [28] reduced the rate, Li et al. [35] retained the original pre-exponential factor.

3.6.17 R23: CO+OH=CO_2+H

Sometimes referred to as the second most important reaction in combustion chemistry reaction R23 is responsible for a large portion of energy release associated with CO burnout, and may play an important role in impacting adiabatic flame temperatures in CO_2 diluted combustion due to CO_2 dissociation, as relevant to the experiments at hand. Keromnes et al. [28] used RRKM/master equation analyses done by Joshi and Wang [125]. Joshi and Wang [125] proposed a double Arrhenius low-pressure-limit rate and, although it recommends fall-off inclusion for extremely high pressures, it provides a fall-off pressure validity check relation, which for the temperature range exceeding those targeted in this study provides the following tabulated limits:

Table 2: R23's fall-off initiation pressure as a function of temperature from Joshi and Wang [125]

T (K)	Fall-of occurs at P (bar) >
900	43
1000	76
1100	127
1200	204
1300	316
1400	476
1500	698
1600	999
1700	1402
1800	1931
1900	2617
2000	3493
2100	4601
2200	5987

In-line with Joshi and Wang, Li et al. [35] determined their own rate expression, and also noted that the pressure dependence due to the involvement of HOCO adduct becomes particularly important at lower temperatures, but at higher temperatures it is assumed to be pressure-independent.

As the CO burnout temperatures are usually in the lower range of the above table, it is unclear whether fall-off could become important in the next generation highly pressurized combustors. However, for conventional gas turbine combustor conditions these pressure independent reaction rates are appropriate. Li et al. [35] discussed several rates, including Troe [168], Zhu et al. [169] , and Senosiain et al.'s [126] theoretical calculations, and observed that the first two over predict the rate at low to intermediate temperatures, whereas the last under predicts the rates at all relevant temperatures. Troe [168] provided a triple modified Arrhenius rate for k_0 and triple modified Arrhenius rate and evaluated collision efficiency with H_2O rendering it a desirable choice for higher pressure lower temperature applications. Hence, combustion code permitting, for applications involving these conditions, Troe [168] serves as a strong alternative able to capture the impact of high H_2O concentration. Recently, Weston et al. also recalculated this rate theoretically [170]. Their rate determination was followed by a shock tube laser absorption spectroscopy study by Nasir and Farooq [171] measuring formation of CO_2, providing three rates for three specific pressures ranges spanning 700-1230 K and 1.2-9.8 bar. Nasir and Farooq [171] stated that their data was in closer agreement with that of Joshi and Wang's [125], relative to that of Weston et al.'s [170], as such the latter was not adopted in this study. Moreover, a more recent shock tube study from Wang et al. [137] simultaneously measuring CO & H_2O behind reflected shockwaves, provided another rate expressions for temperature range 1428-1685 K at a pressure of 1.5 atm, and they confirmed that their data was in very good agreement with that of Joshi and Wang's [125]. The rate provided by Joshi and Wang [125] also has pressure dependence stipulated for He, N_2, Ar, CH_4, and SF6. It appears that while both FFCM-1 [87] and Keromnes et al. [28] reference Joshi and Wang's [125] rate, there is a discrepancy in the activation energy of the first Arrhenius expression relative to the source study.

Finally a recent study by Masunov et al. [172] also points to an autocatalytic effect of supercritical CO_2 impacting the activation barrier and acceleration of $CO+OH=CO_2+H$. This study is followed by a more recent study by Panteleev et al. [173] providing PLOG pressure and temperature dependent rates for the reaction in a CO_2 environment for the pressure and temperature ranges of 1-1000 atm, and 400-1600 K. However, the nature of PLOG rates, confines collider-specific impacts hence this rate is dismissed and is considered to be more applicable to very high sCO_2 diluted environments. Hashemi et al. [130], on the other hand, adopted the PLOG rate of Senosiain et al. [126], which is similar to the prediction of Troe's [168]. Currently, as most experimental studies support the double Arrhenius rate of Joshi & Wang, and they indicate that pressure dependence occurs at higher pressure and temperature combinations, as per the Table 2, this rate is adopted in this study as well. Alternatively Troe's [168] can be adopted if combustion codes could accommodate triple rate expressions for each of the low-pressure-limit as well as the high-pressure-limit rate simultaneously.

3.6.18 R25: HCO (+M) = H + CO (+M)

For this pressure-dependent reaction rate, Keromnes et al. [28] utilized a low-pressure-limit rate from Li et al. [35] who derived this rate from species flux analysis of formaldehyde pyrolysis. Similarly, Aramcomech 1.3 [22] also selected Li et al.'s [35] recommended rate but increased it by a factor of 1.2 for better agreement with experimental data; as it is an optimized rate it is not considered as a candidate rate in this work. Alternatively, FFCM-1 [87] adopts Friedrichs et al.'s [129] theoretical RRKM calculated rates, fitted to shock tube data with bath gas Ar at 1000 K for decomposition of formaldehyde, with relative efficiencies from GRIMech [47]. However, this rate is also at the low-pressure-limit. As the focus of this study is to ensure pressure dependence in the presence of strong colliders such as CO_2 and H_2O are properly captured, the theoretical rate of Yang et al. [128], in-line with Hashemi et al.'s mechanisms [63, 130], is adopted in this study. Yang et al. [128] conducted a theoretical study and calculated a pressure-dependent rate covering a pressure range of 0.01-1000 atm, at 300-2700 K while ensuring their adopted thermochemistry was in good agreement with Active thermochemical tables [89]. The enhanced third-body collider efficiencies were adopted from Hashemi et al.'s mechanism [63].

3.6.19 R26: $HCO+O_2=CO+HO_2$

Keromnes et al., Li et al., and Metcalfe et al. [28, 35, 22] all adopted Timonen et al.'s 1988 rate [132] from a study done in a tubular reactor coupled to a photoionization mass spectrometer for a temperature range of 295-713 K. Alternatively, FFCM-1 [87] used a rate referring to communications with Klippenstein which was slower. Hashemi et al. [63] utilized the more recent rate of Fabheber et al. [131] involving measuring HCO concentrations behind Ar diluted shockwaves of glyoxal pyrolysis at temperatures of 1285-1760 K and different total density ranges for glyoxal/oxygen and glyoxal mixtures. Fabheber et al. [131] then combined their data with low temperature data from the literature to produce a more inclusive rate applicable to the temperature range of 295-1705 K. In-line with Hashemi et al. [63], this more recent rate involving higher temperature experimental data at combustion relevant temperatures is adopted instead of Timonen et al.'s [132].

3.6.20 R27-R30: HCO reactions with H, O, and OH

The four radical recombination reactions involving HCO are R27: $HCO+H=CO+H_2$, R28: $HCO+O=CO+OH$, R29: $HCO+O=CO_2+H$, and $HCO+OH=CO+H_2O$.

For R27, Keromnes et al., Li et al. [28, 35] adopted Timonen et al.'s [134], whereas Hashemi et al. [63] utilized Friedrichs et al.'s [129] which has a 50% faster rate than that of Timonen et al.'s [134]. In this study the more recent rate recommended rate by Baulch et al. [25], whose estimate lies in between the two aforementioned studies is utilized, in-line with FFCM-1 [87].

In the case of R28 Keromnes et al., Li et al. [28, 35] chose the rate by Tsang and Hampson 1986 [24], whereas Hashemi et al. [63] opted for Baulch et al.'s 1992 [112] rate, with is very similar to the aforementioned rate. In this study, in-line with FFCM-1 [87], Baulch et al.'s 2005 more recent recommended rate [25] is adopted, which considered both rates in their review.

For R29, Baulch et al. 2005 [25] rate is also adopted as it is related to R28, in-line with FFCM-1 [87]. This is also in-line with Hashemi et al. [63] who used Baulch et al.'s 1992 [112] rate, and Keromnes et al., and Li et al. [28, 35] who chose the rate by Tsang and Hampson 1986 [24], as all three rates are identical.

Finally for R30, Keromnes et al. [28] selected the rate by Baulch et al.'s 1992 [112], whereas FFCM-1 [87] and Hashemi et al. [63] both utilized Baulch et al. 2005 [25]. The latter is ~6% higher than the former. On the other hand, Li et al. [35] recommended the rate from Tsang and Hampson 1986 [24], which is approximately a third of the other two sources. In this study the rate by Baulch et al. 2005 [25] is adopted.

3.7 CH_4 oxidation mechanism

To construct the hierarchical CH_4 mechanism, in-line with the model development approach of Figure 4, recent literature involving high-pressure experimental IDT data and model validation for small hydrocarbons were first surveyed for candidate mechanisms. CH_4 mechanisms developed by NUIG, the AramcoMECH series, have been used the most by researchers and show favorable performance for high-pressure applications including those involving large quantities of CO_2 [174, 92, 16, 175, 14, 13, 176]. Among the AramcoMECH models, AramcoMECH 2.0 [86], and AramcoMECH 3.0 [92], were selected in this manuscript for further development, as they benefited from updated thermodynamic properties based on Burke et al. [93] work. The well-cited AramcoMECH 2.0 involves 493 species and 2716 reactions. Its successor, AramcoMECH 3.0, includes 581 species and 3,037 reactions. In this work, two mechanisms were constructed by replacing AramcoMECH 2.0 [86], and AramcoMECH 3.0 [92] H_2/CO submechanism with CanMECH 1.0. These models were then used as alternative starting point mechanisms for evaluation, potential improvement, and/or validation, results of which are detailed in section 7.4.

3.8 Sensitivity analysis to kinetic parameters

As combustion mechanisms are large and the interaction of its building blocks are complex, two common diagnostics techniques, namely sensitivity and rate of production analyses, are employed. The former enables identifying the rate controlling or limiting reactions, and the latter enables quantifying the contribution of a reaction to the net production rates of a target species [6]. As such, these techniques are utilized to prioritize which reaction rates are better suited to be subjected to parameter tuning within its uncertainty bounds. To this end, the brute-force approach commonly adopted in the literature [28, 177, 22] evaluates the sensitivity of global reactivity, signified by IDT sensitivities, to variations in kinetics parameter values, namely: the pre-exponential factors as well as center broadening factors and collision efficiencies of pressure-dependent reactions. As ignition delay time measurements are the main validation tool in this modeling effort, this macro variable serves as an appropriate metric for selection of candidates for parameter tuning as well as providing qualitative measure of the extent of tuning appropriate. The approach involves increasing and decreasing the rate of each reaction by a factor of two at the conditions of the experiments. A factor of two is appropriate as most reaction rates' uncertainties are commonly within a factor of two. In these analyses the sensitivity coefficient σ is:

$$\sigma = {log\left(\frac{\tau'}{\tau''}\right)}\Big/{log\left(\frac{a}{1/a}\right)} \tag{3.11}$$

where, τ', and τ'' are the ignition delay times calculated with the increased and decreased reaction rate parameter respectively, and the a is the multiplier by which the parameter has been scaled. A negative sensitivity coefficient represents a reducing effect on IDT, meaning promoting effect on reactivity, whereas a positive one is the reverse, that is indicative of an inhibiting effect on reactivity [177]. To implement such analysis, the rates of reactions are adjusted via doubling and halving their pre-exponential factors. For sensitivities to variations in the center broadening factors, the extent of such variation was commonly less to ensure the center broadening factor does not exceed 1 as that could result in broadening factors larger than 1, which is not physically possible.

It is also important to note that in conducting sensitivity analyses the choice of the definition of ignition criteria in IDT determinations, impacts the results. The method used to arrive at ignition delay times from experimental data is by drawing a tangent to the inflection of OH* emission trace, and extending it until it intersects the baseline OH* emission immediately after passage of the reflected shock wave. The corresponding time of such intersect denotes the ignition time, coincident with runaway increase of OH radicals. However, Chemkin-Pro does not have such means. The means available in Chemkin-Pro are, temperature inflection point, user-specified relative temperature increase, and peak emissions of any user-dictated species. It was observed that based on the choice of ignition criteria different sensitivities and, at times, sensitivities with opposing signs were detected. Consequently, in this work an in-house computer code was used to post-processes the emission traces generated by Chemkin-Pro and determine ignition delay times using the exact same method as those used to process the experimental data. This way the sensitivity analysis results as well as any simulated model validation experiments are using an identical ignition delay time determination method. Moreover, while this process is possible manually the computer code enabled, running thousands of parametric studies with very quick post-processing to generate the data needed for model validation and tuning purposes.

3.9 Shock tube reactor modelling

Selecting an appropriate reactor model able to accurately mimic the shock tube reactor is fundamental to the model validation activities. Based on shock tube's position-time diagram description in section 2.2.1, the "test section" of the shock tube, where the kinetics are explored, behaves like a constant volume reactor. During the ignition process the sudden release of thermal energy is accompanied by a measured sudden rise in pressure, i.e., measured using side-wall pressure transducers. This pressure rise is short lasting, subsides following ignition by relieving itself axially towards the driver section of the shock tube. While modelling this pressure fall-off is complicated, and is necessary for studies investigating evolution of species post ignition, such modelling can be avoided for ignition delay time experiments' simulations. This is due to the fact that the common definition of ignition time is the onset of the runaway increase in OH radial, i.e. mirrored with the explosive rise of its excited radical counterpart, OH*. Hence, OH* emission is commonly measured and the intersection of the tangent to its inflection point with its pre-ignition baseline emission is used to determine the onset of OH's runaway increase, otherwise known as ignition. For the period bounded by the arrival of the reflected shock to the time of OH*'s exponential increase, a constant volume reactor model captures the physically observed pressure spike. Alternatively, the reactor can be modelled as a constant pressure reactor prior to onset of OH*'s exponential increase but, as pressure does not change significantly prior to OH* rise, this approach fails to capture the pressure rise and its associated potential impact on OH* emission profile. It is important to note that shock tubes can be modified to accommodate constrained reaction volume (CRV) strategy [178], to exhibit constant pressure behavior across the ignition experiment. CRV experiments eliminate the observed pressure spike by limiting the quantity of reactive mixture in the driven section to a small volume near the driven section end-wall. However, the shock tube facilities used in this work could not accommodate CRV. Hence, the reactor was not modelled as a constant pressure one for any of the model validation data generated or utilized in this work. As such, for all Chemkin-Pro simulations of the experimental model validation data, the reactor is modeled as a constant volume reactor. Figure 8 shows a typical experimental pressure profile superimposed with different constant volume reactor modelling options.

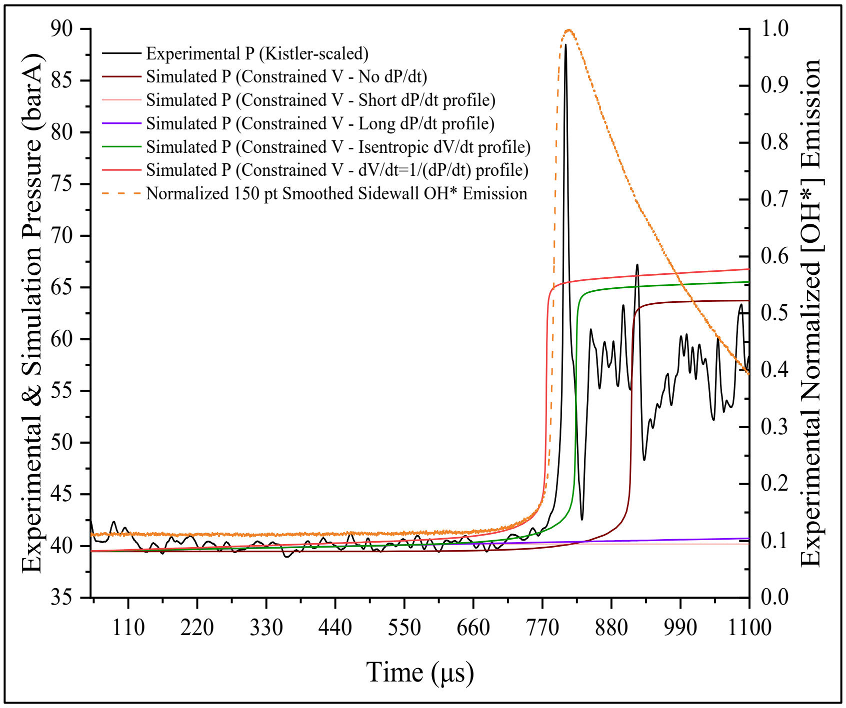

Figure 8: Simulation vs. Experimental Pressure Profiles (barA). Experimental condition of ~39 bar Stoichiometric 4%H_2 combustion in Ar bath. Upper bound Υ of 1.667 applied for isentropic compression of the mixture

While the post ignition reactor condition perturbations are not relevant to studies looking at IDT experiments such as this one, perturbations in the pre-ignition conditions is of great importance, such as the dP/dt effect discussed in section 2.2.1. To incorporate the aforementioned pressure rise into Chemkin-Pro with the constant volume assumption there are two available options in Chemkin-Pro, namely:

1- Constrained reaction volume while solving the energy equation, along with a dV/dt or volume profile (i.e., volume reducing as a function of time to incorporate the corresponding pressure rise)

2- Constrained reaction volume while solving the energy equation, along with a dP/dt or pressure profile (i.e., pressure rising as a function of time to resemble that observed for the facility)

To better understand which choice is more appropriate for the study at hand, Chemkin-Pro's treatment of changes in pressure or volume is important. Thermodynamically, it is expected that an adiabatic increase in pressure or a decrease in volume will both have an associated PV work. Compression processes also have a heat of compression that needs to be accounted for, and assuming such compression happens isentropically, it is important to evaluate how the heat of compression is captured. The reactor at hand is so short-lived that it can be assumed adiabatic, with no wall effects, and is in essence a batch homogeneous reactor, and as such, only the interaction between the gas-phase species are of concern.

For such homogenous 0 dimensional, adiabatic, transient, batch reactor (no mass transport) the conservation equations simplify to:

Mass conservation:

$$\frac{d}{dt}(\rho V) = 0 \tag{3.12}$$

where:

- ρ is the mass density
- V is the reactor volume

Species transient conservation:

$$(\rho V)\frac{dY_k}{dt} = (\dot{\omega}_k V)W_k \tag{3.13}$$

where:

- ρ is the mass density
- V is the reactor volume
- Y_k is the mass fraction of the kth species
- $\dot{\omega}_k$ is the molar rate of production of the kth species by gas-phase chemical reaction per unit volume
- W_k is the molecular weight of species k

Total internal energy of the reactor system is:

$$\frac{dU_{sys}}{dt} = -P\frac{dV}{dt} \tag{3.14}$$

where:

- U_{sys} consists of the internal energy of the system
- $P\frac{dV}{dt}$ is the work done by the control volume (see Figure 2a, reactor is the section of the shock tube in orange, near the driven section end-wall) on the surroundings

Alternatively the time derivative of the internal energy i.e., the LHS of Eq. 3.14 can also be equated with the time derivative of the enthalpy minus the time rate of change of the product of pressure and volume, which for the reactor under study the enthalpy of the system simplifies to that of the gas phase only:

$$\frac{dU_{sys}}{dt} = \frac{dH_{gas}}{dt} - P\frac{dV}{dt} - V\frac{dP}{dt} \tag{3.15}$$

Where:

- H_{gas} is the composite enthalpy of gaseous species

The first term of RHS of equation 3.15 yields a heat balance for the reactor:

$$\frac{dH_{gas}}{dt} = \frac{d(\rho V\bar{h})}{dt} = \rho V\left(\sum_{k=1}^{K_g} Y_k c_{pk}\frac{dT}{dt}\right) + \rho V\left(\sum_{k=1}^{K_g} h_k\frac{dY_k}{dt}\right) + \sum_{k=1}^{K_g} Y_k h_k\frac{d(\rho V)}{dt} \tag{3.16}$$

Where:

- $\bar{h} = \sum_{k=1}^{K_g} Y_k h_k$
- K_g is the number of species in the gas phase
- $h_k = \frac{H_k}{W_k}$
- H_k is the molar enthalpy of species k
- W_k is the molecular weight of species k

To solve the governing equations of the system, substituting equation 3.13 (after rearranging for $\frac{dY_k}{dt}$) into equation 3.16 yields:

$$\frac{dH_{gas}}{dt} = \rho V\left(\sum_{k=1}^{K_g} Y_k c_{pk}\frac{dT}{dt}\right) + \sum_{k=1}^{K_g} h_k(\dot{\omega}_k V)W_k \tag{3.17}$$

Combining equations 3.14 and 3.15 yields:

$$\frac{dH_{gas}}{dt} = V\frac{dP}{dt} \tag{3.18}$$

<u>Conservation of Energy:</u> Combining equation 3.17 and 3.18 yields the transient energy equation for solving the temperature:

$$\frac{dP}{dt} = \rho\left(\sum_{k=1}^{K_g} Y_k c_{pk}\frac{dT}{dt}\right) + \sum_{k=1}^{K_g} h_k(\dot{\omega}_k)W_k \tag{3.19}$$

As such, increase in density, ρ (either by increasing the pressure or by decreasing the volume), enables capturing the positive dP/dt, through the PV work term accounted for in the internal energy conservation equation 3.15.

Moreover, while Chemkin-Pro allows the users to constrain either volume or pressure, and simultaneously implement either a pressure or a volume profile, it is important to demonstrate how it incorporates the contradicting requirements of an enforced pressure profile for a constrained volume simulation, through the ignition process. When volume is constrained the slow pressure change due to dP/dt effect will interfere with the pressure change expected as a consequence of ignition. To demonstrate Chemkin-Pro's modelling options, and how each option incorporates the user inputs, a shock tube experimental test was simulated in the following five ways, using the syngas model developed in this work:

1. Constrained volume with no dP/dt effect
2. Constrained volume with a short duration pressure profile, ending prior to ignition
3. Constrained volume with a long duration pressure profile, extending beyond ignition
4. Constrained volume with pressure rise implemented as a volume decrease, by assuming PV^{Υ}=constant, i.e., assuming the pressure change is isentropic

5. Constrained volume with pressure rise implemented as a volume decrease, by assuming PV=constant, i.e., a change in pressure will only manifests itself as a reciprocal ideal gas change in volume

These results are depicted in Figure 8. Adoption of an approach is determined by its capability to reproduce the experimentally measured parameters, which are test section (reactor) pressure and OH* emission profile up to the ignition point. Figure 8 illustrated the results of the associated simulation pressures superimposed with the experimental scaled pressure recorded. The experimental pressure had to be scaled by a factor of 1.4, to offset the effect of the signal splitting hardware at KAUST's facilities.

Comparison of the cases where dP/dt is accounted for using a pressure profile vs. those using a volume profile, indicate that specification of a pressure profile overrides the constrained volume requirement. This erroneously forces the pressure to respect the input pressure profile even during the ignition process's experimentally observed pressure spike. As, such the reactor better resembles a constant volume one, with simulated pressures similar to the mean of the post ignition pressure oscillations, observed experimentally. Finally, it can be observed that implementation of dP/dt does impact the ignition delay time. This was confirmed by comparing different dP/dt values while monitoring the associated temperature profile and their consequent impact on global reactivity.

Finally, in order to implement an isentropic pressure profile, the measured estimates of dP/dt were converted to their corresponding dV/dt for isentropic compression of each reactive mixture using the relation:

$$\frac{P_2}{P_1} = \left(\frac{V_1}{V_2}\right)^{\gamma} \tag{3.20}$$

Where γ is the ratio of the molar weighted constant pressure and volume specific heats of each mixture.

The associated volume profiles were then implemented into the Chemkin-Pro simulations along with a constant volume reactor model with dynamic solving of the internal energy equation. In these Chemkin-Pro simulations, for example for the syngas simulations, the associated mechanism i.e. CanMECH 1.0 as depicted in Table 1, were implemented along with the associated thermodynamic database. A similar approach was also followed for the CH_4 mechanism.

Finally, in the model improvement and validation process sensitivity analysis simulations discussed in section 3.7 are relied on to detect rate parameters or properties that require further improvement or optimization. With the model development and validation approach defined, the next chapter details the experimental test facilities and methods used to generate novel model validation data in this work.

Chapter 4 Experimental Setup

To fill the knowledge gap existing in terms of model validation data, two shock tube ignition delay time experimental test campaigns were designed, one focusing on H_2 and another on CH_4 oxidation. These test campaigns were conducted at King Abdullah University of Science and Technology's (KAUST) Clean Combustion Research Center (CCRC).

4.1 Design of experiments

Based on review of the literature, the following considerations informed the design of experiments, which will be discussed in the proceeding subsections:

- Techniques to mitigate the effect of impurities on ignition delay time measurements;
- Practical test time limits for shock tube IDT experiments;
- Maximum practical concentrations of polyatomic molecules for manageable IDT uncertainties;
- Suitable diagnostics for IDT measurements of highly bifurcating mixtures; and,
- Maximum fuel concentrations to minimize chance of pre-ignition

Additionally, due to H_2O's high dew point even at ambient conditions, which also increases with pressure, experiments must be designed to preclude water condensation. To this end, a series of flashpoint calculations were conducted in AspenHYSYS and Peng-Robinson equation of state, and it was determined that mixtures' dew points for the high-pressure conditions explored in this work were lower than 130°C, i.e., for both shock tube charge pressures as well as mixing vessel's maximum fill pressures considered. Consequently, the high-pressure H_2O-laden experiments were designed to be conducted with a T_1 of 150°C.

4.1.1 Mitigating effects of impurities on IDT

Recent papers by Urzay et al. [57], Mulvihill and Petersen [58], and Ninnemann et al. [53] show that hydrogen ignition delay time experiments can be highly impacted by the presence of impurities. Urzay et al. [57] proposed a method to quantify these effects using a simplified five-step chemistry, however, its applicability to high-pressure experiments needs further examination. On the other hand, Mulvihill and Petersen [58] investigated the effect of impurities on shock tube ignition delay time experiments numerically and experimentally, and identified that the cleaning of the mixing tank can have a significant impact on reducing the effect of impurities on IDT experiments. Moreover, the authors showed that while highly diluted H_2 experiments are very sensitive to impurity effects, these effects are minimized at dilution levels of less than 94%. Finally, they also showed that CH_4 experiments were insensitive to these impurity effects [58]. Ninnemann et al. [53] conducted shock tube experiments, and confirmed Mulvihill and Petersen's [58] conclusions. Both aforementioned studies showed that the presence of shock tube diaphragm fragments from previous experiments had negligible impact on the IDTs measured, hence removing them is deemed not critical. In this work, a set of experiments were conducted prior to the start of test campaign at equivalence ratio of 1, with H_2 concentration of 2.7% in Ar. Those experiments confirmed that H_2 IDT experiments were shortened at these concentrations when higher impurities, likely from CO_2 cylinders, were present. Consequently to mitigate the impact of impurities in the experimental test campaign a requirement for minimum concentration of 4% H_2 was implemented. It should be noted, that this requirement does not apply to the CH_4 test campaign in-line with the aforementioned studies [58, 57].

In addition, to further minimize the adverse impact of impurities that may accelerate IDT measurements the following procedure was followed:

1- Mixing tank was cleaned with tert-Butyl hydroperoxide (TBHP) prior to starting the H_2 test campaign, followed by overnight vacuuming to lower than 10^{-4} milli-bar;

2- All wetted mixture preparation apparatus and shock tube feed lines were cleaned before the start of the first test campaign with TBHP, followed by overnight vacuuming to lower than 10^{-4} milli-bar;

3- In between each test vacuum shock tube and feed lines were vacuumed to lower than 10^{-4} milli-bar;

4- Shock tube was cleaned with acetone or TBHP prior to the start of each test campaign;

5- Shock tube cleaning was followed by a minimum of five unfueled high concentration oxygen shocks at temperatures of 3000-5000 K to burn off any remaining cleaning agent, followed by vacuuming to lower than 10^{-4} millibar;

6- H_2 test campaigns were conducted immediately after the cleaning procedures, prior to CH_4;

7- Certified high purity feed gases were sourced from the Abdullah Hashim Gases (AHG) with the following purities: H_2 (≥ 99.9999%), CH_4 (≥ 99.999%), O_2 (≥ 99.999%), Ar (≥ 99.9999%), He (99.999%), CO_2 (≥99.995%);

8- The order of tests were controlled to reduce potential cross contamination. As such tests having $CO_2/H_2O/Ar$ and CO_2/Ar as the bath gases, were conducted after conducting tests having only H_2O/Ar and Ar as the bath gas. This was a precautionary measure to eliminate any residual potential impact of impurities on tests which did not contain CO_2, due to its higher HC impurities.

4.1.2 Practical test time limits for IDT experiments

Due to the conflicting requirements of the need to target high temperature experiments at equivalence ratio of 1, and minimum H_2 concentrations of 4% a compromise was needed to reduce the maximum temperature targeted. This is due to the fact that higher fuel and oxidizer concentrations at high pressures and temperatures result in very short ignition delay times, less than 100 μs. Pyror et al. [14] showed that depending on the definition of ignition time, for IDT range of 100-1000 μs, variations of 50 μs were present for mixtures containing less CO_2 and this variation increased to 80 microseconds for mixtures containing CO_2 concentration of 60%. As such, at shorter time scales, the relative cumulative magnitude of uncertainties to IDTs become unacceptably large, rendering the associated IDTs less effective metrics as model validation targets. Consequently, for the experimental test campaigns, conditions having estimated IDTs larger than 100 μs were only kept in the plan.

Conversely, for lower temperature experiments a requirement was put in place to target conditions that resulted in IDTs smaller than 2 milliseconds, to preclude the impact of contact surface or expansion fan arrival prior to ignition in the test section of the shock tube. In fact for a few experiments these effects were encountered which prematurely ended the test time, and hence the results from those experiments were removed from the validation data set.

4.1.3 Maximum fuel concentrations to minimize chance of pre-ignition

While maximum fuel concentration may be indirectly limited by the minimum ignition delay time requirement of larger than 100 μs, it also has direct implications on ignition delay time uncertainties. Pang et al. [52] and Ninnemann et al. [53] both showed hydrogen concentrations of 15% experienced pre-ignition phenomena, whereas lower concentration of 4% H_2 concentrations were much less impacted by it. Ninnemann et al. [53] discussed the undesirable characteristics of pre-ignition phenomena, i.e. reducing ignition delay time due to energy release prior to the main ignition event, reasons for which are not fully understood.

While in this work, CH_4 and H_2 concentrations were less than 5% due to the minimum IDT duration requirement of 100 µs, the maximum fuel limitations informed the model validation data selection process.

4.1.4 Maximum practical concentrations of polyatomic molecules

Presence of large quantities of polyatomic gases result in the bifurcation of the reflected shock [56]. Depending on the extent of bifurcation, ignition delay time measurements may be adversely impacted [54]. These impacts include presence of flow fields at the boundary layer, resulting in cold or hot spots and turbulence, all of which could cause deviations from the ideal homogenous reactor assumption at the test section [13]. To ensure these effects are manageable, the experiments were designed to strike a balance in enabling the exploration of as high a concentration of H_2O and CO_2 while minimizing their impact on the measured validation IDT data generated. Concentrations of up to 65% H_2O and 45% CO_2 are of relevance to oxy-fuel combustion technologies with wet flue gas recirculation. To this end, based on the findings of studies in the recent literature additional limits were imposed on the test plan.

Petersen and Hanson [56] investigated the extent and magnitude of bifurcation, and concluded that it was a strong function of the specific heat ratio of the gas, and to a lesser degree depended on the molecular weight and the incident shock Mach number. The authors concluded that while high levels of bifurcation were apparent, they did not affect the core portion of the post-shock region, which comprised most of the flow area. The conditions they investigated covered gases with molecular weights from 14.7 to 44.0, specific heat ratios of 1.29-1.51, P_5s of 11-265 atm, T_5s of 780-1740 K [56]. This molecular weight range covers CO_2 and H_2O's, and the pressure and temperature ranges are wide and inclusive to high temperature conditions. Their lower limit of specific heat ratio of 1.29 constituted the first limitation imposed on gamma, $\gamma=C_P/C_V$, in this work.

Hargis and Petersen [54] recently investigated the effect of high concentrations of CO_2 versus N_2 on reflected shock bifurcation effects, for conditions of 1 and 10 atm, at temperatures of 1450-1900 K, with 75% dilution, i.e., 0-75%CO_2 concentration with the balance N_2 at increments of 25%, with gamma values of 1.31, 1.33, 1.36, and 1.39. The authors concluded that for mixtures with gamma values of 1.31 and 1.33, the fluid motion due to bifurcation was very high rendering interpretation of pressure data difficult. In addition, suppressed pressure traces due to the CO_2's larger heat capacity rendered pressure-based IDT determinations even more difficult. The authors also reported higher uncertainties associated with higher pressure experiments (~10 bar), and attributed it to more turbulent boundary layers expected at high pressures. The combination of Hargis and Petersen [54] and Petersen and Hanson [56] studies covers the wider pressure range of 1-265 atm, at temperatures of 780-1900 K, which encompasses the conditions targeted in this work. Based on the pressure and emission traces provided by Hargis and Petersen [54] it was concluded that while mixtures with gamma values of 1.31 and 1.33 should be avoided, mixtures with larger gamma values will likely produce IDT model validation targets with manageable uncertainties. As such for this work, the lower bound gamma limit was increased to 1.36.

More recently, Pryor et al. [14] investigated the impact of high CO_2 dilutions of up to 89.5%, at T_5s of 1650-2040 K and P_5s of 0.6-1.2 atm, on stoichiometric CH_4 IDTs, using shock tube end-wall high speed camera imaging. End-wall high speed camera imaging enables direct probing of homogeneity of ignition, versus the non-ideal deflagration process with localized flame kernels. The mixtures investigated showed that high flame area ratios, i.e. ratio of visible flame to cross sectional area of 71% and higher were observed for CO_2 concentrations of 60% and lower [14]. Moreover, the authors noted that the flame area ratio increased with temperature. Pyror et al. also investigated stoichiometric CH_4 IDTs in CO_2 and Argon bath gases with CO_2 concentrations of 30%, 60% and 85% at temperatures of 1300-2000 K and pressures of 6-31 atm. The authors concluded that the uncertainties for the 85% diluted tests were approximately 20%. Based on their findings it is apparent that there is impetus to reduce the concentrations of CO_2 below 60% and target higher T_5 when possible.

To summarize, it was concluded that that mixtures with gamma values larger than 1.36, CO_2 concentrations of <60%, and higher temperatures should be targeted to reduce the impact of bifurcation. Due to the lower specific heat ratios targeted in this work caused by the presence of large concentrations of H_2O and CO_2, H_2O's concentrations had to be limited to 45% to respect the aforementioned constraints. Also as CO_2 concentrations of up to 45% are expected in the flue gases of gaseous- and liquid-fueled pressurized oxy-combustion systems this maximum concentration limit was also imposed for CO_2 in this work.

To respect the practical test time limits, a series of temperature sweeps of ignition delay times were performed using Keromnes et al.'s model for the H_2 test campaign, and using AramcoMECH2.0 and GRI-MECH3.0 for the CH_4 test campaign, targeting higher temperature chemistries. Due to the desire to benchmark and explore these chemistries at low and high pressures, two pressures of 2 and 40 bar were targeted, which culminated in the two test plans, one provided in Table 3 for the H_2 test campaign, and the other detailed in Table 4 for the CH_4 test campaign:

Table 3: Low- and high-pressure H_2 IDT test campaign target conditions

T_5 (K)	P_5 (bar)	Mix group #	Ar mole frac.	CO_2 mole frac.	H_2 mole frac.	H_2O mole frac.	O_2 mole frac.	MW in g/mol	T_1 (K)	Specific heat ratio $\gamma_1 = Cp_{1mix}/Cv_{1mix}$
1225-1325	2	1	0.94	0	0.04	0	0.02	38.3	343	1.64
1225-1325	2	2	0.49	0.45	0.04	0	0.02	40.1	343	1.39
1100-1225	40	3	0.94	0	0.04	0	0.02	38.3	295	1.64
1100-1225	40	4	0.49	0	0.04	0.45	0.02	28.4	423	1.43
1100-1225	40	5	0.49	0.15	0.04	0.30	0.02	32.3	423	1.41
1100-1225	40	6	0.49	0.45	0.04	0	0.02	40.1	423	1.37

Table 4: Low- and high-pressure CH_4 IDT test campaign target conditions

T_5 (K)	P_5 (bar)	Mix group #	CH_4 Mole frac.	O_2 Mole frac.	CO_2 Mole frac.	H_2O Mole frac.	Ar Mole fract.	MW in g/mol	T_1 (K)	Specific heat ratio $\gamma_1 = Cp_{1mix}/Cv_{1mix}$
1550-1750	2	7	0.03	0.06	0	0	0.91	38.8	333	1.62
1550-1750	2	8	0.03	0.06	0.45	0	0.46	40.6	333	1.39
1550-1750	40	9	0.005	0.01	0	0	0.985	39.7	423	1.66
1550-1750	40	10	0.005	0.01	0	0.45	0.535	29.9	423	1.44
1550-1750	40	11	0.005	0.01	0.15	0.30	0.535	33.8	423	1.42
1550-1750	40	12	0.005	0.01	0.45	0	0.535	41.6	423	1.37

It should be noted that low-pressure H_2O- and H_2O/CO_2-laden experiments were originally planned, but, due to technical issues as they were not successful, they were eliminated from the test plan.

4.1.5 Diagnostics for IDT measurements of highly bifurcating mixtures

To determine ignition delay times reliably, accurate means are necessary for pinpointing both the true start time of the experiment, i.e. "time zero" as well as the true "ignition time". In the context of bifurcating mixtures the true time zero can be defined as the time when the core gas has been processed by the planar normal portion of the reflected shock wave. This is due to the fact that while the core portion of the post-shock region where the gases are at T_5, P_5 [56, 54], the boundary layers are not. As such side-wall pressure measurements which are the conventional means to determine time zero, are not suitable for the mixtures targeted in this work. In fact, they predict time zeros that are more delayed that reality, resulting in underestimation of IDTs. Alternatively, Schlieren spike of line of sight lasers traversing the diameter of the shock tube located axially at the test plane has been shown to be fairly immune to boundary layer effects such as bifurcation. As such they are employed in this work to accurately determine the true time zero.

Determination of the ignition time is, however, more controversial. From the work of Pryor et al., as well as Hargis and Petersen [54, 14], it is concluded that different ignition time definitions result in large variations at times around 100% for short IDTs. The most widely accepted definitions of ignition delay time is the time of intersection of extended tangent to OH* emission trace inflection point with base line OH* emission level prior to ignition, and the time of intersection of extended tangent to pressure trace inflection point with base pressure prior to ignition, all measured at the test section of the shock tube. While the latter definition will not be workable for highly bifurcating mixtures, Hargis and Petersen have shown that the former may be more immune to bifurcation effects [54]. The exception to this is localized pre-ignition events reaching the view port of the photomultiplier (PMT). Moreover, while both excited species emission and pressure signals maybe subdued by the presence of high heat capacity quenching bath gases, particularly at low fuel loadings, emissions diagnostics had higher signal to noise ratios (SNR). In this work, for the low-pressure CH_4 test campaign, OH laser absorption spectroscopy (LAS) measurements were also done, similar to Badra et al. [179]. The increase in absorbance of the laser was used to determine the time of ignition, similar to the OH* emission-based ignition time definition. For these measurements, the time of intersection of the tangent of the maximum slope inflection of the OH LAS absorbance with the initial OH LAS absorbance (immediately after passage of the reflected shockwave), was defined to mark the ignition time. In terms of location of diagnostics, both pressure and emissions instruments, as well as the line-of-sight OH LAS laser are commonly located on the side-walls at the test plane. Petersen [180] grouped IDT shock tube experiments into two categories to better assist with decision making on effectiveness of the location of emissions diagnostics, namely:

1- Highly diluted mixtures: mixtures with inert diluents such as Ar or N_2 on the order of 97% by volume or more

2- Undiluted mixtures: mixtures which involve only fuel and oxidizer (air), without additional dilution

Petersen, concluded that while under ideal shock tube conditions, ignition behind reflected shockwave occurs first at the end-wall, under dilute conditions end-wall emission measurements can lead to artificially longer ignition times [180]. The longer apparent ignition time was shown to be a result of the integrated effect of the detector seeing ignition occurring at later times down the length of the driven section [180]. This is also expected to be worsened when there is no significant pressure rise and the ignition event is not abrupt, i.e. when the increase in the excited-state species concentration occurs over a period on the order of a hundred microseconds or greater [180]. As such, these effects are pertinent in this work due to the high dilutions with high heat capacity molecules H_2O and CO_2, and thus end-wall emissions measurements were deemed inappropriate for ignition delay time determinations. As for pressure measurements, because of their lower SNR due to low fuel loadings exacerbated by large concentrations of high heat capacity H_2O and CO_2, they were not deemed useful for IDT determinations.

In summary, in this work, side-wall emission of OH* served as the main diagnostic for determination of ignition time. This diagnostic was also augmented with end-wall emission diagnostics for several tests to detect potential pre-ignition events taking place down the length of the shock tube, and to reaffirm the IDTs determined by side-wall emission measurements. Additionally for the low-pressure CH_4 test campagins OH LAS measurements were also performed as an alternative means for ignition time determinations.

4.2 Shock tube facilities description

King Abdullah University of Science and Technology’s (KAUST) High-Pressure Shock Tube (HPST) and Low-Pressure Shock Tube (LPST) test facilities were used to conduct the experimental test campaigns of this work. These facilities have been described in previous studies [181, 179, 182].

4.2.1 KAUST high-pressure shock tube test facility and diagnostics

At the heart of the test facility is a high-pressure shock tube able to withstand pressures as high as 200 bar, with a large constant internal diameter of 10 cm, a 6.6 m long driven section and a 2.2 m long diver section that is extendable to 6.6 m. The facility has been detailed previously by Burke et al. [181]. The shock tube, its feed line and mixing vessel are jacketed and heat traced. The facility was heated to 150

°C for the water-laden tests of this work, as well as some of the dry tests. The latter was to maintain the leak-tight heated system and minimize emergence of leakage paths brought about by thermal expansion effects associated with temperature changes. For the determination of post-reflected shock temperature, over the last 3.7 meter of the driven section, six piezoelectric PCB112A05 pressure transducers coupled with model 482C signal conditioners and Agilent 53220A 100ps frequency counter/timers are used to accurately measure the incident shock velocity.

To initiate the data acquisition (DAQ) process, and measure the post-reflected shock pressure P_5, a Kistler 603B1 piezoelectric pressure transducer is utilized located on the shock tubes side-wall. It is coupled to a type 5018 charge amplifier, a 15-bit National Instruments BNC-2110, and a Tektronix DPO 3014 Digital Phosphor Oscilloscope to enable effective recording of data generated from the multitude of instruments monitoring the short-lived ideal reactor conditions at the test plane.The average uncertainty in incident shock velocity measurements were ±0.24% for the H_2, and ±0.37% for CH_4 high-pressure test campaigns, respectively. Deviation from linear fit of the multiple velocity measurements, made by the PCB and time counters, was used for each run to calculate these uncertainties. Uncertainties calculated for the reflected shock pressure varied and expectedly were larger for the water and CO_2-laden tests, due to additional errors associated with their pressure-dependent thermodynamic properties, and non-ideal behavior of mixtures prepared, see section 3.3.

Time 0, i.e. the arrival of the normal section of the reflected shock at the test section located 10.48 mm from the driven section end-wall of the shock tube, was determined using a REO precision optical solutions Newport R-32172 fixed wavelength IR HeNe laser at 3392 nm. The laser utilized a VIGO Systems STCC-04 TEC power supply and was coupled with two VIGO Systems S.A. PV1JTE-4/MPDC-F-10 for the detection of the reference and attenuated laser beam intensities.

For the determination of ignition time, a HAMAMATSU 1P21 photomultiplier detector and voltage controller coupled with a THORLABS 307 bandpass filter is used to detect excited OH emission. An identical setup was also used for end-wall emission measurements.

For the determination of ignition time, a HAMAMATSU 1P21 photomultiplier detector and voltage controller coupled with a THORLABS 307 bandpass filter is used to detect excited OH emission. A similar setup is used for both side wall emission as well as end-wall emission detection. End-wall emission and side-wall Kistler pressure signals were used to confirm the detected ignition time when their signals were deemed reliable.

4.2.2 KAUST low-pressure shock tube test facility

KAUST's low-pressure shock tube has a 9 meter long driver as well as a driven section of identical length. The facility has been previously described by Badra et al. [179]. The shock tube and its feed line connected to a mixing vessel are jacketed and heat traced, and can be heated up to 100°C. For the determination of post-reflected shock temperature, over the last 1.5m of the driven section, five piezoelectric PCB pressure transducers coupled with model 482C signal conditioners and Agilent 53220A 350MHz 100ps frequency counter/timers were used to accurately measure the incident shock velocity. The average of the errors of the measured velocities was ±0.23% for the H_2, and ±0.24% for CH_4 low-pressure test campaigns, respectively. Uncertainties calculated for the reflected shock pressure varied and expectedly were larger for the water and CO_2-laden tests, as they introduce additional uncertainties, associated with thermodynamic properties (due to their pressure dependence), as well as additional mixture preparation uncertainties, see section 3.3.

To initiate the data acquisition (DAQ) process, and measure the post-reflected shock pressure P_5, a Kistler 603B piezoelectric pressure transducer is installed at the test section. It is coupled to a type 5018 charge amplifier, a National Instruments BNC-2110 15 bit, and a Tektronix DPO 4104B Digital Phosphor Oscilloscope with 11-bit resolution, to enable effective recording of data generated from the instruments monitoring the short-lived reactor at the test plane.

For the determination of time 0, i.e. the arrival of the normal section of the reflected shock at the test section located 2 cm from the driven section end-wall of the shock tube, either of two laser setups were used. The first laser setup is a REO precision optical solutions Newport R-32172 HeNe laser at a fixed wavelength of 3392 nm, coupled to two VIGO Systems S.A. PV1JTE-4/MPDC-F-10 for the detection of the reference and attenuated laser beam intensities. The second is a 200 mW UV light tuned to 306.69 i.e. coincident with the center of OH's $R_1(5)$ $A^2\Sigma \leftarrow X^2\Pi$. The laser is coupled with a modified PDA10CS-EC detector, as well as a Modified PDA36A-EC, both of which are augmented with a 307 nm Endover Bandpass filter to detect the reference and attenuated laser beam intensity. The Schlieren spike was found to be stronger for the OH laser, relative to those recorded from the HeNe laser.

For the determination of ignition time, a HAMAMATSU 1P21 photomultiplier detector and voltage controller coupled with a THORLABS 307 bandpass filter were used to detect excited OH emission. A similar setup was used for both side-wall and end-wall emission detection. Additionally, for the CH_4 test campaign, OH LAS measurements were also done as a secondary means for the determination of ignition time. The continuous wave (CW) UV laser tuned to 306.69 nm, i.e. $R_1(5)$ in OH A-X (0,0) band, was used to measure the rate of OH LAS absorbance increase for the determination of time of ignition. The laser system included a Spectra-Physics Millenia Price 10.5 pump laser, coupled with CW 1 W Matisse ring dye tunable laser, connected to a CW Spectra Physics frequency doubler, to generate a 200 mW laser tuned to 306.69 nm. The laser beam leaving the wavetrain was then split using a THORLABS beam splitter, and its reference intensity was measured using a modified PDA10CS-EC detector equipped with a 307 nm Endover bandpass filter. The attenuated laser beam intensity was measured, using a modified PDA36A-EC detector with a 307nm Endover bandpass filter. The same ignition time definition used for IDT determinations using the OH* emission, was also applied to OH LAS absorbance.

4.3 Mixture preparation

Mixtures were prepared manometrically for both test facilities. Water was injected in the form of liquid using a Monoject hypodermic syringe (0.816 mm x 3.8 cm) along with a septa valve, followed by vaporization to determine its final partial pressure.

To minimize cross contamination of mixtures and enable effective loading and measurement of the water content of mixtures the following procedure was devised:

1. Prior to every mixture preparation, the mixing vessel and mixture preparation and feed lines were vacuum pumped to pressures below 0^{-4} milli-bar;
2. For H_2O-laden mixtures, the mixing vessel was heated to 150°C for the high-pressure test facility to remain above the dew point of water by at least 25 °C;
3. Fuel and oxidizer were loaded into the mixing vessel and their injection was measured using 0-1000 torr Baratron pressure transducers;
4. Water was then injected using the Monoject syringe and a septa valve. It should be noted that water injection as the fourth or fifth gas was not feasible due to high back pressure of the mixing vessel;
5. Following liquid water injection, mixing vessel pressure rise was monitored until it halted, indicating complete evaporation of liquid water; and,

6. After the mixing vessel pressure plateaued, CO_2 was injected, followed by Argon. Argon was always as the last component to reach the total targeted pressure. The latter ensured that the fuel and oxidizer loadings were not impacted by the less-controlled water injection process.

The HPST facility is equipped with a 100L jacketed and heated stainless steel vessel, along with a magnetic stirrer. However, as the stirrer was malfunctioning, mixtures were prepared and left overnight to ensure homogeneity. For mixture preparation in this facility a set of MKS-Baratron 615A13TRC with 0-1000 torr range was used for H_2, CH_4 and O_2 injection, as well as another set with a range of 0-25,000 torr, for H_2O, CO_2 and Ar injection.

For the H_2O-laden mixtures to minimize chance of condensation in addition to the mixing vessel (MV) being heated to 150°C, the maximum pressure of mixtures were also capped. For mixtures containing 45% H_2O, the maximum MV pressures did not exceed 3675 and 4200 torr for the H_2 and CH_4 tests, respectively. For mixtures containing 30% H_2O, and 15% CO_2 the pressures did not surpass 5500 and 6100 torrs in the H_2 and CH_4 tests, respectively. All connecting piping, valves and manifolds that would come into contact with water were heat traced, preheated to 150 °C and kept at this temperature during the mixture preparation process. Spot checks were performed to ensure equipment were in good working order and the apparatus was properly insulated.

A similar procedure was also followed in the LPST test facility. This facility was equipped with a 21.4 L jacketed and heated stainless steel vessel with a stirrer. Mixtures were prepared using MKS-Baraton 628DX13TBE2B pressure transducers with a range of 0-1000 torr.

4.4 Reactor/Shock tube test section's T_5 and P_5 uncertainties analyses

While shock tube is the main reactor vessel used in these experiments, the idealized reactor near its driven section end-wall probed for the model validation data is in fact much smaller and very short lived. Reaction times that can be accommodated are in the order of a few milliseconds, and as such measurement of temperature is not possible, and instead must be calculated. Similarly, while pressure is measured experimentally due to the noise associated with such measurements, they are typically used to confirm the calculated reactor pressures. To determine the post reflected shock reactor conditions, T_5 and P_5, in this work, the FROSH code developed by Stanford University and recently published by Campbell [183] was adopted. Inputs to the code are the measured values of pre-test driven section temperature and pressure T_1, P_1, the measured incident shock velocity, in addition to thermodynamic properties of feed gases in 7-coefiicient NASA polynomials format as a function of temperature only. However, embedded in these calculations are the following assumptions to determine the temperature and pressure, T_5 and P_5:

1- The mixture does not react during the passage of the incident shock wave. This assumption can be examined by example. A typical incident shock velocity is measured to be approximately 917 m/s. As the test plane is located 1-2 cm from the end-wall, it takes ~10-20 μs for it to reach the end-wall prior to reflecting. The temperature reached after passage of incident shock is 761 K. The reflected shockwave typically has a speed of ~409 m/s, and requires ~24-49 microseconds to reach the test plane. Collectively, the mixture at the test plane has spent as long as 70 μs at a temperature of approximately 761 K. At such relatively low temperatures the reaction rates for the small fuel concentrations considered are negligible and as such, it can be assumed that the mixture has not reacted until it is processed by the reflected shock.

2- The gas components are energetically relaxed, i.e. equilibrium is established between the translational, vibrational and electronic energies of the molecules after passage of the incident shockwave prior to being processed by the reflected shockwave. At non-equilibrium conditions the translational, rotational, vibrational and electronic temperatures of a molecule will not be the same, and the Boltzmann definition of temperature which assumes equilibrium will not be true. If sufficient time is available equilibrium will be achieved post-passage of the incident shock. The timelines for translational, vibrational and electronic relaxation are such that they can be assumed to be shorter than the available time between passage of incident shock wave and the arrival of the reflected one. This enables applying the shock relations in a step wise fashion twice. Once for the processing of the reaction gas at x-t position 1 with the incident shock, to obtain the conditions at x-t location 2 and a section time to the reactive mixture at location 2 being processed by the reflected shockwave to determine the target reactor conditions at x-t location 5. This assumption is valid as the relaxation times are shorter than the previously discussed example time lines at the test plane.

3- As the shock relations implemented into the calculations of T_5 and P_5 are in essence a product of simultaneous solving the mass, momentum and energy conservation equations combined with ideal gas law, deviations from ideal gas behavior are not commonly accounted for in such calculations.

Since the conditions encountered in combustion systems are usually at high temperatures (greater than 1000 K), and lower pressures (below 100 bar), deviations from ideal gas law are commonly neglected. While such deviations from ideal gas law have been shown to have a minimal impact, see section 2.4, the errors introduced by the pressure dependence of thermochemical properties of H_2O and CO_2, are not negligible and must be accounted for under the conditions encountered in this work, see the investigation presented in section 3.3.

To determine the experiment-specific uncertainties associated with the calculated T_5 and P_5, the contribution of each input parameters' test-specific uncertainty were quantified and combined. To this end, in-house codes were written in Matlab and integrated with FROSH to automate evaluation of the following uncertainties:

1- Uncertainties associated with P_1 measurement. This was determined based on the accuracy of the shock tubes' charging pressure transducers, i.e., MKS-Baratron model 615A53TRC, and MKS-Baratron model 628DX13TBE2B for the high and low-pressure shock tubes respectively. Their maximum errors were ±0.12% of reading.

2- Uncertainties associated with T_1. These were determined based on the accuracy of the surface thermocouples which are also used to control the wattage input of the shock tube jacket heaters, for heated tests. This error was reported to be ± 2.1 °C for the K-type thermocouples used for both the LPST and HPST facilities.

3- Uncertainty associated with incident shock velocity measurements, these errors are calculated using KAUST's in-house code which compares the velocities measured by the PCB pressure transducers timed pressure spikes measured using time counters. The code calculates both the incident shock velocity as well as its attenuation rate. As the attenuation rate is supposed to be linear, the error reported is based on the linear fit of the individual velocities measured. The error reported is test-specific but on average it is approximately 0.3% of the velocity.

4- Error associated with thermodynamic properties. While Burchat's thermodynamic properties database [72] includes fit errors for CH_4, H_2, O_2, Ar, CO_2 and H_2O, these uncertainties are only valid at low pressures. As such, for the high-pressure tests in this work, for the case of H_2O and CO_2, a comparison with NIST's high accuracy "thermophysical Properties of Fluid systems" data [90] was completed to quantify and increase the associated uncertainties. It was observed from the discussions in section 3.3, that NIST commonly estimates a higher C_P for H_2O and CO_2 than those estimated by the NASA polynomials at the conditions relevant to this study. Based on comparisons performed, the worst case, i.e. highest pressure lowest temperature conditions, upper bound positive errors for the post-incident and -reflected shock condition were estimated to be 2.2% and 1.4% for H_2O, and 0.46% and 0.8% for CO_2, respectively. As the same thermodynamic database is applied for both conditions, an average of the two provides an approximate measure of the upper bound error. As such for the uncertainty analysis the upper bound error of Burchat's thermodynamic properties database [72] were increased to 1.8% for H_2O, and 0.63% for CO_2 to account for the non-ideal pressure effect on these properties. It should also be noted, as the relations are interrelated, changes in enthalpy and heat capacity were simultaneous and in the same direction for each species.

5- Uncertainties associated with mixture concentrations. While manometrically prepared mixture concentrations are generally very accurate for gaseous mixtures, the errors associated with H_2O and CO_2-laden mixtures are expected to be non-negligible. In this work the errors of the pressure transducers, used to determine the concentrations, were determined based on the pressure transducers' reported accuracies. Moreover, as these gases were both non-ideal, the degree of deviation from ideal gas law was estimated using re-simulation of the mixture preparation process in AspenHYSYS using its Peng-Robinson fluid package. As such, the uncertainties of such non-ideal behavior were also incorporated into uncertainty analysis of mixtures. Depending on the number of mixture components and order of filling, either CO_2, or Ar concentration was adjusted to accommodate the estimated uncertainties.

In order to enable effective combination of the errors, two approaches were followed. One that is commonly adopted in the literature is to assume that the errors are random and orthogonal. The latter is satisfied, due to the small errors in temperature, although other inputs depend on temperature. For the former, at high pressures, H_2O and CO_2's C_p and concentration uncertainties are highly skewed and both were in the same direction. As Cp and concentration errors were also of the same order, RSS errors bars were deemed appropriate, since the positive and negative RSS uncertainties are calculated independently which enables them to capture the skewness in error. RSS errors were also used in graphical representations of IDTs in this work. With these assumptions individual contribution of each of the input parameters, investigated one at a time, can be combined using a root sum of squares analysis (RSS) [183]. The errors are then combined using:

$$\boldsymbol{\varepsilon_{RSS}} = \sqrt{\sum_{\boldsymbol{m=1}}^{\boldsymbol{N}} \left(\frac{\boldsymbol{\Delta R_m}}{\boldsymbol{R}}\right)^{\boldsymbol{2}}} \tag{4.1}$$

where ε_{RSS} is the RSS uncertainty, N is the number of input variables, $\frac{\Delta R_m}{R}$ is the relative error associated with input M. An alternative approach than enables quantification of interdependencies and determination of maximum-uncertainties, is also implemented in this study to determine the worst-case-scenario uncertainties. To this end, similar to the approach of Campbell [183], a Matlab code was developed in this work, enabling examination of all possible combination of input variable errors at three values of: 1) measured (or center value), 2) upper bound uncertainty value 3) lower bound uncertainty value, which incorporate the largest positive and negative deviations, for all input variables. The input errors were those pertaining to T_1, P_1, C_p and H of each species (three to five depending on the mixture), incident shock velocity, concentration error in CO_2, and concentration error in H_2O. This constituted between 3^6=729 to 3^{10}=59,049 matlab parametric runs per experiment, depending on the number of gases present in the mixture. Among the cases ran for each test, with its specific T_1, P_1, incident shock velocity, and concentration errors, the highest and lowest values of T_5 and P_5 were extracted to determine their maximum-uncertainties reported in this work.

4.5 Facility-specific dP/dt effect

The facility-specific dP/dt effect discussed in section 2.2.1 is commonly measured in facilities for different mixtures. Campbell [183] noted that, based on the literature, these effects are more significant for lower pressures and higher temperature experiments, i.e. temperatures above 1400 K and pressures below 10 atm. However, due to the bifurcation effect for the H_2O and CO_2 laden mixtures, side-wall pressure measurements could not be used to quantify the effect. Although such measurements may have been possible using end-wall pressure transducers, the facilities were not equipped to accommodate end-wall pressure measurements. Therefore, previous side-wall measurements performed at the HPST and LPST facilities at KAUST for highly diluted mixtures, were referred to from the literature to estimate this effect. Moreover, pressure traces of experiments with Ar dilutions larger than 94% were reviewed for further insight into the extent of this effect. The longest test in these campagins was ~2 ms for the high-pressure test campaign, and no significant dP/dt was detectable, due to the short test time. As such for the HPST while the estimates of 2-3%/ms and 3%/ms had been reported by Javed et al. [182] and Burke et al. [181], respectively, values of 2-2.5%, were incorporated into the constant volume simulations of this work, as detailed in section 3.9. For the LPST an estimate of 3-4%m/s were reported by Badra et al. [179], and since the Ar-diluted experiments reviewed were shorter, an average value of 3.5%/ms was adopted when simulating the reactor in this work.

Chapter 5 Experimental and Kinetics Study of H_2/CO Oxidation Mechanism at High Pressure in the Presence of H_2O and CO_2

To validate the H_2/CO model developed, CanMECH, this chapter first details the unique shock tube experimental results generated in this work along with an analysis of their uncertainties. These novel experimental data had to be generated as they are crucial to the validation of the kinetics mechanism, and to fill the existing knowledge gap in the literature. This is followed by a description of additional IDT model validation data selected from the literature. Then, model performance evaluation criteria used to assess the model's ability to reproduce experimental validation targets is discussed. Subsequently, the results of a comparative performance evaluation of the untuned CanMECH vis-à-vis Keromnes et al. [28] are presented and discussed. The results of kinetic rate parameter IDT sensitivity and parametric studies to determine suitable tuning parameters as well as the degree of appropriate tuning are detailed. The tuned model's performance evaluation results are then discussed. This is followed by its application to characterize the impact of pressure, temperature, as well as H_2O and CO_2 dilution on the chemistries, extrapolated to pressures exceeding 100 bar.

5.1 Experimental test results

In this work, experimental IDT is defined as the time delay between the second laser Schlieren spike, signifying the arrival of the reflected shock wave at the test plane, and the time of intersection of the tangent to the side-wall OH*'s emission rise's highest slope inflection with its base line value after passage of the reflected shock (see Figure A1 of Appendix B). The same definition of ignition time was also applied to end-wall OH* emission and side-wall Kistler's pressure trace data to confirm consistency and reliability of IDTs determined based on side-wall OH* emission measurements. There were a total of 51 tests with 17 conducted at low pressures and 34 at high pressures for H_2 oxidation.

The results of the low-pressure hydrogen test campaign IDT measurements are summarized in Table 5. It can be observed that the IDT estimates from the different diagnostics corroborate well, with side-wall OH* generally estimating shorter IDTs than others.

Graphical examination of the results show end-wall OH* emission trace commonly exhibits two or more inflections with slightly different slopes during its climb towards peak emission (see Figure A2 in Appendices detailing Test 14's measured signal traces). For such experiments with multiple inflections, while the first inflections produced IDT estimates that corroborated better with the side-wall emission-based ones, they were not commonly the highest sloped inflection. Note that for the IDT estimates listed in Table 5, the highest sloped inflection was used.

Side-wall pressure signal had lower signal to noise ratio relative to emission diagnostics for Ar-diluted experiments. Moreover, it was deemed unreliable for IDT estimation, due to bifurcation effects commonly signified by two distinct peaks and valleys. As such the pressure-based IDT estimates were only reported for Ar-diluted experiments, and the estimates serve a more qualitative confirmatory purpose.

Table 5: IDT measurements of H_2 in Ar and 45%CO_2/Ar baths at φ=1 at ~2 bar

Test ID	T_5 (K)	P_5 (barA)	φ	H_2 mole %	O_2 mole %	Ar mole %	CO_2 mole %	Measured IDT Side-wall OH* (μs)	Measured IDT End-wall OH* (μs)	Measured IDT Side-wall P (μs)
1	917	1.64	1	4.00	2.00	94.00		973	1192	
2	935	1.63	1	4.00	2.00	94.00		832	1120	
3	984	1.65	1	4.00	2.00	94.00		500	527	519
4	1046	1.69	1	4.00	2.00	94.00		342	505	390
5	1065	1.57	1	4.00	2.00	94.00		249	269	246
6	1104	2.07	1	4.00	2.00	94.00		181	199	230
7	1113	1.62	1	4.00	2.00	94.00		198	213	193
8	1121	1.73	1	4.00	2.00	94.00		150	166	133
9	1130	2.18	1	4.00	2.00	94.00		123	139	127
10	1237	2.13	1	4.00	2.00	94.00		60		
11	1014	2.37	1	4.00	2.00	49.00	45.00	629	638	
12	1017	2.08	1	4.00	2.00	49.01	44.99	726	608	
13	1043	2.41	1	4.00	2.00	49.01	44.99	550	543	
14	1077	2.16	1	4.00	2.00	49.01	44.99	312	426	
15	1109	2.31	1	4.00	2.00	49.01	44.99	206	337	
16	1146	2.23	1	4.00	2.00	49.01	44.99	137	270	
17	1211	2.24	1	4.00	2.00	49.01	44.99	66	162	

The measured high-pressure IDT estimates from experiments conducted at HPST at approximately 40 bar in Ar, 45%H_2O/Ar, 30%H_2O/15%CO_2/Ar, and 45%CO_2/Ar bath gases are summarized in Table 6.

Generally, side-wall OH* emission data produced shorter ignition delay times, with higher signal to noise ratio than end-wall emission. For the Ar-diluted, and 30%H_2O/15%CO_2/Ar-laden experiments side-wall emission rise was monotonic with a single distinct inflection point (see Figure A3 in Appendices). The slope was generally steeper for Ar-diluted experiments with a more abrupt sign-reversal of the slope at peak emission. In contrast, H_2O/CO_2/Ar-diluted experiments exhibited a more gradual hill-like ascent and sign-reversal of the slope at peak emission (see Figure A4 in Appendices, for Test 39). For the 45% H_2O/Ar and 45%CO_2/Ar-diluted experiments, side-wall OH* emission trace displayed multiple inflections. In the case of 45% H_2O/Ar diluted experiments, generally the first inflection of side-wall emission was not the highest sloped one, and the multiple inflections exhibited similar slopes (Example Figure A5 in Appendices, for Test 30). For these experiments the definition of ignition time, i.e. the time of intersection of tangent to the steepest slope of the OH* emission rise extended to the baseline OH* defined near time zero, requires further thought. This is due to the fact that it intends to capture the onset of a runaway OH radical production indicating ignition. It is debatable whether extending the tangent to the slightly lower sloped first OH* emission rise inflection back to the baseline OH* emission better captures the onset of runaway OH radical generation or extending the tangent to the highest slope inflection point which may occur slightly later (see Figure A5 in Appendices). Based on the available diagnostics it was not possible to determine the appropriate choice. As such, in this study, while the steepest slope criteria was strictly followed for consistency, the error bars were extended to capture the alternative definition of ignition time based on the first steep rise of side-wall OH* emission. For the 45%CO_2/Ar experiments, typically the first inflection was significantly steeper that the later ones, rendering them less ambiguous (see Figure A6 in Appendices).

For the HPST H_2 experiments end-wall emissions measurements were only performed for Ar-diluted experiments, and similar to the LPST experiments, some of the tests exhibited multiple inflections in the end-wall emission trace. Also, side-wall pressure was deemed unreliable for IDT estimates involving polyatomic bath gases, due to bifurcation effects. These boundary layer effects resulted in noisy double-humped side-wall pressure traces. Side-wall pressure traces were, however, utilized to provide qualitative estimate of IDTs in Ar-diluted experiments similar to the LPST experiments.

Table 6: IDT measurements of stoichiometric H_2 in Ar, 45%H_2O/Ar, 30%H_2O/15%CO_2/Ar and 45%CO_2/Ar baths at ~40 bar

Test ID	T_5 (K)	P_5 (barA)	φ	H_2 mole %	O_2 mole %	Ar mole %	H_2O mole %	CO_2 mole %	Measured IDT Side-wall OH* (μs)	Measured IDT End-wall OH* (μs)	Measured IDT Side-wall P (μs)
18	1084	37.0	1	4.00	2.00	94.00			2012	2035	2019
19	1115	38.6	1	4.00	2.00	94.00			933	939	943
20	1126	39.5	1	4.00	2.00	94.00			748	759	766
21	1130	38.7	1	4.00	2.00	94.00			711	718	723
22	1161	38.7	1	4.00	2.00	94.00			383	387	404
23	1181	39.8	1	4.00	2.00	94.00			261	261	268
24	1196	43.8	1	4.00	2.00	94.00			199	205	216
25	1209	39.6	1	4.00	2.00	94.00			148	153	161
26	1237	41.4	1	4.00	2.00	94.00			85	88	89
27	1106	39.7	1	4.00	2.00	49.03	44.97		1596		
28	1128	40.7	1	4.00	2.00	48.89	45.11		1251		
29	1133	39.7	1	4.00	2.00	49.03	44.97		1284		
30	1158	39.1	1	4.00	2.00	49.04	44.96		979		
31	1189	40.2	1	4.00	2.00	48.89	45.11		833		
32	1206	39.9	1	4.00	2.00	49.04	44.96		595		
33	1222	40.0	1	4.00	2.00	48.89	45.11		548		
34	1242	40.2	1	4.00	2.00	49.04	44.96		410		
35	1108	40.9	1	4.00	2.00	49.00	29.96	15.04	1603		
36	1124	41.0	1	4.00	2.00	49.00	29.96	15.04	1397		
37	1145	41.5	1	4.00	2.00	49.00	30.00	15.00	1113		
38	1154	40.9	1	4.00	2.00	49.00	30.00	15.00	1013		
39	1167	41.6	1	4.00	2.00	49.00	29.96	15.04	806		
40	1180	40.4	1	4.00	2.00	49.00	30.00	15.00	704		
41	1201	40.5	1	4.00	2.00	49.00	30.00	15.00	613		
42	1232	40.4	1	4.00	2.00	49.00	30.00	15.00	461		
43	1133	39.3	1	4.00	2.00	49.00		45.00	1270		
44	1158	39.8	1	4.00	2.00	48.99		45.01	977		
45	1171	40.9	1	4.00	2.00	49.00		45.00	811		
46	1175	43.8	1	4.00	2.00	49.00		45.00	728		
47	1185	41.2	1	4.00	2.00	49.00		45.00	663		
48	1186	39.5	1	4.00	2.00	48.99		45.01	673		
49	1207	40.0	1	4.00	2.00	48.99		45.01	514		
50	1218	42.0	1	4.00	2.00	49.00		45.00	438		
51	1226	40.6	1	4.00	2.00	48.99		45.01	382		

5.2 Uncertainties analyses

Uncertainties associated with the measured IDTs in shock tube facilities were divided into two categories: uncertainties in ignition delay time determinations from experimental data, and uncertainties in T_5 and P_5 determinations, as discussed in section 4.4;

5.2.1 Uncertainties in ignition delay time determinations

Uncertainties associated with IDT determinations are comprised of those pertaining to time zero and time of ignition determinations. Time zero is determined using laser Schlieren spike. For many experiments the fractional transmission signal exhibited two distinct minimums, corresponding to the arrival of the incident and reflected shock waves with little to no uncertainties. For some of the high-pressure H_2O-diluted experiments there were no minima detected, for which, the location of the minima was estimated with ±5 μs uncertainty, based on the relative location of rise of fractional transmission signal and the side-wall pressure from tests with distinct minimums (see Figure A7 in Appendices). The reason behind such observation remains unclear, however, as the IDT data associated with these tests were not an outlier in comparison with the overall experimental IDT trend, the associated data were retained. Moreover, for several low-pressure tests the minima had multiple nearly spaced valleys with similar fractional transmission (see Figure A8 in Appendices). To capture the uncertainty associated with these minimums, unbalanced bounds were placed around the absolute minima selected to capture these valleys. Based on the data available, it was not possible to determine the cause of such behavior. Schlieren spike is a consequence of abrupt density change and it was initially suspected that the oblique shocks in front of and behind the normal portion of the reflected shock wave may have been the culprit resulting in the multiple minimums observed. However, since these effects also presented themselves in the argon-diluted experiments, oblique shocks are not likely the cause. Nevertheless, as the associated uncertainties were small, this was not dwelled on further, but were captured by the error bars reported. Also, for some tests, the reference laser signal was not recorded and only the attenuated laser signal was measured. Based on tests that had both signals, the associated uncertainty was quantified to be less than ±0.5 μs, which was incorporated into the error bars of the affected tests. Finally, for one experiment, test 44, there was no attenuated laser signal, and an uncertainty of ±5 μs was deemed appropriate and incorporated. For this specific experiment time zero was determined based on determination of the relative location of laser Schlieren minimums to the onset of pressure rise observed from other tests with the same mixture composition.

Side-wall OH* emission signal used for IDTs exhibited the highest signal to noise ratio of the diagnostics in place. Low levels of digital filtering, using 2nd order Savitzky-Golay polynomial fit method [184] with ranges a high as 250 points, were applied to the 11-bit high frequency emission data collected by the oscilloscope. The highest level of data smoothing performed was 750 points for a few experiments, which was graphically evaluated and determined to be appropriate. This determination was made visually by superimposing data from different levels of smoothing to detect erroneous perturbation of the overall trend relative to the unsmoothed data. Ignition time uncertainties associated with the determination of steepest slope inflection and the baseline emission signal were test-specific and were observed to be in the order of 1% for Ar and 2% for 45%CO_2/Ar-diluted experiments, and in the order of 5% for H_2O-laden tests. Moreover, based on alternative definitions of ignition time discussed section 5.1 unbalanced additional errors were incorporated into the uncertainty bars of the ignition delay times reported to capture estimates from both plausible ignition time definitions. This was done by expressing the IDT based on the steepest slope definition, and extending its vertical error bar until it includes the IDT estimate determined based on the alternative first rise definition.

The combined uncertainties of test-specific time zero and ignition time determinations are summarized in the IDT's positive and negative percent error columns of Table 7 and Table 8 for the low- and high-pressure experimental test campaigns, respectively.

5.2.2 Uncertainties in T_5 and P_5 determinations

Uncertainties in T_5 and P_5 stem from uncertainties in input parameters. In this work, errors associated with T_1, P_1, measured incident shock velocity, fitting errors of NASA polynomial gas properties and their deviations due to pressure dependency, concentrations of H_2O and CO_2 (from mixture preparation pressure transmitters), and deviations from ideal gas behavior during mixture preparation, were quantified and accounted for. Two combined uncertainties for the experimental data generated in this work were calculated, using the two methods discussed in section 4.4, namely: maximum uncertainty test-specific bounds as well as the root-sum-of-squared (RSS) relative errors. The resulting combined error calculated using both methods are summarized in Table 7 and Table 8.

It can be observed that, as expected, the maximum errors reported for T_5 and P_5, are larger than the RSS relative errors. Additionally, comparison of positive and negative uncertainties in Table 8, show that the errors are not uniform. The main input parameters responsible for such non-uniform uncertainties are the NASA-polynomials used to estimate thermodynamic properties, and the composition uncertainties due to non-ideal gas behavior of the mixtures.

Table 7: Low-pressure H_2 experiments' IDT, T_5, and P_5 maximum and RSS uncertainties

Test ID-Mix group #	T_5 (K)	P_5 (bar)	IDT (μs)	IDT +ve error (%)	IDT +ve error (%)	Max T_5 +ve error (%)	Max T_5 -ve error (%)	RSS T_5 +ve error (%)	RSS T_5 -ve error (%)	Max P_5 +ve error (%)	Max P_5 -ve error (%)	RSS P_5 +ve error (%)	RSS P_5 -ve error (%)
1-1	917	1.64	973	5.1	5.1	0.3	0.3	0.2	0.2	1.7	1.6	1.1	1.1
2-1	935	1.63	832	5.1	5.1	0.3	0.3	0.2	0.2	1.6	1.6	1.1	1.1
3-1	984	1.65	500	5.1	5.1	0.9	0.9	0.7	0.7	2.8	2.7	1.7	1.7
4-1	1046	1.69	342	5.1	5.1	0.5	0.5	0.3	0.3	1.9	1.9	1.2	1.2
5-1	1065	1.57	249	5.2	5.2	0.5	0.5	0.3	0.3	1.9	1.9	1.2	1.1
6-1	1104	2.07	181	5.3	5.3	0.4	0.4	0.3	0.3	1.8	1.8	1.1	1.1
7-1	1113	1.62	198	5.3	6.6	0.6	0.6	0.4	0.4	2.1	2.0	1.2	1.2
8-1	1121	1.73	150	5.3	6.0	0.4	0.4	0.3	0.3	1.8	1.8	1.1	1.1
9-1	1130	2.18	123	5.4	5.4	0.3	0.3	0.2	0.2	1.6	1.6	1.0	1.0
10-1	1237	2.13	60	5.8	5.8	0.5	0.5	0.3	0.3	1.8	1.8	1.1	1.1
11-2	1014	2.37	629	5.1	6.2	0.5	0.5	0.3	0.3	1.7	1.7	1.0	1.0
12-2	1017	2.08	726	5.1	5.1	0.9	0.9	0.7	0.6	2.7	2.6	1.7	1.7
13-2	1043	2.41	550	5.1	5.1	1.0	1.0	0.7	0.7	2.9	2.8	1.8	1.8
14-2	1077	2.16	312	5.2	5.2	0.8	0.8	0.5	0.5	2.4	2.3	1.4	1.4
15-2	1109	2.31	206	5.2	5.2	1.5	1.4	1.1	1.1	3.8	3.7	2.7	2.6
16-2	1146	2.23	137	5.4	5.4	0.4	0.4	0.2	0.2	1.5	1.5	0.9	0.9
17-2	1211	2.24	66	5.8	5.8	0.6	0.6	0.3	0.3	1.8	1.7	1.0	1.0

To reduce these uncertainties, alternative shock wave calculation codes would need to be developed that can incorporate NIST thermodynamic properties data, if available for all gas components and over the relevant temperature and pressure ranges. While there are several computer codes that can incorporate common real gas equations of state with few parameters, they are not appropriate due to the deficiencies of equations of state in appropriately predicting the properties of mixtures containing large quantities of H_2O and, to a lesser extent, CO_2, see analysis in section 3.3. To estimate the uncertainties associated with non-ideal behavior of mixtures prepared, the reported fill procedures were re-simulated in AspenHYSYS using Peng-Robinson equation of state. Concentration deviations were then estimated from the difference of the simulated mixture compositions with theirexperimental counterparts, which were done assuming ideal gas behavior. These deviations were incorporated into the error analysis.

Table 8 illustrates that due to the aforementioned unbalanced uncertainty contributions of the thermodynamic properties of H_2O and CO_2, and the non-ideal behavior of gas mixtures, both the maximum worst-case-scenario uncertainties and the RSS ones are unbalanced. This is however, not the case for Ar-diluted HPST experiment, or for the LPST experiments as observed from the data presented in Table 7.

Table 8: High-pressure H_2 experiments' IDT, T_5, and P_5 maximum and RSS uncertainties

Test ID - Mix group #	T_5 (K)	P_5 (bar)	IDT (μs)	IDT +ve error (%)	IDT -ve error (%)	Max T_5 +ve error (%)	Max T_5 -ve error (%)	RSS T_5 +ve error (%)	RSS T_5 -ve error (%)	Max P_5 +ve error (%)	Max P_5 -ve error (%)	RSS P_5 +ve error (%)	RSS P_5 -ve error (%)
18-3	1084	37.0	2012	1.0	1.7	0.32	0.32	0.20	0.20	1.66	1.63	1.16	1.14
19-3	1115	38.6	933	1.0	1.0	0.39	0.39	0.23	0.23	1.78	1.74	1.17	1.15
20-3	1126	39.5	748	1.0	1.0	0.43	0.43	0.26	0.26	1.83	1.80	1.18	1.17
21-3	1130	38.7	711	1.0	1.0	0.36	0.36	0.22	0.22	1.71	1.68	1.16	1.14
22-3	1161	38.7	383	1.0	1.0	0.43	0.43	0.26	0.26	1.82	1.79	1.17	1.16
23-3	1181	39.8	261	1.0	1.0	0.34	0.34	0.21	0.21	1.66	1.63	1.14	1.12
24-3	1196	43.8	199	1.0	1.0	0.48	0.48	0.30	0.30	1.90	1.87	1.19	1.18
25-3	1209	39.6	148	1.0	2.0	0.31	0.31	0.20	0.20	1.60	1.57	1.13	1.11
26-3	1237	41.4	85	1.0	1.0	0.43	0.43	0.27	0.26	1.80	1.77	1.16	1.14
27-4	1106	39.7	1596	5.0	5.3	0.79	1.39	0.49	0.77	2.80	2.44	1.50	1.36
28-4	1128	40.7	1251	5.0	5.0	0.77	1.38	0.47	0.77	2.72	2.37	1.45	1.30
29-4	1133	39.7	1284	5.1	5.1	0.81	1.42	0.51	0.79	2.82	2.46	1.52	1.37
30-4	1158	39.1	979	5.5	10.8	0.69	1.31	0.40	0.74	2.51	2.16	1.33	1.16
31-4	1189	40.2	833	5.0	13.9	0.75	1.38	0.45	0.77	2.63	2.27	1.40	1.23
32-4	1206	39.9	595	5.9	7.7	0.78	1.41	0.48	0.79	2.69	2.32	1.44	1.27
33-4	1222	40.0	548	5.1	6.0	0.76	1.41	0.47	0.79	2.66	2.29	1.41	1.25
34-4	1242	40.2	410	5.1	5.1	0.74	1.39	0.44	0.78	2.58	2.21	1.37	1.20
35-5	1108	40.9	1603	5.3	9.1	0.63	1.01	0.40	0.54	2.39	2.24	1.27	1.23
36-5	1124	41.0	1397	5.0	5.0	0.65	1.02	0.41	0.55	2.42	2.26	1.29	1.25
37-5	1145	41.5	1113	5.0	11.5	0.69	1.07	0.45	0.58	2.52	2.35	1.35	1.31
38-5	1154	40.9	1013	5.0	11.1	0.69	1.08	0.45	0.58	2.51	2.34	1.35	1.31
39-5	1167	41.6	806	5.0	5.1	0.66	1.05	0.43	0.57	2.44	2.28	1.30	1.26
40-5	1180	40.4	704	2.0	2.0	0.71	1.10	0.47	0.60	2.54	2.36	1.37	1.33
41-5	1201	40.5	613	5.1	5.9	0.74	1.13	0.49	0.62	2.60	2.42	1.41	1.37
42-5	1232	40.4	461	5.0	5.9	0.71	1.11	0.47	0.61	2.52	2.34	1.35	1.31
43-6	1133	39.3	1270	5.0	5.4	0.78	0.88	0.51	0.54	2.39	2.21	1.40	1.37
44-6	1158	39.8	977	5.5	5.5	0.71	0.81	0.44	0.47	2.18	2.01	1.24	1.21
45-6	1171	40.9	811	5.1	5.1	0.67	0.77	0.40	0.44	2.08	1.91	1.16	1.13
46-6	1175	43.8	728	4.9	4.9	0.70	0.80	0.43	0.47	2.14	1.98	1.21	1.18
47-6	1185	41.2	663	2.0	2.0	0.72	0.83	0.45	0.49	2.20	2.04	1.25	1.23
48-6	1186	39.5	673	2.0	2.0	0.78	0.88	0.50	0.53	2.33	2.16	1.35	1.33
49-6	1207	40.0	514	2.0	2.0	0.74	0.84	0.47	0.50	2.23	2.06	1.27	1.25
50-6	1218	42.0	438	2.0	2.0	0.77	0.87	0.49	0.53	2.29	2.12	1.32	1.29
51-6	1226	40.6	382	2.0	2.0	0.78	0.89	0.51	0.54	2.32	2.15	1.34	1.32

5.3 Additional shock tube IDT validation targets from the literature

The concerns and requirements presented in sections 4.1.1, 4.1.4 and 4.1.5 that informed the design of experimental test campaigns of this work, were also applied to filter and select appropriate validation data from the literature. These requirements were the minimum and maximum acceptable H_2 and CO concentrations, to minimize the impact of impurities and potential pre-ignition effects, as well as the maximum polyatomic bath gas concentrations above which inhomogeneous ignition effects are less likely to have been manageable. In this context, the following shock tube IDT model validation datasets were selected from the literature, in addition to those generated in this work:

1- Shao et al.'s [83] stoichiometric 3% H_2 IDT data conducted at 11.4-32.9 bar, at 1179-1376 K with balance Ar, N_2, as well as 10-20%CO_2/Ar and 3.9-13.8 H_2O/Ar. The authors noted that they evaluated the impact of H_2 impurities and determined it to be minimal. Gas dynamics effects' dP/dt values were not reported for the data but, due to the short ignition delay times involved, they are inconsequential.

2- Pang et al.'s [52] stoichiometric 4% H_2 IDT data conducted at 3.42-3.76 bar, at 924-1118 K with balance Ar. A dP/dt of 2%/ms, as suggested by the authors, was applied to the constant volume IDT simulations, after converting it to a dV/dt using the mixture's gamma along with the assumption of isentropic compression.

3- Select datasets from Keromnes et al.'s [28] extensive shock tube IDT data, i.e., tests with with H_2 concentration of approximately 3% and higher. This included, datasets S11, S12, S13, and S16, with fuel concentrations of 3.47%H_2, 12.54%H_2, 2.98%H_2/0.52%CO, and 2.96%H_2/2.96%CO, respectively. Equivalence ratios explored in these datasets were 0.5, 1, and 4, spanning a temperature range of 924-2220 K and pressure range of 0.76-16.8 bar. A dP/dt of 2.15%/ms, based on digitization of pressure traces from the supplemental material, were estimated and converted into dV/dt assuming isentropic compression. Mixture specific dV/dt profiles were calculated for all mixtures using their gammas. These dV/dt profiles, were then implemented in all constant volume model validation simulations of their reported IDT data.

5.4 Model performance evaluation criteria

In order to benchmark and evaluate the effectiveness of models in predicting IDT validation target data as well as their overall performance, three performance evaluation metrics were utilized in this work. To ensure the metrics do not bias larger IDTs which have larger absolute errors, the metrics used relied on relative errors.

The first metric is Root Mean Square Relative Error (RMSRE), utilized to evaluate models' performance for individual sets of data with common composition and similar in pressure, which is defined as:

$$RMSRE = \sqrt{\frac{\sum_{i=1}^{n}\left(\frac{IDT_{predicted,i} - IDT_{Measured,i}}{IDT_{Measured,i}}\right)^2}{n}} \tag{5.1}$$

where $i = 1..N$ is the index of each data point within a dataset of size N

This metric ensures that prediction ability of the model for each individual data point has an equal weight, and provides a measure of the average relative prediction error or deviation of the modelled IDT from the measured IDTs within a dataset.

To compare models' overall performance against incumbent one(s) a modified version of the RMRSE formulation is utilized, i.e.:

$$RMSRE = \sqrt{\frac{\sum_{j=1}^{M}\sum_{i=1}^{N}\left(\frac{IDT_{predicted,ij} - IDT_{Measured,ij}}{IDT_{Measured,ij}}\right)^2}{\sum_{j=1}^{M} N_j}} \tag{5.2}$$

where $j = 1..M$ is the index of each dataset of the overall validation matrix with M datasets

This metric, in essence, treats all model validation data used as if they were from one large dataset, and provides equal weight to all data points. Similar to equation 5.1 it is a measure of the average relative prediction error of the modelled IDT in comparison with its experimentally measured value, but is applied to all data points within the model validation matrix.

A third comparative metric utilized in this work is the relative percent RMSRE, or RPRMSRE, which provides a relative superiority measure in percent for newly developed models relative to a benchmark incumbent one in predicting validation each dataset, as well as the overall matrix, i.e.:

$$RPRMSRE = \frac{RMSRE_{model} - RMSRE_{benchmark}}{RMSRE_{benchmark}} \times 100\% \qquad (5.3)$$

5.5 Model validation results and discussions

In order to develop a model with minimal parameter tuning, the model validation and evolvement process in this work entailed:

1- Evaluating the performance of the reference incumbent model, Keromnes et al. [28], in predicting experimental IDT data;

2- Evaluating the performance of the untuned CanMECH Base model, in predicting experimental IDT data;

3- Benchmarking and comparing CanMECH Base's performance metrics detailed in section 5.4 against the incumbent model. Identifying and categorizing validation datasets that are well replicated by the model versus those that the model struggles to mimic;

4- Conducting IDT sensitivity analyses to identify appropriate reaction rate tuning parameter(s). The sensitivity was done on pre-exponential factors, as well as collision efficiencies and center broadening factors of pressure-dependent reactions; and,

5- Conducting parametric studies to determine the extent of tuning required, by evaluating the performance of the model in predicting all validation datasets. In this process, the three performance evaluation criteria were monitored simultaneously. This was to ensure that the appropriate balance has been struck between reproducing individual datasets as well as improving the overall model performance across all experimental data. It is important to note that the extent of tuning was limited to the uncertainty bounds provided by the original study from which the rate parameter was extracted. The resulting model generated, CanMECH 1.0, is the minimally tuned and validated improved mechanism for H_2/CO combustion modeling.

Table 9 details the values of the three RMSRE-based model performance evaluation metrics for the three models, namely: the untuned CanMECH Base, CanMECH 1.0, as well as the incumbent Keromnes et al. [28].

Table 9 H_2/CO Model Performance Evaluation Results Matrix

Data set ID	Source	Fuel & Bath gas Composition	# of data	Pressure range (bar)	Temperature range (K)	φ	CanMECH 1.0 RMSRE	CanMECH Base RMSRE	Keromnes et al. RMSRE	CanMECH 1.0 vs. Keromnes et al. RPRMSRE (%)
1	This Work	4%H_2/Ar	10	1.6-2.2	917-1237	1	1.418	1.659	1.199	18
		4%H_2/45CO_2/Ar	7	2.1-2.4	1014-1211	1	5.244	5.524	7.378	-29
		Combined at ~ 2bar	**17**	**1.6-2.4**	**917-1211**	**1**	**3.536**	**3.766**	**4.823**	**-27**
2	This Work	4%H_2/Ar	9	37.0-43.8	1084-1237	1	0.067	0.169	0.122	-45
		4%H_2/45%H_2O/Ar	8	39.1-40.7	1106-1242	1	0.192	0.192	0.269	-29
		4%H_2/30%H_2O/15%CO_2/Ar	8	40.4-41.6	1108-1232	1	0.097	0.097	0.179	-46
		4%H_2/45%CO_2/Ar	9	39.3-43.8	1133-1226	1	0.075	0.080	0.075	0
		Combined at ~ 40bar	**34**	**37.0-43.8**	**1084-1242**	**1**	**0.116**	**0.142**	**0.173**	**-33**
3	Shao et al. 2019 [83]	3%H_2/Ar	5	29.1-32.9	1230-1262	1	0.382	0.134	0.453	-16
		3%H_2/Ar	6	17.0-17.6	1184-1224	1	0.243	0.091	0.315	-23
		3%H_2/N_2	5	12.8-13.3	1199-1228	1	0.162	0.162	0.313	-48
		3%H_2/4.4%H_2O/Ar	3	15.9-17.0	1264-1307	1	0.185	0.247	0.348	-47
		3%H_2-9%H_2O-Ar	6	15.2-16.6	1270-1344	1	0.166	0.230	0.354	-53
		3%H_2/13.4%H_2O/Ar	2	15.3-15.7	1282-1376	1	0.093	0.133	0.377	-75
		3%H_2/20%CO_2/Ar	11	11.7-19.3	1185-1268	1	0.203	0.221	0.408	-50
		3%H_2/10%CO_2/Ar	2	11.4-11.9	1179-1180	1	0.294	0.146	0.150	96
		Combined	**40**	**11.4-32.9**	**1179-1376**	**1**	**0.231**	**0.186**	**0.367**	**-37**
4	Pang et al. 2009 [52]	**4%H_2/Ar**	**33**	**3.42-3.76**	**924-1118**	**1**	**0.332**	**0.651**	**0.238**	**40**
5	Keromnes et al. 2013 (S11) [28]	3.47%H_2/N_2	11	0.94-1.05	932-1954	0.5	0.282	0.282	0.245	15
			13	3.91-4.54	1006-1257	0.5	0.313	0.313	0.490	-36
			10	15.1-16.3	1060-1243	0.5	0.321	0.321	0.251	28
		Combined- S11	**34**	**0.94-16.3**	**932-1954**	**0.5**	**0.306**	**0.306**	**0.360**	**-15**
6	Keromnes et al. 2013 (S12) [28]	12.54%H_2/Ar	26	0.92-1.37	943-2136	4	0.208	0.210	0.207	0
			20	3.7-4.5	967-1463	4	0.129	0.232	0.182	-29
			16	14.2-16.6	947-1227	4	0.248	0.286	0.242	3
		Combined-S12	**62**	**0.92-16.6**	**943-2136**	**4**	**0.199**	**0.239**	**0.209**	**-5**
7	Keromnes et al. 2013 (S13) [28]	**2.98%H_2/0.52%CO/46.57%N_2/46.42%Ar**	7	15.0-16.6	1002-1222	**0.5**	**0.443**	**0.453**	**0.455**	**-3**
8	Keromnes et al. 2013 (S16) [28]	2.96%H_2/2.96%CO/Ar	23	0.76-1.18	924-2220	1	0.240	0.231	0.199	20
			23	3.71-5.07	942-1364	1	0.202	0.204	0.226	-11
			16	14.7-16.8	997-1215	1	0.245	0.329	0.225	9
		Combined-S16	**23**	**0.76-16.8**	**924-2220**	**1**	**0.228**	**0.251**	**0.216**	**5**
Overall			**289**	**0.76-43.8**	**917-2220**	**0.5-4**	**0.890**	**0.965**	**1.199**	**-26**

Table 9, has been divided into groups, which are boxed with a solid black border. Within each grouping, each row is dedicated to a subset of data with similar mixture compositions and pressures, for experiments conducted at different temperatures. Each row provides the experimental conditions of the tests, their associated RMSREs depicting each of the three model's performances, as well as the RPRMSRE of CanMECH 1.0 relative to Keromnes et al. mechanism [28]. The last row within each grouping provides the combined conditions and RMSREs as a measure of the performance of each model in predicting all of the IDT data of that grouping. In Table 9, cells that are highlighted in yellow identify the best performing model, having the least RMSRE, for composition- and pressure-specific subsets within each datasets. Cells with an orange fill, distinguish the model that outperforms others in mimicking a complete dataset grouping, with the lowest RMSRE. The last row of Table 9 summarizes the overall RMSRE, that is taking into account all validation data for each model. The cell, with the dark red fill indicates the model with the best overall performance. Finally, the cells in the last column with a green fill distinguish datasets where CanMECH 1.0 has an improved or identical performance relative to the incumbent model. Based on the definition of RPRMSRE, as denoted in section 5.4, a more negative value translates to a larger percentage reduction of the overall RMSRE brought about by the adoption of CanMECH 1.0 in place of Keromnes et al.'s mechanism [28].

In the following paragraphs the results of CanMECH Base mechanism and the incumbent Keromnes et al. models' [28] performance metrics are discussed and benchmarked. The results of sensitivity and parametric studies to identify appropriate tuning parameter(s) and the extent of tuning required are then presented. Lastly, the performance of the tuned CanMECH 1.0 mechanism and its validation are discussed.

Comparison of the individual RMSRE, and combined RMSREs for CanMECH Base and the incumbent, in Table 9, indicates that it outperforms the incumbent in reproducing all of this work's experimental IDT results with the exception of the low-pressure Ar-diluted experiments. In the following discussions, in addition to the three metrics which quantify models' performance, it is equally important to graphically examine the model validation data generated. As such, the graphs of the experimental validation results collected in this work are superimposed by the associated modeled results and examined along with the RMSRE-based metrics of Table 9. In Figure 9 to Figure 14, the vertical error bars of the experimental data represent the combined uncertainties of time 0 determinations and the graphical ignition time estimations using side-wall OH* emission data, as discussed in section 5.2.1. The horizontal error bars of the data are the RSS T_5 uncertainties discussed and tabulated in section 5.2.2.

Figure 9 illustrates the results of the low-pressure (~2 bar) Ar-diluted experimental H_2 IDT measurements at temperatures of 917-1237 K. It can be observed that while all models overpredict the IDTs, Keromnes et al. [28] reproduces the low-pressure Ar-diluted IDT data better. Moreover, the overprediction takes place across the temperature range explored in this work. CanMECH Base model shows the largest deviation from both the experimental data and modeled IDT's using Keromnes et al.'s mechanism [28] at temperatures below 1000 K. These observations are quantified with the larger CanMECH Base RMSRE of 1.659 vs. 1.199 of the incumbent. This RMSRE is also the second largest of all the validation data for the CanMECH Base model.

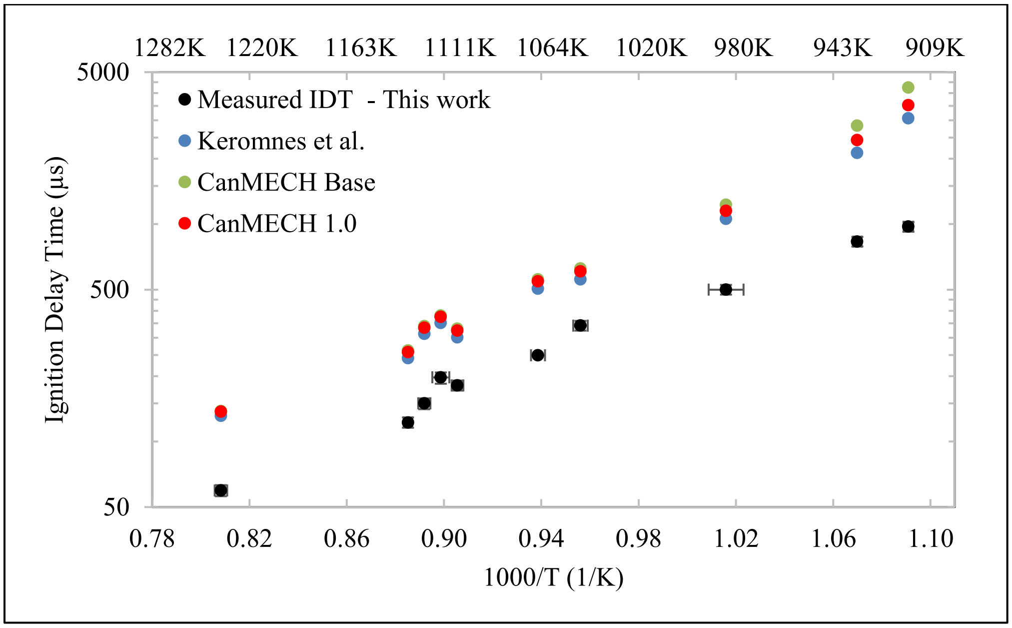

Figure 9: Measured vs. Modelled IDT 4%H_2/Ar φ=1 at ~1.8 bar

Figure 10 superimposes the IDT data of 4%H_2/45%CO_2/Ar at an equivalence ratio of 1 and approximately 2.3 bar, along with the models' estimates of the IDTs. While the models overestimate the measured IDTs at all temperatures, they reproduce the experimental data better at higher temperatures. Figure 10 shows that, in presence of CO_2, the untuned CanMECH Base performs significantly better than the incumbent, also signified by its lower RMSRE. While CanMECH Base's improved performance is promising, the RMSRE calculated for the 45%CO_2-laden low-pressure dataset in this work, is the largest among all validation datasets.

The overall RMSRE of the two low-pressure datasets indicate that CanMECH Base's overall performance (RMSRE of 3.766) in predicting low-pressure experimental results of this work, is superior to that of the incumbent (RMSRE of 4.823).

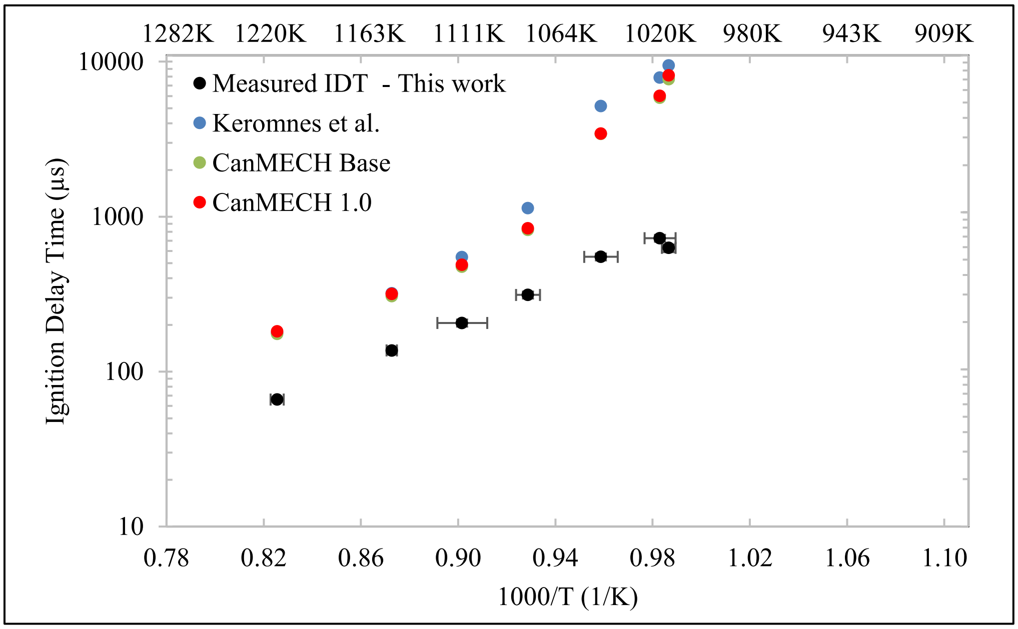

Figure 10: Measured vs. Modelled IDT 4%H_2/45%CO_2/Ar φ=1 at ~2.3bar

Figure 11 depicts the measured IDT data for 4%H_2/Ar φ=1 at 40 bar. Figure 11 and Table 9's RMSREs show that the incumbent performs better than CanMECH Base model in predicting the 40 bar Ar-diluted experimental IDT measurements. It can be observed that while Keromnes et al. mechanism underestimates the IDTs CanMECH Base over-estimates them. A comparison of Figure 9 and Figure 11 also reveals that both models' performance in predicting IDTs in Ar-diluted mixtures has significantly improved with pressure, i.e. the RMSREs were reduced by an order of magnitude for both mechanisms.

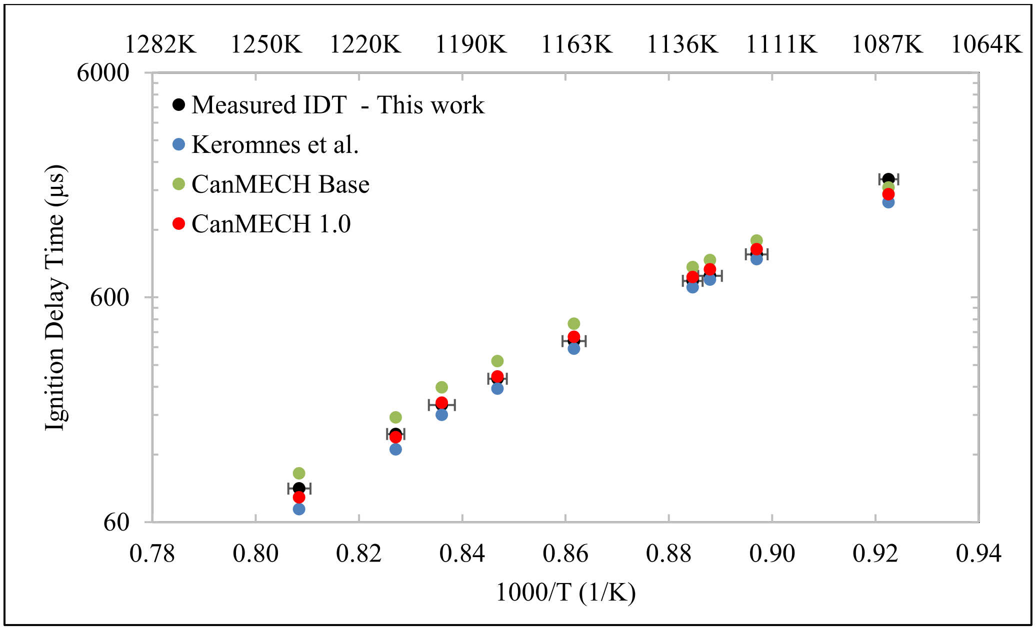

Figure 11: Measured vs. Modelled IDT 4%H_2/Ar φ=1 at 40bar

Figure 12 depicts the results of the novel experimental IDT measurements, that is with high water content at elevated pressure, for 4%H_2/45%H_2O/Ar at φ=1, superimposed with the modelled results. It should be noted that the two CanMECH models have similar predictions, and perfectly overlap. This is also apparent from their identical RMSRE of 0.192. It can be observed that, while all models underestimate IDTs at temperatures higher than 1128 K, CanMECH models have significantly better performance. CanMECH Base's RMSRE is 29% lower than that of the incumbent. This is a clear indication that the mechanism developed without any parameter tuning is better suited to predict the 45% H_2O-laden mixture IDTs as well as their activation energy, which is one of the main objectives of the model development efforts in this work.

Figure 13 is a graph of the measured IDT results for 4%H_2/30%H_2O/15%CO_2/Ar at φ=1 conducted at near 41 bar, superimposed with the modelled predictions. It should be noted that, similar to Figure 12, the two CanMECH models' results perfectly overlap. This is also apparent from their identical RMSRE of 0.097. It is apparent that CanMECH Base predicts the IDT data well, with the exception of a slight underprediction of measurements for the two data points at temperatures higher than 1200 K. CanMECH Base model significantly outperforms the incumbent model, which underpredicts most measurements, except at the lowest temperature. Both models seem to suggest a slightly higher global activation energy than the measurements, but CanMECH Base's modeled activation energy is closer to that of the experimental data. These observations are also corroborated by the calculated RMSRE values of Table 9, which indicate CanMECH Base's RMSRE (0.097) is just over half of that of the incumbent (0.179).

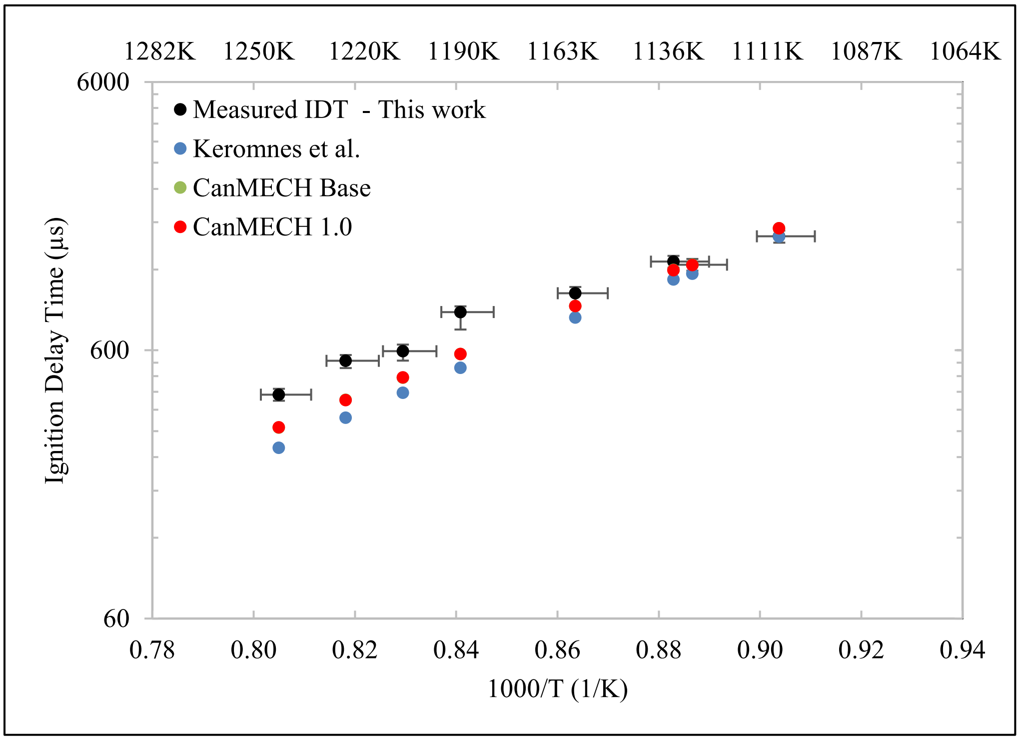

Figure 12: Measured vs. Modelled IDT 4%H_2/45%H_2O/Ar at φ=1 at 40 bar

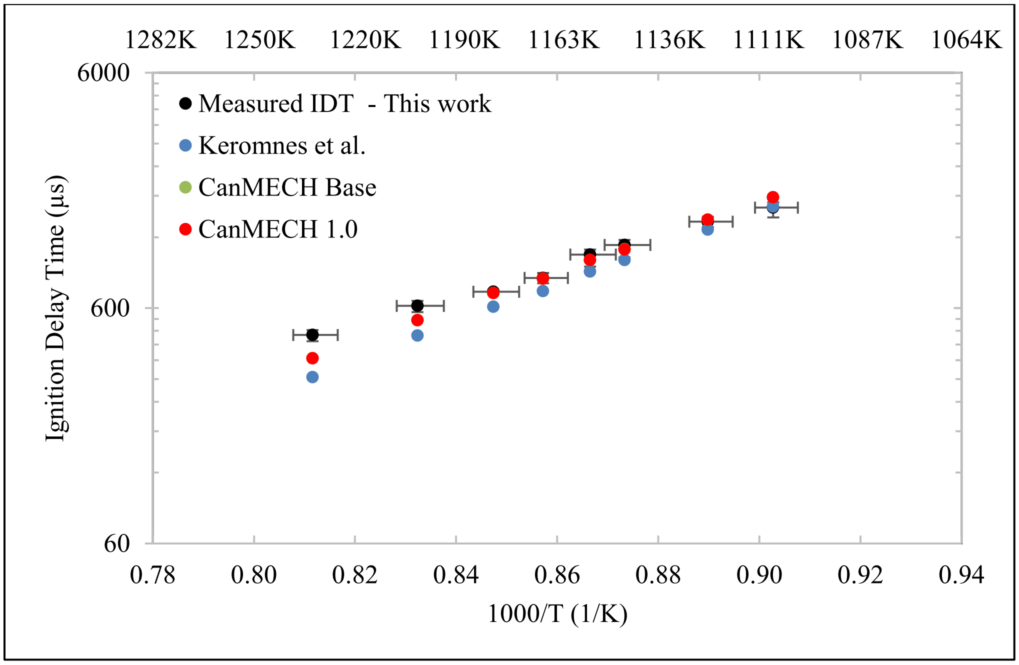

Figure 13: Measured vs. Modelled IDT for 4%H_2/30%H_2O/15%CO_2/Ar φ=1 near 41 bar

Figure 14 is a plot of the measured IDTs for 4%H_2/45%CO_2/Ar φ=1 at 41 bar, along with the three model IDT estimates. It is clear that all three models have very similar performance. RMSRE of CanMECH Base vs. that of Keromnes et al. [28] suggests that the incumbent is slightly better at predicting the measured IDTs.

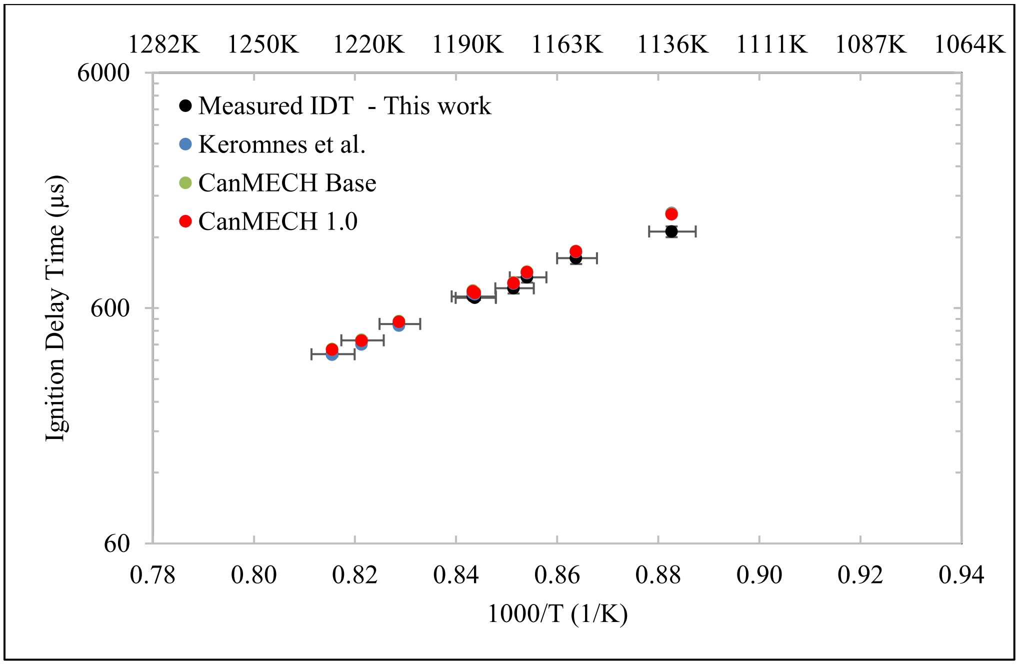

Figure 14: Measured vs. Modelled IDT 4%H_2/45%CO_2-Ar φ=1 at 41 bar

In an effort to validate and increase the robustness of the mechanism, in addition to the experimental validation data generated in this work, models' performances in reproducing other IDT validation targets from the literature were also examined. The first validation dataset is from the recent work of Shao et al. [83] conducted using Stanford University's shock tube test facilities. Table 9 RMSRE's indicate CanMECH Base was significantly better than the incumbent model in predicting the novel H_2O- and CO_2-laden IDT targets of Shao et al. data [83]. Table 9 also indicates that CanMECH Base outperforms the incumbent, for every subset of data grouped by composition as well, signified by their corresponding RMSREs. These IDT validation dataset spanned a pressure range of 11.4 to 32.9 bar, with bath gases ranging from 4.4-13.4%H_2O/Ar, Ar, N_2, and 10-20%CO_2/Ar [83]. As such, it is highly relevant to the validation objectives of this work.

To further evaluate the model's performance at lower pressures, another data set by Pang et al. [52], with identical composition to those of the Ar-diluted experiments of this work, was selected from the literature. Pang et al.'s [52] shock tube IDT study was conducted at 924-1118 K, 3.42-3.76 bar, at Stanford University's shock tube test facilities. The study's P_5 pressures [52], are higher than the low-pressure (~2bar) Ar-diluted experiments of this work, but lower than Shao et al.'s [83] 3%H_2/1.5%O_2/Ar experiments conducted at near 17 and 33 bar. Figure 15 is a graph of Pang et al.'s

[52] experimental IDT measurements, along with the original study's reported uncertainties of T_5. The figure also superimposes the constant volume modeled IDT results of the three mechanisms, with 2%/ms dP/dt correction, converted and implemented as a dV/dt by assuming isentropic compression.

It can be observed that the incumbent Keromnes et al. mechanism [28] performs significantly better than CanMECH Base. CanMECH Base systematically overpredicts the IDTs. Comparison of Table 9's RMSREs of Keromnes et al. and CanMECH Base mechanism indicates that incumbent model's predictions are better by more than a factor of two.

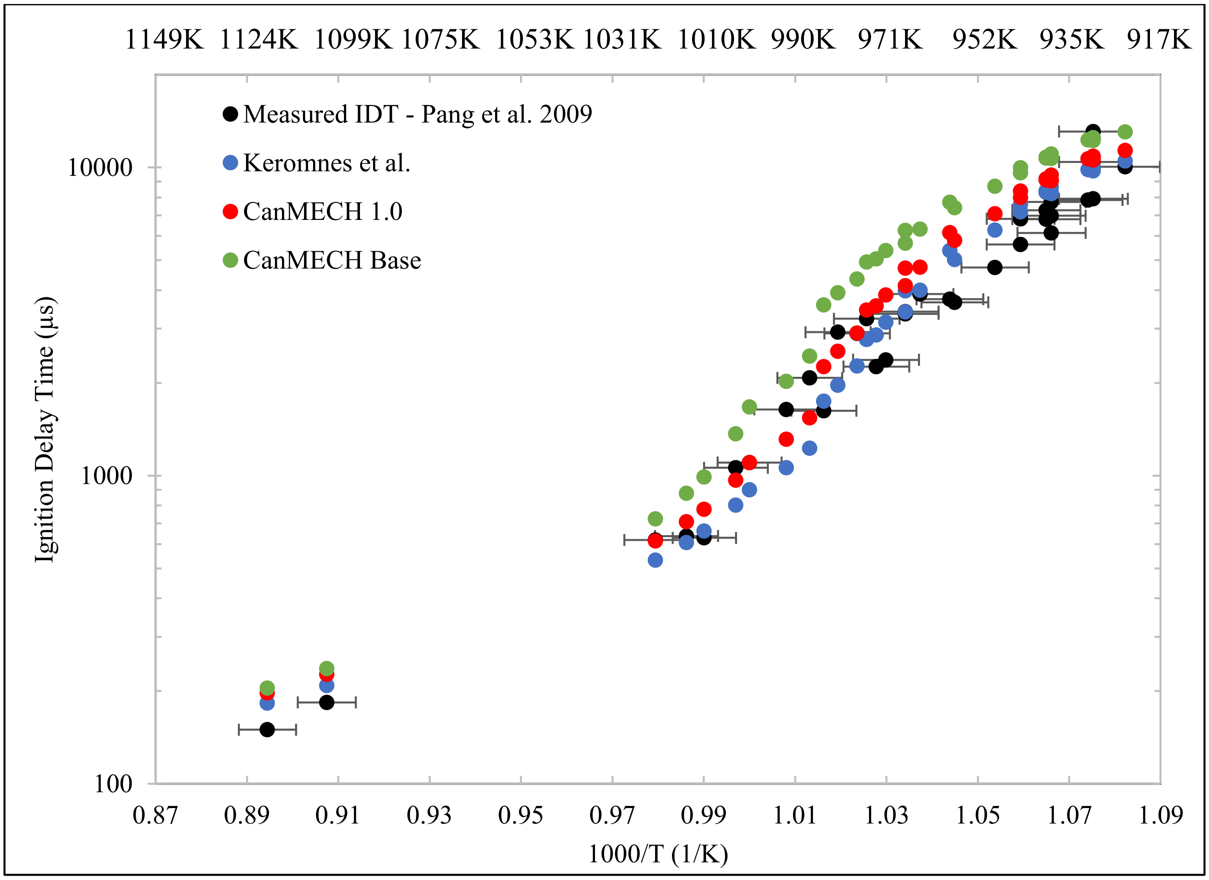

Figure 15: Measured IDT from Pang et al. [52] for 4%H_2/Ar φ=1 at superimposed with modelled IDT results using Keromnes et al. [28], CanMECH Base, and CanMECH 1.0 Mechanisms

Four additional sets of IDT validation data from Keromnes et al.'s study [28], conducted at the German Research Institute for Aviation and Space Flight's (DLR) shock tube test facility, also met the model validation criteria of this work. The first set (Table S11 from Keromnes et al.'s [28] supplementary material) involved 3.47%H_2/N_2 at φ=0.5, and was tested at three discrete pressures of approximately 1, 4 and 16 bar, and 932-1954 K. This dataset validates the performance of the models for lean H_2 mixtures, in nitrogen bath gases at different pressures. Table 9's RMSREs indicate that while the incumbent performs better at pressures of 1 and 16 bar, and CanMECH Base brings significant improvements to the incumbent's larger RMSREs observed at 4 bar. Moreover, CanMECH Base's performance is not significantly different from that of Keromnes et al. [28] at pressures of 1 and 16 bar. The combined RMSRE of the data for the three pressures show that adoption of CanMECH Base brings about 15% improvement in IDT prediction ability.

The second validation dataset adopted from Keromnes et al.'s [28] supplementary material, is listed in its Table S12. It involves a hydrogen rich mixture with φ=4, 12.4%H_2/Ar, at discrete pressures of 1, 4, and 16 bar, covering a temperature range of 943-2136 K [28]. Table 9 indicates both CanMECH Base and Keromnes et al. [28] have reasonable performances, signified by their RMSREs at each of the three pressures. The incumbent has superior performance to CanMECH Base at all three pressure points. The two models have similar RMSREs at low and high pressures, however, the incumbent performs better, with CanMECH Base's RMSRE being 54% higher relative to Keromnes et al.'s [28].

The third validation dataset extracted from Keromnes et al. [28] supplementary material is provided in its Table S13. This dataset involves a mixture of H_2 and CO, and enables direct evaluation of the CO sub-mechanism of CanMECH model at pressures near 16 bar, at 1002-1222 K. The dataset involves a fuel lean environment composed of 2.98%H_2/0.52%CO/46.57%N_2/46.42%Ar at an equivalence ratio of 0.5. Table 9 indicates that CanMECH Base performs slightly better than the incumbent, signified by its 2.6% lower RMSRE.

The last validation dataset is also obtained from Keromnes et al. [28] supplementary materials. Its Table S16 lists experimental IDT data for 2.96%H_2/2.96%CO/Ar conducted at stoichiometric conditions with φ=1, at 1, 4, and 16 bar, covering a temperature range of 917-2220 K. This validation dataset enables validation of the CO mechanism at equivalence ratio of 1 at different pressures and across a larger temperature range. Table 9 indicates that while CanMECH Base performs better at 4 bar, Keromnes et al. [28] performs better at 1 bar and significantly better at 16 bar. The combined RMSREs of the two models at the three pressures for this dataset indicates that, Keromnes et al. outperforms CanMECH Base with an overall RMSRE of 0.216 vs. 0.251.

Based on an examination of the RMSREs for each validation data set the following overall observations across all experiments can be made:

1- CanMECH Base performs significantly better for all H_2O- and CO_2- laden H_2 IDT validation targets examined in this work.

2- CanMECH Base performs better for high-pressure Ar-diluted experiments, i.e., at 30 and 40 bar.

3- Keromnes et al. mechanism [28] performs better for the low-pressure Ar-diluted experiments. In particular, CanMECH Base mechanism needs to be improved for both Pang et al. dataset [52] and the low-pressure Ar-diluted experiments of this work.

4- A consistent conclusion cannot be made about the two model's performance at intermediate pressures of 16-17 bar, in Ar and N_2 diluted mixtures.

These conclusions suggest, that bath-gas-dependent reaction rates involving Ar are likely candidates for parameter tuning. Moreover, any tuning should only impact the lower pressure IDT predictions. To identify appropriate tuning parameters this study resorts to IDT sensitivity analyses conducted at different pressures and temperatures. To minimize the number of tuning parameters, they must have a substantial desirable impact only on the IDT data where the incumbent's predictions are better than CanMECH Base's. The tuning parameter adjustments must also have a minimal impact on other IDT predictions or, ideally, further improve them. To this end the proceeding paragraphs discuss the results of pressure-dependent sensitivity analyses conducted for the experimental IDTs of this work, as well as Pang et al.'s [52], to identify appropriate candidate tuning parameters. As pressure-dependent sensitivity analyses are conducted at a specific temperature, it is important to explore the effect of temperature variations on IDT-sensitivities and the chemistries involved (see next paragraph).

To understand the effect of temperature on the detailed hydrogen combustion chemistry, competition between the multiple chain branching explosive reaction pathways is commonly put into context in terms H_2-O_2's Z-shaped explosion limit curve, which characterizes the impact of temperature, as well as pressure. However, distinguishing the effect of temperature from other parameters, is not as easy as those for HC combustion mechanisms. A complex condition-specific interplay of elementary reactions are involved. H radicals play a crucial role in determining the H_2-O_2 reactions, similar to HC oxidation mechanisms. Glassman and Yetter [6] lists competing explosive pathways for hydrogen oxidation, which involves consumption of H either through elementary reaction R1: $H+O_2=O+OH$ as the main chain branching reaction, or through R9: $H+O_2(+M)=HO_2(+M)$, providing a few chain propagating and branching pathways. The ratio of rate constants of these reactions $k_1/k_9(M)$, where M is the concentration of a third body colliding/stabilizing molecule, provides a measure for which of the above two paths prevail. For instance, the second explosion limit of H_2 is observed when this ratio is near 0.5 [6].

Glassman and Yetter [6] also noted that generally at high temperatures and low-pressures R1 prevails, which along with R2: $O+H_2=H+OH$, R3: $OH+H_2=H+H_2O$, and -R4: $O+H_2O=OH+OH$ builds the radical pool necessary for explosive reaction.

HO_2, on the other hand, is a metastable radical and is less reactive than OH and O, and R9 which produces it, is characterized as a chain terminating reaction. At high pressures, and/or in the presence of strong colliders, R9's dominance increases, and HO_2 can play a chain-propagating role in building the radical pool. At such conditions, HO_2 reactions with other radicals, its recombination or its attack on the fuel, gains importance and provides several chain propagating and/or chain branching pathways. Such pathways include H_2O_2 formation through R14: $HO_2+HO_2=H_2O_2+O_2$ and/or R17: $HO_2+H_2=H_2O_2+H$ followed by it decomposition through R15: $H_2O_2(+M)=OH+OH$, or directly lead to chain branching via R11: $HO_2+H=OH+OH$, among others. Since these pathways are exothermic, these slow reactions, can compete with R1 and lead to explosive combustion. It is important to consider that, while HO_2 may require somewhat higher temperatures than the three more reactive radicals H, O, and OH, its rate of formation decreases relative to other reactions with increased temperature, as its activation energy is 0.

Hence, to generally delineate the impact of temperature, conditions that rely on reaction paths involving HO_2 and H_2O_2 similar to the low temperature HC combustion mechanisms, are referred to as those resembling low temperature chemistry, in this work. In-line with this terminology, conditions where R1 dominates, which commonly involves higher temperatures, are referred to as those resembling high temperature chemistry. Finally, condition that involve a fair competition between R1 and R9, as the dominant rate limiting reaction, are referred to as those resembling intermediate temperature chemistry, in this work.

To capture the effect of temperature on the chemistry, selected temperature dependent IDT-sensitivities are also conducted for the 40 bar experimental test campaigns. This enables determining whether a low, medium, or high temperature chemistry is dominant. It also shows whether conclusions made on the appropriate choice of tuning parameter at one temperature would still be valid at other temperatures across the temperature span of the experimental IDTs.

Figure 16 summarizes the results of an IDT sensitivity analysis conducted at pressures of 2, 4, and 40 bar at 1209 K, for 4%H_2/Ar φ=1. This analysis illustrates IDT sensitivities and the variation of the IDT-sensitive rate parameters, with non-negligible sensitivity coefficients ($\max|\sigma| \geq 0.02$), at three pressures relevant to the model validation data used in this work.

Focusing on the sensitivity results at 2 bar, it can be observed that, IDT is decreased mainly by an increased rate of R1: $H+O_2=O+OH$, and to lesser extents by R2: $O+H_2=H+OH$, R3: $OH+H_2=H+H_2O$ and R10: $H_2+O_2=H+HO_2$, whereas, it is increased by an increase in Ar-specific low-pressure-limit rate of R9: $H+O_2(+M)=HO_2(+M)$ (R9-A0-Ar). As such, to improve the fit of the low-pressure Ar-dilute data, potential kinetic rate parameters that can be tuned are limited to R1, R2, R9, R3, and R10.

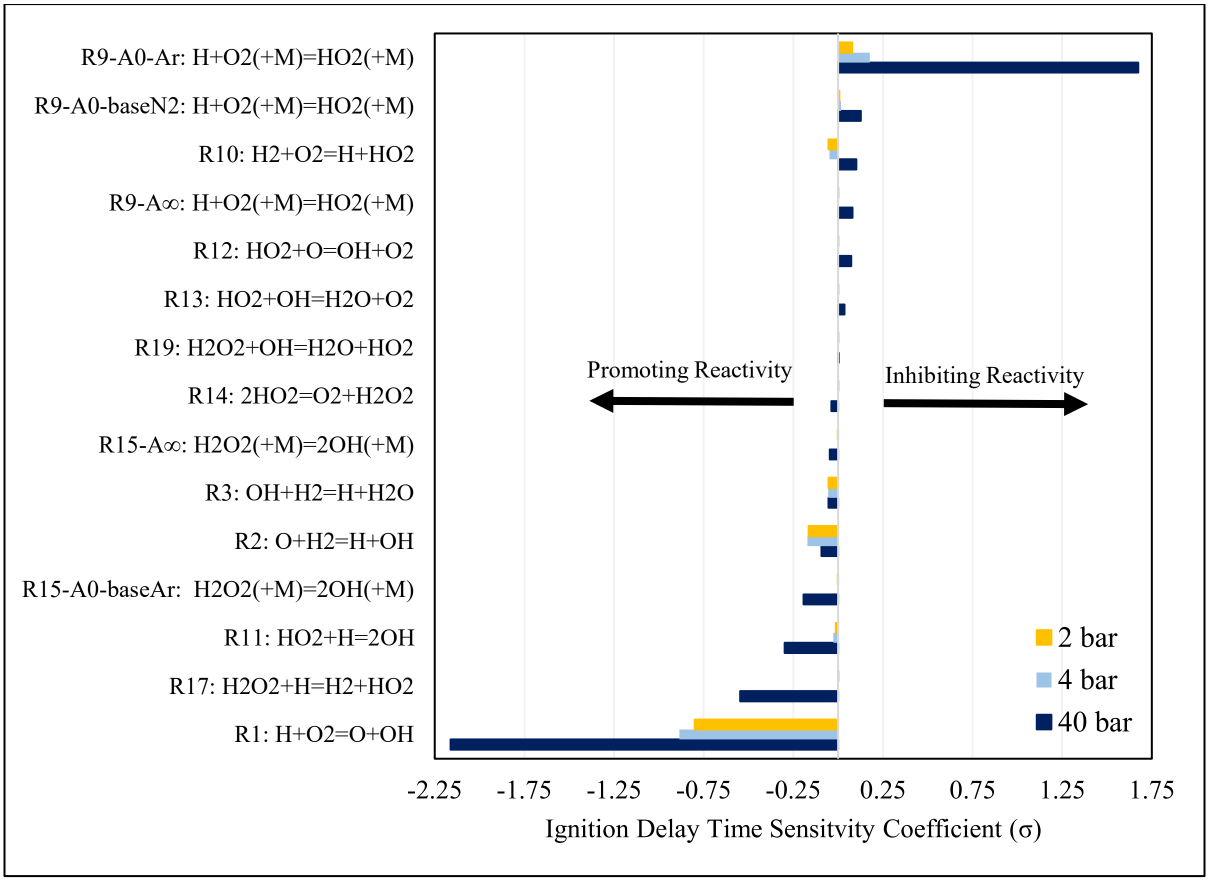

Figure 16: IDT-sensitive reaction rate parameters (max|σ|≥0.02) for 4%H_2/Ar φ=1 at 1209 K and pressures of 2, 4 and 40 bar

To understand the effect of temperature change, a graph of variation of IDT as a function of temperature at ~2 bar can be examined. Figure 17 provides an IDT temperature sweep for 4%H_2/Ar φ=1 at 2 bar over the temperature range of 940-2200 K. It can be observed that the change in log(IDT) vs. 1000/T is linear for temperatures above 1000 K. This suggests that for the majority of tests, at 2 bar in Ar, the chemistry is not expected to change, with the exception of tests 1-3 (see Table 5) which were run at temperatures below 1000 K. For tests 1-3, the chemistry appears to have started to shift into intermediate temperature chemistry, indicated by the non-negligible slope increase of the plot of log(IDT) vs. 1000/T, at temperatures below 1000 K.

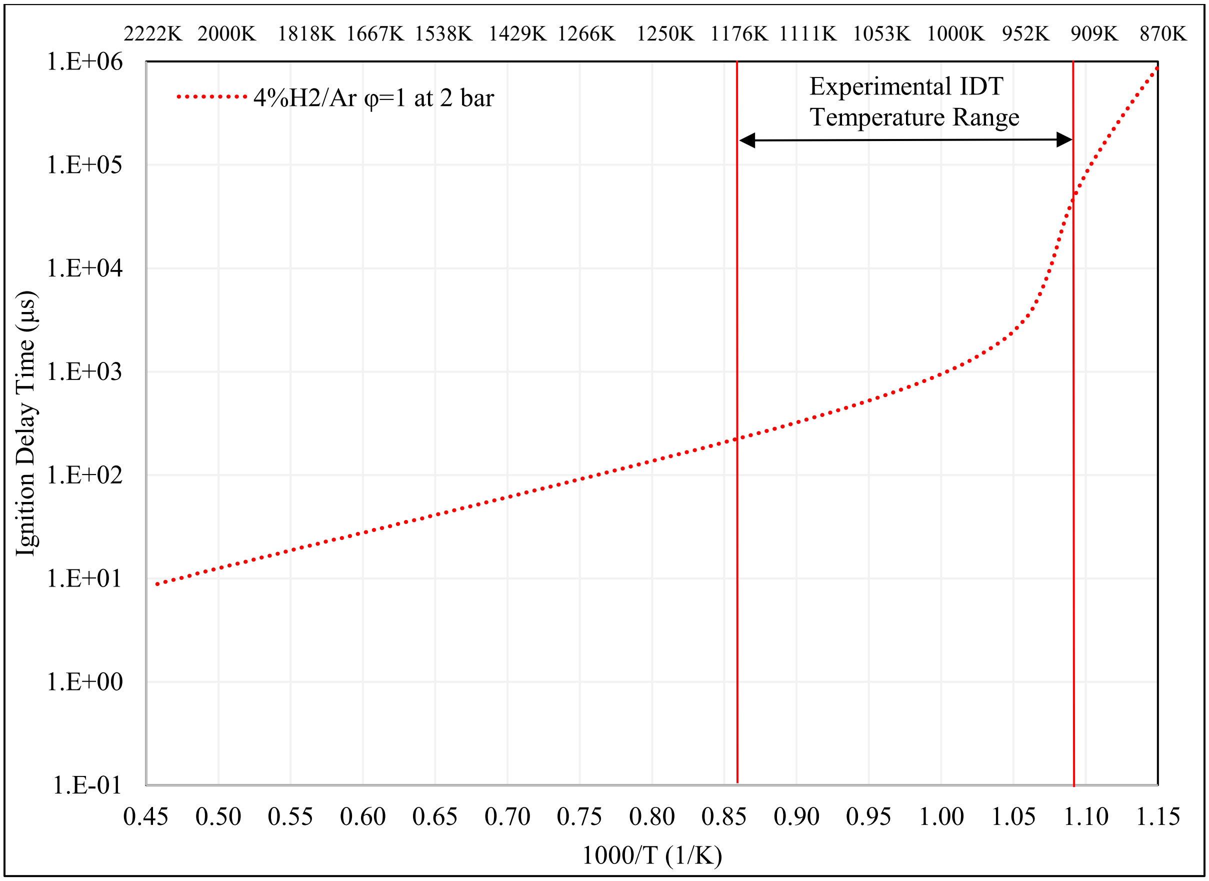

Figure 17: IDT Variation with temperature for 4%H_2 φ=1 at 2 bar

To better understand the IDT-sensitive reaction rate parameters at lower temperatures and at slightly higher pressures of 3.7 bar, relevant to Pang et al.'s [52] experimental data, Figure 18 depicts the results of a pressure-dependent IDT-sensitivity analysis conducted at a temperature of 1000 K. It details all IDT-sensitive rate parameters with max|σ|≥0.02 for 4%H_2/Ar φ=1 at 1000 K and pressures of 2, 3.7 and 40 bar. It can be observed that the conclusions drawn related to IDT-sensitive reaction rate parameters at 1209 K, also apply at 1000 K. Moreover, from the results of the 2 bar analysis at 1000 K, it is observed that R9 has a more pronounced contribution, whereas R3's contribution is subdued to insignificance relative to those observed at 1209 K. This eliminates R3 from the list of potential candidates for parameter tuning and changes the previously prioritized order of potential candidates to R1, R9, R2, and R10.

Shifting focus to the 3.7 bar results of Figure 18, in a decreasing order of importance, reactions R1, R9 Ar-specific and BaseN_2 low-pressure-limit rates, and to lesser extents R11: HO_2+H=OH+OH, R17:

H_2O_2+H=H_2+HO_2, and R2 are controlling the overall reactivity. The effect of R1, and R9's Ar-specific low-pressure-limit rate are significantly larger than others, rendering them as likely candidates for tuning. It is important to note that their larger impact is also signified by their much larger sensitivity coefficient extending the bounds of the sensitivity chart from -2.16/+1.67 (Figure 17) to -3.16/+2.84. As R17 is inconsequential to the 2 bar IDT data it is unlikely to be the primary tuning parameter. Combining the results of 2 and 3.7 bar IDT sensitivities at 1000 and 1209 K, it can be concluded that R17, R10, R11, and R9's Base N_2 low-pressure-limit rates are unlikely to be the primary tuning parameter, as they have small impact on IDTs of both 1000 and 1209 K at 2 bar. As such the revised list of potential candidates can be further narrowed down to R1, R9 and R2.

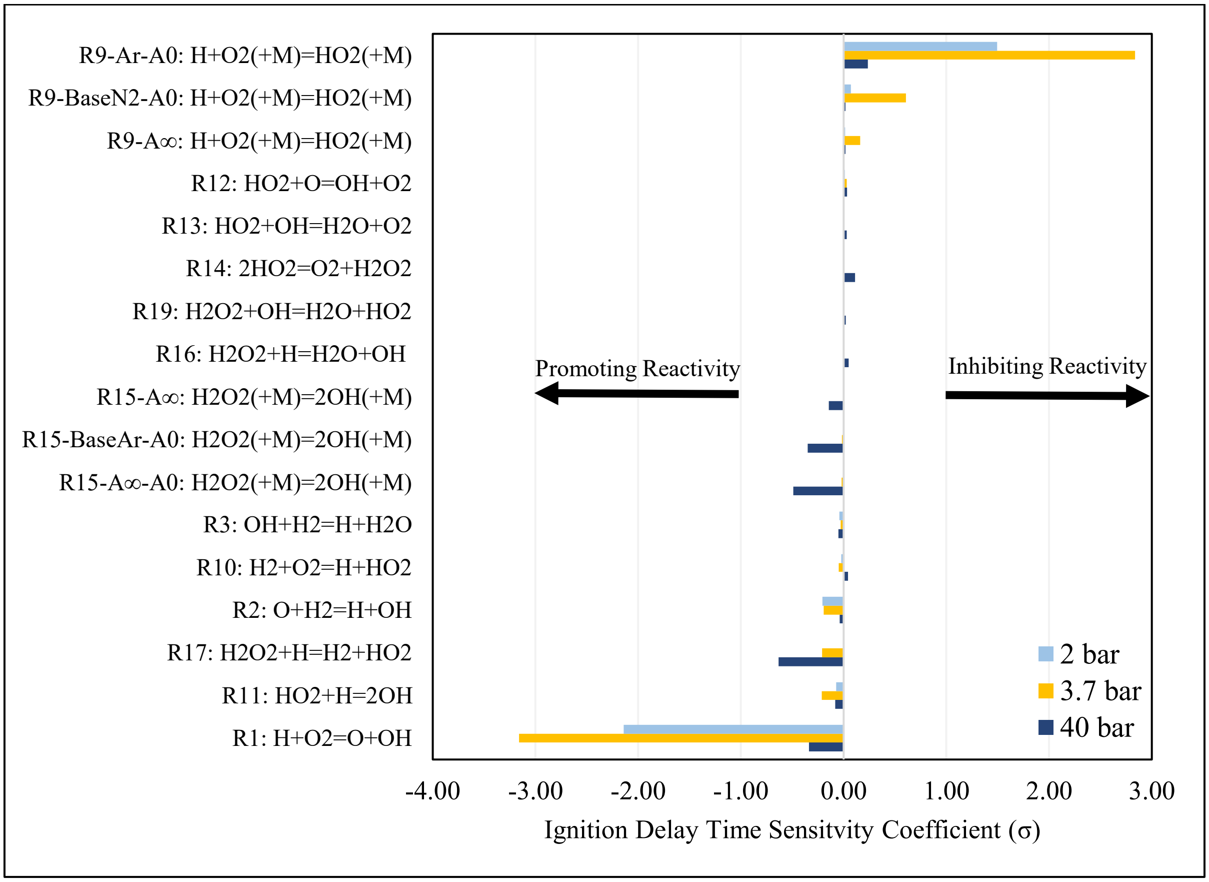

Figure 18: IDT-sensitive reaction rate parameters (max|σ|≥0.02) for 4%H_2/Ar φ=1 at 1000 K and pressures of 2, 3.7 and 40 bar

Looking at the 40 bar sensitivity results of Figure 16, there are significantly more reactions that contribute to the overall reactivity, and thus it can be concluded that the chemistry is more complex at higher pressures. Notably, R9 and R17 appear to have a significantly increased contribution relative to the sensitivity analysis results observed at 2 and 4 bar. Also, R10's sensitivity switches sign and exhibits an inhibiting effect instead. In addition to R1, R17, and R11, the Ar-specific low-pressure-limit rate of R15: $H_2O_2(+M)=OH+OH(+M)$, as well as its high-pressure-limit rate, also promote reactivity significantly. Based on an examination of Figure 9 and Figure 11 it can be observed that the models overpredict the measured IDTs at both 2 and 40 bar near 1209 K. As such, if only one rate were to be adjusted to achieve the desired effect at both pressures, it is unlikely to be R10, as it increases reactivity at 2 bar but decreases it at 40 bar. R17, R11 and R15 are also less likely candidates, as at 1209 K, they only impact the high-pressure IDTs. This limits the remaining possible candidates for parameter tuning to R1, the Ar-specific low-pressure-limit rate of R9: $H+O_2(+M)=HO_2(+M)$, and to a lesser extent R2. To ensure that the conclusions drawn based on the results of the 40 bar IDT-sensitivity analysis conducted at 1209 K, apply to other temperatures relevant to this study, a temperature dependent IDT-sensitivity analysis is conducted at 40 bar. Figure 19, summarizes the 12 IDT-sensitive kinetic parameters with $\max|\sigma|\geq 0.1$ for the extended temperature range of 975-1650 K, for 4%H_2/Ar $\varphi=1$. It can be observed that the temperature range explored experimentally falls closer to the intermediate to lower temperature chemistry. However, it is important to observe that, with the exception of an increased dominance of R1 and R9, there is no major change in sensitivities of rate determining kinetic rate parameters, within the experimental temperature range. This ensures that the conclusions drawn from IDT sensitivities at 1209 K and 40 bar, are applicable to all experimental data within the explored IDT temperature range bounded by the vertical red lines in Figure 19.

In contrast to the Ar-diluted experimental data of validations data sets 1 and 4, which require an increased reactivity to improve CanMECH Base's prediction ability, the water laden data of this work call for a reduction of the model reactivity at higher temperatures. Figure 12 and Figure 13 show that for the 45% and 30% H_2O-laden experimental data of this work, a decrease in overall reactivity at temperatures above 1128 and 1200 K, respectively, should reduce the RMSRE of the fit. Also the CO_2-laden experimental data of this work should remain unperturbed. To this end, in order to identify the most suitable tuning parameter(s), it is important to understand the sensitivity of reaction rate parameters to model prediction ability for the H_2O- and CO_2-laden datasets at temperatures of 1200 K and higher.

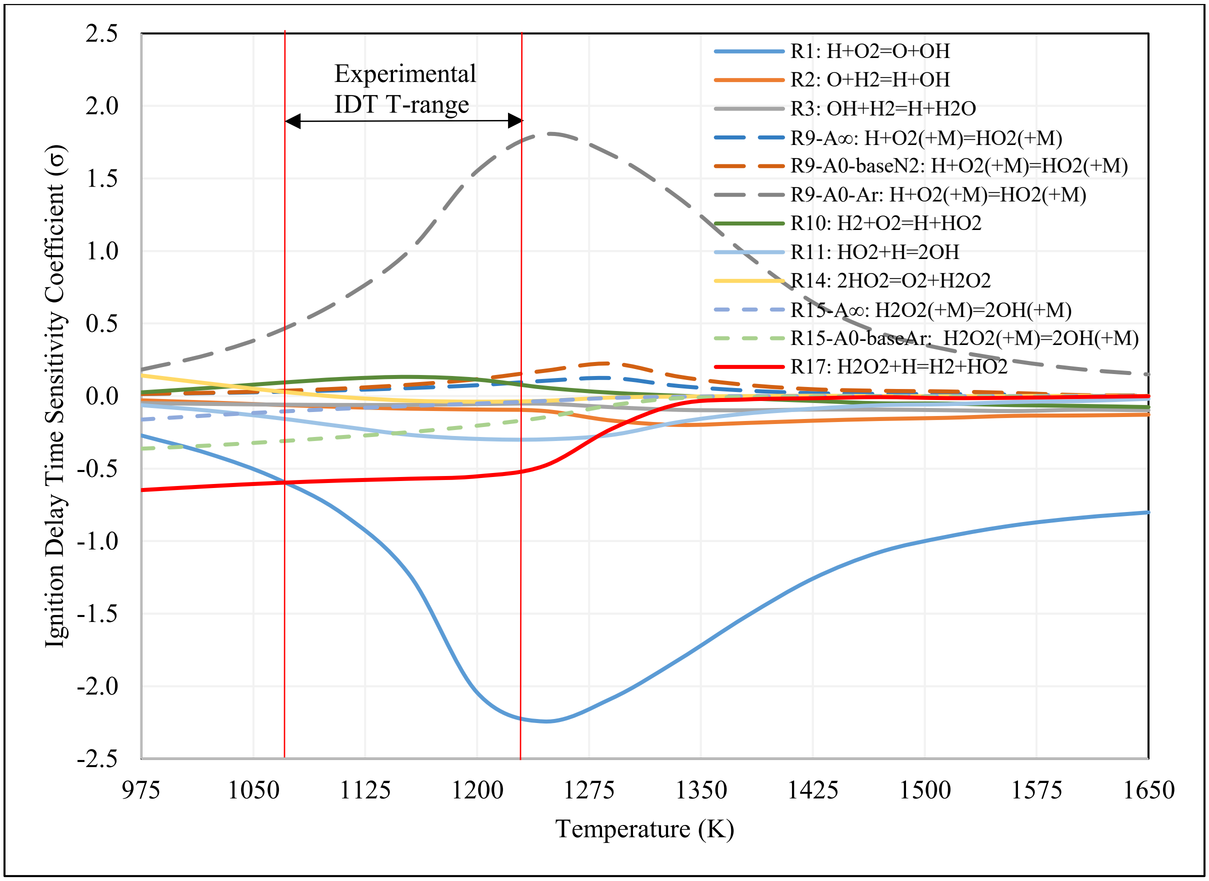

Figure 19: IDT Sensitivity of Reactions for 4%H_2/Ar φ=1 at 40 bar

Figure 20 depicts the IDT-sensitive rate parameters at pressures of 2, and 40 bar for the 45%H_2O-laden data at 1222 K. At 40 bar, R17, R3, R1, R19, R14, R15 and R4 are the dominating reactions that decrease IDT, sorted from the most to least impactful. R13, R9, and R10 are the most inhibiting to reactivity, respectively. In contrast to the previous sensitivity analyses, R9's Ar-specific low-pressure-limit rate's dominant effect is completely replaced by its H_2O-specific low-pressure-limit rate. This reaffirms the Ar-specific limiting rate as a potential tuning parameter, as it leaves the fit of 45% H_2O-laden data nearly unperturbed. Also, since R17, R3 and R1 increase the reactivity of the H_2O-laden experiments, it is concluded that, while increasing their rate would improve the fit of Ar-diluted experiments of validation data sets 1 and 4, such tuning would worsen the fit of H_2O-laden data, which is undesirable. As such R17, R3, and R1 are unlikely to be suitable candidates for tuning. R14 and R15 were not identified as impactful rate parameters for validation data set 4, as such they are less appropriate choices for parameter tuning. This leaves only R9's Ar-specific low-pressure-limit rate, and R2 as potential tuning parameters. To evaluate whether these conclusions apply across the experimental IDT temperature range, Figure 21, which depicts IDT-sensitivity variations of Kinetics parameters across an extended temperature range of 975-2025 K for 4%H_2/45%H_2O/Ar with φ=1 at 40 bar, is examined. The absence of R9's Ar-specific low-pressure-limit and R2 in Figure 21 confirms that the shortlisted tuning parameters will not have an impact on the H_2O-laden IDT predictions.

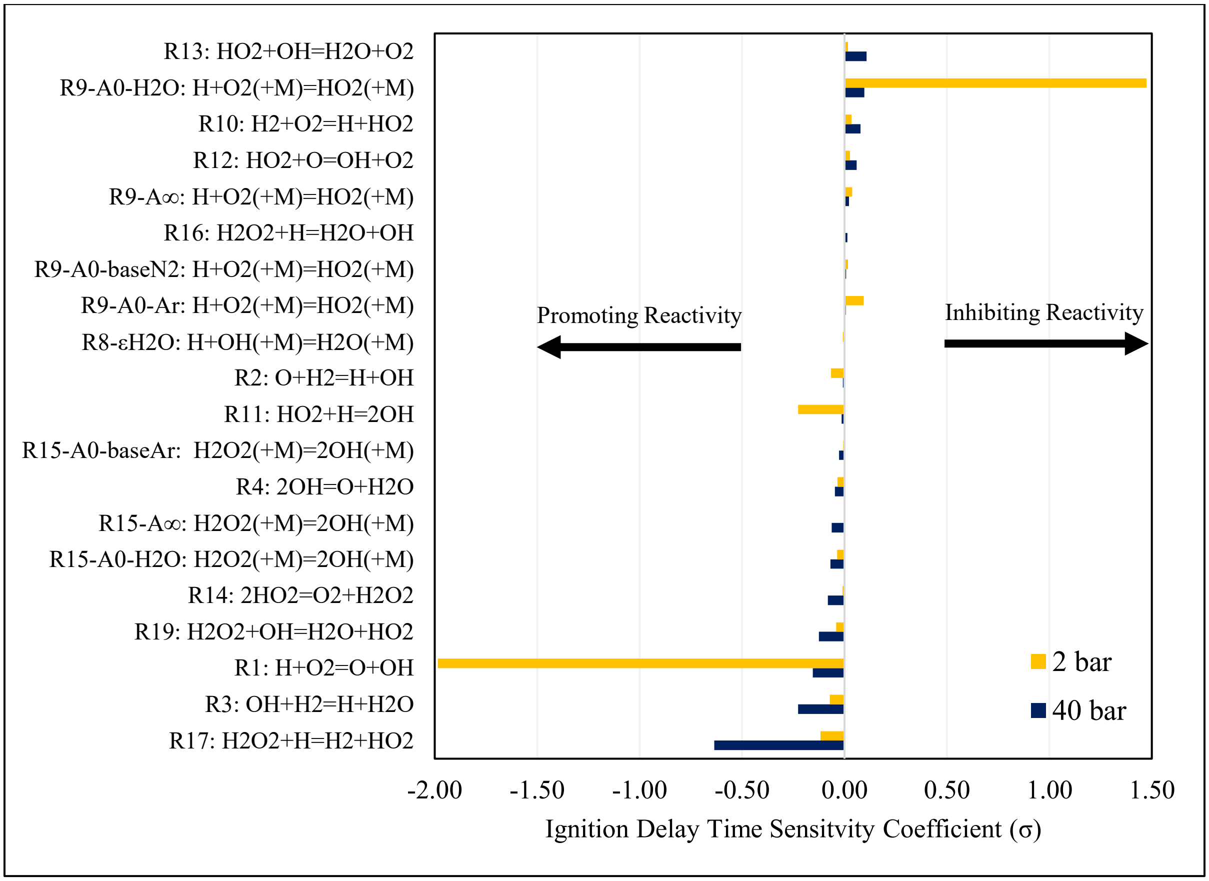

Figure 20: IDT-sensitive reaction rate parameters (max|σ|≥0.02) for 4%H_2/45%H_2O/Ar φ=1 at 1222 K and pressures of 2 and 40 bar

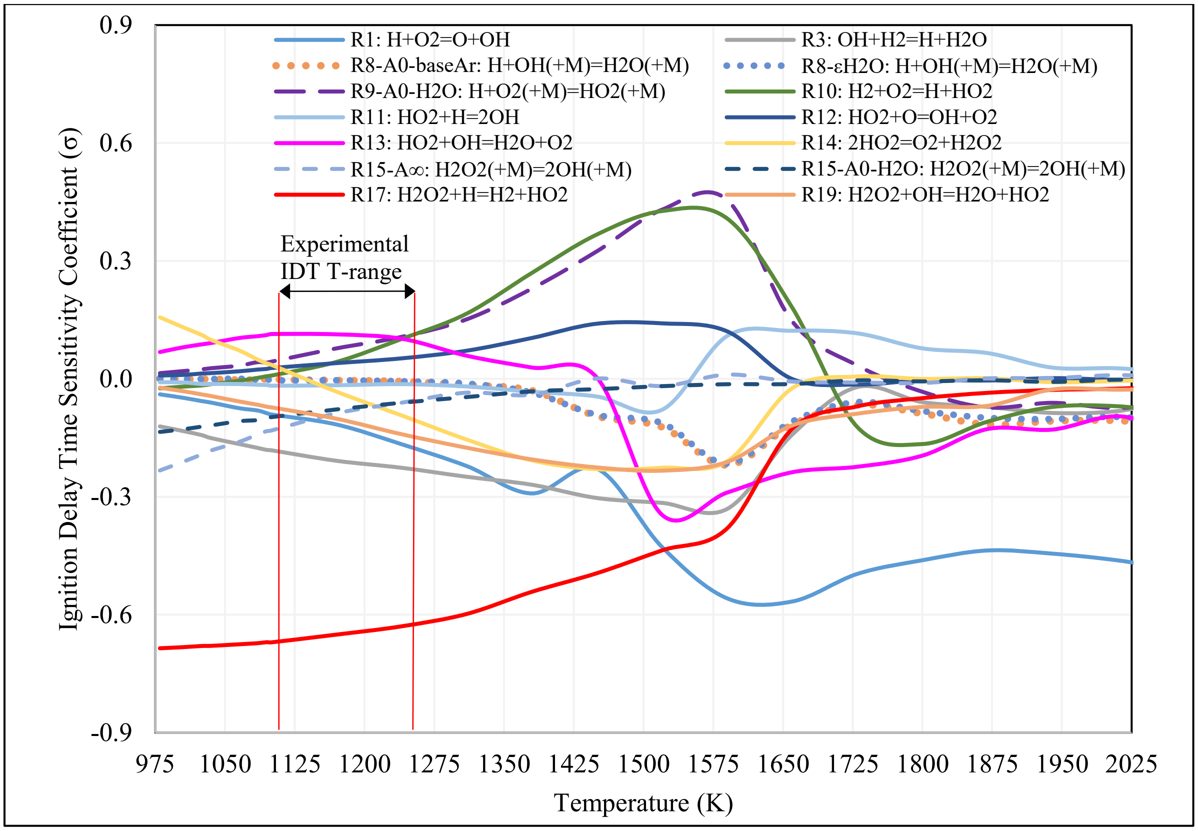

Figure 21: IDT Sensitivity of Reactions for 4%H_2-45%H_2O/Ar φ=1 at 40 bar

To confirm appropriateness of the tuning parameters, it is important to understand their impact on IDTs in bath gases composed of 30%H_2O/15%CO_2/Ar and 45%CO_2/Ar as well. Figure 22 lists the important reaction rate parameters with max|σ|≥0.02 for the 4%H_2/30%H_2O/15%CO_2/Ar mixtures with φ=1 at 1232 K and pressures of 2, and 40 bar. It can be observed that the sensitivities closely resemble those of the 45%H_2O, except R9's Ar- and CO_2-specific low-pressure-limit rates now appear on the list of sensitive reactions. This is due to the reduced concentration of H_2O, which is 23 times stronger collider than Ar [83]. Fortunately, the impact of R9's CO_2- and Ar-specific low-pressure-limit rate, is only non-negligible at low pressures relative to that of R9-A0-H_2O. As such adjustment of R9's Ar-specific low-pressure-limit rate is expected to be inconsequential to CanMECH Base's performance in predicting the 30%H_2O/15%CO_2-laden IDT data of this work. R2 on the other hand seems to have a reactivity promoting effect, which is undesirable. This is because to improve the fit of Ar-diluted data its rate needs to be increased, but such increase would adversely impact the fit of 30%H_2O/15%CO_2-laden

IDTs. Hence, the only remaining parameter tuning appears to be R9's Ar-specific low-pressure-limit rate (R9-A0-Ar).

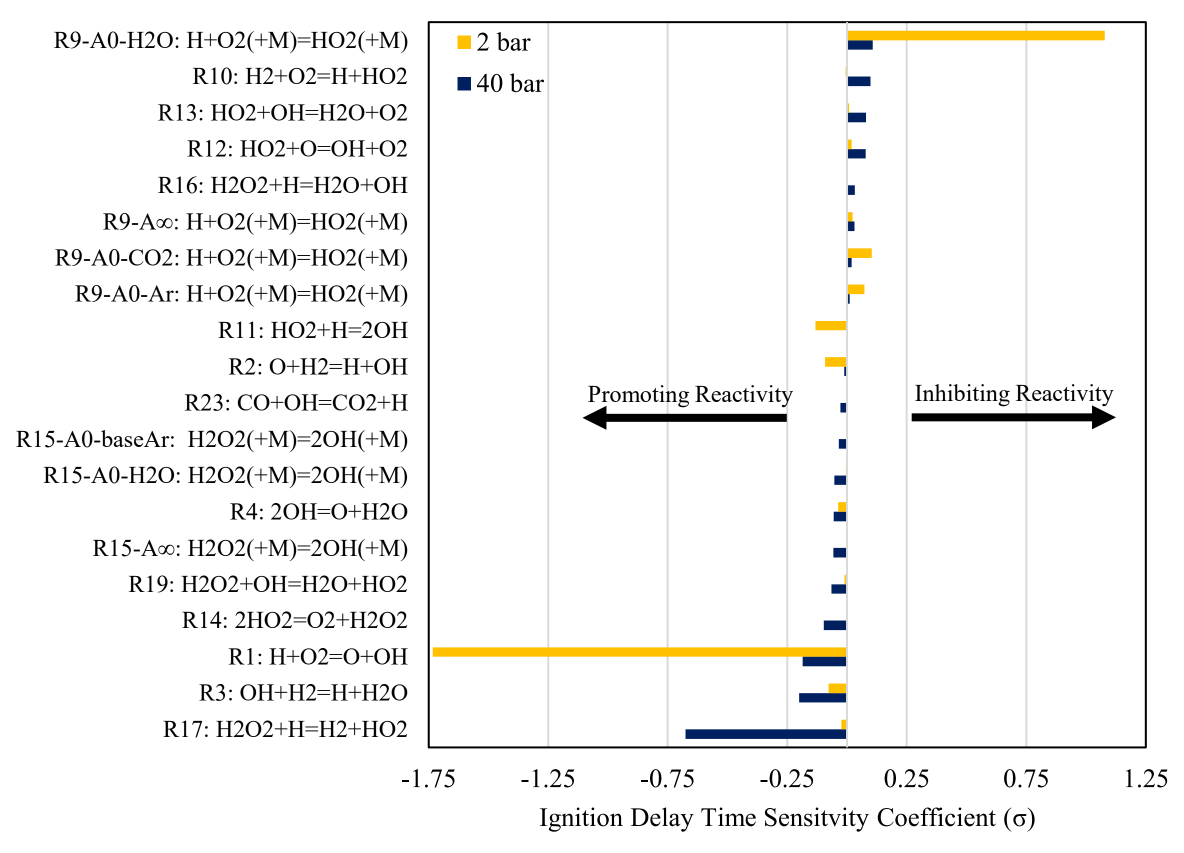

Figure 22: IDT-sensitive reaction rate parameters (max|σ|≥0.02) 4%H_2/30%H_2O/15%CO_2/Ar φ=1 at 1232 K and pressures of 2, and 40 bar

To ensure that suitability of R9's Ar-specific as the primary tuning parameter inclusively applies across the temperature range explored experimentally, temperature dependent IDT sensitivities are examined. Figure 23 illustrates the variation of sensitivities as a function of temperature for IDT-sensitive reaction rate parameters, for 4%H_2/30%H_2O/15%CO_2/Ar φ=1. Similar to the 45%H_2O Figure 23 shows that R14 is the only reaction that changes sign, within the experimental temperature range. However, it is not one of the candidate parameters considered for tuning. It also illustrates that other rate parameters' sensitivity trendsdo not undergo drastic changes within the experimental temperature range.These validate the conclusions drawn regarding tuning parameters, based on the sensitivity analysis results of Figure 22, conducted at 1232 K.

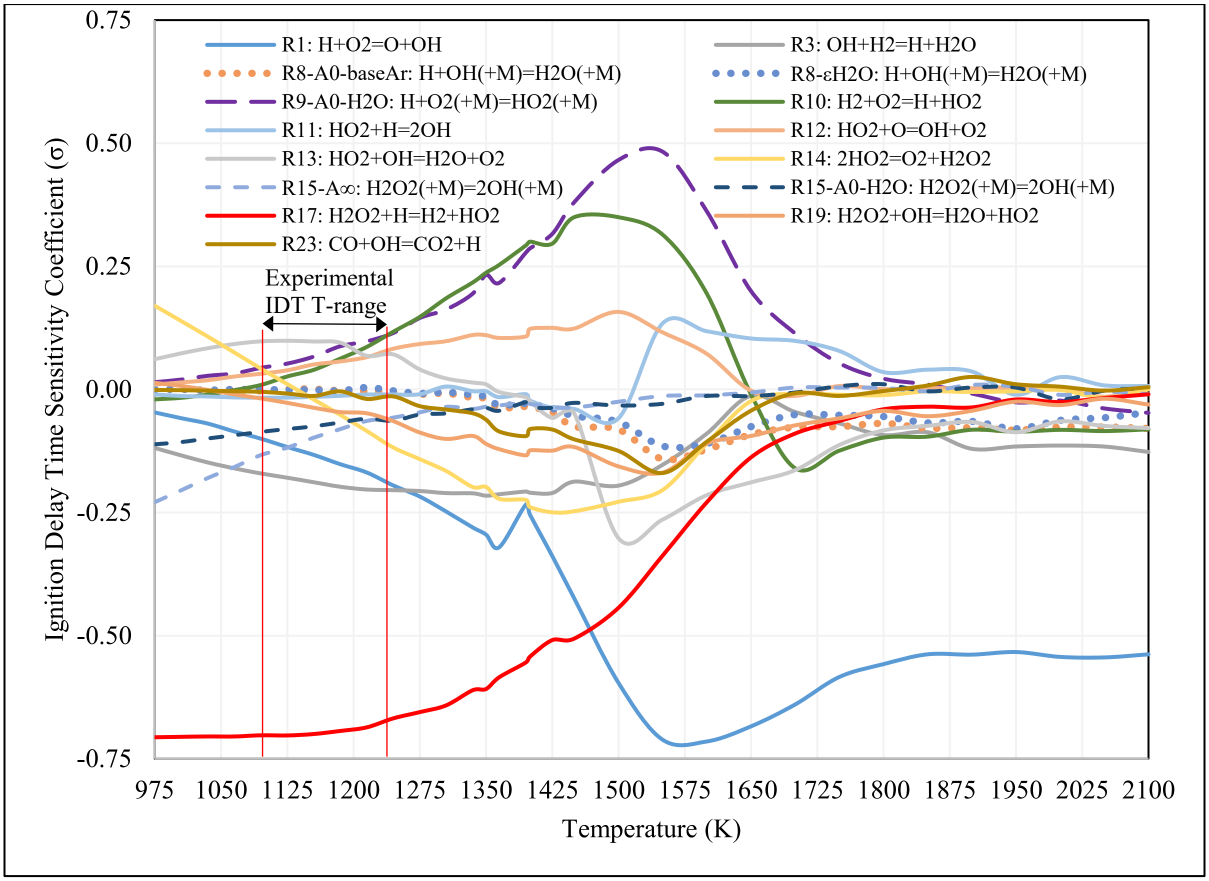

Figure 23: IDT Sensitivity of Reactions for 4%H_2/30%H_2O/15%CO_2/Ar φ=1 at 40 bar

Figure 24 details the IDT-sensitive reaction rate parameters for 4%H_2/45%CO_2/Ar φ=1 at 1226 K and pressures of 2, and 40 bar. Examining the low-pressure (~2 bar) sensitivity results, indicates that the range of sensitivity coefficients Figure 24's x-axis is reduced by a factor of 2 relative to Ar- and H_2O-laden sensitivity analyses. This change in scale must be taken into consideration for correct interpretation of data. Nevertheless, at 2 bar, R9's CO_2- and Ar-specific low-pressure-limit rates and R12 increase ignition delay times, while R1, R2, R10, R3 and R11 decrease them. As reduced IDTs are desired for the fit of low-pressure Ar- and CO_2-diluted modeled IDTs, R9's Ar-specific low-pressure-limit rate's negative sensitivity confirms its suitability for parameter adjustments. Examining the data at 40 bar, illustrates that R9's CO_2- and Ar-specific low-pressure-limit rates, R10, R12, R16, R13 and R19 increase IDTs, while R1, R17, R14 and R11, R23, R15, R2, R3, R9's H_2O-specific low-pressure-limit rate decrease them. Building on the results of the sensitivity analysis at 2 bar, 40 bar sensitivity of R9's small Ar-specific low-pressure-limit rate, suggests that tuning this parameter should also impact

IDTs, which could also benefit from a small reduction in the modelled IDTs to improve the fit. Finally, to check the applicability of conclusions across the experimentally explored temperature range, Figure 25 depicts IDT sensitivity analysis results as a function of temperature for experiments with 45% CO_2 dilution. Based on the results of Figure 25 no noteworthy variation in the chemistry is expected over the temperature range explored experimentally. As such the conclusions drawn from Figure 24 with respect to the appropriate choice of tuning parameter, are not contested.

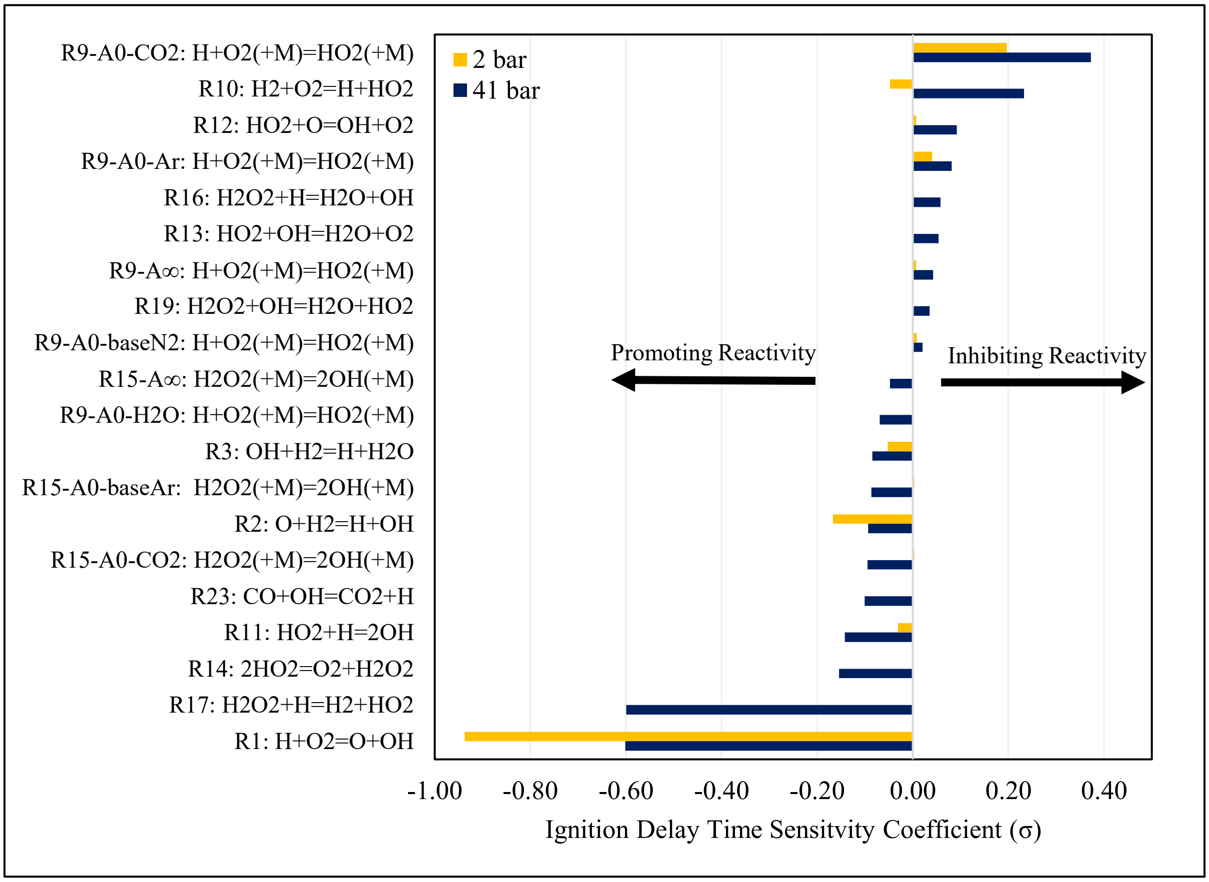

Figure 24: IDT-sensitive reaction rate parameters (max|σ|≥0.02) 4%H_2/45%CO_2/Ar φ=1 at 1226 K and pressures of 2, and 40 bar

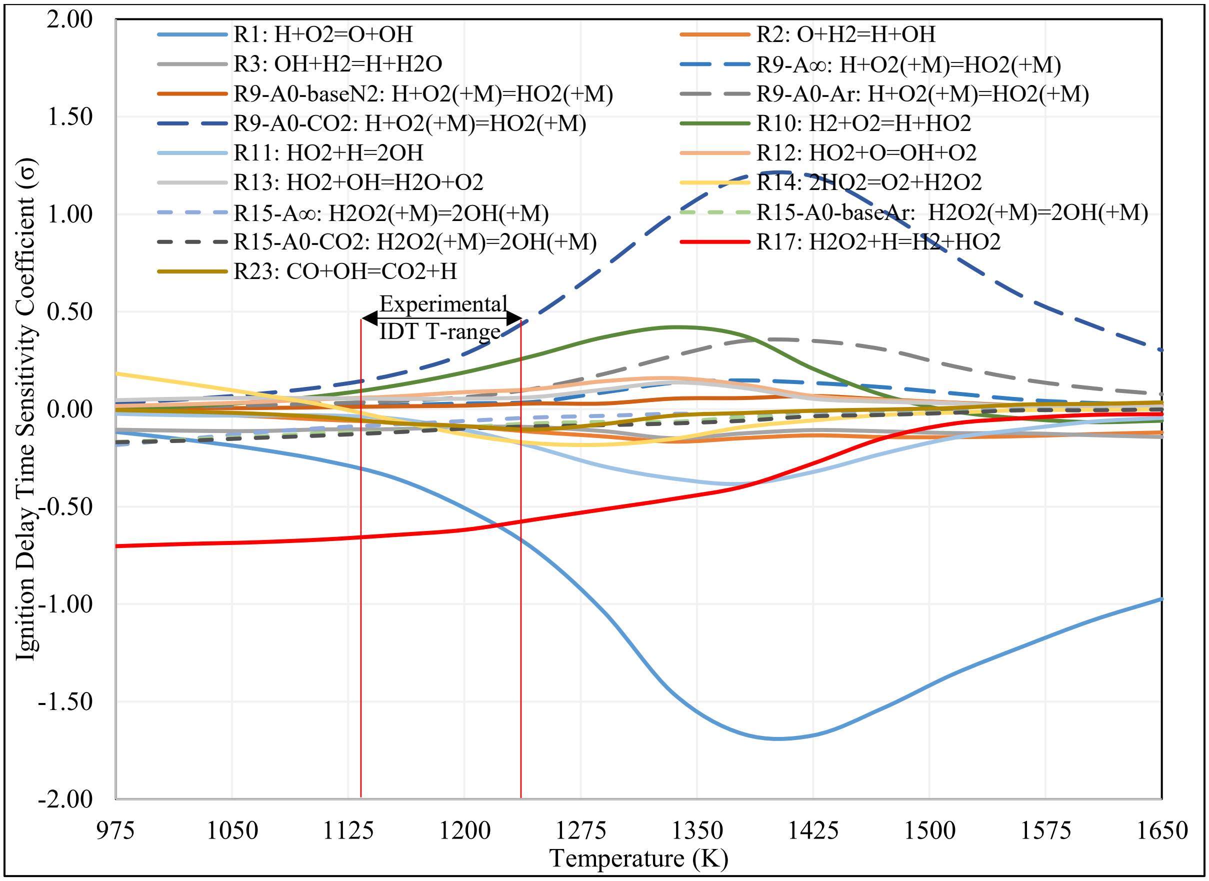

Figure 25: IDT Sensitivity of Reactions for 4%H_2/45%CO_2/Ar φ=1 at 40 bar

Based on the above sensitivity analyses, the only reaction rate that will universally improve the fit of the analyzed datasets, where CanMECH Base does not perform as well as Keromnes et al. [28], is R9's Ar-specific low-pressure-limit rate. This parameter is also expected to have little effect on the H_2O- and CO_2-laden IDT data of this work.

Among the three tunable parameters for this reaction, namely: the temperature exponent, "n", activation energy "E_a" and the pre-exponential A-factor "A", since an obvious temperature dependent lack of fit was not apparent in either of Figure 9, Figure 10, Figure 11 or Figure 15, the pre-exponential factor, A, was selected for tuning.

To determine the extent of tuning appropriate, a parametric study was conducted on the pre-exponential factor of R9's Ar-specific low-pressure-limit rate constant. Table 10 provides the results of this parametric study, detailing the RMSRE's as a function of the extent of tuning of the pre-exponential factor of R9's: $H+O_2(+M)=H+O_2(+M)$ Ar-specific low-pressure-limit rate constant. The source of this reaction's original rate parameters, Shao et al.'s 2019 study [83], reported a maximum uncertainty of ±12% for this rate. Hence, the extent of tuning had to be limited to ±12%. From sensitivity analyses, it was observed that increasing this reaction rate reduces reactivity at low and high pressures. As such in order to reduce the predicted IDTs, a rate multiplier with a value smaller than 1 and larger or equal to 0.88 (-12% adjustment), is desired. Table 10, details the results of a stepwise parametric study examining pre-exponential multiplier values of 0.95, 0.92, 0.9, 0.89, and 0.88. From the last column of Table 10 it can be observed that for the final tuned CanMECH 1.0 with only one parameter tuned, i.e. the collider-specific low-pressure-limit-rate of Argon, for R9: $H+O_2(+M)=H+O_2(+M)$ with a pre-exponential value of 0.88, outperforms the incumbent Keromnes et al. mechanism for the majority of datasets. Moreover, the last row of Table 10 lists the overall RMSRE for the different pre-exponential multiplier values considered in this parametric study. It can be observed that CanMECH 1.0 exhibits the lowest overall RMSRE after reducing the rate of the collider-specific low-pressure-limit-rate of Argon, for R9 by 12% (0.88 multiplier). Also, relative to the incumbent model of Keromnes et al. [28] CanMECH 1.0 brings about a 26% reduction in overall RMSRE (last column's last row), signifying its improved prediction ability of all IDT validation data of Table 9. In addition to the overall performance metrics it is also important to understand the effect of the implemented parameter tuning on individual datasets.

Table 10 shows that RMSREs of the 2 bar Ar- and CO_2-diluted experimental IDTs of this work, which consistently decrease with a decrease in R9's reaction rate, reaching their minimum for the rate multiplier value of 0.88. While CanMECH Base's RMSRE has reduced by over 15% for the low-pressure Ar-diluted test, its RMSRE is still higher than Keromnes et al.'s [28], as observed from its calculated RPRMSRE of +18%. Re-examination of Figure 9 shows that the implemented parameter tuning has narrowed the error gap relative to the experimental results. While further reduction of Ar's low-pressure-limit would have reduced the deviation, the reported uncertainty of 12% for this rate by Shao et al. [83], prohibited applying a rate multiplier lower than 0.88 (-12% adjustment). It should be noted that Keromnes et al. [28] utilizes a rate that has a 13% lower pre-exponential factor for Ar's low–pressure-limit rate relative to CanMECH 1.0. This corresponds to implementing a tuning multiplier value of 0.77.

Table 10: RMSRE results of parametric study of R9’s Ar-specific low-pressure-limit rate’s A-factor

Data set ID	Source	Fuel & Bath gas Composition	# of data	Pressure range (barA)	Temperature range (K)	φ	CanMECH Base - R9-Ar-A0x0.88 **CanMECH 1.0 RMSRE**	R9-Ar-A0x0.89 RMSRE	R9-Ar-A0x0.90 RMSRE	R9-Ar-A0x0.92 RMSRE	R9-Ar-A0x0.95 RMSRE	CanMECH Base RMSRE	**Keromnes et al. [28] RMSRE**	**CanMECH 1.0 vs. Keromnes et al. RPRMSRE Error (%)**
1	This Work	4%H_2/Ar	10	1.6-2.2	917-1237	1	1.418	1.437	1.457	1.478	1.543	1.659	1.199	18
		4%H_2/45CO_2/Ar	7	2.1-2.4	1014-1211	1	5.244	5.270	5.296	5.321	5.397	5.524	7.378	-29
		Combined at ~ 2bar	**17**	**1.6-2.4**	**917-1211**	**1**	**3.536**	**3.557**	**3.577**	**3.598**	**3.660**	**3.766**	**4.823**	**-27**
2	This Work	4%H_2/Ar	9	37.0-43.8	1084-1237	1	0.067	0.068	0.072	0.079	0.108	0.169	0.122	-45
		4%H_2/45%H_2O/Ar	8	39.1-40.7	1106-1242	1	0.192	0.191	0.192	0.192	0.192	0.192	0.269	-29
		4%H_2/30%H_2O/15%CO_2/Ar	8	40.4-41.6	1108-1232	1	0.097	0.097	0.097	0.097	0.098	0.097	0.179	-46
		4%H_2/45%CO_2/Ar	9	39.3-43.8	1133-1226	1	0.075	0.076	0.075	0.076	0.078	0.080	0.075	0
		Combined at ~ 40bar	**34**	**37.0-43.8**	**1084-1242**	**1**	**0.116**	**0.116**	**0.117**	**0.119**	**0.125**	**0.142**	**0.173**	**-33**
3	Shao et al. [83]	3%H_2/Ar	5	29.1-32.9	1230-1262	1	0.382	0.362	0.342	0.321	0.254	0.134	0.453	-16
		3%H_2/Ar	6	17.0-17.6	1184-1224	1	0.243	0.230	0.218	0.205	0.163	0.091	0.315	-23
		3%H_2/N_2	5	12.8-13.3	1199-1228	1	0.162	0.162	0.162	0.162	0.162	0.162	0.313	-48
		3%H_2/4.4%H_2O/Ar	3	15.9-17.0	1264-1307	1	0.185	0.187	0.191	0.196	0.206	0.247	0.348	-47
		3%H_2-9%H_2O-Ar	6	15.2-16.6	1270-1344	1	0.166	0.172	0.177	0.182	0.200	0.230	0.354	-53
		3%H_2/13.4%H_2O/Ar	2	15.3-15.7	1282-1376	1	0.093	0.097	0.099	0.103	0.113	0.133	0.377	-75
		3%H_2/20%CO_2/Ar	11	11.7-19.3	1185-1268	1	0.203	0.200	0.197	0.196	0.199	0.221	0.408	-50
		3%H_2/10%CO_2/Ar	2	11.4-11.9	1179-1180	1	0.294	0.282	0.269	0.258	0.217	0.146	0.150	96
		Combined	**40**	**11.4-32.9**	**1179-1376**	**1**	**0.231**	**0.224**	**0.217**	**0.211**	**0.196**	**0.186**	**0.367**	**-37**
4	Pang et al. [52]	**4%H_2/Ar**	**33**	**3.42-3.76**	**924-1118**	**1**	**0.332**	**0.357**	**0.383**	**0.411**	**0.497**	**0.651**	**0.238**	**40**
5	Keromnes et al. (S11) [28]	3.47%H_2/N_2	11	0.94-1.05	932-1954	0.5	0.282	0.282	0.282	0.282	0.282	0.282	0.245	15
			13	3.91-4.54	1006-1257	0.5	0.313	0.313	0.313	0.313	0.313	0.313	0.490	-36
			10	15.1-16.3	1060-1243	0.5	0.321	0.321	0.321	0.321	0.321	0.321	0.251	28
		Combined- S11	**34**	**0.94-16.3**	**932-1954**	**0.5**	**0.306**	**0.306**	**0.306**	**0.306**	**0.306**	**0.306**	**0.360**	**-15**
6	Keromnes et al. (S12) [28]	12.54%H_2/Ar	26	0.92-1.37	943-2136	4	0.208	0.208	0.209	0.209	0.209	0.210	0.207	0
			20	3.7-4.5	967-1463	4	0.129	0.127	0.125	0.128	0.152	0.232	0.182	-29
			16	14.2-16.6	947-1227	4	0.248	0.251	0.252	0.253	0.263	0.286	0.242	3
		Combined-S12	**62**	**0.92-16.6**	**943-2136**	**4**	**0.199**	**0.199**	**0.199**	**0.200**	**0.209**	**0.239**	**0.209**	**-5**
7	Keromnes et al. (S13) [28]	**2.98%H_2/0.52%CO/ 46.57%N_2/46.42%Ar**	7	15.0-16.6	1002-1222	**0.5**	**0.443**	**0.442**	**0.445**	**0.444**	**0.448**	**0.453**	**0.455**	**-3**
8	Keromnes et al. (S16) [28]	2.96%H_2/2.96%CO/Ar	23	0.76-1.18	924-2220	1	0.240	0.239	0.238	0.229	0.226	0.231	0.199	20
			23	3.71-5.07	942-1364	1	0.202	0.196	0.191	0.186	0.181	0.204	0.226	-11
			16	14.7-16.8	997-1215	1	0.245	0.243	0.242	0.244	0.263	0.329	0.225	9
		Combined-S16	**23**	**0.76-16.8**	**924-2220**	**1**	**0.228**	**0.225**	**0.223**	**0.218**	**0.221**	**0.251**	**0.216**	**5**
Overall			**289**	**0.76-43.8**	**917-2220**	**0.5-4**	**0.890**	**0.896**	**0.902**	**0.9073**	**0.9268**	**0.965**	**1.199**	**-26**

For the 2-bar CO_2 diluted data of this work, it can be observed that the RMSREs consistently reduce with smaller values of the rate multiplier. Graphical examination of Figure 10 corroborates with the RMSREs and shows that the parameter tuning has a desirable but small impact on the modelled IDTs for $4\%H_2/45\%CO_2/Ar$ $\varphi=1$ at ~2.3bar. Their impact is also smaller relative to that observed for the low-pressure Ar-diluted experiments. This is due to the increased concentration of CO_2 displacing Ar, which has a five times larger third body collision efficiency than Ar when it comes to R9: $H+O_2(+M)=HO_2(+M)$. Nevertheless, an RPRMSRE of -29% indicates that CanMECH 1.0 has a 29% better performance, relative to the incumbent. Moreover, the combined RMSRE for dataset 1 suggests a 27% improvement of the relative errors, as indicated by the overall RPRMSRE.

For the 40-bar Ar-diluted predicted IDT (dataset 2), the RMSREs consistently decrease with reduced reaction rate multiplier values, reaching their minimum for the multiplier value of 0.88. While prior to tuning, Keromnes et al.'s mechanism [28] had the lowest RMSRE for this data, after 12% reduction of the tuned rate, CanMECH 1.0 now exhibits the lowest RMSRE. Relative to the incumbent, CanMECH 1.0 has brought about a 45% improvement, signified by its RPRMSRE. Figure 11 is another clear testament to the improved RMSREs and illustrates that CanMECH 1.0 mimics the global activation energy of the experimental data more closely, as well.

RMSREs of Table 10 also illustrate that for the 45% H_2O-laden as well as the $30\%H_2O/15\%CO_2$-laden experimental data the tuning parameter is inconsequential toward the fit of the data. Figure 12 and Figure 13 show that, CanMECH 1.0 provides significantly better estimates of the measured IDTs and their global activation energy than the incumbent. This is signified by the RPRMSREs of -29% and -46% for the 45% H_2O-laden as well as the $30\%H_2O/15\%CO_2$-laden data, respectively. The inconsequential effect of the tuning parameter, is revealed by the perfect overlap of CanMECH Base and CanMECH 1.0 results of Figure 12 and Figure 13. This suggests that in-line with the sensitivity analysis results, the displacement of nearly half of the Ar (from 94% down to 49%) by the 23 times more effective third body collider H_2O dwarfs its contribution as a collider in reaction 9's net rate. As such tuning Ar's low-pressure-limit rate is inconsequential to the $45\%H_2O$- and $30\%H_2O/15\%CO_2$-laden mixtures. Examination of the RMSREs of the $45\%CO_2$ experimental IDTs of this work also indicates that the maximum implemented parameter tuning does produce the lowest RMSRE and further improves the fit, relative to both CanMECH Base and Keromnes et al. [28]. While CanMECH Base was not as good as the incumbent in representing these IDT data, after implementing the tuning, CanMECH 1.0 now performs equally well relative to the incumbent, signified by the RPRMSRE value of 0. Overall, adoption of CanMECH 1.0 brings about a 33% improvement relative to the incumbent when it comes to representing the high-pressure novel IDT experimental data of this work.

Examination of the RMSREs of dataset 3 shows that while the tuning parameter improves the fit of H_2O-laden and 20%CO_2-laden data, it adversely impacts the fit of Ar-diluted and 10%CO_2 diluted experiments. This is expected as the rate adopted for R9's Ar-specific low-pressure-limit, is from Shao et al.'s study [83], which is also the source of validation dataset 3. Shao et al. [83] optimized this rate parameter to obtain the best fit for their Ar-diluted experimental data. As such any tuning of this rate is expected to result in an increased RMSRE for Shao et al.'s data [83]. Examination of the RPRMSREs, however, indicate that CanMECH 1.0 outperforms Keromnes et al. in predicting all but one of Shao et al.'s validation data set [83]. This dataset is for a mixture of 3%H_2/1.5%O_2/10%CO_2/Ar, contains only two IDT measurements, and while RPRMSRE suggests a 96% improvement, CanMECH 1.0's predictions are still within the unusually large error bounds of experimental data, see Figure A9 in the appendices. Hence, the seemingly high RPRMSRE is not of concern for these uncertain data which has large reported uncertainties of ± 39% and ±42% [83]. The overall RPRMSRE suggests that an overall 37% improved RMSRE is expected with CanMECH 1.0 relative to Keromnes et al. [28], in predicting Shao et al.'s [83] complete IDT validation dataset.

Results of the parametric study for Pang et al.'s data [52] illustrate that RMSREs reduce with smaller rate multiplier values. The minimum RMSRE is achieved with the minimum rate multiplier value of 0.88. Figure 15 shows that, while Keromnes et al.'s mechanism [28] performs better for the lower temperature data, due to the scatter of experimental data both models capture many of the data points within their uncertainty bars. The improved performance of Keromnes et al.'s model is again attributed to their 13% lower pre-exponential factor of Ar's low-pressure-limit rate relative to the already reduced rate of CanMECH 1.0. Moreover, reproducibility of the low-temperature IDT experimental results, such as that of Pang et al [52], as noted by the Ninnemann et al. [53] is highly sensitive to accurate measurements of the dP/dt effect, which is not commonly available. The incumbent model has a better performance signified by an RPRMSRE of 40%, however, the implemented parameter tuning has significantly improved the performance of CanMECH 1.0 relative to CanMECH Base.

Comparison of the RMSREs of the N_2-diluted IDTs of validation dataset 5 in Table 10, shows that the tuning parameter is inconsequential as the reactive mixture does not contain any Argon. The

RPRMSRE value of -15% indicates that CanMECH 1.0 brings about significant improvement relative to the incumbent model.

Table 10 illustrates that for the hydrogen rich mixture of validation dataset 6 diluted in Ar, the tuning parameter improves the model fit at all three discrete pressures of 1, 4 and 16 bar. Moreover, the combined RPRMSREs indicate that CanMECH 1.0 brings about a 5% improved RMSREs relative to Keromnes et al. mechanism [28].

The RMSRE results of validation dataset 7 in Table 10 indicates that the tuning parameter brings about small improvements in the overall fit of the validation data relative to CanMECH Base mechanism. CanMECH 1.0 outperforms the incumbent, signified by the negative RPRMSRE, suggesting a 3% reduced RMSREs relative to Keromnes et al.'s mechanism [28].

Finally examination of the parametric study results for dataset 8 from Table 10, indicates that while parameter tuning has slightly increased the RMSRE for the 1 bar 2.96%H_2/2.96%CO/2.96%O_2/Ar IDT data, it has improved both the 4 and 16 bar data. Keromnes et al. [28] outperforms CanMECH 1.0 for the 1 bar and to a lesser extent 16 bar data. CanMECH 1.0 brings about an 11% improvement in RMSREs for the 4 bar data. Overall, for dataset 8 the RPRMSRE suggests that the incumbent model has a 5% lower RMSRE than CanMECH 1.0.

In conclusion:

1- Out of the twenty five subsets of validation data examined, CanMECH 1.0 outperformed Keromnes et al.'s mechanism [28] for 16 subsets, and had an identical performance for another two;
2- Considering all model validation datasets, CanMECH 1.0 has brought about a 26% improvement in RMSRE relative to Keromnes et al.'s mechanism [28]; and
3- Of particular importance, CanMECH 1.0 significantly outperforms Keromnes et al.'s mechanism [28] in predicting shock tube IDT for H_2O- and CO_2- laden reactive mixtures, as well as all IDT data at pressures of 17-43.8 bar.

This concludes the model validation work culminating in the development of the improved mechanism CanMECH 1.0. This validated kinetics model is used to delineate the impact of bath gas composition and pressure in the next section. Moreover, it is also utilized to generate extrapolated IDT predictions and sensitivities at conditions of potential interest to highly pressurized oxy-fuel combustion applications.

Chapter 6 Effects of Pressure and Presence of H_2O and CO_2 Bath Gases on Hydrogen Combustion Chemistry

6.1 Introduction

To understand the effects of pressure and high H_2O and CO_2 concentrations on combustion chemistry a mechanism with minimal tuning parameters and validated for such conditions is needed. CanMECH 1.0 mechanism is uniquely better positioned than other mechanisms, as it exhibits a superior performance in reproducing shock tube IDT validation targets, with only one minimally tuned kinetic parameter. Relative to incumbent models which implement multiple tuning parameters to improve the local fit of validation targets, CanMECH 1.0 relies on unperturbed reaction rate parameters from theoretical or experimental elementary rate determination studies. Moreover, it has been validated at pressures of 2 to 40 bar in bath gases including 0-45% CO_2/Ar, 0-45%H_2O/Ar, Ar, N_2, Ar/N_2, for H_2 and H_2/CO reactive mixtures at different equivalence ratios.

Figure 26 depicts a temperature sweep of ignition delay times at 40 bar, for the four different bath gases explored in this work. Examination of each curve, shows that the variation of ignition delay time with temperature exhibits an S-shaped curve with near Arrhenius behavior (linear log (IDT) vs. 1/T) at the high- and low-temperature ends. Tracing each curve from high to low temperatures, reveals that all three curves exhibit an increase of the global activation energy, followed by a decrease at the low temperature end. Such variations in slope are attributed to potential changes in the chemistry involved. Comparison of the curves with each other shows that bath gas composition also has a significant impact on the modelled IDTs. These observations also corroborate with those made from the examination of temperature-dependent IDT sensitivity charts, i.e. Figure 19, Figure 21, Figure 23, and Figure 25. These figures, as well as Figure 26 show that the transition to a higher temperature regime occurs at temperatures above 1350 K, 1550 K, and 1650 K and 1700 K for the 94%Ar, 45%CO_2/49%Ar, 30%H_2O/15%CO_2/49%Ar, and 45%H_2O/49%Ar bath gases, respectively. Moreover, Figure 26 shows that presence of H_2O causes the largest shift of low-temperature chemistry's dominance from low to high temperatures. A similar trend is also observed for CO_2-diluted IDTs, but to a lesser extent. It is also apparent that the effect of 30%H_2O/15%CO_2 dilution is similar to that of 45%H_2O dilution. Figure 26 also suggests, that at higher temperatures, IDTs increase with increased H_2O and CO_2 dilutions. However, at lower temperatures larger H_2O concentrations decrease IDTs, whereas higher CO_2

concentrations increase them. The presence of 30-45%H_2O reduces ignition delay times relative to 45%CO_2 mixtures at temperatures below 1250 K. Also at temperatures below 1000 K, the presence of 45%H_2O/49%Ar results in lower ignition delay times relative to mixtures with 94%Ar dilution. This suggests that the effect of bath gases on the chemistry involved is complex, and requires further exploration. At 40 bar, experimental and modeling results suggest that the presence of H_2O and/or CO_2 also extends the temperature span over which the chemistry transitions from a low-temperature to a high-temperature chemistry, see Figure 26. Pressure-dependent IDT sensitivity bar charts of section 5.5 (Figure 16, Figure 18, Figure 20, Figure 22, Figure 24), also suggest that increases in pressure brings about significant additional changes in dominant chemical pathways. It is important to recall from section 5.5, that high-pressure and intermediate- to low-temperature chemistries are signified by the dominance of rate limiting reactions involving HO_2 and H_2O_2, in contrast with high-temperature low-pressure chemistries where R1: $H+O_2=OH+O$ dominates the reactivity as the main chain branching reaction.

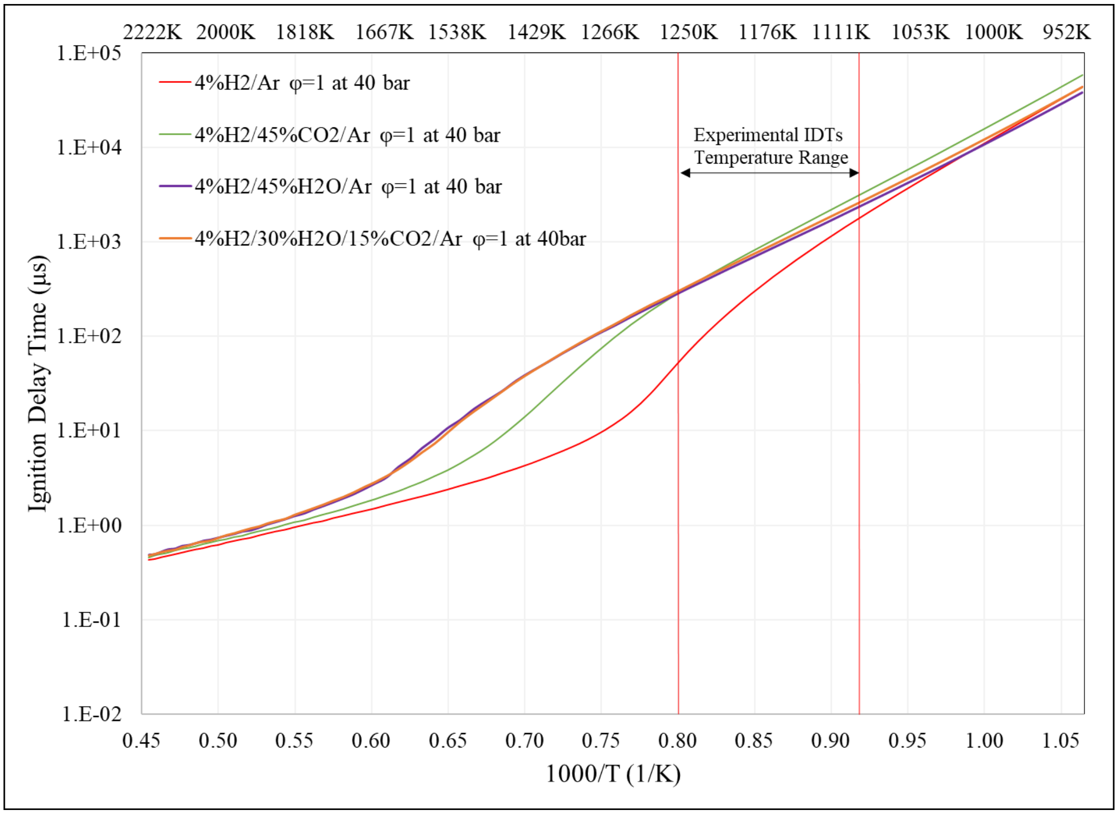

Figure 26: IDT variation with temperature & bath gas composition for 4%H_2 φ=1 at 40 bar

In order to segregate and understand the effect of bath gas compositions, pressure and combinations thereof, a systematic approach is followed in this section. A subsection has been dedicated to each bath gas effect, starting with the most common and well understood bath gas Ar, followed by CO_2 and finally H_2O. For each bath gas the approach detailed below is followed:

1- IDT temperature sweeps spanning 950-2200 K are analyzed at 2, 40 and 150 bar;
2- IDT sensitivities as a function of pressure are reviewed to:
    a. identify which rate parameters the IDTs are most sensitive to; and,
    b. detect changes in chemistry, indicated by variations in IDT sensitivity trends;
3- Rate of production (ROP) analyses are conducted at conditions coincident with validated experimental data, at the higher end of the experimental temperature range, 1200-1250 K. Careful analysis of which enables deciphering the impact of pressure vs. bath gases;
4- IDT senstivities as a function of temperature at pressures of 40 and 150 bar are also reviewed, to show at what temperatures beyond those analyzed here, major changes in reactive pathways should be expected; and,
5- For H_2O- and CO_2-diluted bath gases, IDT temperature sweeps at extrapolated conditions, involving different concentrations of these gases are presented. These sweeps are analyzed to map the concentration-dependent impact of these bath gases on IDT trends.

For all these analyses, CanMECH 1.0 was used, including those explored extrapolated conditions (e.g. 150-300 bar), outside the validation range of available kinetics models, relevant to indirect and direct pressurized oxy-fuel combustion systems.

6.2 Chemistry of Argon-diluted combustion at different pressures

As many kinetic studies involve Ar, as an inert bath gas, to understand the effect of pressure it is prudent to start with the simpler $4\%H_2/2\%O_2/Ar$ mixture. Figure 27 depicts IDT temperature sweeps for a $4\%H_2/2\%O_2/Ar$ mixture at 2, 40 and 150 bar. The figure illustrates the combined effect of pressure and temperature on IDTs. Examination of each of the three S-shaped curves, pertaining to 2, 40, and 150 bar, suggests that potential changes are taking place in the chemistry as a function of temperature. At the higher temperature end, chemistry transitions take place near 1650 K, 1450 K and 1000 K for the 150, 40 and 2 bar conditions. It can also be observed that with increased pressure, the relative shift in IDT trends across this transition becomes less, and the transition takes place less abruptly. Simulated IDTs have an inverse relationship with pressure at temperatures above 1500 K and below 900 K.

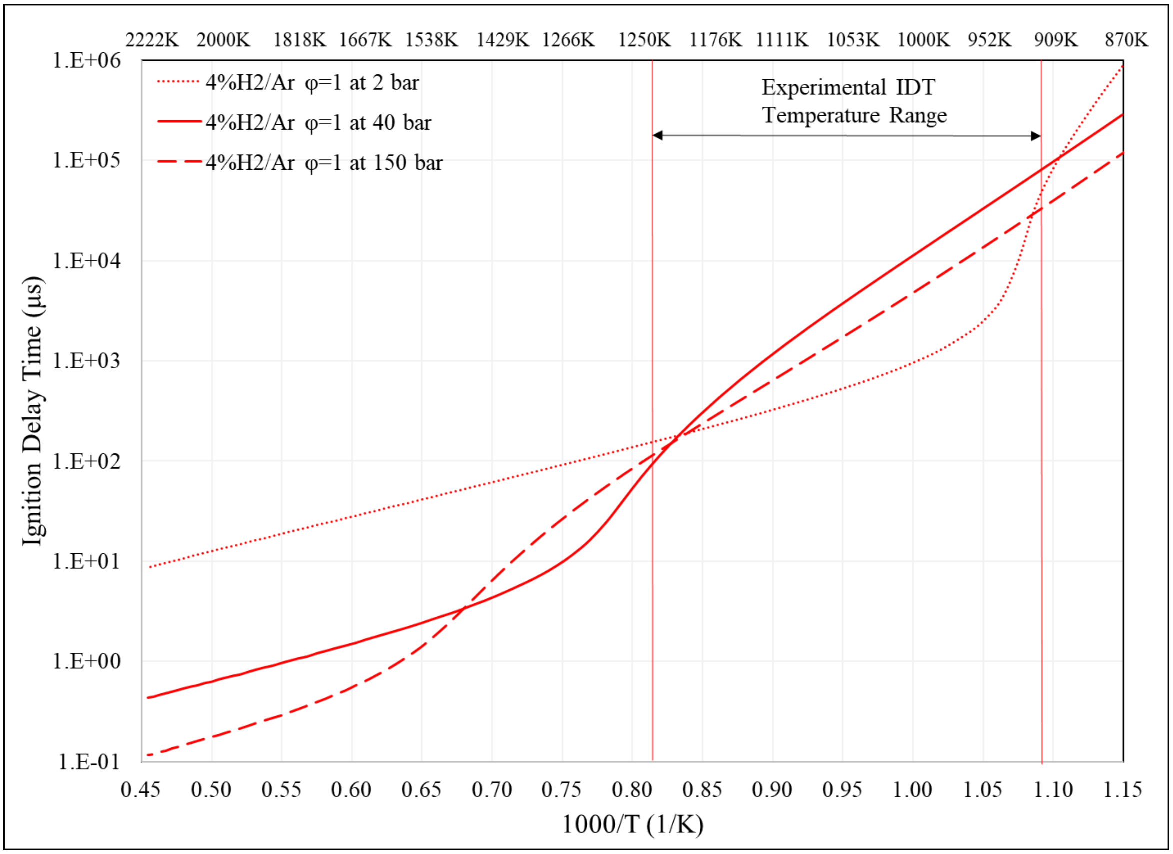

Figure 27: IDT variation with temperature & pressure for 4%H_2/Ar φ=1 at 2, 40, and 150 bar

To better understand the effect of pressure it is useful to explore the source of differences in the chemistries at 1000 K, and 1209 K. This is because at 1000 K at 40 and 150 bar, the chemistry has already transitioned from high-temperature to a low-temperature chemistry, wheras at 2 bar, it is on the cusp of transitioning. Moreover, at 1209 K the IDTs of the three different pressures cross each other simultaneously, and while at 2 bar the chemistry appears to be similar to high temperatures, at 40 bar it is in the middle of a transition, and at 150 bar the chemistry has likely transitioned to lower temperature and high pressure regime.

Figure 28 depicts the effect of pressure on IDT-sensitivities to important reaction rate parameters (with max $|\sigma|\geq 0.1$), for 4%H_2/Ar at 1000 K. The three target pressures of 2, 40 and 150 bar, have been marked by the vertical red lines. Figure 28 shows that at 1000K:

a. At 2 bar, IDTs are most senstive to R9: $H+O_2(+M)=HO_2(+M)$, and R1: $H+O_2=O+OH$, followed to lesser extent by R2: $O+H_2=H+OH$ and R11: $HO_2+H=2OH$;

b. At 40 bar, IDTs are most sensitive to R17: $H_2+HO_2=H+H_2O_2$, followed by R15: $H_2O_2(+M)=OH+OH(+M)$, R1, R9 and to lesser extents to R14: $HO_2+HO_2=O_2+H_2O_2$, and R11; and,
c. At 150 bar, similar to 40 bar R17 and R15 dominate sensitivities, but R14 sensitivity becomes the third largest. R1 and R9 have lower IDT senstivities, and R11's sensitivity is nearly negligible.

Figure 29 illustrates IDT sensitivity coefficients as a function of pressure for 4%H_2/Ar φ=1 at 1209 K. This figure shows that at 1209 K:

a. At 2 bar, IDTs are sensitive to R1, R2, R9, R3: $OH+H_2=H+H_2O$ and R10: $H_2+O_2=H+HO_2$ rates, the chemistry is not undergoing transition and is well into the high-temperature low-pressure regime;
b. At 40 bar, IDTs are close to the peak of transitioning regime, and are sensitive to R1, R9, R17, R11, R10, R15, and to lesser extents R2 and R3; and,
c. At 150 bar, R17, R1, R9, R15, R11, R10, R3 and to a lesser extent R2, are the critical rate parameters impacting IDTs.

Comparison of sensitivities of Figure 28 (1000 K) with Figure 29 (1209 K) reveals that, an increase in temperature:

a. At 2 bar, renders IDTs less sensitive to R9, but more senstivie to R2. Sensitivities of IDTs to R1 and R11 are also reduced, whereas, they become more sensitive to R3 and R10. The sensitivities suggest that, the chemistry is well into the high-temperature chemistry regime at 1209 K, as such, it is dominated by the chain branching reactions R1-R3. At 1000 K, the chemistry is in a transitional state, signified by larger IDT sensitivities to R9 and R11, which impact the HO_2 radical pool;
b. At 40 bar, makes IDTs most sensitive to R1 and R9, instead of R17. Also IDTs are more sensitive to R11: $HO_2+H=OH+OH$, instead of R15: $H_2O_2(+M)=OH+OH(+M)$, which alter OH producing paths. Finally IDTs appear to be less sensitive to R14: $HO_2+HO_2=O_2+H_2O_2$, but more sensitive to R10: $H_2+O_2=H+HO_2$. These suggest that H_2O_2 chemistry is likely more rate controlling at lower temperatures; and,
c. At 150 bar, causes IDTs to be less sensitive to R15, and more sensitive to R1, R9, R10, and R3. Also, the sensitivity to R14 falls below the threshold of $\max|\sigma|\geq 0.1$. These show that IDTs

are likely becoming more dependent on HO_2 chemistry rather than H_2O_2 chemistry with increase in temperature.

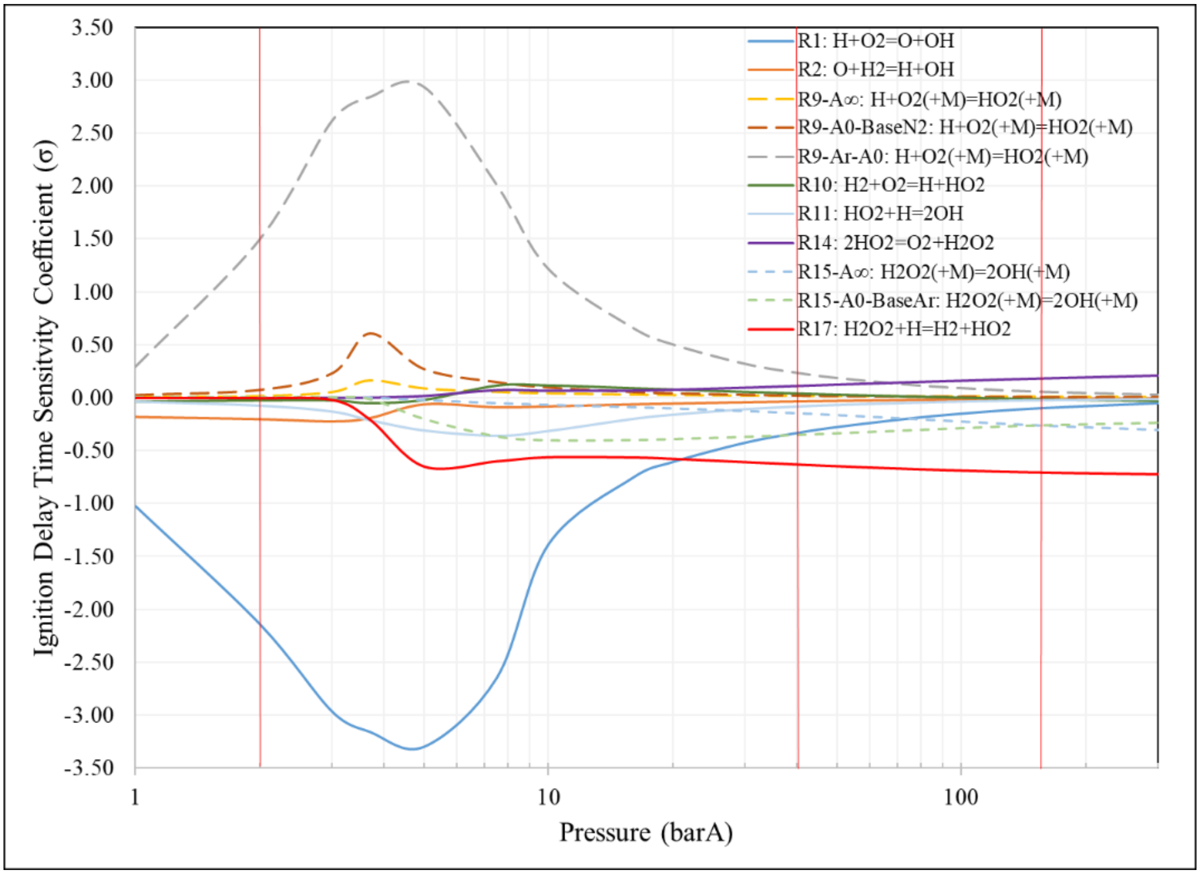

Figure 28: IDT-sensitive (max |σ|≥0.1) reaction rate parameters sensitivity coefficients vs. pressure for 4%H_2/Ar φ=1 at 1000 K for pressures of 1-300 bar

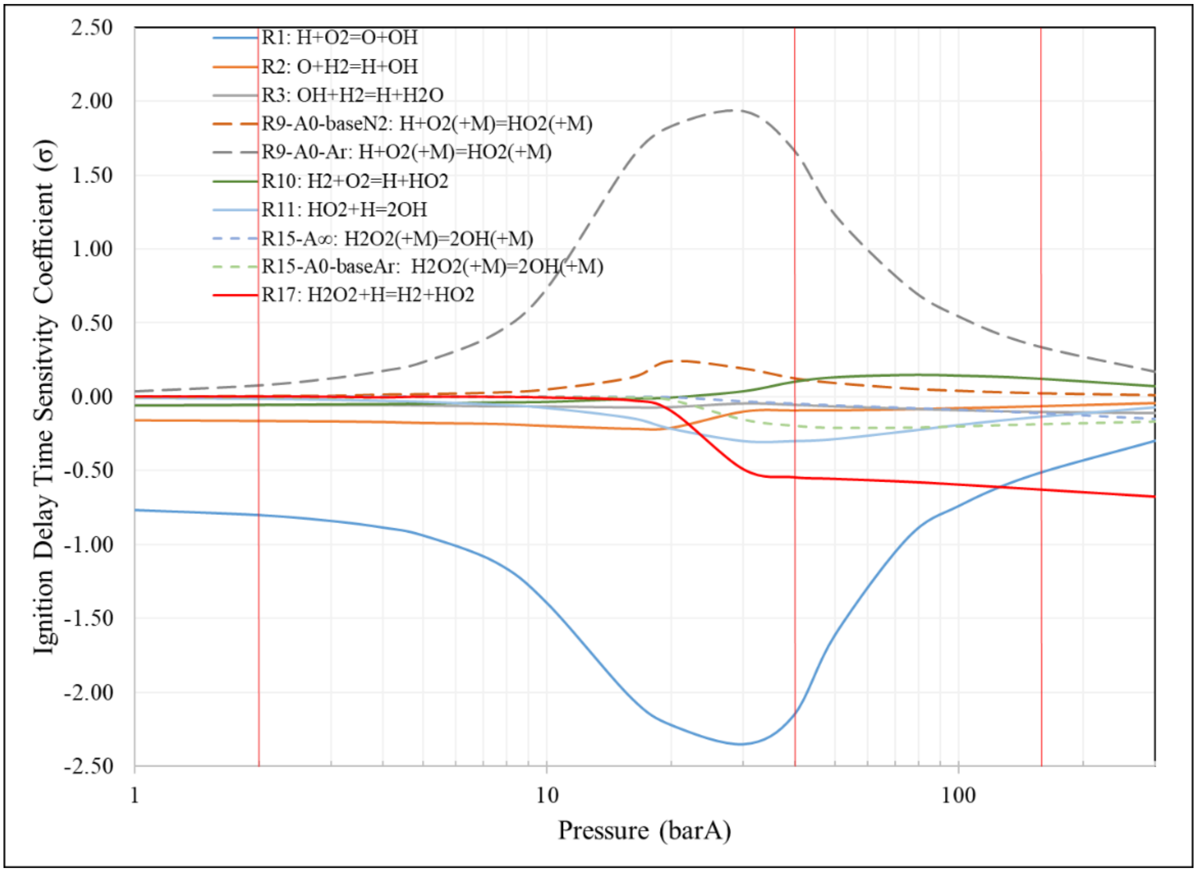

Figure 29: IDT-sensitive (max |σ|≥0.1) reaction rate parameters sensitivity coefficients vs. pressure for 4%H_2/Ar φ=1 at 1209 K

To characterize the change in dominant reactive pathways associated with increase in pressure, detailed rate of production (ROP) analyses were conducted for two of the experimental tests of this work, tests #10 and #25, performed at 2 and 40 bar. An additional ROP was also performed at an extrapolated pressure of 150 bar for test #25.

Test #10 involves 4%H_2/Ar φ=1 tested at 1237 K and 2.13 bar. This test is a representative example of high-temperature low-pressure H_2 combustion chemistry. This is because, Figure 27 and Figure 29 illustrated that, at 1209 K and 2 bar, the chemistry is already in the high-temperature regime, hence at the higher temperature condition of test #10 (1237 K) it will be in the same regime, as well.

Test #25 was at a similar temperature, 1209 K, with the same mixture composition, but was conducted at 39.6 bar.

The third ROP analysis is conducted for the same gas composition and temperature (1209 K) but at 150 bar.

It should be noted that the three ROPs are representative of the following three different IDT regimes, namely:

1- A high-temperature low-pressure regime at 2 bar;
2- An intermediate-temperature and -pressure regime at 40 bar; and,
3- A low-temperature and high-pressure regime at 150 bar.

In order to appropriately interpret the reactive pathways vis-à-vis the experimental modeled IDTs it is important to emphasize the following:

1- OH* emission is measured to define experimental ignition time, but OH* does not directly impact the kinetics. As such, runaway OH radical mole fraction increase is used as the main indicator for ignition, in the ROP analyses in this chapter;
2- In addition to the OH-based IDT, IDTs from other indicators, specifically OH* and temperature (time of inflection), were also calculated. The ROP data beyond the longest calculated IDT were discarded in the analyses, as they do not impact ignition; and,
3- A bottom up approach is used starting with OH ROP, to determine the dominant reactive pathway(s) by tracing the source(s) of OH. If the major OH production path(s) involves other radical and/or intermediate species (H, O, HO_2, H_2O_2, HCO, CO), their ROPs are subsequently analyzed. This process is repeated until the source of all involved radical(s) and/or reaction intermediate(s) with signficant contribution are mapped.

The above outlined approach is followed in all ROP analyses of this chapter for all bath gases. In-line with the approach, for the first ROP analysis, conducted for test #10, in the low-pressure high-temperaure regime, at 2 bar and 1237 K, its modeled IDT estimates are first examined. For this test the calculated OH*-based, OH-based, and time of inflection of temperature IDTs are 137, 131 and 155 μs, respectively. Hence the data beyond 155 μs is ignored.

Figure 30 illustrates the modeled evolution of critical reaction intermediates, superimposed with normalized temperature, pressure, and OH* mole fraction. These parameters were normalized by dividing all simulated values of each parameter by its maximum value. Figure 30 shows that, the chemistry involves large H, O and OH radical pool buildup. HO_2 and H_2O_2 do not appear to be present at any signficant concentration at any point prior to ignition.

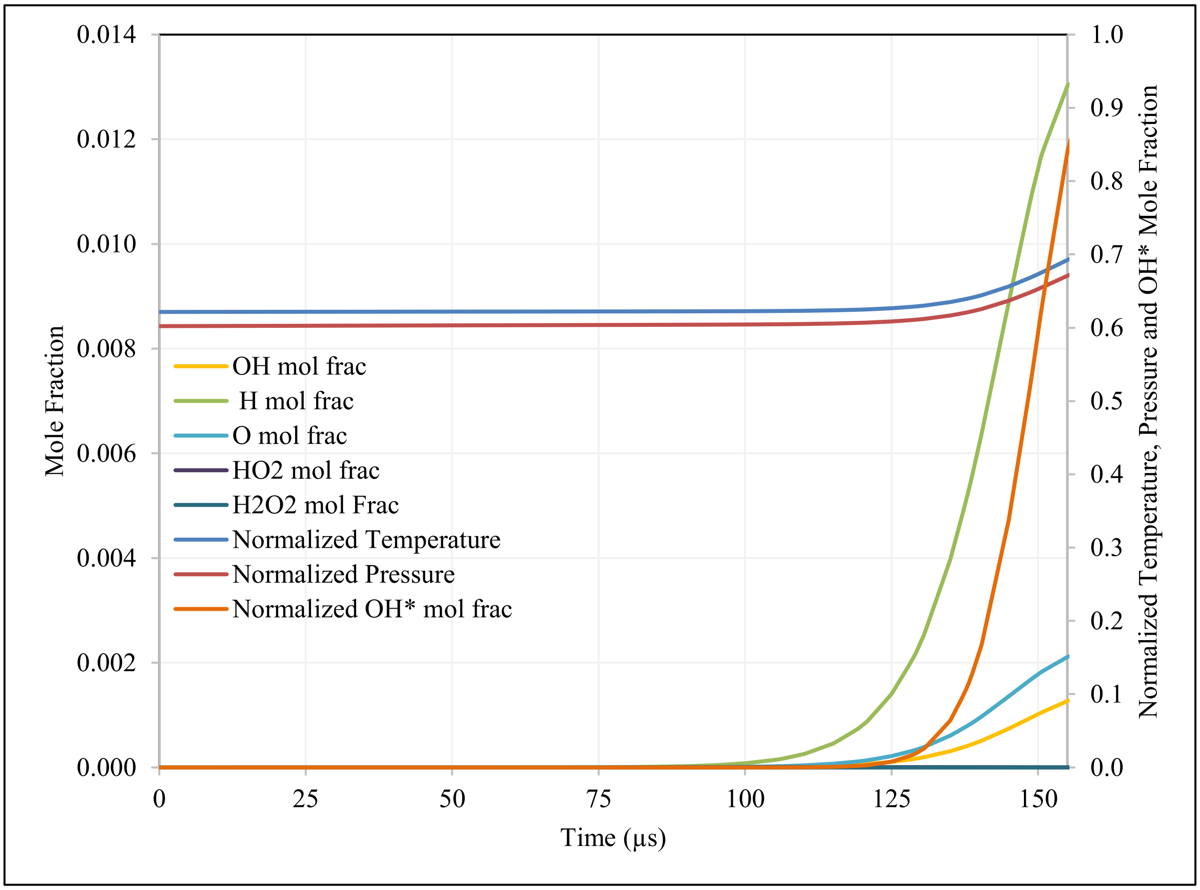

Figure 30: Mole fraction traces of radicals and reaction intermediates, superimposed with normalized temperature, pressure and OH* mole fraction for Test #10 – 4%H_2/Ar φ=1 at 1237 K and 2.13 bar

ROP analysis of 4%H_2/Ar φ=1 at 2 bar in Ar bath:

To demonstrate the procedure followed to graphically analyze and determine dominant reaction pathways, the ROP plots examined for Test #10, are provided in this section as an example case. It should be noted for all other reaction pathways analyses of this chapter, the associated ROP plots are provided in Appendix C, instead. Figure 31 depicts the results of an ROP analysis for OH radical production for Test #10. In this figure reactions with positive ROPs lead to production of OH radicals whereas, the ones with negative ROPs consume them. As the absolute values of ROPs of reactions are very small at the early stages of the ignition delay period, it is also important to normalize individual reactions' ROPs by the sum of all positive ROPs through reactions that produce the target species. Equation 6.1, depicts the normalized rate of production formulation utilized to generate the normalized ROP plots of this chapter.

$$C_{ji}^{p} = \frac{\nu_{j,i} \cdot q_i}{\sum_{i=1}^{m} \max\left(\nu_{j,i}, 0\right) q_i} \tag{6.1}$$

where:

- C_{ji}^{p} is the rate of production of species j through reaction i
- $\nu_{j,i}$ is the stoichiometric coefficient of species j in reaction i
- q_i, is the rate of reaction i (mol/cm^3-s)

This approach is followed for all ROP analyses in this chapter. The combination of the absolute and normalized ROPs enable understanding both the absolute and relative contributions of reactions to the radical pool build up leading to the ignition event. To this end, Figure 32, provides the associated normalized OH-ROP for test #10.

Figure 31, and Figure 32, show that R1: $H+O_2=O+OH$, R2: $O+H_2=H+OH$ and to a much lesser extent R11: $HO_2+H=OH+OH$ are the main OH producing reactions, and R3: $OH+H_2=H+H_2O$ is its main consumer. This dominance starts from the intial stages and persists until ignition. As R11's relative contribution to building the OH radical pool is smaller than 10% this path is not further investigated. It should also be noted that in Figure 32 as reaction paths involving R2 and R1 both produce OH and are known to commonly participate in the same reaction pathway together, a normalized sum of their ROPs are also included in the normalized OH ROP graphs of this chapter. This enables identifying the time at which the pathway involving R1+R2 becomes dominant relative to others, when other competing reaction(s) are present.

The rate of OH production through R1 and R2 is contingent on the presence of H and O radicals, as such, it is important to determine the main reactions that generate these radicals.

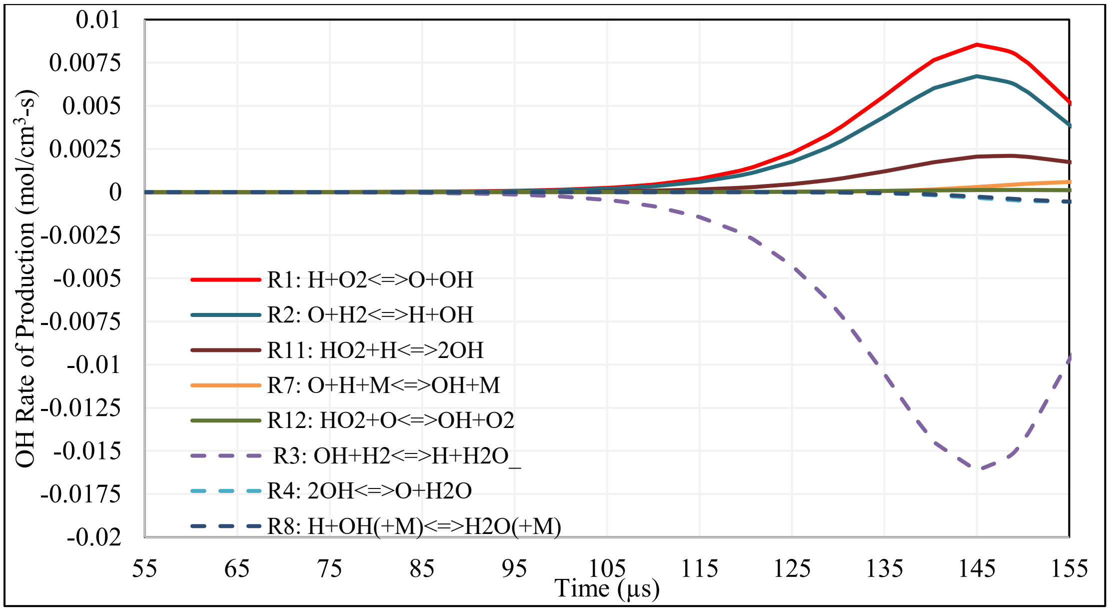

Figure 31: OH rate of production (ROP) analysis for Test #10 – 4%H_2/Ar φ=1 at 1237 K and 2.13 bar

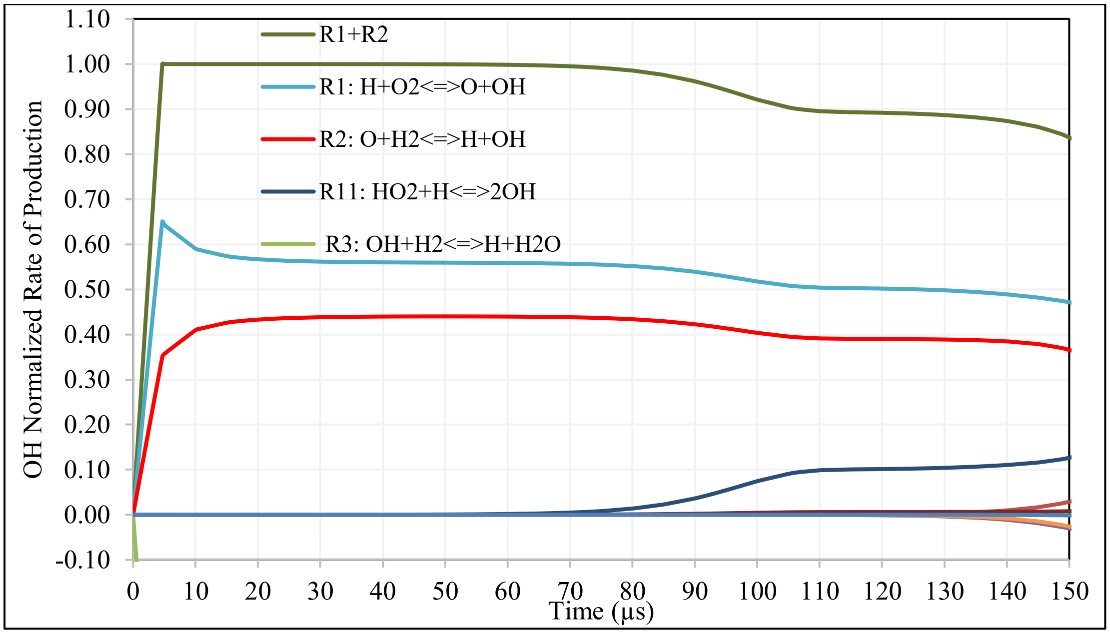

Figure 32: Nomralized OH rate of production (ROP) analysis for Test #10 – 4%H_2/Ar φ=1 at 1237 K and 2.13 bar

Figure 33 and Figure 34 provide the absolute and normalized H radical ROP analyses results. These figures illustrate that the H radical is mainly produced through reaction R3: $OH+H_2=H+H_2O$, followed by R2: $O+H_2=H+OH$ throughout the IDT period. However, in order for R2 to proceed, O radical generation must have preceded this process.

Figure 35 and Figure 36 provide the absolute and normalized O ROP. They illustrate that the ROP of O radical is dominated by R1: $H+O_2=O+OH$.

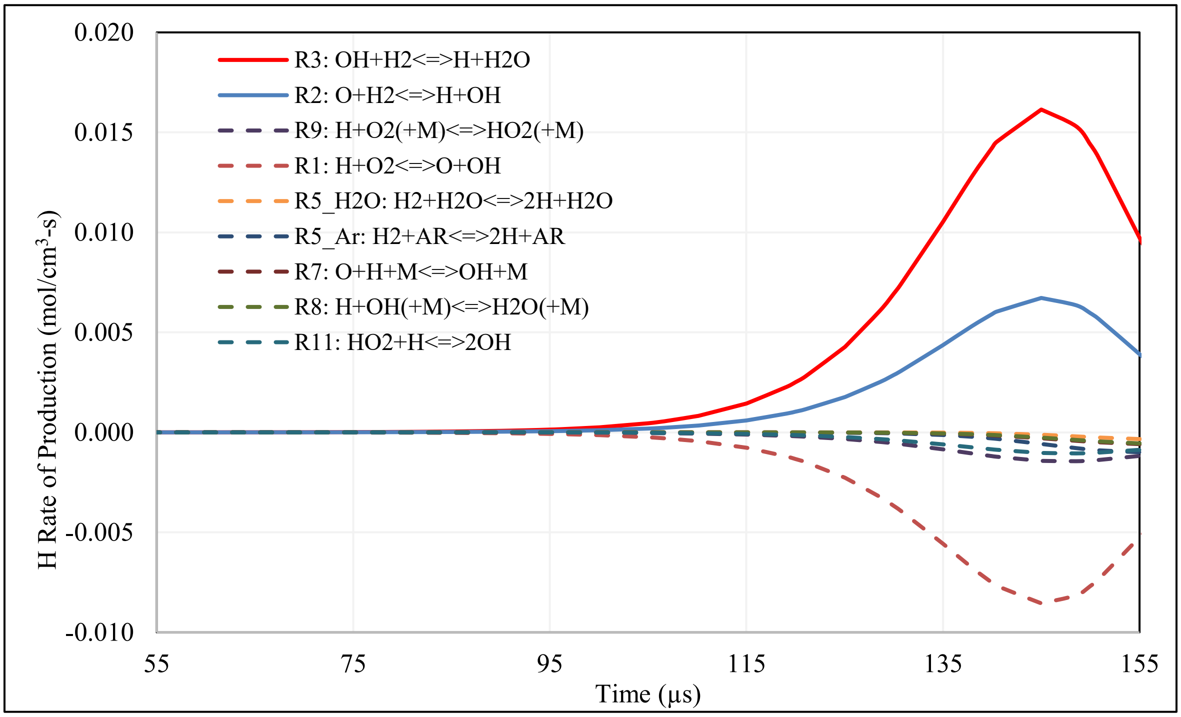

Figure 33: H rate of production analysis for Test #10 – 4%H_2/Ar φ=1 at 1237 K and 2.13 bar

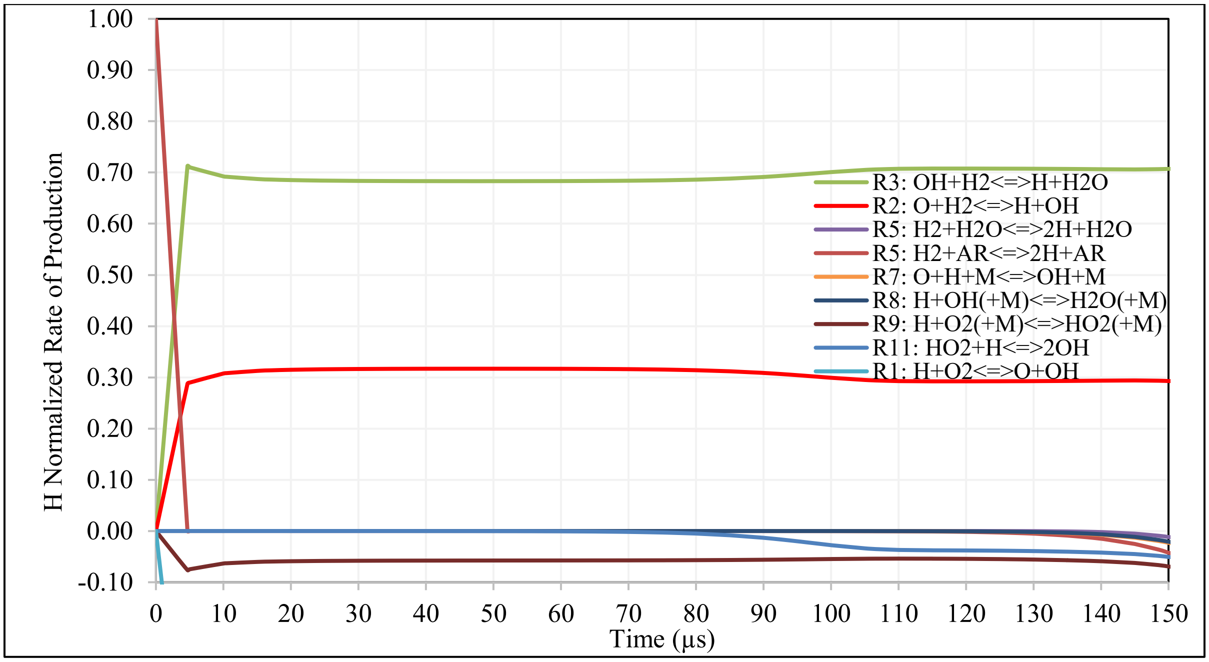

Figure 34: Normalized H rate of production analysis for Test #10 – 4%H_2/Ar φ=1 at 1237 K and 2.13 bar

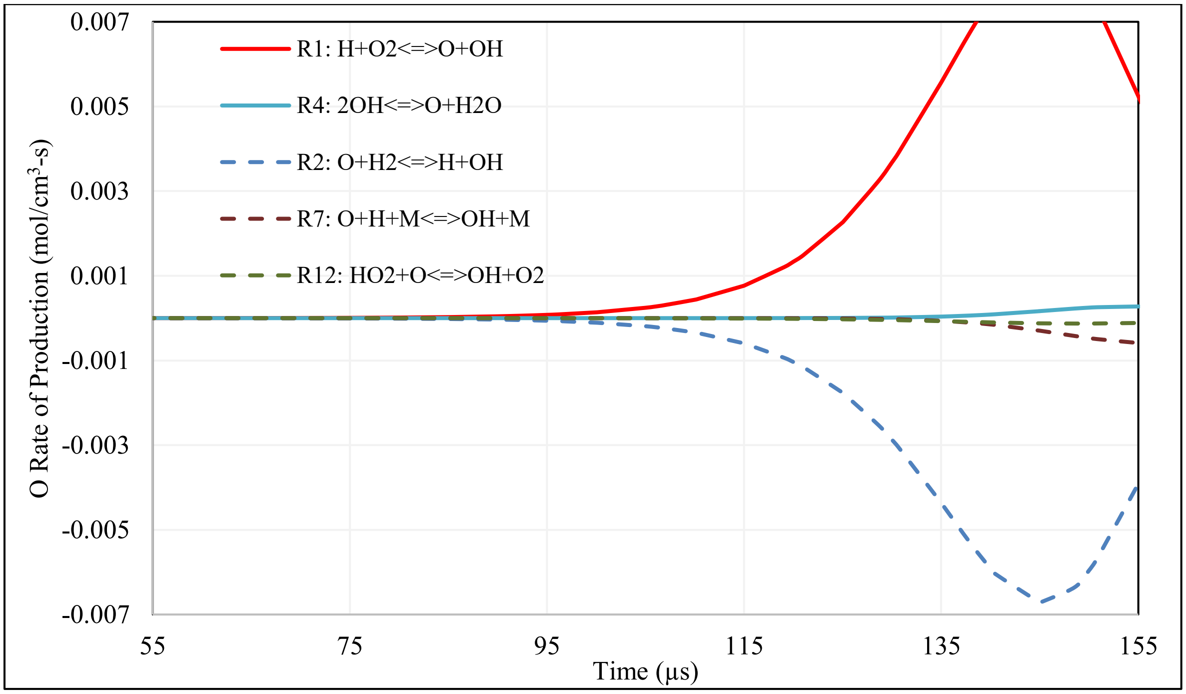

Figure 35: O rate of production analysis for Test #10 – 4%H_2/Ar φ=1 at 1237 K and 2.13 bar

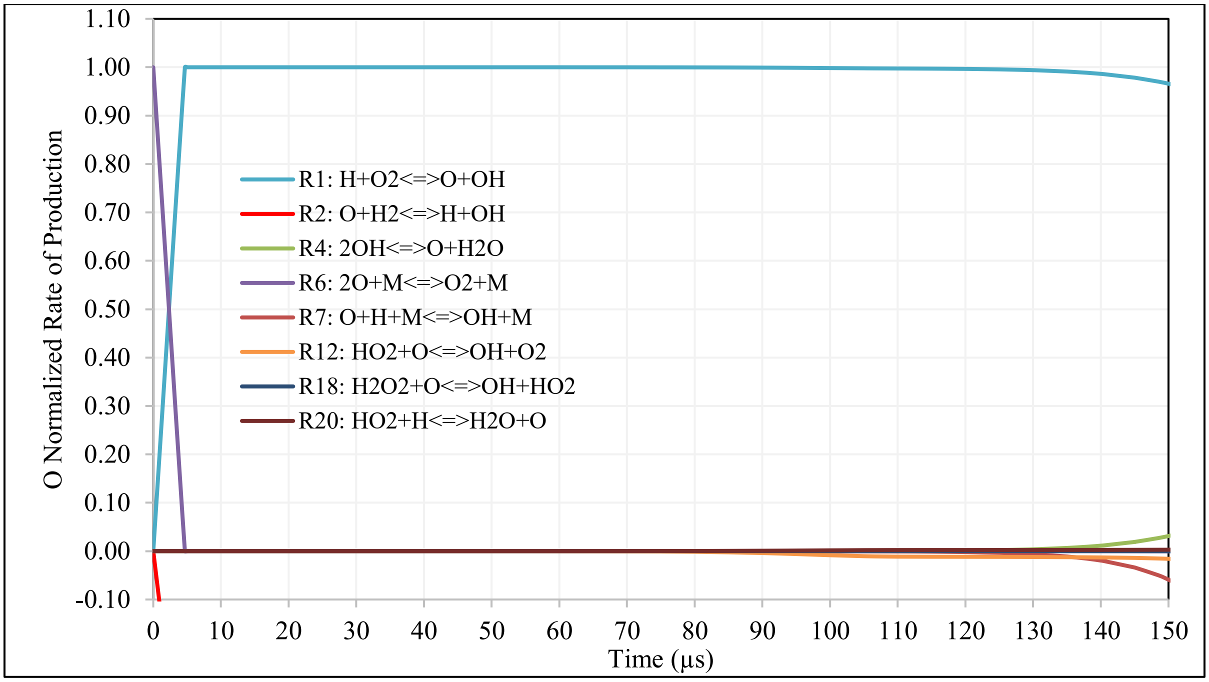

Figure 36: Normalized O rate of production analysis for Test #10 – 4%H_2/Ar φ=1 at 1237 K and 2.13 bar

From these figures (Figure 31 to Figure 36) it is concluded that, at 2 bar and 1237 K, representing the high-temperature low-pressure chemistry, the dominant reaction pathway following chain initiation, involves:

R1: $H+O_2=O+OH$

R2: $O+H_2=H+OH$

R3: $OH+H_2=H_2O+H$

ROP analysis of 4%H_2/Ar φ=1 at ~40 bar in Ar bath:

With an understanding of the dominat pathway to ignition for the high-temperature and low-pressure (~2 bar) regime, ROP analysis of test #25, at 40 bar, provides insight into the effect of increase of pressure. This increase in pressure was shown to push the chemistry into transitional intermediate-temperature regime at 40 bar (see Figure 27). For test #25, OH*-based and OH-based IDT estimates are both 143 µs, and the time of inflection of temperature points to an IDT of 144 µs. As such, the data beyond 144 µs were discarded for reaction pathway analyses. Figure 37, depicts the profiles of all radicals' mole fractions as well as those of H_2O_2, superimposed with normalized temperature, pressure and OH* mole fraction. Comparison of Figure 37 and Figure 30 (test #10 at ~2 bar) shows that the order of increase of radical concentrations changes from H, O, OH*, and OH (test #10), to HO_2, H_2O_2, H, OH and O. Also the order of largest radical pool buildup changes from H, O, OH to H, OH and O for test #25.

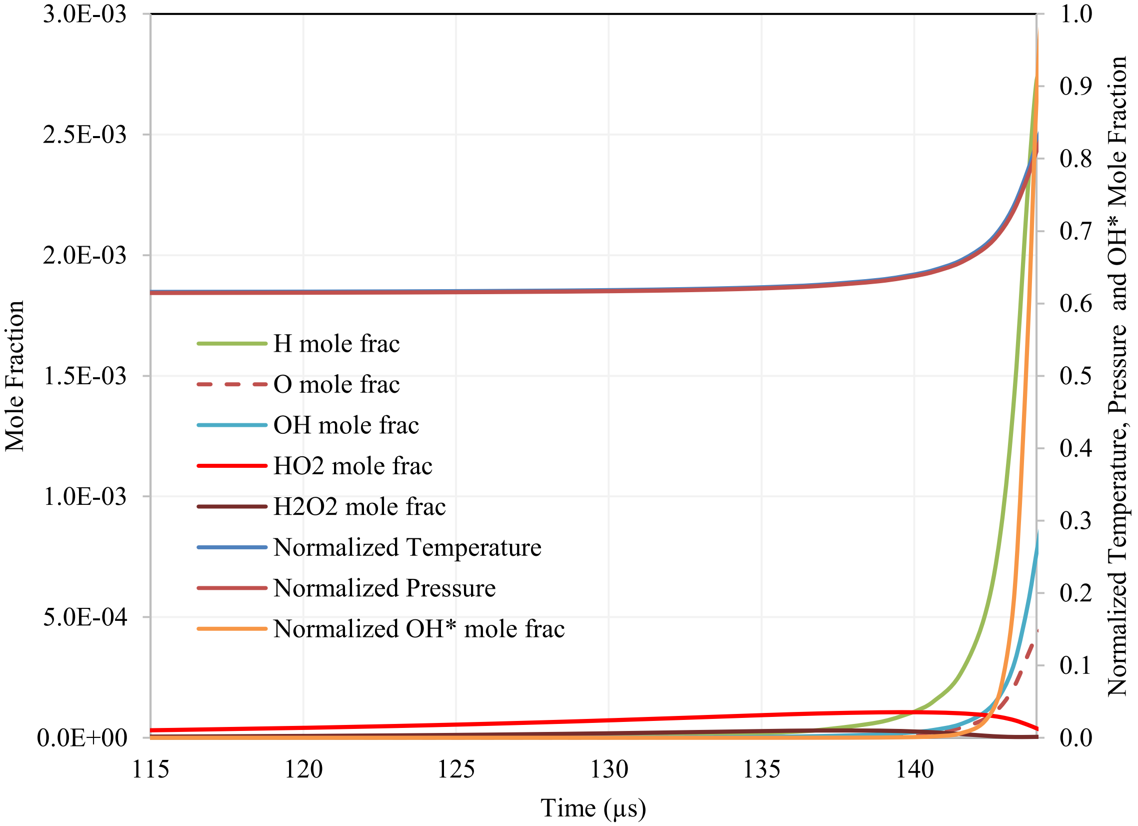

Figure 37: Mole fraction traces of radicals and reaction intermediates, superimposed with normalized temperature, pressure and OH* mole fraction for Test #25 – 4%H_2/Ar φ=1 at 1209 K and 39.6 bar

To understand the underlying reaction pathways involved ROP analyses were performed for OH, H, O and HO_2 radicals for for test #25 (see Figure A10 to Figure A17). From these ROP analyses it is concluded that, in an Ar bath at 40 bar and 1209 K, the dominant OH production pathway:

For the initial 125 µs, is:

R1: $H+O_2=O+OH$

R2: $O+H_2=H+OH$

R3: $OH+H_2=H_2O+H$

For 125 μs - ignition at 144 μs, is:

R3: $OH+H_2=H_2O+H$

R9: $H+O2=HO_2$

R11: $H+HO_2=OH+OH$

ROP analysis of 4%H_2/Ar φ=1 at 150 bar in Ar bath:

Having understood the dominant OH production pathways at 40 bar, in order to characterize the impact of increasing the pressure to even higher pressures, an additional set of ROP analyses are needed. As such, the dominant reactive pathways were examined at 1209 K, at an extrapolated pressure of 150 bar for 4%H_2/Ar φ=1. It should be noted that the IDT regime at this condition has transitioned to a low-temperature high-pressure regime, see IDT temperature sweep graph at 150 bar (Figure 27) and pressure-dependent IDT sensitivity graph at 1209 K (Figure 29). This is a shift from the IDT regime of test #25 above, which was in a transitional intermediate-temperature and -pressure regime (see Figure 27 and Figure 29).

At the extrapolated test condition of 1209 K and 150 bar, the OH*-based, OH-based, temperature inflection-based IDT estimates are 148, 148, and 149 μs. As such, for its reaction pathways analyses, the data beyond 149 μs are dismissed. Figure 38 illustrates the evolution of temperature, pressure, H_2O_2 and all radical species for this extrapolated case. This figure also shows that at 150 bar, HO_2 and H_2O_2 pools build up to much larger concentrations than H, OH, and O, until they are surpassed by H and then OH very close to the ignition event. Comparison of Figure 38, Figure 37 and Figure 30 shows that, in contrast to the 150 bar simulated case, test #25 at 40 bar, and test #10 at 2 bar exhibited significantly larger peak H, O and OH mole fractions relative to those of HO_2 and H_2O_2 during the IDT period.

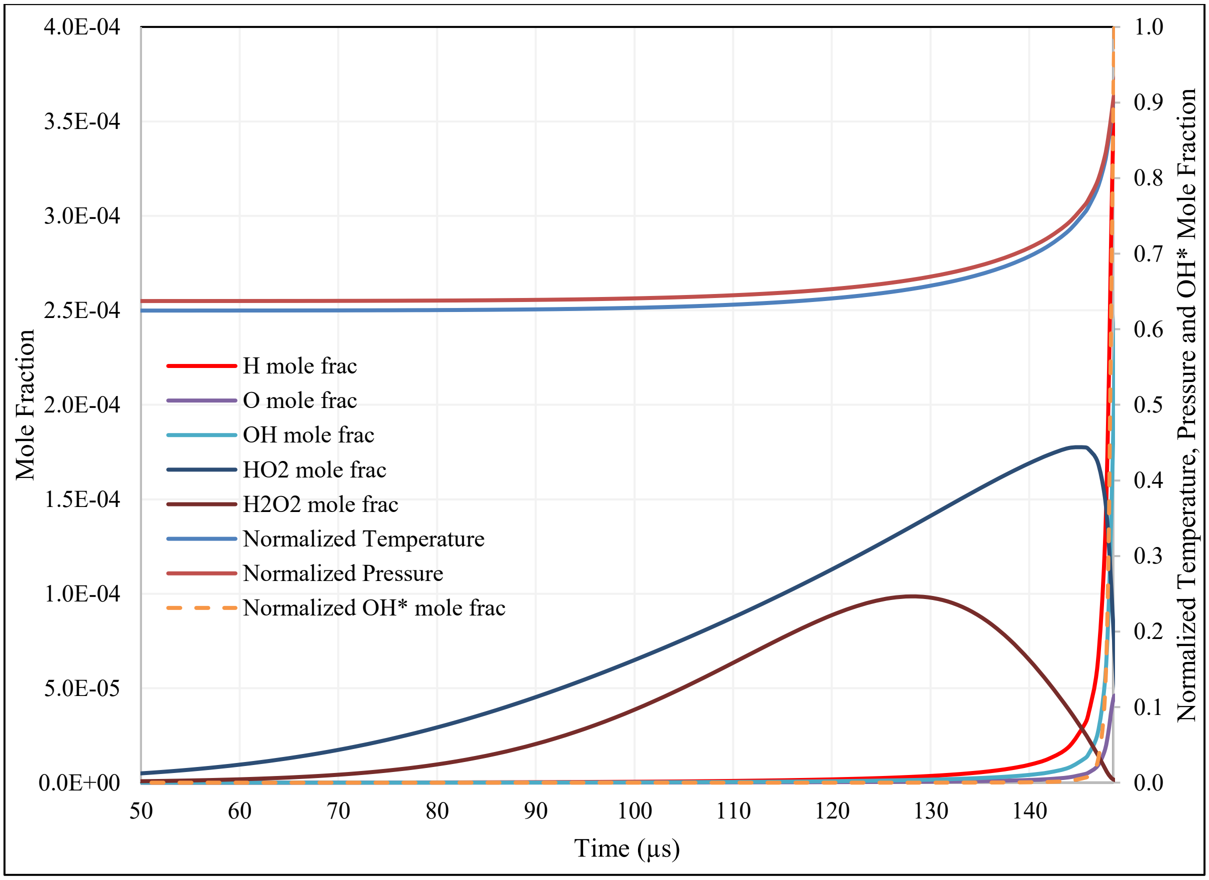

Figure 38: Mole fraction traces of radicals and reaction intermediates, superimposed with normalized temperature, pressure and OH* mole fraction for 4%H_2/Ar φ=1 at 1209 K and 150 bar

To understand the role of these radicals and determine the dominant reaction pathways, detailed ROP analyses were conducted (see Figure A18 to Figure A27 of Appendix C).

ROP analyses show that at 150 bar and 1209 K, for the reactive mixture involving 4%H_2 φ=1, in an Ar bath:

For the intial 0-8 µs, the dominant path to OH production is:

R1: $H+O_2=O+OH$

R2: $O+H_2=H+OH$

R3: $OH+H_2=H_2O+H$

For 8-70 µs, the dominant path to OH production switches to:

R3: $OH+H_2=H_2O+H$

R9: $H+O_2=HO_2$

-R17: $HO_2+H_2=H_2O_2+H$

R15: $H_2O_2(+M)=OH+OH(+M)$

For 70-132 μs the dominant path to OH then becomes:

R3: $OH+H_2=H_2O+H$

R9: $H+O_2=HO_2$

R14: $HO_2+HO_2=H_2O_2+O_2$

R15: $H_2O_2(+M)=OH+OH(+M)$

For 132 μs to ignition at149 μs, the dominant path leading to OH is:

R3: $OH+H_2=H_2O+H$

R9: $H+O2=HO_2$

R11: $H+HO_2=OH+OH$

Table 11 provides a comparative summary of the ROP analyses results in Ar bath gas at pressures of 2, 40 and 150 bar. This table illustrates that with:

a. An increase of pressure from 2 to 40 bar, a new dominant path involving HO_2 chemistry, i.e. R3+R9+R11, presents itself at the later stages of ignition, in addition to R1+R2+R3, which is dominant a the earlier stages of the ignition delay period;

b. An increase of pressure from 40 to 150 bar, two additional dominant pathways appear, involving H_2O_2 chemistry. These pathways are preceeded by R1+R2+R3 for a short period of time, and both rely on R3+R9+R15 for the generation of H, HO_2 and OH radicals. However, for the generation of H_2O_2, the earlier dominant path involving R3+R9+R15 relies on –R17: $HO_2+H_2=H_2O_2+H$, whereas the later one relies on R14: $HO_2+HO_2=O_2+H_2O_2$. Finally, at the later stage of the ignition delay period, close to the ignition event, these paths are surpassed by R3+R9+R11.

Table 11: Comparison of reactive pathways for 4%H_2 φ=1 in Ar bath at pressures of 2, 40 and 150 bar

Ar bath at ~2 bar and 1237 K	Ar bath at ~40 bar and 1209 K	Ar bath at 150 bar and 1209 K
IDT Regime: High T + Low P	IDT Regime: Intermediate T and P (peak of transition)	IDT Regime: Low T + High P (transition to low T chemistry is nearing completion)
Dominant path (0-ignition/155 μs): R1: $H+O_2=O+OH$ R2: $O+H_2=H+OH$ R3: $OH+H_2=H_2O+H$	Dominant path (0-125μs): R1: $H+O_2=O+OH$ R2: $O+H_2=H+OH$ R3: $OH+H_2=H_2O+H$	Dominant path (0-8 μs): R1: $H+O_2=O+OH$ R2: $O+H_2=H+OH$ R3: $OH+H_2=H_2O+H$
	Dominant path (125-ignition/144 μs) R3: $OH+H_2=H_2O+H$ R9: $H+O2=HO_2$ R11: $H+HO_2=OH+OH$	Dominant path (8-70μs): R3: $OH+H_2=H_2O+H$ R9: $H+O_2=HO_2$ -R17: $HO_2+H_2=H_2O_2+H$ R15: $H_2O_2(+M)=OH+OH(+M)$
		Dominant path (70-132 μs): R3+R9+R15 +R14: $HO_2+HO_2=H_2O_2+O_2$
		Dominant path (132 μs – ignition/149 μs): R3: $OH+H_2=H_2O+H$ R9: $H+O_2=HO_2$ R11: $H+HO_2=OH+OH$

Corroboration of the ROP analyses results with the pressure-dependent IDT sensitivities of Figure 29 for 4%H_2/Ar φ=1 at 1209 K, shows that:

a. At 2 bar, representative of high-temperatures low-pressure IDT regime, IDTs are most sensitive to R1, R2, R9, R3 & R10: $H_2+O_2=H+HO_2$ rates. This corroborates well with ROP analyses which suggest a dominant reaction pathway involving R1+R2+R3;

b. At 40 bar, IDTs are close to the peak of the transitional intermediate-temperature and -pressure regime, and are sensitive to R1, R9, R17, R11, R10, R15, and to lesser extent R2 and R3. These corroborate well with the ROP analyses presented, with dominant reaction pathways initially involving R1+R2+R3, followed by R3+R9+R11 at the later stages. Positive IDT senstivities (inhibiting reactivity) to –R10, can be explained as it competes with R11 and R1 for HO_2 and H radicals, to reproduce the reactants for the latter half of ignition delay period, see normalized OH and H ROP analyses of test #25 (Figure A11 and Figure A13). Moreover, ROP analyses clarified that although the IDT sensitivities to R17 rate were significant, at its nominal rate parameter values the dominant pathways do not directly involve this reaction; and,

c. At 150 bar, while the same list of IDT-sensitive rate parameters were present as in the 40 bar case, their order of importance was different at 150 bar, i.e., R17, R1, R9, R15, R11, R10, R3 and to lesser extent R2. This corroborates well with the ROP analysis results which revealed that the path involving R3+(-R17)+R9+R15 is responsible for building the initial radical pool.

To understand the impact of temperature on the chemistry involved at 40 and 150 bar at temperatures beyond those explored experimentally in this work, temperature-dependence of IDT sensitivities were analyzed. Figure 39, summarizes the 12 IDT-sensitive kinetic parameters with max$|\varphi|$ greater than 0.1 for a temperature range of 975-1650 K at 40 bar. Similarly, Figure 40 depicts the results of the same analysis conducted at 150 bar for a temperature range of 975-2025 K.

At 40 bar, the senstivities confirm that the experimental temperature range falls closer to the intermediate- to low-temperature regime where, in addition to R1+R2+R3, generation of HO_2 through R9: $H+O_2(+M)=HO_2(+M)$, and OH through R11: $H+HO_2=OH+OH$ are also competitive. Moreover, at the lower end of the experimental temperature range based on the increased senstivities of R15, H_2O_2 chemistry is expected to dominate. Examining the complete temperature range indicates that R1 and R9's competition peaks at ~1250 K and dominates the chemistry at temperatures larger than 1075 K. Also, R10 switches sensitivity at 1400 K, above which, increasing its rate decreases IDTs. Also while R14 has an IDT increasing effect at temperatures below 1080 K, it switches sign at this temperature and promotes reactivity up to temperatures of 1325 K, after which its IDT sensitivity becomes negligible.

At 150 bar, Figure 40 illustrates that the chemistry involves an almost identical set of IDT-sensitive reactions with similar relative sensitivities with, as in the case of 40 bar. Similarly, R9 and R10 increase IDTs, and R1, R17, R15, R11, R14, R2, and R3 decrease them. However, at 150 bar R13: $HO_2+OH= H_2O+O_2$ also appears to play a non-negligible role in reducing IDTs throughout the temperature range of 975-2025 K, which was not the case at 40 bar. This observation is likely due to the larger HO_2 radical pool buildup at higher pressures and its positive sensitivity coefficient is indicative of its chain terminating effect.

Further comparison of the variation of sensitivity coefficients in Figure 39 and Figure 40 and the temperature spans over which they change, suggest that increasing the pressure shifts and stretches the low and transitional chemistries to higher temperatures. At the low temperature end, similar relative sensitivities are observed at 1050 K and 975 K, for the 40, and 150 bar cases. This suggests a shift of approximately 75 K at low temperatures. At the high temperature end, similar relative sensitivities are observed at 1650 and 2025 K, at 40 and 150 bar. Hence the shift is now stretched by an additional ~325 K with an increase in pressure of 110 bar (from 40 to 150 bar).

This concludes the mapping of the effect of temperature and pressure on the chemistry of Ar-diluted reactive mixtures. The proceeding sections investigate the impact of presence of CO_2, followed by H_2O, in addition to these pressure and temperature effects.

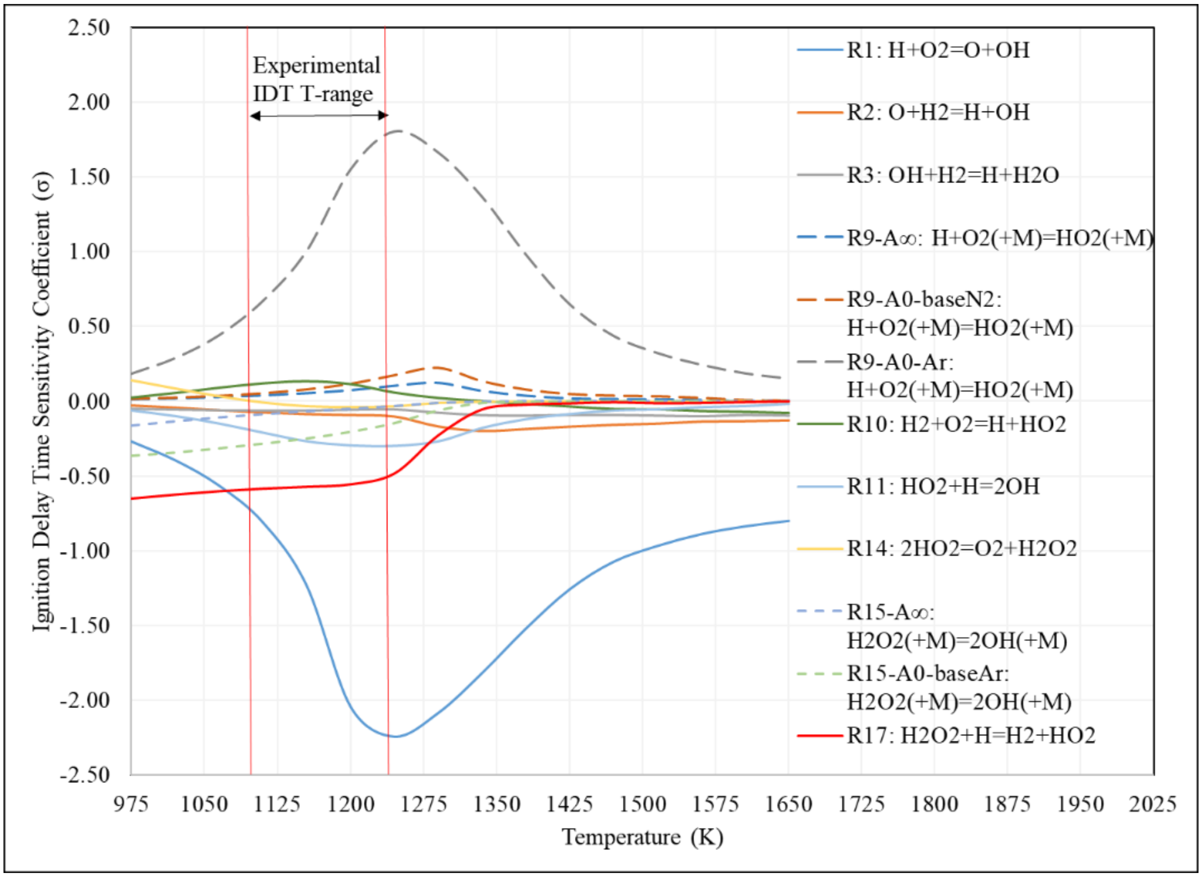

Figure 39: IDT-sensitive (max |σ|≥0.1) reaction rate parameters sensitivity coefficients vs. temperature for 4%H_2/Ar φ=1 at 40 bar

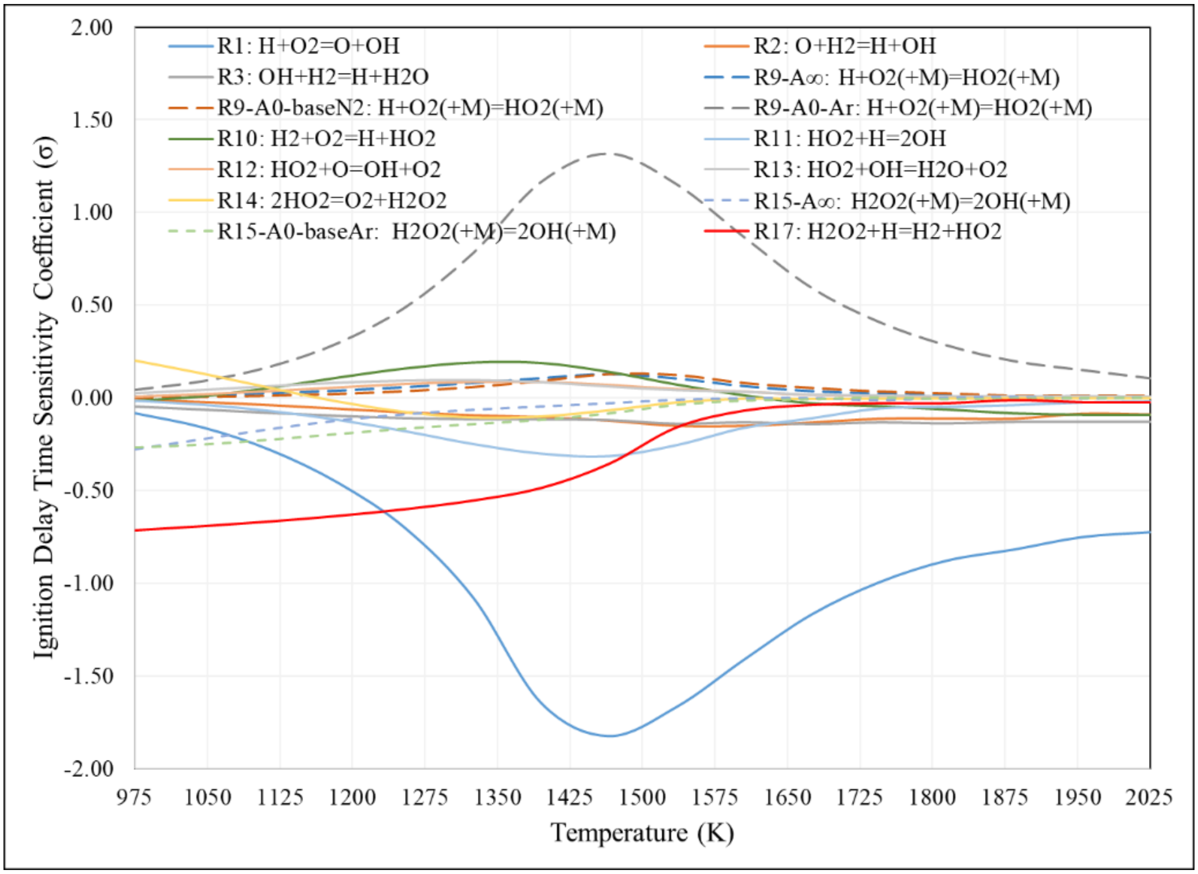

Figure 40: IDT-sensitive (max |σ|≥0.1) reaction rate parameters sensitivity coefficients vs. temperature of Reactions for 4%H_2/Ar φ=1 at 150 bar

6.3 Effect of presence of CO_2 on combustion chemistry at different pressures

In order to map the impact of CO_2 it is important to capture its effect at different pressures and at different concentrations. Figure 41 illustrates the variation of IDTs with temperature and pressure for 4%H_2/45%CO_2/Ar φ=1 at 2, 40, and 150 bar. It can be observed from this figure that in the presence of 45%CO_2 increasing pressure generally reduces the ignition delay time, at temperatures above 1665 K, and below 1000 K. Similar to the case of no CO_2 dilution (Figure 27), the transition from high to low temperature regime shifts to higher temperatures with pressure. This temperature increases from approximately 1120 K at 2 bar to 1660 K and above 1800 K, at 40 and 150 bar, respectively. With increases in pressure the temperature span, over which the impact of transition in chemistry is visible, stretches; the transition is less abrupt, and its impact on the IDTs as well as the change in global activation energy at the high vs. low temperature ends, is less.

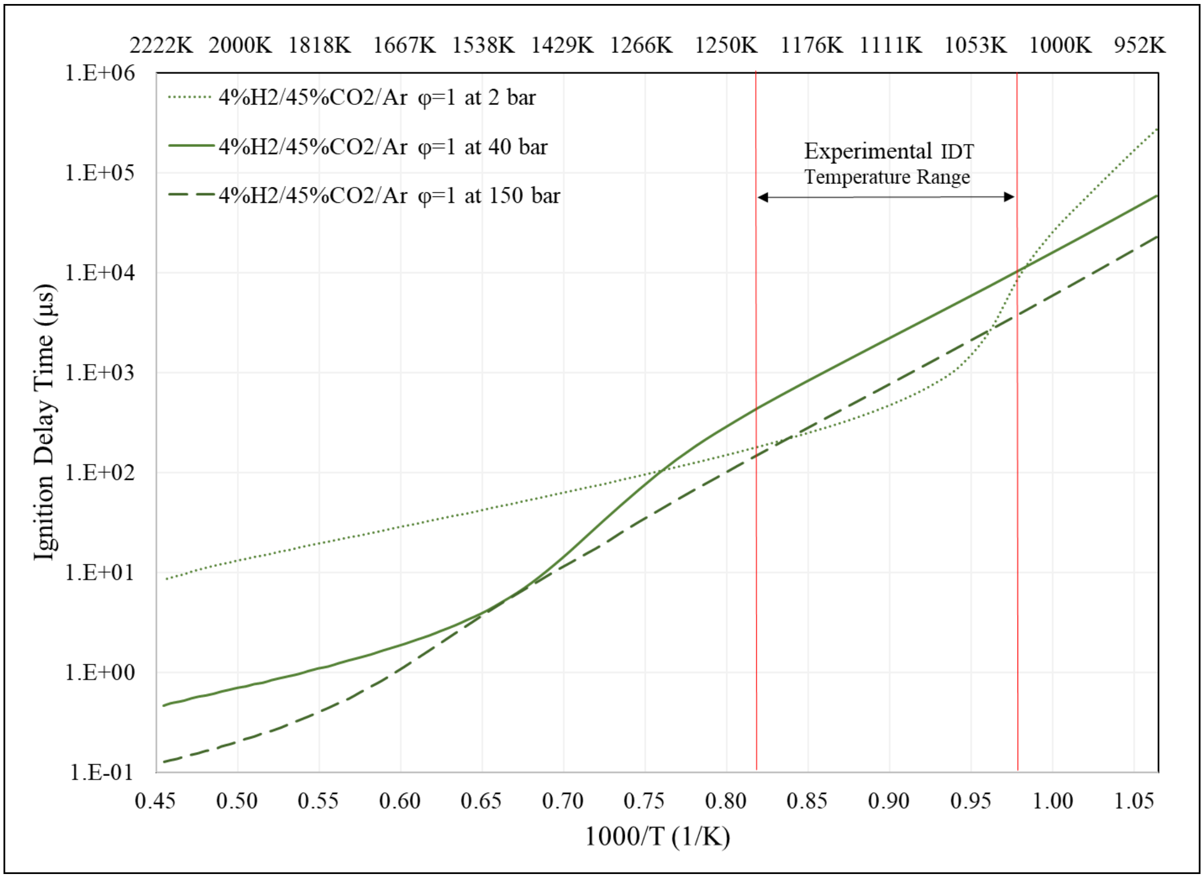

Figure 41: IDT variation with temperature & pressure for 4%H_2/45%CO_2/Ar φ=1 at 2, 40, and 150 bar

The effect of pressure is also investigated through pressure-dependent IDT sensitivity analyses at 1226 K, as seen in Figure 42. The temperature of 1226 K was selected as it lies in the upper end of the experimentally explored temperature range, and corresponds to an experimental validation test condition, conducted at 40 bar in 45%CO_2/Ar bath gas, i.e., test #51. It can be observed that at 2 bar, in-line with the observations of Figure 41, high-temperature low-pressure chemistry is dominant. Figure 42, shows that at 1226 K:

a. At 2 bar, IDTs are most sensitive to R1, R9, R2, R3, R10 and R11;

b. At 40 bar, the IDTs are sensitive to R1, R17, R9, R10, R12, R14, R13, R11, R2, R3, R23 and R15, in order of priority. It is also observed that an increase in pressure has increased relative senstivities to R17, R9, R10, R11, R12, R13, R14, R23, and R15. It should be noted that all of these, with the exception of R23, and R15, involve HO_2. Moreover, three involve H_2O_2, i.e. R17, R14 and R15; and,

c. At 150 bar, IDTs are most sensitive to R17, R10, R15, R9, R14, and to lesser extents to R3, R23, R1, and R2. It is also important to note that, increasing pressure has lowered sensitivity to R1, R11, R12, and R13 to near-negligible levels. Whereas, it has significantly increased the relative senstivities to R17, and R15, R10 and R14, three of which (R17, R15 and R14) involve H_2O_2. Also R10 and R14's IDT sensitivity coefficients change sign with increase in pressure at ~70 and 90 bar, respectively.

Comparison of Figure 42, with its Ar-diluted counterpart at 1209 K, Figure 29, reveals that:

a. At 2 bar, IDTs sensitivities are relatively similar, but R11's relative sensitivity slightly increases;
b. At 40 bar, IDTs are less sensitive to R15, but sensitivities to R9, R10, R12, R14, and R13 and R23: $CO+OH=CO_2+H$ increase. Appearance of R23 is a direct consequence of the presence of CO_2 and confirms the importance of inclusion of CO submechanism even when the only carbon containing specie is the CO_2 molecules of bath gas. The comparison also shows that the transition to low-temperature, high-pressure regime is further along, even though, the analysis was done at a slightly higher temperature (1226 K for CO_2 vs. 1209 K in Ar); and,
c. At 150 bar, the chemistry appears to have nearly completed the transition to the low-temperature chemistry. IDT senstivities increase to R17, R15, R14, R10 and sensitivity to R23 remains present. However, IDT senstivities decrease to R1, R11 and R2.

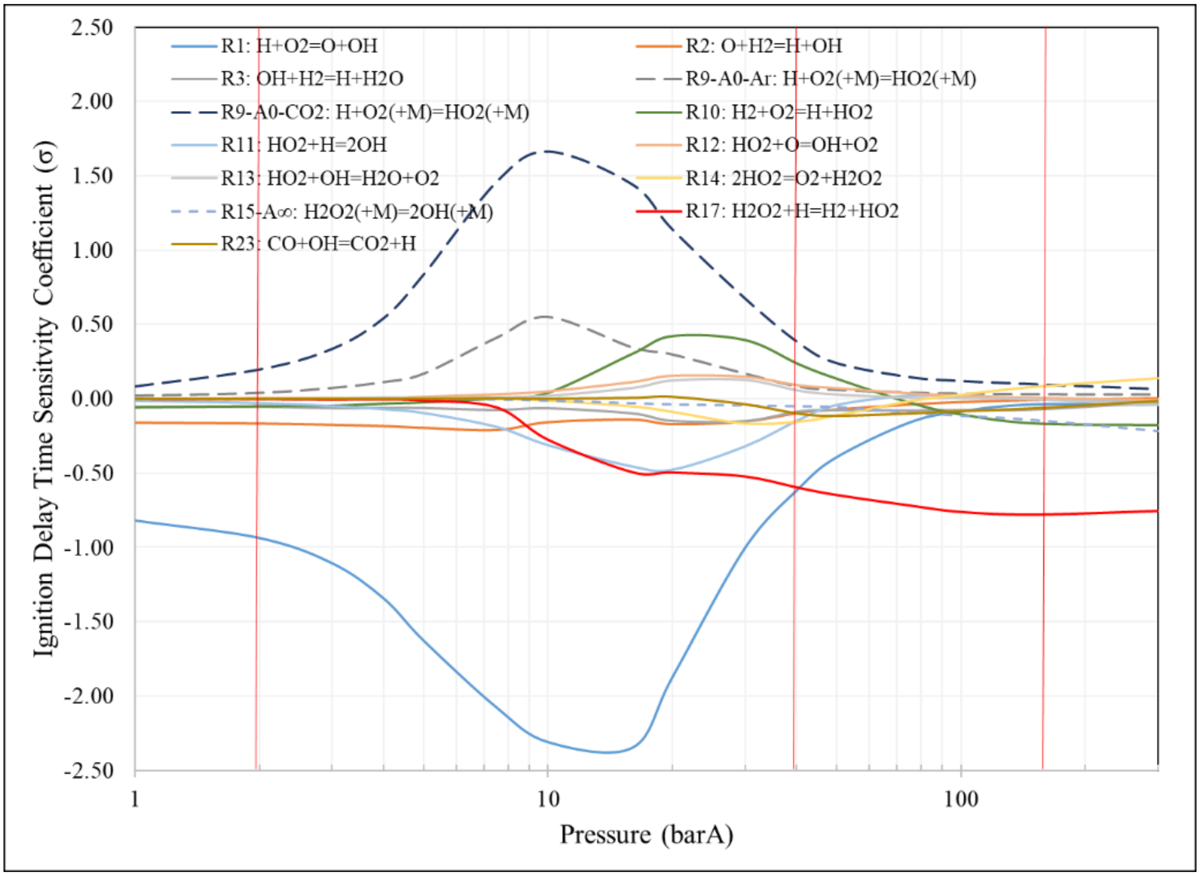

Figure 42: IDT-sensitive (max |σ|≥0.1) reaction rate parameters sensitivity coefficients vs. pressure for 4%H_2/45%CO_2/Ar φ=1 at 1226 K

With pressure-dependent IDT senstivities analyzed, to deconvolute the chemical pathways involved, rate of production analyses were conducted at two conditions, namely:

1- At the condition of experimental validation test #51, involving 4%H_2/45%CO_2/Ar with φ=1 conducted at 1226 K at 40.6 bar; and,
2- Variant of test #51, extrapolated to 150 bar, with other conditions remaining the same.

<u>ROP analysis of 4%H_2 φ=1 at ~40 bar in 45%CO_2/Ar bath:</u>

In-line with the approach assumed for the Ar-diluted ROP analyses, for test #51, the OH*-, OH-, and temperature inflection-based IDTs were calculated to be 399, 386, 449 μs. Hence, simulated data beyond 449 μs were dismissed and not used for the ROP analyses of this test. This test involved a 4%H_2 φ=1 reactive mixture, and was conducted at 1226 K, 40.6 bar in a 45%CO_2/Ar bath.

Figure 43 depicts the evolution of H, O, OH, HO_2, H_2O_2, HCO in addition to the normalized evolution of OH*, CO, temperature and pressure for Test #51. It should be noted that in this figure, temperature, pressure, OH* and CO mole fractions were normalized by dividing their values by their peak simulated values. OH* had to be normalized due to its low maximum mole fraction of 5.12×10^{-16}, and CO due to its high maximum mole fraction of 7.06×10^{-3}. In the presence of CO_2, there is a non-negligible quantity (maximum 0.7% by mole) of CO generated at these conditions. It is also clear that the HO_2 and H_2O_2 are present in significantly larger concentrations than H, OH and O (i.e., a factor of 7 and 3 larger than the H radical). Comparison of Figure 43 with its Ar-diluted counterpart of at 1209 K, Figure 37, reveals that the maximum radical concentrations are two orders of magnitude lower at high pressures and 45% CO_2 dilution. Furthermore, the H and O radical pool has mainly been replaced by H_2O_2 and HO_2 pools. Comparison of Figure 43 and Figure 37 shows that the chronological order of increase of radical concentrations remains the same: the excited OH* buildup preceeds OH and O radicals', and its buildup takes place at an exponentially faster rate than H radical, in the presence of CO_2. Also the order of largest radical pool buildup changes from H, OH and O for test #25, to HO_2, H_2O_2, and to much lesser extents H, OH and O for test #51. This change is very significant as in the Ar-diluted case H radical mole fraction was about 20 times more than that of HO_2, and 2 orders of magnitude more than H_2O_2. Similarly, OH and O were present at 10X and 5X larger concentrations relative to HO_2, respectively. Examining the absolute value of mole fractions of radicals, suggests that this large relative shift is more a consequence of significantly lower H, OH, and O radical pool buildup, as the HO_2 and H_2O_2 absolute peak concentrations have increased by less than a factor of 2. To understand the dominance of reactive pathways, ROP analyses results are examined. Figure A28 to Figure A36 of Appendix C detail ROP plots for OH, H, O, H_2O_2 and HO_2 for test #51.

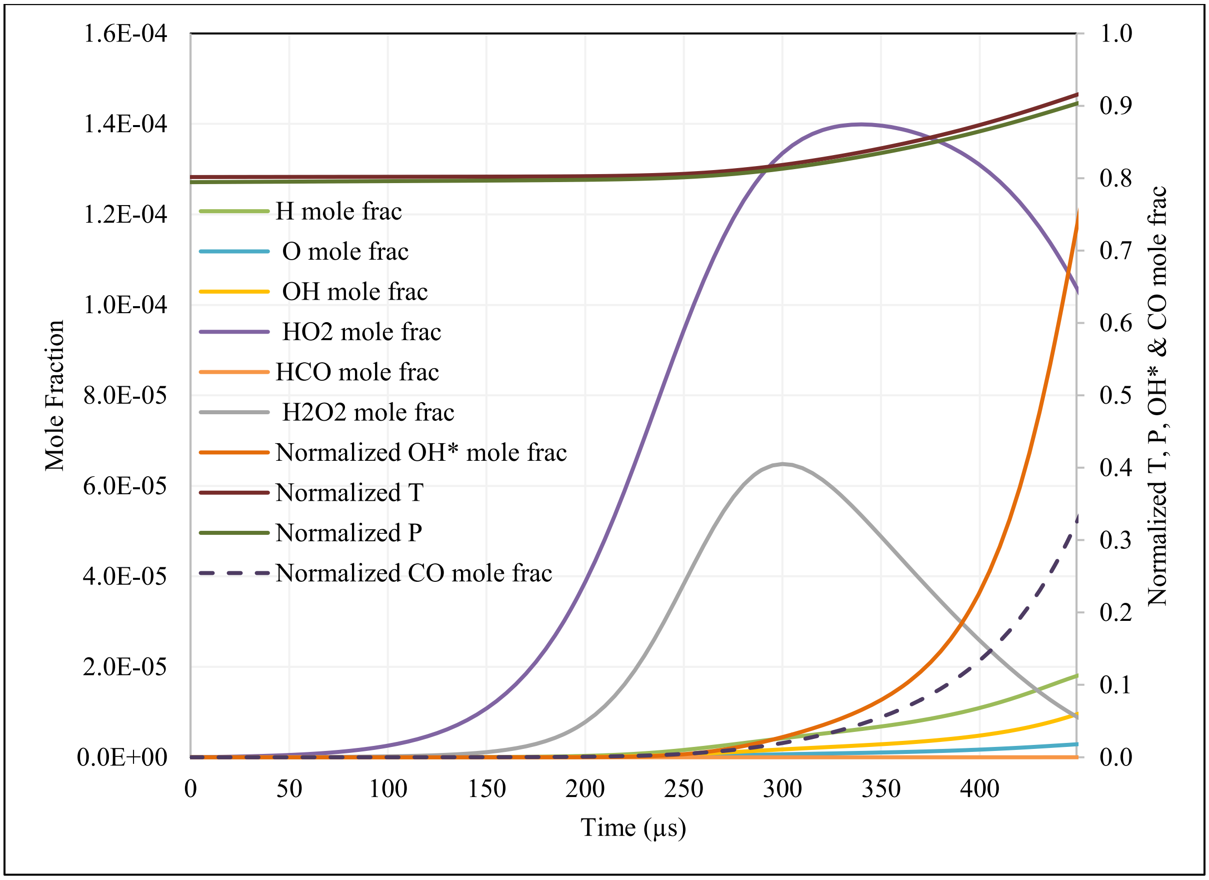

Figure 43: Mole fraction traces of radicals and reaction intermediates, superimposed with normalized temperature, pressure and OH* and CO mole fraction for Test #51 – 4%H_2/45%CO_2/Ar φ=1 at 1226 K at 40.6 bar

These ROP plots show that at 1226 K and 40.6 bar in the presence of 45%CO_2 the dominant reaction path leading to OH production:

For the first 25 μs is:

R1: $H+O_2=OH+O$

R2: $O+H_2=OH+H$

R3: $OH+H_2=H+H_2O$

For 25-170 μs is:

R3: $OH+H_2=H+H_2O$

R9: $H+O_2(+M)=HO_2(+M)$

-R17: $HO_2+H_2=H_2O_2+H$

R15: H_2O_2=OH+OH

For 170 µs to 280 µs is:
R3: OH+H_2=H+H_2O
R9: H+O_2(+M)=HO_2(+M)
R14: HO_2+HO_2= H_2O_2+O_2
R15: H_2O_2=OH+OH

For 275 µs to ignition at 449 µs is:
R3: OH+H_2=H+H_2O
R9: H+O_2(+M)=HO_2(+M)
R11: HO_2+H=OH+OH

Based on the reaction pathways determined by the 40 bar ROP analysis it is important to examine these results against the IDT-sensitvity results of Figure 42 conducted at 45%CO_2/Ar, 1226 K and pressures of 1-300 bar.

At 40 bar, the IDTs were shown to be sensitive to R1, R17, R9, R10, R12, R14, R13, R11, R2, R3, R23 and R15, in order of priority. Considering the multiple competing pathways competition of R11, R9, and R1 with –R10 and –R23 for H radical explains their large sensitivities. HO_2-ROP profile in Figure A35 of Appendix C, indicates that while R9 is the only producer of HO_2, -R17, R14, R11, followed by -R10: H+HO_2=H_2+O_2 are its main consumers. This explains the large positive IDT sensitivity coefficients for -R10, as well as R14, as they compete with –R17 and R11 for HO_2 radicals. Also, as R11 and R14 contribute to ignition pathways by producing H_2O_2, and OH, they have negative senstivities, but –R10, which consumes HO_2 and H to re-produce reactants for the most part, inhibits ignition and has a positive IDT sensitivity coefficient.

To delineate the effect of CO_2 bath gas versus Argon, Table 12 provides a side-by-side comparison of the reactive pathways identified at 40 bar for 4%H_2 φ=1 in Ar and 45%CO_2/Ar baths. It can be observed that in the presence of 45% CO_2, two additional pathways involving H_2O_2 decomposition, become dominant, in contrast with the Ar-diluted case. This shows that 45%CO_2 pushes the high-pressure low temperature chemistry, involving H_2O_2, to higher temperatures. Also, the high temperature path through R1+R2+R3 becomes short-lived in the presence of CO_2. However, the dominant reaction pathway immediately preceeding ignition, involving R3+R9+R11, remains common to both Ar and 45%CO_2/Ar baths.

Table 12: Comparison of reactive pathways for ignition of 4%H_2 φ=1 in 45%CO_2/Ar vs. in Ar bath at 40 bar

Ar bath at ~40 bar and 1209 K	45%CO_2/Ar bath at 40.6 bar 1226 K
IDT Regime: Intermediate T & P (peak of transition)	IDT Regime: Intermediate T & P (nearing transition to low T)
Dominant path (0-125μs): R1: $H+O_2=O+OH$ R2: $O+H_2=H+OH$ R3: $OH+H_2=H_2O+H$	Dominant path (0-25μs): R1: $H+O_2=O+OH$ R2: $O+H_2=H+OH$ R3: $OH+H_2=H_2O+H$
	Dominant path (0-170 μs): R3: $OH+H_2=H+H_2O$ R9: $H+O_2(+M)=HO_2(+M)$ -R17: $HO_2+H_2=H_2O_2+H$ R15: $H_2O_2=OH+OH$
	Dominant path (170-280 μs): R3+R9+R15 +R14: $HO_2+HO_2= H_2O_2+O_2$
Dominant path (125-ignition/144 μs): R3: $OH+H_2=H_2O+H$ R9: H+O2=HO_2 R11: $H+HO_2=OH+OH$	Dominant path (280-ignition at 449 μs): R3: $OH+H_2=H+H_2O$ R9: $H+O_2(+M)=HO_2(+M)$ R11: $HO_2+H=OH+OH$

ROP analysis of 4%H_2 φ=1 at 150 bar in 45%CO_2/Ar bath:

To understand the chemistry change brought about by increasing the pressure in the presence of 45%CO_2, the ignition delay process for test #51 is resimulated at an extrapolated pressure of 150 bar. Figure 44 depicts the evolution of radicals and reaction intermediates, superimposed with normalized temperature, pressure, OH* and CO mole fractions for 4%H_2/45%CO_2/Ar φ=1 at 1226 K at 150 bar. The normalized parameters were calculated by dividing their time-dependent values by their respective maximum simulated values, i.e., maximum OH* and CO mole fractions of 4.11×10^{-17} and 0.005, respectively. IDT estimates using OH*, OH, and temperature inflection time for this test were, 140, 100 and 181 μs, respectively, as such the data beyond 181 μs were discarded.

Comparing Figure 44 with test #51 at 40.6 bar (Figure 43) shows that increasing the pressure to 150 bar has increased peak mole fractions of HO_2 (~12%), and H_2O_2 (~2X larger). In contrast, increasing the pressure has decreased H, OH and O radical pools' peak mole fractions by more than an order of magnitude at 150 bar.

Comparison of Figure 44 with its Ar-diluted extrapolated counterpart at 150 bar (Figure 38), reveals that with the introduction of 45% CO_2, OH, H, and O peak concentrations have reduced by approximately two orders of magnitude. Moreover, HO_2 and H_2O_2 peak concentrations have both increased by ~10%.

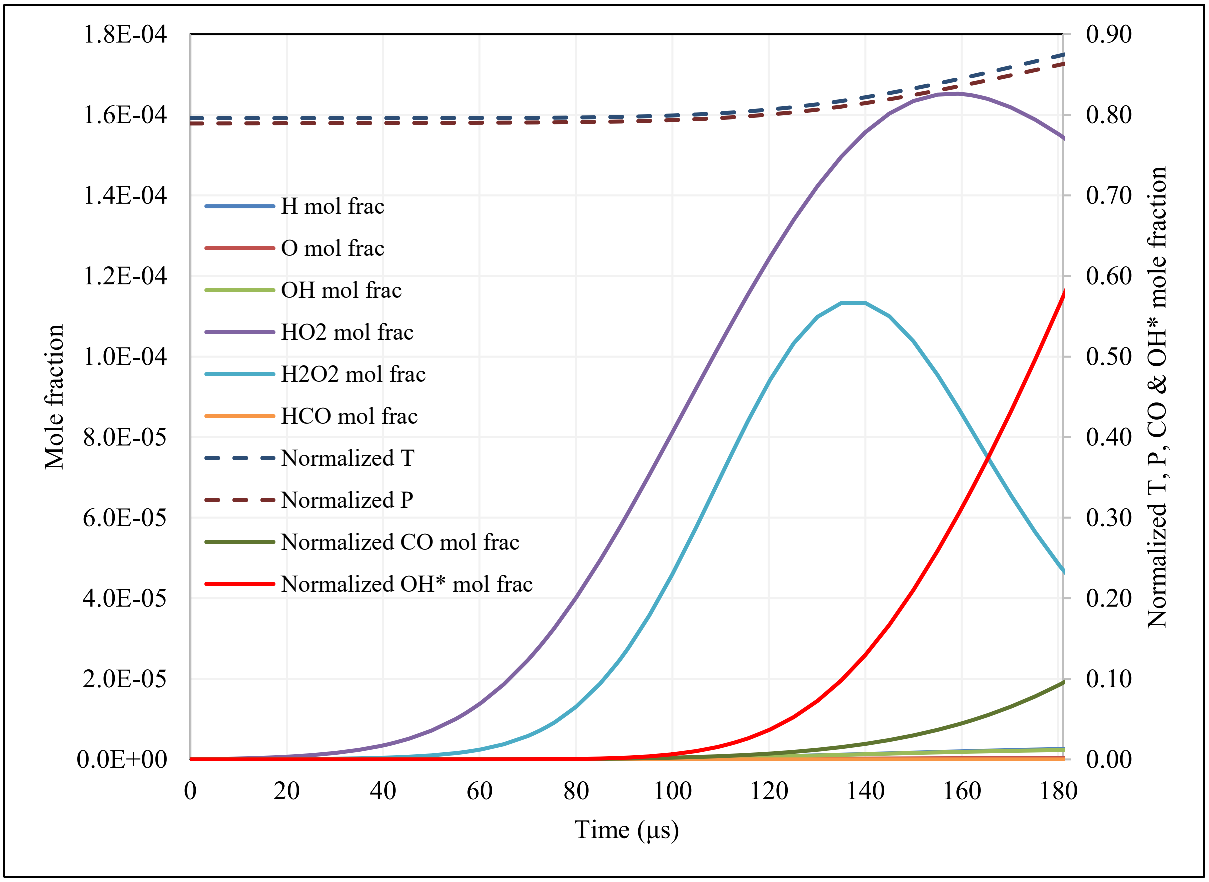

Figure 44: Mole fraction traces of radicals and reaction intermediates, superimposed with normalized temperature, pressure and OH* and CO mole fraction for 4%H_2/45%CO_2/Ar φ=1 at 1226 K at 150 bar

In order to understand the reaction pathways leading to ignition, rate of production analyses are conducted for radicals and reaction intermediates for test #51 at extrapolated condition of 150 bar. ROP plots of OH, H_2O_2, HO_2 and H (see Figure A37 to Figure A44 of Appendix C), illustrate that for

4%H_2/45%CO_2/Ar φ=1 at 1226 K at 150 bar, the chemistry leading to OH production traverses the following dominant pathways:

For the initial 0-65 µs:
R3: $OH+H_2=H+H_2O$
R9: $H+O_2(+M)=HO_2(+M)$
-R17: $HO_2+H_2=H_2O_2+H$
R15: $H_2O_2=OH+OH$

For 65-180 µs (until ignition):
R3: $OH+H_2=H+H_2O$
R9: $H+O_2(+M)=HO_2(+M)$
R14: $HO_2+HO_2= H_2O_2+O_2$
R15: $H_2O_2=OH+OH$

In addition, the ROP analyses show that the chemistry also involves the following alternate pathways:

For 0-85 µs:
R1: $H+O_2=O+OH$
R2: $O+H_2=H+OH$
R3: $OH+H_2=H_2O+H$

For 85-180 µs (until ignition):
R3: $OH+H_2=H+H_2O$
R9: $H+O_2(+M)=HO_2(+M)$
R11: $HO_2+H=OH+OH$

Corroborating the reaction pathways from the ROP analyses at 150 bar, with the pressure-dependent IDT senstivities of Figure 42 illustrate that, at 150 bar, IDTs are most sensitive to R17, R10, R15, R9, and R14, and to lesser extents to R3, R23, R1, and R2. These senstivities corroborate well with the ROP analysis results, as four out of the five most sensitive reactions (R17, R15, R9 and R14) are an integral part of the reaction pathways presented. In addition, R10 proceeds in the reverse direction -R10: $H+HO_2=H_2+O_2$ at the intial stages of ignition which may partially explains its negative sensitivity. However, as –R10 is also highly exothermic (~-220 kJ/mol, near 1200 K) the heat generated associated with the consumption of HO_2 and H, could explain its net promoting effect on reactivity.

Table 13 illustrates the change in reaction pathways brought about by an increase of pressure from 40 bar to 150 bar in the presence of 45%CO_2. It can be observed that at 150 bar the two main dominant paths rely on H_2O_2 decomposition through R15 to build the OH radical pool necessary for ignition. This is in contrast with its counterpart at 40 bar, which at the initial stages relied on R1+R2+R3, and prior to ignition on R3+R9+R11. These paths become secondary alternate ones for OH generation at 150 bar in the presence of 45% CO_2.

Table 13: Summary of reaction pathways at 40 vs. 150 bar in 45%CO_2/Ar bath gas

45%CO_2/Ar bath at 40.6 bar 1226 K	45%CO_2/Ar bath at 150 bar 1226 K
IDT Regime: Intermediate T and P (transition nearing low T)	IDT Regime: Low T high P
Dominant path (0-25 µs): R1: $H+O_2=O+OH$ R2: $O+H_2=H+OH$ R3: $OH+H_2=H_2O+H$	
Dominant path (25-170 µs): R3: $OH+H_2=H+H_2O$ R9: $H+O_2(+M)=HO_2(+M)$ -R17: $HO_2+H_2=H_2O_2+H$ R15: $H_2O_2=OH+OH$	Dominant path (0-65 µs): R3: $OH+H_2=H+H_2O$ R9: $H+O_2(+M)=HO_2(+M)$ -R17: $HO_2+H_2=H_2O_2+H$ R15: $H_2O_2=OH+OH$
Dominant path (170-280 µs): R3+R9+R15 +R14: $HO_2+HO_2= H_2O_2+O_2$	Dominant path (65-ignition/180µs): R3+R9+R15 +R14: $HO_2+HO_2= H_2O_2+O_2$
Dominant path (280-ignition at 449 µs): R3: $OH+H_2=H+H_2O$ R9: $H+O_2(+M)=HO_2(+M)$ R11: $HO_2+H=OH+OH$	
	Alternate path (0-85 µs): R3: $OH+H_2=H_2O+H$ R1: $H+O_2=O+OH$ R2: $O+H_2=H+OH$
	Alternate path (85-ignition/180µs) R3: $OH+H_2=H+H_2O$ R9: $H+O_2(+M)=HO_2(+M)$ R11: $HO_2+H=OH+OH$

Table 14 summarizes the reaction pathways at 150 bar for Ar vs. 45%CO_2/Ar bath gases to enable delineation of the bath gas effect at this pressure. It is apparent that in the presence of CO_2, the importance of H_2O_2 decomposition through R15 to build the OH radical is more dominating. Additionally, the introduction of 45% CO_2, demotes the paths through R3+R9+R11 and R1+R2+R3 to alternate pathways. These paths were dominant at 150 bar in the presence of pure Ar.

Table 14: Summary of reaction pathways at 150 bar in Ar vs. 45%CO_2/Ar bath

Ar bath at 150 bar and 1209 K	45%CO_2/Ar bath at 150 bar 1226 K
IDT Regime: Low T + High P (transition to low T chemistry is nearing completion)	IDT Regime: Low T high P
Dominant path (0-8 µs) R1: $H+O_2=O+OH$ R2: $O+H_2=H+OH$ R3: $OH+H_2=H_2O+H$	
Dominant path (8-70 µs): R3: $OH+H_2=H_2O+H$ R9: $H+O_2=HO_2$ -R17: $HO_2+H_2=H_2O_2+H$ R15: $H_2O_2(+M)=OH+OH(+M)$	Dominant for the initial 0-65 µs: R3: $OH+H_2=H+H_2O$ R9: $H+O_2(+M)=HO_2(+M)$ -R17: $HO_2+H_2=H_2O_2+H$ R15: $H_2O_2=OH+OH$
Dominant path (70-132 µs): R3+R9+R15 +R14: $HO_2+HO_2=H_2O_2+O_2$	Dominant path (65-ignition/180µs): R3+R9+R15 +R14: $HO_2+HO_2=H_2O_2+O_2$
Dominant path (132-ignition/149 µs): R3: $OH+H_2=H_2O+H$ R9: $H+O_2=HO_2$ R11: $H+HO_2=OH+OH$	
	Alternate path (0-85 µs): R3: $OH+H_2=H_2O+H$ R1: $H+O_2=O+OH$ R2: $O+H_2=H+OH$
	Alternate path (85-ignition/180µs) R3: $OH+H_2=H+H_2O$ R9: $H+O_2(+M)=HO_2(+M)$ R11: $HO_2+H=OH+OH$

It is also of interest to understand what the effect of temperature variation is in the presence of CO_2 at different pressures. To this end, temperature-dependent IDT sensitivity analyses at the two pressures of 40 and 150 bar are conducted in this work. Figure 45 and Figure 46 illustrate the variation of IDT sensitivity coefficients of rates with temperature for 4%H_2/45%CO_2/Ar $\varphi=1$ at 40 and 150 bar, respectively. Comparison of these graphs illustrates that R17 has a dominating contribution at higher pressures, and its impact stretches to higher temperatures with pressure. Figure 45 shows that R17's sensitivity reduces to -0.5 around 1300 K at 40 bar, and at 150 bar it reaches this value at 1550 K, see Figure 46. At 150 bar, and temperatures above 1240 K, R11 IDT sensitivity switches sign and exhibits a significant positive sensitivity whereas it exhibits a strong negative sensitivity at 40 bar at least up to 1650 K. Moreover, increasing R10: H_2+O_2=H+HO_2 rate decreases IDTs at 40 bar at temperatures of up to 1500 K, after which it decreases them. At 150 bar increasing R10's rate consistently decreases IDTs, and it is in the top 3 IDT sensitive reactions at temperatures of 1275-2025 K. It can be observed that the higher temperature chemistry at 150 bar at temperatures above 1275 K is a different chemistry which requires further investigation. Highly negative IDT sensitivity coefficients of R10, and R13, along with positive IDT sensitivity coefficient of R3, were not encountered so far in this study, with the exception of R10 involvement as a potential chain initiation step. Furthermore, the aforementioned reactions' IDT sensitivities switch over yet again in addition to R23 in the temperature range of 1725-1875 K, which likely points to yet another change in dominant chemical pathways, which would benefit from further investigation.

Overall, from a comparison of the scales of the vertical axes of Figure 45 and Figure 46, it is concluded that overall IDTs are less sensitive to R9 and R1 at higher pressures in the presence of 45%CO_2. Also, the temperature span over which R9 and R1's competition peaks, stretches and covers a larger temperature range. With increased pressure, HO_2 and H_2O_2 chemistries dominate the overall chemistry at higher temperatures, which provide multiple alternate pathways for reactivity. For 45%CO_2, by comparing the IDT temperature sweeps of Figure 41, and IDT senstivities of Figure 46 at 150 bar, it can be concluded that with increased pressure the changes in competing chemical pathways, with temperature, exhibit a net cancelling effect leaving overall reactivity nearly unpurturbed. This is observed from the less distinct change in ignition delay times at high pressures with variations in temperature. It can also be concluded that in addition to R9 and R1, accurate rate determinations of R17, R3, R15, R10, and R14 are instrumental to reliable predictions of the mechanism. Accurate bath-gas specific rate parameters are also of critical importance especially for R9, and R15.

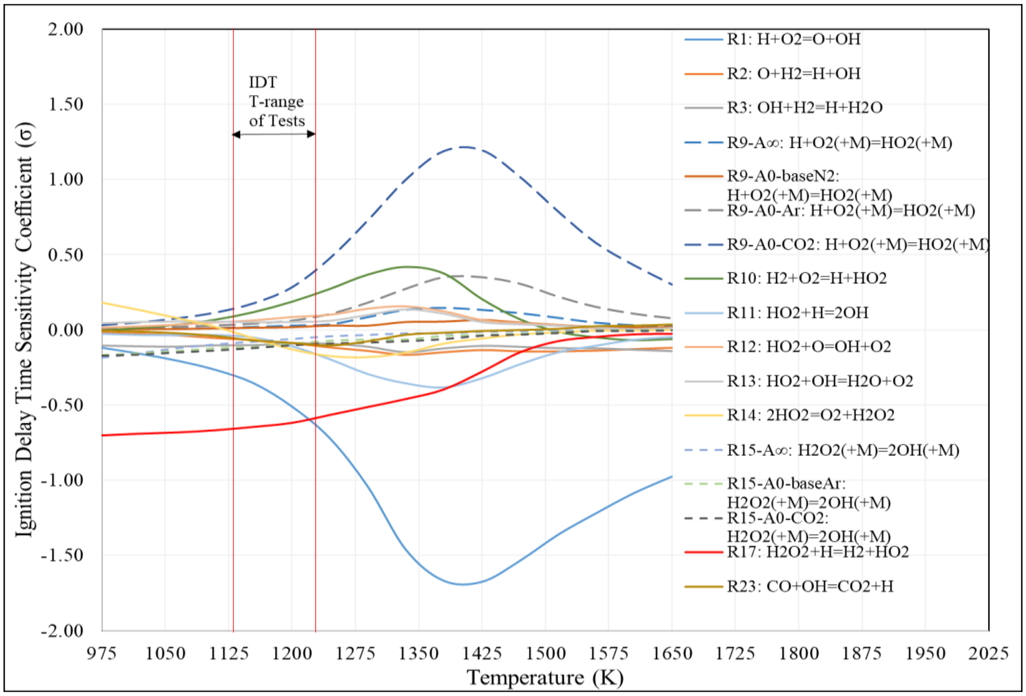

Figure 45: IDT sensitivities for 4%H_2/45%CO_2/Ar φ=1 at 40 bar for 975-1650 K

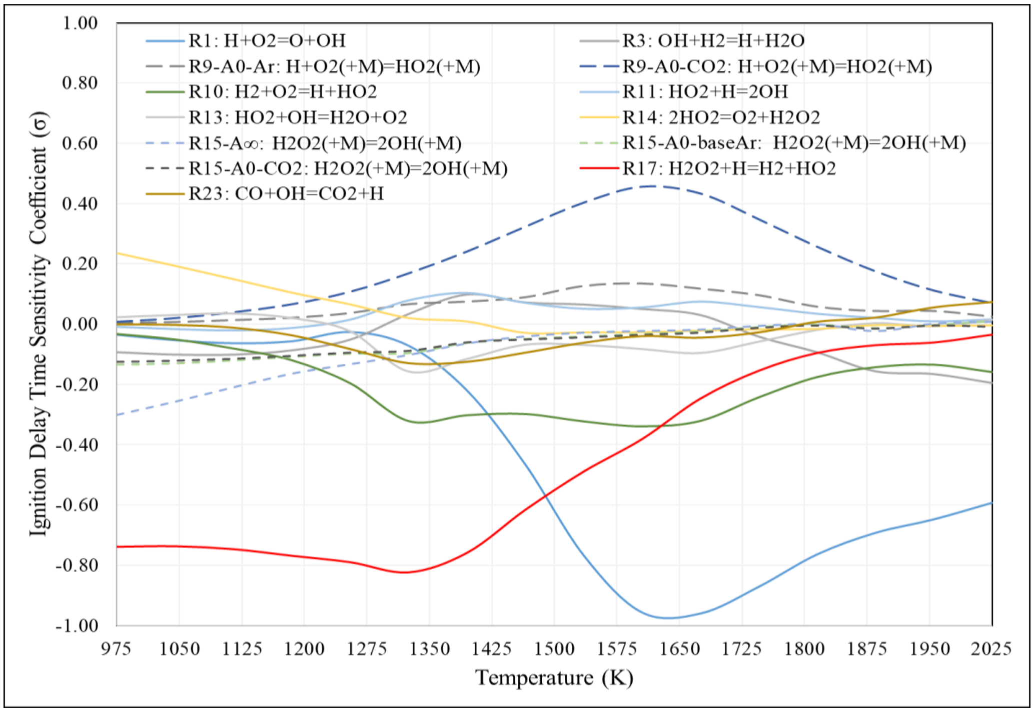

Figure 46: IDT sensitivities for 4%H_2/45%CO_2/Ar φ=1 at 150 bar for 975-2025 K

With the effect of pressure and temperature mapped for CO_2 dilution of 45%, it is also of interest to explore the impact of different CO_2 concentrations at each pressure.

Figure 47 depicts an IDT temperature sweep at concentrations of 0-65% CO_2 with the balance Ar at 2 bar. It can be observed that, increasing the concentration of CO_2, consistently increases the ignition delay time at temperatures below 1250 K, whereas at higher temperatures such increase does not have a noticeable effect. It is also apparent that the temperature at which deviation from high temperature chemistry starts to reveal itself is pushed to higher temperatures with increased concentration of CO_2 in the bath gas. Figure 47 indicates that, the transition starts near 1000, 1075, 1150, 1225, 1260, and 1270 K for 5%, 15%, 30%, 45%, 65% CO_2 dilutions, respectively at 2 bar. Based on these results, the effect of CO_2 addition on the temperature at which the chemistry transitions, reduces at higher dilutions of CO_2.

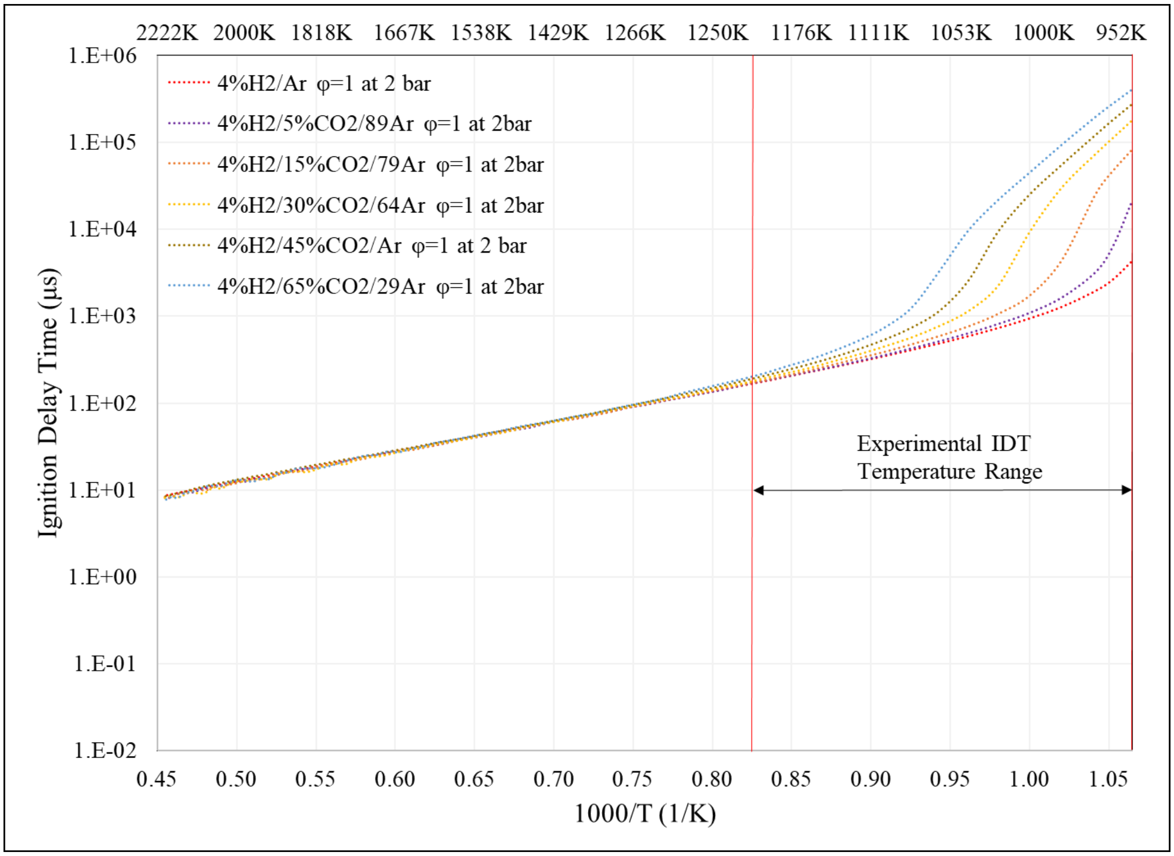

Figure 47: IDT temperature sweep for $4\%H_2/0\text{-}65\%CO_2/Ar$ φ=1 at 940-2200 K, 2 bar

Figure 48, provides IDT temperature sweep for 4%H_2/0-65%CO_2/Ar φ=1 at 940-2200 K, at 40 bar. This figure illustrates that incremental increase of CO_2 concentration from 0 to 65% increases the simulated IDTs. However, similar to the previously described pressure effect it is observed that higher dilution rates of CO_2 result in similar effect to increasing the pressure on IDTs. It can be observed that with increased CO_2 concentration, the transition from one chemistry to another is less abrupt, and has a less noticeable impact, as apparent from a comparison of 45%CO_2/Ar case with 65%CO_2/Ar case in Figure 48. At sufficiently high concentrations, in addition to the less abrupt IDT effect due to chemistry transition, the temperature span over which this takes place stretches. This is similar to the trend changes observed with increased pressure on IDTs. This generally results in increases in IDTs for larger concentrations of CO_2. Deviations from this general statement is observed due to the out of phase transitional chemistry effects, which occur at different temperatures for different pressures and concentrations of CO_2.

Finally, Figure 49, summarizes the results of IDT temperature sweep for 4%H_2/0-65%CO_2/Ar φ=1 at 940-2200 K, 150 bar. It illustrates that at 150 bar, the combined effect of higher CO_2 concentrations and pressure changes on chemistry has less of an overall impact on IDTs. The boundaries between potential variations in reaction paths become less distinguishable, to the point that for the case of 65%CO_2 dilution, the impact of the change in chemistry as a function of temperature on ignition delay times is almost unnoticeable.

This concludes the analyses of the effects of CO_2 and pressure on kinetics of hydrogen oxidation. The next section details the results of a similar set of analyses pertinent to H_2O-diluted bath gases.

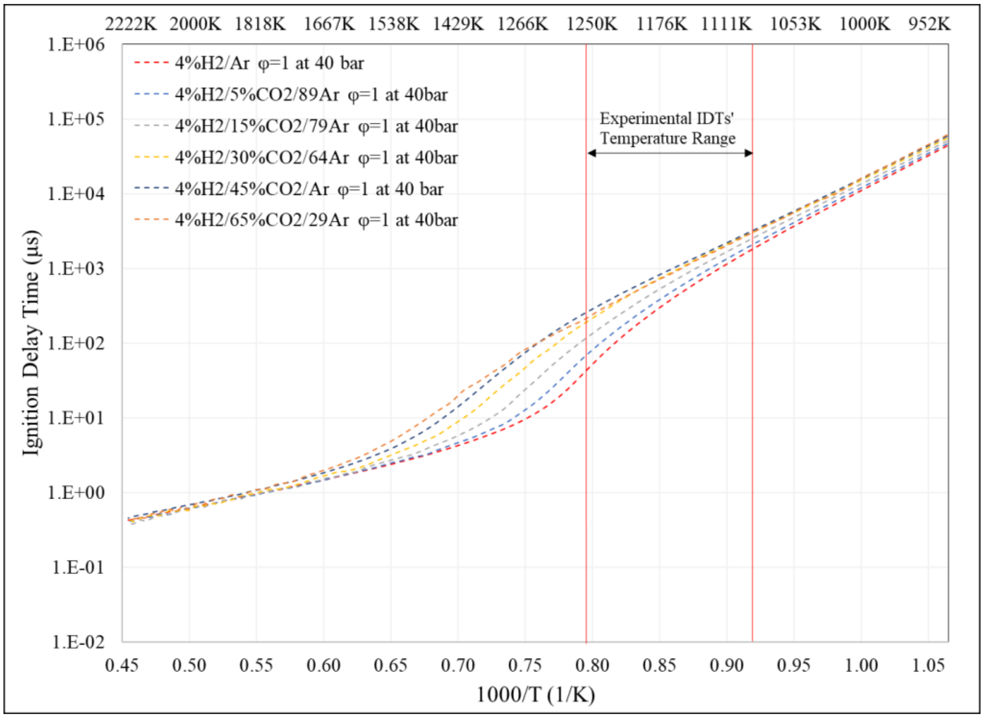

Figure 48: IDT temperature sweep for 4%H_2/0-65%CO_2/Ar φ=1 at 940-2200 K, 40 bar

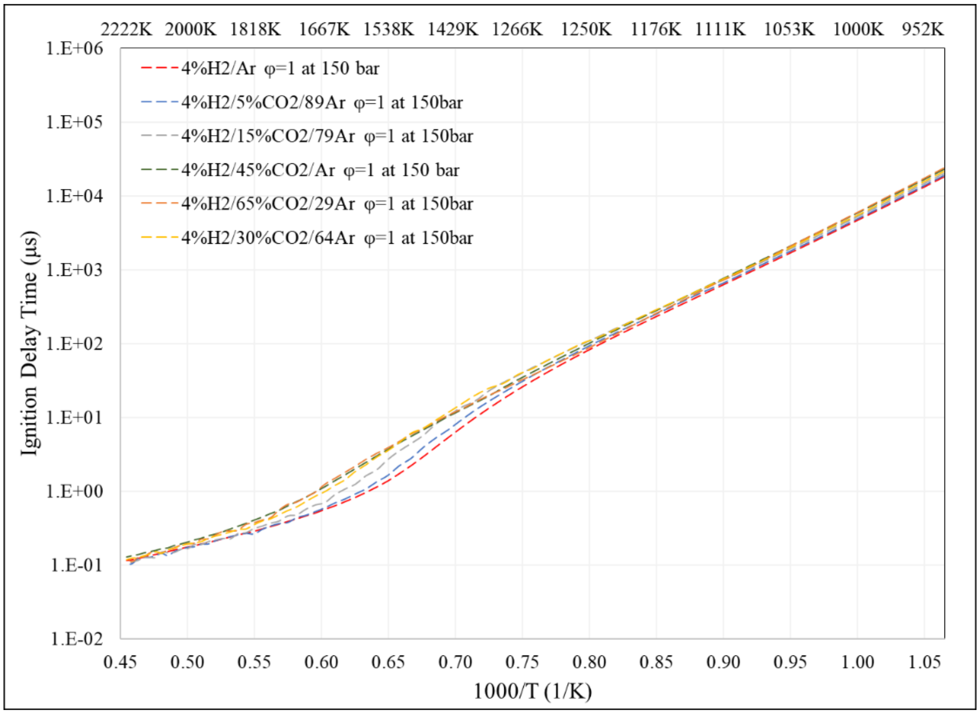

Figure 49: IDT temperature sweep for 4%H_2/0-65%CO_2/Ar φ=1 at 940-2200 K, 150 bar

6.4 Effect of presence of H_2O on combustion chemistry at different pressures

In order to map the dominant chemical pathways in presence of H_2O, evaluation of individual and combined impacts of pressure, H_2O concentrations and temperature are desired. In this section, the effect of pressure is first explored at H_2O concentrations of 45%, where experimental validation data is available at 40 bar. Pressure dependence of IDT sensitivities are examined at pressures of 1-300 bar, at an H_2O concentration of 45% and temperature of 1222 K. This temperature was selected, as it lies in the narrow temperature range of 1209-1237 K, within which kinetic pathways were analyzed in detail for Ar and 45%CO_2/Ar baths. In addition, it corresponds to a validated experiment containing 45%H_2O/Ar at 40 bar, i.e. test #33. Detailed chemical pathways at pressures of 40 and 150 bar are then explored for 45% H_2O concentration at 1222 K. Temperature dependence of IDT sensitivities are also analyzed for further insight into chemistry variations with temperature within the range of 975-2025 K, at pressures of 40 and 150 bar in 45%H_2O/Ar bath. Finally, parametric IDT temperature sweeps are conducted, at pressures of 2, 40 and 150 bar, for different concentrations of H_2O from 0 to 65%, to map the effect of different H_2O concentrations in the bath gas.

Figure 50 depicts the results of IDT temperature sweeps at three different pressures of 2, 40 and 150 bar, for 4%H_2/45%H_2O/Ar at $\varphi=1$. Examination of the results for the 2 bar IDT temperature sweep suggests that a change in chemistry, signified by change in slope of log IDT vs. 1000/T plot, is taking place between temperatures of 1025 K and 1300 K. Examination of the results of 40 bar IDTs shows a similar but less steep change taking place, over a larger temperature span of 1200-1700 K. Finally, at 150 bar, the slope of this change is even less, barely detectable and spans an even larger temperature range of 1400 to 2000 K. Comparison of Figure 50 with its Ar-only diluted counterpart at similar conditions (Figure 27) shows that, for pressures of 2, 40 and 150 bar, transition to high-temperature chemistry shifts from ~1000, 1450, and 1650 K for Ar-only baths, to 1300 K, 1750, and 2000 K for 45% H_2O/Ar baths. Figure 41 shows that, for 45%CO_2/Ar-diluted mixture at pressures of 2, 40 and 150 bar, the same transitions occur at 1120, 1660 and 1800 K, respectively. As such, it is concluded that presence of 45%H_2O has the strongest effect relative to Ar-only and 45%CO_2/Ar bath gases in stretching the temperature span over which such transitions takes place, as well as making the boundaries separating them less clear.

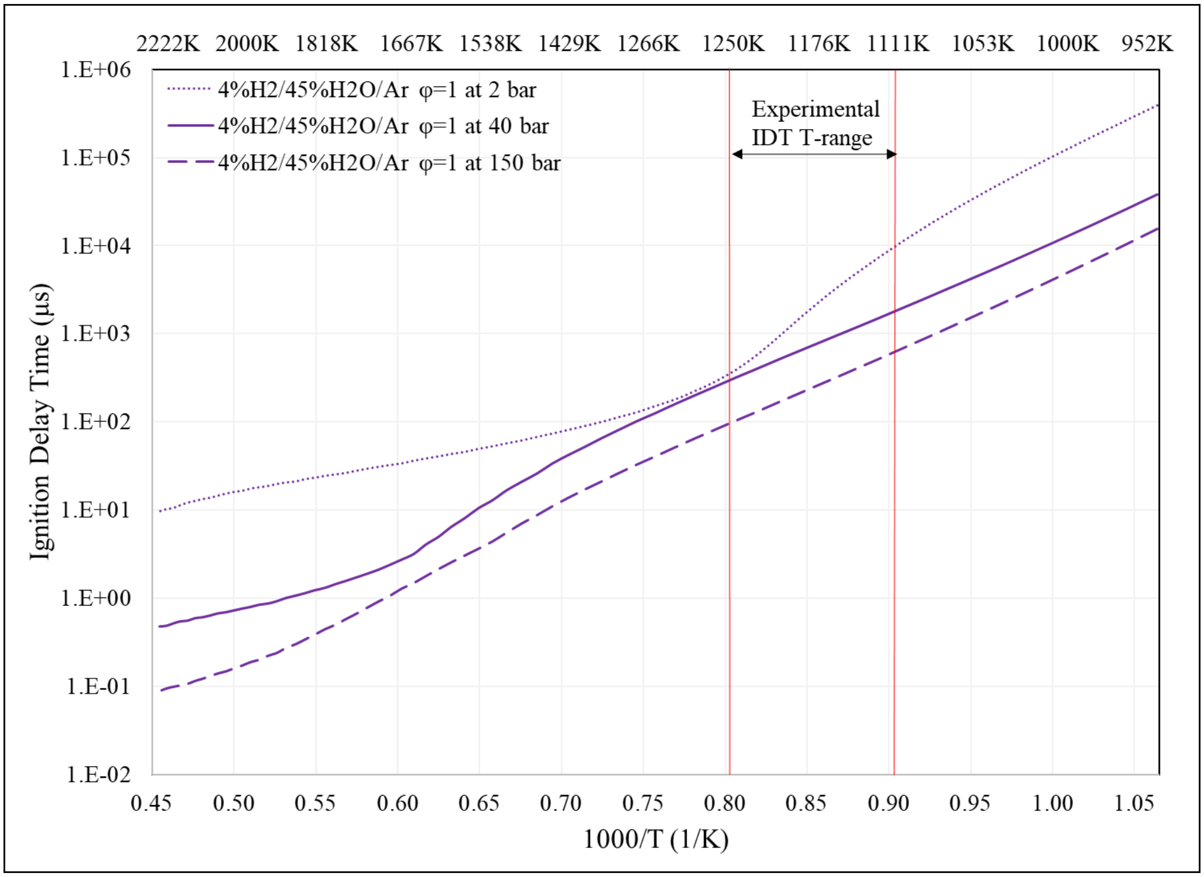

Figure 50: IDT variation with temperature & pressure for 4%H_2/45%H_2O/Ar φ=1 at 2, 40, and 150 bar

For further insight into the chemistries involved, Figure 51 depicts IDT sensitivity coefficients of important reaction rate parameters as a function of pressure at 1222 K for the 4%H_2/45%H_2O/Ar φ=1. Figure 51 shows that in presence of 45%H_2O/Ar:

a. At 2 bar, IDTs are most sensitive to R1, R9, R11, R17, R10, R3, R19, R12 and R13. With the exception of R1 and R3, all of these reactions involve HO_2.

b. At 40 bar, the IDTs are sensitive to R17, R3, R1, R19, R13, R9, R10, R14, R12 and R15 in order of priority. The increase in pressure has increased relative senstivities of R17, R3, R19, R13, R12 and R15, and has significantly reduced those of R1, R9, and R11.

c. At 150 bar, IDTs are most sensitive to R17, R3, R15, R13, R19, and to lesser extents R1, R9 R10, R12, R14 and R11. Increasing pressure has increased relative sensitivities of R17, R13 and R15, has reversed the sign of R10 and R14 senstivities, and has lowered sensitivities of

R1, R9, and R12 to negligible levels. It also has reversed the sign of R10 and R14's IDT sensitivity coefficient, such that they exhibit an IDT decreasing and an IDT increasing effect for pressures larger than ~80 and 120 bar, respectively.

Comparison of Figure 51 with its Ar-diluted counterpart (Figure 29) shows that introducing 45%H_2O:

a. At 2 bar, has made IDTs newly sensitive to R17, R19, R12, and R13, more sensitive to R11, and insensitive to R2. Reactions R19: H_2O_2+OH=H_2O+HO_2, R13: HO_2+OH=H_2O+O_2 involve H_2O and HO_2.
b. At 40 bar, has increased senstivities to R17, R3, R19, R13, R14, and R12, and has reduced senstivities to R1, R9, R11, and R15. It also has rendered IDTs insensitive to R2.
c. At 150 bar, has increased relative sensitivities to R17, R3, R15, R13, R19. It has also made IDTs less sensitive to R1, R9, and R11 and insensitive to R2.

Comparison of Figure 51 with its 45%CO_2/Ar-diluted counterpart (Figure 42) illustrates that, by replacing the 45%CO_2 with 45%H_2O:

a. At 2 bar, IDTs have become newly sensitive to R17, R19, R12, and R13, nearly insensitive to R2, and more sensitive to R11.
b. At 40 bar, the IDTs have become sensitive to R19, significantly less sensitive to R1 and R9, and to lesser extent to R10, and R11. IDTs have become more sensitive to R3, R13, and R12. It should also be noted due to absence of CO_2, sensitivity to R23 is absent.
c. At 150 bar, IDTs have become sensitive to R19, more sensitive to R3 and R13 and less sensitive to R17, R10, R14, R9.

Moreover, comparison of the sensitivies at 40 and 150 bar of Figure 51 and Figure 42, indicate a similar switch over of the sensitivities of R14: HO_2+HO_2=O_2+H_2O_2 and R10: H_2+O_2=H+HO_2, to those observed in the case of 45%CO_2/Ar diluted mixtures at similar temperature (1226 K). This comparison also shows that, H_2O-specific low-pressure-limit rate sensitivity of R9 is so dominating for the 45% H_2O-diluted mixture that the Ar-specific low-pressure-limit rate's sensitivity is no-longer relevant. Comparison of other reactions' sensitivities of Figure 51 and Figure 42 reveals that the relative sensitivities of R3: OH+H_2=H+H_2O and R13: HO_2+OH=H_2O+O_2 significantly increase in the presence of 45%H_2O. Similarly, larger senstivities to R19 point to its increased impact on IDTs. These differences call for a more in depth analysis of reaction pathways in the presence of 45% H_2O.

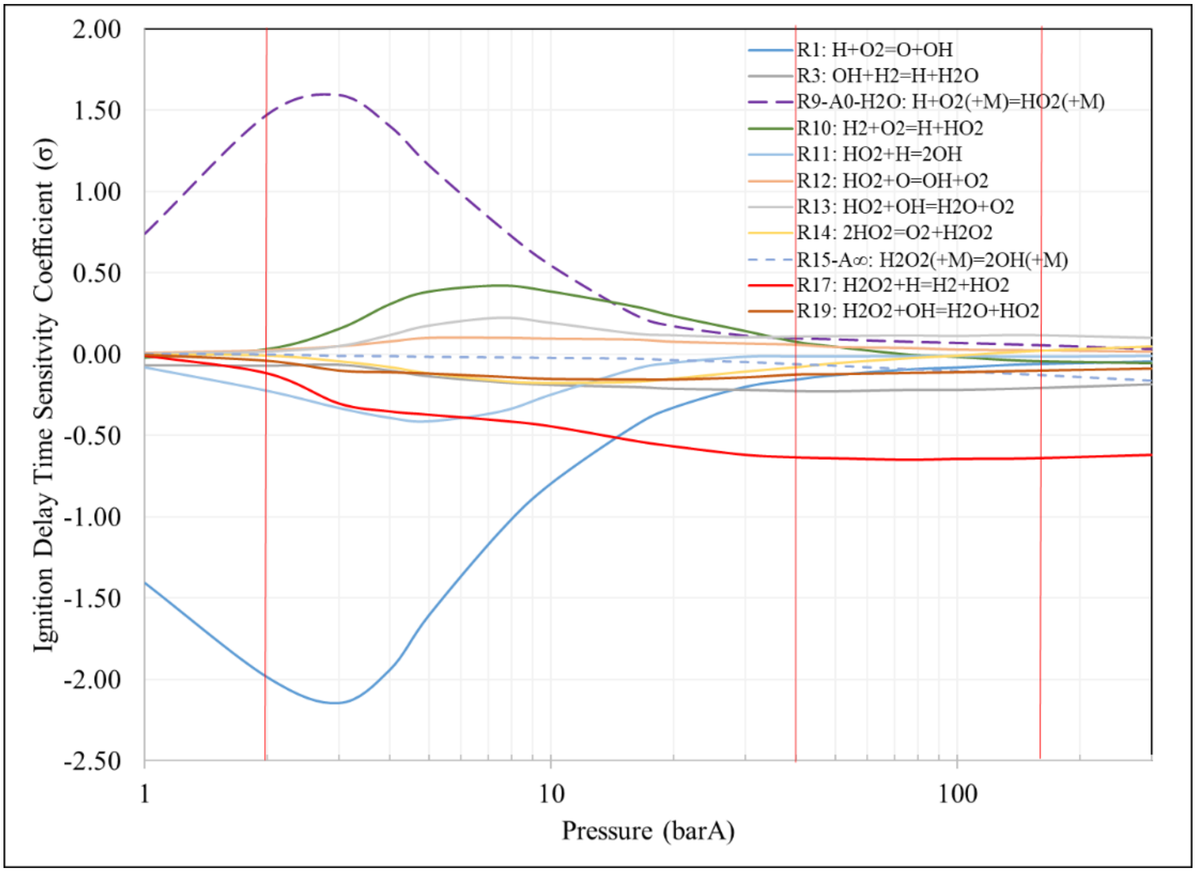

Figure 51: IDT-sensitive (max |σ|≥0.1) reaction rate parameters sensitivity coefficients vs. pressure for 4%H_2/45%H_2O/Ar φ=1 at 1222 K

ROP analysis of 4%H_2 φ=1 at ~40 bar in 45%H_2O/Ar bath:

ROP analyses were performed for a validated experiment in 45%H_2O/Ar bath, Test #33, conducted at 1222 K and 40 bar. This test was selected as its pressure and temperature conditions were similar those of test #25 (in Ar) and test #51 (in 45%CO_2) for which reaction pathways were analyzed in detail. Test #25 was conducted at 1209 K and 39.6 bar and test #51 at 1226 K and 40.6 bar. Figure 52, depicts the evolution of mole fraction of radicals and reaction intermediates, superimposed with normalized temperature, pressure and OH* mole fraction for Test #33.

In-line with the approach assumed for the previous ROP analyses, the OH*-, OH-, and temperature inflection-based IDTs were calculated to be 393, 457 and 440 µs, repectively. As such ROP data beyond 457 µs, were discarded.

Figure 52 illustrates that HO_2 radical pool build up is the largest followed by H_2O_2, which are then followed by a small buildup of OH and H radicals.

Comparisons of Figure 52 with its Ar- and CO_2-diluted counterparts at 40 bar (see Figure 37, and Figure 43) reveal that in the presence of 45% H_2O during the IDT period, maximum mole fraction of:

a. OH: was 2 orders of magnitude smaller than for Ar, and 20% lower than that of 45%CO_2 bath;
b. HO_2: doubled relative to in Ar bath, and was 40% larger than its value in 45%CO_2/Ar;
c. H_2O_2: was 90% higher and 13% lower relative to its counterparts in Ar and 45%CO_2/Ar baths;
d. H: was 490X and 3X lower than in Ar and 45%CO_2/Ar; and,
e. O: was 3 and 1 orders of magnitude lower in Ar and 45%CO_2/Ar, respectively.

Also, in the presence of 45% H_2O, mole fraction of HO_2 is 26X and nearly two and three orders of magnitude larger than OH, H, and O respectively. Examining the absolute value of mole fractions of radicals, suggests that shift in ratio of mole fractions of HO_2 and H_2O_2 vis-à-vis those of H, OH and O are a result of the significant reduction of the the latter three radicals' buildup. To understand the dominant reaction pathways ROP analyses results are examined.

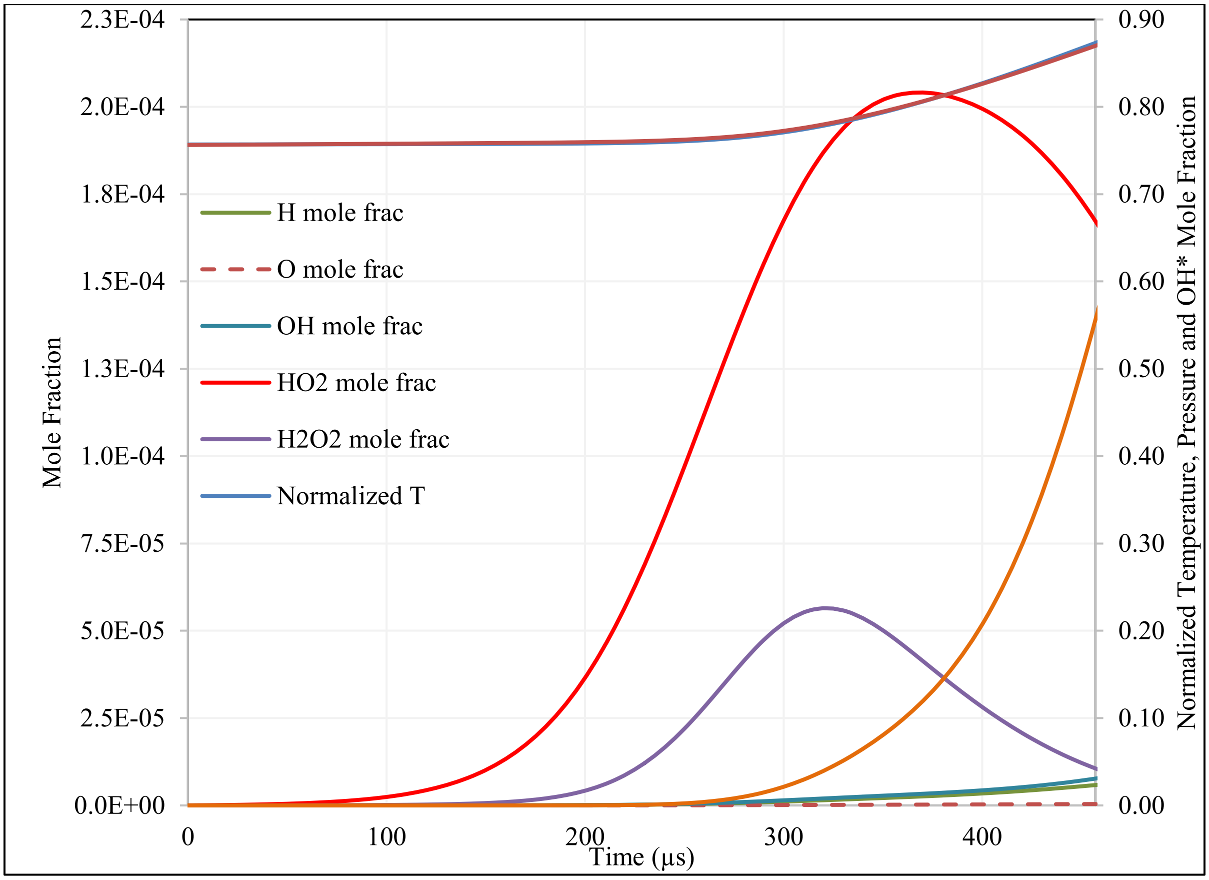

Figure 52: Mole fraction traces of radicals and reaction intermediates, superimposed with normalized temperature, pressure and OH* mole fraction for Test #33 – 4%H_2/45%H_2O/Ar φ=1 at 1222 K and 40 bar

Figure A45 to Figure A53 of Appendix C detail OH, H_2O_2, HO_2, H and O ROP analyses results for test #33. The analyses illustrate that at pressures of 40 bar and in the presence of 45% H_2O, the following OH production pathways are important:

Dominant path for the initial 170 µs:

R3: $OH+H_2=H+H_2O$

R9: $H+O_2(+M)=HO_2(+M)$

-R17: $H_2+HO_2=H+H_2O_2$

R15: $H_2O_2(+M)=OH+OH(+M)$

Dominant path from 175 µs to ignition at 457 µs

R3: $OH+H_2=H+H_2O$
R9: $H+O_2(+M)=HO_2(+M)$
R14: $HO_2+HO_2=O_2+H_2O_2$
R15: $H_2O_2(+M)=OH+OH(+M)$

Alternate path for the intial 200 μs:
R3: $OH+H_2=H+H_2O$
R9: $H+O_2(+M)=HO_2(+M)$
-R19: $H_2O+HO_2=OH+H_2O_2$
R15: $H_2O_2(+M)=OH+OH(+M)$

Alternate path from 200 μs to ignition at 457 μs:
R3: $OH+H_2=H+H_2O$
R9: $H+O_2(+M)=HO_2(+M)$
R11: $HO_2+H=2OH$

The above proposed pathways corroborate well with the IDT sensitivities identified, which showed that at 40 bar, the IDTs were most sensitive to R17, R3, R1, R19, R13, R9, R10, R14, R12 and R15 in order of priority. The two largest senstivities of R17 and R3 can be explained due to their critical role in the first dominant pathway, responsible for building the initial H radical and H_2O_2 pool.

R3's roll is more critical to in the presence of 45% H_2O, as indicated by its 10X and ~3X larger IDT sensitivity coefficients, relative to those observed for the Ar- and 45%CO_2/Ar baths, respectively. Involvement of R3 in all pathways, and H radical's significantly lower mole fractions and high production rates in the presence of 45% H_2O, point to H radical and in turn R3's important role in the reaction pathways.

Negative sensitivity coefficients of R1 and R15 are attributed to their chain branching nature, producing O and OH radicals. Similarly, R19's contribution to the OH and H_2O_2 pool, which is an integral part of the alternate pathway listed, explains its negative IDT sensitivity coefficient calculated. Finally, the chain terminating nature of R13: $HO_2+OH=H_2O+O_2$, –R10: $H+HO_2=O_2+H_2$ and R12: $HO_2+O=OH+O_2$ explains their non-negligible positive IDT sensitivities. This concludes the reaction pathway determination for 45%H_2O/Ar bath.

In order to delineate the impact of presence of 45%H_2O vs. 45%CO_2 vs. pure Argon at 40 bar, it is beneficial to compare the dominant reactive pathways identified for each bath gas. To this end, Table 15, depicts the pathways based on ROP and sensitivity analyses presented in section 6.2, for test #25 (in Ar), and in section 6.3 for test #51 (in 45%CO_2/Ar), alongside those of test #33 (in 45%H_2O/Ar). It can be observed that in the presence of 45%H_2O, in contrast to both Ar and 45%CO_2/Ar baths, the path through R3+R9+R11, is no longer dominant and has become an alternate path. Moreover, the path through, R3+R9+(-R19)+R15, has gained significance and serves as an alternate path in the presence of H_2O.

Table 15: Comparison of reactive pathways for ignition of 4%H_2 φ=1 in Ar vs. 45%CO_2/Ar vs. 45%H_2O/Ar bath at 40 bar

Ar bath at ~40 bar and 1209 K	45%CO_2/Ar bath at 40.6 bar 1226 K	45%H_2O/Ar bath at 40 bar 1222 K
IDT Regime: Intermediate T & P (peak of transition)	IDT Regime: Intermediate T & P (nearing transition to low T)	IDT Regime: Low T and intermediate P (transition nearing low T)
Dominant path (0-125µs): R1: $H+O_2=O+OH$ R2: $O+H_2=H+OH$ R3: $OH+H_2=H_2O+H$	Dominant path (0-25µs): R1: $H+O_2=O+OH$ R2: $O+H_2=H+OH$ R3: $OH+H_2=H_2O+H$	
	Dominant path (25-170 µs): R3: $OH+H_2=H+H_2O$ R9: $H+O_2(+M)=HO_2(+M)$ -R17: $HO_2+H_2=H_2O_2+H$ R15: $H_2O_2=OH+OH$	Dominant path (0-170 µs): R3: $OH+H_2=H+H_2O$ R9: $H+O_2(+M)=HO_2(+M)$ -R17: $H_2+HO_2=H+H_2O_2$ R15: $H_2O_2(+M)=OH+OH(+M)$
	Dominant path (170-280 µs): R3+R9+R15 +R14: $HO_2+HO_2= H_2O_2+O_2$	Dominant path (170-ignition/457 µs) R3+R9+R15 +R14: $HO_2+HO_2= H_2O_2+O_2$
Dominant path (125-ignition/144 µs): R3: $OH+H_2=H_2O+H$ R9: $H+O2=HO_2$ R11: $H+HO_2=OH+OH$	Dominant path (280-ignition at 449 µs): R3: $OH+H_2=H+H_2O$ R9: $H+O_2(+M)=HO_2(+M)$ R11: $HO_2+H=OH+OH$	
		Alternate path (0-200 µs): R3+R9+R15 -R19: $H_2O+HO_2=OH+H_2O_2$
		Alternate path (200 µs–ignition/457 µs): R3: $OH+H_2=H+H_2O$ R9: $H+O_2(+M)=HO_2(+M)$ R11: $HO_2+H=OH+OH$

ROP analysis of 4%H_2 φ=1 at 150 bar in 45%H_2O/Ar bath:

With the bath gas effect better understood at 40 bar it is also important to understand the effect of presence of H_2O at higher pressures of 150 bar. This also enables delineation of the pressure effect from that of the bath gas. Hence, test #33 was resimulated and analyzed at a higher pressure of 150 bar. For this test the calculated IDTs were 127, 121 and 140 µs, based on OH*, OH, and temperature inflection time, respectively. As such, all data beyond 140 µs were discarded.

Figure 53 illustrates the evolution of OH, H, O, HO_2 and H_2O_2 mole fractions superimposed by the normalized (by maximum value) temperature, pressure, and OH* mole fractions. This figure illustrates that HO_2 radical pool build up is the largest followed by H_2O_2.

Comparison of Figure 53 with its counterpart at 40 bar, Figure 52 reveals that at 150 bar peak mole fractions of:

a. OH was 24% lower;
b. HO_2 was 20% higher;
c. H_2O_2 had doubled; and,
d. H and O were both 2.4X lower than their counterparts at 40 bar.

Comparisons of Figure 53 with its counterparts at 150 bar, in Ar and 45%CO_2/Ar baths (Figure 38 and Figure 44) show that for the 45%H_2O/Ar bath the maximum mole fraction of:

e. OH: was 36X and 2X lower relative to Ar and 45%CO_2/Ar baths;
f. HO_2: was 36% and 48% higher than those in Ar and 45%CO_2/Ar;
g. H_2O_2: was 15% and 2% higher relative to those in Ar and 45%CO_2/Ar baths;
h. H: was 156X and 13% lower than in Ar and 45%CO_2/Ar; and,
i. O: was 287X and 2X lower in Ar and 45%CO_2/Ar, respectively.

In order to understand the reaction pathways involved ROP analyses of radicals and intermediate species are conducted for the extrapolated case at 150 bar in 45%H_2O/Ar bath. Figure A54 to Figure A61 illustrate the OH, H_2O_2, HO_2, and H absolute and normalized ROP plots for test #33 at 150 bar.

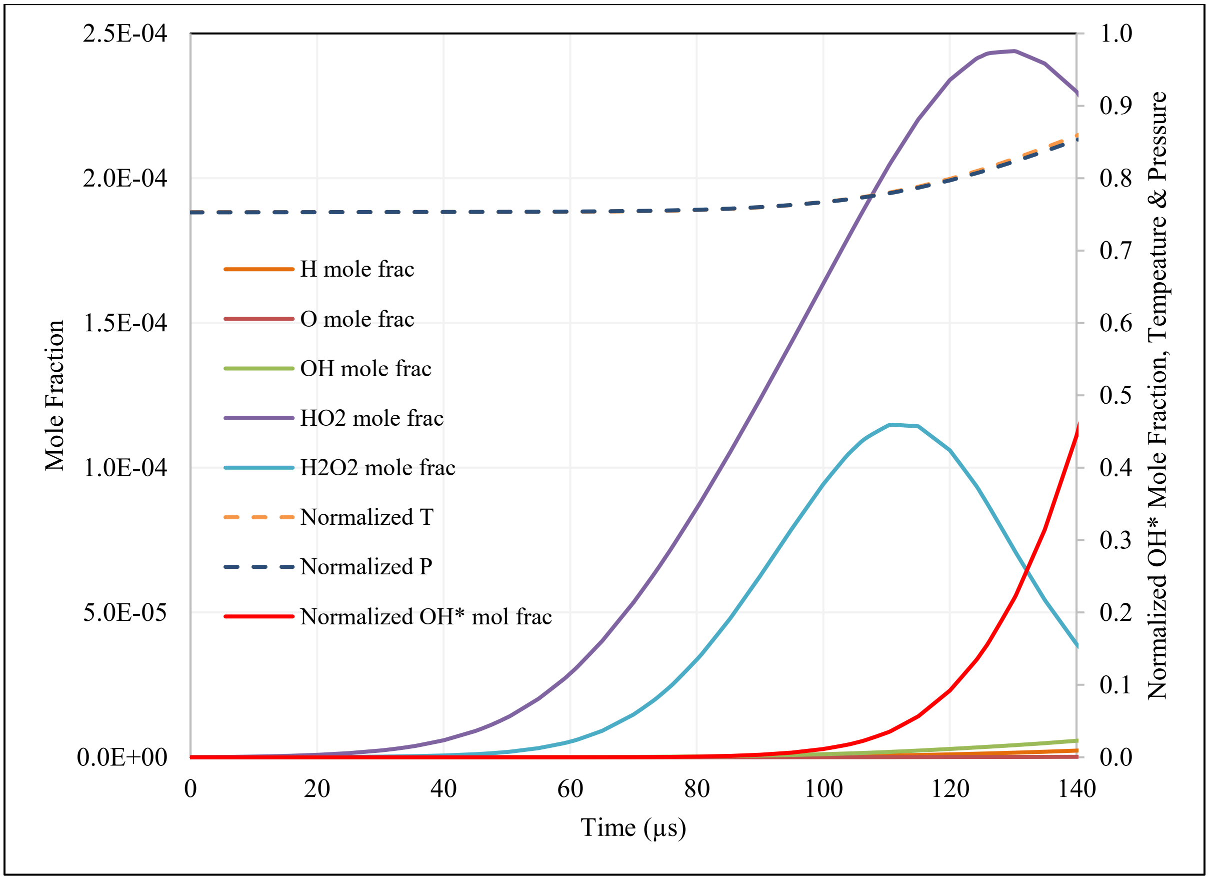

Figure 53: Mole fraction traces of radicals and reaction intermediates, superimposed with normalized temperature, pressure and OH* mole fraction for 4%H_2/45%H_2O/Ar φ=1 at 1222 K and 150 bar

ROP analyses reveal that for 4%H_2/45%H_2O/Ar φ=1 at 1222 K and 150 bar, for production of OH the:

Dominant reaction path for the first 55 μs, is:

R3: $OH+H_2=H+H_2O$

R9: $H+O_2(+M)=HO_2(+M)$

-R17: $HO_2+H_2=H_2O_2+H$

R15: $H_2O_2(+M)=OH+OH$

Dominant path from 55 μs until ignition at 140 μs, is:

R3: $OH+H_2=H+H_2O$

R9: $H+O_2(+M)=HO_2(+M)$

R14: $HO_2+HO_2=H_2O_2+O_2$

R15: $H_2O_2(+M)=OH+OH$

Alternate path from 0-60 μs, is:

R3: $OH+H_2=H+H_2O$

R9: $H+O_2(+M)=HO_2(+M)$

-R19: $H_2O+HO_2=H_2O_2+OH$

R15: $H_2O_2(+M)=OH+OH$

The above proposed reaction paths are confirmed through corroboration with the pressure-dependent IDT sensivities of Figure 51 at 150 bar. This figure showed that at 150 bar, IDTs were most sensitive to R17, R3, R15, R13, R19, and to lesser extents R1, R9, R10, R12, R14 and R11.

-R17 and -R19 role in building the H_2O_2 pool, in addition to simultaneous production of H and OH by –R17 and –R19 explains their observed sensitivities.

Normalized OH ROP analysis (Figure A55) shows that R13 in fact proceeds in the reverse direction and takes on a chain branching role for the first 30 μs. It, however, switches direction and takes on a chain terminating role until ignition. Normalized HO_2 and H ROP plots (Figure A59 and Figure A61) show that R10 for the initial 50 μs of reaction time, plays a chain branching role, after which it reverses direction, and becomes a radical recombining chain terminating reaction. Dominance of the path through R15: $H_2O_2(+M)=OH+OH(+M)$, has significantly increased with pressure, which explains its increased relative sensitivity. Conversely, the chain terminating reactions R13: $HO_2+OH=H_2O+O_2$, and R12: $HO_2+O=OH+O_2$ all exhibit positive IDT sensitivities. Also R10 IDT reducing effect, as indicated by its negative senstivity at 150 bar, is either due to its initial (first 50 μs) H-producing role (seeFigure A61), or due to its exothermic, temperature increasing effect when it proceeds in its reverse direction later on in the IDT period. –R10: $H+HO_2=H_2+O_2$ has a a heat of reaction of -220 kJ/mol at 1200 K.

Combining the above findings, and comparing the reaction paths with those at 40 bar, enables understanding the pressure effect. Table 16 provides a summary of reaction pathways at 40 vs. 150 bar in 45%H_2O/Ar bath gas. This table shows that the increase in pressure has not impacted the dominant reaction paths, although it has changed their relative contributions. With increased pressure dominance of alternate path through R3+R9+(-R19)+R15 has increased, whereas the relative contributions of alternate paths through R1+R2+R3 as well as R3+R9+R11 have decreased. Their peak contribution to OH radical pool were less than 20%, as such, they were not included as alternate paths at 150 bar.

Table 16: Summary of reaction pathways at 40 vs. 150 bar in 45%H_2O/Ar bath gas

45%H_2O/Ar bath at 40 bar 1222 K	45%H_2O/Ar bath at 150 bar 1222 K
IDT Regime: Low T and intermediate P (transition nearing low T)	IDT Regime: Low T and high P
Dominant path (0-170 μs): R3: $OH+H_2=H+H_2O$ R9: $H+O_2(+M)=HO_2(+M)$ -R17: $H_2+HO_2=H+H_2O_2$ R15: $H_2O_2(+M)=OH+OH(+M)$	Dominant path (0-55 μs): R3: $OH+H_2=H+H_2O$ R9: $H+O_2(+M)=HO_2(+M)$ -R17: $H_2+HO_2=H+H_2O_2$ R15: $H_2O_2(+M)=OH+OH(+M)$
Dominant path (170-ignition/457 μs) R3+R9+R15 +R14: $HO_2+HO_2= H_2O_2+O_2$	Dominant path (55-ignition/140 μs) R3+R9+R15 +R14: $HO_2+HO_2= H_2O_2+O_2$
Alternate path (0-200 μs): R3+R9+R15 -R19: $H_2O+HO_2=OH+H_2O_2$	Alternate path (0-60 μs): R3+R9+R15 -R19: $H_2O+HO_2=OH+H_2O_2$
Alternate path (200 μs–ignition/457 μs): R3: $OH+H_2=H+H_2O$ R9: $H+O_2(+M)=HO_2(+M)$ R11: $HO_2+H=OH+OH$	

To delineate the different bath gases effects at 150 bar it is also important to compare the reaction pathways identified for each. Table 17 provides a comparison of these reaction pathways in Ar vs. 45%CO_2/Ar vs. 45%H_2O/Ar bath at 150 bar. It can be observed in the presence of either 45%CO_2/Ar or 45%H_2O/Ar the reaction path through R3+R9+R11 is no longer dominant in contrast to the case of pure Ar bath. Moreover, all dominant reaction paths involved rely on R15 as the main means of production of OH. One newly significant pathway has also emerged in the presence of 45%H_2O/Ar through R3+R9+(-R19)+R15.

Table 17: Comparison of reactive pathways for ignition of 4%H_2 φ=1 in Ar vs. 45%CO_2/Ar vs. 45%H_2O/Ar bath at 150 bar

Ar bath at 150 bar and 1209 K	45%CO_2/Ar bath at 150 bar 1226 K	45%H_2O/Ar bath at 150 bar 1222 K
IDT Regime: Low T + High P (transition to low T chemistry is nearing completion)	IDT Regime: Low T high P	IDT Regime: Low T and high P
Dominant path (0-8 µs) R1: $H+O_2=O+OH$ R2: $O+H_2=H+OH$ R3: $OH+H_2=H_2O+H$		
Dominant path (8-70 µs): R3: $OH+H_2=H_2O+H$ R9: $H+O_2=HO_2$ -R17: $HO_2+H_2=H_2O_2+H$ R15: $H_2O_2(+M)=OH+OH(+M)$	Dominant for the initial 0-65 µs: R3: $OH+H_2=H+H_2O$ R9: $H+O_2(+M)=HO_2(+M)$ -R17: $HO_2+H_2=H_2O_2+H$ R15: $H_2O_2=OH+OH$	Dominant path (0-55 µs): R3: $OH+H_2=H+H_2O$ R9: $H+O_2(+M)=HO_2(+M)$ -R17: $H_2+HO_2=H+H_2O_2$ R15: $H_2O_2(+M)=OH+OH(+M)$
Dominant path (70-132 µs): R3+R9+R15 +R14: $HO_2+HO_2=H_2O_2+O_2$	Dominant path (65-ignition/180µs): R3+R9+R15 +R14: $HO_2+HO_2=H_2O_2+O_2$	Dominant path (55-ignition/140 µs) R3+R9+R15 +R14: $HO_2+HO_2=H_2O_2+O_2$
Dominant path (132-ignition/149 µs): R3: $OH+H_2=H_2O+H$ R9: $H+O_2=HO_2$ R11: $H+HO_2=OH+OH$		
	Alternate path (0-85 µs) R1: $H+O_2=O+OH$ R2: $O+H_2=H+OH$ R3: $OH+H_2=H_2O+H$	
	Alternte path (85-ignition/180 µs): R3: $OH+H_2=H_2O+H$ R9: $H+O_2=HO_2$ R11: $H+HO_2=OH+OH$	
		Alternate path (0-60 µs): R3+R9+R15 -R19: $H_2O+HO_2=OH+H_2O_2$

Comparison of the dominant pathways and ROP analyses of 45%H_2O diluted mixtures vs. reactive mixtures in 45%CO_2 vs. reactive mixtures in pure Ar, at pressures of 40 and 150 bar illustrates the following:

1- At 150 bar, OH production is dominated by H_2O_2 decomposition through R15: H_2O_2(+M)=OH+OH(+M) at the initial stages for all bath gases, except for Ar, it is preceeded by a shortlived dominance of R1+R2+R3.

2- At 150 bar, for all bath gases, these initial stages involving H_2O_2 production, take place first through -R17: HO_2+H_2=H_2O_2+H, and later through R14: HO_2+HO_2= H_2O_2+O_2.

3- At 150 bar after the intial stages the dominant reaction path:
   a. For Ar, becomes R3+R9+R11; and
   b. For 45%H_2O and 45%CO_2, remains R3+R9+R14+R15.

4- At 40 bar, the initial stages of reactivity are dominated by R1+R2+R3 for both Ar and 45% CO_2.

5- At 40 bar, the initial stages OH production:
   a. For Ar, involves R1+R2+R3;
   b. For 45%CO_2, involves R1+R2+R3, followed by R3+R9+R15-R17; and,
   c. For 45%H_2O, involves R3+R9+R15-R17.

6- At 40 bar after the intial stages the dominant reaction path:
   a. For Ar, becomes R3+R9+ R11;
   b. For 45%CO_2, becomes R3+R9+ R11 until ignition; and,
   c. For 45%H_2O, becomes R3+R9+R14+R15, involving H_2O_2.

7- At 2 bar, the dominant reaction path in Ar involves only R1+R2+R3, and is independent of reaction pathways involving HO_2 and H_2O_2.

With the reaction pathways understood at different pressures for 45%H_2O at 1222 K, to gain insight into the effect of temperature on pressurized combustion chemistry, temperature-dependent IDT sensitivity analyses are conducted.

Figure 54 depicts IDT sensitivity variations of kinetics parameters for an extended temperature range of 975-2025 K for 4%H_2/45%H_2O/Ar with $\varphi=1$ at 40 bar. The figure illustrates that sensitivities change over the temperature range of 1222 K-2025 K. There is a drastic change taking place near 1450-1750 K. Within this region R3, R11, R12, R14, R10, and even R9 sensitivities change sign. This is important as, with the exception of R10 and R12, the other reactions were shown to be instrumental to pathways leading ignition near 1226 K. The chemistry over this 300 K span, even though in a transitional regime, is at high enough temperatures, relevant to combustor design, which necessitates further investigation. Moreover, at temperatures above 1750 K, yet another dominant chemistry change may be emerging, signified by a change in sign of sensitivity coefficient of R9, which also calls for further analysis.

Over the complete temperature span explored experimentally in this work, it can be observed that reactivity is not as dominated by R9 and R1 as it is at higher temperatures (>1250 K). Comparison of Figure 54 with its Ar-diluted counterpart at similar conditions (see Figure 19) reveals that the sensitivity bounds shrink from +1.75/-2.25 in Ar, to +0.45/-0.7 in 45% H_2O/Ar. This suggests a significant increase in IDT-sensitivities of other reactions, relative to those of R1 and R9.

Comparison of Figure 54 with its 40 bar Ar-only- and 45%CO_2-diluted counterparts at similar conditions, Figure 19 and Figure 45, reveals unique features brought about by the presence of 45% H_2O. For example the emergence of IDT sensitive reactions -R19: $HO_2+H_2O=H_2O_2+OH$ and R8: $H+OH(+M)=H_2O(+M)$. The near equivalent sensitivity of R8's low- and high-pressure-limit rate suggests that the reaction is likely in the fall-off regime. As such, implementation of a pressure-dependent rate is important, which is an advantage of CanMECH 1.0 to models like Keromnes et al. [28], which assumes this reaction to be at its low-pressure limit.

Moreover, R9's Ar-specific rate low-pressure-limit rate, which was a tuned parameter of CanMECH 1.0 (see section 5.5), is not an IDT-sensitive parameter across the extended temperature range of 975-2025. This shows that it is more important to have an accurate H_2O-specific low-pressure-limit rate for R9, with its own center broadening factor and temperature dependencies, which was done in CanMECH 1.0, without any tuning.

Another unique feature of presence of H_2O is the change in sensitivity sign of R9 at temperatures above 1750 K. This needs to be explored, as in the other bath gases this reaction always inhibited reactivity.

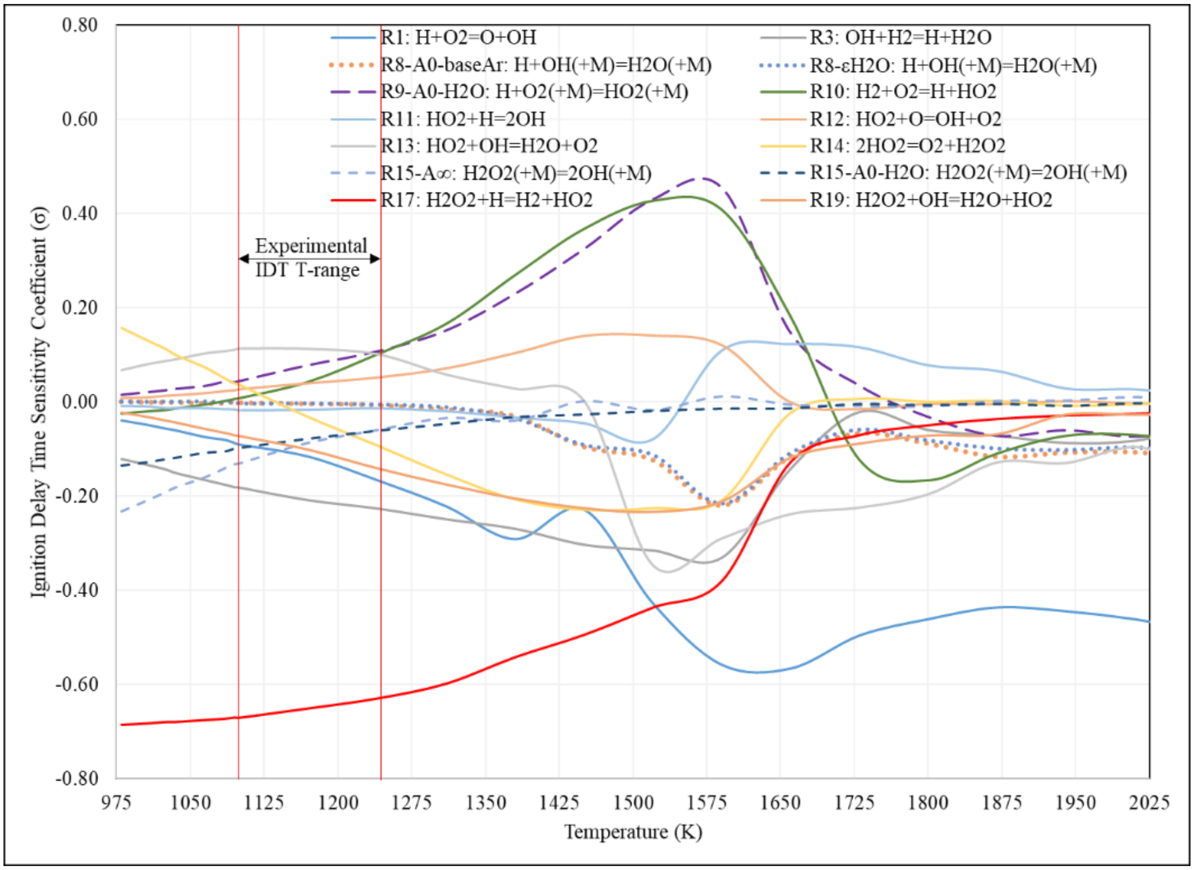

Figure 54: IDT-sensitive (max |σ|≥0.1) reaction rate parameters sensitivity coefficients vs. temperature for 4%H_2-45%H_2O/Ar φ=1 at 40 bar

More generally, comparison of sensitivities with Ar- and CO_2-diluted ones from Figure 19 and Figure 45, shows that the presence of H_2O shifts the chemistry towards that resembling a lower temperature one at higher temperatures. To delineate these chemistries, the temperature at which R9 and R1's IDT sensitivities peak provides a useful reference point for comparison. The peak competition of R9 and R1 occurs at 1575 K for 45%H_2O-diluted bath gas vs. at 1250, and 1400 K for its Ar- and CO_2/Ar-diluted counterparts, see Figure 39 and Figure 45.

To complete the mapping of the combined temperature and pressure effect, Figure 55, depicts the IDT sensitivity of important reactions (max |σ|≥0.1) for 4%H_2-45%H_2O/Ar φ=1 at 150 bar, over the extended temperature range of 920-2200 K. It can be observed that the IDT sensitivities of R1 and R9 relative to other reactions', have subsided the most, among all mixtures and pressure conditions explored so far in this work. Moreover, R9, appears to be deeper in the fall-off regime, as indicated by the increased sensitivity to R9’s high-pressure-limit rate vis-à-vis the reduced sensitivity to its low-pressure-limit rate at 150 bar.

At 150 bar, sensitivities of R15 are significant at temperatures of up to 1600 K, whereas at 40 bar it becomes insignificantly sensitive below 1500 K, see Figure 54.

R8’s IDT decreasing effect is delayed with increase in pressure from 40 to 150 bar, from 1400 K to 1800 K.

R4: 2OH=O+H_2O also appears in the list of sensitive reactions whereas that was not the case for any of the temperature dependent IDT analyses presented in this work so far, namely: Figure 39, Figure 40, Figure 45, Figure 46, and Figure 54.

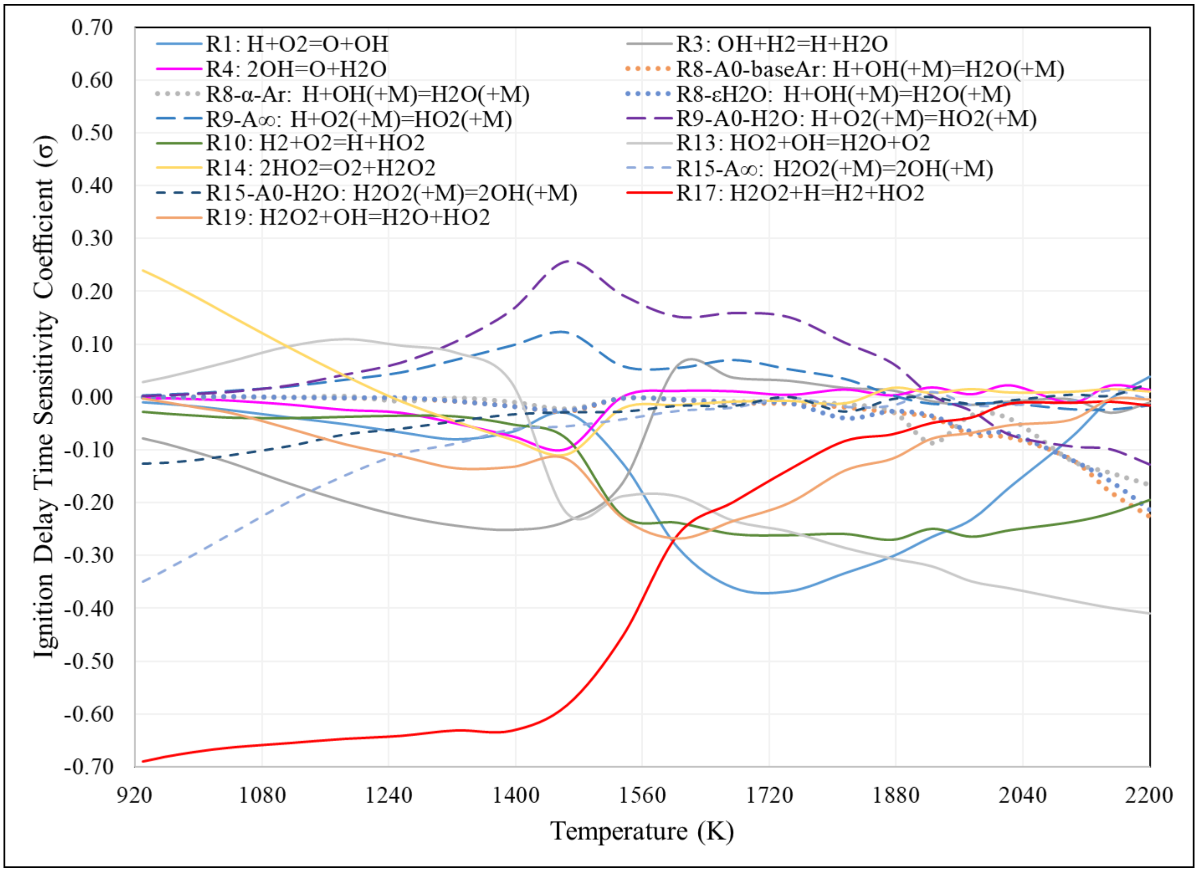

Figure 55: IDT-sensitive (max |σ|≥0.1) reaction rate parameters sensitivity coefficients vs. temperature for 4%H_2-45%H_2O/Ar φ=1 at 150 bar

This concludes the analysis in mapping the combined effect of pressure and temperature for 45%H_2O/Ar-diluted mixtures. The analyses suggest that the chemistry at higher temperatures and pressures have unique features that must be explored as possible future work. There are three major shifts in reaction pathways that take place at temperatures beyond those analyzed in detail in this work, which remain to be understood.

Finally, to map the effect of different concentrations of H_2O along with pressure and temperature on IDTs, parametric IDT temperature sweeps are conducted at H_2O concentrations of 0-65%, at pressures of 2, 40 and 150 bar, and temperatures of 940-2200 K.

Figure 56, Figure 57, and Figure 58 depict IDT temperature sweeps at concentrations of 0-65% H_2O with the balance Ar at 2, 40 and 150 bar, respectively.

Figure 56, shows that increasing the concentration of H_2O, increases IDTs at temperatures below 1500 K, and at higher temperatures it does not have a noticeable effect. Moreover, with increased concentrations of H_2O, the temperature at which deviation from high temperature chemistry starts to reveal itself is pushed to higher temperatures. Figure 56, indicates that the transition starts at roughly 1000, 1175, 1250, 1270, 1350, 1475, 1500, 1525 K for 2%, 5%, 10%, 20%, 30%, 45%, 55%, and 65% H_2O dilutions, respectively, at 2 bar. Comparison of Figure 56 with its counterpart generated for CO_2 (Figure 47), indicates H_2O pushes the lower temperature chemistry to higher temperatures, more than CO_2, and even at low concentrations H_2O, e.g. 2%, has a large impact on increasing IDTs.

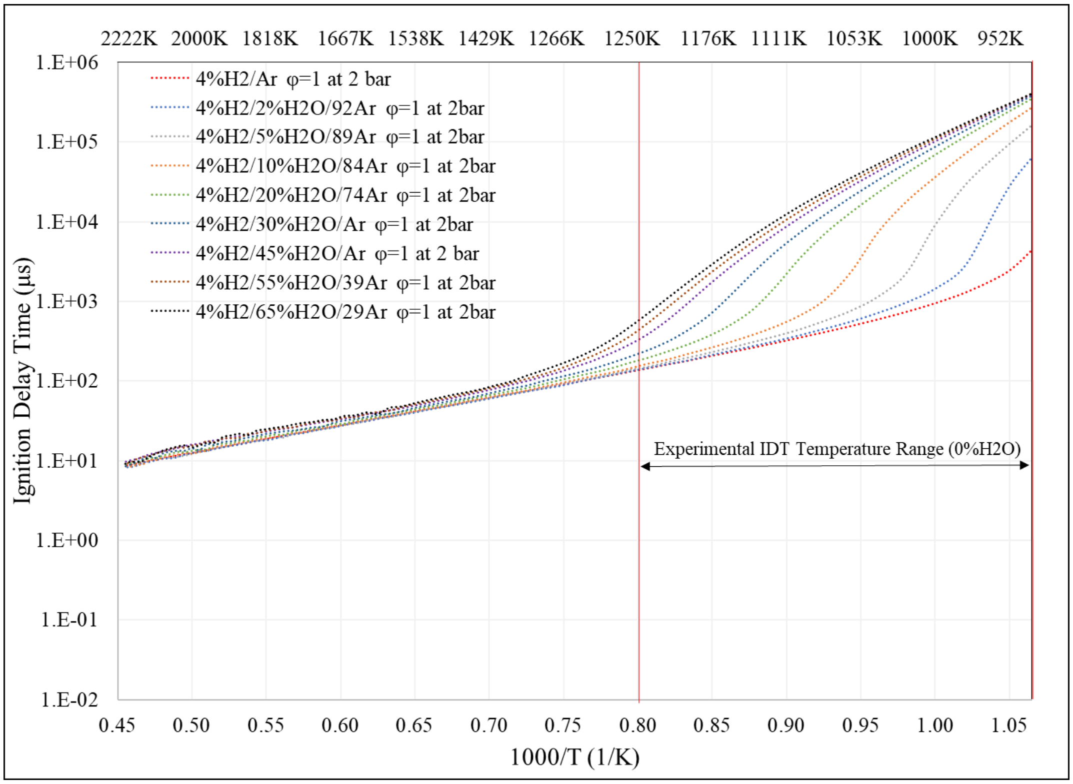

Figure 56: IDT temperature sweep for 4%H_2/0-65%H_2O/Ar φ=1 at 940-2200 K, 2 bar

Figure 57, provides IDT temperature sweeps for 4%H_2/0-62%H_2O/Ar φ=1 at 940-2200 K, at 40 bar. This figure illustrates that incremental increase of H_2O concentration from 0 to approximately 35% increases the simulated IDTs. However, increases in H_2O concentrations beyond 35%, reduces the IDTs observed at temperatures in the range of 1150-1800 K. Also, as the H_2O concentration increases, the transition from one chemistry to another (through the "S-shape" of the graphs) is less noticeable and stretches over a larger temperature span. This is similar to the effect of increased pressure on IDTs. A feature unique to H_2O diluted mixtures is that its presence reduces ignition delay time at the low temperature end, relative to both Ar and CO_2-diluted bath gases. For example, for 62%H_2O concentration, IDTs at temperatures below 1020 K are lower than its Ar-only diluted counterpart. This is in contrast with CO_2-diluted chemistries which increase the IDTs at low temperatures, see Figure 48. Comparison with Figure 48 also indicates that H_2O dilution, shifts the dominance of chemistry with low-temperature high-pressure features to higher temperatures, more than in the case of CO_2 dilution.

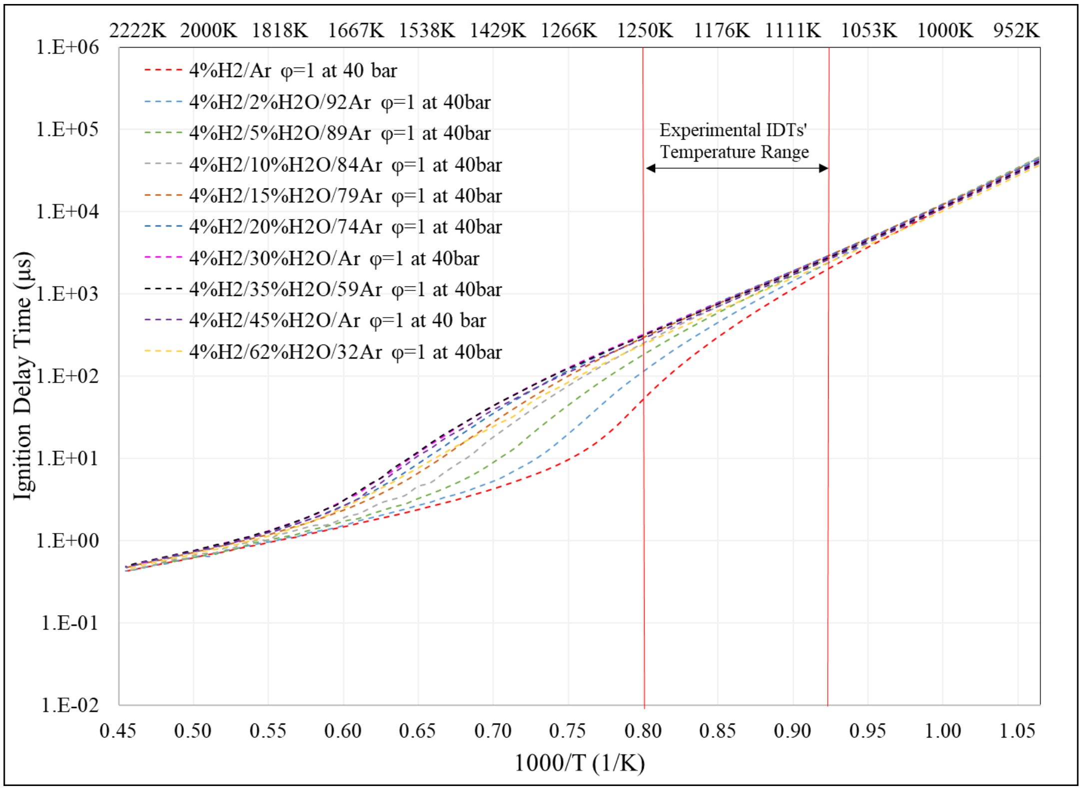

Figure 57: IDT temperature sweep for 4%H_2/0-65%H_2O/Ar φ=1 at 940-2200 K, 40 bar

Figure 58 shows the results of IDT temperature sweeps for 4%H_2/0-65%H_2O/Ar φ=1 at 940-2200 K at 150 bar. The figure shows that with increased concentration of H_2O, the boundaries between potential variations in reaction paths become less distinguishable, to the point that at 65% H_2O dilution, such chemistry effects become unnoticeable. A unique feature of 150 bar H_2O-laden conditions, is that with increased concentrations of H_2O, IDTs become the lowest over larger temperature spans, both at higher and lower temperatures. To the point that at the highest H_2O concentration of 65%H_2O, this mixture exhibits the lowest ignition delay time for temperatures below 1260 K and above 1800 K. While this effect is small, it is signifies an increase in global reactivity, over larger temperature ranges, at higher pressures in presence of large concentrations of H_2O. Moreover, there appears to be a mid-range concentration of H_2O, for which, IDTs are at their maximum. At 150 bar this concentration is 20% for H_2O. Comparison of Figure 58 with Figure 57 shows that this concentration has changed from 35% to 20%, when the pressure is increased from 40 bar to 150 bar.

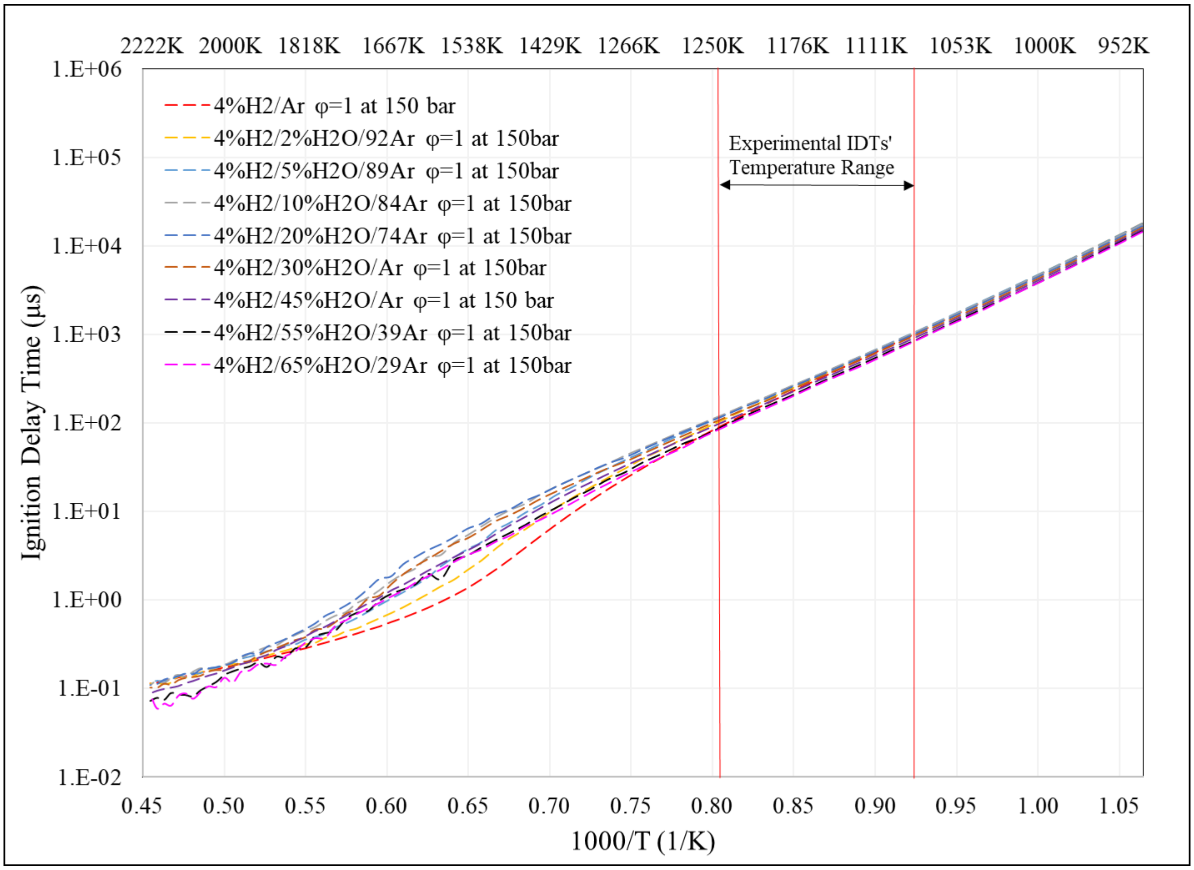

Figure 58: IDT temperature sweep for 4%H_2/0-65%H_2O/Ar φ=1 at 940-2200 K, 150 bar

This concludes the analysis and mapping of the individual and combined effect of pressure and temperature H_2O concentrations, on combustion kinetics. Next section briefly discusses the combined effect of presence of H_2O and CO_2 at different pressures and temperatures.

6.5 Effect of presence of 30%H_2O/15%CO_2 on combustion chemistry at different pressures

With the individual effects of pressure, temperature, and concentrations of H_2O and CO_2 mapped, this section explores the impact of simultaneous presence of these bath gases.

Figure 59 depicts IDT variation with temperature and pressure for 4%H_2/30%H_2O/15%CO_2/Ar φ=1 at 2, 40, and 150 bar. It can be observed that, with increased pressure, IDTs generally reduce. The exception is for the 2 bar simulated IDTs which become shorter than those at 40 bar for temperatures between 1180 and 1270 K. This is a result of dominance of the faster high temperature chemistry at low pressures and at temperatures above ~1260 K. However, after the chemistry has transitioned to the low-temperature low-pressure one, IDTs of 2 bar exceed their 40 bar counterparts.

Figure 60 superimposes IDT temperature sweep results for 4%H_2 in 30%H_2O/15%CO_2/Ar, 45%H_2O/Ar and 45%CO_2/Ar at $\varphi=1$ at pressures of 40 and 150 bar, at 940-2200 K. This figure shows that:

a. At 40 bar, the effect of 30% H_2O is more dominanting than the 15%CO_2, indicated by the near-complete overlap of 30%H_2O/Ar with 45%H_2O/Ar at 40 bar. Moreover, at this pressure, the presence of 30%H_2O/15%CO_2/Ar reduces IDTs at temperatures below 1250 K, relative to those in 45%CO_2/Ar bath, but slightly increases them relative to their 45%H_2O-diluted counterparts.

b. At 150 bar, the impact of bath gas has a reduced impact, relative to those at 40 bar. IDT sweeps of 30%H_2O/15%CO_2/Ar resemble those of 45%H_2O/Ar more closely than the 45%CO_2/Ar-diluted mixtures. The presence of 30% H_2O/15%CO_2, reduces IDTs relative 45%CO_2/Ar at temperatures lower than 1270 K and above 1800 K, and slightly increase IDTs relative to those with 45%H_2O/Ar bath gas over the aforementioned temperature spans.

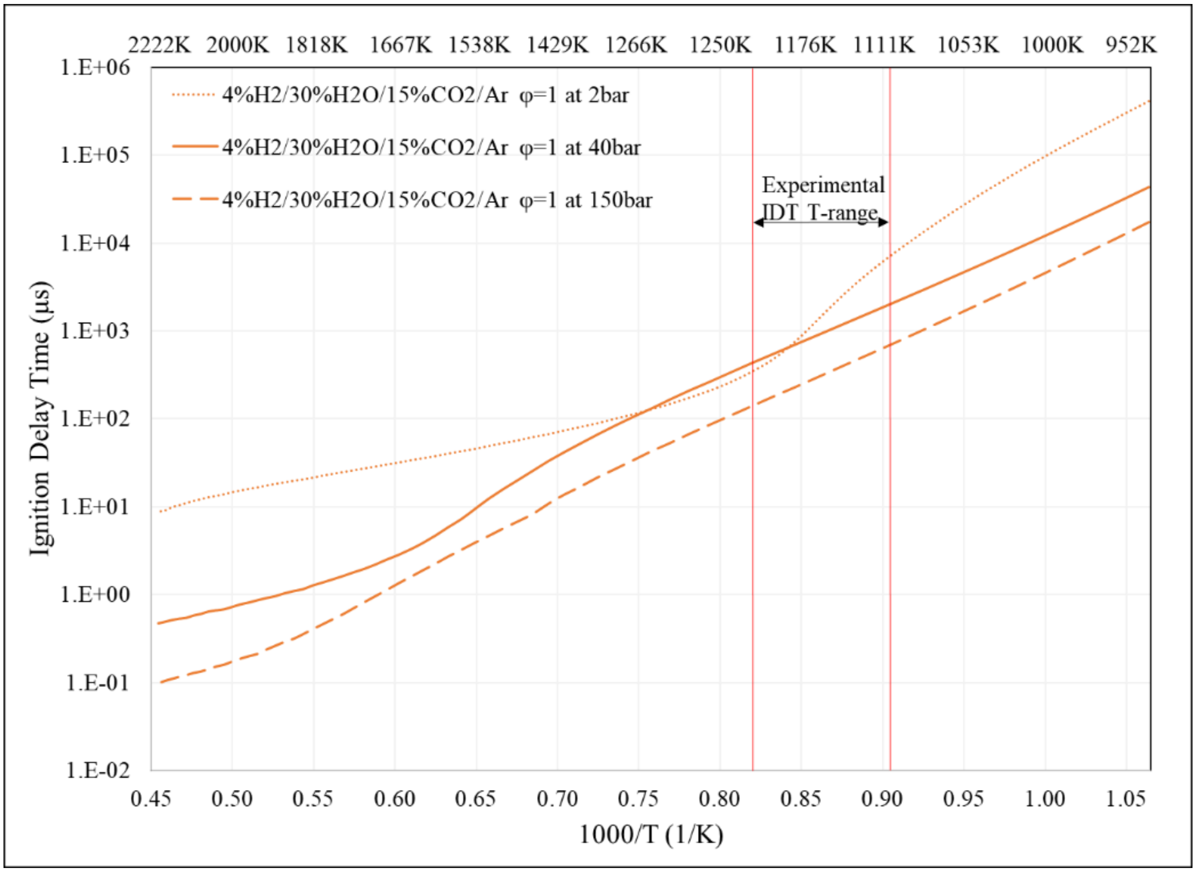

Figure 59: IDT variation with temperature & pressure for 4%H_2/30%H_2O/15%CO_2/Ar φ=1 at 2, 40, and 150 bar

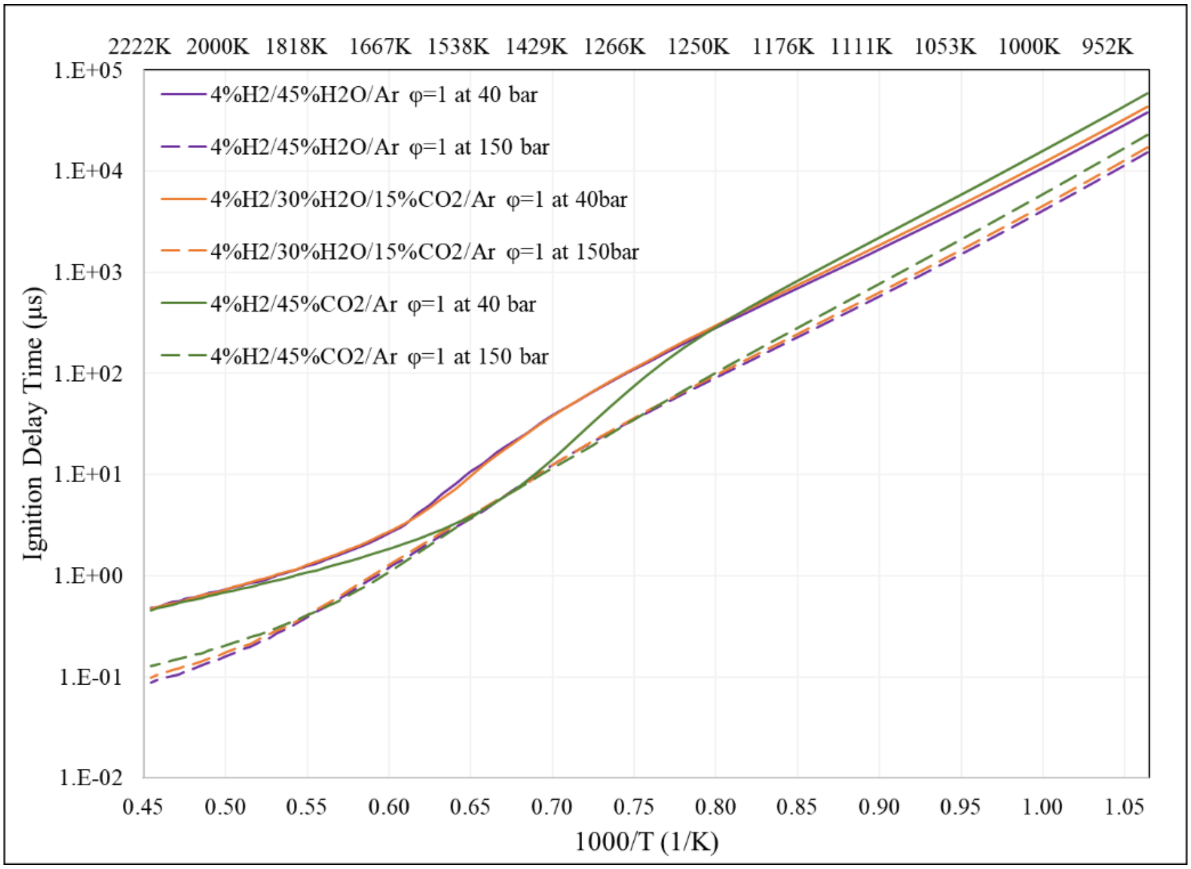

Figure 60: IDT variation with temperature & pressure for 4%H_2 in 30%H_2O/15%CO_2/Ar, 45%H_2O/Ar and 45%CO_2/Ar at φ=1 at 40 and 150 bar

For further insight into the potential changes in chemistry, pressure and temperature dependent IDT-senstivities are examined.

Figure 61 depicts pressure-dependent IDT sensitivity analysis for 4%H_2/30%H_2O/15%CO_2/Ar φ=1 at 1232 K. Comparison of this figure with the pressure-dependent IDT sensitivity chart of 45%H_2O/Ar at 1209 K (Figure 51), reveals that the trends are nearly identical with the exception of a small change in R9's sensitivity.

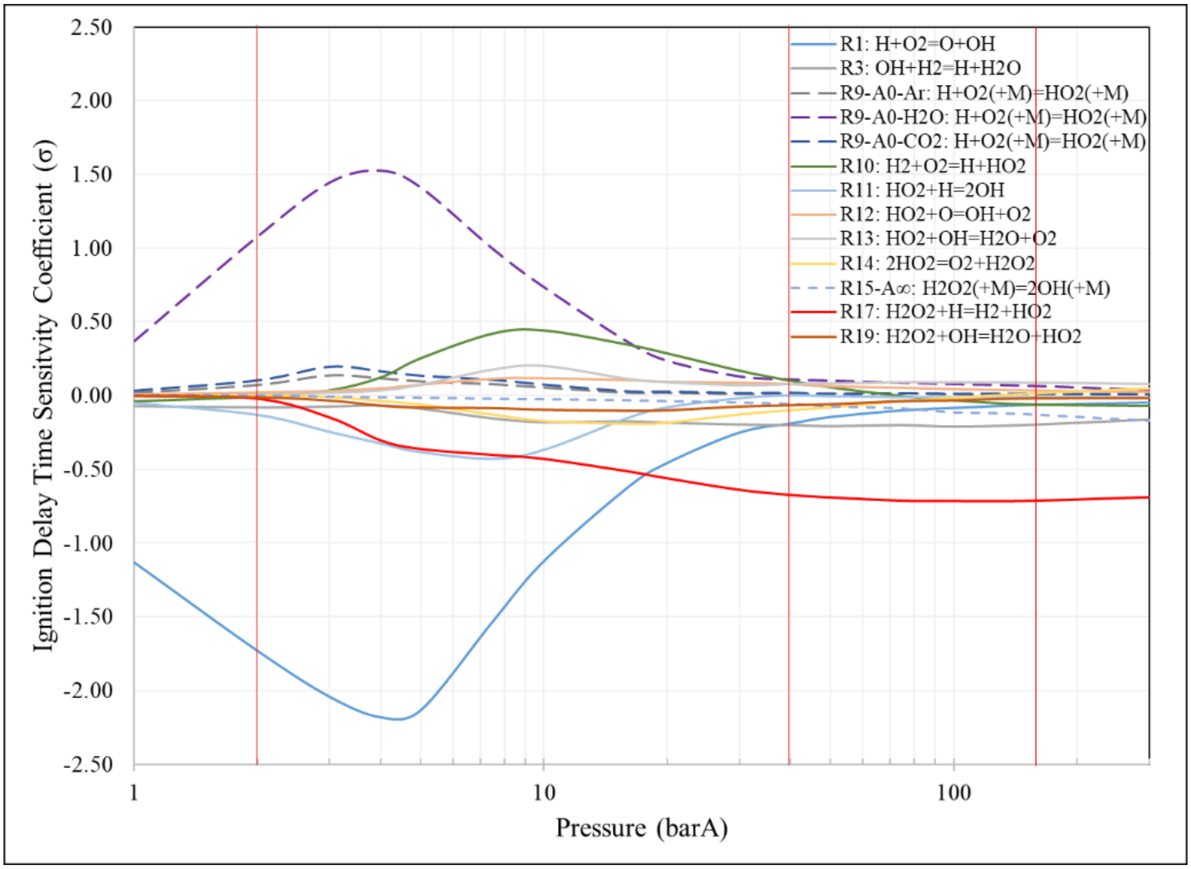

Figure 61: IDT-sensitive (max |σ|≥0.1) reaction rate parameters sensitivity coefficients vs. pressure for 4%H_2/30%H_2O/15%CO_2/Ar φ=1 at 1232 K

As such, it can be concluded that the change in chemistry brought about by addition of 15%CO_2, by reducing H_2O concentration by the same amount, is nearly negligible and does not appear to impact the reaction pathways significantly.

To gain further insight into potential changes that could present themselves arise at temperatures higher and lower than the 1232 K probed, it is prudent to look at temperature-dependent IDT sensitivities.

Figure 62 illustrates IDT-sensitive (max |σ|≥0.1) reaction rate parameters sensitivity coefficients vs. temperature for 4%H_2/30%H_2O/15%CO_2/Ar φ=1 at 40 bar. Similar to the 45%H_2O-diluted sensitivities at 40 bar (see Figure 21), the relative dominance of R1 and R9 subsides in the presence of 30%H_2O and 15%CO_2. Moreover, as a consequence of the presence of 15%CO_2 in the bath gas, there is one IDT-sensitive reaction from the CO chemistry added to the list of important reactions, -R23: CO+OH=CO_2+H. This confirms that CO_2 does breakdown to form CO, as observed in temperature-dependent IDT senstivities in 45%CO_2/Ar bath (see Figure 25). This reaction plays a promoting role at higher temperatures, with peak sensitivity near 1550 K. Higher temperature chemistry is not necessarily less complicated, but R1 becomes dominant at slightly lower temperatures of 1550 K vs. at 1600 K for mixtures containing 45% H_2O dilution (see Figure 54). This indicates that H_2O has a stronger impact in shifting the chemistry explored towards lower temperature chemistry than CO_2. R9 and R1's competition peaks at approximately 1550 K whereas it had peaked at 1575 K and 1250 K for 45%H_2O/Ar- and Ar-diluted experiments respectively, see Figure 54 and Figure 39.

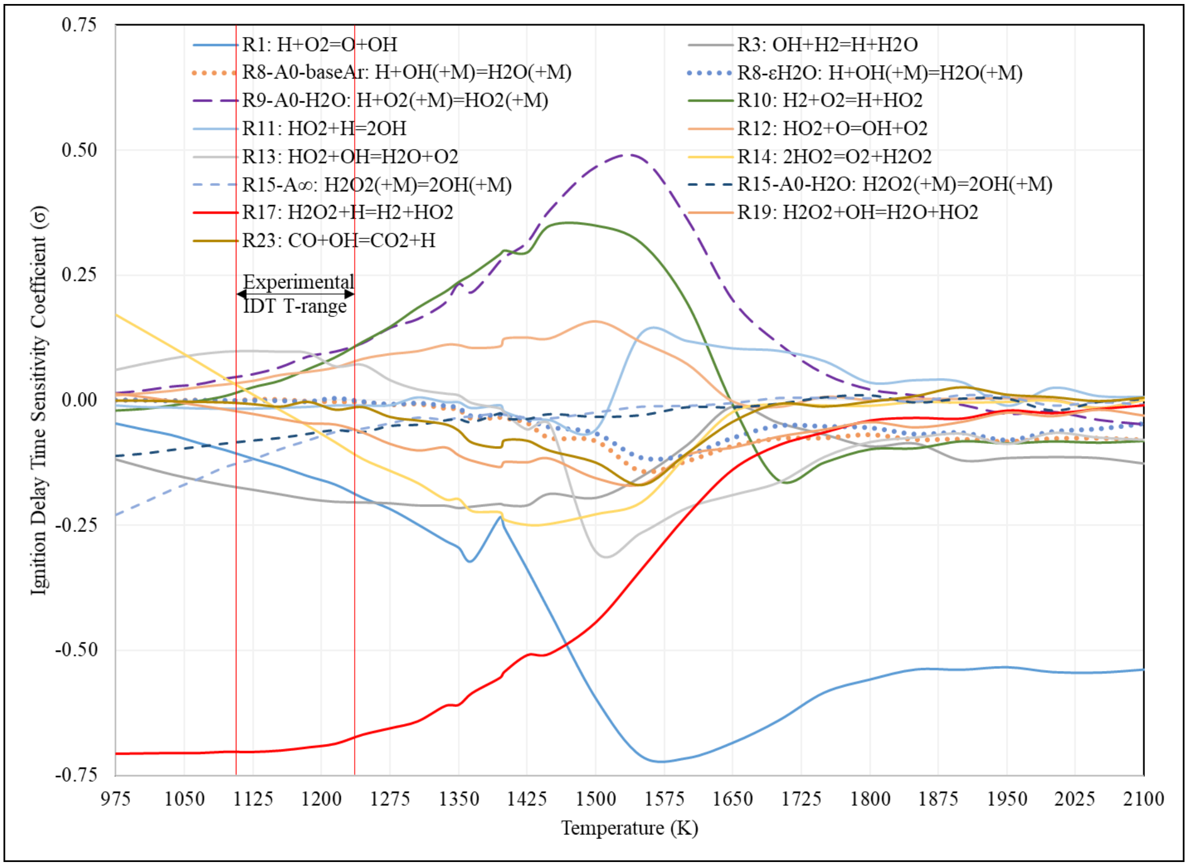

Figure 62: IDT-sensitive (max |σ|≥0.1) reaction rate parameters sensitivity coefficients vs. temperature for 4%H_2/30%H_2O/15%CO_2/Ar φ=1 at 40 bar

Figure 63 depicts IDT-sensitive (max |σ|≥0.1) reaction rate parameters sensitivity coefficients as a function of temperature for 4%H_2/30%H_2O/15%CO_2/Ar φ=1 at 150 bar, over a temperature range of 920-2200 K. The observations are near identical to those of for 45%H_2O bath gas (see Figure 55). Two minor differences were the larger magnitude of –R19: $H_2O+HO_2=H_2O_2+OH$ sensitivity, and absence of -R4: O+H_2O=OH+OH. Comparison of the temperature-dependent IDT raw data shows that IDT-sensitivities to both reactions decrease with the reduction of H_2O concentration in the bath gas from 45%H_2O to 30%H_2O. It should be noted that reaction pathways involving these reactions had smaller contributions to ignition in 45%CO_2, but a path through –R19 served as an alternate one for 45%H_2O baths. This was illustrated in their resepective OH ROP analyses at 150 bar, see Figure A37 and Figure A54.

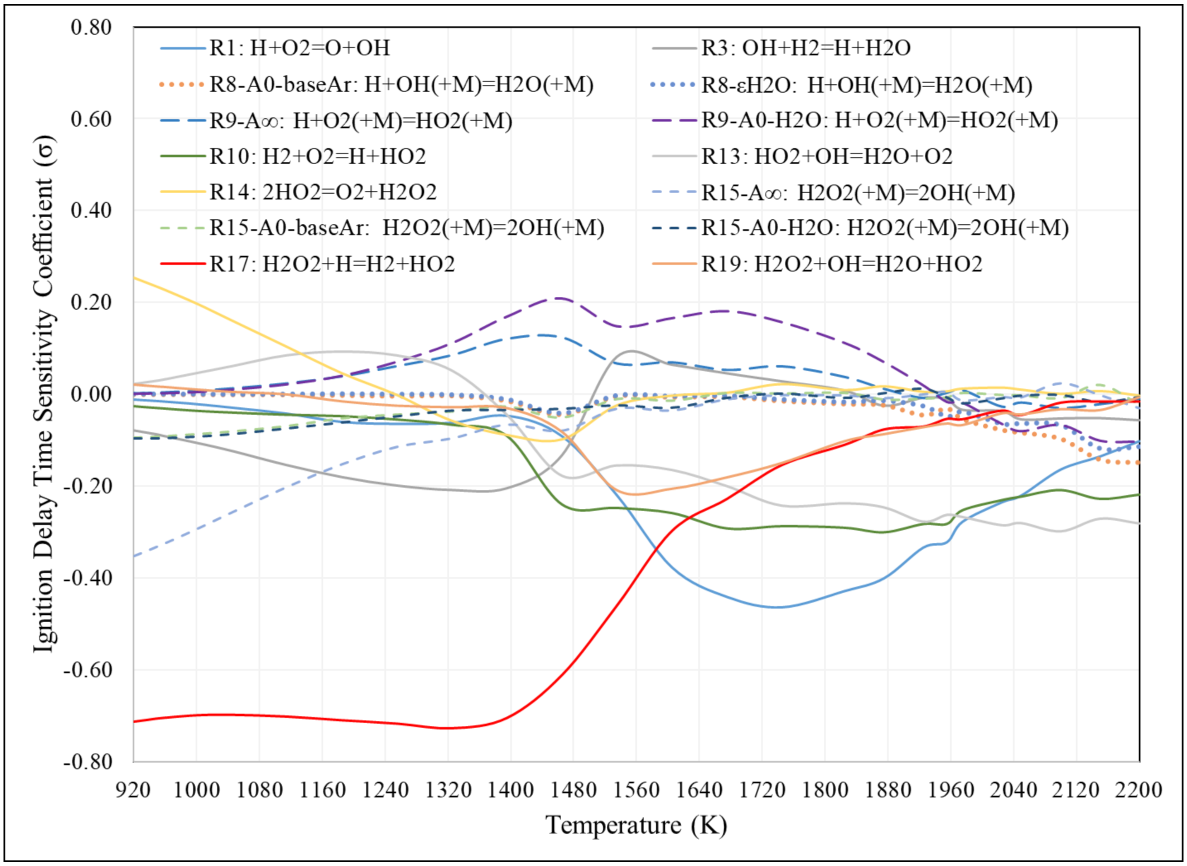

Figure 63: IDT-sensitive (max |σ|≥0.1) reaction rate parameters sensitivity coefficients vs. temperature for 4%H_2/30%H_2O/15%CO_2/Ar φ=1 at 150 bar

In conclusion, the chemistry of 4%H_2/30%H_2O/15%CO_2/Ar adopts features from chemical pathways involved in ignition of 4%H_2/45%H_2O/Ar and 4%H_2/45%CO_2/Ar. However, overall results of IDT temperature sweeps and IDT sensitivities at different pressures and temperatures show that the chemistry in presence of 30%H_2O/15%CO_2 more closely resembles that observed in the presence of 45%H_2O/Ar.

This concludes the investigation into the effects of pressure and presence of H_2O and CO_2 bath gases on hydrogen combustion chemistry.

The next chapter, Chapter 7, investigates the effect of pressure and presence of H_2O and CO_2 bath gases on methane's combustion chemistry, and presents the results of novel experimental test campaigns, as well as their subsequent utilization to develop a validated CH_4 oxidation mechanism.

Chapter 7 Experimental and Kinetics Study of CH_4 Oxidation Mechanism at High Pressure in the Presence of H_2O and CO_2

To validate the CH_4 mechanisms constructed based on AramcoMECH 2.0 [86], and AramcoMECH 3.0 [92] (see section 3.7), this chapter details the results of the unique shock tube IDT test campaigns conducted in this work. These data fill an existing knowledge gap and are integral to the kinetics model validation. The results of the uncertainty analysis performed on the experimental data are also discussed. Additional model validation data adopted from Shao et al.'s [175] recent experimental shock tube study are presented. Models' performances are then evaluated, and validation results are tabulated and discussed.

7.1 Experimental test results

In-line with section 5.1, experimental IDTs are defined to be the difference between time-zero, signified by the laser Schlierern spike, and ignition time based on intersection of the tangent to the steepest rise of side-wall OH* with its baseline value after passage of reflected shock (see Appendix B Figure A1). The same definition is also applied to determine IDTs using OH cocentration measurement (using UV LAS), end-wall OH* emission, and side-wall pressure signals. For the purpose of model validation side-wall OH* is the main signal relied on for model performance evaluation and reporting purposes. This is because side-wall OH* is more reliable than end-wall OH*, and side-wall pressure for bifurcating mixtures, see section 4.1.5. Also, for both H_2 and CH_4 test campaigns it was the diagnostic that was included for all tests, and its signal was successfully recorded for the largest number of experiments. A total of 49 IDT tests were conducted, with CH_4 as the fuel at three pressures of 2, 40 and 50 bar, spanning a temperature range of 1486-1896 K.

The results of the low-pressure methane IDT test campaign are summarized in Table 18. It can be observed that for the Ar-diluted experiments, IDTs based on side-wall OH* and pressure corroborate better with each other than they do with [OH] LAS. It should be noted that the OH* emission and [OH] LAS signals had higher signal to noise ratio as compared to side-wall pressure signal. For consistency, the side-wall OH*-based IDT was reported and used for model validation.

The 45% CO_2 diluted tests 60-63 exhibited a two-step rises in the side-wall OH* signal (two inflections), suggesting potential localized energy release, and likely inhomogeneities in the ignition event (see Figure A62 to Figure A65). It should be noted that for easier visualization and comparison, in all graphical representations of raw data, normalization of the measured signals was done by dividing the instantaneous signal value by its peak value recorded across the test's time span. Moreover, digital filtering of signals were done using 2nd order Savitzky-Golay polynomial fit method [184]. For tests 62-63, and 65-67 (see Figure A64 to Figure A69), the side-wall OH* signal saturated prior to peaking. Also, the OH LAS signal exhibited discontinuous multi-step rises (multiple inflections), for tests 60, 61, 66 and 67 (see Figure A62, Figure A63, Figure A68 and Figure A69). A careful corroboration of the emission with the OH LAS signal, enabled estimating the associated uncertainties for each test (see test-specific rationale in section 7.2.1). Overall, the localized OH* emission, as well as OH concentration changes observed prior to the main ignition event, are potential indications of inhomogenous reactivity, which is undersirable. However, as the IDT trends did not exhibit significant scatter, and often only one diagnostic detected such effects, these inhomogenous effects are believed to be more localized and likely closer to the boundary layer. As such, they are not expected to have severely impacted the estimates, hence, the data is retained for model validation purpose.

In the presence of 45% CO_2, the pressure rise measured by the Kistler at the side-wall appear to be much weaker than for the Ar-diluted tests, and strongly confounded by the boundary layer effects of bifurcation. As such pressure-based IDT estimates were unreliable for estimation of the ignition time (see Figure A62 to Figure A69).

Table 18: IDT measurements of CH_4 in Ar and 45%CO_2/Ar baths at φ=1 at ~2 bar

Test ID	T_5 (K)	P_5 (barA)	φ	CH_4 mole %	O_2 mole %	Ar mole %	CO_2 mole %	Measured IDT Side-wall OH* (μs)	Measured IDT [OH] LAS (μs)	Measured IDT Side-wall P (μs)
52	1486	2.3	1	3.44	6.87	89.69		935	982	939
53	1536	2.4	1	3.44	6.87	89.69		647	666	648
54	1545	2.3	1	3.44	6.87	89.69		526	534	474
55	1639	2.3	1	3.44	6.87	89.69		252	264	252
56	1664	2.3	1	3.44	6.87	89.69		177	188	171
57	1708	2.4	1	3.44	6.87	89.69		125	131	123
58	1738	2.3	1	3.44	6.87	89.69		88	96	96
59	1770	2.3	1	3.44	6.87	89.69		89	103	94
60	1565	2.0	1	3.00	6.00	46.00	45.00	820	697	
61	1577	2.1	1	3.00	6.00	46.00	45.00	567	595	
62	1606	2.0	1	3.00	6.00	46.00	45.00	511	557	
63	1668	1.9	1	3.00	6.00	46.00	45.00	358	394	
64	1728	1.8	1	3.00	6.00	46.00	45.00	273	329	
65	1738	1.8	1	3.00	6.00	46.00	45.00	187	203	
66	1740	1.8	1	3.00	6.00	46.00	45.00	201	250	
67	1805	1.8	1	3.00	6.00	46.00	45.00	94	153	

Table 19 details the IDT estimates for the 40 and 50 bar Ar-, 45%H_2O/Ar-, 30%H_2O/15%CO_2/Ar-, and 45%CO_2/Ar-diluted shock tube experiments. In this test campaign the definition of IDT is consistent with the previous test campaigns. Side-wall OH* and CH* emissions, end-wall OH* emission, and side-wall Kistler pressure signals were used to determine the time of ignition, when possible. However, as the side-wall CH*-based estimates were significantly lower and did not corroborate with the other signals, as such it was not reported.

Table 19: IDT measurements of CH_4 in Ar and 45%CO_2/Ar baths at φ=1 at ~40 and 50 bar

Test ID	T_5 (K)	P_5 (barA)	φ	CH_4 mole %	O_2 mole %	Ar mole %	H_2O mole %	CO_2 mole %	Measured IDT Side-wall OH* (μs)	Measured IDT End-wall OH* (μs)	Measured IDT Side-wall P (μs)
68	1577	40.1	1.00	0.50	1.00	98.50			765	780	742
69	1649	41.2	1.00	0.50	1.00	98.50			361	381	337
70	1692	41.7	1.00	0.50	1.00	98.50			237	255	230
71	1742	42.1	1.00	0.50	1.00	98.50			140	142	134
72	1805	42.0	1.00	0.50	1.00	98.50			75	77	
73	1561	39.8	0.93	0.476	1.024	98.50			832	848	769
74	1615	39.6	0.93	0.476	1.024	98.50			403	424	402
75	1536	37.9	1.00	0.50	1.00	52.62	45.88		1255	1089	
76	1552	37.3	1.00	0.50	1.00	52.62	45.88		804	854	
77	1567	39.5	1.00	0.50	1.00	52.62	45.88		680	814	
78	1617	37.9	1.00	0.50	1.00	53.91	44.60		467	500	
79	1640	37.6	1.00	0.50	1.00	52.62	45.88		295	363	
80	1723	37.5	1.00	0.50	1.00	53.91	44.60		97	121	
81	1568	39.6	1.00	0.50	1.00	53.51	30.30	14.69	678	750	
82	1612	39.5	1.00	0.50	1.00	53.51	30.30	14.69	483	529	
83	1618	40.9	1.00	0.50	1.00	53.50	30.00	15.00	280	349	
84	1674	40.9	1.00	0.50	1.00	53.50	30.00	15.00	183	254	
85	1685	41.5	1.00	0.50	1.00	53.50	30.00	15.00	107	121	
86	1708	39.1	1.00	0.50	1.00	53.50	30.00	15.00	64	72	
87	1724	38.7	1.00	0.50	1.00	53.50	30.00	15.00	47	57	
88	1795	37.8	1.00	0.50	1.00	53.50	30.00	15.00	24	26	
89	1645	52.8	1.00	0.50	1.00	53.50	30.00	15.00	714	856	
90	1704	53.3	1.00	0.50	1.00	53.50	30.00	15.00	477	557	
91	1753	53.1	1.00	0.50	1.00	53.50	30.00	15.00	321	360	
92	1782	51.5	1.00	0.50	1.00	53.50	30.00	15.00	197	224	
93	1845	51.5	1.00	0.50	1.00	53.50	30.00	15.00	67	78	
94	1896	49.6	1.00	0.50	1.00	53.50	30.00	15.00	30	27	
95	1599	41.0	1.00	0.499	1.001	53.48		45.02	755	830	
96	1631	39.5	1.00	0.499	1.001	53.48		45.02	578	599	
97	1691	40.1	1.00	0.499	1.001	53.48		45.02	330	357	
98	1723	39.7	1.00	0.499	1.001	53.48		45.02	233	265	
99	1733	40.2	1.00	0.499	1.001	53.48		45.02	224	252	
100	1775	39.2	1.00	0.499	1.001	53.48		45.02	138	169	

For the Ar-diluted experiments, IDTs were measured at two equivalence ratios of 1 and 0.93 for 0.5% CH_4 fuel molar concentration. The pressure rises associated with ignition, measured using side-wall Kistler were noisy, and had large unceratinties. As such, side-wall pressure-based estimates were deemed less reliable. IDT estimates using side-wall OH* were 1-7% smaller relative to those using end-wall OH*. The inflection of side-wall OH* emission rise was very distinct, however end-wall OH* emission rises exhibited multiple inflections for tests 69-72 and 74 (see Figure A70). In the case of multiple inflections, the estimates based on the steepest slope were reported. This increase was followed by the side-wall pressure rise recorded by Kistler.

For the 45% H_2O-diluted tests, it was not possible to determine IDTs from side-wall pressure signal. This is because the boundary layer pressure rise due to bifurcation could not be distinguished from the pressure rise due to ignition. Moreover, the observed pressure rise was weak and noisy for the 45% H_2O-diluted experiments (see Figure A71 to Figure A76). Both side-wall OH* and end-wall OH* signals were very noisy. Side-wall OH* was less noisy than end-wall OH* signal. The emission rise signals were observed to be weak. The side-wall OH* baseline was on a rise for test 75 and 76 (See Figure A71 and Figure A72). It was not possible to indentify the reason for such slow rise in the emission signal. However, for the determination of the IDT the baseline emission value used corresponded to the OH* emission value immediately after passage of the reflected shock for all tests. Morover, for the 45% H_2O-diluted tests, the fractional transmission signal for time zero determination either exhibited a local or no minima coincident with the arrival of the reflected shock (see Figure A77). Instead, it increased with the arrival of the reflected shock. This increase was followed by the side-wall Kistler pressure rise, as expected.

For the 30%H_2O/15%CO_2/Ar diluted tests the side-wall pressure signal was not usable for IDT determination, as the pressure rise associated with ignition was very weak and heavily masked by the boundary layer bifurcation effects (see Figure A78). The side-wall and end-wall OH* signals were very noisy, however, digital filtering was found to be very effective as the emission rises displayed distinct inflection points (see Figure A80). The estimates were more reliable, as the rise of the smoothed data was not oscillatory. While side-wall OH*-based estimates were lower than the end-wall OH* estimates, the estimates from the two signals corroborated well. For time zero determination the fractional transmission signal displayed a clear minima coincident with the arrival of the reflected shock, and was very reliable (see Figure A81). The detected minimas preceeded the side-wall pressure rise recorded by Kistler.

For the 45% CO_2/Ar-diluted tests, in-line with the previous mixtures containing H_2O and CO_2, the side-wall Kistler pressure signal was not usable for IDT determinations, as a distinct pressure rise coincident with the emission rise of the ignition event, was not detectable. The side-wall and end-wall OH* emission signals were less noisy than the H_2O-laden experiments. For time zero determination laser Schlieren fractional transmission signal exhibited either a local minima or no minima at all. It instead increased in a step-wise fashion similar to the 45% H_2O-diluted tests. In contrast to the 45%H_2O-diluted tests however, this rise was detected after the side-wall pressure rise. These observations are further discussed in section 7.2.1.

7.2 Uncertainty Analysis

In-line with section 5.2, the uncertainties associated with experimental results are categorized into those pertaining to ignition delay time estimations and those pertaining to the shock tube reaction condition, T_5 and P_5 determinations.

7.2.1 Uncertainties in ignition delay time determinations

For the low-pressure Ar- and CO_2-diluted experiments laser Schlieren fractional transmission signal typically showed a distinct minima or displayed two to three closely spaced peak and valleys, and were always less than +6/-8 μs of the main peak or valley (see Figure A82). As discussed in section 5.2.1, the cause of these oscillations could not be determined. While the smallest minima was utilized for IDT determination, uncertainties were extended to include other peaks and valleys as signifiers of true time zero.

For the low-pressure Ar-diluted ignition time determinations, the positive and negative uncertainty bounds associated with the reported IDTs based on side-wall OH*, were extended to include IDT estimates based on side-wall pressure and [OH] LAS signals.

For the low-pressure CO_2-diluted tests, side-wall OH*-based IDTs' unbalanced uncertainty bounds were determined through careful analysis of both diagnostics. For tests 60 and 61, side-wall OH* exhibited a two-step rise. Similarly side-wall OH LAS absorbance also exhibited a multi-step rise discontinuous rise. These observations suggest likely inhomogeneous localized reactivity (see Figure A62 and Figure A63). These inhomogeneities may be responsible for some of the scatter observed in the overall IDT trend (see Figure 65). For test 62, while sidewall OH* exhibited a two-step rise, OH LAS demonstrated a distinct single inflection point (see Figure A64). The OH* emission detected by the side-wall detector is likely localized as the line-of-sight OH LAS absorbance rise occurs after the two-step emission signal rise. Similarly, for test 63, while OH* indicated a closely spaced two-step rise, OH LAS had one main rise, which is deemed reliable according the logic presented for test 62 (Figure A65). For tests 64 and 66, side-wall OH* emission rises had distinct points of inflection which preceeded side-wall OH LAS absorbance signal rise. While side-wall OH LAS illustrated a delayed two-step rise, homogeneous ignition likely had occurred prior to these rises (see Figure A66 and Figure A68). For test 65 both side-wall OH* and OH LAS showed distinct rises which point to a similar estimate of IDT (see Figure A67). For test 67, side-wall OH* emission saturated prior to peaking, and potentially inflecting, while side-wall OH LAS showed a three-step rise (see Figure A69). The relatively lower-slope monotonic rise of the emission signal combined with its saturation was concerning. Since the third rise of OH LAS signal was the steepest, the estimated uncertainties were extended to include this OH LAS-based IDT, culminating in an exceptionally large positive uncertainty of 65% designated for this test (see Table 20 and Figure 65).

For the high-pressure tests, time zero was determined using laser Schlieren signal. For the Ar- and 30%H_2O-15%CO_2/Ar-diluted tests, the Schlieren spike was distinct and clear. However, for several tests only the attenuated laser signal was available. Based on the estimated errors associated with unavailability of the reference laser signal discussed in section 5.2.1, error bars of +/-0.5 μs were included. For other tests no additional uncertainties were detected. In contrast, laser Schlieren spikes were not detected for any of the 45%H_2O-diluted experiments. Instead, the laser fractional transmission displayed an abrupt multi-step climb, initiated prior to the rise of the side-wall pressure signal associated with the arrival of the reflected shock wave (see Figure A77). As such, unbalanced uncertainties were extended to include any purturbations in the fractional transimission signal, prior to its larger amplitude rise, in case they signified a potentially weak spike. Additionally, in the positive direction, the uncertainties were extended up to the start of the second rise of side-wall pressure. The uncertainty bounds incorporated for the 45%H_2O/Ar-diluted tests spanned, +8/-5 μs. The start of the side-wall pressure rise was found to be coincident with the laser Schlieren spike of the 30%H_2O-15%CO_2/Ar-diluted tests. This is also in-line with the observations and the approach assumed for the uncertainty calculations of the high-pressure H_2 test campaign experiments discussed in section 5.2.1.

For the 45%CO_2/Ar-diluted tests no Schlieren spike was observed for any of the tests. For these tests, in contrast to the 45%H_2O/Ar-diluted tests, the rise in fractional transmission signal of the Schlieren laser occurred near or slightly after the second rise of the side-wall pressure had initiated. This observation suggests that negative uncertainties should be extended to include the initial side-wall pressure rise, as it has been shown by researchers that the fractional transmission minima preceeds the side-wall pressure rise for CO_2-diluted tests [56, 54]. As such uncertainties spanning +5/-5 μs were included for these tests.

For the high-pressure ignition time determinations, in the case of Ar-diluted experiments, the signal was not noisy. Savitzky-Golay filtering of 2nd order was applied to 250 to 500 point increments for both side-wall and end-wall OH* emission rises. The appropriate smoothing level was determined visually, by testing multiple smoothing levels, and determining when a noticeable shift from the approximate tangents drawn using noisier data with lower filtering occurs. Uncertainties of 3% of the IDT measurement were applied to the IDTs based on the afformentioned smoothing levels and variations in steepest tangent graphical determinations.

The uncertainties associated with the 45%H_2O/Ar-diluted experiments were larger, as both side-wall and end-wall OH* signals were weak and noisy. The weak signal is expected as H_2O is twice as effective as CO_2, and three orders of magnitude more effective than Ar in de-exciting OH* to OH. This can be observed by comparing the rate constants of reactions $OH^*+H_2O=OH+H_2O$ and $OH^*+CO_2=OH+CO_2$ adopted from Tamura et al. [185], and OH*+Ar=OH+Ar adopted from Paul et al. [186] (see Figure A83). Weaker signals also require larger amplification which increases the recorded signals noise. Savitzky-Golay filtering of 2nd order was applied to 3000 to 7500 point increments to enable IDT estimations for the side-wall OH* signal. Similarly, end-wall OH* required smoothing increments of 3000-8000 points were necessary to enable ignition time estimations, with the exception of test 75 which required an exceptionally high smoothing level of 10000. Digital filters in the range of 100-10000 point increments were tested to determine the appropriate level necessary for every test. Due to higher levels of digital filtering applied to tests containing 45% H_2O, uncertainty bounds were increased to ±7% as a minimum and summed with uncertainties associated with each tests' time zero determination error. The exceptions were tests 75 and 76 for which side-wall OH*-based estimates were less certain (see Figure A71 and Figure A72). Tests 75 and 76 displayed a peculiar side-wall OH* emission rise which initiated prior to the start of the test. The cause of this rise was not determined. While these tests were the lowest temperature tests, i.e. at 1536 K and 1552 K, such initial OH* emission rise was not observed for the next lowest temperature test, i.e. test 77 conducted at 1567 K (see Figure A71 to Figure A73). Nonetheless, these data were retained because the end-wall OH* did not display such rise, and the side-wall OH*-based IDT estimates did not excessively deviate from the near linear trends of log IDT vs. 1000/T (see Figure 67). However, their uncertainty determination approach differed. For test 75, while both side-wall OH* and end-wall OH* required significant digital filtering, 5000 and 10000 point, end-wall OH*-based was deemed more reliable. However, unlike other tests, it predicted a longer IDT. For tests that were more reliable side-wall IDTs were on average 15.4% smaller than end-wall OH*-based IDTs. As such for test 75, the negative uncertainty of the reported side-wall OH*-based IDT was extended to include a value 15.4% smaller than the end-wall IDT based estimate, resulting in a -27% negative uncertainty relative to the reported side-wall OH*-based estimate. For test 76's negative uncertainties, a similar approach was assumed. To determine the negative uncertainty bound of the side-wall OH*-based IDT, the true value was assumed to lie within the -15.4% of the end-wall OH*-based IDT estimate (~ -10% relative to the reported side-wall OH*-based IDT estimate). For tests 75 and 76, positive uncertainty bounds were retained at +7% due to the high levels of digital filtering applied to both end-wall and side-wall signals.

The side-wall and end-wall OH* emission trends recorded for the 30%H_2O/15%CO_2-diluted tests exhibited significantly less noise than their 45% H_2O diluted counterparts. 2nd order Savitzly-Golay digital filters applied to side-wall OH* signals spanned 500-5000 point increment. However, the majority of the tests required less than 2000 point digital filtering. Similarly, for the end-wall OH* while the majority of tests required less than 5000 point digital filter, the range spanned 2500-10000. Digital filter was shown to be more effective for the 30%H_2O/15% CO_2 experiments than for the 45% H_2O-diluted ones. As such minimum uncertainties of 6% were designated due to the generally high levels of digital filtering. However, as many of these tests were conducted at higher temperatures (for most tests above 1675 K) these uncertainty bounds had to be increased for tests conducted at the lower temperature end. This is due to the fact that the relative uncertainties were more sensitive to the slope of the tangent selected (graphically determined), than their higher temperature counterparts.For the two lowest temperature tests, i.e. test 81 and test 82, due to the larger levels of digital filtering exceeding 5000, the minimum designated uncertainties were increased to 7% (see Figure A78 and Figure A79). Overall, the estimated uncertainties associated with the 30%H_2O/15%CO_2-diluted tests varied between 6-16.8% (see Table 21).

For the 45%CO_2-diluted tests side-wall and end-wall OH* signal noise levels were low. Digital filtering levels of 400-1500 and 700-1400 points were sufficient for reliable time of ignition estimations, respectively, which points to these experiments' higher signal-to-noise ratio relative their H_2O-laden counterparts. As such an estimate of ±5% in addition to the test-specific time zero uncertainties were applied to each test, in determining the uncertainties associated with ignition delay time estimations.

In summary, test-specific unbalanced positive and negative IDT combined uncertainties were estimated by adding the time zero uncertainties with the ignition time estimation uncertainties. These combined uncertainties are tabulated in Table 20 and Table 21, and were designated byvertical error bars for graphical representation of experimental IDTs of this work, (see section 7.4). The next section discusses the uncertainties associated with T_5 and P_5 determinations of the CH_4 IDT test campaigns.

7.2.2 Uncertainties in T_5 and P_5 determinations

Determination of T_5 and P_5 uncertatinties includes the combined effect of errors associated with 1) T_1, P_1, 2) measured incident shock velocity, 3) fitting errors of NASA polynomial gas properties and their deviations due to pressure dependency, 4) concentrations of H_2O and CO_2 and 5) deviations from ideal gas behavior during mixture preparation. Combined maximum as well as the root-sum-of-squared (RSS) relative errors were generated, using the methods discussed in section 4.4. These uncertainty estimates are listed in Table 20 and Table 21, for the low- and high-pressure CH_4 test campaigns, respectively. In these tables the mixture group numbers of the test ID column refer to the target mixture groups of section 4.1.4 (see Table 4: Low- and high-pressure CH_4 IDT test campaign target conditions).

Table 20 illustrates that the P_5 and T_5 errors associated with the low-pressure Ar-diluted tests (Tests 52-7 to 59-7), are generally larger than those of their 45%CO_2/Ar-diluted counterparts (Tests 60-8 to 67-8). This is due to the fact that these uncertainties are strongly impacted by the incident shock velocity measurement error, and the averages of this error were 0.42% and 0.37% for the Ar- and CO_2-diluted tests, respectively.

Table 20: Low-pressure CH_4 experiments' IDT, T_5, and P_5 maximum and RSS uncertainties

Test ID - Mix group #	T_5 (K)	P_5 (barA)	IDT (µs)	IDT +ve error (%)	IDT -ve error (%)	Max T_5 +ve error (%)	Max T_5 -ve error (%)	RSS T_5 +ve error (%)	RSS T_5 -ve error (%)	Max P_5 +ve error (%)	Max P_5 -ve error (%)	RSS P_5 +ve error (%)	RSS P_5 -ve error (%)
52-7	1486	2.3	935	5.0	0.3	0.71	0.71	0.51	0.51	2.11	2.07	1.25	1.24
53-7	1536	2.4	647	2.9	1.4	0.55	0.55	0.37	0.36	1.82	1.79	1.08	1.07
54-7	1545	2.3	526	1.5	10.7	0.52	0.52	0.34	0.34	1.77	1.74	1.05	1.04
55-7	1639	2.3	252	5.2	1.7	0.80	0.80	0.59	0.59	2.22	2.17	1.32	1.31
56-7	1664	2.3	177	8.5	3.6	0.95	0.94	0.74	0.73	2.46	2.41	1.50	1.49
57-7	1708	2.4	125	8.8	1.8	0.82	0.82	0.61	0.61	2.23	2.19	1.33	1.32
58-7	1738	2.3	88	13.7	0.0	0.74	0.74	0.54	0.54	2.09	2.05	1.23	1.22
59-7	1770	2.3	89	20.3	0.0	0.77	0.76	0.56	0.56	2.12	2.08	1.25	1.24
60-8	1565	2.0	820	0.7	1.3	0.65	0.68	0.38	0.39	1.86	1.78	1.04	1.03
61-8	1577	2.1	567	2.1	1.1	0.65	0.68	0.38	0.39	1.86	1.77	1.04	1.03
62-8	1606	2.0	511	9.0	3.7	0.48	0.52	0.27	0.28	1.54	1.46	0.89	0.88
63-8	1668	1.9	358	8.1	6.2	1.04	1.07	0.73	0.74	2.58	2.47	1.57	1.55
64-8	1728	1.8	273	2.3	30.6	0.49	0.53	0.27	0.29	1.54	1.46	0.89	0.87
65-8	1738	1.8	187	9.6	5.7	0.40	0.44	0.23	0.25	1.37	1.30	0.84	0.83
66-8	1740	1.8	201	0.0	11.4	0.67	0.70	0.40	0.41	1.86	1.78	1.04	1.02
67-8	1805	1.8	94	65.0	20.3	0.66	0.70	0.40	0.41	1.85	1.76	1.03	1.01

Table 21, illustrates that for the CO_2- and H_2O-laden tests, the reported uncertainties are significantly larger and more unbalanced than both low-pressure tests and high-pressure Ar-diluted experiments. This non-uniformity observed for these uncertainties are attributed to the unbalanced errors associated with NASA-polynomials used to estimate thermodynamic properties, and the composition uncertainties due to non-ideal gas behavior of the mixtures. As described in section 4.4 only the upper bound error of thermodynamic properties database had to be increased to 1.8% for H_2O, and 0.63% for CO_2 to account for the non-ideal pressure effect on these properties, which causes the unbalanced error bars. Whereas the lower bound error bound for H_2O and CO_2 remained at -0.5% and -0.4%, respectively. Also in-line with the approach discussed in section 5.2.2, HYSYS simulations were conducted to estimate the errors in compositions of mixtures prepared with the assumption of ideal gas behavior. Also as discussed in section 4.4 RSS errors listed in Table 20, and Table 21 are used in graphical representations of the data in the proceeding sections.

Table 21: High-pressure CH_4 experiments' IDT, T_5, and P_5 maximum and RSS uncertainties

Test ID - Mix group #	T_5 (K)	P_5 (barA)	IDT (μs)	IDT +ve error (%)	IDT -ve error (%)	Max T_5 +ve error (%)	Max T_5 -ve error (%)	RSS T_5 +ve error (%)	RSS T_5 -ve error (%)	Max P_5 +ve error (%)	Max P_5 -ve error (%)	RSS P_5 +ve error (%)	RSS P_5 -ve error (%)
68-9	1577	40.1	765	3.0	3.0	0.96	0.95	0.75	0.75	2.49	2.44	1.52	1.50
69-9	1649	41.2	361	3.0	3.0	1.00	0.99	0.79	0.78	2.53	2.48	1.55	1.54
70-9	1692	41.7	237	3.0	3.0	0.95	0.94	0.74	0.74	2.42	2.37	1.46	1.45
71-9	1742	42.1	140	3.0	3.0	1.04	1.03	0.83	0.82	2.56	2.51	1.58	1.57
72-9	1805	42.0	75	3.0	3.0	0.98	0.97	0.76	0.76	2.42	2.37	1.47	1.46
73-9	1561	39.8	832	3.0	3.0	1.01	1.00	0.80	0.80	2.59	2.54	1.60	1.59
74-9	1615	39.6	403	3.0	3.0	0.92	0.92	0.72	0.71	2.42	2.37	1.46	1.45
75-10	1536	37.9	1255	7.4	27.2	0.94	1.73	0.61	0.98	2.93	2.50	1.61	1.42
76-10	1552	37.3	804	7.6	11.2	0.84	1.63	0.52	0.93	2.71	2.29	1.46	1.25
77-10	1567	39.5	680	7.7	7.7	0.89	1.68	0.56	0.95	2.80	2.38	1.52	1.32
78-10	1617	37.9	467	8.1	8.1	0.87	1.67	0.55	0.95	2.74	2.32	1.48	1.29
79-10	1640	37.6	295	8.7	9.7	0.92	1.73	0.59	0.99	2.84	2.41	1.55	1.35
80-10	1723	37.5	97	12.1	15.2	0.88	1.70	0.56	0.97	2.72	2.28	1.48	1.27
81-11	1568	39.6	678	7.0	7.0	0.83	1.30	0.58	0.74	2.68	2.43	1.46	1.40
82-11	1612	39.5	483	7.0	7.0	0.79	1.27	0.54	0.71	2.58	2.33	1.38	1.32
83-11	1618	40.9	280	6.0	6.4	0.75	1.23	0.52	0.69	2.51	2.27	1.33	1.27
84-11	1674	40.9	183	6.0	6.0	0.76	1.25	0.52	0.70	2.50	2.26	1.33	1.26
85-11	1685	41.5	107	7.5	6.0	0.76	1.25	0.52	0.70	2.50	2.25	1.32	1.26
86-11	1708	39.1	64	6.0	6.0	0.80	1.30	0.56	0.73	2.59	2.33	1.39	1.33
87-11	1724	38.7	47	6.0	6.0	0.91	1.40	0.66	0.81	2.80	2.53	1.55	1.49
88-11	1795	37.8	24	9.1	16.8	0.81	1.31	0.57	0.75	2.58	2.32	1.38	1.31
89-11	1645	52.8	714	6.1	6.1	0.95	1.43	0.70	0.84	2.90	2.64	1.64	1.58
90-11	1704	53.3	477	6.1	9.2	0.88	1.37	0.63	0.79	2.74	2.48	1.51	1.45
91-11	1753	53.1	321	6.2	8.7	0.81	1.31	0.56	0.74	2.58	2.32	1.38	1.32
92-11	1782	51.5	197	6.3	7.6	0.82	1.33	0.58	0.75	2.61	2.35	1.40	1.34
93-11	1845	51.5	67	6.7	6.7	0.54	1.06	0.33	0.59	2.04	1.79	1.03	0.94
94-11	1896	49.6	30	8.7	13.4	0.76	1.27	0.52	0.72	2.45	2.18	1.28	1.21
95-12	1599	41.0	755	5.7	5.7	0.87	0.99	0.58	0.63	2.32	2.14	1.34	1.31
96-12	1631	39.5	578	5.9	5.9	0.87	1.00	0.59	0.63	2.32	2.13	1.34	1.31
97-12	1691	40.1	330	6.7	5.2	0.85	0.98	0.56	0.61	2.25	2.06	1.28	1.25
98-12	1723	39.7	233	7.2	5.0	0.94	1.07	0.65	0.69	2.42	2.23	1.42	1.39
99-12	1733	40.2	224	7.2	7.2	0.85	0.98	0.57	0.61	2.24	2.06	1.27	1.24
100-12	1775	39.2	138	8.6	8.6	0.90	1.03	0.61	0.66	2.32	2.13	1.34	1.31

7.3 Additional shock tube IDT validation targets from the literature

To ensure that the model produced is robust, it is critical to include experiments from other experimental facilities and expand the range of temperature, pressure and equivalence ratio. It is also beneficial to evaluate the model's performance in predicting the kinetics of slightly larger intermediate hydrocarbons involved in the breakdown of methane. Methane oxidation is also known to lead to formation of larger hydrocarbons temporarily prior to breaking down again to form CO_2 and H_2O [6]. As such, a recent experimental IDT test campaign conducted by Shao et al. [175] was chosen to validate the kinetic models. This experimental test campaign spanned a temperature range of 950-1800 K, a pressure range of 14-64 bar, equivalence ratios of 1 and 2, and involved, methane (1.96 and 3.85 mole %), ethylene (1.32 and 2.66 mole %), propene (0.88 mole %), as well as binary mixtures of these fuels. Moreover, as the study was more recent (2018), dP/dt effect were also capped and reported (2%/ms), unlike earlier studies predating the discovery of this effects, such as the well-cited large validation datasets of Petersen et al. [60, 62]. As such, in this thesis, in addition to the new high-pressure data generated at KAUST's LPST and HPST test facilities, Shao et al.'s [175] experimental shock tube IDT tests conducted at Stanford University's high-pressure shock tube facilities, were also adopted for the CH_4 model validation work. In-line with the approach detailed in section 5.5 the validation data were simulated in Chemkin using constant volume simulations. The dP/dt of 2%/ms, was converted to a dV/dt profile using the mixture's gamma along with the assumption of isentropic compression.

7.4 Model validation results and discussions

For the CH_4 mechanism, validation the model performance evaluation criteria detailed in 5.4, namely, root mean square relative error (RMSRE) and the relative percent RMSRE (RPRMSRE) were used. To evaluate, validate and recommend an improved CH_4 mechanism:

1. The performance of the first incumbent model AramcoMECH 2.0 [86] in predicting the experimental IDT validate datasets was evaluated;
2. The performance of another incumbent mechanism AramcoMECH 3.0 [92], which is a larger successor model to AramcoMECH 2.0, was also evaluated for comparison in reproducing the experimental IDT validation datasets;
3. The H_2/CO submechanism of AramcoMECH 2.0 [86] was replaced with CanMECH 1.0 developed in Chapter 5, and the performance of the model was evaluated;
4. The H_2/CO submechanism of AramcoMECH 3.0 was replaced with CanMECH 1.0, and the performance of the model was also evaluated for comparison purposes; and,
5. The model with the best performance was then recommended for future development and/or usage.

Table 22 details the values of the three RMSRE-based model performance evaluation metrics for four models, namely: AramcoMECH 2.0 modified with CanMECH 1.0, AramcoMECH 3.0 modified with CanMECH 1.0 H_2/CO sub-mechanism, AramcoMECH 2.0 [86], and AramcoMECH 3.0 [92]. It should be noted that as the incumbent models are AramcoMECH 2.0 and AramcoMECH 3.0, the generated RPRMSREs are deteremined relative to these mechanisms.

Table 22, similar to Table 9, has been organized into groups, with each grouping (boxed in black borders) dedicated to a subset of data with similar mixture compositions and pressures. Each row also contains the source study, range of experimental conditions, and the RMSREs of the four models. It can be observed that the model generated by replacing AramcoMECH 2.0 [86] H_2/CO mechanism with CanMECH 1.0 has the lowest overall RMSRE (0.880). This model is henceforth referred to as CanMECH 2.0, and constitutes the CH_4 mechanism recommended for further performance evaluation. Each row of Table 22 also lists the RPRMSRE of the best performing model (CanMECH 2.0) relative to the incumbent models, AramcoMECH 2.0 [86] and AramcoMECH 3.0 [92]. Each grouping's last row provides the combined RMSREs as a measure of the performance of each model in predicting all of the IDT data of that dataset. Cells that are highlighted in yellow in Table 22 identify the best performing model in predicting subsets of IDT data sharing the same composition- and/or pressure-range. Cells highlighted in orange point to the model that outperforms (lowest RMSRE) others in predicting each grouping's IDT validation data. Finally Table 22's last row details the overall performance of each model in predicting all of the validation datasets considered in this work, and the cell with the dark red fill distinguishes the model with the best overall performance. The last two columns of Table 22, list the RPRMSRE's of CanMECH 2.0 relative to the incumbent AramcoMECH models. In these columns the cells highlighted in green indicate the datasets that CanMECH 2.0 is able to predict better than the incumbent model.

Comparison of individual and combined RMSRE's indicate that CanMECH 2.0 has a better overall performance in predicting the high-pressure dataset of this work, as well as Shao et al.'s [175] data. AramcoMECH 2.0 and 3.0 display a better overall performance in predicting low-pressure data of this work. For a more thorough analysis of the models performance in predicting this works IDT validation data, it is beneficial to graphically examine their prediction ability in tandem. To this end, CanMECH 2.0's performance is benchmarked against AramcoMECH 2.0 [86] and AramcoMECH 3.0's [92], in Figure 64 to Figure 70. The horizontal and vertical error bars of the experimental data depicted in these figures represent the combined RSS errors of T_5 (see section 7.2.2) and ignition delay time estimates using the side-wall OH* emission signal (see 7.2.1), respectively. These uncertainties are also tabulated in Table 20 and Table 21 of section 7.2.2.

Table 22: CH_4 Model Performance Evaluation Results Matrix

Dataset ID	Source	Fuel & Bath gas Composition	# of data	Pressure range (barA)	Temperature range (K)	φ	Modified AramcoMECH 2.0 [H_2/CO mechanism replaced by CanMECH 1.0] (**CanMECH 2.0**) RMSRE	Modified AramcoMECH 3.0 [H_2/CO mechanism replaced by CanMECH 1.0] RMSRE	AramcoMECH 2.0 RMSRE	AramcoMECH 3.0 RMSRE	CanMECH 2.0 vs. AramcoMECH 2.0 RPRMSRE (%)	CanMECH 2.0 vs. AramcoMECH 3.0 RPRMSRE (%)
1	This Work	3.436%CH_4/Ar	8	1.81-2.06	1486-1770	1	1.540	1.544	1.432	1.436	8	7
2		3%CH_4/45%CO_2/Ar	8	2.26-2.38	1565-1805	1	1.479	1.485	1.341	1.345	10	10
		Combined	**16**	**1.81-2.38**	**1486-1705**	**1**	**1.510**	**1.515**	**1.387**	**1.391**	**9**	**9**
3	This Work	0.5%CH_4/Ar	5	40.1-42.1	1577-1805	1	0.228	0.229	0.171	0.175	33	30
4		0.476%CH_4/Ar	2	39.6-39.8	1561-1615	0.93	0.382	0.383	0.328	0.332	16	15
5		0.5%CH_4/45%H_2O/Ar	6	37.3-39.5	1536-1723	1	0.713	0.728	0.760	0.763	-6	-7
6		0.5%CH_4/30%H_2O/15%CO_2/Ar	8	37.8-41.5	1568-1795	1	2.676	2.803	2.839	2.928	-6	-9
7		0.5%CH_4/30%H_2O/15%CO_2/Ar	6	49.6-53.3	1645-1896	1	0.446	0.444	0.418	0.399	7	12
8		0.5%CH_4/45%CO_2/Ar	6	39.2-41.0	1599-1775	1	0.887	0.909	0.862	0.870	3	2
		Combined	**33**	**37.3-53.3**	**1536-1896**	**0.93-1**	**1.423**	**1.484**	**1.496**	**1.537**	**-5**	**-7**
9	Shao et al. 2018	1.96%CH_4/Ar	13	13.7-15.7	1420-1752	1	0.092	0.093	0.102	0.103	-10	-11
10		1.96%CH_4/Ar	8	51.7-59.0	1437-1663	1	0.088	0.088	0.095	0.096	-7	-8
11		3.85%CH_4/Ar	14	13.5-15.0	1464-1782	2	0.163	0.163	0.141	0.140	16	16
12		1.32%C_2H_4/Ar	13	15.7-16.9	1132-1317	1	0.165	0.174	0.262	0.266	-37	-38
13		1.32%C_2H_4/Ar	10	60.3-64.1	1095-1311	1	0.209	0.185	0.149	0.159	41	32
14		2.66%C_2H_4/Ar	10	15.9-16.6	1122-1268	2	0.099	0.121	0.122	0.136	-19	-27
15		0.88%C_3H_6/Ar	8	14.7-15.9	1255-1488	1	0.178	0.232	0.175	0.308	2	-42
16		0.54%CH_4/0.96%C_2H_4/Ar	6	15.4-16.5	1133-1340	1	0.220	0.182	0.097	0.108	126	103
17		0.25%C_2H_4/0.72%C_3H_6/Ar	1	15.0	1324	1	0.193	0.479	0.286	0.607	-32	-68
18		0.53%C_2H_4/0.53%C_3H_6/Ar	2	15.1-15.8	1212-1329	1	0.132	0.345	0.169	0.449	-22	-71
19		0.88%C2H4/0.29%C_3H_6/Ar	2	15.0-15.7	1206-1326	1	0.054	0.266	0.067	0.354	-19	-85
		Combined	**87**	**13.5-64.1**	**1095-1782**	**1-2**	**0.154**	**0.175**	**0.159**	**0.206**	**-3**	**-25**
		Overall	**136**	**1.81-64.1**	**1095-1896**	**0.93-2**	**0.880**	**0.908**	**0.886**	**0.910**	**-1**	**-3**

Figure 64 depicts the results of the shock tube IDT data conducted at KAUST's LPST for stoichiometric 3.436% CH_4/Ar at pressures of 2.26-2.38 bar. It can be observed that all models overpredict the experimental data over the explored temperature range of 1486-1770 K. AramcoMECH 2.0 [86] performs best. AramcoMECH 2.0 [86] and AramcoMECH 3.0 [92] have similar performance (RMSRSEs of 1.432 and 1.436) and perform better than CanMECH 2.0 which has an RMSRE of 1.54. The three models also appear to capture the global activation energy reasonably well.

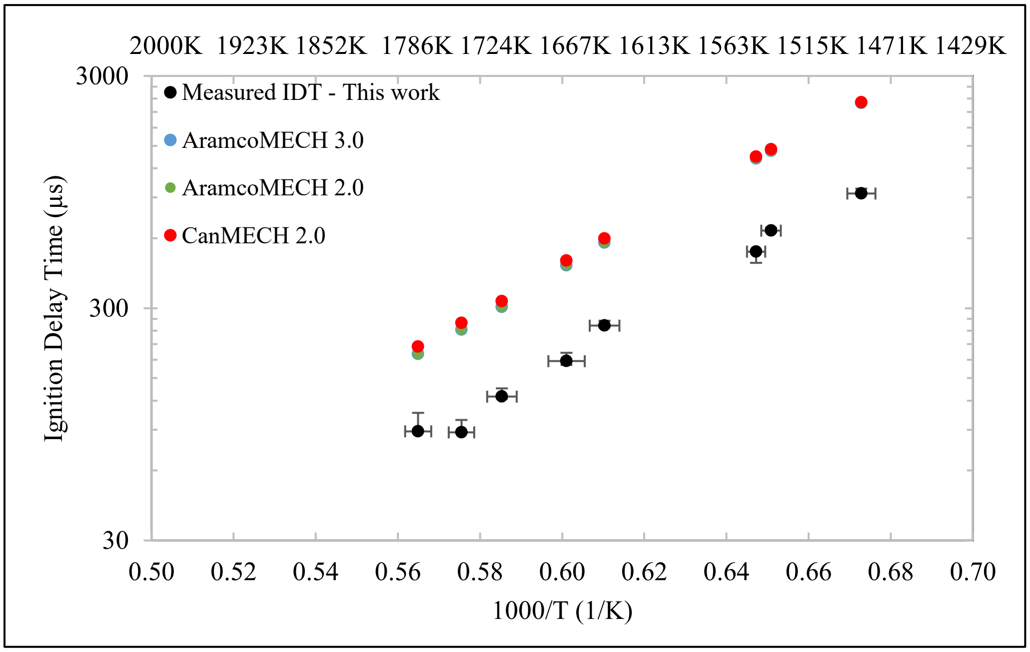

Figure 64: Measured vs. Modelled IDT 3.44%CH_4/Ar φ=1 at ~ 2.3 bar

Figure 65 illustrates the low-pressure experimental IDT results for 3%CH_4-45%CO_2/Ar at φ=1 conducted at pressures of 1.81-2.06 bar, and 1565-1805 K. All three models overpredict the IDTs and AramcoMECH 2.0 [86] and AramcoMECH 3.0 [92] have very similar performance with RMSREs of 1.341 and 1.345. Their performance in predicting this 45%CO_2-laden data is better than CanMECH 2.0 (RMSRE of 1.479). AramcoMECH 2.0 [86] has the best performance.

Overall RMSREs point to AramcoMECH 2.0 [86] as the best peforming model in predicting the low-pressure IDT data of this work. AramcoMECH 3.0 [92] was the second best model, followed by CanMECH 2.0. This is also reflected by the positive RPRMSRE indicating that adopting CanMECH 2.0 worsens the prediction ability of both AramcoMECH 2.0 [86] and AramcoMECH 3.0 [92] by 9%.

Also, from Table 22 RMSRE, it is apparent that replacing AramcoMECH 3.0's H_2/CO mechanism by CanMECH 1.0 does not bring any advantage in either of the low-pressure 3.44%CH_4/Ar (RMSRE

1.544) or the 3%CH_4-45%CO_2/Ar (RMSRE 1.485), even though it constitutes a larger mechanism. Figure 65 also illustrates that considering the scatter and uncertainties of the data, the three models' IDT trends have similar overall activation energies to that of the experiments.

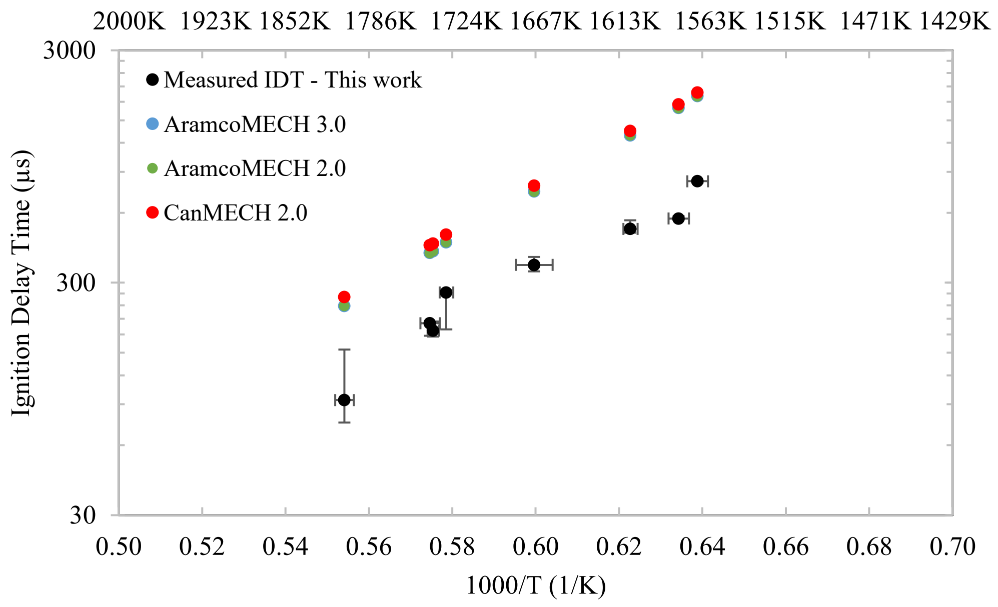

Figure 65: Measured vs. Modelled IDT 3%CH_4-45%CO_2/Ar φ=1 at ~ 1.9 bar

Figure 66 depicts high-pressure IDT data for 0.5%CH_4/Ar at φ=1, spanning 40.1-42.1 bar and 1577-1805 K, having round-shaped markers. The figure includes two additional IDT data conducted with 0.476%CH_4/Ar, at φ=0.93, pressures of 39.6-39.8 bar, at temperatures of 1561 and 1615 K, designated in square-shaped markers. Figure 66 shows that while all three models overpredict the data the performance of the models significantly improved relative to their low-pressure counterparts, indicated by an order of magnitude lower RMSREs. AramcoMECH 2.0 [86] and AramcoMECH 3.0 [92], have similar RMSREs of 0.171 and 0.175, respectively, and perform better than CanMECH 2.0 having an RMSRE of 0.228. AramcoMECH 2.0 [86] performs best having the lowest RMSRE. The overall RPRMSREs indicate that adopting CanMECH 2.0 increases the RMSREs by 33% and 30% relative to AramcoMECH 2.0 [86] and AramcoMECH 3.0 [92], respectively.

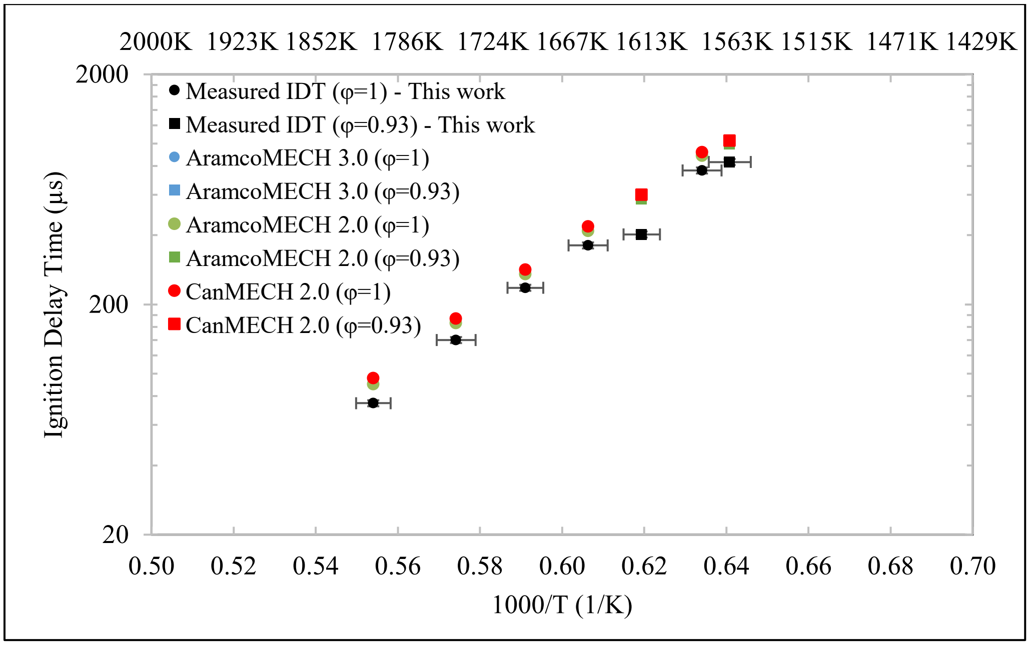

Figure 66: Measured vs. Modelled IDT 0.5%CH_4/Ar (round markers) at φ=1 ~41.4 bar and 0.476%CH_4/Ar (square markers) at φ=0.93, ~ 39.7 bar

Figure 67 provides a graph of the measured and modelled IDTs of 0.5%CH_4-45%H_2O/Ar at φ=1, pressures of 37.3-39.5 bar and temperatures of 1536-1723 K. All three models overestimate the IDT data, and also appear to be underestimating the global activation energy. This 45%H_2O-diluted data is of particular importance to pressurized oxy-fuel systems. It is apparent that CanMECH 2.0 outperforms both AramcoMECH 2.0 [86] and AramcoMECH 3.0 [92]. Barring the low-pressure data of this work, this dataset has the third highest RMSRE, among other datasets. CanMECH 2.0 predictions have an RMSRE of 0.713, whereas AramcoMECH 2.0 [86] and AramcoMECH 3.0 [92] have RMSREs of 0.760 and 0.763 respectively. The negative RPRMSRE values indicate that adopting CanMECH 2.0 is expected to bring about improvements of 6% and 7% relative to AramcoMECH 2.0 [86] and AramcoMECH 3.0 [92], respectively.

Figure 68 depicts the measured and modelled IDT data for 0.5%CH_4-30%H_2O-15%CO_2/Ar at φ=1, spanning temperatures of 1568-1795 K, and pressures of 37.8-41.5 bar. All three models overestimate the measurements, and underpredict the global activation energy. CanMECH 2.0 with an RMSRE of 2.676 outperforms AramcoMECH 2.0 [86] and AramcoMECH 3.0 [92] with RMSRE of 2.839, and and 2.928. This dataset has the highest RMSRE of all, as such an improvement of 6% and 9% in

RPRMSREs relative to the incumbent models is a significant improvement brought about by the adoption of CanMECH 2.0.

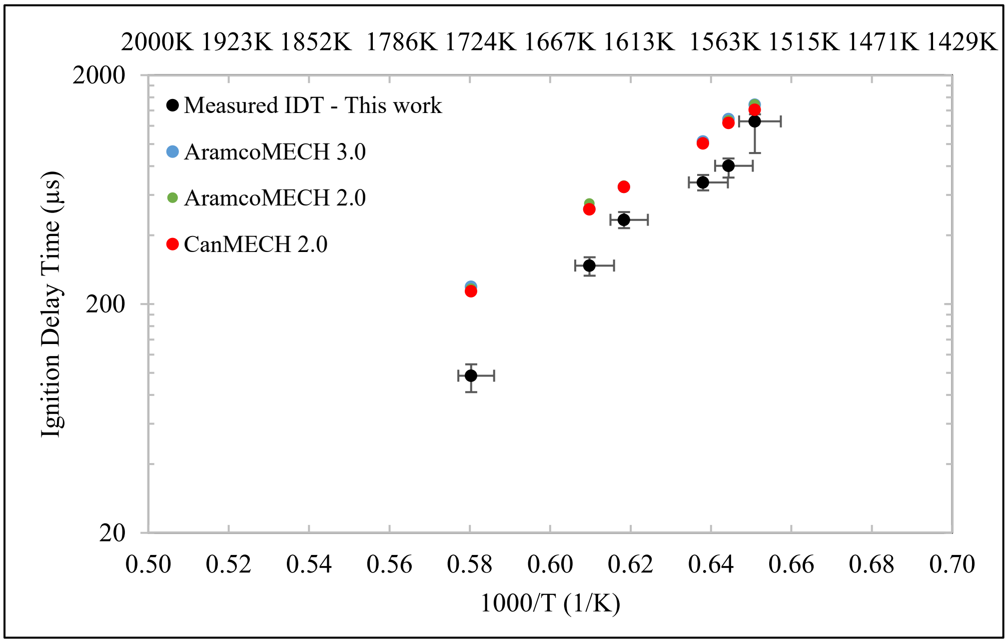

Figure 67: Measured vs. Modelled IDT 0.5%CH_4-45%H_2O/Ar at φ=1 ~37.9 bar

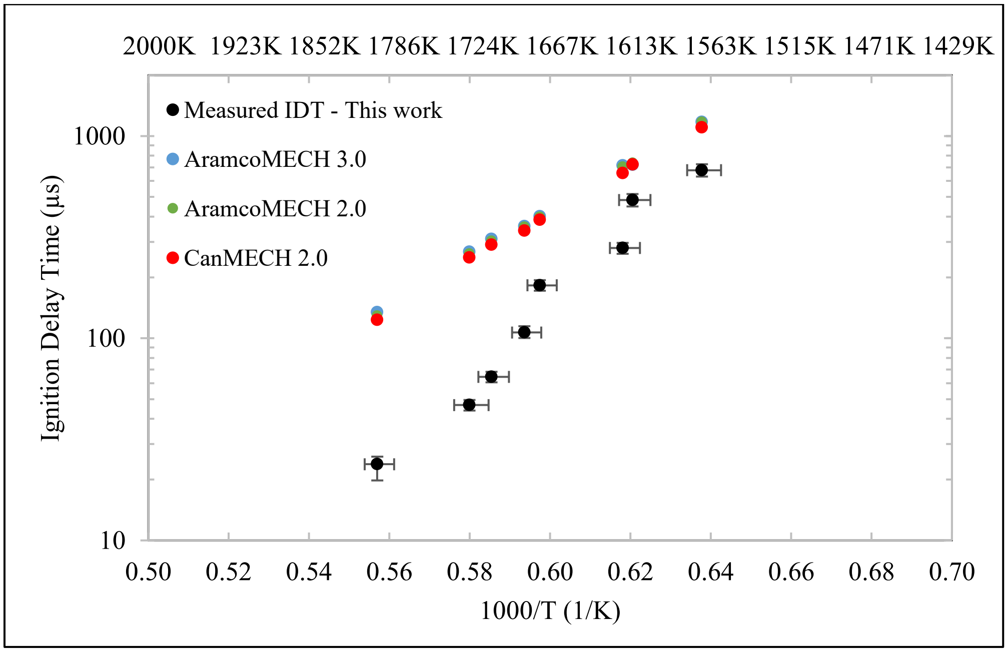

Figure 68: Measured vs. Modelled IDT 0.5%CH_4-30%H_2O-15%CO_2/Ar at φ=1 ~39.8 bar

Figure 69 depicts both measured and modelled IDTs for 0.5%CH_4-30%H_2O-15%CO_2/Ar at φ=1 spanning temperatures of 1645-1896 K and pressures across the range of 49.6-53.3 bar. It can be observed that all three models underpredict the data at temperatures below 1850 K, but for the data at 1896 K while AramcoMECH 2.0 [86] and AramcoMECH 3.0 [92] overpredict this data, CanMECH 2.0 predicts this point well. Comparison of Figure 69 with Figure 68, suggests that there may be potential change in chemistry brought about by the 10 bar pressure increase that the models are unable to capture. This is because whereas at 40 bar (see Figure 68) the models overpredict IDTs they underpredict them at near 52 bar. In-line with the observations from Figure 68 the models appear to underpredict the global activation energy at 52 bar as well. In terms of overall model performance AramcoMECH 3.0 [92] has the best performance with an RMSRE of 0.399 followed by AramcoMECH 2.0 [86] and CanMECH 2.0 with RMSREs of 0.418 and 0.446 respectively. Adopting CanMECH increases the RMSREs by 7% and 12% relative to AramcoMECH 2.0 [86] and AramcoMECH 3.0 [92], respectively.

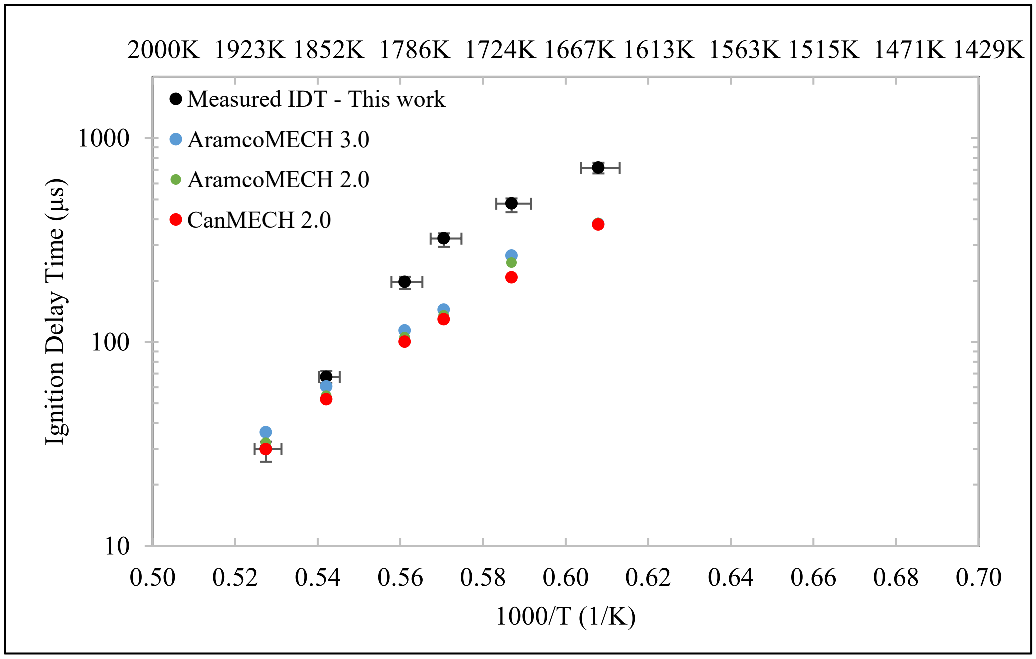

Figure 69: Measured vs. Modelled IDT 0.5%CH_4-30%H_2O-15%CO_2/Ar at φ=1 ~52.0 bar

Figure 70 superimposes the measured and modelled IDT data for 0.5%CH_4-45%CO_2/Ar at φ=1, conducted at pressures of 39.2-41.0 bar and temperatures of 1599-1775 K. All three models overestimate the measured IDTs. It can be observed from the near perfect overlap of the data that the three models have similar performances. RMSREs of Table 22, enable ranking performance with AramcoMECH 2.0 [86] being the best with an RMSRE 0.862, followed closely by AramcoMECH 3.0 [92] (RMSRE 0.870) and CanMECH 2.0 (RMSRE 0.887). RPRMSREs show that adopting CanMECH 2.0 slightly increases the RMSREs by 3% and 2% relative to AramcoMECH 2.0 [86] and AramcoMECH 3.0 [92], respectively.

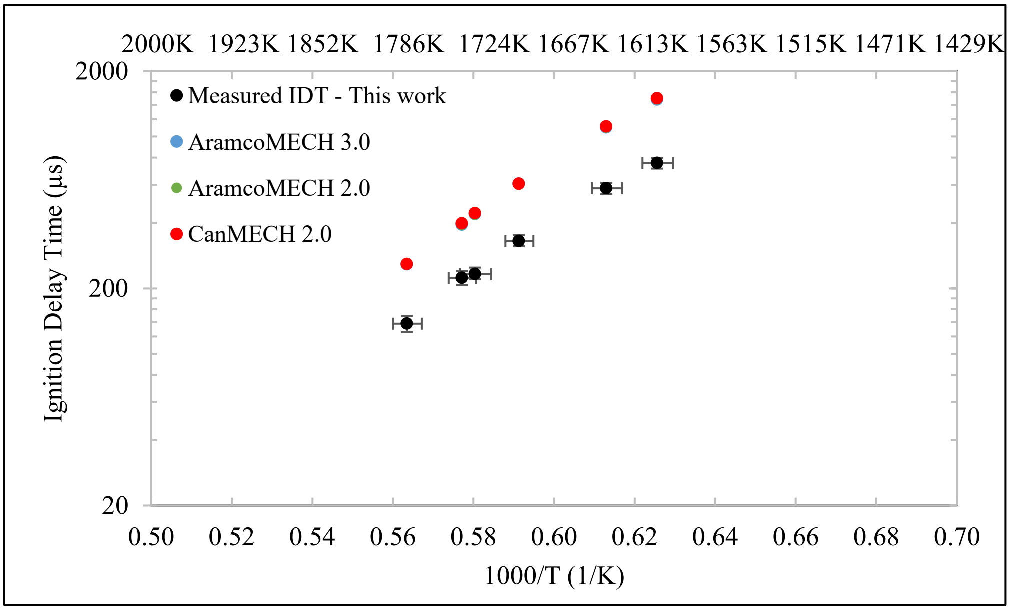

Figure 70: Measured vs. Modelled IDT 0.5%CH_4-45%CO_2/Ar at φ=1 ~39.9 bar

The overall RMSREs illustrate that with the improvements brought about by CanMECH 2.0 in predicting the 45%H_2O- and 30%H_2O-15%CO_2-diluted IDT data at 40 bar it has the best overall performance in predicting the high-pressure IDT dataset of this work, with an overall RMSRE of 1.42. Adopting CanMECH 2.0 for these pressurized oxy-fuel mixtures brings about an overall 5% and 7% improvement to AramcoMECH 2.0 [86] and AramcoMECH 3.0 [92], respectively.

It is also important to note that with the exception of experiments conducted for 30%H_2O-15%CO_2/Ar ~52.0 bar (Figure 69), a systematic overprediction of the 2 and 40 bar experimental IDTs is apparent for all bath gases by all three models (see Figure 64 to Figure 70). To understand the source of such errors, it is important to evaluate the models' performance against other experimental data from the literature. To this end, the prediction ability of the models were also evaluated against shock tube validation data of Shao et al. [175].

Comparison of the three models RMSREs of Table 22, for validation dataset 9 of Shao et al. [175], show that the for 1.96%CH_4/Ar at φ=1, spanning 13.7-15.7 bar and 1420-1752 K, adopting CanMECH 2.0 brings a 10% and 11% improvement relative to AramcoMECH 2.0 [86] and AramcoMECH 3.0 [92], as indicated by the RPRMSRE values. Moreover, CanMECH 2.0's low RMSRE of 0.092 suggests that a systematic prediction error is not present at these intermediate pressures, unlike the low- and high-pressure experimental data of this work.

Validation dataset 10 of Shao et al. [175], involves the same mixture as dataset 9, but is conducted at higher pressures of 51.7-59.0 bar, and temperatures of 1437-1663 K. Table 22 RPRMSREs indicate that CanMECH 2.0 again brings about improvements of 7% and 8%, relative to AramcoMECH 2.0 [86] and AramcoMECH 3.0 [92]. This is encouraging as this dataset is the highest pressure stoichiometric CH_4/Ar IDT validation dataset of this work, for which CanMECH 2.0 performs better than the incumbent models. Also, the low RMSRE of 0.088 of CanMECH 2.0 in predicting this dataset, dismisses the existence of a systematic prediction error, in contrast with the low- and high-pressure experimental data of this work (datasets 1-5 and 7).

Comparison of high RMSREs of datasets 1 and 3 of this work with Shao et al.'s [175] validation datasets 9 and 10, suggests that the systematic error observed in the former could have experimental origins. This is because these datasets involved overlapping temperature ranges and stoichiometric (φ=1) ignition of CH_4 in Ar bath. It was not however, possible to conclusively attribute these errors to experiments, as the pressures explored in this work differed from those of Shao et al., and a source of error was not identified upon a second review of neither the raw experimental data nor the experimental procedure followed in this work.

Validation datasetset 11 of Shao et al. [175], explores a fuel rich mixture involving 3.85%CH_4/Ar at φ=2, spanning intermediate pressures of 13.5-15.0 bar and temperatures of 1464-1782 K. For this rich mixture Table 22 shows that AramcoMECH 3.0 [92] performs best with an RMSRE of 0.140, followed closely by AramcoMECH 2.0 [86] and CanMECH 2.0 with RMSREs of 0.141 and 0.163, respectively. CanMECH 2.0 increase the RMSREs by 16% relative to both of the incumbent models as indicated by the RPRMSREs of Table 22.

Table 22 RMSREs indicate that for stoichiometric C_2H_4/Ar mixture of validation experiments of dataset 12 of Shao et al. [175], spanning temperatures of 1132-1317 K and pressures of 15.7-16.9 bar CanMECH 2.0 outperforms AramcoMECH 2.0 [86] and AramcoMECH 3.0 [92]. This is shown by the

37% and 38% improvement brought about to the RMSREs of 0.266 and 0.262 of AramcoMECH 2.0 [86] and AramcoMECH 3.0 [92], respectively.

Dataset 13 of Shao et al. [175], involves the same stoichiometric mixture of ethylene, but at higher pressures of 60.3-64.1 bar and at lower temperatures of 1095-1311 K. RMSREs of Table 22 indicate that AramcoMECH 2.0 [86] performs best (RMSRE of 0.149) followed closely by AramcoMECH 3.0 [92] and CanMECH 2.0 with RMSREs of 0.159 and 0.209. It should be noted that while RPRMSREs values of 41% and 32% may seem large, as the incumbent models' RMSREs are very low, these high relative percent RMSREs are not of concern, and the three models' performance are not very different.

Table 22 RMSREs illustrate that for the fuel rich 2.66%C_2H_4/Ar at φ=2, spanning intermediate pressures of 15.9-16.6 bar and temperatures of 1122-1268 K, of dataset 14 adopted from Shao et al. [175], CanMECH 2.0 is the best performing model. Relative to AramcoMECH 2.0 [86] and AramcoMECH 3.0 [92], CanMECH 2.0 reduces the RMSREs by 19% and 27% respectively.

Validation dataset 15 of Shao et al. [175] involves a stoichiometric mixture of the larger hydrocarbon C_3H_6 at a concentration of 0.88% in an Ar bath. This validation dataset spans temperatures of 1255-1488 K and pressures of 14.7-15.9 bar, Table 22 RMSREs show that while AramcoMECH 2.0 [86] is the best performing model with an RMSRE of 0.175, CanMECH 2.0's performance is very similar with an RMSRE of 0.178. AramcoMECH 3.0 [92], however, has a significantly larger RMSRE. Expectedly, RPRMSREs indicate that while adopting CanMECH 2.0 brings about a 42% improvement relative to AramcoMECH 3.0 [92], it increases the RMSRE relative to AramcoMECH 2.0 [86], but by only 2%.

Validation datasets 16 to 19 involve binary mixtures of the three hydrocarbons CH_2, C_2H_4, and C_3H_6 adopted from Shao et al. [175]. Dataset 16 of Table 22 involves a stoichiometric mixtures of 0.54%CH_4/0.96%C_2H_4/Ar, at temperatures of 1133-1340 K and pressures of 15.4-16.5. The very high RPRMSREs of 126% and 103% listed for CanMECH 2.0 relative to AramcoMECH 2.0 [86] and AramcoMECH 3.0 [92] for this dataset, are not a cause for concerns. This is because these values are calculated relative to the very low RMSRE values of 0.097 and 0.108 for AramcoMECH 2.0 [86] and AramcoMECH 3.0 [92]. As such all three models in fact perform reasonably well.

Validation dataset 17 involves a stoichiometric binary fuel mixture of 0.25%C_2H_4/0.72%C_3H_6/Ar, at 15 bar and 1324 K. RPRMSREs illustrate that CanMECH 2.0 brings about improvements of 32% and

68% relative to AramcoMECH 2.0 [86] and AramcoMECH 3.0 [92]. As the incumbent models RMSREs were large i.e., 0.607 and 0.286 for AramcoMECH 2.0 [86] and AramcoMECH 3.0 [92], this improvement is valuable.

Validation dataset 18 from Shao et al. [175] involves a stoichiometric mixture of 0.53%C_2H_4/0.53%C_3H_6/Ar tested at temperatures of 1212-1329 K and pressures of 15.1-15.8 bar. Table 22 RMSREs shows that CanMECH 2.0 performs best with an RMSRE of 0.132, followed by AramcoMECH 2.0 [86] and AramcoMECH 3.0 [92] with RMSREs of 0.169 and 0.449. The negative RPRMSREs of 22% and 71%, illustrate that adopting CanMECH 2.0 brings about significant improvement relative to the incumbent models.

Validation dataset 19 from Shao et al. [175] involves a stoichiometric mixture containing 0.88%C_2H_4/0.29%C_3H_6/Ar. The IDT tests were conducted at temperatures of 1206-1326 K and pressures of 15.0-15.7 bar. RPRMSREs suggest that adopting CanMECH 2.0 brings about 19% and 85% improvement relative to the incumbent models AramcoMECH 2.0 [86] and AramcoMECH 3.0 [92]. This suggests that relative to AramcoMECH 3.0 [92], with an RMSRE of 0.354 adopting CanMECH 2.0 brings about a noticeable improvement.

Overall for the 11 datasets of Shao et al. [175] adopting CanMECH 2.0 performs best with an overall RMSRE of 0.880. CanMECH 2.0 brings about a 3% and a 5% improvement overall relative to the incumbent models AramcoMECH 2.0 [86] and AramcoMECH 3.0 [92], respectively, as indicated by the RPRMSRE values.

Table 22, illustrates that overall, for the 136 shock tube IDT data considered in this work, spanning temperatures of 1095-1896 K, pressures of 1.81-64.1 bar, equivalence ratios of 0.93-1, involving fuels CH_4, C_2H_4, C_3H_6, in bath gases containing 0-45%CO_2, 0-45%H_2O, and Ar, CanMECH 2.0 performs best, with an overall RMSRE of 0.88. Relative to AramcoMECH 2.0 [86] and AramcoMECH 3.0 [92], having overall RMSREs of 0.89 and 0.91, CanMECH 2.0 brings about 1% and 3% overall improvement.

Based on the results of the performance evaluation conducted by the graphical examination of the IDT data of this work (see Figure 64 to Figure 70), and the RPRMSRE values of Table 22, the following are deduced from the work presented in this chapter:

1. CanMECH 2.0, outperforms the incumbent models AramcoMECH 2.0 [86] and AramcoMECH 3.0 [92], by 5% and 7% respectively, in predicting the new high-pressure (40-50 bar) IDT validation data of this work involving bath gases 45%H_2O, 30%H_2O-15%CO_2 and 45%CO_2;
2. CanMECH 2.0, outperforms the incumbent models AramcoMECH 2.0 [86] and AramcoMECH 3.0 [92] by 3% and 35% respectively in predicting Shao et al. [175] intermediate- to high-pressure (13.5-64.1 bar) IDT validation data involing CH_4, C_2H_4, and C_3H_6 and mixtures thereof;
3. AramcoMECH 2.0 [86] and AramcoMECH 3.0 [92] outperformed CanMECH 2.0 in predicting the low-pressure (~2 bar) IDTs of this work, with CanMECH 2.0 having 9% higher RMSREs relative to these incumbent models.
4. Overall the newly proposed CH_4 detailed kinetics model constructed, CanMECH 2.0 brings an overall improvement of 1% and 3% in predicting the complete validation dataset considred in this work. Hence this model is recommended for future model improvement and adoption.

Chapter 8 Conclusions and Recommendations

8.1 Conclusions

In this thesis the impacts of high pressures, as well as H_2O and CO_2 concentrations on oxy-combustion kinetics were investigated both experimentally and through modelling. From the research conducted the following conclusions are made:

1. Low-pressure shock tube IDT data for 4% H_2 stoichiometric reactive mixture, in Ar and 45%CO_2/Ar, at temperatures spanning 917-1237 K and pressures in the range of 1.6-2.4 bar, revealed that IDTs in 45%CO_2/Ar bath were larger than those in Ar-diluted mixtures. Uncertainties in T_5 (mean: ± 0.4%) and P_5 (mean: ± 1.3%) stemmed mainly from the incident shock velocity measurement errors.
2. Novel high-pressure shock tube IDT data for 4% H_2 stoichiometric reactive mixtures, in Ar, 45%H_2O/Ar, 30%H_2O/15%CO_2/Ar and 45%CO_2/Ar, at temperatures of 1084-1242 K and pressures of 37-44 bar, demonstrated that IDTs in 45%H_2O/Ar, 30%H_2O/15%CO_2/Ar and 45%CO_2/Ar were larger than those in Ar-diluted mixtures. For Ar-diluted tests uncertainties of T_5 (mean: ±0.24%) and P_5 (mean: +1.16/-1.15%), mainly stemmed from incident shock velocity measurement errors. On the other hand, for the 45%H_2O/Ar, 30%H_2O/15%CO_2/Ar and 45%CO_2/Ar, the main sources of error of T_5 (mean: +0.46/-0.61%) and P_5 (mean: +1.35/1.27%), in addition to incident shock velocity measurements, pertained to the assumptions of ideal thermodynamic properties and ideal P-V-T behavior of mixtures prepared.
3. A new and improved H_2/CO mechanism with minimal parameter tuning, CanMECH 1.0 was developed by:
    a. Constructing an untuned reaction mechanism, evaluating its performance using the new IDT experimental data of this work, as well as other data from the literature;
    b. Conducting sensitivity analyses which identified the Ar-specific low-pressure-limit rate of R9: $H+O_2(+M)=HO_2(+M)$ as the target tuning parameter to improve the model's performance; and,

   c. Carrying out a parameteric study, which illustrated that a 12% reduction of the pre-exponential factor of the Ar-specific low-pressure-limit rate of R9 results in the best fit. This tuning was then implemented and the resulting model, was named CanMECH 1.0.

4. Performance comparison of CanMECH 1.0 showed it outperformed the well-cited Keromnes et al. mechanism [28], for 16 out of 22 shock tube IDT validation datasets, and had an identical performance for another two. Overall, adopting CanMECH 1.0 was shown to bring about a 26% improvement in predicting all the shock tube IDT validation datasets considered in this work. Of particular importance, CanMECH 1.0 performed better in predicting the IDTs of H_2O- and CO_2-laden mixtures, as well as all IDT data at pressures of 17-43.8 bar.

5. Reaction pathways analyses (Rate-of-production, pressure- and temperature-dependent IDT sensistivities, IDT temperature sweeps) conducted over the temperature range of 1209-1237 K (upper end of experimental temperature range) showed, that:
   a. At 2 bar in Ar bath, a low-pressure high-temperature IDT regime is dominant. At this condition OH production is dominated by the reaction pathway R1: $H+O_2=OH+O$ and R2: $O+H_2=OH+H$ and R3: $OH+H_2=H+H_2O$
   b. With increase in pressure, the formation of HO_2 through R3 + R9: $H+O_2(+M)=HO_2(+M)$ forms an integral part of dominant paths producing OH, such that:
      i. At 40 bar:
         1. For Ar bath, R3+R9+R11: $HO_2+H=OH+OH$ becomes a delayed dominant path, with R1+R2+R3 dominant at earlier stages;
         2. For 45%CO_2 bath, R3+R9+R11 becomes a delayed dominant path, with R1+R2+R3 dominant at initial stages (very short lived), and paths involving R15: $H_2O_2(+M)=OH+OH(+M)$ become dominant in between;
         3. For 45%H_2O bath, paths through R3+R9+R15 completely dominate, and R3+R9+R11 provides a delayed non-dominant alternate path;

ii. At 150 bar:

    1. For Ar bath, R3+R9+R11 becomes a delayed dominant path, R1+R2+R3 dominance is limited to short-lived initial stages, and paths involving R15: $H_2O_2(+M)=OH+OH(+M)$ become dominant in between;
    2. For 45%CO_2 bath, paths through R3+R9+R15 completely dominate, and the paths R1+R2+R3 (at initial stages) and R3+R9+R11 (preceeding ignition) provide non-dominant alternate paths;
    3. For 45%H_2O bath, paths through R3+R9+R15 completely dominate, and provide a non-dominant alternate path as well;

For the dominant paths involving R3+R9+R15, H_2O_2 is initially produced through -R17: $HO_2+H_2=H_2O_2+H$, and later through R14: $HO_2+HO_2= H_2O_2+O_2$, for all bath gases.

For H_2O an additional non-dominant path involving R3+R9+R15 and –R19: $HO_2+H_2O=OH+H_2O_2$ becomes competitive, dominance of which increases with increased pressure.

In summary, in the temperature range of 1209-1226 K, at low pressures (~2 bar) OH is produced mainly through R1+R2+R3. Increasing the pressure to 40 bar increases OH production through R3+R9+R11 pathway involving HO_2. Increasing the pressure further to 150 bar, increases dominance of OH production pathways involving H_2O_2 i.e., R3+R9+R15 which includes –R17 and to a lesser extent -R19 (only in 45%H_2O at initial stages) and R14 (at later stages). Addition of H_2O strongly favors dominance of H_2O_2 pathways leading to ignition. Addition of CO_2 favors dominance of H_2O_2, more than Ar, but less than H_2O.

6. IDT temperature sweeps and temperature-dependent IDT sensitivity analyses show that the chemistry of reactive mixtures in 30%H_2O/15%CO_2 is nearly the same as those in 45%H_2O/Ar. Impact of presence of H_2O is significantly larger than that of CO_2.
7. Temperature-dependent IDT sensitivity analyses showed that while the reaction paths explored are understood at 40 and 150 bar at 1200-1250 K, these conclusions are not

extendable to higher temperatures. Variations of IDT-sensitivities suggest that the chemistries change significantly at higher temperatures. This is the case both at 40 and 150 bar for 45%H_2O/Ar, 45%CO_2/Ar and 30%H_2O/15%CO_2/Ar baths.

8. Log IDT vs. 1000/T plots, for T between 950 and 2200 K and pressures of 2, 40 and 150 bar, exhibited an S-shaped trend for all bath gases, respresenting three different IDT regimes. The low- and high-temperature regimes were separated by a transitional regime, over which dominant reaction pathways switch. It is concluded that:
    a. Increases in pressure cause the temperature span over which transitional regime dominates to stretch and make the boundaries separating the three different regimes less distinct. Also, increases in pressure shifts the dominance of low-temperature regime to higher temperatures.
    b. Increasing concentrations of H_2O (0-65%) and CO_2 (0-65%) exhibit a similar effect to that of pressure. Additionally:
        i. At 2 bar, increasing concentration of either CO_2 or H_2O, increases IDTs;
        ii. At 40 bar, IDTs increase with increases in H_2O concentrations of up to 35%, after which IDTs generally decrease with higher H_2O concentrations;
        iii. At 40 bar, IDTs generally increase with increases in CO_2 concentrations of up to 45%, after which it nearly plateaus;
        iv. At 150 bar, IDTs increase with increases in H_2O concentrations of up to 20%, after which IDTs generally decrease for higher H_2O concentrations; and,
        v. At 150 bar, IDTs increase with increases in CO_2 concentrations of up to around 45%, after which IDTs decrease with higher CO_2 concentrations.
9. Low-pressure shock tube IDT experimental data involving stoichiometric 3-3.44% CH_4, at pressures of 1.8-2.4 bar, temperatures of 1486-1805 K in bath gases containing Ar, and 45%CO_2/Ar, were generated. Analysis of uncertainties revealed that uncertainties of reported T_5 (mean: ±0.46%), and P_5 (mean: ±1.1%), mainly stemmed from the incident shock velocity measurements, whereas graphical IDT determination uncertainties were a result of combination of signal quality, and noise levels.

10. New high-pressure shock tube IDT experimental tests with 0.48-0.5% CH_4, at equivalence ratios of 0.93-1.0, pressures of 37-53 bar, temperatures of 1536-1896 K, were carried out. Main source of uncertainties in reported IDTs were attributed to signal quality and noise levels. Uncertainties in reported T_5 (mean: ±0.77%), and P_5 (mean: ±1.5%) of the reactor pertained to the incident shock velocity measurement errors in Ar baths. Additionally, for the H_2O and CO_2-diluted tests uncertainties of T_5 (mean: +0.57/-0.76%), P_5 (mean: +1.4/-1.32%) in addition to incident shock velocity measurements, pertained to the assumptions of ideal thermodynamic properties and ideal P-V-T behavior of mixtures prepared.
11. Using the hierarchical model development approach presented, a CH_4 mechanism called CanMECH 2.0 was constructed. CanMECH 2.0 was assembled by replacing the H_2/CO submechanism of the well-cited C_1-C_4 kinetics model AramcoMECH 2.0 [86], with CanMECH 1.0.
12. Performance of CanMECH 2.0, AramcoMECH 2.0 [86], and its successor AramcoMECH 3.0 [92] were evaluated, in reproducing the shock tube IDT validation datasets of this work as well as those from Shao et al. [175]. Overall, the untuned CanMECH 2.0 outperformed AramcoMECH 2.0 [86] and AramcoMECH 3.0 [92] by 1% and 3%, respectively.
13. Of particular importance CanMECH 2.0 performed better than AramcoMECH 2.0 [86] and AramcoMECH 3.0 [92] by 5% and 7% in reproducing high-pressure (37-53 bar) IDT data of this work. It performed better (6-7% improvement) than the two incumbents for the 45%H_2O-laden IDT dataset of this work, which is of particular importance. CanMECH 2.0 also brought about a 3% and 25% overall improvement relative to AramcoMECH 2.0 [86] and AramcoMECH 3.0 [92] in predicting Shao et al.'s high pressure (13.5-64.1 bar) IDT data involving CH_4, C_2H_4 and C_3H_6.

8.2 Recommendations

The following two sets of recommendations are expected to help formulate impactful future work from an experimental and modeling points of view, respectively.

On the experimental front:

1. End-wall high speed camera imaging should be conducted, to explore the homogeneity of ignition for all mixtures in particular those containing 45% H_2O.

2. Higher concentrations of CH_4 should be explored, for the H_2O- and CO_2-laden experiments, as they are very effective OH* quenchers. Concentrations of 1% should provide a suitable starting point for high pressure experiments (~40 bar).
3. The cause of multiple rises in side-wall OH* and side-wall CH*, observed for many of the tests in this work, should be explored. These multiple inflections could be pointing to potentially significant localized energy release or ignition. End-wall pressure measurement is highly recommended as it is likely less impacted or potentially immune to the boundary layer, reflected shock bifurcation effects, as such it can:
    a. determine how important the localized emission detection is, in perturbing the temperature and pressure of the core section of the shock tube
    b. help delineate which emission rise corresponds to the main ignition event
4. Special attention should be given to minimize the noise by adjusting the gain of recording devices, e.g. oscilloscope, to minimize the extent of digital filtering required for data post-processing. Moreover, it is important to ensure that the peak emission of all diagnostics side-wall and end-wall OH* or CH* are captured for every test, to enable exploring other IDT definitions. This is based on the observation that peak CH* and OH* emission may provide alternative validation tools for the slow rise of emission signals observed for the H_2O- and CO_2-laden experiments.
5. The reasons behind, an absence of pressure spike in the case of 45%H_2O-diluted high-pressure IDTs should be explored. Testing of different lasers with different laser properties to detect the Schlieren spike, may be helpful, to enable more accurate detection of the arrival of normal portion of the reflected shock wave.

On the modeling front, based on the modeling approach devised and detailed in Chapter 3:

1- RMG should be utilized to detect missing reactions both pressure-dependent and pressure-independent, over a wider temperature range of 700-2000 K, and pressure range of 2-300 bar. CanMECH 1.0 and CanMECH 2.0 should be augmented to include these reactions.

2- Sensitivity analyses with RMG should be conducted to identify the critical reaction rate parameters for CanMECH 2.0 (CH_4 mechanism). If those rates are pressure-dependent, whether they are expressed in Chebyshev or PLOG format, it is imperative to express them using Troe formulation. This is to ensure H_2O's significantly enhanced effect is properly delineated and captured vis-à-vis other bath gases.

3- The same procedure followed for the development of CanMECH 1.0 should be repeated to identify the appropriate tuning parameters as well as the extent of tuning appropriate for CanMECH 2.0.

4- If pressures above the critical point of either H_2O or CO_2 are being explored, theoretical or experimental re-evaluation of reaction rates are imperative, as these bath gases forcefields are expected to impact the kinetics, and may even contribute chemically through unexplored reaction pathways, as suggested by Wang et al. [172].

Bibliography

[1] International Energy Agency, "World Energy Outlook 2020 - Executive Summary," International Energy Agency, Paris, 2020.

[2] D. J. Dillon, V. White, R. J. Allam, R. A. Wall and J. Gibbins, "Oxy Cobmsution Processes for CO2 Capture from Power plant," IEA Greenhouse Gas R&D Programme, Cheltenham, 2005.

[3] L. Mancuso and N. Ferrari, "CO2 capture at coal based power and hydorgen plants," IEAGHG, Cheltenham, 2014.

[4] International Energy Agency, "CCUS in Clean Energy Transitions," IEA, Paris, 2020.

[5] A. Beigzadeh, A. Shafeen, M. Abbassi, C. Salvador and K. E. Zanganeh, "Optimized Multi-pollutant Control in Oxy-fuel Combustion Systems Using CO2 Capture and Compression Process," *Energy Procedia,* vol. 63, pp. 8134-8143, 2014.

[6] I. Glassman and R. A. Yetter, Combustion, 4th Edition, Burlington, MA: Elsevier, 2008.

[7] N. T. Weiland and C. W. White, "Performance and cost assessment of a natural gas-fueled direct sCO2 power plant," National Energy Technology Laboratory, Pittsburgh, March 15, 2019.

[8] K. Zanganeh, A. Shafeen, C. Salvador and A. Beigzadeh, "G2 Technology for production of power, water or steam and pipeline-ready pressurized CO2," in *5th Oxyfuel Combusiton Research Network Meeting*, Wuhan, October 27-30, 2015.

[9] K. Brun, P. Friedman and R. Dennis, Fundamentals and Applications of Supercritical Carbon Dioxide (SCO2) Based Power Cycles, Duxford: Elsevier - WOODHEAD PUBLISHING, 2017.

[10] R. Allam, S. Martin, B. Forrest, J. Fetvedt, X. Lu, D. Freed, W. G. Brown Jr., T. Sasaki, M. Itoh and J. Manning, "Demonstration of the Allam Cycle: An Update on the Development Status of a High Efficiency Supercritical Carbon Dioxide Power Process Employing Full Carbon Capture," *Energy Procedia,* vol. 114, pp. 5948-5966, 2017.

[11] C. White, D. Gray, J. Plunkett, W. Shelton, N. Weiland and T. Shultz, "Techno-economic Evaluation of Utility-Scale Power Plants Based on the Indirect sCO2 Brayton Cycle," National Energy Technology Laboratory, Pittsburgh, September 25, 2017.

[12] M. Ilinich, K. Zanganeh, T. Robertson, H. Dole, D. Seo, H. Radfarnia, H. Saari and A. Beigzadeh, "The effect of elevated temperatures and pressure on five metallic materials in quasi-static supercritical CO2 environment," in *7th International Supercritical CO2 Power Cycles Symposium*, San Antonio, 2020.

[13] O. Pryor, S. Barak, J. Lopez, E. Ninnemann, B. Koroglu, L. Nash and S. S. Vasu, "High Pressure Shock Tube Ignition Delay Time Measurements During Oxy-Methane Combustion With High Levels of CO2 dilution," *Journal of Energy Resources Technology,* vol. 139, no. 4, pp. 042208-1-6, 2017.

[14] O. Pryor, S. Barak, B. Koroglu, E. Ninnemann and S. S. Vasu, "Measurements and interpretation of shock tube ignition delay times in highly CO2 diluted mixtures using multiple diagnostics," *Combustion and Flame,* vol. 180, pp. 63-76, 2017.

[15] B. Koroglu, O. M. Pryor, J. Lopez, L. Nash and S. S. Vasu, "Shock tube ignition delay times and methane time-histories measurements during excess CO2 diluted oxy-methane," *Combustion and Flame,* vol. 164, pp. 152-163, 2016.

[16] J. Shao, R. Choudhary, D. F. Davidson, R. K. Hanson, S. Barak and S. Vasu, "Ignition delay times of methane and hydrogen highly diluted in carbon dioxide at high pressures up to 300 atm," *Proceedings of the Combustion Institute,* vol. 37, pp. 4555-4562, 2019.

[17] S. Barak, E. Ninnemann, S. Neupane, F. Barnes, J. Kapat and S. Vasu, "High-Pressure Oxy-Syngas Ignition Delay Times With CO2 Dilution: Shock Tube Measurements and Comparison of the Performance of Kinetic Mechanisms," *Journal of Engineering for Gas Turbines and Power,* vol. 141, pp. 021011-1-021011-7, 2019.

[18] F. Battin-Leclerc, J. M. Simmie and E. Blurock, Cleaner Combustion: Developing Detailed Kinetic Models, London: Springer, 2013.

[19] V. P. Zhukov and V. A. Sechenov, "Spontaneous Ignition of Methane–Air Mixtures in a Wide Range of Pressures," *Combustion, Explosion, and Shock Waves,* vol. 39, no. 5, pp. 487-495, 2003.

[20] Y. Kochar, J. Sietzman, T. Lieuwen, W. Metcalfe, S. Burke, H. Curran, M. Krejci, W. Lowry, E. Petersen and G. Bourque, "LAMINAR FLAME SPEED MEASUREMENTS AND MODELING OF ALKANE BLENDS AT ELEVATED PRESSURES WITH VARIOUS DILUENTS," in *Proceedings of ASME Turbo Expo 2011*, Vancouver, 2011.

[21] V. P. Zhukov, "Kinetic model of alkane oxidation at high pressure from methane to n-heptane," *Combustion Theory and Modeling,* vol. 13, no. 3, pp. 427-442, 2009.

[22] W. K. Metcalfe, S. M. Burke, S. S. Ahmed and H. J. Curran, "A Hierarchical and Comparative Kinetic Modeling Study of C1-C2 Hydrocarbon and Oxygenated Fuels," *International Journal of Chemical Kinetics,* vol. 45, no. 10, pp. 638-675, 2013.

[23] C. N and K. R. Westberg, "Chemical kinetic data sheets for high-temperature chemical reactions," *Journal of Physical and Chemical Rerference data,* vol. 12, no. 3, pp. 531-590, 1983.

[24] W. Tsang and H. R. F, "Chemical Kinetic Data Base for Combustion Chemistry. Part I. Methane and Related compounds," *Journal of Physical and Chemical Rerference data,* vol. 15, no. 3, pp. 1087-1222, 1986.

[25] D. L. Baulch, C. T. Bowman, C. J. Cobos, R. A. Cox, T. Just, J. A. Kerr, M. J. Pilling, D. Stocker, J. Troe, W. Tsang, R. W. Walker and W. J, "Evaluated Kinetic Data for Combustion Modeling: Supplement II," *Journal of Physical and Chemical Rerference data,* vol. 34, no. 3, pp. 757-1397, 2005.

[26] "Evaluated Kinetic Data for High-Temperature Reactions," *Journal of Chemical and Physical Reference Data,* vol. 15, no. 2, pp. 465-592, 1986.

[27] M. J. Pilling, *Combustion Chemistry,* New Jersey: Combustion Energy Research Frontier - Summerschool, 2013.

[28] A. Keromnes, W. K. Metcalfe, K. A. Heufer, N. Donohoe, A. K. Das, C.-J. Sung, J. Herzler, C. Naumann, P. Griebel, O. Mathieu, M. C. Krejci, E. L. Petersen, W. J. Pitz and H. J. Curran, "An experimental and detailed chemical kinetic modeling study of hydrogen and syngas mixture oxidation at elevated pressures," *Combustion and flame,* vol. 160, pp. 995-1011, 2013.

[29] Z. Hong, D. F. Davidson and R. K. Hanson, "An improved H2/O2 mechanism based on recent shock tube/laser absorption measurements," *Combustion and Flame,* vol. 158, no. 4, pp. 633-644, 2011.

[30] M. P. Burke, M. Chaos, Y. Ju, F. L. Dryer and S. J. Klippenstein, "Comprehensive H2/O2 Kinetic Model for High-Pressure Combustion," *International Journal of Chemical Kinetics,* vol. 44, no. 7, pp. 444-474, 2012.

[31] A. A. Konnov, "Yet another kinetic mechanism for hydrogen combustion," *Combustion and Flame,* vol. 203, pp. 14-22, 2019.

[32] V. A. Alekseev, M. Christensen and A. A. Konnov, "The effect of temperature on the adiabatic burning velocities of diluted hydrogen flames: A kinetic study using an updated mechanism," *Combustion and Flame,* vol. 162, pp. 1884-1898, 2015.

[33] A. A. Konnov, "On the role of excited species in hydrogen combustion," *Combustion and flame,* vol. 162, pp. 3755-3772, 2015.

[34] J. Li, A. Kazakov and F. L. Dryer, "An Updated Comprehensive Kinetic Model of Hydrogen Combustion," *International Journal of Chemical Kinetic,* vol. 36, no. 10, pp. 566-575, 2004.

[35] J. Li, Z. Zhao, A. Kazakov, M. Chaos, F. L. Dryer and J. J. Scire, JR., "A comprehensive Kinetic Mechanism for CO, CH2O, and CH3OH Combustion," *International Journal of Chemical Kinetics,* vol. 39, no. 3, pp. 109-136, 2007.

[36] C. Olm, I. G. Zsely, R. Palvolgyi, T. Varga, T. N. Nagy, H. J. Curran and T. Turanyi, "Comparison of the performance of several recent hydrogen combustion mechanisms," *Combustion and Flame,* vol. 161, pp. 2219-2234, 2014.

[37] M. Goswami, J. G. H. van Griensven, R. J. M. Bastiaans, A. A. Konnov and L. P. H. de Goey, "Experimental and modeling study of the effect of elevated pressure on lean high-hydrogen syngas flames," *Proceedings of Combustion Institute,* vol. 35, pp. 655-662, 2015.

[38] T. Varga, T. Nagy, C. Olm, I. G. Zsely, R. Palvolgyi, E. Valko, G. Vincze, M. Cserhati, H. J. Curran and T. Turanyi, "Optimization of a hydrogen combustion mechanism using both direct and indirect measurements," *Proceedings of the Combustion Institute,* vol. 35, pp. 589-596, 2015.

[39] J. Li, A. Kazakov and F. L. Dryer, "An Updated Comprehensive Kinetic Model of Hydrogen Combustion," *International Journal of Chemical Kinetic ,* vol. 36, no. 10, pp. 566-575, 2004.

[40] Z. Hong, D. F. Davidson, B. E. A and H. R. K, "A new shock tube study of the H+O2->OH+O reaction rate using tunable diode laser absorption of H2O near 2.5 m," *Proceedings of Combustion Institute,* vol. 33, pp. 309-316, 2011.

[41] Z. Hong, R. D. Cook, D. F. Davidson and R. K. Hanson, "A shock tube study of OH+ H2O2→ H2O+ HO2 and H2O2+ M→ 2OH+ M using laser absorption of H2O and OH," *The Journal of Physical Chemistry A,* vol. 114, no. 18, pp. 5718-5727, 2010.

[42] C. Olm, I. G. Zsely, T. Varga, H. J. Curran and T. Turanyi, "Comparison of the performance of several recent syngas combustion mechanisms," *Combustion and Flame,* vol. 162, pp. 1793-1812, 2015.

[43] ANSYS, *Chemkin-Pro Theory Manual 17.2,* San Diego: ANSYS, Inc, 2016.

[44] R. W. Bates, D. M. Golden, R. K. Hanson and C. T. Bowman, "Experimental study and modeling of the reaction H+O2+M->HO2+M (M=Ar, N2, H2O) at elevated pressures and temperatures between 1050 and 1250 K," *Physical Chemistry Chemical Physics,* vol. 3, no. 12, pp. 2337-2342, 2001.

[45] A. W. Jasper, M. C. Oana and J. A. Miller, ""Third Body" collision efficiencies for combustion modeling: Hydrocarbons in atomic and diatomic baths," *Proceedings of the combustion Institute,* vol. 35, no. 1, pp. 197-204, 2014.

[46] M. P. Burke and R. Song, "Evaluating Mixture Rules for Multi-Component Pressure Dependence: H+O2(+M)=HO2(+M)," *Proceedings of the Combustion Institute ,* vol. 36, no. 1, pp. 245-253, 2017.

[47] G. P. Smith, D. M. Golden, M. Frenklach, N. W. Moriarty, B. Eiteneer, M. Goldenberg, C. T. Bowman, H. R. K, S. Song, W. C. J. Gardiner, V. Lissianski and Z. Qin, "GRI-MECH 3.0," [Online]. Available: http://www.me.berkeley.edu/gri_mech/. [Accessed 20 June 2017].

[48] R. K. Hanson, *Quantitative laser Diagnostics for Combustion Chemistry and Propulsion,* Princeton: Combustion Energy Research Frontier Summer School, 2013.

[49] R. K. Hanson, *Quantitative Laser Diagnostics for Combustion Chemistry and Propulsion,* Princeton: Combustion Energy Research Frontier Summer School, 2015.

[50] D. J. Beerer and V. G. McDonell, "An experimental and kinetic study of alkane autoignition at high pressures and intermediate temperatures," *Proceedings of the Combustion Institute,* vol. 33, no. 1, pp. 301-307, 2011.

[51] Z. Hong, G. A. Pang, S. S. Vasu, D. F. Davidson and R. K. Hanson, "The use of driver inserts to reduce non-ideal pressure variations behind reflected shock waves," *Shock Waves,* vol. 19, no. 2, pp. 113-123, 2009.

[52] G. A. Pang, D. F. Davidson and H. R. K, "Experimental study and modeling of shock tube ignition delay times for hydrogen–oxygen–argon mixtures at low temperatures," *Proceedings of the Combustion Institute,* vol. 32, no. 1, pp. 181-188, 2009.

[53] E. Ninnemann, B. Koroglu, O. Pryor, S. Barak, L. Nash, Z. Loparo, J. Sosa, K. Ahmed and S. Vasu, "New insights into the shock tube ignition of H2/O2 at low to moderate temperatures using high-speed end-wall imaging," *Combustion and Flame,* vol. 187, pp. 11-21, 2018.

[54] J. W. Hargis and E. L. Petersen, "Methane Ignition in a Shock Tube with High Levels of CO2 dilution: Consideration of the Reflected-Shock Bifurcation," *Energy & Fuels,* vol. 29, pp. 7712-7726, 2015.

[55] J. Hargis, Methane ignition in a shock tube with high levels of CO2 dilution, College station: Texas A&M University, 2015.

[56] E. L. Petersen and R. K. Hanson, "Measurement of reflected-shock bifurcation over a wide range of gas composition and pressure," *Shock Waves,* vol. 15, pp. 333-340, 2006.

[57] J. Urzay, N. Kseib, D. F. Davidson, G. Iaccarino and R. K. Hanson, "Uncertainty-quantification analysis of the effects of residual impurities on hydrogen-oxygen in shock tubes," *Combustion and Flame,* vol. 161, pp. 1-15, 2014.

[58] C. R. Mulvihill and E. L. Petersen, "Concerning shock-tube ignition delay times: An experimental investigation of impurities in the H2/O2 system and beyond," *Proceedings of the combustion institute,* vol. 37, no. 1, pp. 259-266, 2019.

[59] S. M. Walton, X. He, B. T. Zigler, M. S. Wooldrige and A. Atreya, "An experimental investigation of iso-octane ignition phenomena," *Combustion and Flame,* vol. 150, pp. 246-262, 2007.

[60] E. L. Petersen, D. F. Davidson, M. Rohrig and R. K. Hanson, "SHOCK-INDUCED IGNITION OF HIGH-PRESSURE H2-O2-Ar AND CH4-O2-Ar MIXTURES," in *31st Joint Propulsion Conference and Exhibit*, San Diego, 1995.

[61] E. L. Petersen, M. Rohrig, D. F. Davidson, R. K. Hanson and C. T. Bowman, "HIGH-PRESSURE METHANE OXIDATION BEHIND REFLECTED SHOCK WAVES," in *Twenty-Sixth Symposium (International) on Combustion*, Napoli, The Combustion Institute, 1996, pp. 799-806.

[62] E. L. Petersen, D. F. Davidson and R. K. Hanson, "Ignition Delay Times of Ram Accelerator CH4/O2/Diluent Mixtures," *Journal of Propulsion and Power,* vol. 15, no. 1, pp. 82-91, 1999.

[63] H. Hashemi, J. M. Christensen, S. Gersen, H. Levinsky, K. S. J and P. Glarborg, "High-pressure oxidation of methane," *Combustion and Flame,* vol. 172, pp. 349-364, 2016.

[64] T. Le Cong, P. Dagaut and G. Dayma, "Oxidation of Natural Gas, Natural Gas/Syngas Mixtures, and Effect of Burnt Gas Recirculation: Experimental and Detailed Kinetic Modeling," *Journal of Engineering for Gas Turbines and Power,* vol. 130, pp. 041502-1-10, 2008.

[65] P. S. Veloo, Y. L. Wang, F. N. Egolfopoulos and C. K. Westbrook, "A comparative experimental and computational study of methanol, n-butanol flames," *Combustion and Flame,* vol. 157, pp. 1989-2004, 2010.

[66] N. Donohoe, A. Huefer, W. K. Metcalfe, H. J. Curran, M. L. Davis, O. Methieu, D. Plichta, A. Morones, E. L. Petersen and F. Guthe, "Ignition delay times, laminar flame speeds, and mechanism validation for natural gas/hydrogen blends at elevated pressures," *Combustion and Flame,* vol. 161, no. 6, pp. 1432-1443, 2014.

[67] R. K. Hanson, R. M. Spearrin and C. S. Goldenstein, Spectroscopy and Optical Diagnostics for Gases, Springer, 2016.

[68] C. L. Rasmussen, J. G. Jakobsen and P. Glarborg, "Experimental Measurements and Kinetic Modeling of CH4/O2 and CH4/C2H6/O2 Conversion at High Pressure," *International Journal of Chemical Kinetics,* vol. 40, no. 12, pp. 778-807, 2008.

[69] L. M. Raff, PRINCIPLES OF PHYSICAL CHEMISTRY, New Jersey: Prentice-Hall, 2001.

[70] B. M. Wong, D. M. Matheu and W. H. J. Green, "Temperature and Molecular Size Dependence of the High-Pressure Limit," *Journal of Physical Chemistry A,* vol. 107, no. 32, pp. 6206-6211, 2003.

[71] M. Moshfeghian, "Petroskills," 1 July 2009. [Online]. Available: http://www.jmcampbell.com/tip-of-the-month/2009/07/variation-of-natural-gas-heat-capacity-with-temperature-pressure-and-relative-density/. [Accessed 21 June 2017].

[72] A. Burcat, "Burcat's thermodynamic data," Laboratory for Chemical Kinetics., [Online]. Available: http://garfield.chem.elte.hu/Burcat/burcat.html.

[73] A. Burcat and B. Ruscic, "Third Millennium Ideal Gas and Condensed Phase Thermochemical Database for Combustion with Updates from Active Thermochemical Table," U.S. Department of Energy's Argonne National Laboratory, Argonne, 2005.

[74] C. W. Gao, J. W. Allen, W. H. Green and R. H. West, "Reaction Mechanism Generator: Automatic construction of chemical kinetic mechanisms," *Computer Physics Communications,* vol. 203, pp. 212-225, 2016.

[75] X. Wang and C. K. Law, "An analysis of the explosion limits of hydrogen-oxygen mixtures," *The Journal of Chemical Physics,* vol. 146, no. 20, pp. 134305-1-12, 2013.

[76] J. Troe, "Theory of Thermal Unimolecular Reactions in the Fall-off Range. I. Strong Collision Rate Constants," *Ber. Bunsenges. Phys. Chem.,* vol. 87, pp. 161-169, 1983.

[77] R. G. Gilbert and J. Troe, "Theory of Thermal Unimolecular Reactions in the Fall-off Range. II. Weak Collision Rate Constants," *Ber. Bunsenges. Phys. Chem.,* vol. 87, pp. 169-177, 1983.

[78] R. G. Gilbert, K. Luther and J. Treo, "Theory of Thermal Unimolecular Reactions in the Fall-off Range. II. Weak Collision Rate Constants.," *Berichte der Bunsengesellschaft für physikalische Chemie,* vol. 87, no. 2, pp. 169-177, 1983.

[79] S. J. Klippenstein, "From theoretical reaction dynamics to chemical modeling of combustion," *Proceedings of the Combustion Institute,* vol. 36, no. 1, pp. 77-111, 2017.

[80] A. N. Mazas, D. A. Lacoste and T. Schuller, "EXPERIMENTAL AND NUMERICAL INVESTIGATION ON THE LAMINAR FLAME SPEED OF CH4/O2 MIXTURES DILUTED WITH CO2 AND H2O.," in *Proceedings of ASME Turbo Expo 2010: Power for Land, Sea and Air*, Glasgow, 2010.

[81] N. Donohoe, K. A. Heufer, C. J. Aul, E. L. Petersen, G. Bourque, R. Gordon and H. J. Curran, "Influence of steam dilution on the ignition of hydrogen, syngas and natural gas blends at elevated pressures," *Combustion and flame,* vol. 162, no. 1, pp. 1126-1135, 2015.

[82] T. Turanyi and A. S. Tomlin, Analysis of Kinetic Reaction Mechanisms, Heidelberg: Springer, 2014.

[83] J. Shao, R. Choudhary, A. Susa, D. F. Davidson and R. K. Hanson, "Shock tube study of the rate constants for H+O2+M ->HO2+M(M=Ar, H2O, CO2, N2) at elevated pressures," *Proceedings of the Combustion Institute,* vol. 37, pp. 145-152, 2019.

[84] A. E. Masunov, E. E. Wait, A. A. Atlanov and S. S. Vasu, "Quantum Chemical Study of Supercritical Carbon Dioxide Effects on Combustion Kinetics," *The Journal of Physical Chemistry,* vol. 121, pp. 3728-3735, 2017.

[85] P. H. Stewart, C. W. Larson and D. M. Golden, "Pressure and temperature dependence of reactions proceeding via a bound complex. 2. Application to 2CH3 → C2H5 + H," *Combustion and Flame,* vol. 75, pp. 25-31, 1989.

[86] Y. Li, C.-W. Zhou, K. P. Somers, K. Zhang and H. J. Curran, "The oxidation of 2-butene: A high pressure ignition delay, kinetic modeling study and reactivity comparison with isobutene and 1-butene," *Proceedings of the combustion Institute,* vol. 36, pp. 403-411, 2017.

[87] G. P. Smith, Y. Tao and H. Wang, "Foundational Fuel Chemistry Model Version 1.0 (FFCM-1)," Stanford University, 31 05 2016. [Online]. Available: http://nanoenergy.stanford.edu/ffcm1. [Accessed 2017].

[88] E. Goos, "Thermochemical Database for Combustion with updates from Active Thermochemical Tables," German Aerospace Center (DLR), Institute of Combustion Technology, Chemical kinetics, 2017. [Online]. Available: http://www.dlr.de/vt/en/desktopdefault.aspx/tabid-7603/12862_read-32379/. [Accessed 12 July 2017].

[89] B. Ruscic, "Active Thermochemical Tables (ATcT)," US Argonne National Laboratory, 2020. [Online]. Available: http://atct.anl.gov/. [Accessed 24 November 2020].

[90] National Institute of Standards and Technology, "NIST Chemistry Webbok, SRD 69," U.S. Secretary of Commerce on behalf of the United States of America. All rights reserved, 2018. [Online]. Available: https://webbook.nist.gov/chemistry/fluid/. [Accessed 6 January 2021].

[91] National Institute of Standards and Technology, "NIST Chemistry WebBook, SRD 69," U.S. Secretary of Commerce on behalf of the United States of America, 2018. [Online]. Available: https://webbook.nist.gov/chemistry/form-ser/. [Accessed 6 January 2021].

[92] C.-W. Zhou, Y. Li, U. Burke, C. Banyon, K. P. Somers, S. Ding, S. Khan, J. W. Hargis, T. Sikes, O. Mathieu, E. L. Petersen, M. AlAbbad, A. Farooq, Y. Pan, Y. Zhang, Z. Huang, J. Lopez, Z. Loparo, S. S. Vasu and H. J. Curran, "An experimental and chemical kinetic modeling study of 1,3-butadiene combustion: Ignition delay time and laminar flame speed measurements," *Combustion and Flame,* vol. 197, pp. 423-438, 2018.

[93] S. M. Burke, J. M. Simmie and H. J. Curran, "Critical Evaluation of Thermochemical Properties of C1-C4 Species: Updated Group-Contributions to Estimate Thermochemical Properties," *Journal of Physical and Chemical Reference Data,* vol. 44, no. 1, pp. 013101-1to28, 2015.

[94] J. W. Allen, F. Goldsmith and W. H. Green, "Automatic estimation of pressure-dependent rate coefficients," *Physical Chemistry Chemical Physics,* vol. 14, no. 3, pp. 1131-1155, 2011.

[95] J. E. Dove, S. Halperin and S. Raynor, "Deviations from the linear mixture rule in non-equilibrium chemical kinetics," *The journal of chemical physics,* vol. 81, pp. 799-811, 1984.

[96] ANSYS, Ansys Chemkin-Pro Theory Manual 2020 R2, Canonsburg, Pennsylvania, U.S.: ANSYS, 2020.

[97] J. W. Sutherland, P. M. Patterson and R. B. Klemm, "RATE CONSTANTS FOR THE REACTION, O(3P)+H2O=OH+OH, OVER THE TEMPERATURE RANGE 1053 TO 2033 K USING TWO DIRECT TECHNIQUES," in *Twenty-Third Symposium (International) on Combustion*, Orleans, The Combustion Institute, 1990, pp. 51-57.

[98] K.-Y. Lam, D. F. Davidson and R. K. Hanson, "A Shock Tube Study of H2+OH→H2O+H Using OH Laser Absorption," *International Journal of Chemical Kinetics,* vol. 45, no. 6, pp. 363-373, 2013.

[99] J. V. Michael and J. W. Sutherland, "Rate Constant for the Reaction of H with H2O and OH with H2 by the Flash Photolysis-Shock Tube Technique over the Temperature Range 1246-2297K," *Journal of Physical Chemistry ,* vol. 92, no. 13, pp. 3853-3857, 1988.

[100] G. Altinay and G. R. Macdonald, "Determination of the Rate Constant for the OH(X2Π) + OH(X2Π) →H2O + O(3P) Reaction Over the Temperature Range 295 to 701 K," *The Jounral of Physical Chemistry A,* vol. 118, no. 1, pp. 38-54, 2014.

[101] M. S. Wooldrige, R. K. Hanson and C. T. Bowman, "A Shock Tube Study of the OH + OH -> H2O + O Reaction," *International Journal of Chemical Kinetics,* vol. 26, no. 4, pp. 389-401, 1994.

[102] N. Cohen and W. K. R, "Chemical Kinetic Data Sheets for High-Temperature Chemical Reactions," *Journal of Physical Chemistry Reference Data,* vol. 12, no. 3, pp. 531-590, 1983.

[103] W. C. Gardiner, Combustion Chemistry, New York: Springer-Verlag, 1984.

[104] V. Naudent, J. Sandra and C. E. Paillard, "A High Temperature Chemical Kinetics Study of the Reaction: OH+Ar=H+O+Ar by Atomic Resonance Absorption Spectrophotometry," *Combustion Science and Technology,* vol. 164, pp. 113-128, 2001.

[105] S. R. Sellevåg, Y. Georgievskii and J. A. Miller, "Kinetics of the Gas-Phase Recombination Reaction of Hydroxyl Radicals to Form Hydrogen Peroxide," *The Journal of Physical Chemistry A,* vol. 113, no. 16, pp. 4457-4467, 2009.

[106] N. K. Srinivasan and J. V. Michael, "The Thermal Decomposition of Water," *International Journal of Chemical Kinetics,* vol. 38, no. 3, pp. 211-219, 2006.

[107] J. Troe, "Detailed modeling of the temperature and pressure dependence of the reaction H+O2 (+M)→HO2 (+M)," *Proceedings of the combustion institute,* vol. 28, no. 2, pp. 1463-1469, 2000.

[108] R. X. Fernandes, K. Luther, J. Troe and V. G. Ushakov, "Experimental and modelling study of the recombination reaction H+O 2 (+M) - HO2 (+M) between 300 and 900 K, 1.5 and 950 bar, and in the bath gases M = He, Ar, and N2," *Physical Chemistry Chemistry Physics,* vol. 10, no. 29, pp. 4313-4321, 2008.

[109] J. V. Michael, S. M-C, J. W. Sutherland, J. J. Carroll and A. F. Wager, "Rate Constants For H + O2 + M → HO2 + M in Seven Bath Gases," *The Journal of Physical Chemistry A,* vol. 106, no. 21, pp. 5297-5313, 2002.

[110] V. J. Michael, J. W. Sutherland, L. B. Harding and A. F. Wagner, "INITIATION IN H2/O2: RATE CONSTANTS FOR H2 + O2 → H + HO2 AT HIGH TEMPERATURE," *Proceedings of the Combustion Institute,* vol. 28, no. 2, pp. 1471-1478, 2000.

[111] M. A. Mueller, R. A. Yetter and F. L. Dryer, "Flow Reactor Studies and Kinetic Modeling of the H2/O2/NOX and CO/H2O/O2/NOX Reactions," *International Journal of Chemical Kinetics,* vol. 31, no. 10, pp. 705-724, 1999.

[112] D. L. Baulch, C. J. Cobos, R. A. Cox, C. Esser, P. Frank, T. Just, J. A. Kerr, M. J. Pilling, J. Troe, R. W. Walker and J. Warrantz, "Evaluated Kinetic Data for Combustion Modelling," *Journal of Physical and Chemical Reference Data,* vol. 21, no. 3, pp. 411-734, 1992.

[113] A. Fernández-Ramos and A. J. C. Varandas, "A VTST Study of the H + O3 and O + HO2 Reactions Using a Six-dimensional DMBE Potential Energy Surface for Ground State HO3," *The Journal of Physical Chemistry A,* vol. 106, no. 16, pp. 4077-4083, 2002.

[114] Z. Hong, K.-Y. Lam, R. Sur, S. Wang, D. F. Davidson and R. K. Hanson, "On the rate constants of OH+HO2 and HO2+HO2: A comprehensive study of H2O2 thermal decomposition using multi-species laser absorption," *Proceedings of the Combustion Institute,* vol. 34, no. 1, pp. 565-571, 2013.

[115] L. F. Keyser, "Kinetics of the reaction OH+HO2->H2O+O2 from 254 to 382 K," *Journal of physical chemistry,* vol. 92, pp. 1193-1200, 1988.

[116] C. Kappel, K. Luther and J. Troe, "Shock wave study of the unimolecular dissociation of H2O2 in its falloff range and of its secondary reactions," *Physical Chemistry Chemical Physics,* vol. 4, no. 18, pp. 4392-4398, 2002.

[117] H. Hippler, J. Troe and J. Willner, "Shock wave study of the reaction HO2+HO2→H2O2+O2 : Confirmation of a rate constant minimum near 700 K," *The Journal of Chemical Physics,* vol. 93, no. 3, pp. 1755-1760, 1990.

[118] J. Troe, "The thermal dissociation/recombination reaction of hydrogen peroxide H2O2(+M)<=>2OH(+M) III. Analysis and representation of the temperature and pressure dependence over wide ranges," *Combustion and Flame,* vol. 158, no. 4, pp. 594-601, 2011.

[119] Z. Hong, A. Farooq, E. A. Barbour, D. F. Davidson and R. K. Hanson, "Hydrogen Peroxide Decomposition Rate: A Shock Tube Study Using Tunable Laser Absorption of H2O near 2.5 µm," *Journal of Physical Chemistry A,* vol. 113, no. 46, pp. 12919-12925, 2009.

[120] R. Zellner, F. Ewig, R. Paschke and G. Wagner, "Pressure and temperature dependence of the gas-phase recombination of hydroxyl radicals," *Journal of Physical Chemistry ,* vol. 92, no. 14, pp. 4184-4190, 1988.

[121] R. Forster, M. Frost, D. Fulle, H. Hamann, H. Hippler, A. Schlepegrell and J. Troe, "High pressure range of the addition of HO to HO, NO, NO2, and CO. I. Saturated laser induced fluorescence measurements at 298 K," *J. Chem. Phys.,* vol. 103, pp. 2949-2958, 1995.

[122] B. A. Ellingson, D. P. Theis, O. Tishchenko, J. Zheng and D. G. Truhlar, "Reactions of Hydrogen Atom with Hydrogen Peroxide," *The Journal of Physical Chemistry A,* vol. 111, no. 51, p. 13554–13566, 2007.

[123] J. Troe, "Thermal dissociation and recombination of polyatomic molecules," *Syposium (International) on Combustion,* vol. 5, no. 1, pp. 667-680, 1975.

[124] P. R. Westmoreland, J. B. Howard, J. P. Longwell and A. M. Dean, "Prediction of rate constants for combustion and pyrolysis reactions by bimolecular QRRK," *AIChE,* vol. 32, no. 12, pp. 1971-1979, 1986.

[125] A. V. Joshi and H. Wang, "Master equation modeling of wide range temperature and pressure dependence of CO + OH → products," *International Journal of Chemical Kinetics,* vol. 38, no. 1, pp. 57-73, 2006.

[126] J. P. Senosiain, S. J. Klippenstein and J. A. Miller, "A complete statistica analysis of the reaction between OH and CO," *Proceedings of the combustion institute,* vol. 30, pp. 945-953, 2005.

[127] X. You, H. Wang, E. Goos, C.-J. Sung and S. J. Klippenstein, "Reaction kinetics of CO + HO(2) --> products: ab initio transition state theory study with master equation modeling," *J Phys Chem A,* vol. 111, no. 19, pp. 4031-4042, 2007.

[128] X. Yang, T. Tan, P. Dievart, E. A. Carter and Y. Ju, "Theoretial assessment on reaction kinetics HCO and CH2OH unimolecular decomposition," *8th US National Combustion Meeting,* vol. 2, pp. 1732-1740, 2013.

[129] G. Friedrichs, J. T. Herbon, D. F. Davidson and R. K. Hanson, "Quantitative detection of HCO behind shock waves: The thermal decomposition of HCO," *Physcial chemistry chemical physics,* vol. 4, pp. 5778-5788, 2002.

[130] H. Hashemi, J. G. Jacobsen, C. T. Rasmussen, J. M. Christensen, P. Glarborg, S. Gersen, M. v. Essen, H. B. Levinsky and S. J. Klippenstein, "High-pressure oxidation of ethane," *Combustion and Flame,* vol. 182, pp. 150-166, 2017.

[131] N. Fabheber, G. Friedrichs, P. Marshall and P. Glarborg, "Glyoxal Oxidation Mechanism: Implications for the Reactions HCO + O2 and OCHCHO + HO2," *The Journal of Physical Chemistry A,* vol. 119, no. 28, pp. 7305-7315, 2015.

[132] R. S. Timonen, E. Ratajczak and D. Gutman, "Kinetics of the reactions of the formyl radical with oxygen, nitrogen dioxide, chlorine, and bromine," *Journal of Physcal Chemistry,* vol. 92, no. 3, pp. 651-655, 1988.

[133] S. J. Klippenstein, *Personal Communication,* 2011.

[134] R. S. Timonen, E. Ratajczak and D. Gutman, "Kinetics of the reaction between formyl radicals and atomic hydrogen," *Journal of Physical Chemistry,* vol. 91, no. 3, pp. 692-694, 1987.

[135] C.-H. Wang, A. E. Masunov, T. C. Allison, S. Chang, C. Lim, Y. Jin and V. S. Subith, "Molecular Dynamics of Combustion Reactions in Supercritical Carbon Dioxide. 6. Computational Kinetics of Reactions between Hydrogen Atom and Oxygen Molecule H + O2 ⇌ HO + O and H + O2 ⇌ HO2," *The journal of physical chemistry A,* vol. 123, pp. 10772-10781, 2019.

[136] D. A. Masten, R. K. Hanson and C. T. Bowman, "Shock Tube Study of the Reaction H+O2=OH+O Using OH Laser Absorption," *Journal of Physical Chemistry ,* vol. 94, no. 18, pp. 7119-7128, 1990.

[137] S. Wang, D. F. Davidson and R. K. Hanson, "Shock Tube and Laser Absorption Study of CH2O Oxidation via Simultaneous Measurements of OH and CO," *The Journal of Physical Chemistry A,* vol. 121, no. 45, pp. 8561-8568, 2017.

[138] R. C. Oldenborg, G. W. Loge, D. M. Harradine and W. K. R, "Kinetic Study of the OH 4- H2 Reaction from 800 to 1550 K," *The Journal of Physical Chemistry ,* vol. 96, no. 21, pp. 8426-8430, 1992.

[139] D. F. Davidson, A. Y. Chang and R. K. Hanson, "Laser photolysis shock tube for combustion kinetics studies," in *Twenty-Second Symposium (International) on Combustion*, The combustion Institute, 1988, pp. 1877-1885.

[140] Y. Bedjanian, G. Le Bras and G. Poulet, "Kinetic Study of OH+OH and OD+OD Reactions," *Journal of Physical Chemistry A,* vol. 103, no. 35, pp. 7017-7025, 1999.

[141] M. Sangwan and L. N. Krasnoperov, "Disproportionation Channel of Self-Reaction of Hydroxyl Radical, OH+OH →H2O+O, Studied by Time-Resolved Oxygen Atom Trapping," *The Journal of Physical Chemistry A,* vol. 116, no. 48, pp. 11817-11822, 2012.

[142] M. Sangwan, E. N. Chesnokov and L. N. Krasnoperov, "Reaction OH + OH Studied over the 298-834 K Temperature and 1-100 bar Pressure Ranges," *The Journal of Physical Chemistry A,* vol. 116, no. 24, pp. 6282-6294, 2012.

[143] M. P. Burke, S. J. Klippenstein and L. B. Harding, "A quantitative explanation for the apparent anomalous temperature dependence of OH+HO2=H2O+O2 through multi-scale modeling," *Proceedings of the Combustion Institute,* vol. 34, no. 1, pp. 547-555, 2013.

[144] M.-K. Bahng and R. G. Macdonald, "Determination of the Rate Constant for the OH(X2Π) + OH(X2Π) → O(3P) + H2O Reaction over the Temperature Range 293−373 K†," *The Journal of Physical Chemistry A,* vol. 111, no. 19, pp. 3850-3861, 2007.

[145] T. L. Nguyen and J. F. Stanton, "Ab Initio Thermal Rate Calculations of HO + HO = O(3P) + H2O Reaction and Isotopologues," *The Journal of Physical Chemistry A,* vol. 117, no. 13, pp. 2678-2686, 2013.

[146] T. Varga, C. Olm, T. Nagy, I. G. Zsley, E. Valko, R. Palvolgyi, H. J. Curran and T. Turanyi, "Development of a Joint Hydrogen and Syngas Combustion Mechanism Based on an Optimization Approach," *International Journal of Chemical Kinetics,* vol. 48, no. 8, pp. 407-422, 2016.

[147] S. R. Sellevåg, Y. Georgievskii and J. A. Miller, "The Temperature and Pressure Dependence of the Reactions H + O2 (+M)→HO2 (+M) and H + OH (+M)→H2O(+M)," *The Journal of Physical Chemistry A,* vol. 112, no. 23, pp. 5085-5095, 2008.

[148] A. A. Konnov, "Remaining uncertainties in the kinetic mechanism of hydrogen combustion," *Combustion and flame,* vol. 152, no. 4, pp. 507-528, 2008.

[149] J. Hahn, L. Krasnoperov, K. Luther and J. Troe, "Pressure dependence of the reaction H + O2(+Ar) → HO2(+Ar) in the range 1–900 bar and 300–700 K," *Physical Chemistry Chemical Physics,* vol. 6, no. 9, pp. 1997-1999, 2004.

[150] I. Janik, D. M. Bartels, T. W. Marin and C. D. Jonah, "Reaction of O2 with the Hydrogen Atom in Water up to 350 °C," *The Journal of Physical Chemistry A,* vol. 111, no. 1, pp. 79-88, 2007.

[151] J. A. Miller, M. J. Pilling and J. Troe, "Unravelling combustion mechanisms through a quantitative understanding of elementary reactions," *Proceedings of the Combustion Institute,* vol. 30, no. 1, pp. 43-88, 2005.

[152] L. B. Harding, S. J. Klippenstein, H. Lischka and R. Shepard, "Comparison of multireference configuration interaction potential energy surfaces for H + O2 → HO2: the effect of internal contraction," *Theoretical Chemistry Accounts,* vol. 133, p. 1429, 2014.

[153] D. F. Davidson, *Personal Communications,* 2017.

[154] R. R. Baldwin and R. W. Walker, "Rate constants for hydrogen + oxygen system, and for H atoms and OH radicals + alkanes," *Journal of the Chemical Society, Faraday Transactions 1: Physical Chemistry in Condensed Phases,* vol. 75, no. 0, pp. 140-154, 1979.

[155] M. A. Mueller, T. J. Kim, R. A. Yetter and F. L. Dryer, "Flow Reactor Studies and Kinetic Modeling of the H2/O2 Reaction," *International Journal of Chemical Kinetics,* vol. 31, no. 2, pp. 113-125, 1999.

[156] O. Setokuchi, M. Sato and S. Matuzawa, "A Theoretical Study of the Potential Energy Surface and Rate Constant for an O(3P) + HO2 Reaction," *The Journal of Physical Chemistry A,* vol. 104, no. 14, pp. 3204-3210, 2000.

[157] Z. Hong, S. S. Vasu, D. F. Davidson and R. K. Hanson, "Experimental Study of the Rate of OH + HO2 -> H2O + O2 at High Temperatures Using the Reverse Reaction," *The Journal of Physical Chemistry A,* vol. 114, pp. 5520-5525, 2010.

[158] M. Monge-Palacios and M. Sarathy, "Ab initio and transition state theory study of the OH + HO2 → H2O + O2(3Σg−)/O2(1Δg) reactions: yield and role of O2(1Δg) in H2O2 decomposition and in combustion of H2," *Physical Chemistry Chemical Physics,* vol. 20, no. 6, pp. 4478-4489, 2018.

[159] H. Hashemi, J. M. Christensen, S. Gersen and P. Glarborg, "Hydrogen oxidation at high pressure and intermediate temperatures: Experiments and kinetic modeling," *Proceedings of the Combustion Institute,* vol. 35, no. 1, pp. 553-560, 2015.

[160] J. Troe, "Ultraviolettspektrum und Reaktionen des HO2-Radikals im thermischen Zerfall von H2O2," *Berichte der Bunsengesellschaft für physikalische Chemie,* vol. 73, no. 10, pp. 946-952, 1969.

[161] D. D. Zhou, K. Han, P. Zhang, L. B. Harding, M. J. Davis and R. T. Skodje, "Theoretical Determination of the Rate Coefficient for the HO2 + HO2 → H2O2+O2 Reaction: Adiabatic Treatment of Anharmonic Torsional Effects," *The Journal of Physical Chemistry A,* vol. 116, no. 9, pp. 2089-2100, 2012.

[162] G. Mittal, C. J. Sung and R. A. Yetter, "Autoignition of H2/CO at elevated pressures in a rapid compression machine," *International Journal of Chemical Kinetics,* vol. 38, no. 8, pp. 516-529, 2006.

[163] R. R. Baldwin, D. Jackson, R. W. Walker and S. J. Webster, "Interpretation of the slow reaction and second limit of hydrogen oxygen mixtures by computer methods," *Transactions of the Faraday Society,* vol. 63, pp. 1676-1686, 1967.

[164] D. Lee and S. Hochgreb, "Hydrogen autoignition at pressures above the second explosion limit (0.6–4.0 MPa)," *International Journal of Chemical Kinetics,* vol. 30, no. 6, pp. 385-406, 1998.

[165] X. Lu, Q. Meng, B. Fu and D. H. Zhang, "Rate coefficients of the H + H2O2 → H2 +HO2 reaction on an accurate fundamental invariant-neural network potential energy surface," *The Journal of Chemical Physics,* vol. 149, pp. 174303-1-7, 2018.

[166] P. F. Conforti, M. Braunstein, B. J. Braams and J. M. Bowman, "Global potential energy surfaces for O(P3)+H2O(A11) collisions," *The journal of chemical physics,* vol. 133, pp. 164312-1-10, 2010.

[167] A. W. Jasper and R. Dawes, "Non-Born–Oppenheimer molecular dynamics of the spin-forbidden reaction O(3P) + CO(X 1Σ+) → CO2(X̃Σg+1)," *The journal of chemical Physics,* vol. 139, pp. 154313-1-13, 2013.

[168] J. Troe, "Modeling the temperature and pressure dependence of the reaction HO+CO=HOCO=H+CO2," *Symposium (Internation) on Combustion,* vol. 27, no. 1, pp. 167-175, 1998.

[169] R. S. Zhu, G. W. Diau, M. C. Lin and A. M. Mebel, "A Computational Study of the OH(OD) + CO Reactions: Effects of Pressure, Temperature, and Quantum-Mechanical Tunneling on Product Formation," *J. Phys. Chem. A,* vol. 105, no. 50, pp. 11249-11259, 2001.

[170] R. E. Weston, Jr., T. L. Nguyen, J. F. Stanton and J. R. Barker, "HO + CO Reaction Rates and HD Kinetic Isotope Effects Master Equation Models with ab Initio SCTST Rate Constants," *The Journal of Physical Chemistry A,* vol. 117, pp. 821-835, 2013.

[171] A. Farooq and E. F. Nasir, "A Shock-Tube Study of the CO + OH Reaction Near the Low-Pressure Limit," *The Journal of Physical Chemistry A,* vol. 120, no. 22, pp. 3924-3928, 2016.

[172] A. E. Masunov, E. Wait and S. S. Vasu, "Chemical Reaction CO+OH• → CO2+H• Autocatalyzed by Carbon Dioxide: Quantum Chemical Study of the Potential Energy Surfaces," *The Journal of Physical Chemistry A,* vol. 120, pp. 6023-6028, 2016.

[173] S. V. Panteleev, A. E. Masunov and S. S. Vasu, "Molecular Dynamics Study of Combustion Reactions in a Supercritical Environment. Part 2: Boxed MD Study of CO + OH →CO2 + H Reaction Kinetics," *The Journal of Physical Chemistry A,* vol. 122, no. 4, pp. 897-908, 2018.

[174] R. Li, G. He, F. Qin, C. Pichler and A. A. Konnov, "Comparative analysis of detailed and reduced kinetic models for CH4 + H2 combustion," *Fuel,* vol. 246, pp. 244-258, 2019.

[175] J. Shao, D. F. Davidson and R. K. Hanson, "A shock tube study of ignition delay times in diluted methane, ethylene, propene and their blends at elevated pressures," *Fuel,* vol. 225, pp. 370-380, 2018.

[176] V. Samu, T. Varga, K. Brezinsky and T. Turanyi, "Investigation of ethane pyrolysis and oxidation at high pressures using global optimization based on shock tube data," *Proceedings of the Combustion Institute,* vol. 36, no. 1, pp. 691-698, 2017.

[177] C. J. Aul, W. K. Metcalfe, S. M. Burke, H. J. Curran and E. L. Petersen, "Ignition and kinetic modeling of methane and ethane fuel blends with oxygen: A design of experiments approach," *Combustion and Flame ,* vol. 160, no. 7, pp. 1153-1167, 2013.

[178] M. F. Campbell, A. M. Tulgestke, D. F. Davidson and R. K. Hanson, "A second-generation constrained reaction volume shock tube," *Review of scientific instruments,* vol. 85, no. 5, p. 055108, 2014.

[179] J. Badra, A. E. Elwardany, F. Khaled, S. S. Vasu and A. Farooq, "A shock tube and laser absorption study of ignition delay times and OH reaction rates of Ketones: 2-Butanone and 3-buten-2one," *Combustion and Flame,* vol. 161, pp. 725-734, 2014.

[180] E. L. Petersen, "INTERPRETTING ENDWALL AND SIDEWALL MEASUREMENTS IN SHOCK-TUBE IGNITION STUDIES," *Combustion Science and Technology,* vol. 181, pp. 1123-1144, 2009.

[181] S. M. Burke , U. Burke, R. M. Donagh, O. Mathieu, I. Osorio, C. Keesee, A. Morones, E. L. Petersen, W. Wang, T. A. DeVerter, M. A. Oehlschlaeger, B. Rhodes, R. K. Hanson, D. F. Davidson, B. W. Weber, C.-J. Sung, J. Santner, Y. Ju, F. M. Hass, F. L. Dryer, V. N. Evgeniy, E. J. Nilsson, A. A. Konnov, M. Alrefae, F. Khaled, A. Farooq, P. Dirrenberger, P.-A. Glaude, F. Battin-leclerc and H. J. Curran, "An experimental and modeling study of propene oxidation. Part 2: Ignition delay time and flame speed measurements," *Combustion and Flame,* vol. 162, no. 2, pp. 296-314, 2015.

[182] T. Javed, C. Lee, M. AlAbbad, K. Djebbi, M. Beshir, J. Badra, H. Curran and A. Farooq, "Ignition studies of n-heptane/iso-octane/toluene blends," *Combustion and Flame,* vol. 171, pp. 223-233, 2016.

[183] M. F. Campbell, "Studies of biodiesel surrogates using novel shock tube techniques," Stanford University, Stanford, 2014.

[184] A. Savitzky and M. J. E. Golay, "Smoothing and Differentiation of Data by Simplified Least Squares Procedures.," *Analytical Chemistry,* vol. 36, no. 8, pp. 1627-1639, 1964.

[185] M. Tamura, P. A. Berg, J. E. Harrington, J. Luque, J. B. Jeffries, G. P. Smith and D. R. Crosley, "Collisional Quenching of CH(A), OH(A), and NO(A) in Low Pressure Hydrocarbon Flames," *Combustion and Flame,* vol. 114, no. 3-4, pp. 502-514, 1998.

[186] P. H. Paul, J. L. Durant and J. A. Gray, "Collisional electronic quenching of OH A 2Σ (v'=0) measured at high temperature in a shock tube," *The Journal of Chemical Physics,* vol. 102, no. 21, pp. 8378-8384, 1995.

[187] U.S. Energy Information Administration, "International Energy Outlook 2016," US EIA Office of Communications, Washington , 2016.

[188] M. Colombo, M. d. Prisco and P. Martinelli, "A New Shock Tube Facility for Tunnel Safety," *Experimental Mechanics,* vol. 51, no. 7, pp. 1143-1154, 2011.

[189] M. Goswami, E. N. Volkov and L. P. H. de Goey, "Heat Flux Method: Past, Present & Future," in *3rd Heat Flux Burner Workshop*, Berlin, 2014.

[190] P. E. L and H. R. K, "Measurement of reflected-shock bifurcation over a wide range of gas composition and pressure," *Shock Waves,* vol. 15, no. 5, pp. 333-340, 2006.

[191] B. Ruscic, "The Active Thermochemical Tables," U.S. Argonne National Laboratory, 2017. [Online]. Available: http://atct.anl.gov/. [Accessed 12 July 2017].

[192] *Email communications with Professor David F. Davidson at Stanford University,* May 2017.

[193] A. N. Pirraglia, J. V. Michael, J. W. Sutherland and R. B. Klemm, "A flash photolysis-shock tube kinetic study of the H atom reaction with O 2 : H + O 2 ⇌ OH + O (962 K ≤ T ≤ 1705 K) and H + O 2 + Ar → HO 2 + Ar (746 K ≤ T ≤ 987 K)," *Journal of Physical Chemistry,* vol. 93, no. 1, pp. 282-291, 1989.

[194] R. R. Baldwin, M. E. Fuller, J. S. Hillman, D. Jackson and R. W. Walker, "Second limit of hydrogen + oxygen mixtures: the reaction H + HO2," *Journal of the Chemical Society, Faraday Transactions 1: Physical Chemistry in Condensed Phases,* vol. 70, no. 0, pp. 635-641, 1974.

Appendix A: Sample RMG Simulation

Table A1: RMG Pressure-Dependent Automatically Generated Reaction Mechanism at 1000 K and 40 bar with 4%H_2/2%O_2/45%H_2O/Ar

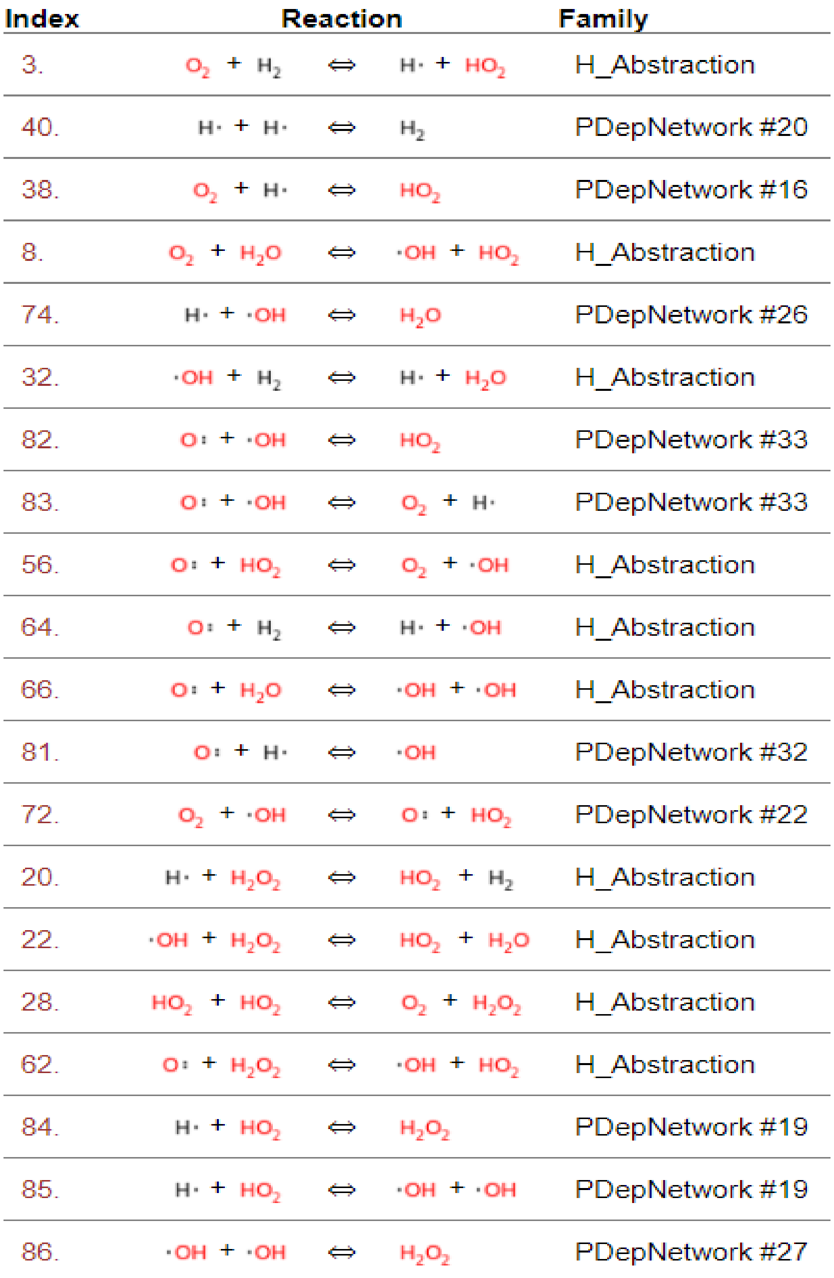

Index	Reaction	Family
3.	O_2 + H_2 ⇔ H· + HO_2	H_Abstraction
40.	H· + H· ⇔ H_2	PDepNetwork #20
38.	O_2 + H· ⇔ HO_2	PDepNetwork #16
8.	O_2 + H_2O ⇔ ·OH + HO_2	H_Abstraction
74.	H· + ·OH ⇔ H_2O	PDepNetwork #26
32.	·OH + H_2 ⇔ H· + H_2O	H_Abstraction
82.	O: + ·OH ⇔ HO_2	PDepNetwork #33
83.	O: + ·OH ⇔ O_2 + H·	PDepNetwork #33
56.	O: + HO_2 ⇔ O_2 + ·OH	H_Abstraction
64.	O: + H_2 ⇔ H· + ·OH	H_Abstraction
66.	O: + H_2O ⇔ ·OH + ·OH	H_Abstraction
81.	O: + H· ⇔ ·OH	PDepNetwork #32
72.	O_2 + ·OH ⇔ O: + HO_2	PDepNetwork #22
20.	H· + H_2O_2 ⇔ HO_2 + H_2	H_Abstraction
22.	·OH + H_2O_2 ⇔ HO_2 + H_2O	H_Abstraction
28.	HO_2 + HO_2 ⇔ O_2 + H_2O_2	H_Abstraction
62.	O: + H_2O_2 ⇔ ·OH + HO_2	H_Abstraction
84.	H· + HO_2 ⇔ H_2O_2	PDepNetwork #19
85.	H· + HO_2 ⇔ ·OH + ·OH	PDepNetwork #19
86.	·OH + ·OH ⇔ H_2O_2	PDepNetwork #27

RMG input file for Table A1’s mechanism generated is detailed below:

```
# -*- coding: utf-8 -*-
"""
Created on Tue Jun 11 18:46:12 2019
@author: abeigzad
"""
database(
    thermoLibraries = ['BurkeH2O2','BurcatNS','primaryThermoLibrary'],
    reactionLibraries = [],
    seedMechanisms = [],
    kineticsDepositories = ['training'],
    kineticsFamilies = 'default',
    kineticsEstimator = 'rate rules',
)
species(
    label='H2',
    reactive=True,
    structure=SMILES("[H][H]"),
)
species(
    label='O2',
    reactive=True,
    structure=SMILES("[O][O]"),
)
species(
    label='H2O',
    reactive=True,
    structure=SMILES("[H]O[H]"),
)
species(
    label='AR',
    reactive=False,
    structure=SMILES("[Ar]"),
)
species(
    label='CO2',
    reactive=True,
    structure=SMILES("C(=O)=O"),
)
simpleReactor(
    temperature=(1000,'K'),
    pressure=(40.0,'bar'),
    initialMoleFractions={
        "H2": 0.04,
        "O2": 0.02,
        "H2O": 0.45,
```

```
        "CO2": 0.0,
        "AR": 0.49,
    },
    terminationRateRatio=0.001,
    terminationTime=(1e2,'s'),
)
simulator(
    atol=1e-16,
    rtol=1e-8,
)
model(
    toleranceKeepInEdge=0.0,
    toleranceMoveToCore=0.1,
    toleranceInterruptSimulation=0.1,
    maximumEdgeSpecies=100000,
)
pressureDependence(
        method='Reservoir State',
        maximumGrainSize=(0.05,'kcal/mol'),
        minimumNumberOfGrains=1000,
        temperatures=(300,2100,'K',8),
        pressures=(1,300, 'bar', 8),
        interpolation=('Chebyshev', 6, 4),
        maximumAtoms=16,
 )
options(
    units='si',
    name='Aug920pdepHHRRSFR',
    generateSeedEachIteration=False,
    saveRestartPeriod=None,
    saveSeedToDatabase=False,
    generateOutputHTML=True,
    generatePlots=False,
    verboseComments=True,
    saveEdgeSpecies=False,

    saveSimulationProfiles=True,
    trimolecularProductReversible=True,
    keepIrreversible=False,
    saveSeedModulus=-1
)
```

Appendix B: H_2 Experimental IDT Supplementary Plots

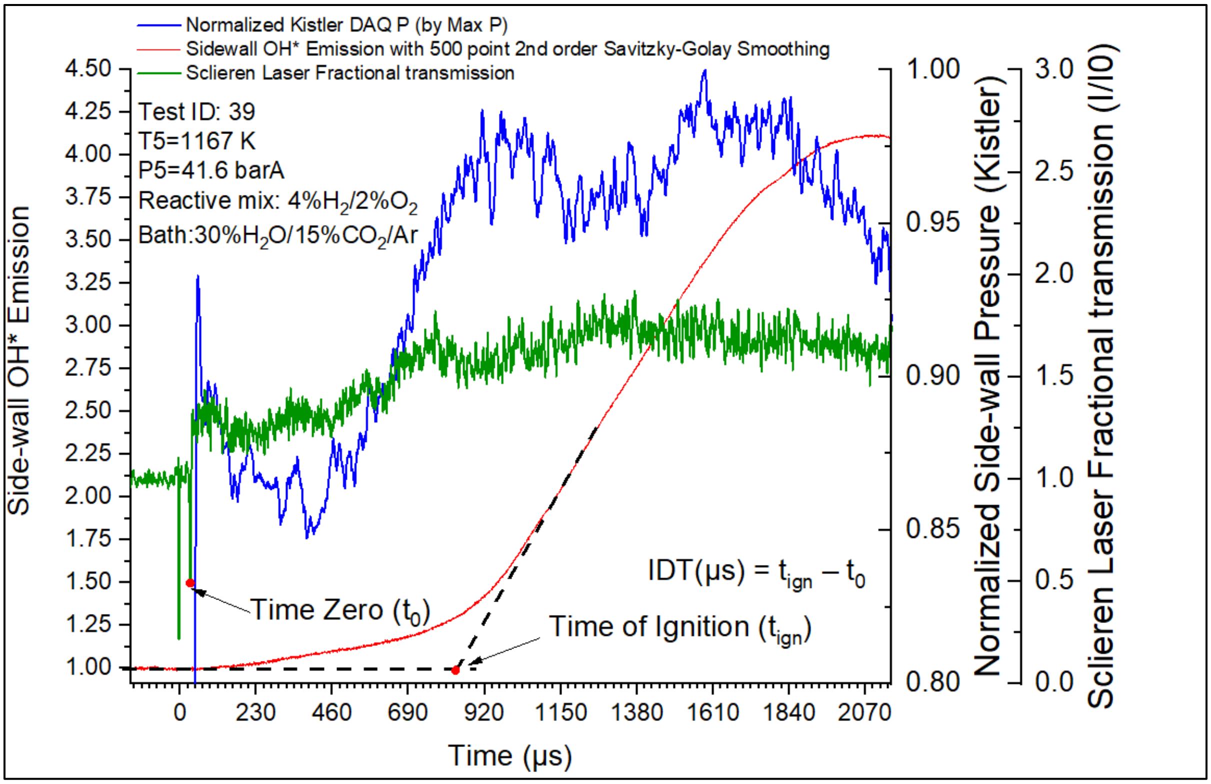

Figure A1: Test 39 Side-wall OH* (with digital filtering) & Fractional Transmission of Schlieren Laser used for Time Zero and Ignition Time determinations, in addition to Normalized Side-wall Kistler Pressure Signal

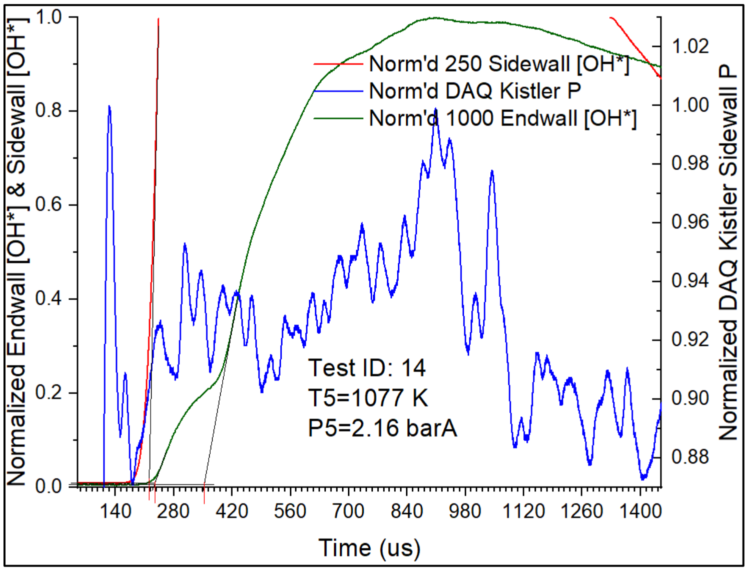

Figure A2: Test ID 14 Normalized 250 point smoothed side-wall OH* emission, Normalized 1000 point smoothed end-wall OH* emission, Normalized side-wall Kistler pressure traces, with mixture composition 4%H_2/2%O_2/Ar

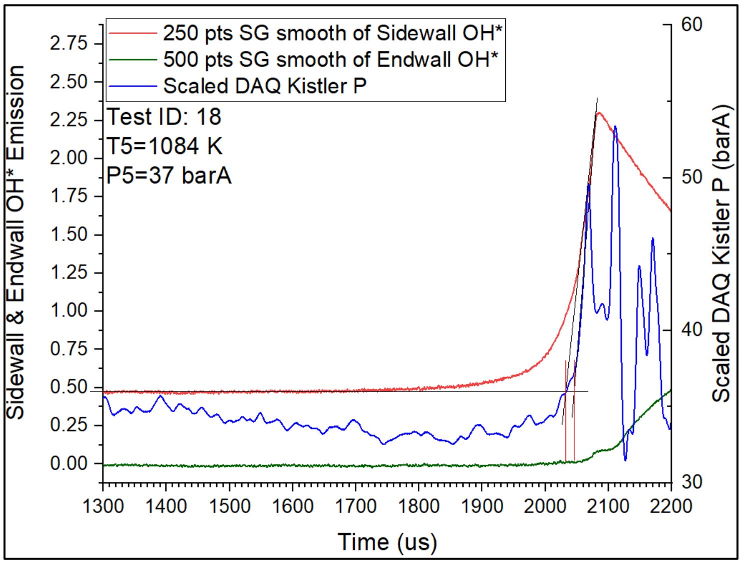

Figure A3: Test ID 18: 250- and 500-point-smoothed side-wall and end-wall OH* emission, and scaled side-wall Kistler pressure traces, with mixture composition 4%H_2/2%O_2/Ar

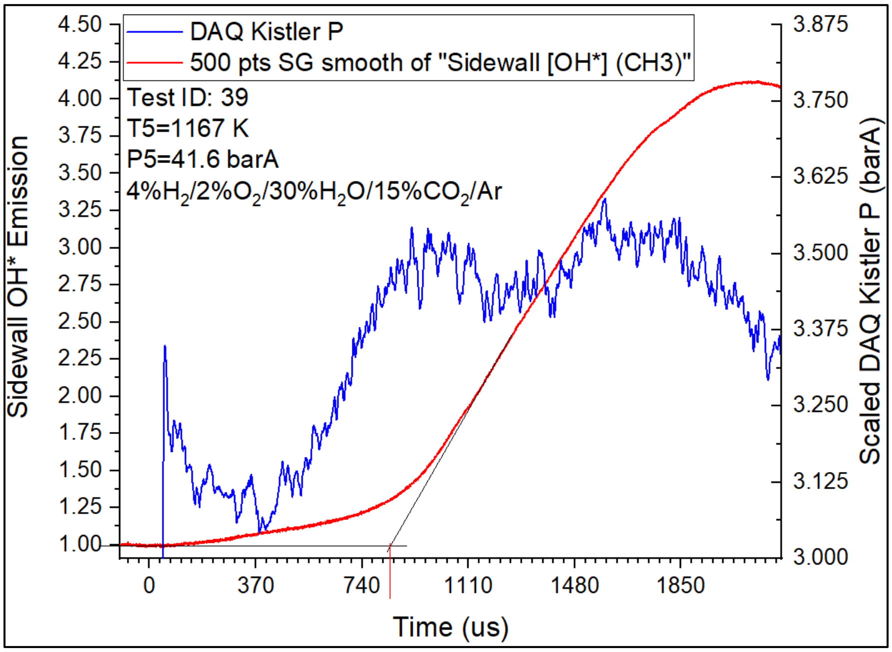

Figure A4: Test ID 39 500-point-smoothed side-wall OH* emission, and scaled side-wall Kistler pressure traces, with mixture composition 4%H_2/2%O_2/30%H_2O/15%CO_2/Ar

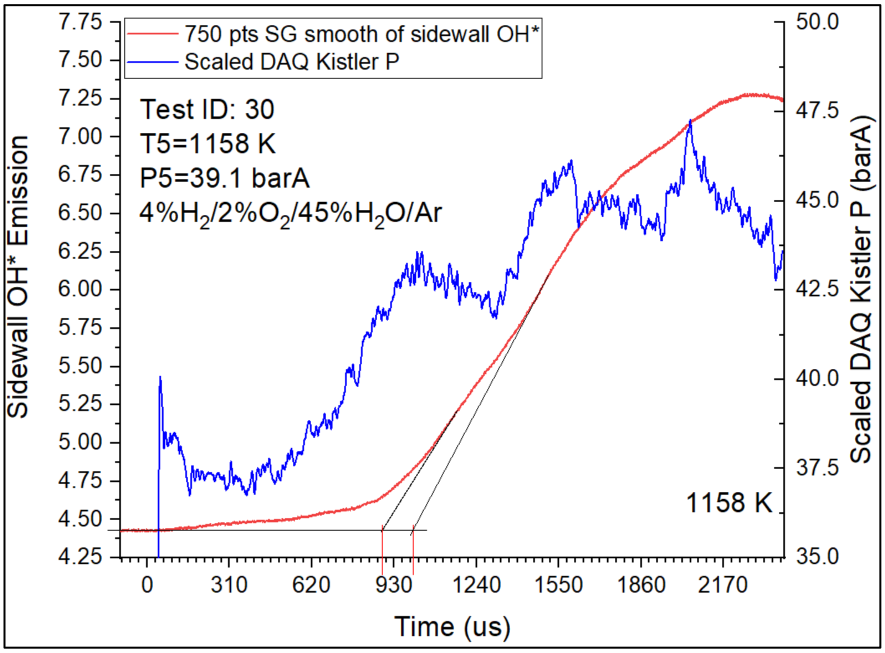

Figure A5: Test ID 30 750-point-smoothed side-wall OH* emission, and scaled side-wall Kistler pressure traces, with mixture composition 4%H_2/2%O_2/45%H_2O/Ar

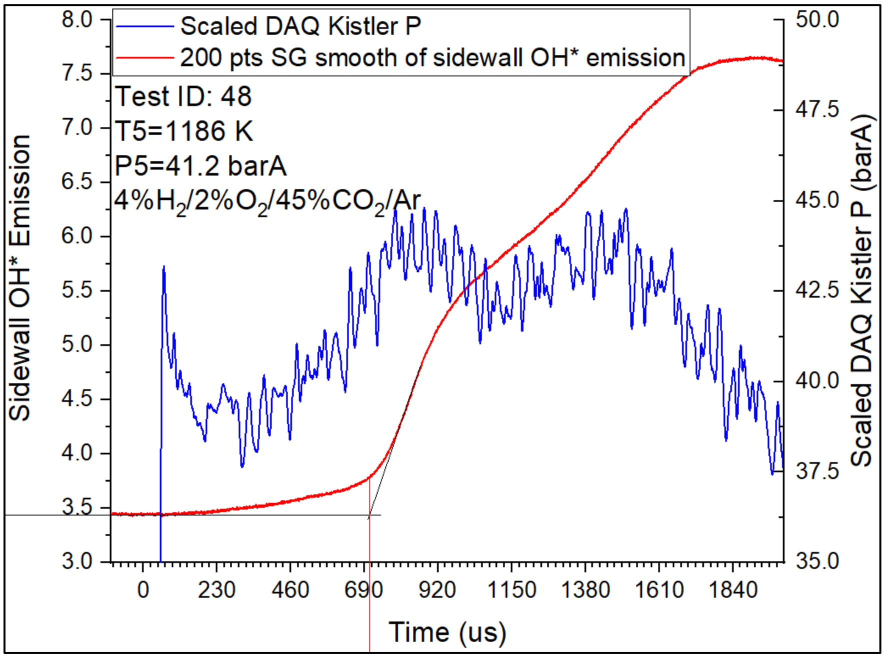

Figure A6: Test ID 48 200-point-smoothed side-wall OH* emission, and scaled side-wall Kistler pressure traces, with mixture composition 4%H_2/2%O_2/45%CO_2/Ar

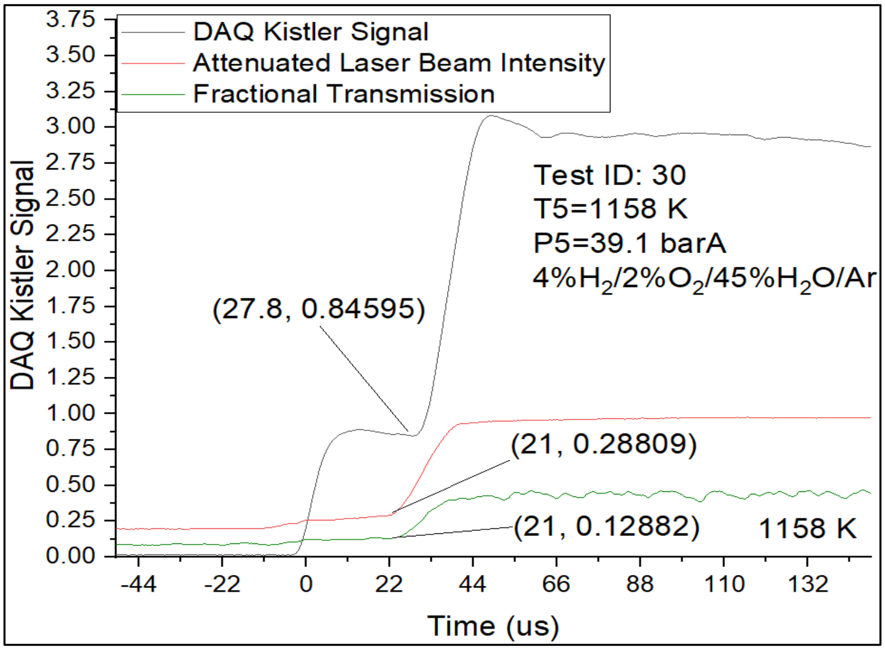

Figure A7: Test 30's Side-wall Kistler, HeNe laser's attenuated laser beam intensity and its fractional transmission

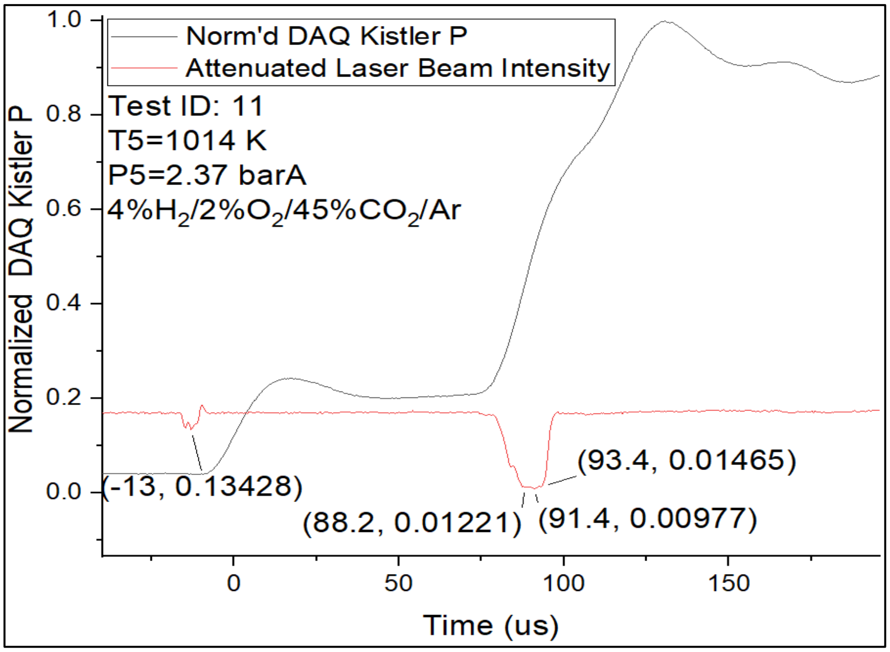

Figure A8: Test 11's Side-wall Kistler, HeNe laser's attenuated laser beam intensity

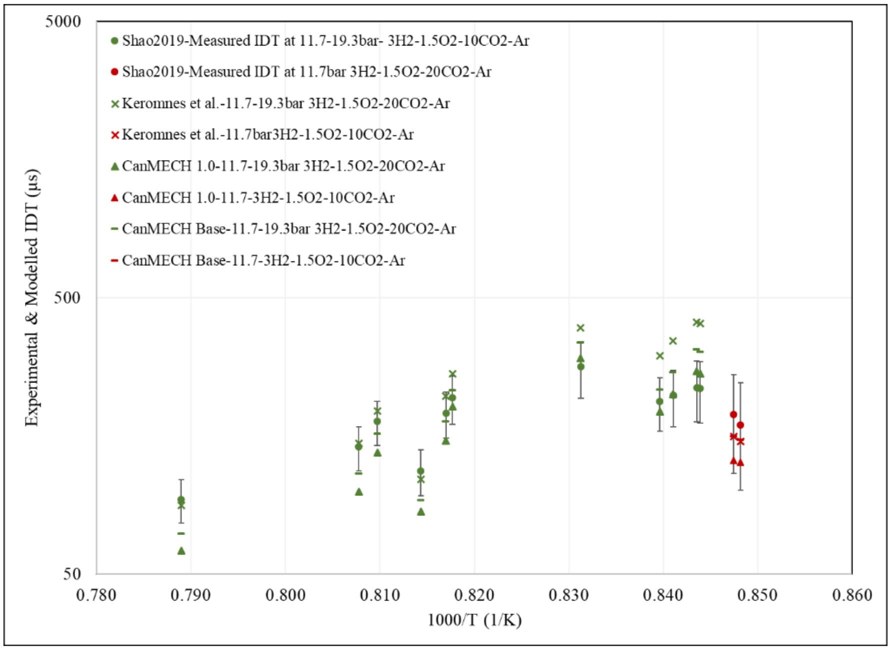

Figure A9: Models performance in predicting Shao et al.'s (Proc. Combust. Inst. 37 (2019) 145-152.) 3%H_2/1.5%O_2/10%CO_2/Ar and 3%H_2/1.5%O_2/20%CO_2/Ar experimental IDTs

Appendix C: H_2 Rate of Production Analyses

<u>ROP analyses results of Test #25– 4%H_2/Ar φ=1 at 1209 K and 39.6 bar:</u>

Figure A10 and Figure A11 depict the absolute and normalized OH ROP for test #25. These figures show that OH generation is dominated by R1+R2 for the initial 125 μs, after which R11: HO_2+H=2OH dominates until ignition at ~144 μs. Comparison of this figure with its lower-pressure counterpart, test #10 (see Figure 31), shows that by increasing the pressure to 40 bar, another pathway through R11, involving HO_2 chemistry, has become dominant at the later stages of IDT period. To understand the chain of reactions involved, it is important to understand the H, HO_2 and to a lesser extent O radical build up.

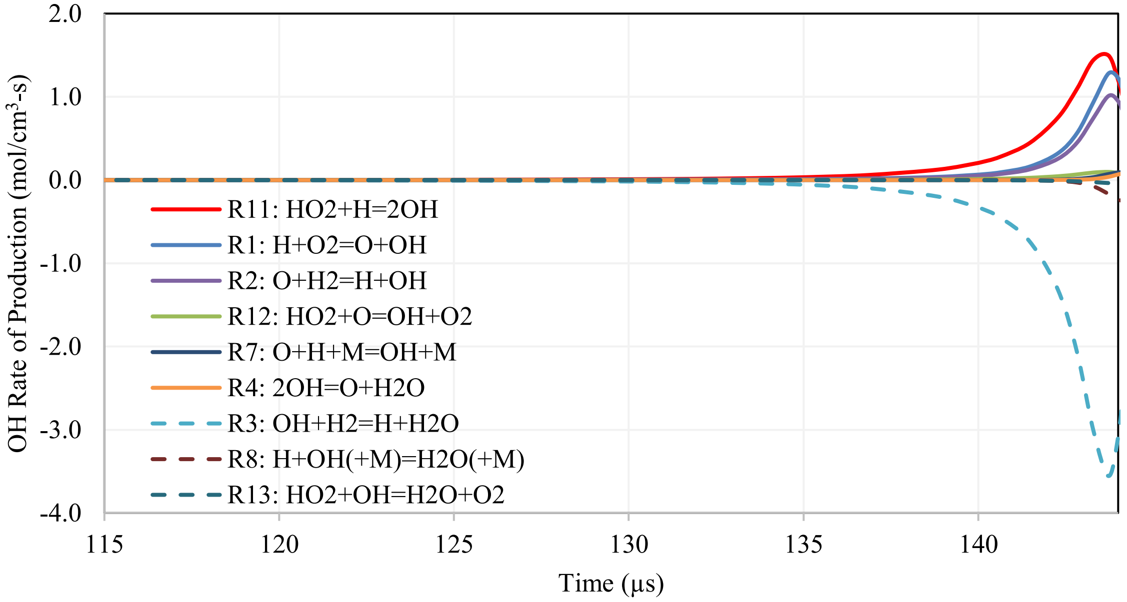

Figure A10: OH rate of production analysis for Test #25 – 4%H_2/Ar φ=1 at 1209 K and 39.6 bar

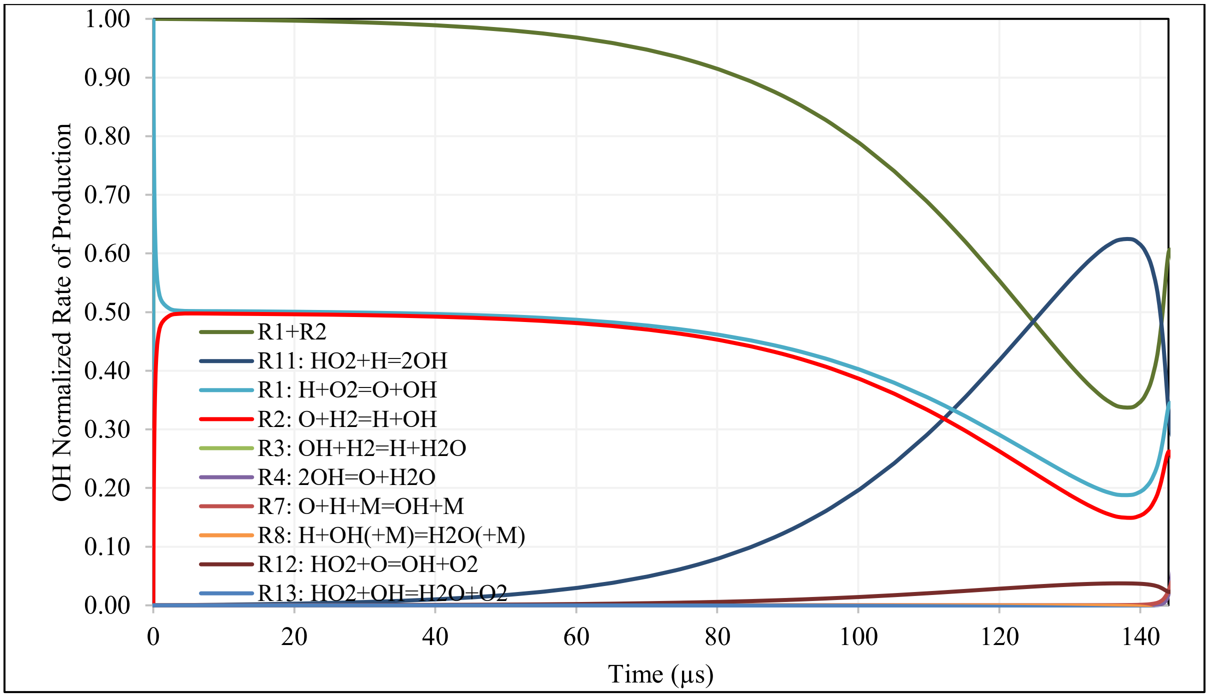

Figure A11: Normalized OH rate of production analysis for Test #25 – 4%H_2/Ar φ=1 at 1209 K and 39.6 bar

Figure A12 and Figure A13 depict test #25's absolute and normalized H ROP. It can be observed that, similar to test #10, H production is dominated by R3 throughout the IDT period, but is also produced to smaller extents through R2. To complete the picture, involving first dominant path through R1+R2, O ROP is analyzed.

Figure A14 andFigure A15, provide the absolute value and normalized O ROP graphs. These figures show that O generation is dominated by R1 for test #25, in-line with the path observed for test #10.

To understand the path dominant at the later stage of IDT period, involving R11, HO_2 ROP is examined. Figure A16 and Figure A17 illustrate the HO_2 ROP analyses results for test #25. Similar to test #10, HO_2 is produced mainly by R9 throughout the IDT period. It is important to note that while pressure-dependent IDT sensitivities of Figure 29 at 1209 K suggested potential involvement of R17, the ROP figures (Figure A10 to Figure A17) clarify that at its base rate parameter values, R17 does not participate in a dominant reaction path.

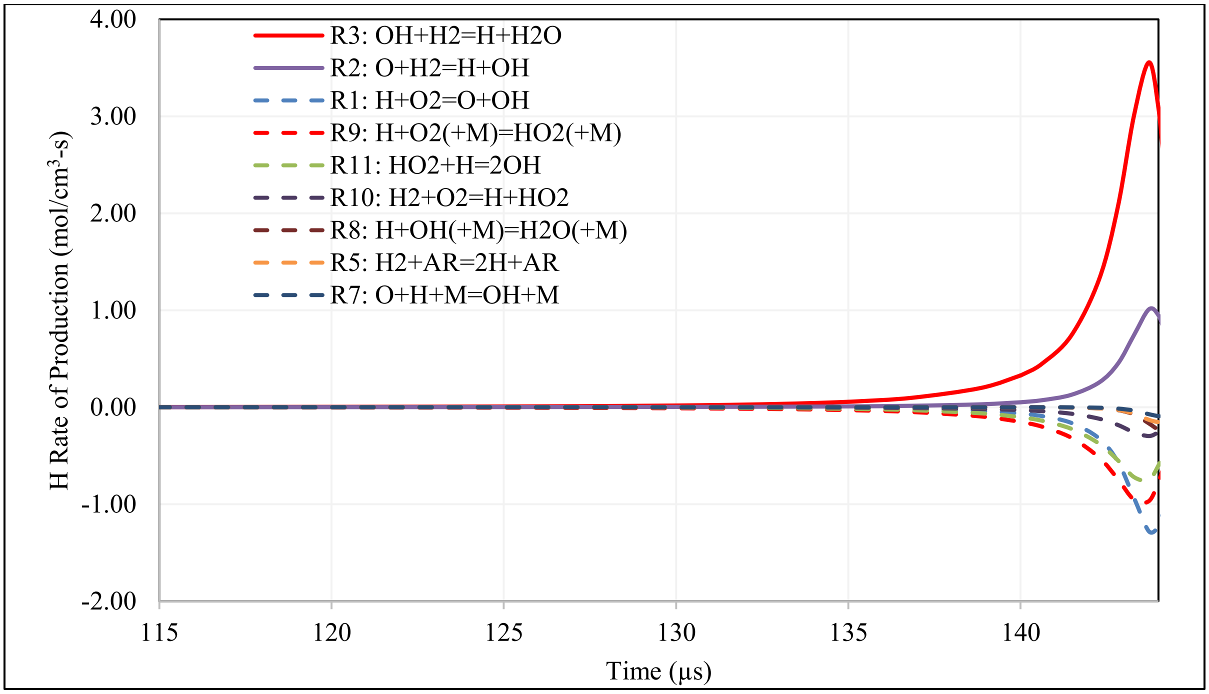

Figure A12: H rate of production analysis for Test #25 – 4%H_2/Ar φ=1 at 1209 K and 39.6 bar

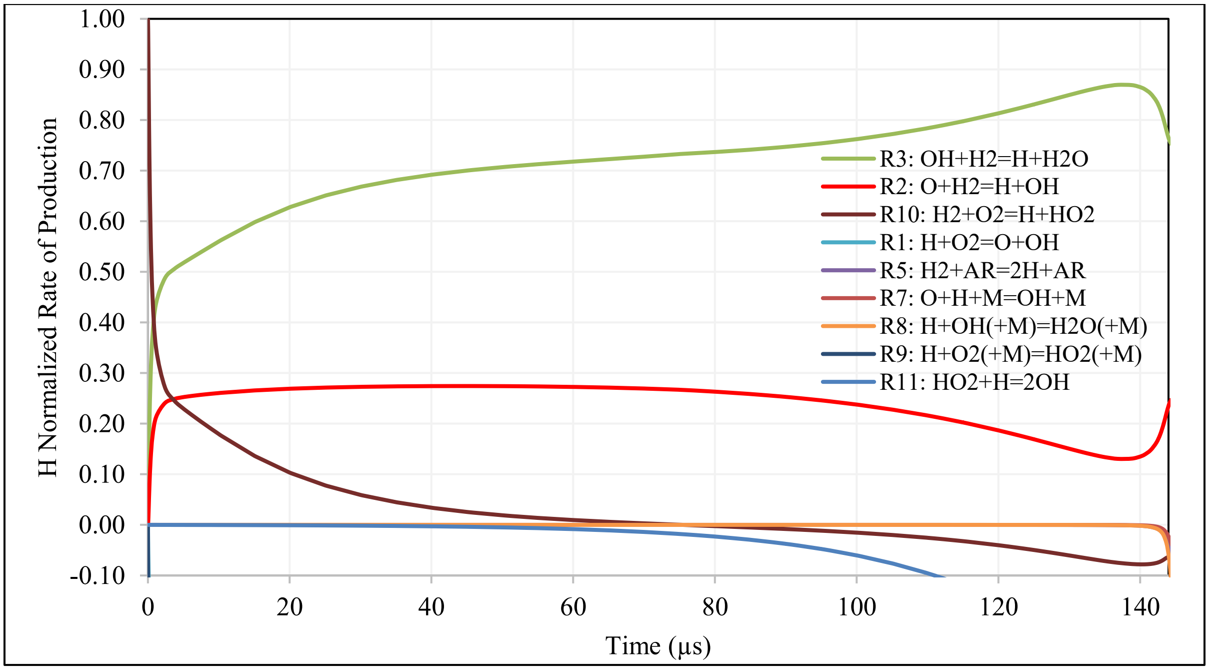

Figure A13: Normalized H rate of production analysis for Test #25 – 4%H_2/Ar φ=1 at 1209 K and 39.6 bar

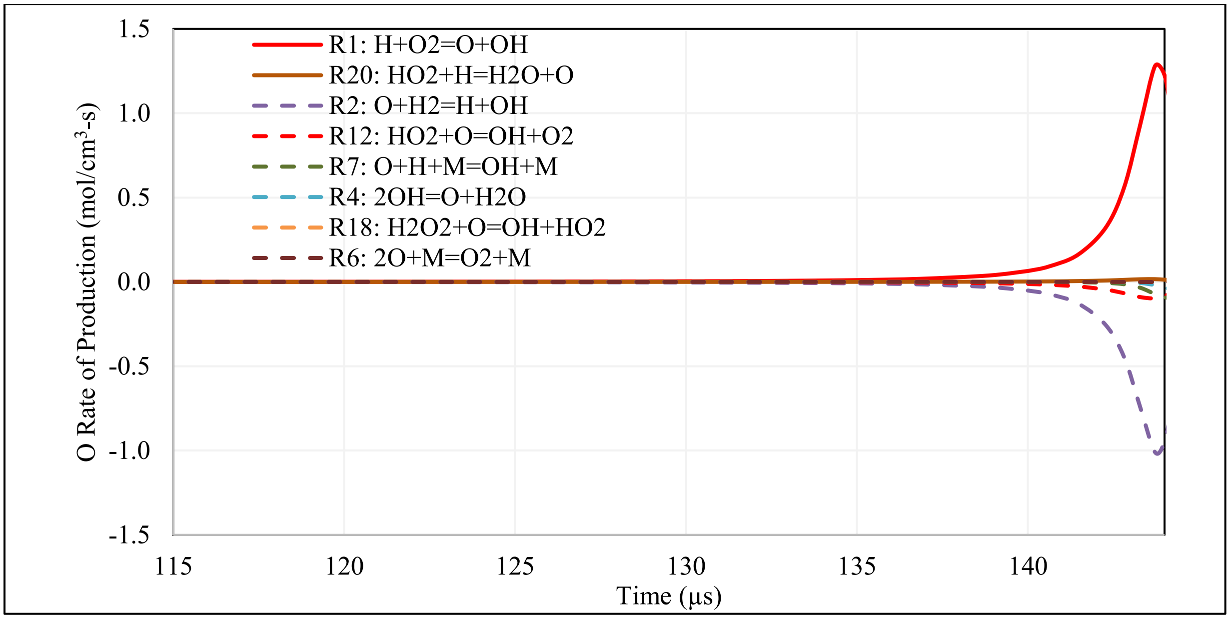

Figure A14: O rate of production analysis for Test #25 – 4%H_2/Ar φ=1 at 1209 K and 39.6 bar

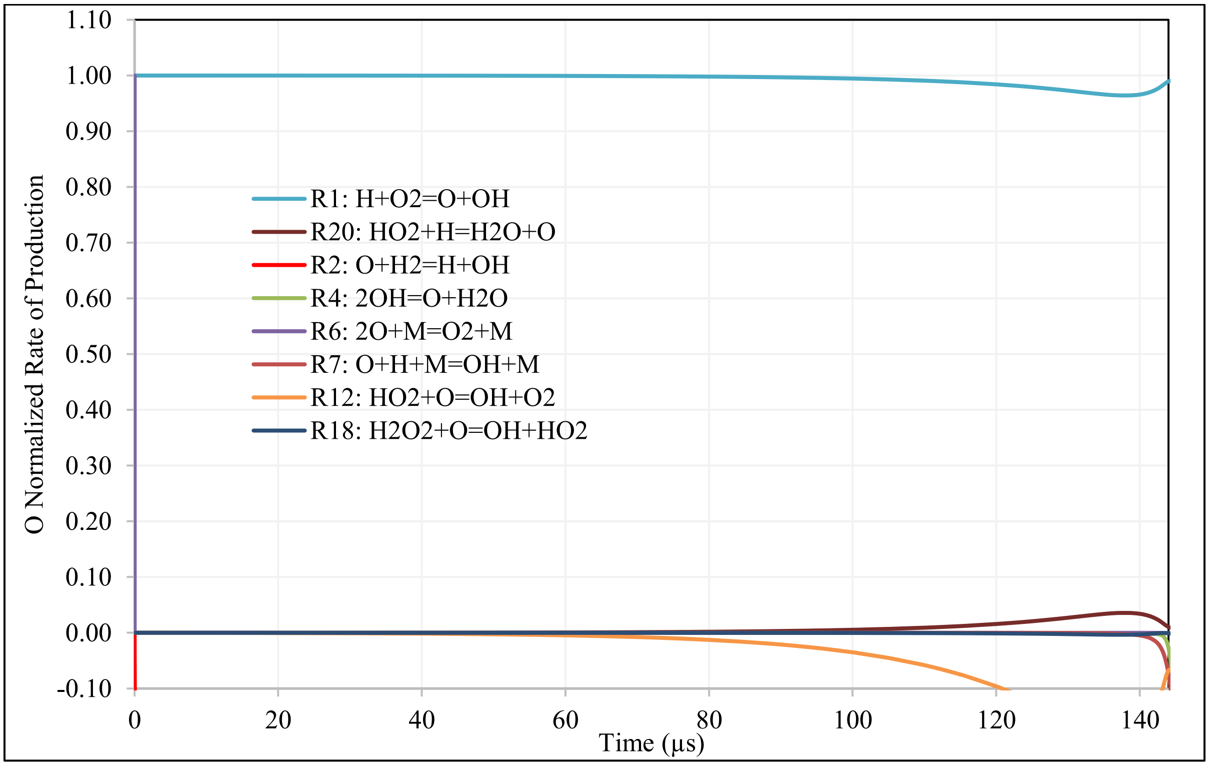

Figure A15: Normalized O rate of production analysis for Test #25 – 4%H_2/Ar φ=1 at 1209 K and 39.6 bar

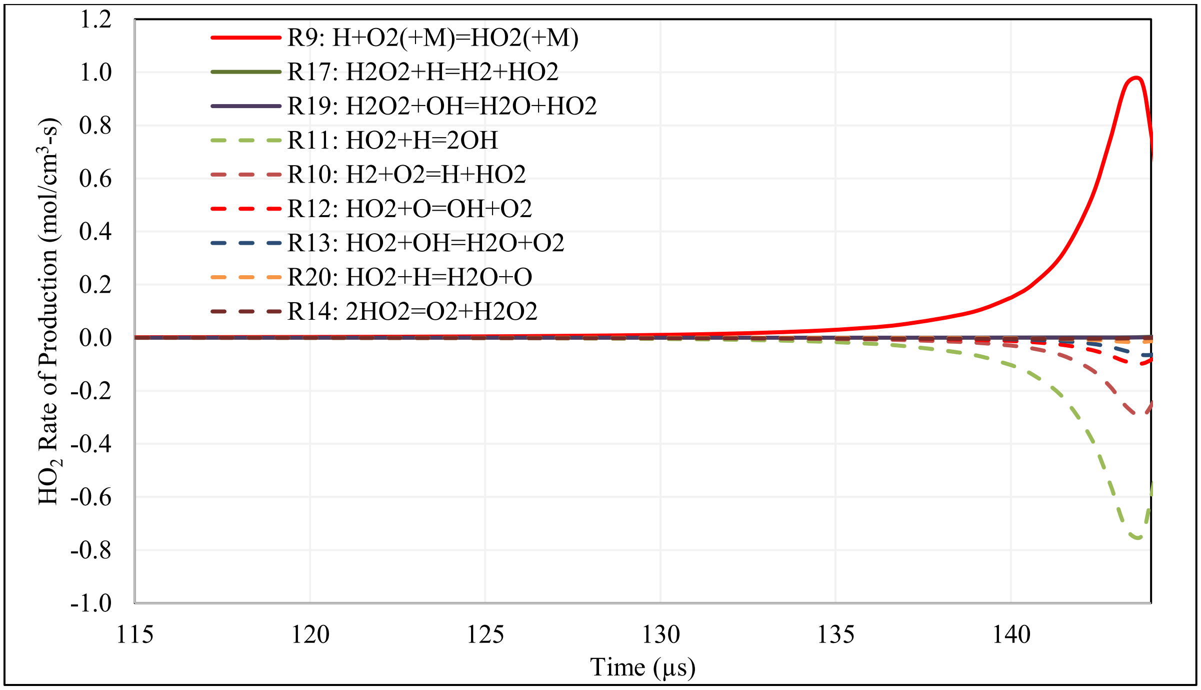

Figure A16: HO_2 rate of production analysis for Test #25 – 4%H_2/Ar φ=1 at 1209 K and 39.6 bar

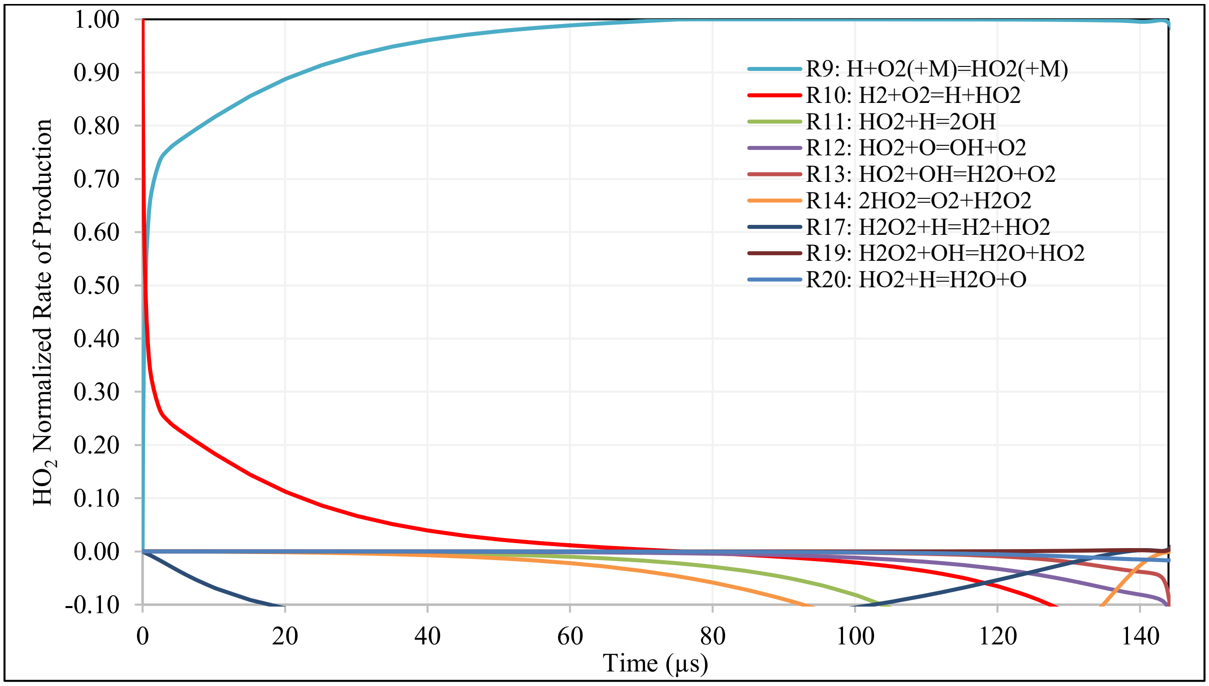

Figure A17: Normalized HO_2 rate of production analysis for Test #25 – 4%H_2/Ar φ=1 at 1209 K and 39.6 bar

<u>ROP analyses results of extrapolated Test #25– 4%H_2/Ar φ=1 at 1209 K and 150 bar</u>

Figure A18 and Figure A19 depict the absolute and normalized OH ROP results for 4%H_2/Ar φ=1 at 1209 K and 150 bar. While Figure A18 points to R11 as the dominant path, the normalized ROP results of Figure A19 show that for the initial 8 µs, a path through R1+ R2, and from 8-134 µs, another path involving R15: H_2O_2(+M)=OH+OH(+M) dominate. Finally the third path through R11, identified fromFigure A18, surpasses the others in producing OH. As such, H, O, H_2O_2 and HO_2 rates of production impact reactivity at this condition.

Figure A20 andFigure A21, illustrate the H radicals ROP analyses at 1209 K and 150 bar. It can be observed that H radicals are mainly produced through R2+R3 and to a lesser extent by R10 (initially).

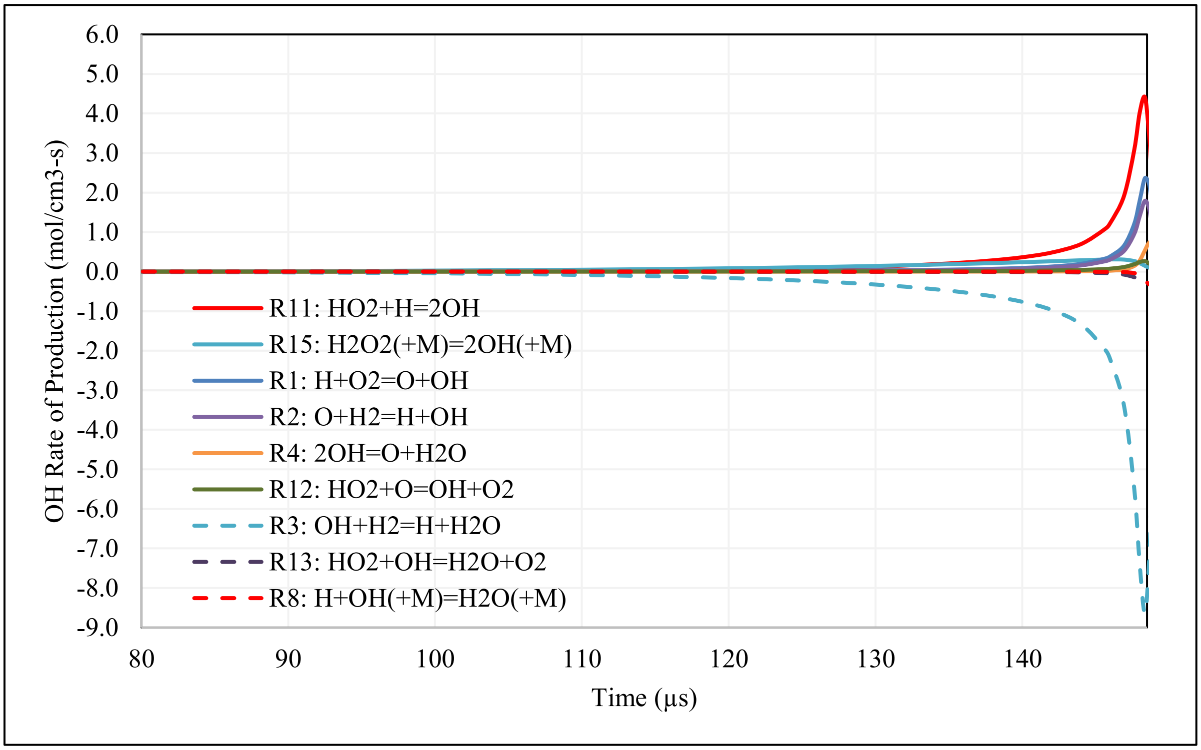

Figure A18: OH rate of production analysis for 4%H_2/Ar φ=1 at 1209 K and 150 bar

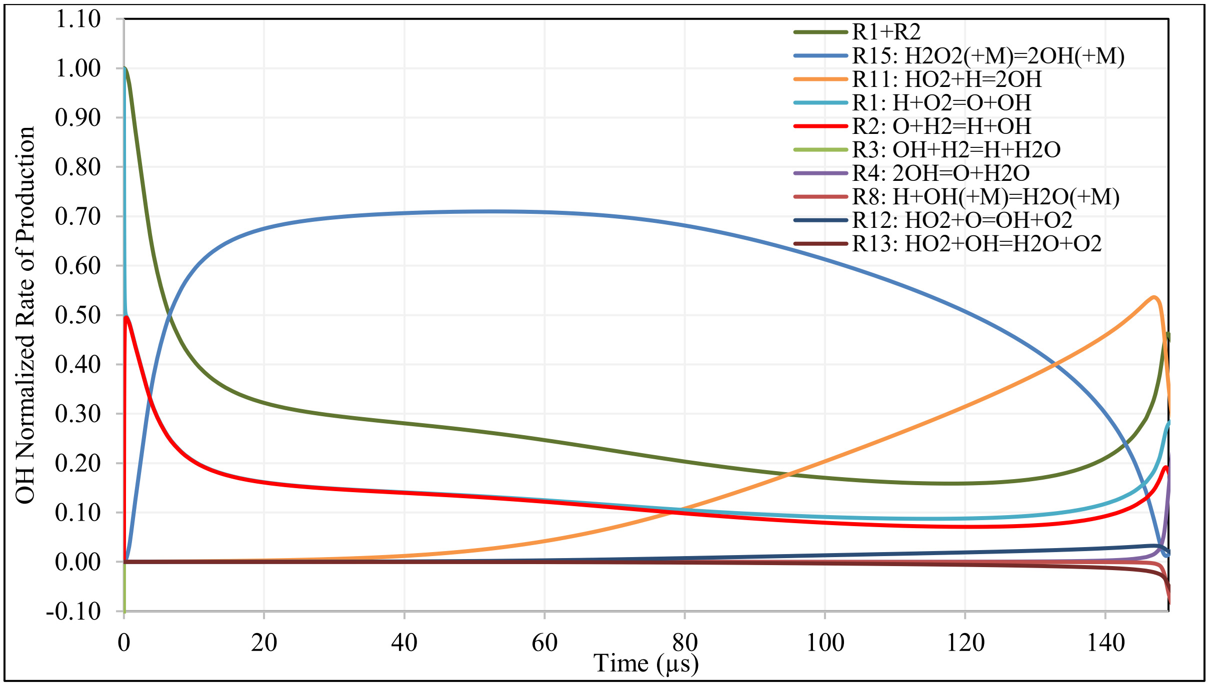

Figure A19: Normalized OH rate of production analysis for 4%H_2/Ar φ=1 at 1209 K and 150 bar

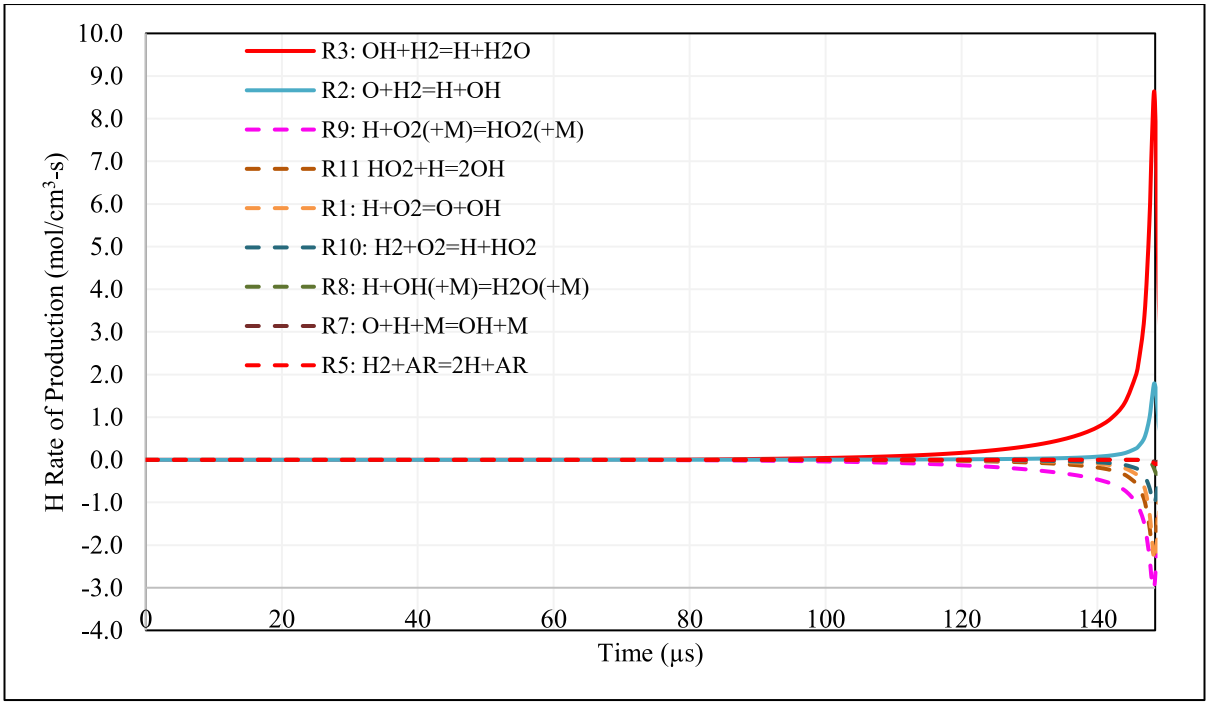

Figure A20: H rate of production analysis for 4%H_2/Ar φ=1 at 1209 K and 150 bar

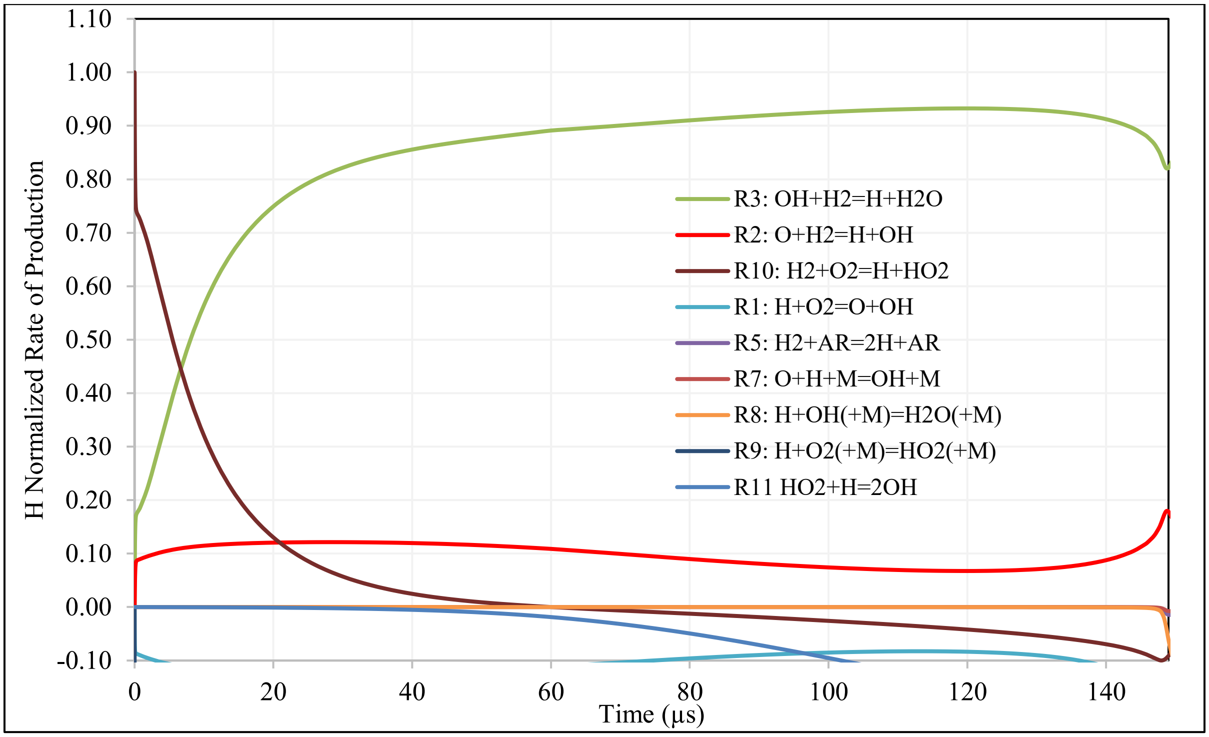

Figure A21: Normalized H rate of production analysis for 4%H_2/Ar φ=1 at 1209 K and 150 bar

Figure A22 and Figure A23 detail the O radical's absolute and normalized rates of production for the same extrapolated case. R1's dominant role as the main producer of O during the IDT period is clear. Combining the OH, H and O ROPs it is concluded that for the first 8 µs the path through R1+R2+R3 dominates. To understand the path(s) involving R15, H_2O_2 ROP is analyzed. Figure A24 and Figure A25 present the H_2O_2 ROP analyses results for the same test. They illustrate that –R17: HO_2+H=H+H_2O_2 is responsible for building the H_2O_2 radical pool for the initial 70 µs, after which R14: HO_2+HO_2=O_2+H_2O_2 becomes significantly faster until ignition. This shows that there are now two paths leading to H_2O_2, both of which rely HO_2 radical pool, i.e., -R17+R15 and R14+R15.

Figure A26 and Figure A27provide the absolute and normalized ROP profiles of HO_2. They illustrate that HO_2 is solely generated through R9, which ties its fate back to the H radical produced mainly by R3. This clarifies the two dominant paths through R15, i.e. R3+(-R17)+R9+R15 and

R3+R14+R9+R15. Similarly, these figures also illustrate that the delayed path to OH production involving R11: HO_2+H=2OH involves R3+R9+R11.

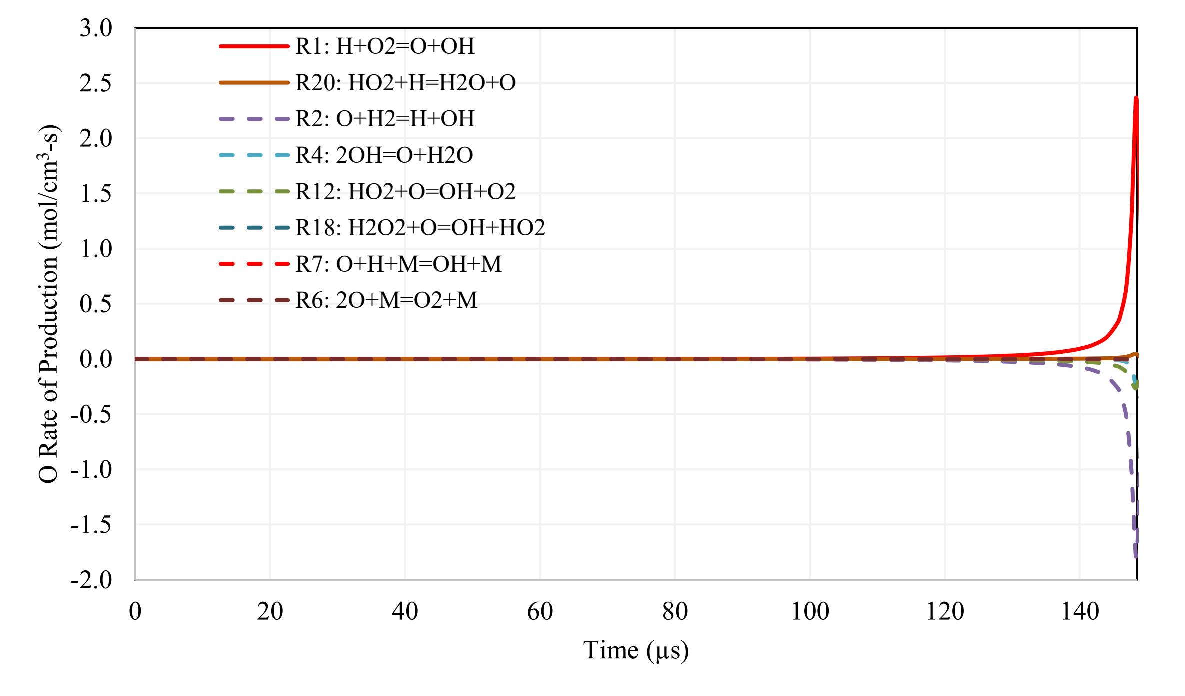

Figure A22: O rate of production analysis for 4%H_2/Ar φ=1 at 1209 K and 150 bar

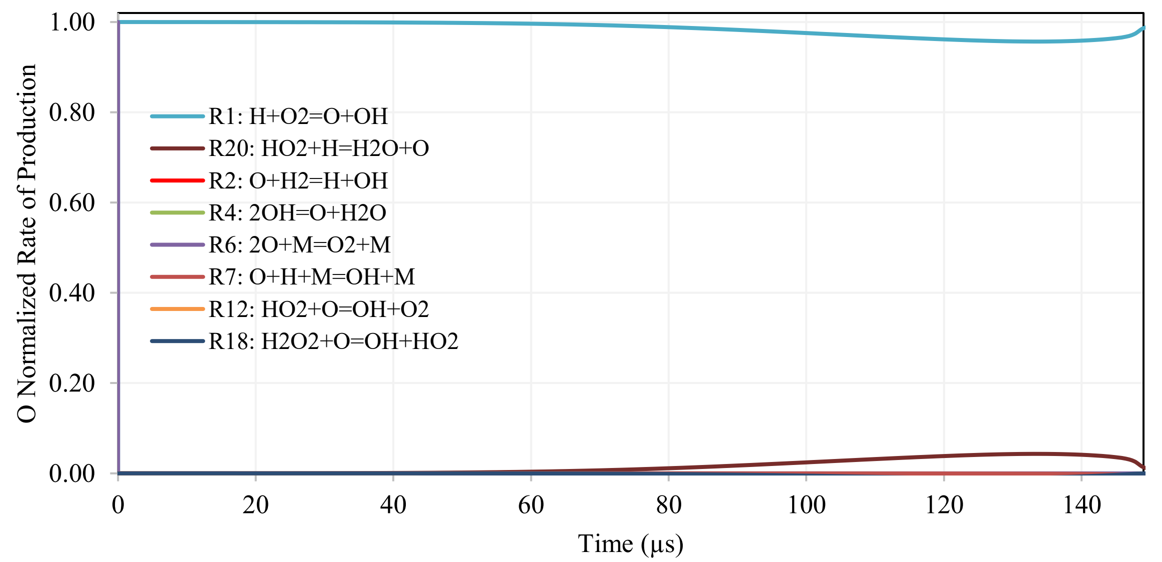

Figure A23: Normalized O rate of production analysis for 4%H_2/Ar φ=1 at 1209 K and 150 bar

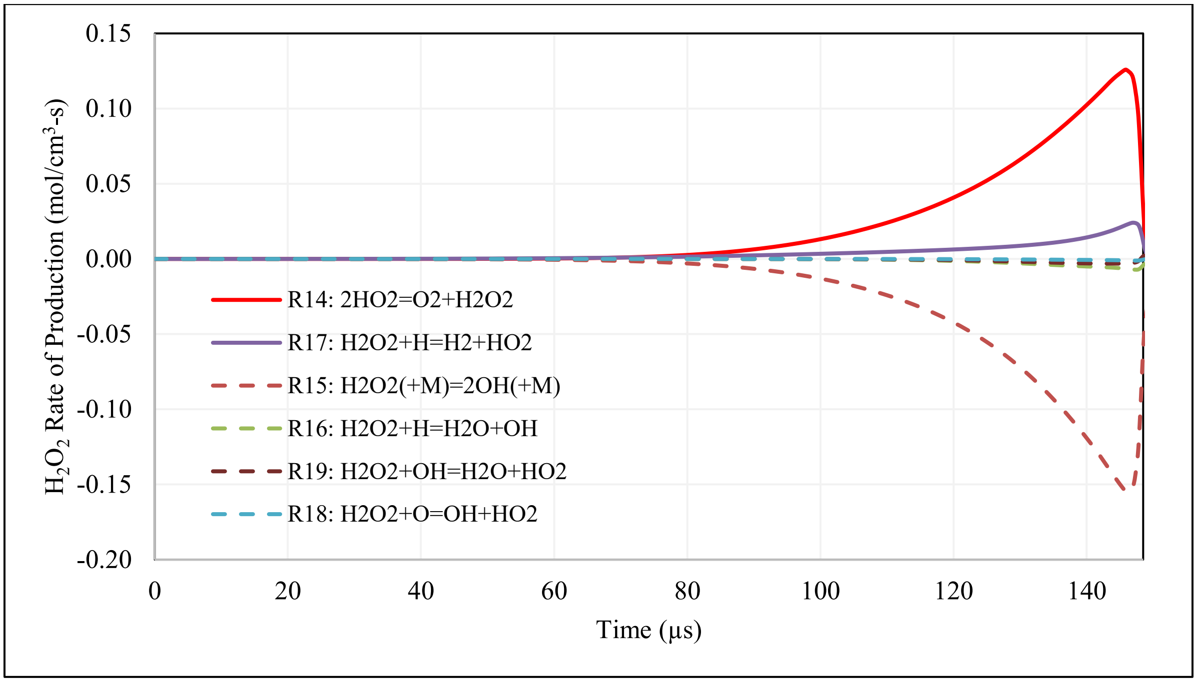

Figure A24: H_2O_2 rate of production analysis for 4%H_2/Ar φ=1 at 1209 K and 150 bar

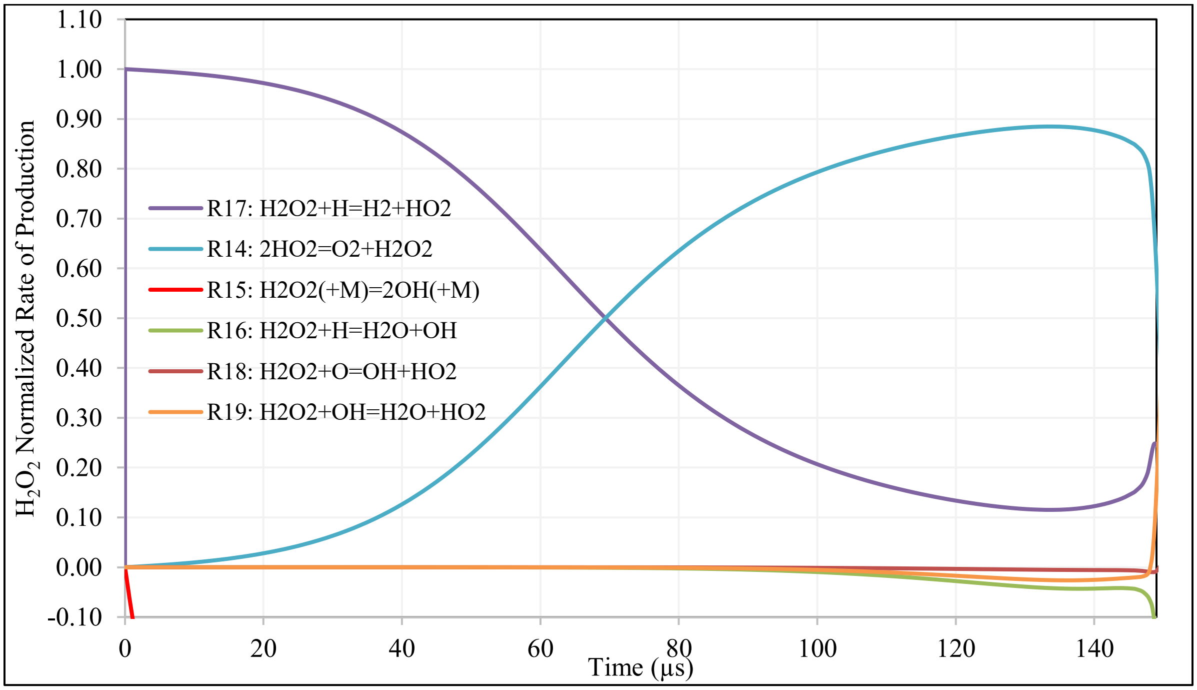

Figure A25: Normalized H_2O_2 rate of production analysis for 4%H_2/Ar φ=1 at 1209 K and 150 bar

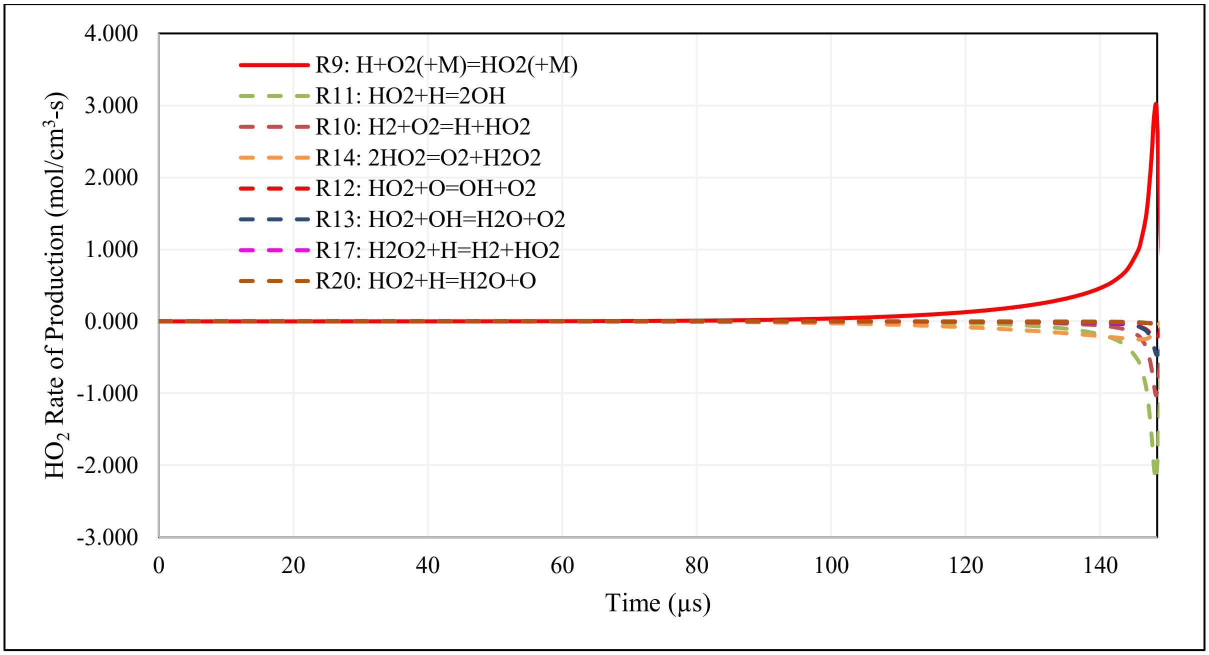

Figure A26: HO_2 rate of production analysis for 4%H_2/Ar φ=1 at 1209 K and 150 bar

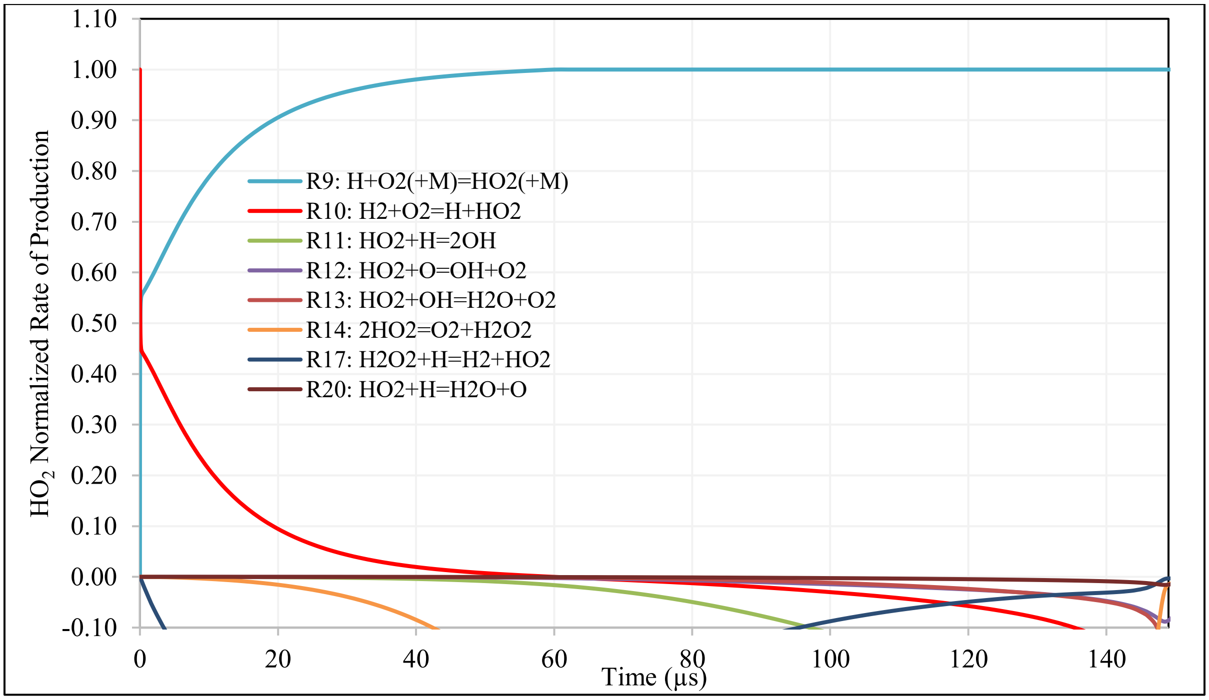

Figure A27: Normalized HO_2 rate of production analysis for 4%H_2/Ar φ=1 at 1209 K and 150 bar

ROP analyses results of Test #51, for 4%H_2/45%CO_2/Ar φ=1 at 1226 K, 40.6 bar

Figure A28 and Figure A29, illustrate the OH-radical ROP analysis for Test #51. They reveal that, in a chronological order: R1+R2, followed by R15: H_2O_2(+M)=OH+OH(+M) and R11: H+HO_2=OH+OH, are the main producers of OH. While less important, the new chain propagating path involving –R23: CO_2+H=CO+OH, has also appeared in the list of OH producers, in the presence of 45%CO_2. It can also be observed that relative to OH ROP analyses for the same mixture in Argon bath (see Figure A10) the radical pool buildup and the ignition event is less abrupt. To understand the reactive pathways it is important to investigate H, O, H_2O_2, and HO_2 ROPs.

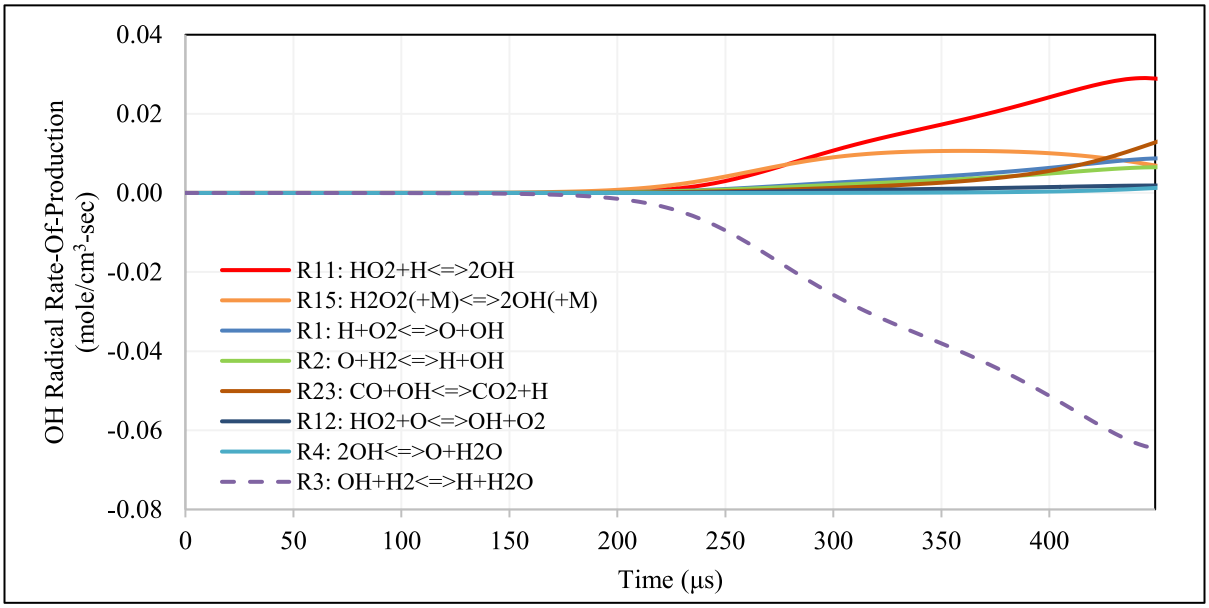

Figure A28: OH rate of production analysis of Test #51, for 4%H_2/45%CO_2/Ar φ=1 at 1226 K, 40.6 bar

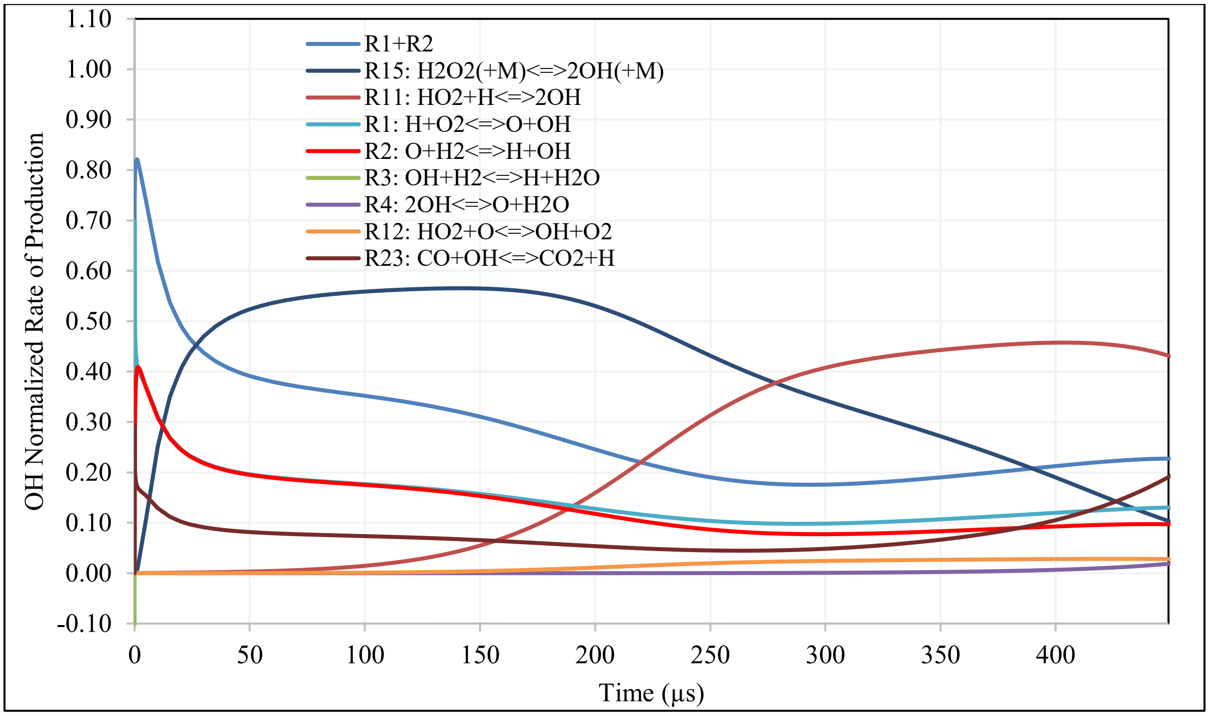

Figure A29: Normalized OH rate of production analysis of Test #51, for 4%H_2/45%CO_2/Ar φ=1 at 1226 K, 40.6 bar

Figure A30 and Figure A31 provide a graph of absolute and normalized H-radical ROPs for test #51. These figures show that, while R3: $OH+H_2=H+H_2O$, –R17: $HO_2+H_2=H+H_2O_2$, and R2 are the dominant suppliers of H radical pool, R9 and R11 are its main consumers. Relative to the Ar-diluted counterpart ofFigure A31, Figure A13, in the presence of 45% CO_2, –R17 has become the second largest supplier of H radicals for the first half of the ignition delay period. This in contrast with the observations for the case of pure Ar bath, where –R17 contribution to the H-radical pool was insignificant.

Figure A32, depicts the normalized O ROP for test #51. This figure shows that R1 is the main producer of this radical. These ROP plots (Figure A28 toFigure A32), illustrate that for the initial 25 μs of reaction time, the dominant reaction reaction path is R1+R2+R3.

Figure A33 and Figure A34 depict the absolute and normalized H_2O_2 ROP profiles of test # 51. These figures clearly indicate that the main producer of H_2O_2 is –R17 for the initial 170 μs, after which R14: $HO_2+HO_2=O_2+H_2O_2$ is more dominant in producing H_2O_2. To complete the understanding associated with the reaction pathways it is important to analyze HO_2 ROP.

Figure A35 and Figure A36 provide the absolute and normalized HO_2 ROP profiles for test #51. They illustrate that R9 is the dominant producer of HO_2, however, R10 also supplies the HO_2 radical pool to a much smaller extent for the first 100 µs, after which it reverses direction and consumes it.

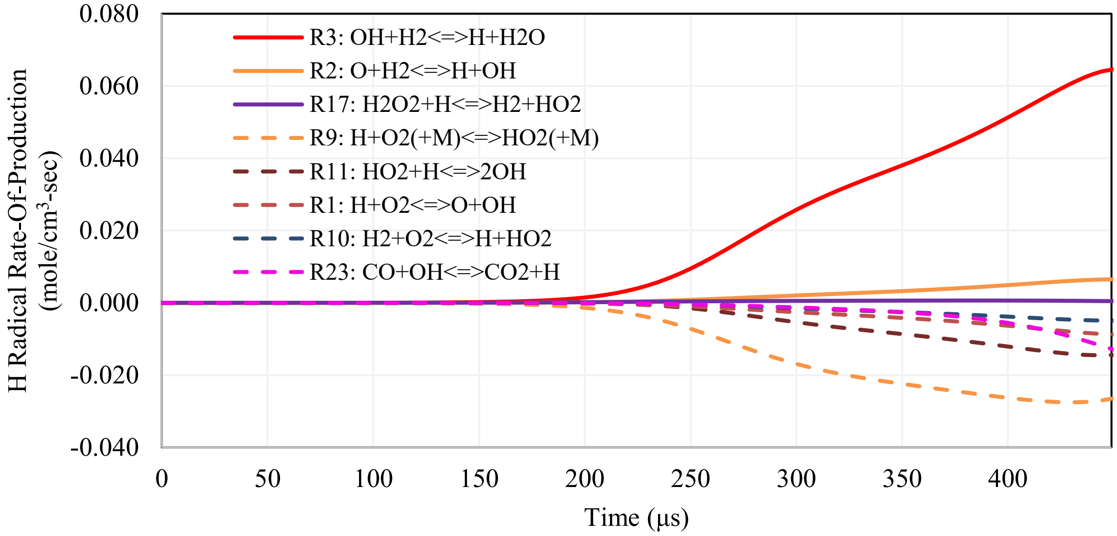

Figure A30: H rate of production analysis of Test #51, for 4%H_2/45%CO_2/Ar φ=1 at 1226 K, 40.6 bar

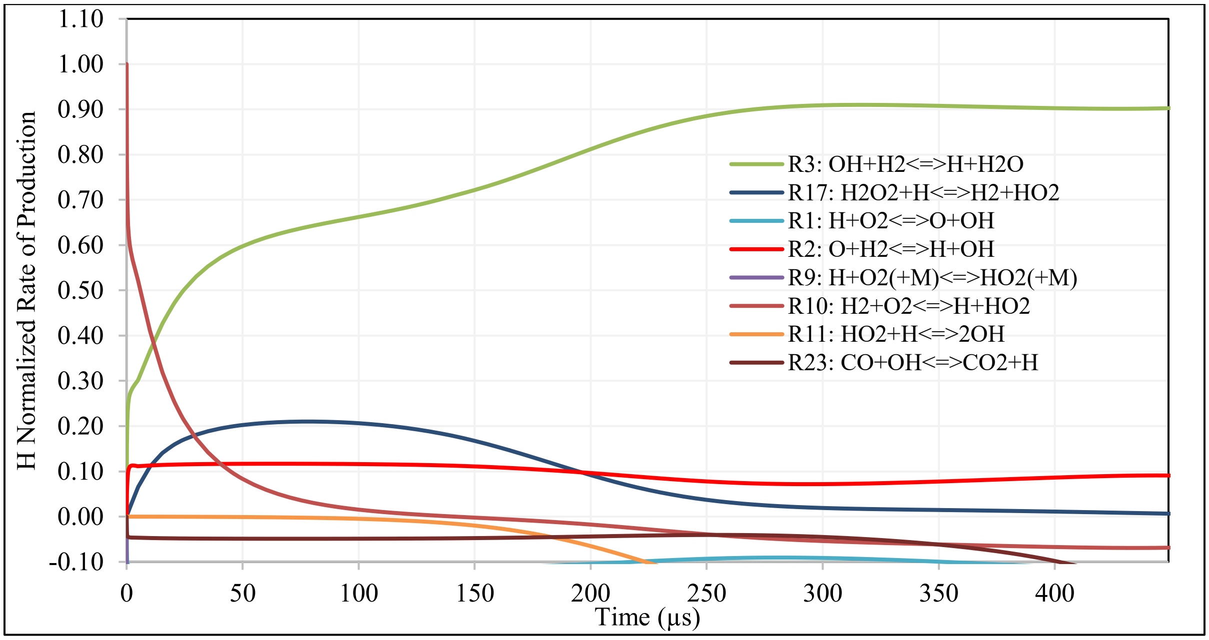

Figure A31: Normalized H rate of production analysis of Test #51, for 4%H_2/45%CO_2/Ar φ=1 at 1226 K, 40.6 bar

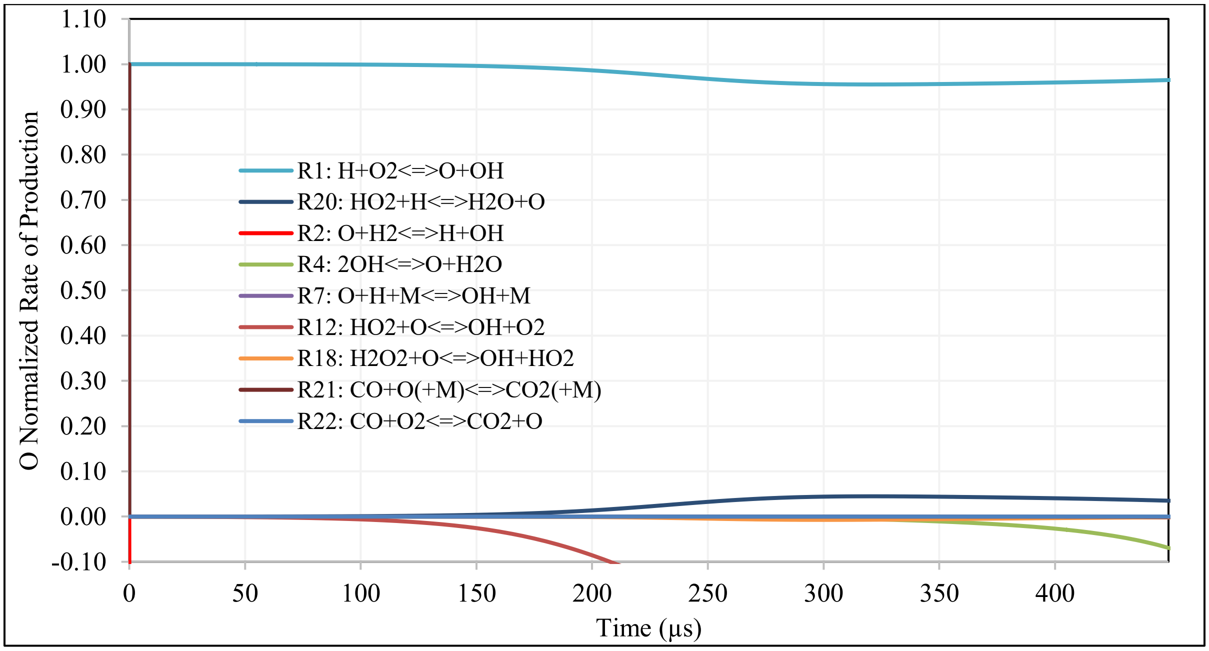

Figure A32: Normalized O rate of production analysis of Test #51, for 4%H_2/45%CO_2/Ar φ=1 at 1226 K, 40.6 bar

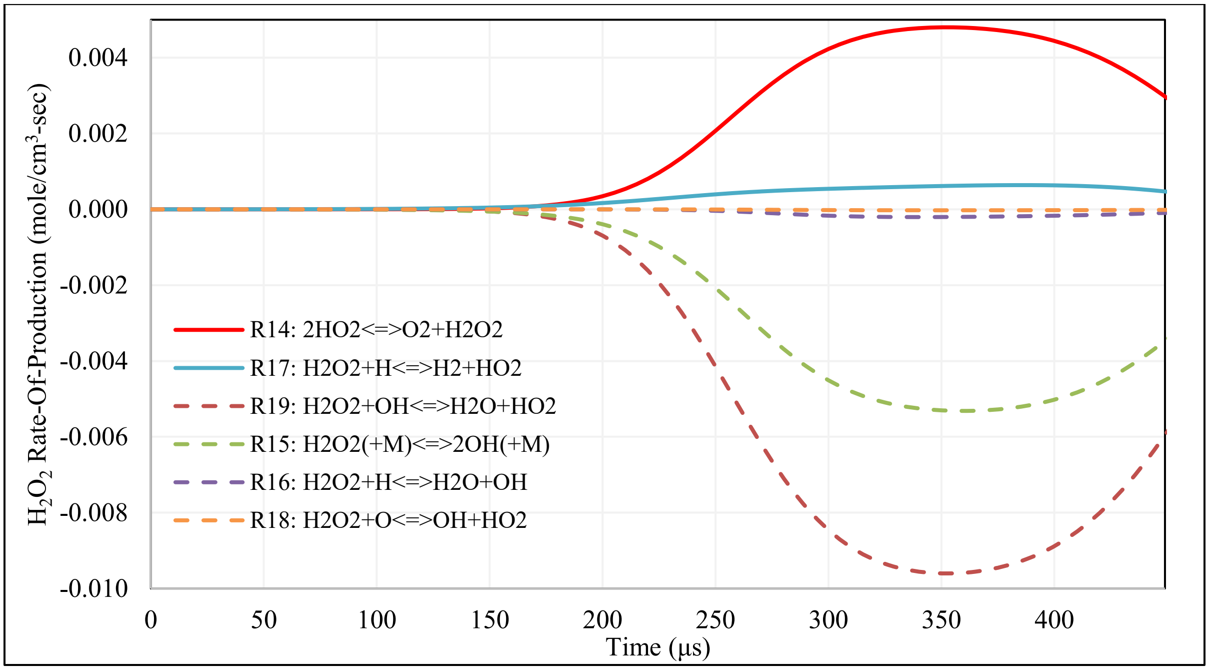

Figure A33: H_2O_2 rate of production analysis of Test #51, for 4%H_2/45%CO_2/Ar φ=1 at 1226 K, 40.6 bar

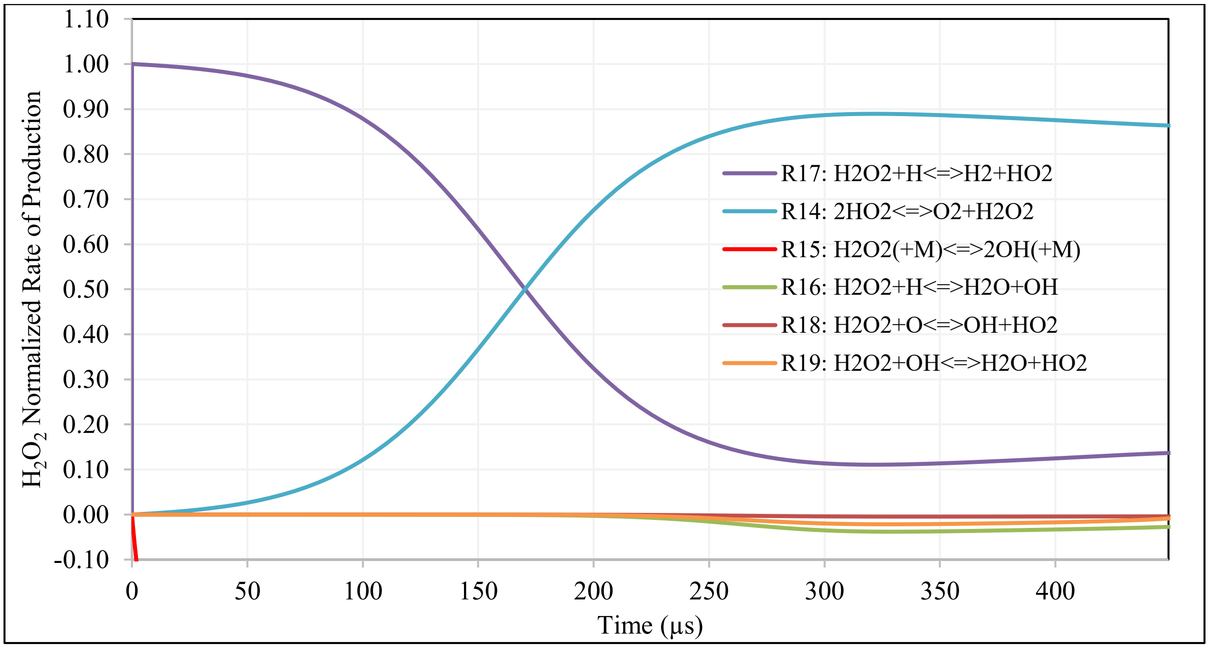

Figure A34: Normalized H_2O_2 rate of production analysis of Test #51, for 4%H_2/45%CO_2/Ar φ=1 at 1226 K, 40.6 bar

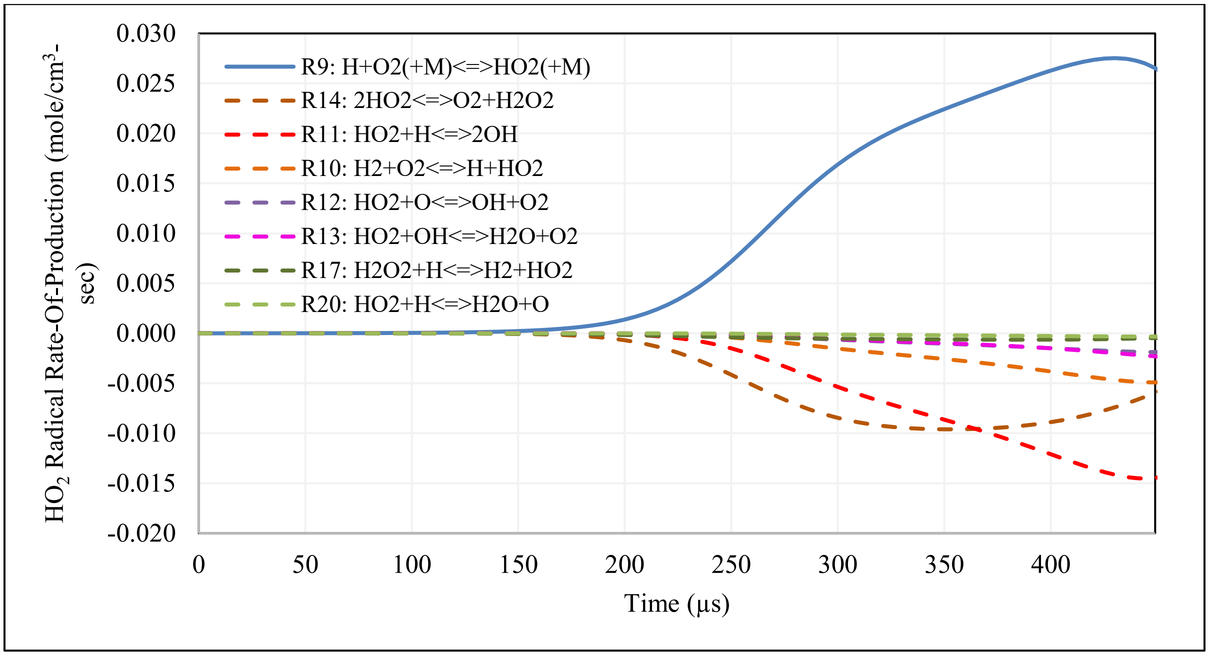

Figure A35: HO₂ rate of production analysis of Test #51, for 4%H₂/45%CO₂/Ar φ=1 at 1226 K, 40.6 bar

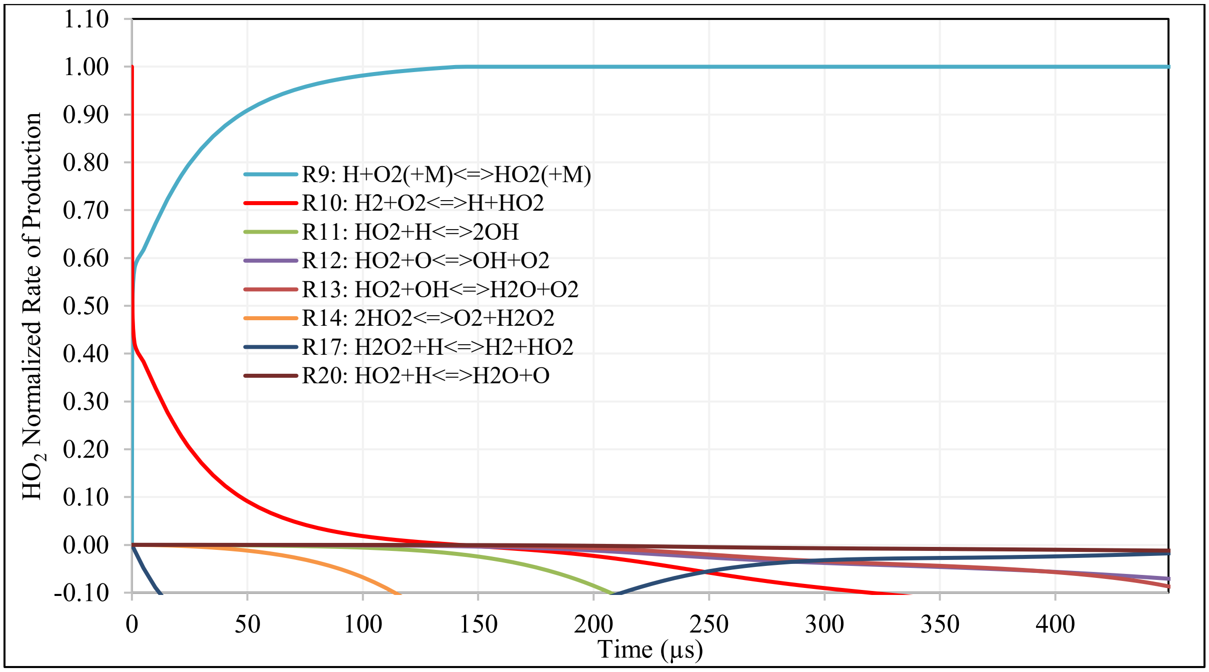

Figure A36: Normalized HO₂ rate of production analysis of Test #51, for 4%H₂/45%CO₂/Ar φ=1 at 1226 K, 40.6 bar

ROP analyses results of Test #51 at extrapolated pressure of 150 bar, for 4%H_2/45%CO_2/Ar φ=1 at 1226 K

Figure A37 and Figure A37 depict the OH-ROP of 4%H_2/45%CO_2/Ar φ=1 at 1226 K at 150 bar. These figures show that at 150 bar, the dominant OH generation path involves only R15: H_2O_2(+M)=OH+OH(+M). Alternate less dominant paths (<25% normalized contribution to OH) through R1+R2 at the earlier stages and through R11: HO_2+H=OH+OH at the later stages are also present. Relative to the OH ROP analysis at the same condition but at 40 bar (seeFigure A28), R15 has become the sole dominant OH producing reaction throughout the ignition delay time period at this higher pressure. At 40 bar, R15 was dominant, but only for the first half of IDT period, and for the second half R11 became the main producers of OH.

Figure A39 and Figure A40 illustrate the H_2O_2 ROP analyses results at 150 bar. It can be observed that the dominant paths to the generation of H_2O_2, involve –R17: HO_2+H_2=H_2O_2+H for the initial 65 µs, followed by R14: HO_2+HO_2=H_2O_2+O_2 until ignition at 181 µs. It is however, important to note that for the first 65 µs, the path through –R17 is the dominant contributor to the H_2O_2 pool. As the fate of H_2O_2 is tied to HO_2, pathways producing this radical are analyzed.

Figure A41 and Figure A42 summarize the results of HO_2 ROP analyses for 4%H_2/45%CO_2/Ar φ=1, 1226 K and 150 bar. It can be observed that the main producer of HO_2 is R9: H+O_2(+M)=HO_2(+M).

To complete the understanding of the dominant reactive pathways, it is important to look at how the H radical is produced.

To this end, Figure A43 and Figure A44 illustrate the results of H ROP analyses at 150 bar in the presence of 45% CO_2. They indicate that H is mainly produced through R3, and to a lesser extent R17 and R2. They also show that H is consumed mainly by R9, R11, -R23, and to a lesser extent R1 and –R10. Comparing Figure A44 with its equivalent at 40 bar, Figure A31, illustrates that R17's contribution has increased from 20% at 40 bar to 30% at 150 bar. This increase in contribution is also accompanied by a decrease in contribution of R2 at 150 bar.

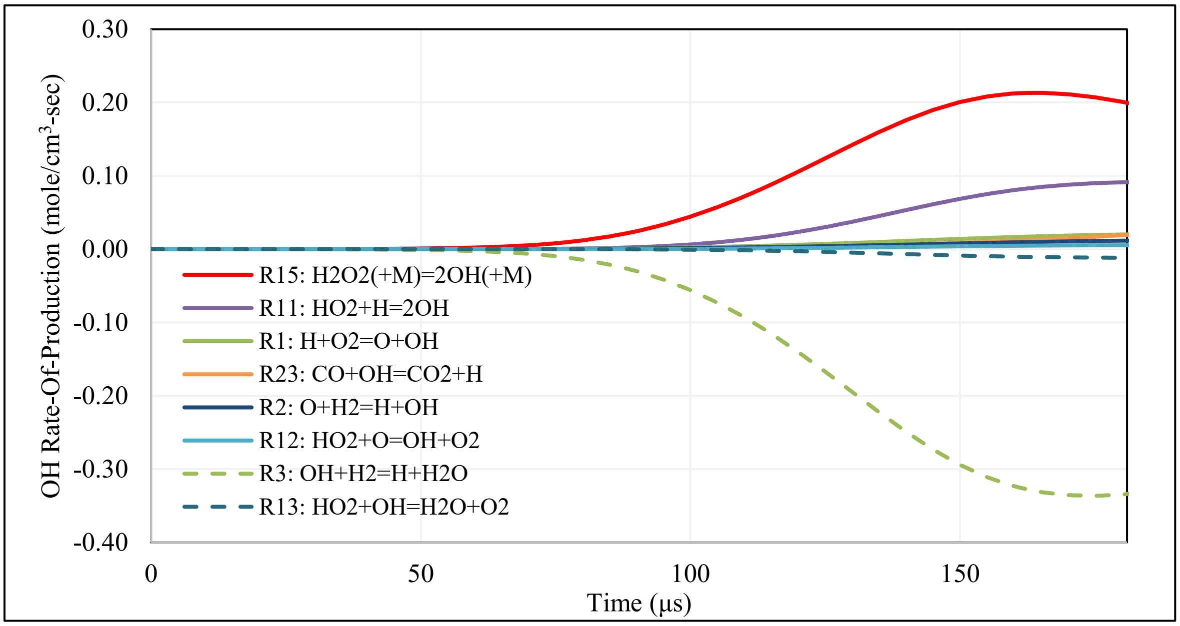

Figure A37: OH rate of production analysis of 4%H_2/45%CO_2/Ar φ=1 at 1226 K at 150 bar

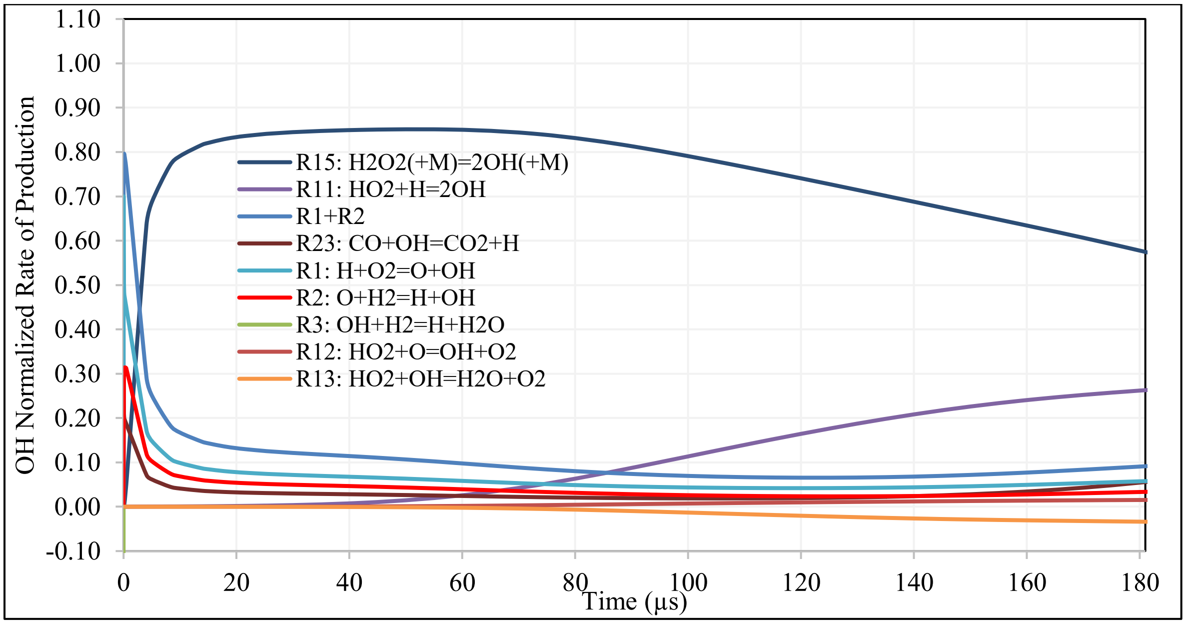

Figure A38: Normalized OH rate of production analysis of 4%H_2/45%CO_2/Ar φ=1 at 1226 K at 150 bar

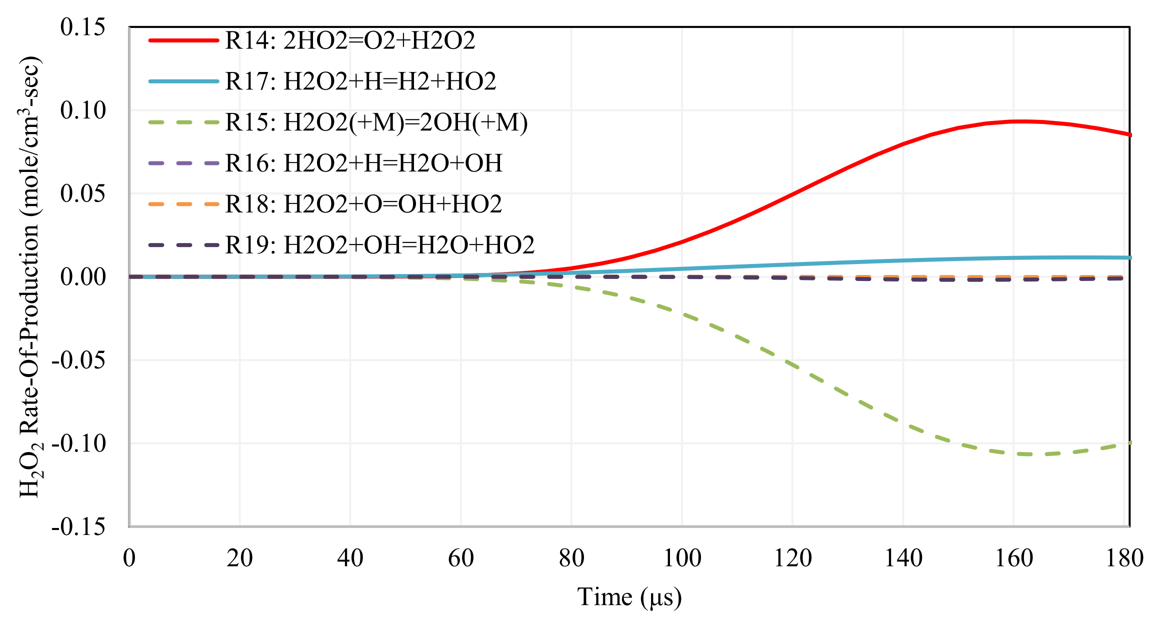

Figure A39: H_2O_2 rate of production analysis of 4%H_2/45%CO_2/Ar φ=1 at 1226 K at 150 bar

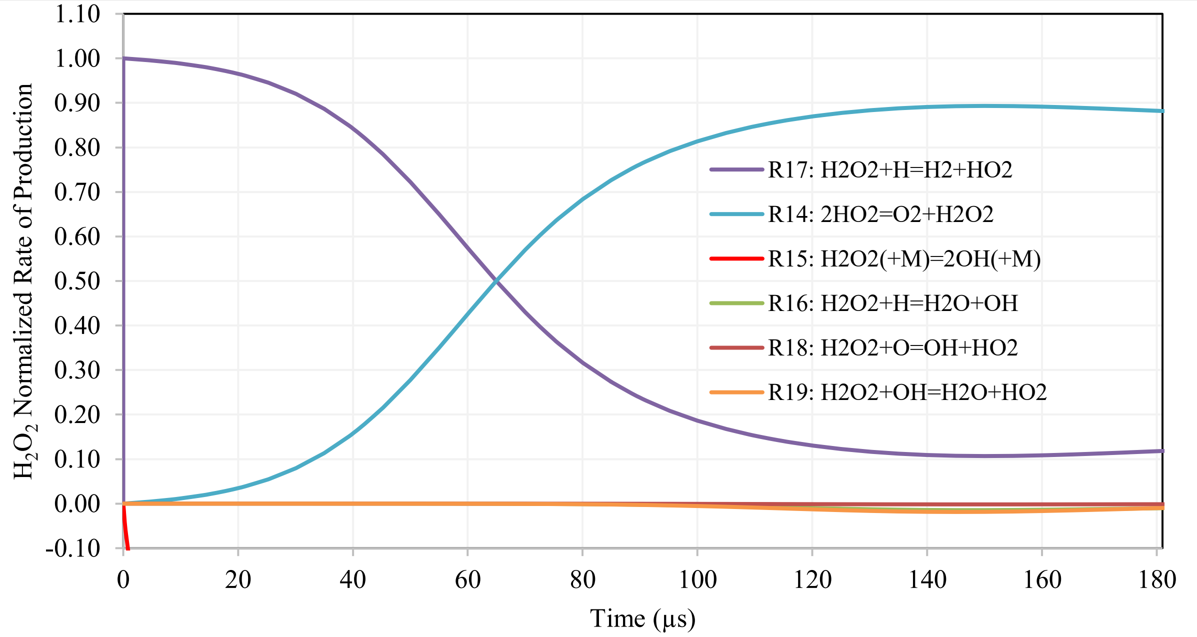

Figure A40: Normalized H_2O_2 rate of production analysis of 4%H_2/45%CO_2/Ar φ=1 at 1226 K at 150 bar

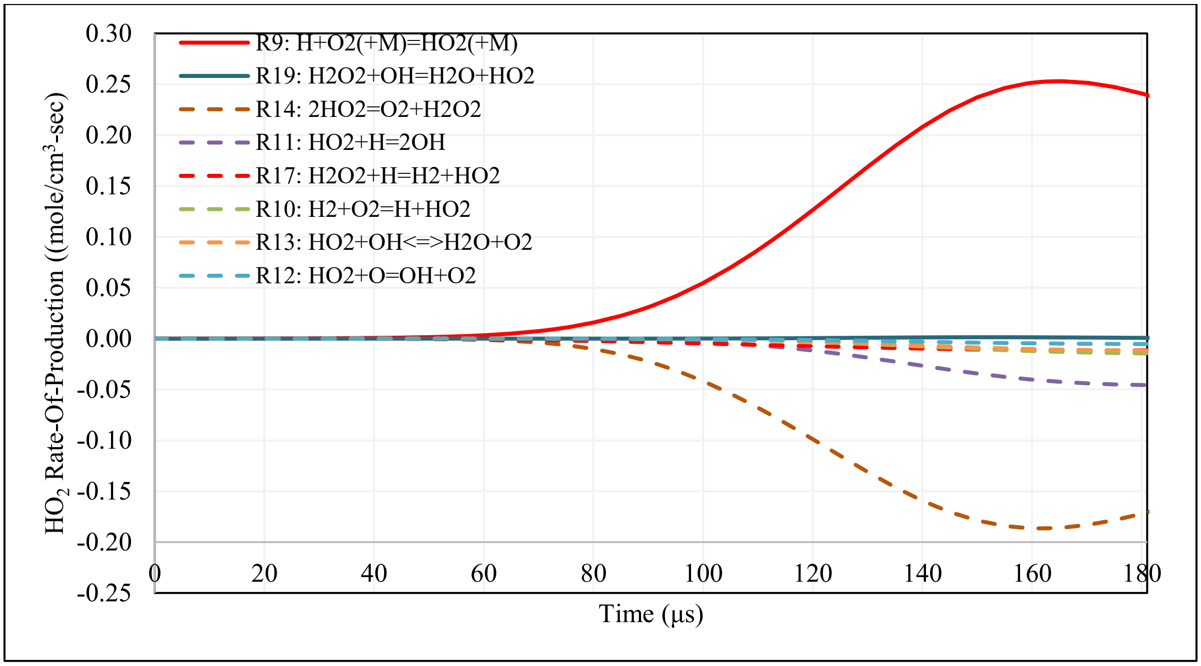

Figure A41: HO_2 rate of production analysis of $4\%H_2/45\%CO_2/Ar$ φ=1 at 1226 K at 150 bar

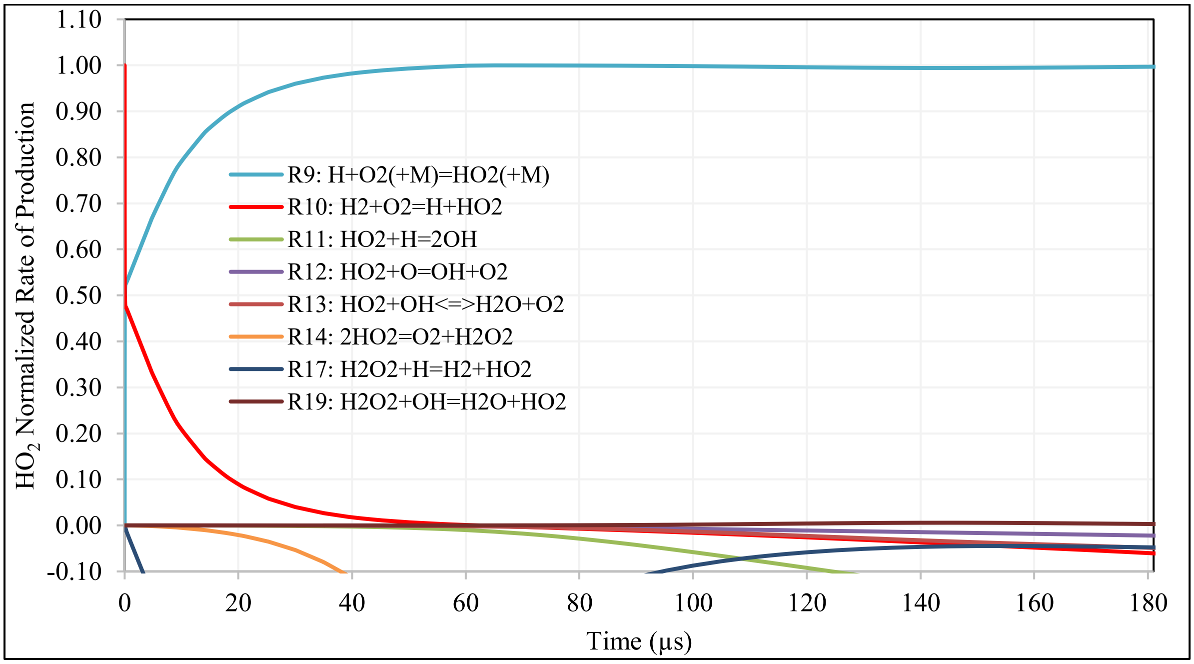

Figure A42: Normalized HO_2 rate of production analysis of $4\%H_2/45\%CO_2/Ar$ φ=1 at 1226 K at 150 bar

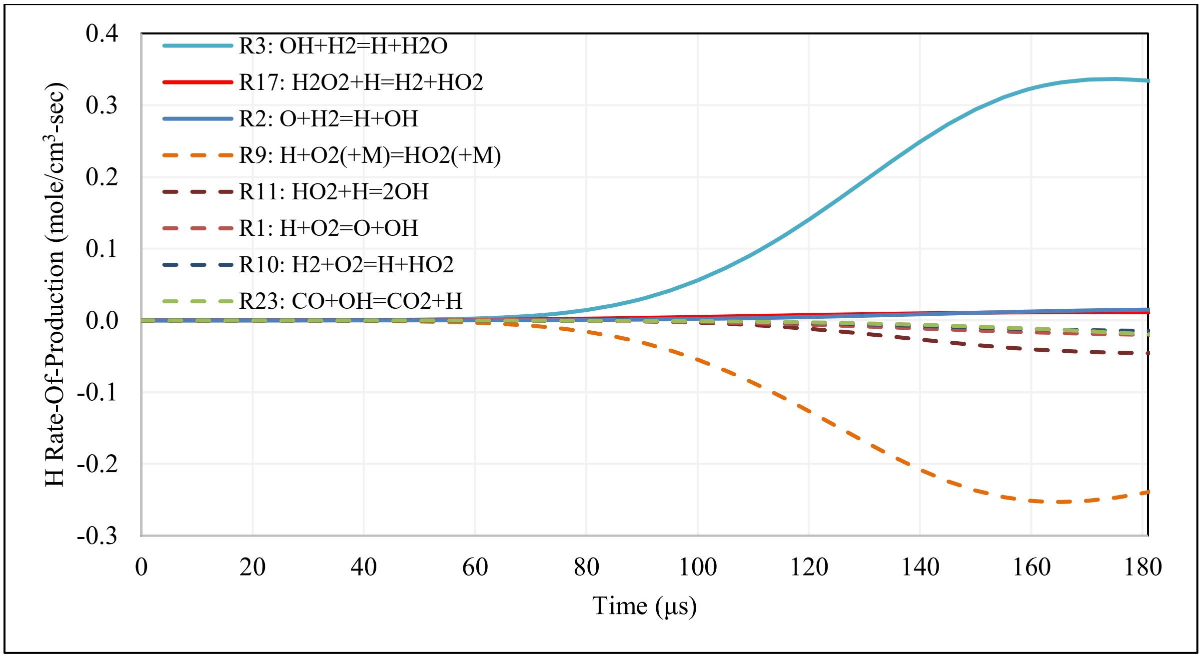

Figure A43: H rate of production analysis of 4%H_2/45%CO_2/Ar φ=1 at 1226 K at 150 bar

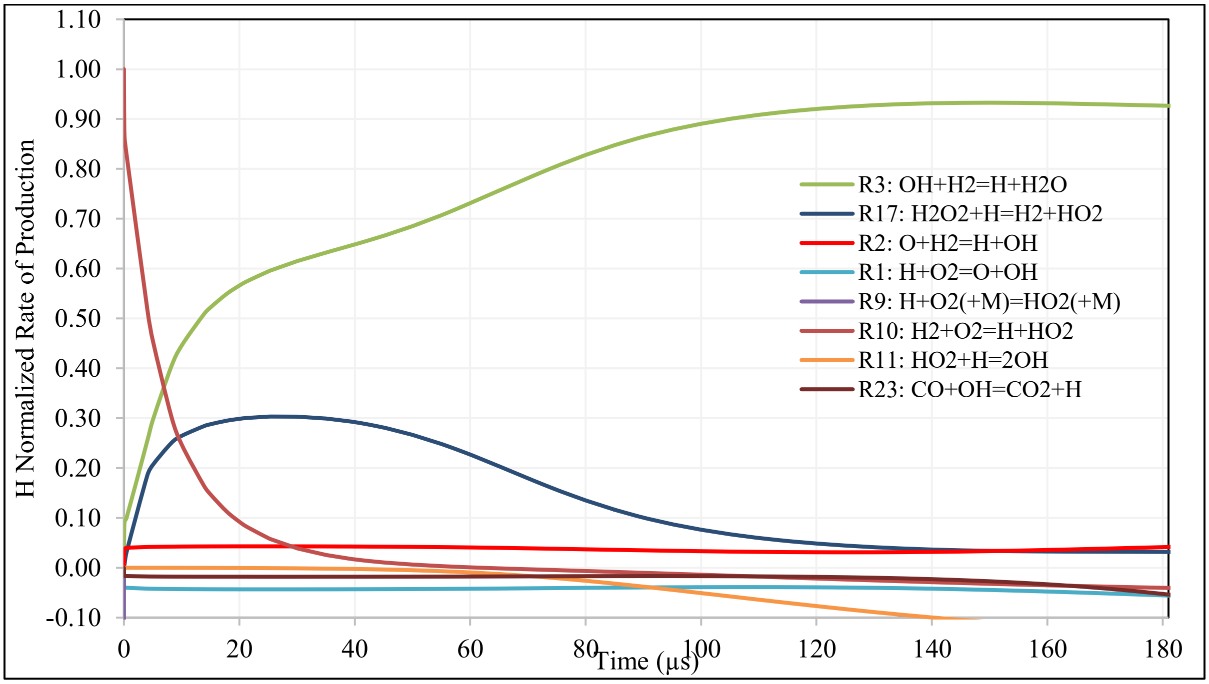

Figure A44: Normalized H rate of production analysis of 4%H_2/45%CO_2/Ar φ=1 at 1226 K at 150 bar

ROP analysis for Test #33 – 4%H_2/45%H_2O/Ar φ=1 at 1222 K and 40 bar

Figure A45 andFigure A46, illustrate the absolute and normalized OH ROP analyses for test #33, and shows that OH is mainly produced through H_2O_2 decomposition through R15: H_2O_2(+M)=OH+OH, and for the initial 200 μs –R19: H_2O=HO_2=OH+H_2O_2 along with R1+R2 have approximately a 10% contribution to the OH pool. Subsequently beyond 200 μs R11: HO_2+H=OH+OH contribution increases and reaches a maximum of 30% at ignition, but it does not dominate at any point in the IDT period.

To better understand the contributions of these pathways it is important to look into H_2O_2, H, HO_2 and O's ROP, in order of priority.

Comparisons of Figure A45 with the OH ROP in Ar (Figure A11) and in 45%CO_2/Ar (Figure A29) reveal that in the presence of 45%H_2O, the relative OH production path through –R19 and –R4: O+H_2O=OH+OH have gained importance. More importantly, the paths through R11, as well as R1+R2, are no longer fast enough to dominate OH production.

Figure A47 and Figure A48 depict the results of H_2O_2 ROP analyses. These figures indicate that H_2O_2 is produced by -R17: H_2+HO_2=H_2O_2+H for the first 170 μs, after which R14: HO_2+HO_2=O_2+H_2O_2, takes over as the main producer of H_2O_2 until ignition at 457 μs. It should also be noted that in the presence of 45%H_2O, for the initial 200 μs, the pathway through -R19: H_2O+HO_2=H_2O_2+OH produces H_2O_2 (~10-25%) as well as OH (5-10%). As such its combined impact, since all H_2O_2 decompose to two OH, translates to peak contributions of upwards of 30%, to the OH pool. Hence the path involving this chain branching reaction now serves as an alternate non-negligable path.

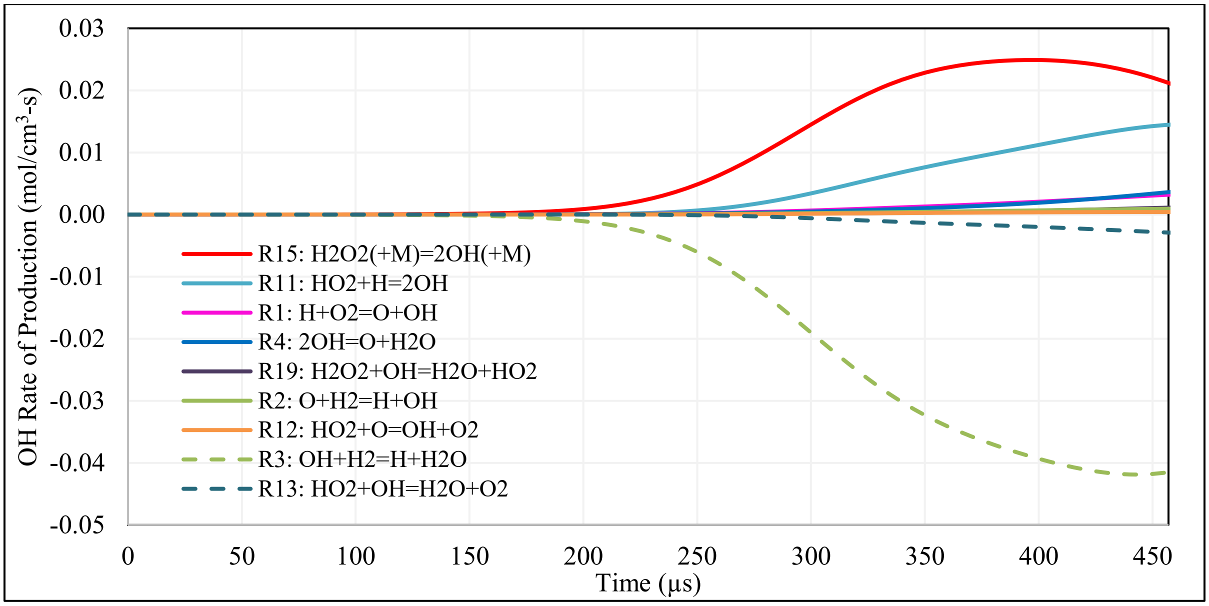

Figure A45: OH rate of production analysis for Test #33 – 4%H_2/45%H_2O/Ar φ=1 at 1222 K and 40 bar

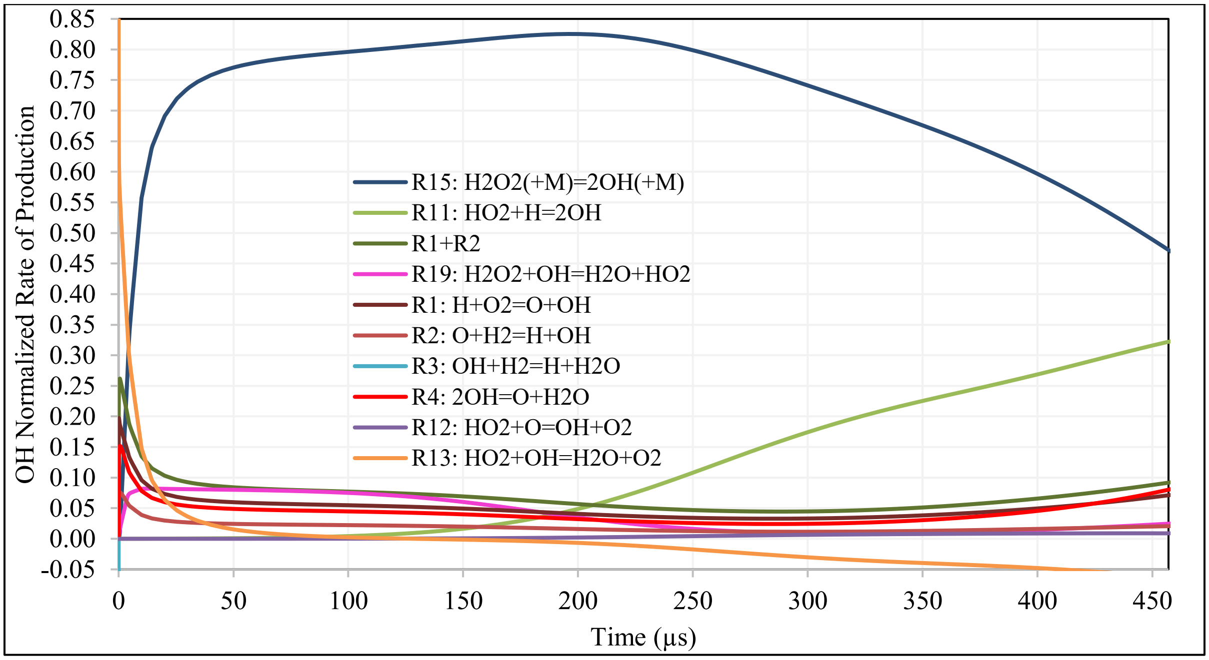

Figure A46: Normalized OH rate of production analysis for Test #33 – 4%H_2/45%H_2O/Ar φ=1 at 1222 K and 40 bar

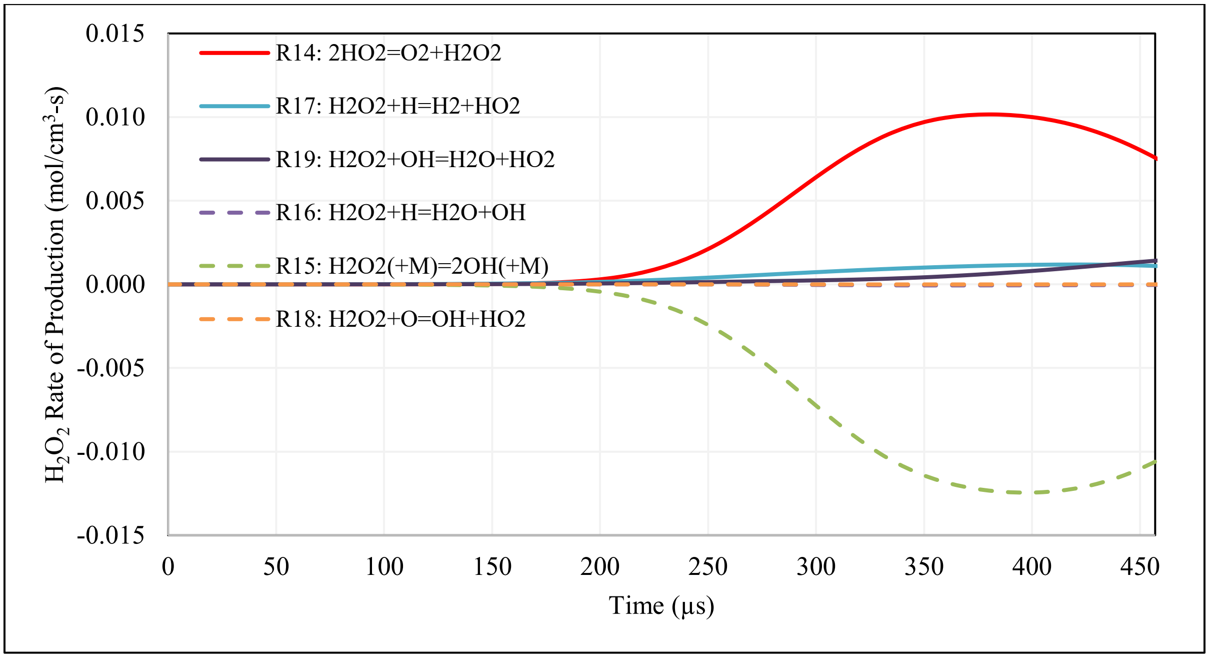

Figure A47: H_2O_2 rate of production analysis for Test #33 – 4%H_2/45%H_2O/Ar φ=1 at 1222 K and 40 bar

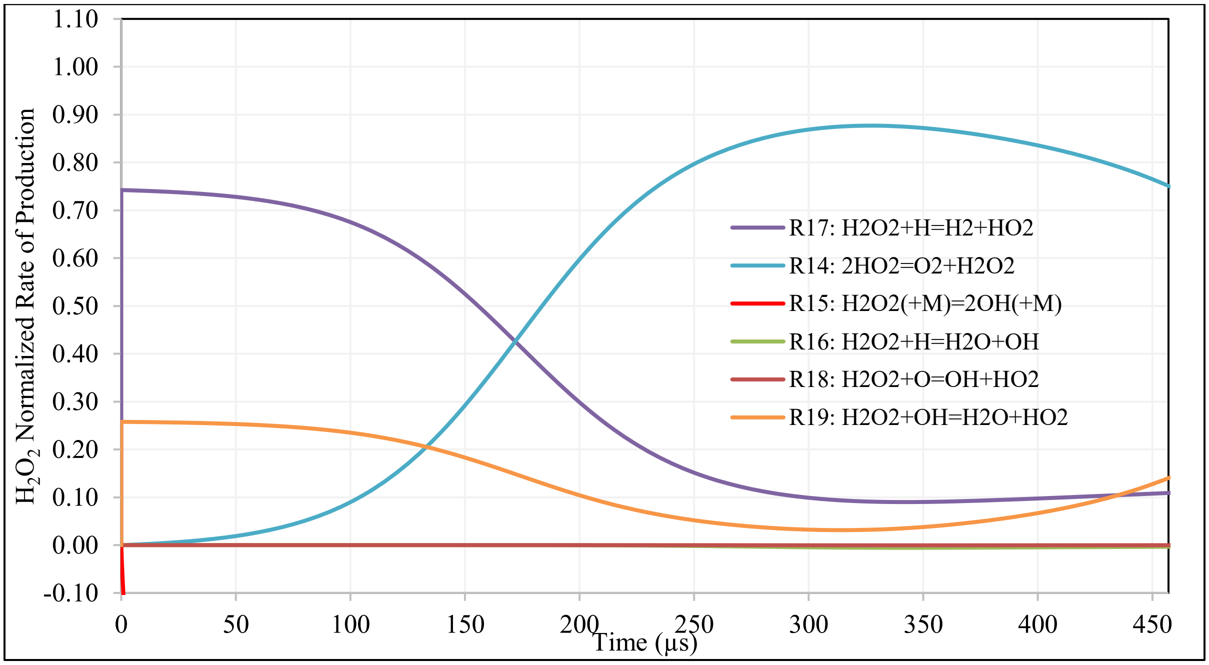

Figure A48: H_2O_2 rate of production analysis for Test #33 – 4%H_2/45%H_2O/Ar φ=1 at 1222 K and 40 bar

Figure A49 and Figure A50 depict absolute value and normalized HO_2 ROP analyses results. They indicate that the main HO_2 producer is the pressure-dependent reaction R9: $H+O_2(+M)=HO_2(+M)$. Also, the main consumers of HO_2, are R14, R11. R10 initially produces HO_2 but switches sign and becomes chain terminating after ~150 µs.

Figure A51 and Figure A52 provide the absolute and normalized H ROP analyses for test #33. It can be observed from these figures that while R3: $OH+H_2=H+H_2O$ dominates H production throughout the ignition delay period, -R17: $HO_2+H_2=H+H_2O_2$ produces as large as 22% it at the intial stages of reactivity. In order to complete the analysis of all radicals involved, the remaining less important ROP in the low temperature chemistry involved is that of O. Figure A53 depicts that O is produced mainly through R1 and to a small extent through R20: $HO_2+H=H_2O+O$.

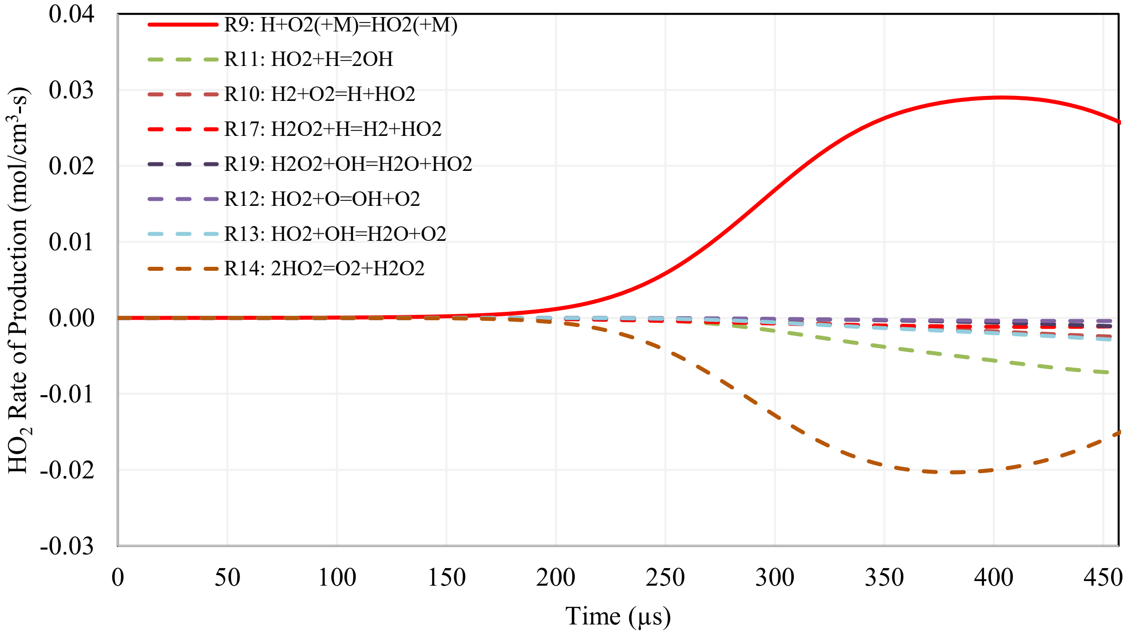

Figure A49: HO_2 rate of production analysis for Test #33 – 4%H_2/45%H_2O/Ar φ=1 at 1222 K and 40 bar

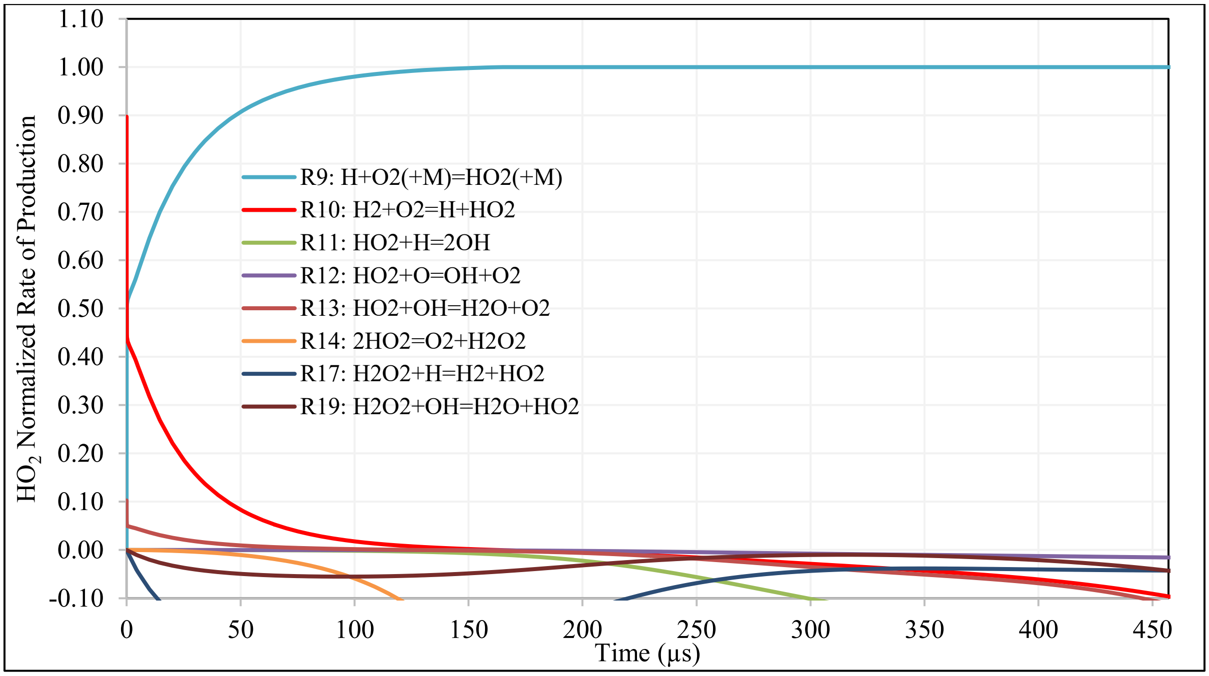

Figure A50: Normalized HO_2 rate of production analysis for Test #33 – 4%H_2/45%H_2O/Ar φ=1 at 1222 K and 40 bar

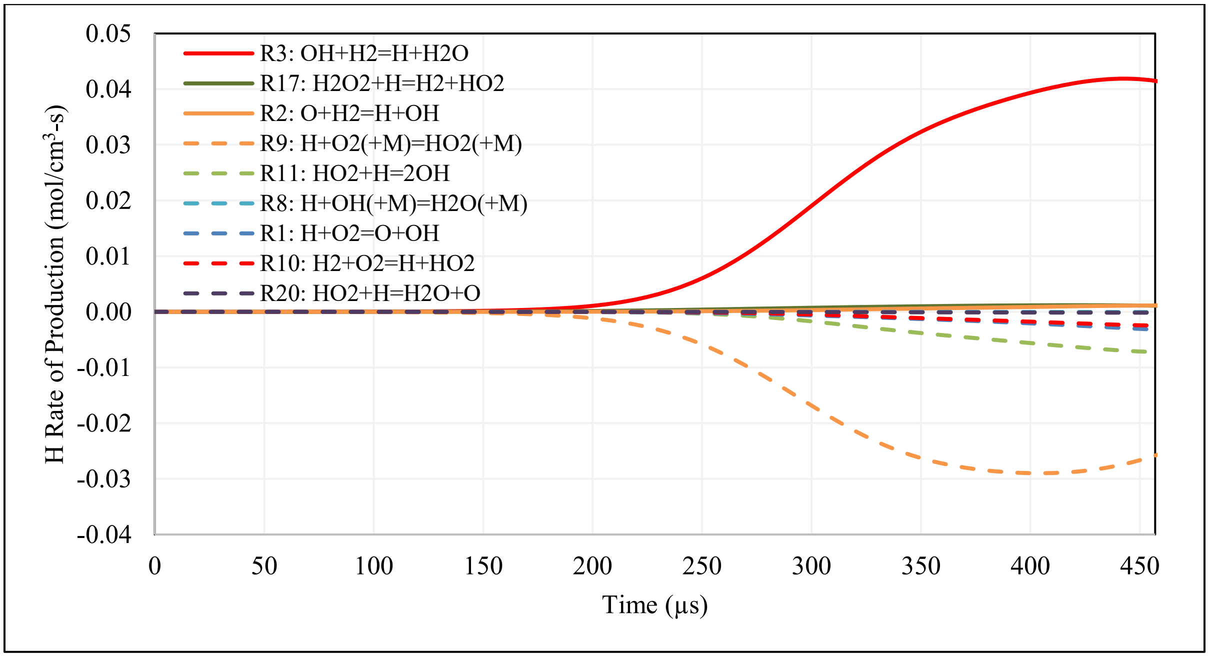

Figure A51: H rate of production analysis for Test #33 – 4%H_2/45%H_2O/Ar φ=1 at 1222 K and 40 bar

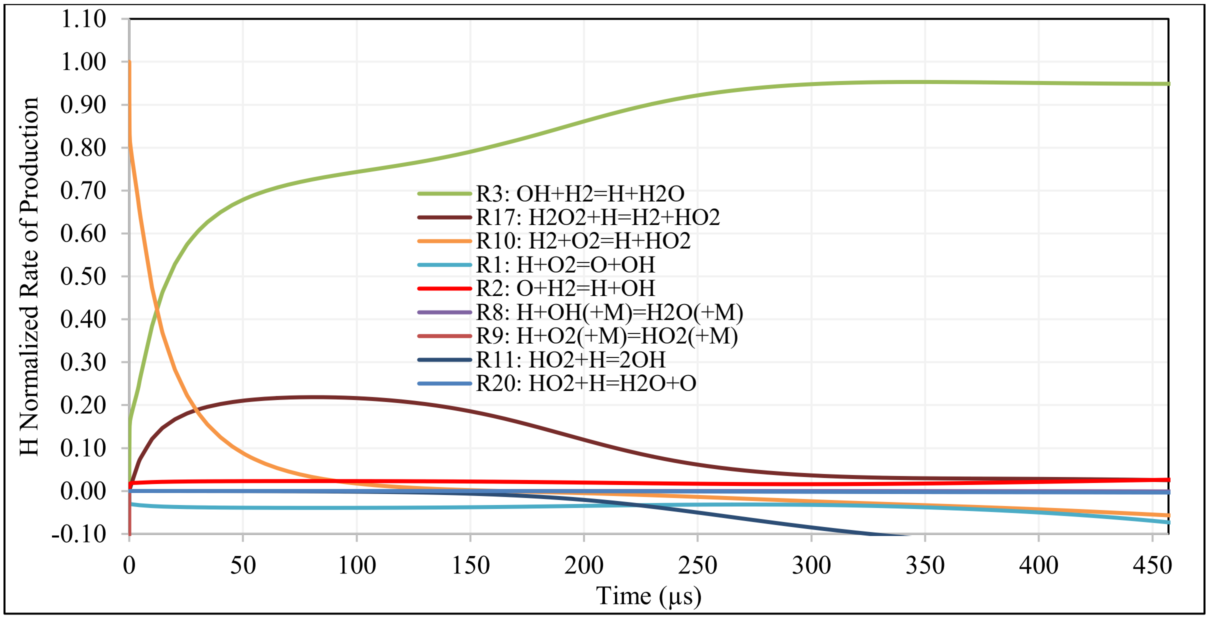

Figure A52: Normalized H rate of production analysis for Test #33 – 4%H_2/45%H_2O/Ar φ=1 at 1222 K and 40 bar

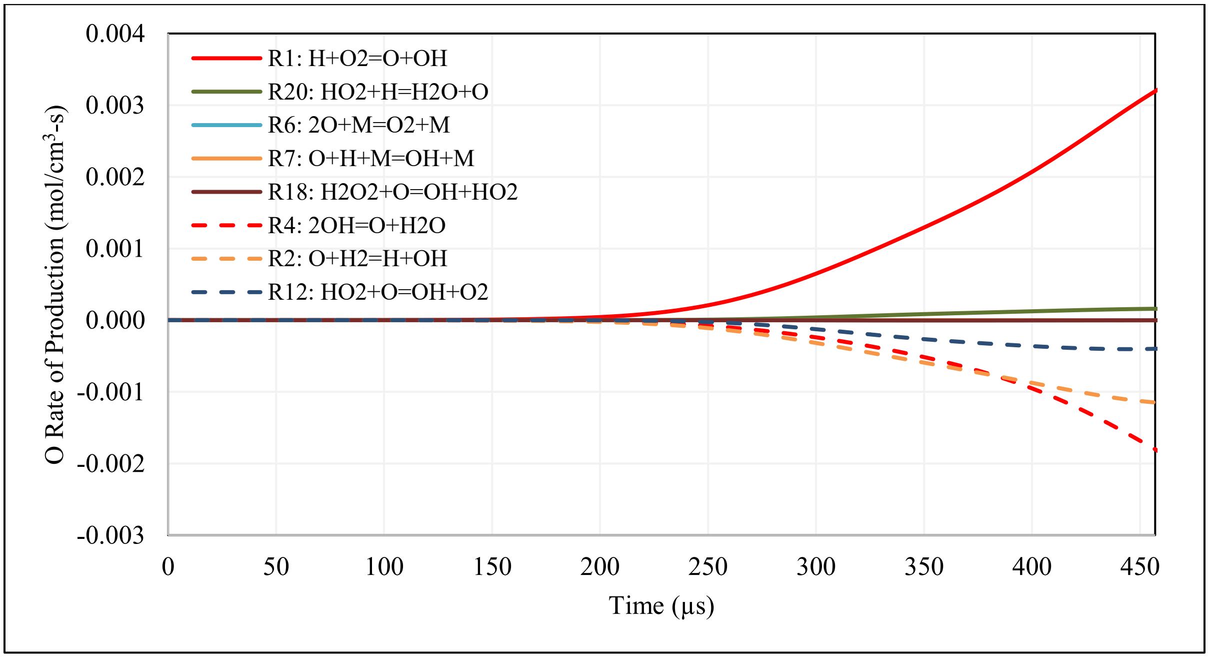

Figure A53: O rate of production analysis for Test #33 – 4%H_2/45%H_2O/Ar φ=1 at 1222 K and 40 bar

ROP analysis for Test #33 – 4%H_2/45%H_2O/Ar φ=1 at 1222 K and 150 bar

Figure A54 and Figure A55 depict the absolute and normalized values of OH ROP for 4%H_2/45%H_2O/Ar φ=1 at 1222 K and 150 bar. These figures illustrate that R15: H_2O_2(+M)=OH+OH(+M) is the main path for OH generation, followed by -R19: H_2O+HO_2=H_2O_2+OH (< 15% contribution) for the first half of the ignition delay period and R11: HO_2+H=OH+OH for the second half (< 15% concribution). The main consumers of OH on the other hand are R3: OH+H_2=H+H_2O and to much lesser extent R13: HO_2+OH=H_2O+O_2.

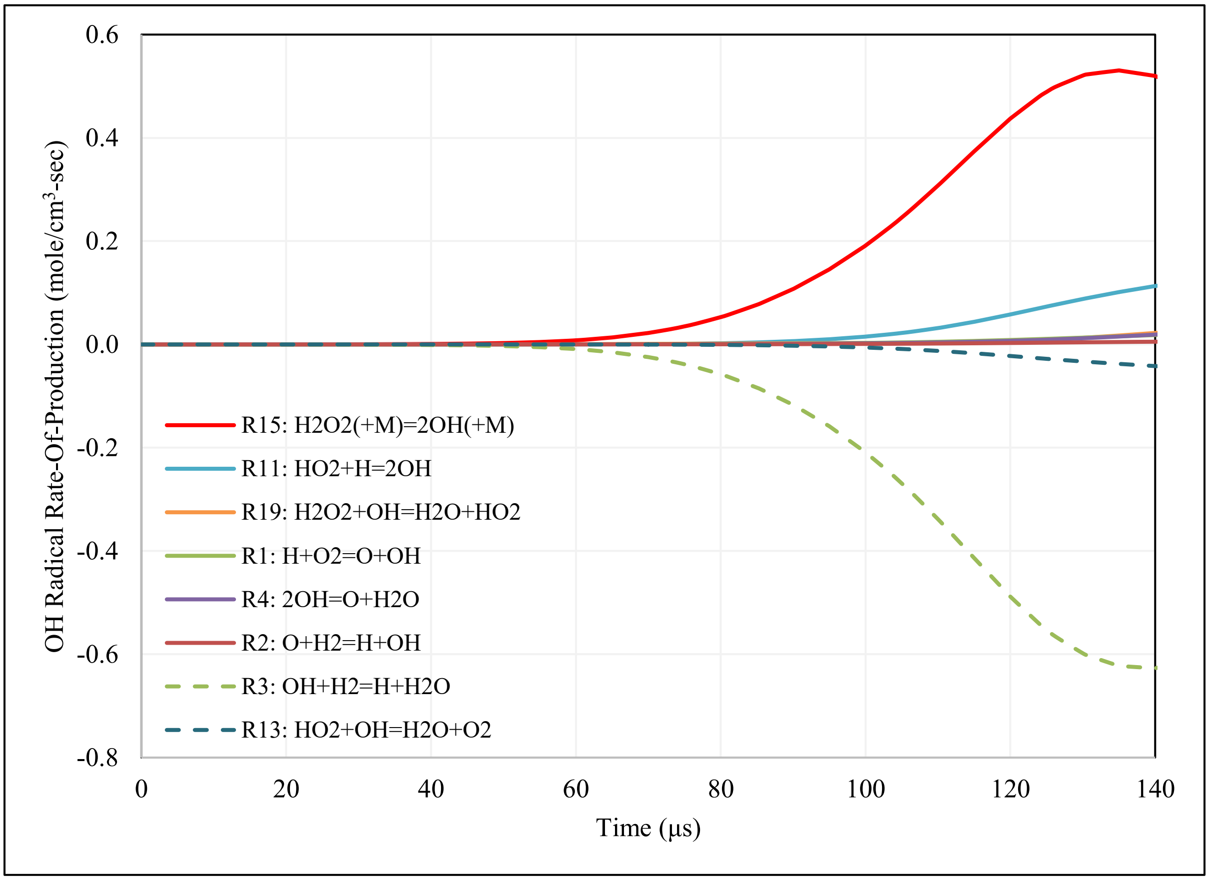

Figure A54: OH rate of production analysis for 4%H_2/45%H_2O/Ar φ=1 at 1222 K and 150 bar

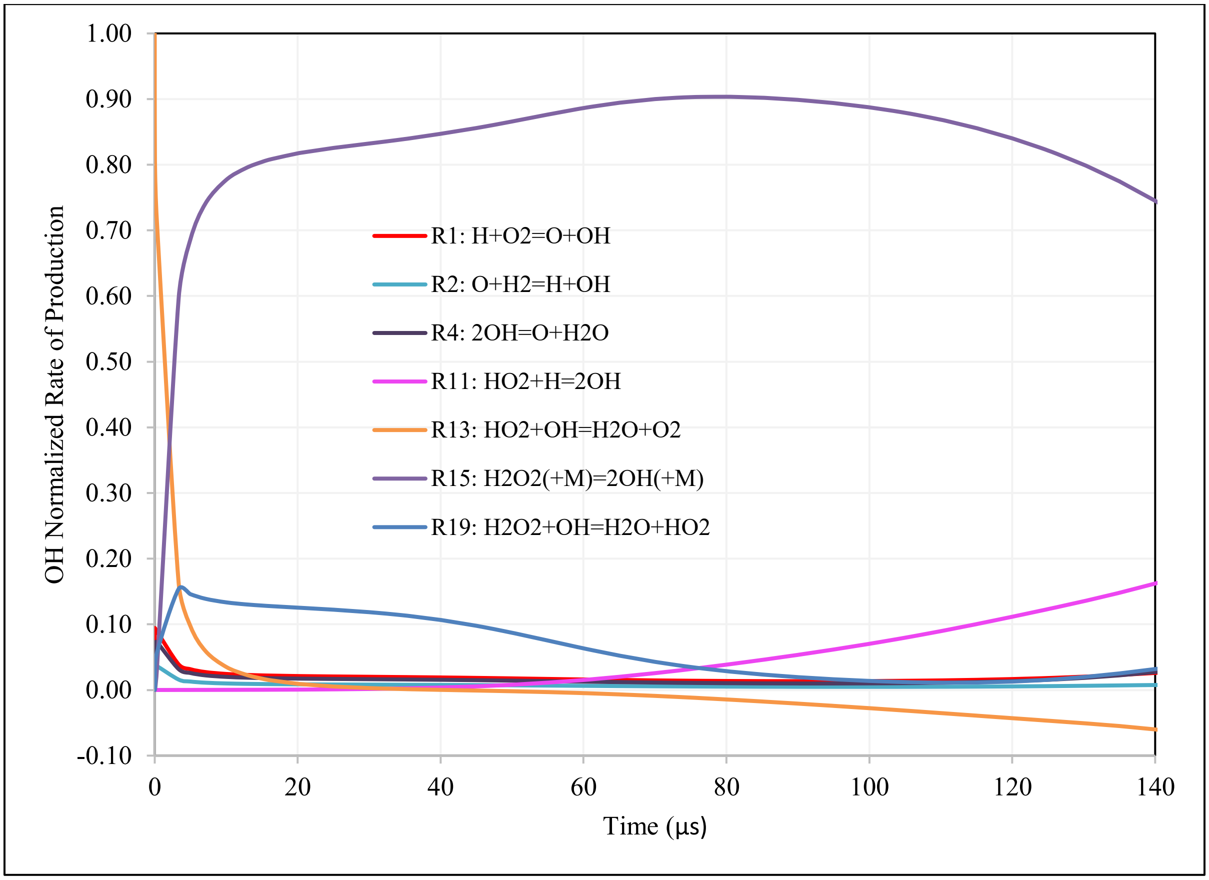

Figure A55: Nomralized OH rate of production for 4%H_2/45%H_2O/Ar φ=1 at 1222 K and 150 bar

Figure A56 and Figure A57 depict H_2O_2 ROP analysis for 4%H_2/45%H_2O/Ar φ=1 at 1222 K and 150 bar. It can be observed that H_2O_2 is produced mainly through -R17: $HO_2+H_2=H_2O_2+H$ for the initial 55 µs, after which it is surpassed by R14: $HO_2+HO_2=H_2O_2+O_2$ until ignition. –R19: $HO_2+H_2O=H_2O_2+OH$ serves as an alternate path producing H_2O_2, which has a peak contribution of ~26%. Note that –R19 simultaneously contributes up to 15% to the OH radical pool, and H_2O_2 is decomposed to two OH through R15. Hence, R19's peak combined contribution to the OH pool has increased to ~40%. It is important to note that the rate of production of H_2O_2 through R14 has increased by 20X at 150 bar, relative to 40 bar. Considering this reaction is bimolecular and pressure has increased by a factor of 3.75, suggests that the rate should have increased by ~14X. The additional increase is attributed to the aformentiond ~20% larger HO_2 concentration (based on comparison of peak values), as it impacts R14 rate twice (1.2x1.2=1.44X), but impacts the ROP of alternate paths -R17 and R19 by ~a factor of 1.2X. Hence, to identify the reaction paths involved, HO_2 and H ROP analyses are conducted.

Figure A58 and Figure A59 depict HO_2 ROP analyses results for 4%H_2/45%H_2O/Ar φ=1 at 1222 K and 150 bar. They show that the main producer of HO_2 is R9. It is also mainly consumed by R14, and to lesser extents by –R17, R11, R13, -R19 and R10.

To identify how HO_2 is produced it is important to investigate reaction paths that produce H. Figure A60 and Figure A61 illustrate the results of H ROP analysis for 4%H_2/45%H_2O/Ar φ=1 at 1222 K and 150 bar. They indicate that H is produced through R3: $OH+H_2=H+H_2O$, followed by –R17: $HO_2+H_2=H_2O_2+H$ (up to 25%).

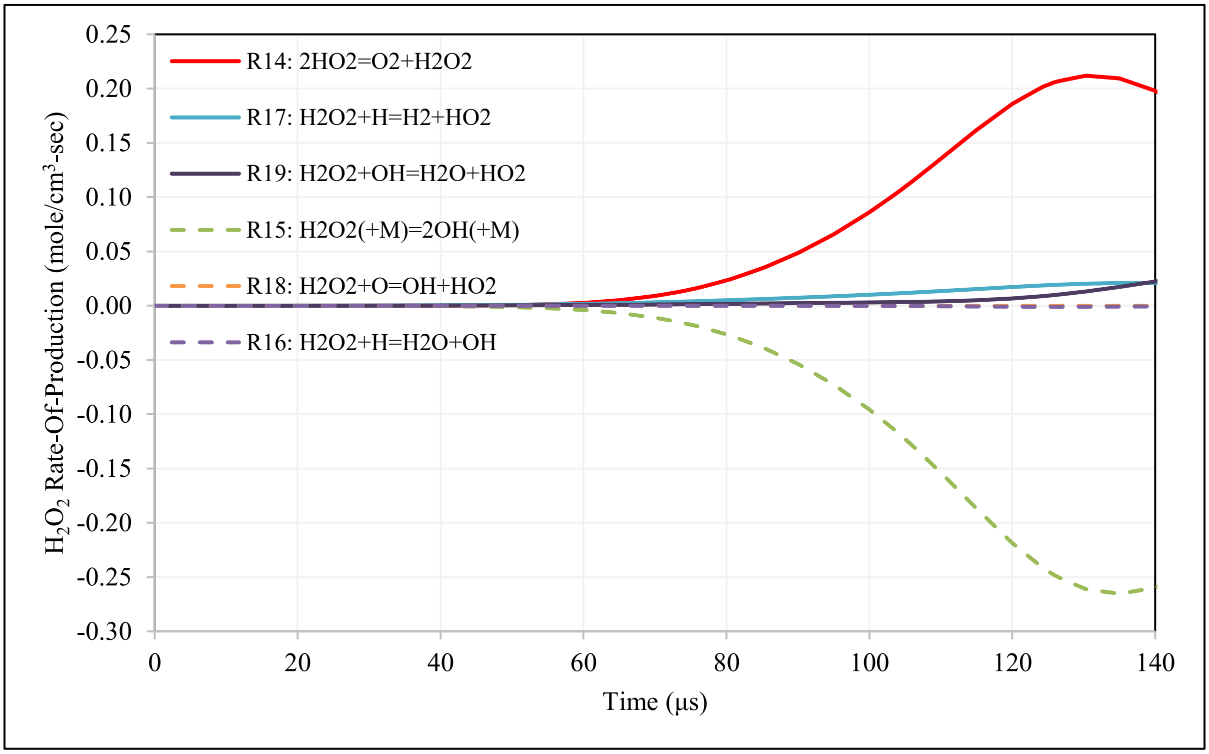

Figure A56: H_2O_2 rate of production analysis for 4%H_2/45%H_2O/Ar φ=1 at 1222 K and 150 bar

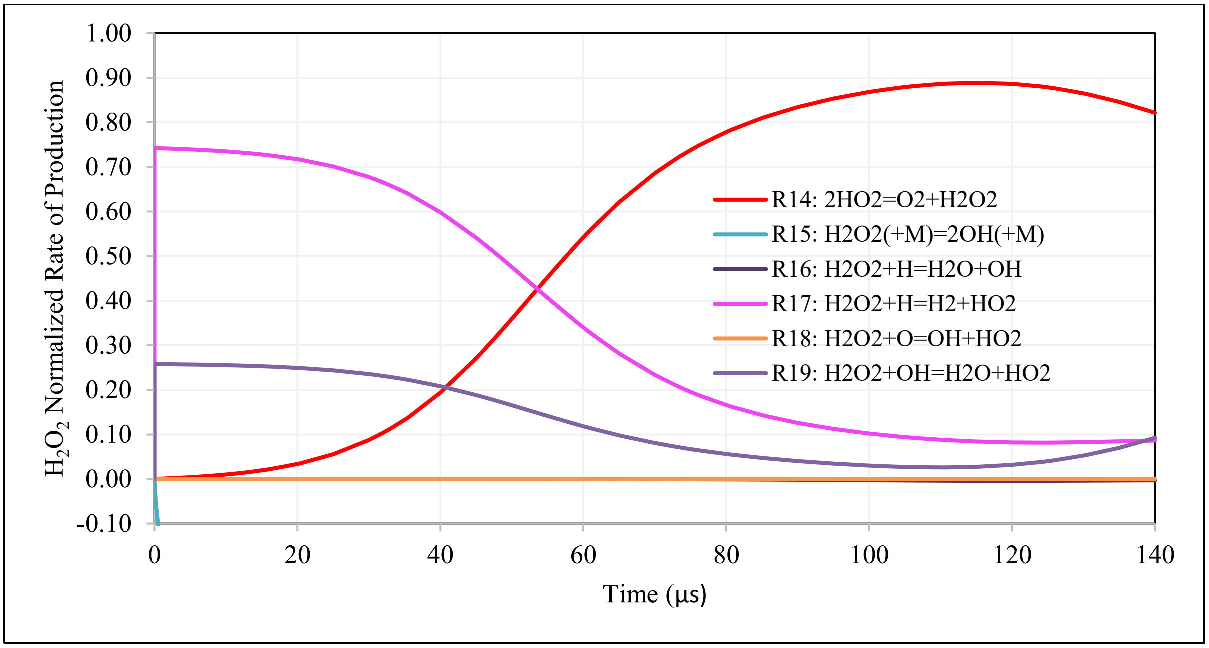

Figure A57: Normalized H_2O_2 rate of production for 4%H_2/45%H_2O/Ar φ=1 at 1222 K and 150 bar

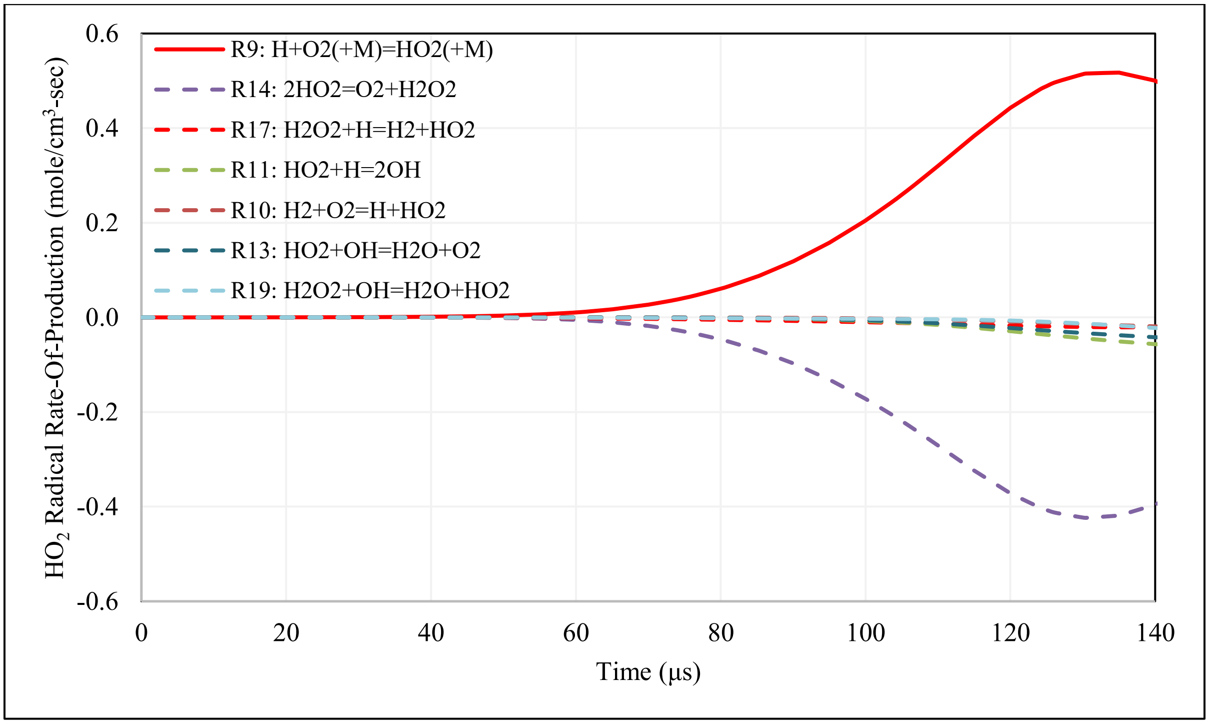

Figure A58: HO_2 rate of production analysis for 4%H_2/45%H_2O/Ar φ=1 at 1222 K and 150 bar

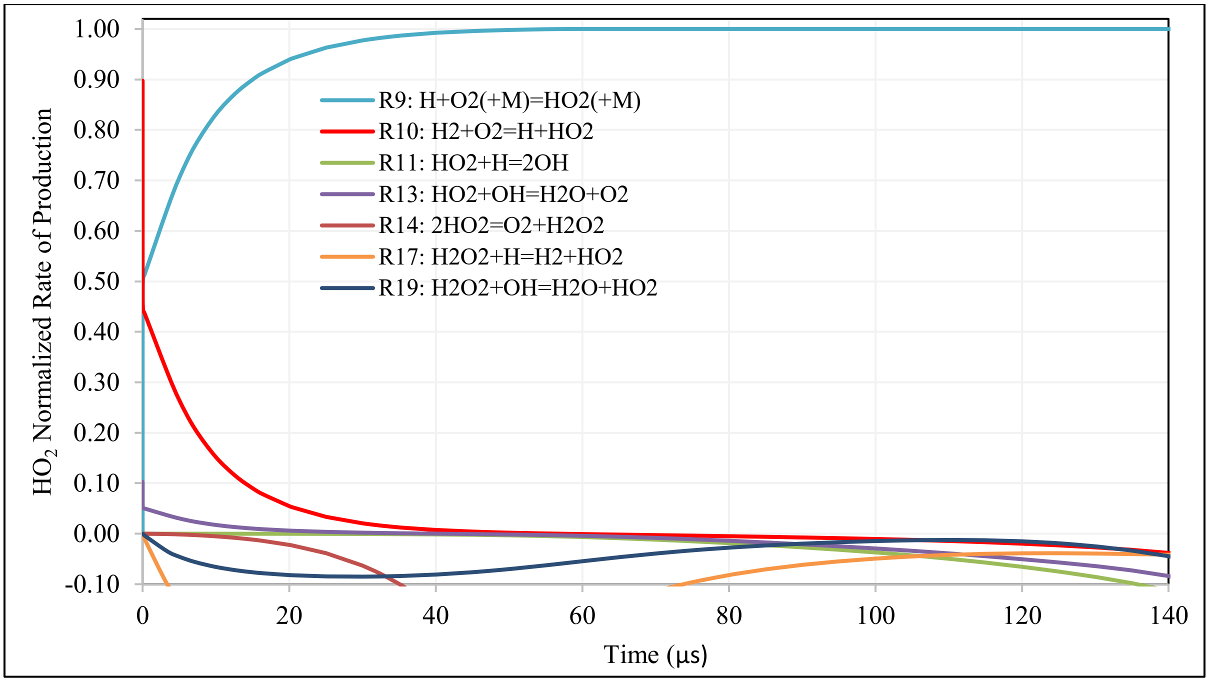

Figure A59: Normalized HO_2 rate of production for 4%H_2/45%H_2O/Ar φ=1 at 1222 K and 150 bar

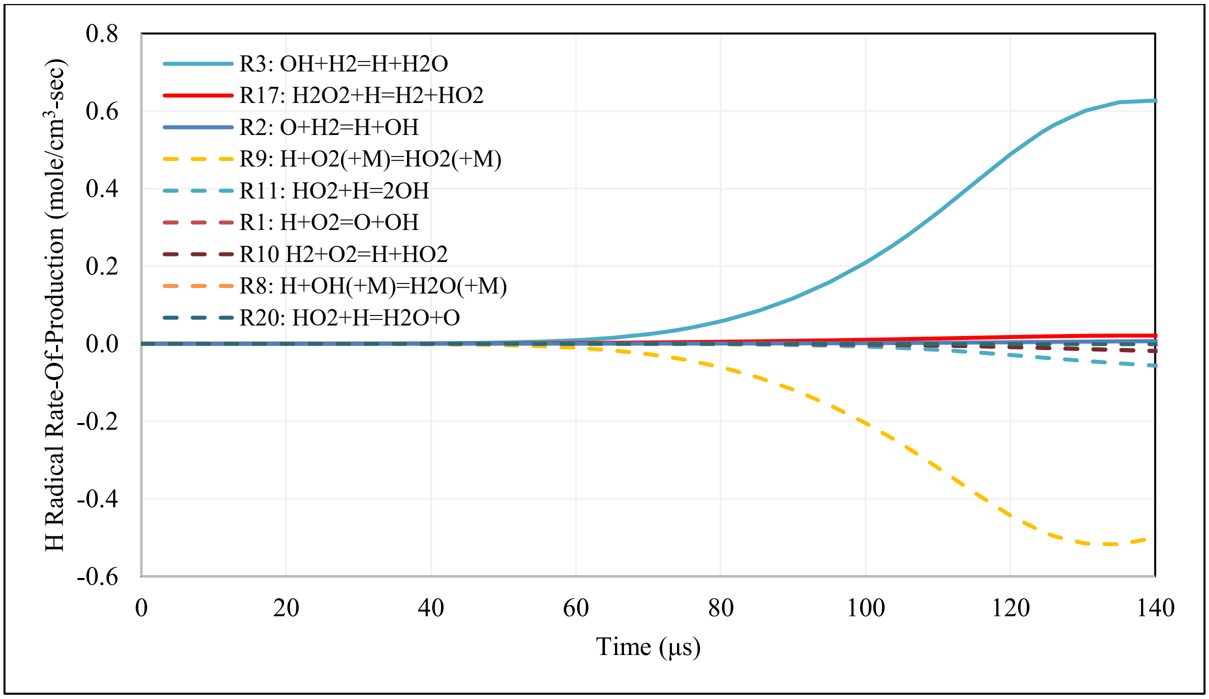

Figure A60: H rate of production analysis for 4%H_2/45%H_2O/Ar φ=1 at 1222 K and 150 bar

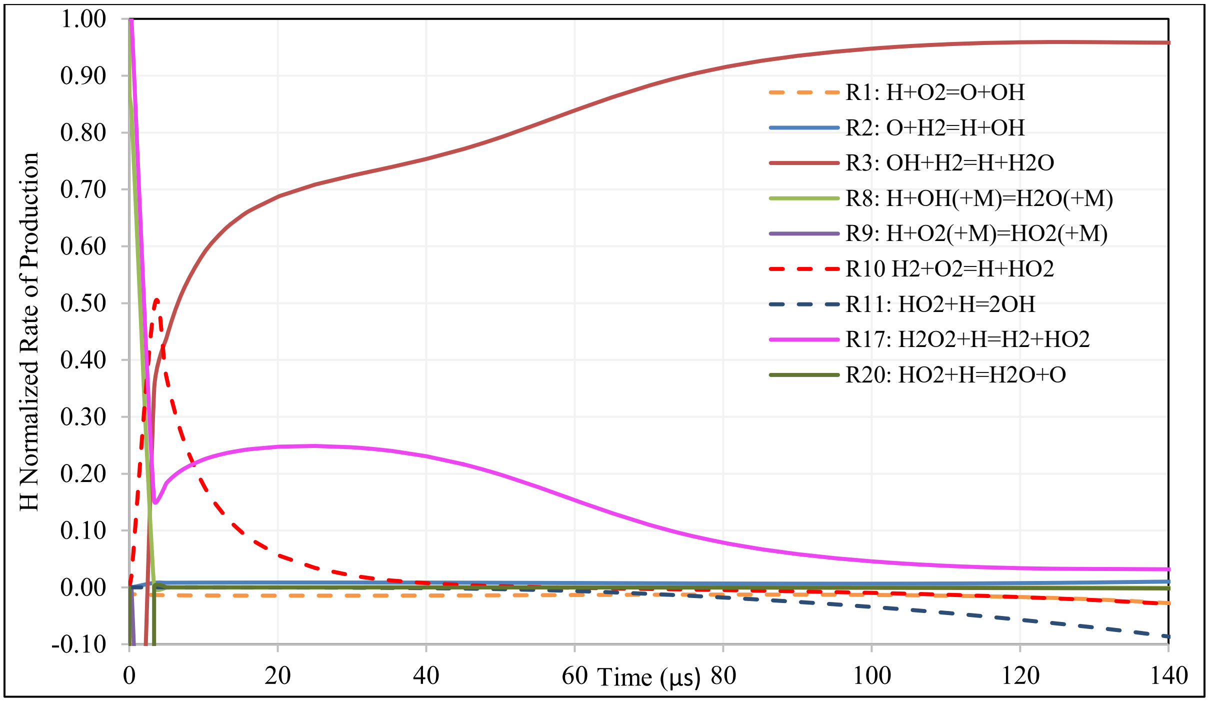

Figure A61: Normalized H rate of production for 4%H_2/45%H_2O/Ar φ=1 at 1222 K and 150 bar

Appendix D: CH₄ Experimental IDT Supplementary Plots

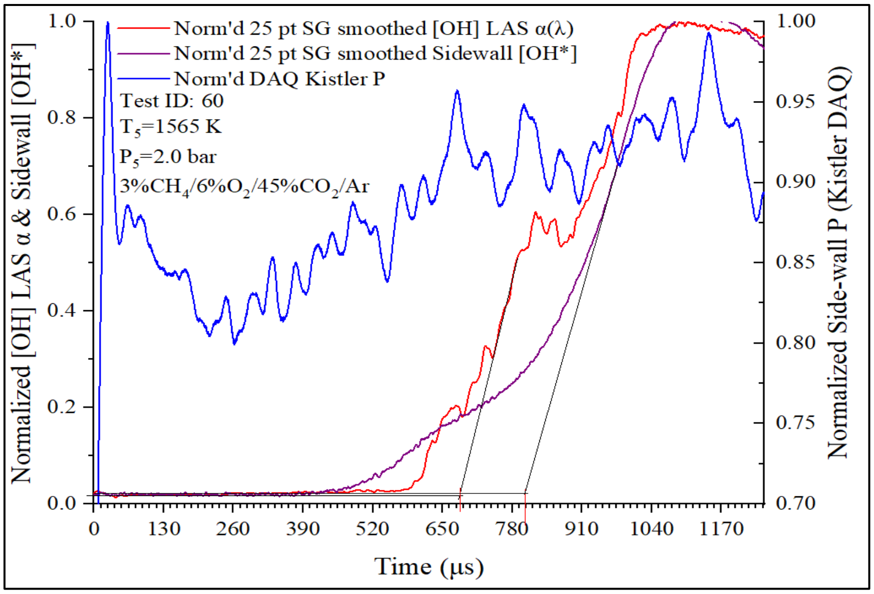

Figure A62: Test 60 side-wall OH* emission, OH LAS absorbance, and side-wall Kistler pressure traces

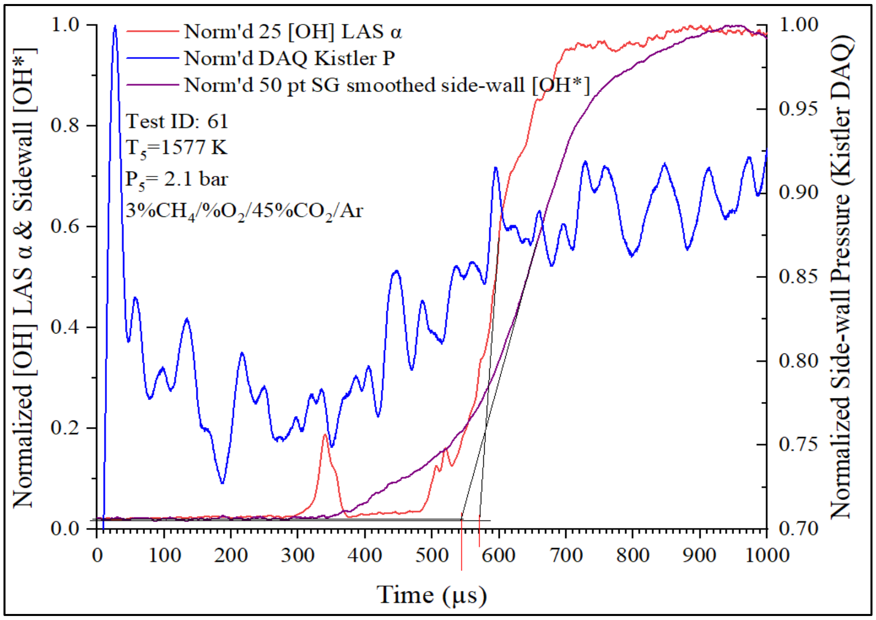

Figure A63: Test 61 side-wall OH* emission, OH LAS absorbance, and side-wall Kistler pressure traces

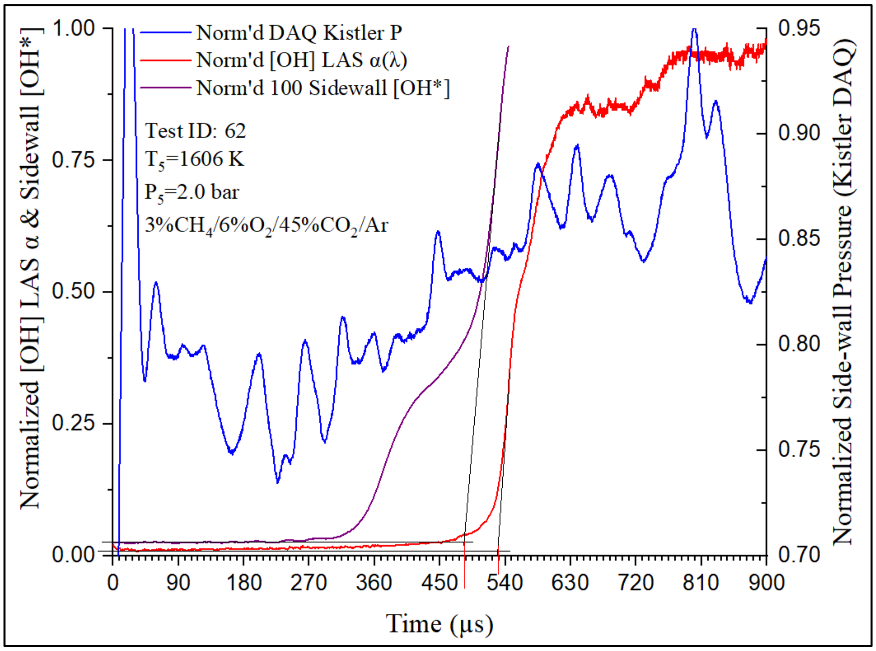

Figure A64: Test 62 side-wall OH* emission, OH LAS absorbance, and side-wall Kistler pressure traces

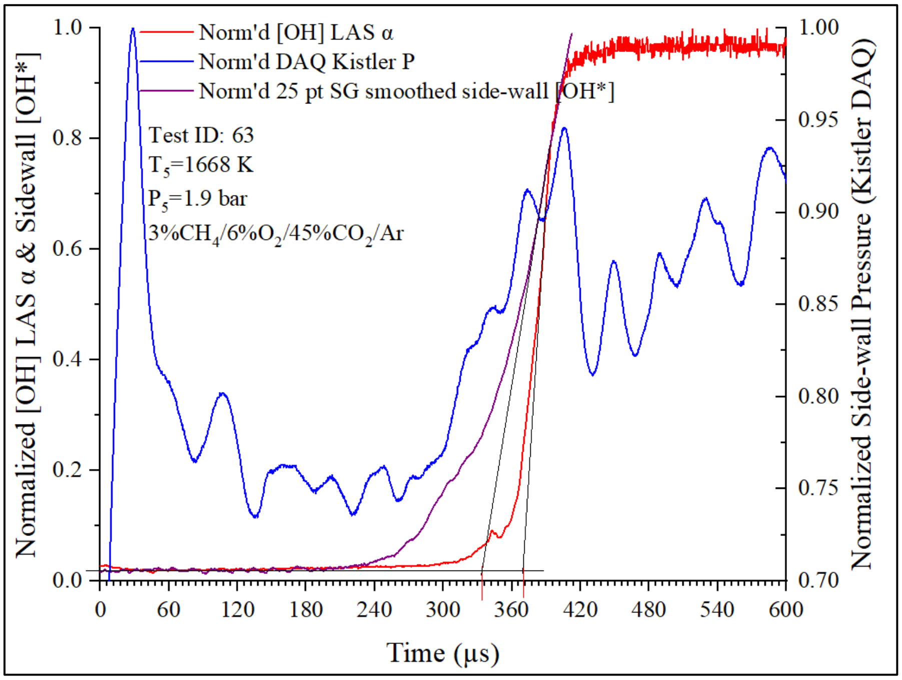

Figure A65: Test 63 side-wall OH* emission, OH LAS absorbance, and side-wall Kistler pressure traces

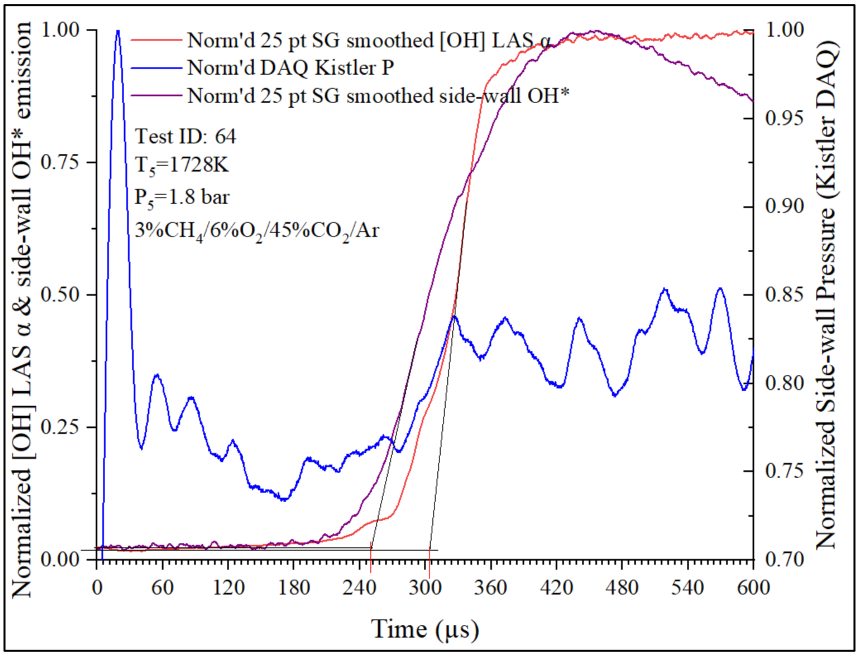

Figure A66: Test 64 side-wall OH* emission, OH LAS absorbance, and side-wall Kistler pressure traces

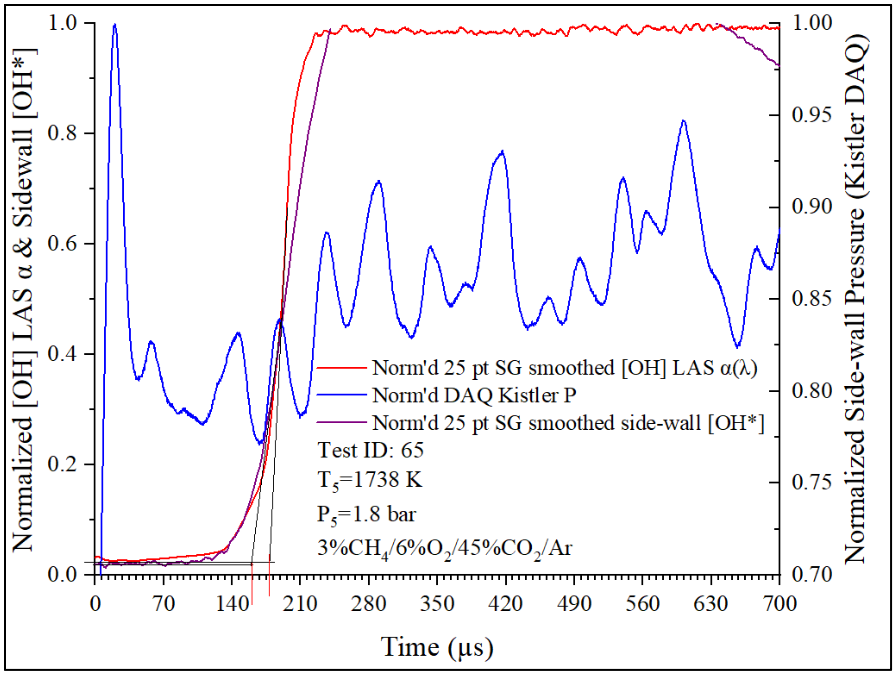

Figure A67: Test 65 side-wall OH* emission, OH LAS absorbance, and side-wall Kistler pressure traces

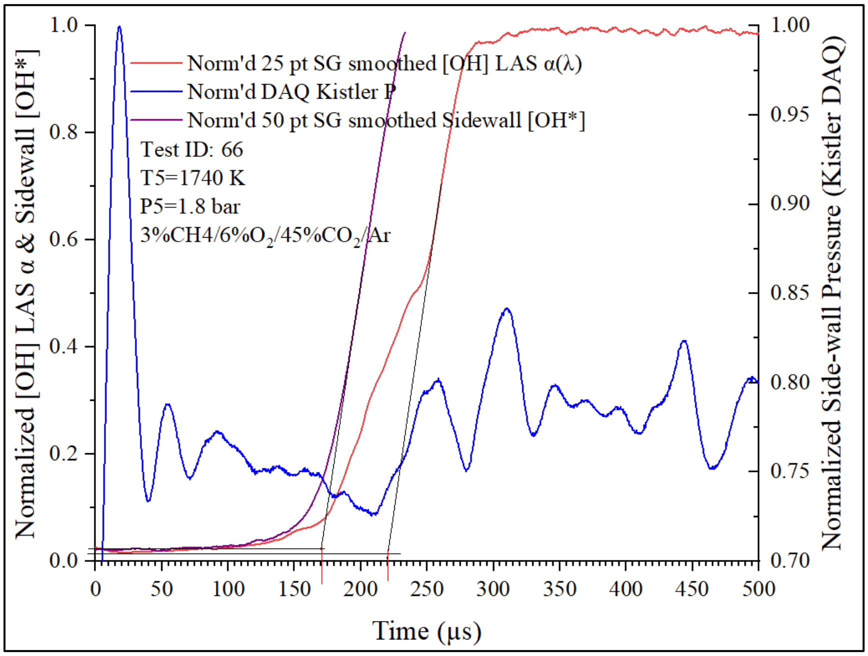

Figure A68: Test 66 side-wall OH* emission, OH LAS absorbance, and side-wall Kistler pressure traces

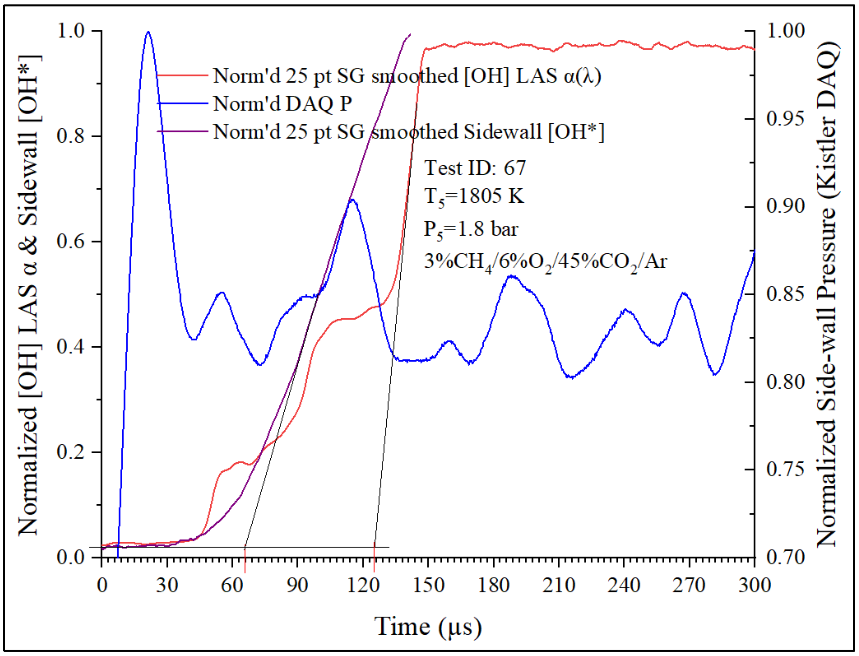

Figure A69: Test 67 side-wall OH* emission, OH LAS absorbance, and side-wall Kistler pressure traces

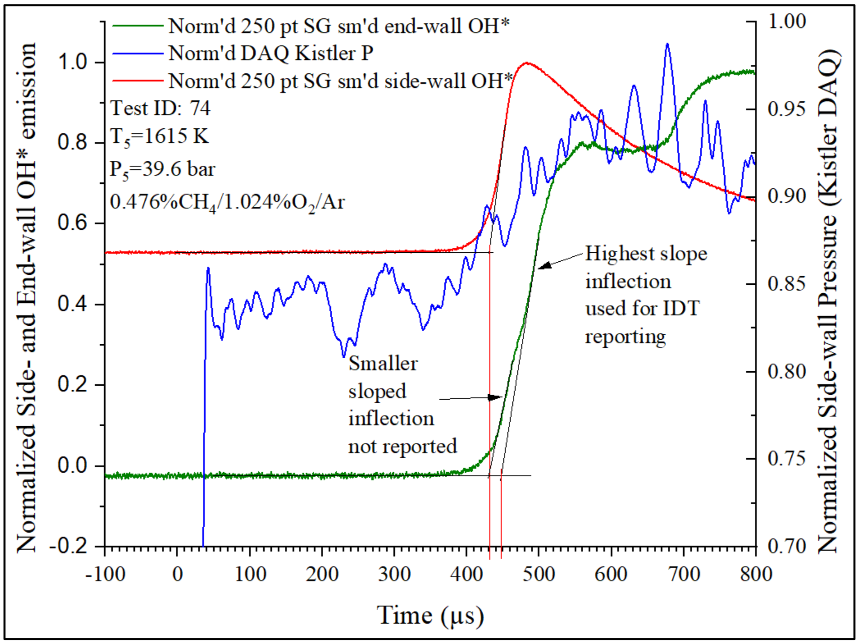

Figure A70: Test 74 normalized side-wall OH*, pressure (Kistler), and end-wall OH* emission traces

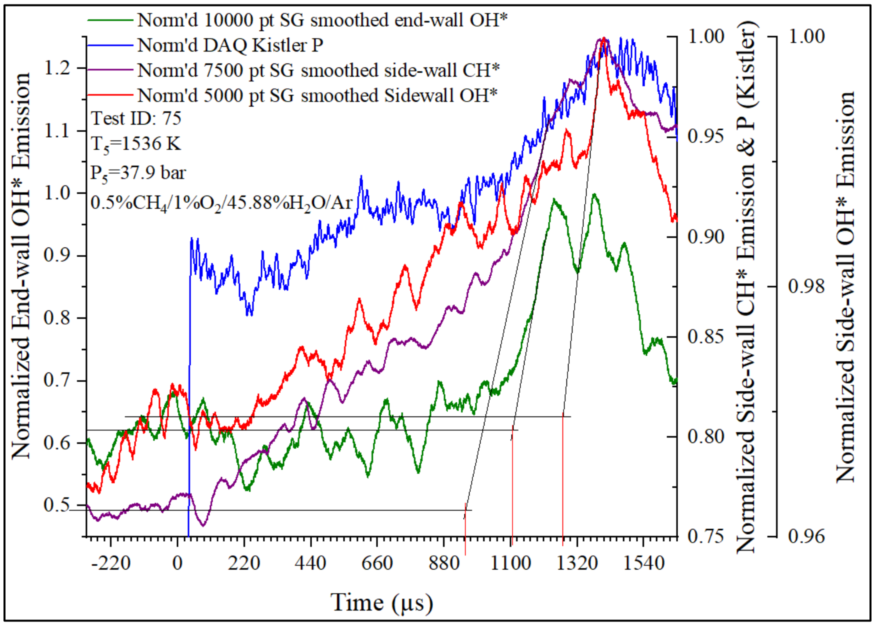

Figure A71: Test 75 normalized side-wall OH*, CH*, pressure (Kistler), and end-wall OH* emission traces

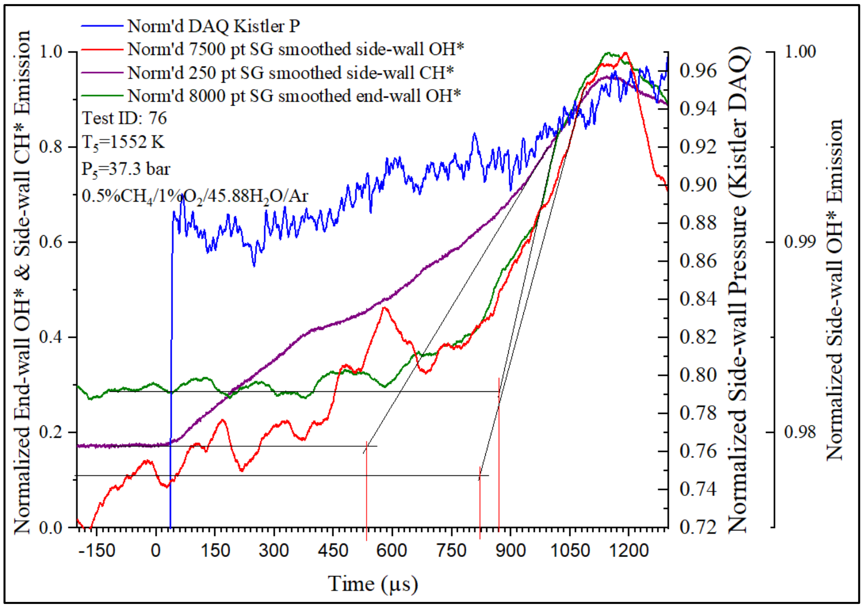

Figure A72: Test 76 normalized side-wall OH*, CH*, pressure (Kistler), and end-wall OH* emission traces

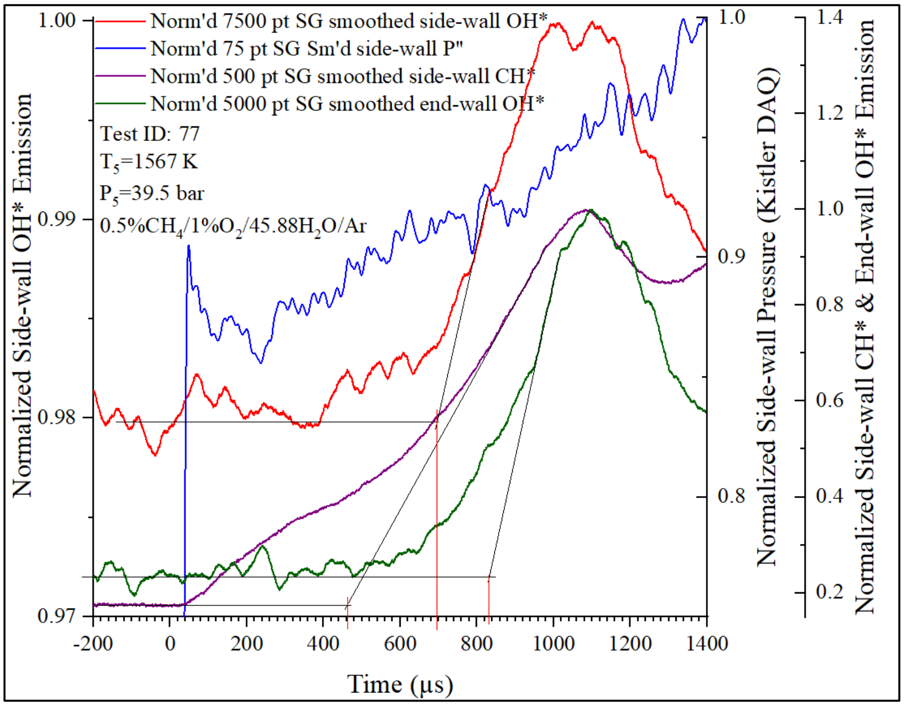

Figure A73: Test 77 normalized side-wall OH*, CH*, pressure (Kistler), and end-wall OH* emission traces

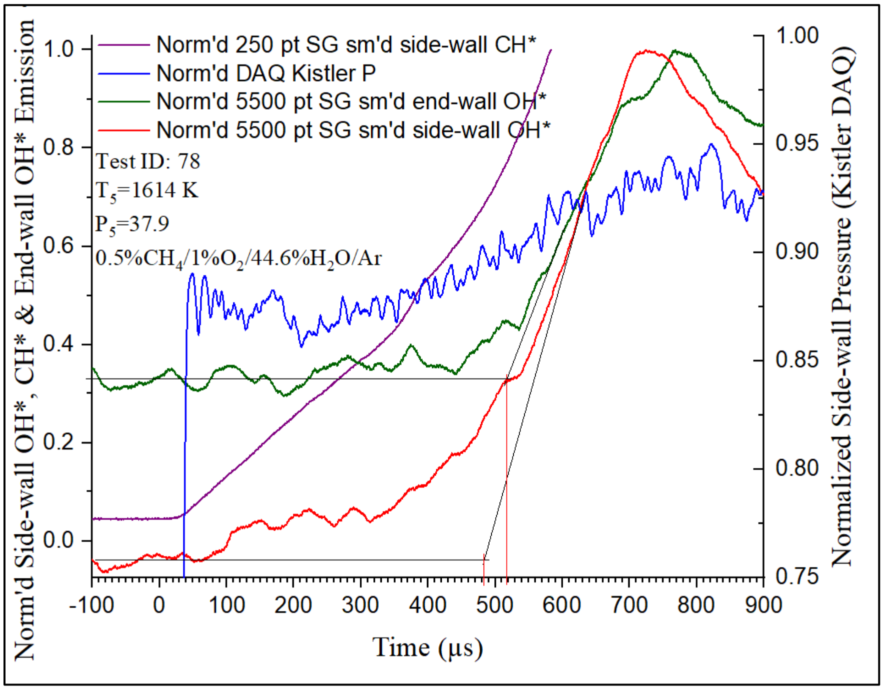

Figure A74: Test 78 normalized side-wall OH*, CH*, pressure (Kistler), and end-wall OH* emission traces

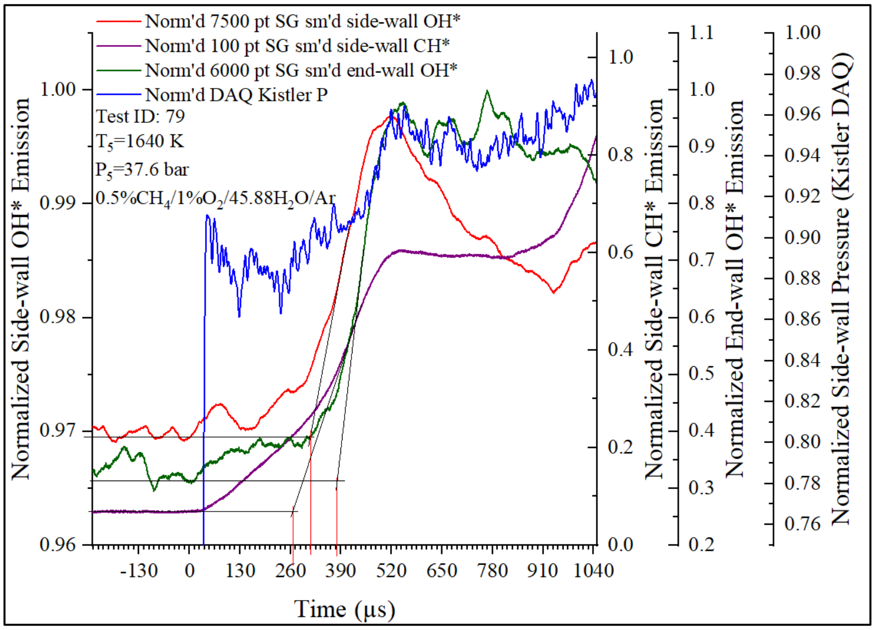

Figure A75: Test 79 normalized side-wall OH*, CH*, pressure (Kistler), and end-wall OH* emission traces

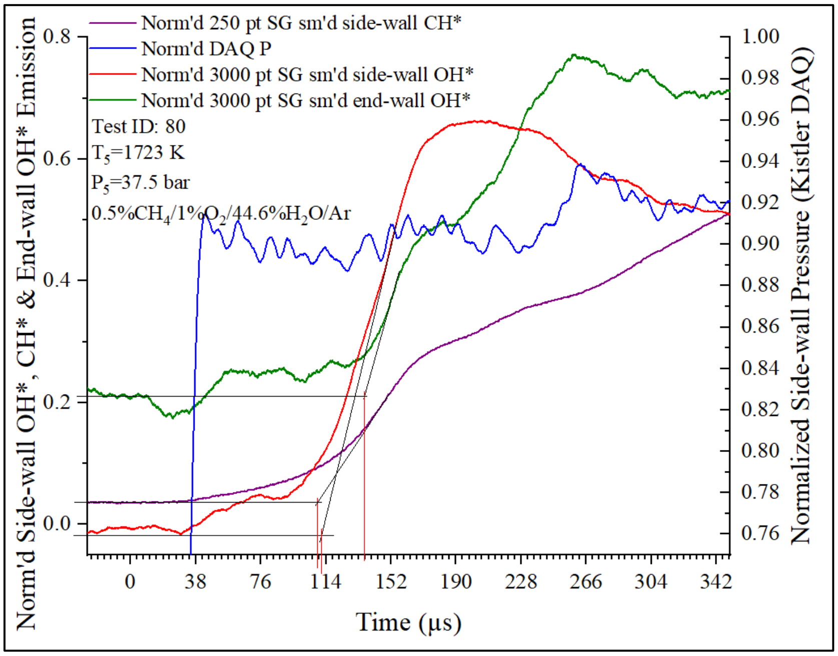

Figure A76: Test 80 normalized side-wall OH*, CH*, pressure (Kistler), and end-wall OH* emission traces

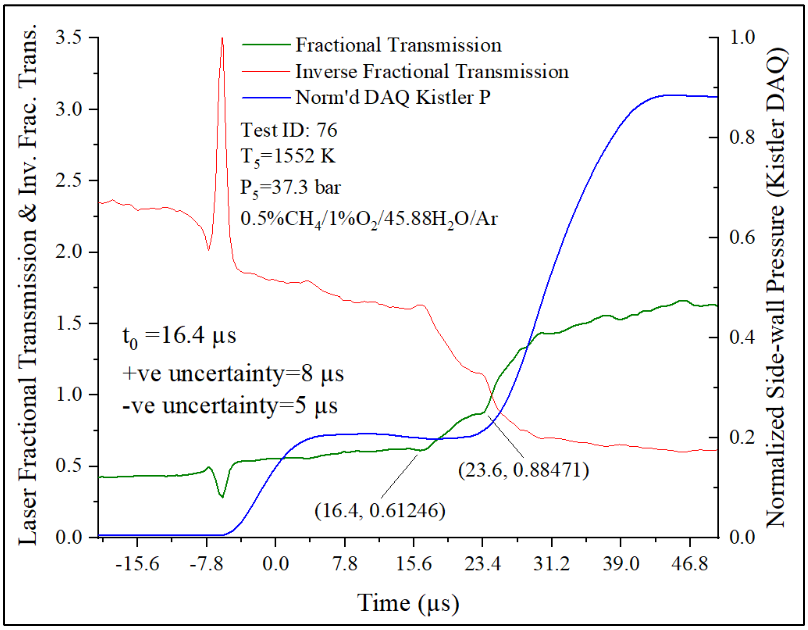

Figure A77: Test 76 Schlieren laser fraction transmission, inverse fractional transmission and side-wall pressure (Kistler) traces

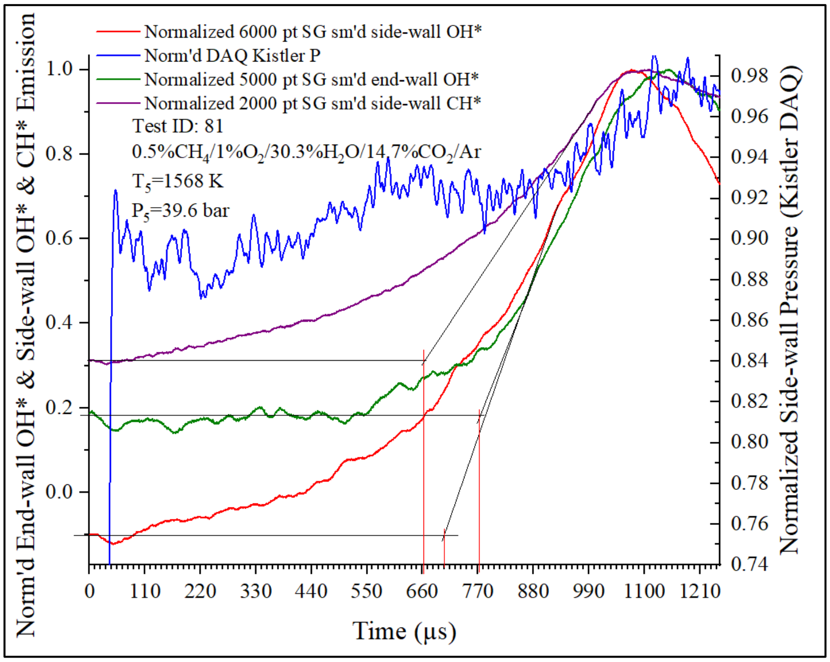

Figure A78: Test 81 normalized side-wall OH*, CH*, pressure (Kistler), and end-wall OH* emission traces

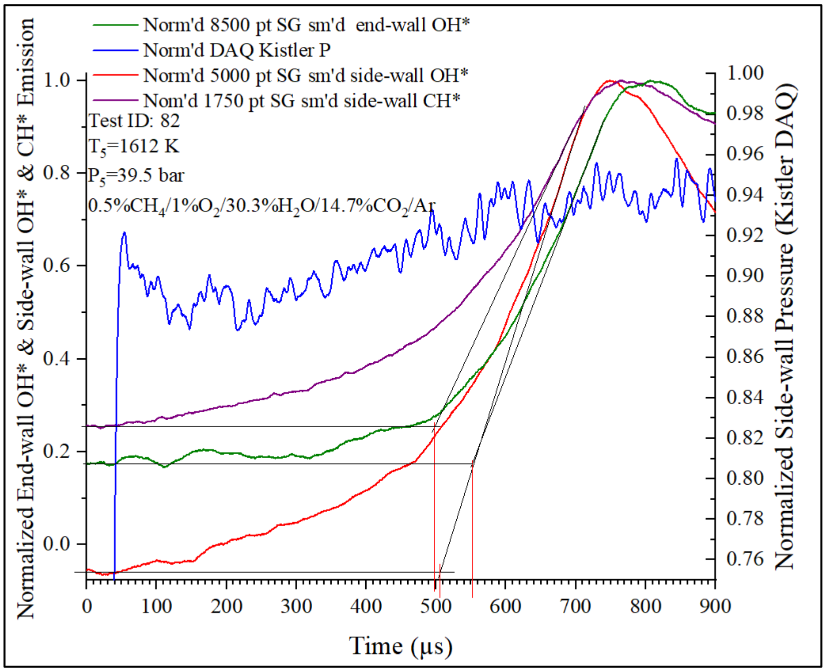

Figure A79: Test 82 normalized side-wall OH*, CH*, pressure (Kistler), and end-wall OH* emission traces

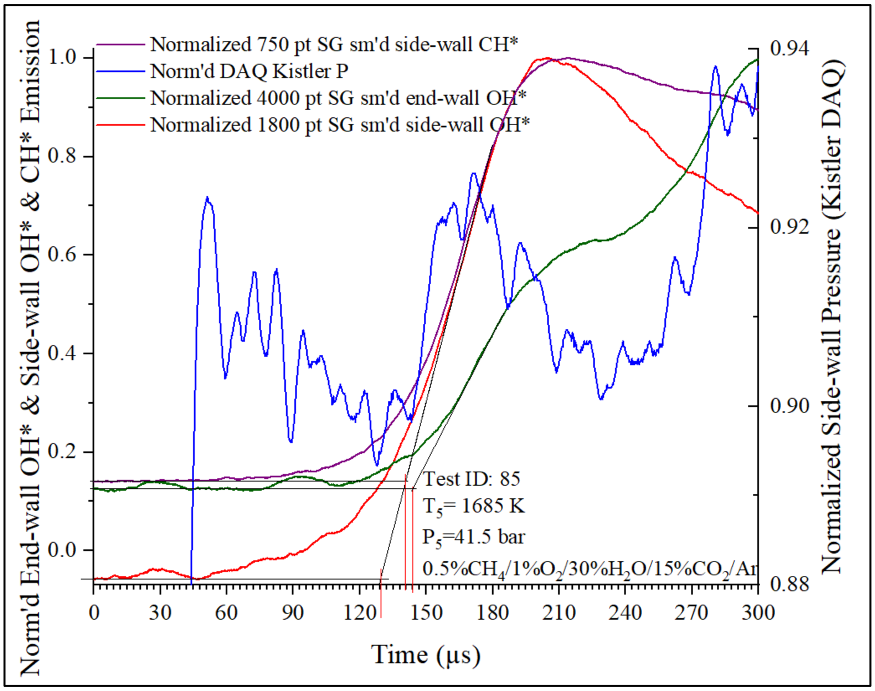

Figure A80: Test 85 Schlieren laser fraction transmission, inverse fractional transmission and side-wall pressure (Kistler) traces

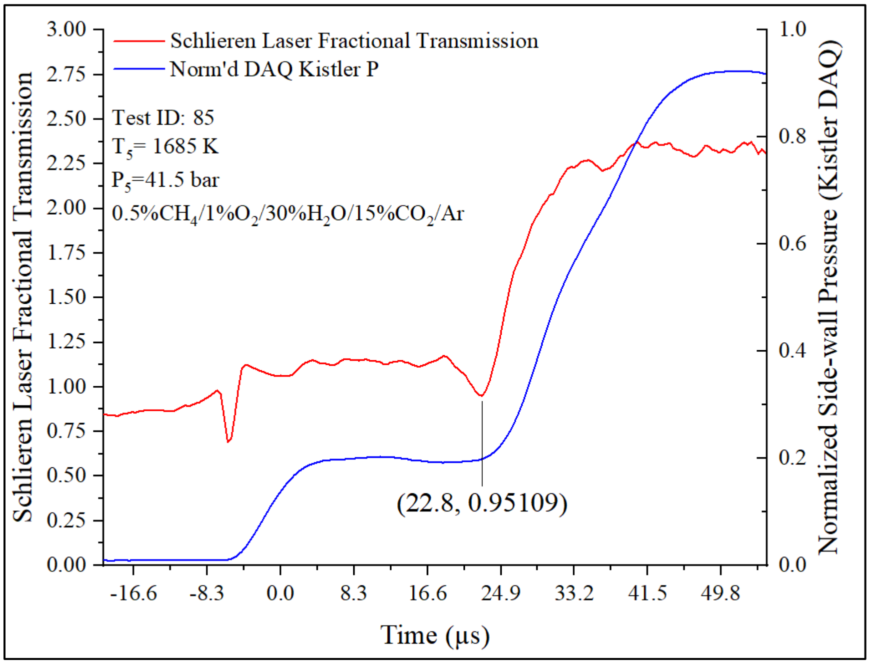

Figure A81: Test 85 Schlieren laser fractional transmission and side-wall pressure (Kistler) traces

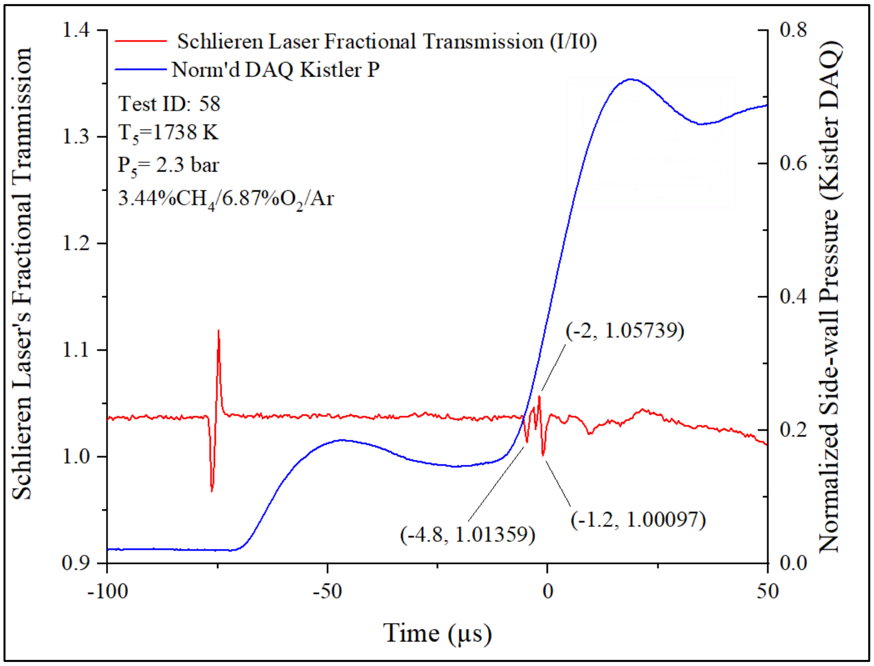

Figure A82: Test 58 Schlieren laser fractional transmission and side-wall pressure (Kistler) traces

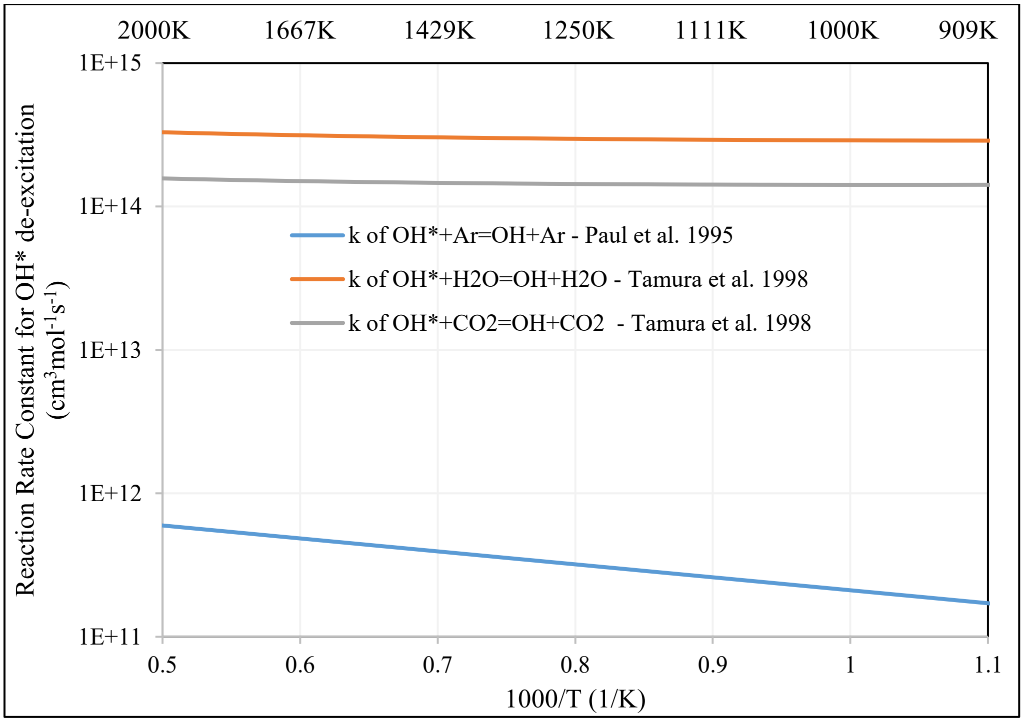

Figure A83: Reaction rate constants of OH*+H_2O=OH+H_2O and OH*+CO_2=OH+CO_2 adopted from Tamura et al., Combust. Flame 114 (1998) 502-514, and OH*+Ar=OH+Ar adopted from Paul et al., J. Chem. Phys. 102 (1995) 8378-8384.